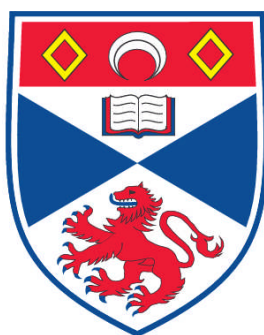


**REVERSIBLE SOLID OXIDE FUEL CELLS AS ENERGY
CONVERSION AND STORAGE DEVICES**

Stephen R. Gamble

**A Thesis Submitted for the Degree of PhD
at the
University of St. Andrews**



2011

**Full metadata for this item is available in
Research@StAndrews:FullText
at:**

<http://research-repository.st-andrews.ac.uk/>

Please use this identifier to cite or link to this item:

<http://hdl.handle.net/10023/2454>

This item is protected by original copyright

**This item is licensed under a
Creative Commons License**

Reversible Solid Oxide Fuel Cells as Energy Conversion and Storage Devices

Stephen Gamble, PhD thesis

3rd November 2011

Dedication and acknowledgments

This work is dedicated to my lovely (and patient) wife, Gillian Gamble, who first met me when I was thinking of starting it, married me during it, and has encouraged me all the way through it.

I would like to give my heartfelt thanks to my supervisor, Prof. John Irvine, for the opportunity to do this work, and also his many helpful suggestions, guidance and discussions, without which this work would not have been possible.

I would also like to especially thank Andy (Jiancong) Ren, a fellow PhD student, who works at the University of Strathclyde, who collaborated extensively with me on the reversible SOFC computer model, for his hard work, and patience with many computer model revisions. It was a pleasure to work with him. I would also like to thank Andrew Roscoe and Graeme Burt at the University of Strathclyde, for their input into the computer modelling work.

I would like to thank some of my colleagues in Prof. John Irvine's research group, who particularly helped me: firstly Paul Connor, for help with software, equations, many practical questions related to building equipment, etc., whose extensive knowledge about many things has greatly benefitted my work. Mark Cassidy and Cristian Savaniu provided their time and expertise to discuss cell fabrication. Dragos Neagu used his knowledge of the Mathematica software to help me, Richard Clarke helped me with integration, and lightened the office mood with many stories. I would also like to thank all the other members of our research group, past and present, for advice and help, deep lunchtime conversations and laughter. I would like to mention Jim Rennie, who helped to design and build to exacting standards, a piece of equipment for me, and Julie Nairn who helped me with many lab-related matters. In the mechanical workshop, George Anthony and Bobby Cathcart made pieces of equipment for me.

I would also like to thank my friend, William Simpson, who helped me to better understand integration, and for good times with him and all my friends. I would like to thank my mother, father and sister for their moral support. Finally, I would like to acknowledge my PhD funders - the EPSRC and the Carbon Trust.

"I think it's tragic that scientific advances have caused many people to imagine that they know it all, and that God is irrelevant or nonexistent. The fact is that everything we learn reveals more things that we do not understand." —Donald E. Knuth (on Proverbs 3:16)

Declarations

1. Candidate's declarations:

I, Stephen Gamble, hereby certify that this thesis, which is approximately 80,000 words in length, has been written by me, that it is the record of work carried out by me and that it has not been submitted in any previous application for a higher degree. I was admitted as a research student in October, 2007 and as a candidate for the degree of PhD in October, 2008; the higher study for which this is a record was carried out in the University of St Andrews between 2007 and 2011.

Date signature of candidate

2. Supervisor's declaration:

I hereby certify that the candidate has fulfilled the conditions of the Resolution and Regulations appropriate for the degree of PhD in the University of St Andrews and that the candidate is qualified to submit this thesis in application for that degree.

Datesignature of supervisor

3. Permission for electronic publication:

In submitting this thesis to the University of St Andrews I understand that I am giving permission for it to be made available for use in accordance with the regulations of the University Library for the time being in force, subject to any copyright vested in the work not being affected thereby. I also understand that the title and the abstract will be published, and that a copy of the work may be made and supplied to any bona fide library or research worker, that my thesis will be electronically accessible for personal or research use unless exempt by award of an embargo as requested below, and that the library has the right to migrate my thesis into new electronic forms as required to ensure continued access to the thesis. I have obtained any third-party copyright permissions that may be required in order to allow such access and migration, or have requested the appropriate embargo below.

The following is an agreed request by candidate and supervisor regarding the electronic publication of this thesis:

(i) Access to printed copy and electronic publication of thesis through the University of St Andrews.

Date signature of candidate

signature of supervisor

Abstract

A reversible solid oxide fuel cell (RSOFC) system could buffer intermittent electrical generation, e.g. wind, wave power by storing electrical energy as hydrogen and heat. RSOFC were fabricated by thermoplastic extrusion of $(\text{La}_{0.8}\text{Sr}_{0.2})_{0.95}\text{MnO}_{3-\delta}$ (LSM) ceramic support tubes, which were microstructurally stable with 55% porosity at 1350 °C. A composite oxygen electrode of LSM-YSZ was applied, providing a homogeneous substrate for a 20 μm - 30 μm thick YSZ electrolyte. A dip-coated 8YSZ slurry, and a painted commercial 3YSZ ink gave sintered densities of 90% and nearly 100% at 1350 °C, respectively. A porous NiO/YSZ fuel electrode was also painted on. A Ag/Cu reactive air braze was unsuccessful at forming a void-free joint between the RSOFC and a 316 stainless steel gas delivery tube, as the braze did not penetrate the oxidation layer on the steel. Two alumina-based ceramic cements failed to fully seal the cell to an alumina gas delivery tube, due to thermal expansion coefficient mismatches and porosity after curing. Therefore, the maximum open circuit voltage (OCV) obtained during RSOFC testing was 0.8 V at 440 °C. LSM-YSZ symmetrical cell performance measurements with oxygen pressure showed a diffusion polarisation, which was assigned to dissociative adsorption and surface diffusion of oxygen species. A collaborative RSOFC system software model showed ohmic and activation losses dominated the RSOFC, and diffusion losses were insignificant. Pressurisation from 1 to 70 bar increased the RSOFC Nernst voltage by 11% at 900 °C, and reduced the entropy of the gases, reducing heat production and increasing electrical efficiency. A 500 kg Sn/Cu phase change heat store prevented the system overheating. Over a 16 h discharge-charge RSOFC cycle in the range 5 mol.% - 95 mol.% hydrogen in steam, at 20.4 A per cell or 3250 A m⁻², the electrical energy storage efficiency was 64.4%.

Contents

Declarations	3
Abstract	4
Contents	5
List of Figures	11
List of Tables	19
Nomenclature	21
1 Introduction and context	27
1.1 Energy conversion and storage	27
1.1.1 Energy: The cause of, and solution to, many of the world's problems	27
1.1.2 Energy storage: UK context	28
1.1.3 Energy storage methods	29
1.2 Fuel cells, electrolyzers and reversible fuel cells	31
1.2.1 Fuel cell types and principles of operation	31
1.2.2 Energy storage by a reversible solid oxide fuel cell system	33
1.3 Reversible SOFC geometry and fabrication	34
1.3.1 Cell geometry	34
1.3.2 Cell materials	35
1.3.3 Cell microstructure	37
1.3.4 Fabrication methods	39
1.3.5 Proposed reversible SOFC design	44
1.4 Reversible SOFC microstructural characterisation	45
1.5 Reversible SOFC performance	47
1.5.1 Symmetrical cell testing	47
1.5.2 Whole cell testing	49
1.5.3 Reported reversible SOFC performance	50
1.6 Modelling of reversible SOFC systems	52
1.7 Thesis and objectives	53
References	55

2	Experimental and methodology	63
2.1	Fabrication methods	63
2.1.1	YSZ electrolyte pellet manufacture	63
2.1.2	Tape casting	64
2.1.3	Screen printing	65
2.1.4	Extrusion	66
2.1.5	Dip coating	72
2.1.6	Hand painting of reversible cell layers	75
2.1.7	Sealing reversible SOFC	76
2.1.8	Leak testing reversible SOFC	77
2.1.9	Current collection and short circuit testing for the reversible SOFC	79
2.1.10	Brazing	81
2.2	Characterisation methods	84
2.2.1	Optical microscopy	84
2.2.2	Scanning electron microscopy (SEM)	84
2.2.3	Energy dispersive X-Ray spectroscopy (EDX)	85
2.2.4	Thermal gravimetric analysis	86
2.2.5	Particle size distribution analysis	86
2.3	Testing symmetrical half cells	87
2.3.1	AC impedance on tape cast cells at ambient pressure	87
2.3.2	Impedance spectroscopy on pellet symmetrical cells at high pressure	88
2.4	Testing of RSOFC	90
2.4.1	Test setup	90
2.4.2	Testing procedure	92
2.5	Modelling a reversible SOFC system	93
2.5.1	Data collection and analysis for semi-empirical equations	93
2.5.2	Assembling the software model and obtaining results	99
2.6	Conclusions	99
	References	101
3	Oxygen electrode testing with symmetrical cells	103
3.1	Tape-cast symmetrical cells	103
3.1.1	Introduction	103
3.1.2	Impedance spectroscopy results	104
3.1.3	Thermal ageing of symmetrical cells	106
3.2	Pellet symmetrical cells	110
3.2.1	Introduction	110
3.2.2	Symmetrical cell testing	111
3.2.3	Impedance spectroscopy results	112
3.2.4	Assignment of arcs in impedance spectra	115
3.3	Conclusions	120

References	121
4 Extrusion	123
4.1 Extrusion with handheld ram extruder	123
4.1.1 Comparison of two solvents for the extrusion mix	123
4.1.2 Extrusion die ratios (length: diameter) and surface fracture	124
4.1.3 Understanding water absorption of cellulose	127
4.1.4 Pinholes in extruded tubes - air bubbles	130
4.2 Extrusion with mechanised screw extruder	131
4.2.1 Water and cellulose based extrusion	131
4.2.2 Thermoplastic extrusion: cellulose pore former	132
4.2.3 Thermoplastic tube extrusion: graphite pore former	136
4.2.4 Porosity analysis of tubes with ImageJ software	139
4.2.5 Conclusions	142
References	145
5 Brazing	147
5.1 Introduction	147
5.1.1 A brazed joint as a seal and interconnect	147
5.2 Silver-copper brazes	147
5.2.1 Initial trial of copper-silver braze	147
5.2.2 Silver-copper braze (40 mol.% Cu)	148
5.2.3 Variation of the braze silver-copper ratio	149
5.3 Braze-LSM composites	154
5.3.1 Introduction	154
5.3.2 Comparison of copper and steel substrates	155
5.3.3 Braze interlayers	157
5.3.4 Titanium coated stainless steel substrates	159
5.4 Conclusions	164
References	167
6 Reversible SOFC preparation	169
6.1 Painting LSM-YSZ oxygen electrode	169
6.2 Producing the 8YSZ electrolyte	170
6.2.1 Dip coating 8YSZ slurries Y-7.4A and Y-3.4B	172
6.2.2 Dip-coating 8YSZ slurries Y-3.4C, Y-5.2D and Y-7.3D	175
6.2.3 Dip-coating 8YSZ slurries Y-7.4A2 and Y-3.4B2	176
6.2.4 Dip coating 8YSZ slurry Y-3.4B2	180
6.2.5 Dip-coating 8YSZ slurries Y-3.4F and Y-7.3G	184
6.2.6 Dip-coating 3YSZ slurries H, Y-10.0I, Y-7.5J, and Y-4.9K.	192
6.2.7 Dip coating 8YSZ slurries Y-7.3G and Y-7.3G2 on recipe M-gra10 LSM tubes	194

6.2.8	Dip coating 8YSZ slurry Y-7.3L and Y-7.4L2.	194
6.2.9	Painting with 8YSZ inks	196
6.3	Production of the NiO/8YSZ fuel electrode	203
6.3.1	NiO/8YSZ dip coating on Y-3.4C, Y-5.2D, and Y-7.3E 8YSZ slurry coated tubes	203
6.3.2	NiO/8YSZ dip-coating on Y-7.4A and Y-3.4B 8YSZ slurry coated tubes	204
6.3.3	NiO/8YSZ dip-coating on Y-7.4A2 and Y-3.4B2 8YSZ slurry coated tubes	205
6.3.4	NiO/8YSZ ink painting on RSOFC	206
6.4	Sealing the reversible SOFC to the support, leak testing	209
6.4.1	Sealing to the 316 stainless steel gas delivery pipe and current collector	209
6.4.2	Sealing to an alumina gas delivery tube	210
6.5	Current collection and short circuit testing	213
6.6	Conclusions	215
References		217
7	Electrochemical testing of reversible SOFC	219
7.1	Introduction	219
7.1.1	Summary of all tests	219
7.2	Testing RSOFC with dip-coated YSZ electrolytes	220
7.3	Testing RSOFC with painted YSZ electrolytes	222
7.4	Conclusions	231
References		233
8	Reversible SOFC computer model	235
8.1	Rationale for the reversible SOFC system and model	235
8.2	Cell voltage, geometry, losses, and power.	236
8.2.1	Nernst voltage and standard voltage	236
8.2.2	Cell geometry	239
8.2.3	Ohmic resistance of the cell components	240
8.2.4	Activation polarisation resistance	241
8.2.5	Diffusion polarisation resistance	245
8.2.6	Cell voltage and total losses	251
8.2.7	Impedance modelling of the RSOFC	253
8.2.8	Power outputs and inputs of the reversible SOFC system	254
8.2.9	Operating range of the reversible system	254
8.3	Heat modelling in the reversible cell system	259
8.3.1	Electrochemical heat production/consumption	260
8.3.2	Ohmic heat production	261
8.3.3	Heat losses to surroundings	262
8.3.4	Cell and stack geometry and heat capacities.	263

8.3.5	Heat capacity of the system gases	264
8.3.6	The phase change heat store	267
8.3.7	Fuel cell and electrolysis cell heat balances	269
8.4	Electrical efficiency and energy storage	274
8.4.1	Electrical efficiency with cell current	274
8.4.2	Electrical efficiency during a RSOFC cycle	275
8.4.3	Limits of the energy storage capacity of the system	279
8.5	Implementation of the model in software	279
8.5.1	Model design, power and controls	279
8.6	Further work	281
8.7	Conclusions	282
References		285
9 Discussion and conclusions		287
10 Future work		293
10.1	Oxygen electrode symmetrical cells	293
10.2	Extrusion	293
10.3	Brazing	294
10.4	Reversible SOFC preparation	294
10.5	Electrochemical testing of reversible SOFC	295
10.6	Reversible SOFC computer model	296
A List of publications		299
B Equation fits and semi-empirical equations		301
B.1	Data from chapter 3	301
B.1.1	Temperature calibration for pellet symmetrical cell measurements . .	301
B.1.2	Example of equivalent circuit modelling fit	303
B.2	Data from chapter 8	304
B.2.1	Semi-empirical equations: resistivity and surface diffusion losses in the RSOFC	304
B.2.2	Semi-empirical equations: thermodynamics, heat production/consumption, and heat capacity	309
Bibliography		315

List of Figures

1.1.1	Renewable energy generation in Scotland	28
1.1.2	Renewable energy generation methods comparison: predictability and continuity	29
1.1.3	UK electrical demand over 10 days	30
1.2.1	Solid oxide fuel cell and solid oxide electrolysis cell	32
1.2.2	Reversible solid oxide fuel cell cycle	33
1.2.3	Thermodynamics of electrolysis as a function of temperature	34
1.3.1	Planar and tubular SOFC geometries	35
1.3.2	Triple phase boundaries in a composite SOFC electrode	36
1.3.3	Typical SOFC/SOEC schematic	36
1.3.4	Schematic of proposed tubular RSOFC	44
1.4.1	Schematic of a scanning electron microscope	45
1.5.1	Symmetrical cell schematic	47
2.1.1	Schematic of tape casting process	64
2.1.2	Lamination of tapes to produce a symmetrical cell	65
2.1.3	Handheld ram extruder	67
2.1.4	Handheld ram extruder die assembly	67
2.1.5	Mechanised single screw extruder	69
2.1.6	Die assembly schematic for mechanised single screw extruder	70
2.1.7	12 V DC motor used for dip coating	74
2.1.8	MACOR and alumina rings used for sealing RSOFC	77
2.1.9	Rubber bung apparatus used for leak testing RSOFC	78
2.1.10	Red dye leak testing apparatus	78
2.1.11	RSOFC-H-cell4-4 and H-cell4-5 pre-test	80
2.3.1	Equivalent circuit used to model impedance results from tape cast symmetrical cells	87
2.3.2	Symmetrical cell testing setup	88
2.3.3	Equivalent circuit used to model impedance results from pellet symmetrical cells	89
2.4.1	Schematic of the first test setup for testing RSOFC	91
2.4.2	Fitting and wiring of RSOFC in pressure vessel test jig	91
2.4.3	Second test setup for testing RSOFC: with flowing oxygen	92

2.5.1	$R_{diff,surface}$ as a function of temperature and pressure. The vertical axis is $R_{diff,surface}$, in the range $0 \Omega - 1.5 \Omega$, the axis pointing towards the observer is temperature (800°C to 1000°C , far to near), and the axis pointing away from the observer is pressure, from 1 bar to 5 bar, left to right. Data are from symmetrical cell measurements, and the surface plot was obtained by trial and error. The plot and fit was obtained in collaboration with Dragos Neagu, a PhD student at the University of St Andrews.	96
3.1.1	Impedance spectra of tape cast samples tested in air and oxygen	104
3.1.2	Impedance spectra of tape cast samples tested in air at different temperatures	105
3.1.3	Area specific polarisation resistance of symmetrical tape cast samples . . .	106
3.1.4	Area specific polarisation resistance of tape cast samples over 160 h. . . .	107
3.1.5	Comparison of impedance arcs for tape cast symmetrical cells before and after 140 h testing, in air and oxygen	108
3.1.6	Cross-section of microstructure of tape cast symmetrical cells before and after testing	108
3.1.7	EDX on tape cast symmetrical cells after testing in oxygen for 162 h. . . .	109
3.2.1	Gold current collection grid on pellet symmetrical cell	111
3.2.2	Microstructure of symmetrical cell electrode and current collector	113
3.2.3	Electrical equivalent circuit used to model pellet symmetrical cells	113
3.2.4	Impedance spectra at different temperatures for a pellet symmetrical cells	114
3.2.5	Area specific polarisation resistance for two pellet symmetrical cells as a function of temperature	115
3.2.6	Area specific polarisation resistance of arc C, measured on a pellet symmetrical cell	116
3.2.7	Area specific polarisation resistance of arc C as a function of temperature and oxygen pressure	116
3.2.8	Area specific polarisation resistance of arc B, as a function of temperature and pressure	119
4.1.1	A comparison of LSM tubes made with water based, and polyethylene glycol based extrusion recipes	125
4.1.2	As extruded LSM tubes showing surface defects	126
4.1.3	Water absorption of cellulose over 24 hours	127
4.1.4	Photograph of 4 tubes extruded with different cellulose-water ratios	129
4.1.5	Monomer repeating unit of 2-hydroxyethylcellulose	129
4.1.6	LSM tubes extruded from extrusion recipe H-cell12, before and after sintering	130
4.1.7	LSM tube surface flaw at different focal lengths, after sintering	131
4.2.1	LSM tubes with longitudinal cracks, after sintering	131
4.2.2	Comparison of cross sections after sintering, of an LSM tube that was solvent extracted, and one that was not	134

4.2.3	Voids in an LSM tube, arising from lumps of cellulose that burned out during sintering	135
4.2.4	Thermal gravimetric analysis of various thermoplastic extrusion components	136
4.2.5	SEM image of graphite pore former	136
4.2.6	Comparison of LSM powder, as received and after coarsening by sintering	137
4.2.7	Particle size distribution measurements on LSM as received, and coarsened LSM powder	138
4.2.8	Comparison of LSM tube made with cellulose pore former, and LSM tube made with coarsened LSM, and graphite pore former	139
4.2.9	Image analysis of cross section of LSM tubes made with different pore formers, and particle sizes of LSM	140
4.2.10	Pressure, temperatures and motor current logged during extrusion with a mechanical screw extruder	141
4.2.11	Comparison of LSM tubes as extruded, and after sintering	142
5.2.1	Microstructure of reduced copper particles, and pictures of LSM and 316 stainless steel tubes before and after brazing	148
5.2.2	Braze absorbed into LSM tube microstructure	148
5.2.3	Silver-copper oxide phase diagram	149
5.2.4	LSM tubes and stainless steel supports before and after brazing	149
5.2.5	Pictures of LSM tubes brazed to 316 stainless steel tubes, with various braze compositions	150
5.2.6	Cross section of LSM tube brazed with 4 mol% CuO, balance silver, to 316 stainless steel tube	151
5.2.7	EDX analysis of phases in braze:316 stainless steel interface	152
5.2.8	EDX analysis of layer between silver layer and LSM in brazed joint	153
5.2.9	Cross sections of LSM tubes brazed to 316 stainless steel tubes at various braze compositions	154
5.3.1	Braze:LSM composites on copper or stainless steel before and after brazing	156
5.3.2	Cross section of braze:LSM composites on 316 stainless steel after brazing	157
5.3.3	EDX analysis of braze:LSM composite to stainless steel interface	158
5.3.4	Braze:LSM composites with or without braze interlayers, on 316 stainless steel after brazing	158
5.3.5	Cross section of braze:LSM composites on stainless steel composites, with or without braze interlayers, after brazing	159
5.3.6	Stainless steel with braze:LSM composite pellets, after brazing	160
5.3.7	Cross sections of braze:LSM composite pellets on steel, with and without titanium coatings, after brazing	161
5.3.8	Braze:LSM composite pellets, on stainless steels, after brazing, compared with bare steels	162
5.3.9	Stainless steels with either no Ti coats, or 2 Ti coats, after brazing composite braze:LSM pellets to it.	163

6.1.1	A painted coat of LSM-YSZ ink before drying, on LSM tubes	170
6.2.1	Particle size distribution measurements on 8YSZ dip-coating slurries . . .	172
6.2.2	Optimal micrographs of surface of 8YSZ sintered electrolyte	173
6.2.3	Cross sections of LSM tubes with 8YSZ electrolyte from slurries Y-7.4A and Y-3.4B	174
6.2.4	LSM tubes with sintered 8YSZ electrolyte from slurries Y-3.4C, Y-5.2D and Y-7.3D	175
6.2.5	Cross section of LSM tubes with 8YSZ dip-coated electrolyte	176
6.2.6	LSM tubes pre-coated with LSM-YSZ, after one sintered coat of 8YSZ, and after second dip coat of 8YSZ	177
6.2.7	Cross section of LSM tubes with YSZ electrolyte made with different slurries	177
6.2.8	Porosities of 8YSZ electrolytes made by dip-coating different slurries . . .	179
6.2.9	EDX analysis of cross section of 2xY-3.4B2 slurry coated 8YSZ electrolyte	180
6.2.10	Pictures of LSM tubes, with or without LSM-YSZ coatings, and sub- sequent coats of 8YSZ, before and after sintering	181
6.2.11	Pictures of LSM tubes, with or without LSM-YSZ coatings, and sub- sequent coats of 8YSZ, before and after sintering, after second YSZ coating	182
6.2.12	Cross section of LSM tube with LSM-YSZ layer and 3x8YSZ dip-coated, sintered layers	182
6.2.13	EDX analysis of RSOFC, showing Ni-YSZ and YSZ layers on LSM substrate	183
6.2.14	Comparison of the penetration of YSZ into LSM tubes, for a tube with a pre-coated LSM layer, and a tube without this layer	183
6.2.15	Cross section of RSOFC with dense LSM-YSZ layer	184
6.2.16	Particle size distribution measurements on 8YSZ dip-coating slurry Y-7.3G	185
6.2.17	Comparison of two 8YSZ surfaces made by dip-coating an LSM tube . . .	186
6.2.18	Comparison of an 8YSZ dip-coated surface at two different magnifications	186
6.2.19	Various flaws in 8YSZ dip-coated surfaces	187
6.2.20	SEM cross section of 1xY-7.4A, 3xY-3.4F 8YSZ dip-coated tube	188
6.2.21	Surface of a 1xY-7.3G 8YSZ coating	189
6.2.22	Surface of a 1xY-7.3G, 1xY-3.4F 8YSZ coating	189
6.2.23	Cross section of sample in fig. 6.2.22	190
6.2.24	Surface of tubes coated with various 8YSZ Y-7.3G slurries	191
6.2.25	LSM tubes dip-coated with 3YSZ slurries Y-10.0I, Y-7.5J, and Y-4.9K, before and after sintering	193
6.2.26	Particle size distribution measurements on 3YSZ slurry Y-4.9K	193
6.2.27	Comparison of unsintered, and pre-sintered LSM tubes coated with 8YSZ slurries and sintered	194
6.2.28	LSM tubes coated with recipe Y-7.3G and recipe Y-7.3L 8YSZ slurries . .	195
6.2.29	Cross section of 8YSZ dip-coated tubes with NiO-YSZ coatings	195
6.2.30	Recipe M-gra10 LSM tubes with a sintered layer of painted 8YSZ ink, and a cross section after sintering, with ceramic sealant on the outside	196

6.2.31	Comparison of the particle size distribution of a 3YSZ-C commercial screen printing ink, and an in-house 8YSZ screen printing ink	197
6.2.32	Comparison of tubes painted with 8YSZ ink, and 3YSZ-C ink	198
6.2.33	Cross section of tube coated with 3YSZ-C ink, showing dense 3YSZ electrolyte	198
6.2.34	Comparison of commercial 3YSZ, and in-house 8YSZ screen printing inks, on LSM tubes after sintering	200
6.2.35	Surface of 3YSZ and 8YSZ electrolytes after sintering	200
6.2.36	Comparison of 3YSZ-C ink and 8YSZ ink coated tubes after sintering . . .	201
6.2.37	Dense electrolyte from 3YSZ-C ink, and flaws seen in this layer	202
6.3.1	Cross section of NiO/YSZ layer on RSOFC	203
6.3.2	Pinhole in LSM substrate of RSOFC-H-cell4-5	204
6.3.3	NiO-YSZ coated onto YSZ on LSM tubes made with extrusion recipe H-cell6205	
6.3.4	Painted NiO/YSZ ink on 8YSZ electrolyte, on LSM tubes	205
6.3.5	EDX analysis of RSOFC cross section showing YSZ and NiO/YSZ layers	206
6.3.6	NiO/YSZ ink on RSOFC before sintering, with drips down tubes after sintering	206
6.3.7	NiO/YSZ on RSOFC before and after sintering, and cross section after sintering	207
6.3.8	NiO/YSZ bands painted on RSOFC before and after sintering	208
6.3.9	NiO/YSZ bands on RSOFC after sintering, with a 3YSZ-C electrolyte . .	208
6.4.1	Red dye leaks tests on RSOFC-H-cell4-1, and H-cell4-4	209
6.4.2	Cross section of sealed end of RSOFC-M-gra10-4	212
6.5.1	Current collection on RSOFC-H-cell4-4	213
6.5.2	RSOFC with nickel mesh and copper wire current collector, and nickel paste	214
6.5.3	RSOFC-M-gra10-4 and M-gra10-6 with their current collectors	214
7.2.1	RSOFC-H-cell4-4 after testing	220
7.2.2	RSOFC-M-gra8-4 pre-testing	221
7.2.3	RSOFC-M-gra8-5 after testing	222
7.3.1	Temperature and oxygen pressure during testing of RSOFC-M-gra10-4 . .	222
7.3.2	RSOFC-M-gra10-4 after testing	223
7.3.3	Cross section of RSOFC-M-gra10-4 after testing	224
7.3.4	EDX analysis on cross section of RSOFC-M-gra10-4 after testing	225
7.3.5	Red dye leak tests of RSOFC-M-gra10-6 after testing	225
7.3.6	Red dye leak tests of RSOFC-M-gra10-27, after testing	226
7.3.7	Impedance data from RSOFC-M-gra10-27 at OCV, during testing	227
7.3.8	RSOFC-M-gra10-27 after testing: sealing problems	228
7.3.9	Red dye leak testing on RSOFC-M-gra10-28, after testing	229
7.3.10	Cross section of RSOFC-M-gra10-27, showing dense 3YSZ electrolyte and crack	230
7.3.11	Red dye leak test of RSOFC-M-gra10-10, after testing	231

8.2.1	Nernst potential of RSOFC as a function of state of charge and system pressure	238
8.2.2	Schematic of modelled RSOFC	239
8.2.3	Ohmic resistance of the components of the modelled RSOFC	241
8.2.4	Activation overpotential of RSOFC, at three different values of pre-exponential coefficient	244
8.2.5	Diffusion of fuel gases above and inside the RSOFC - illustration	245
8.2.6	Modelled fuel electrode diffusion losses in the RSOFC	248
8.2.7	Surface diffusion polarisation in the RSOFC as a function of temperature and pressure	249
8.2.8	Randle's cell for modelling surface diffusion polarisation	250
8.2.9	Voltage drop from surface diffusion polarisation on the RSOFC oxygen electrode as a function of current density	251
8.2.10	Cumulative losses/overpotentials in the RSOFC as a function of current density	252
8.2.11	Electrical equivalent circuit used to model the impedance of the RSOFC	253
8.2.12	Simulated impedance of the RSOFC at two different temperatures	253
8.2.13	RSOFC I/V and power curves modelled at three different temperatures	256
8.2.14	RSOFC power and I/V curves modelled at four different system pressures	257
8.2.15	RSOFC power and I/V curves modelled at four different system states of charge	258
8.3.1	Net electrical power and net heat production by the RSOFC as a function of current density	261
8.3.2	Total and area specific heat loss from the RSOFC system to the surroundings	263
8.3.3	Time taken for RSOFC system to overheat without heat store	266
8.3.4	Heat capacities of RSOFC system components with no heat store	267
8.3.5	Heat capacities of RSOFC system components with a heat store	269
8.3.6	RSOFC cycles at 20.4 and 40.8 A per cell, showing heat flows	271
8.3.7	RSOFC cycles at 20.4 and 40.8 A per cell, showing heat store and hydrogen state of charge with temperature	273
8.4.1	Power output/input and electrical conversion efficiency as a function of RSOFC current	275
8.4.2	RSOFC cycles at 20.4 and 40.8 A per cell, showing the electrical conversion efficiency, and temperature during the cycle	276
8.5.1	RSOFC system modelled in Matlab/Simulink: main model block	280
B.1.1	YSZ pellet resistivity data plot and two fits	301
B.1.2	Impedance data plots with fits from equivalent circuit model	303
B.2.1	Data plot and fit of Vstandard values	304
B.2.2	Data plot and fit of of LSC resistivity values	305
B.2.3	YSZ resistivity data values plot and linear fit	306
B.2.4	Nickel metal resistivity values data plot and fit	307
B.2.5	Rdiff,surface data with 3D surface plot fit	308

B.2.6	Rdiff,surface data with 3D surface plot fit of maximum frequency of arc .	309
B.2.7	Data plots and fits of thermodynamic parameters of the fuel cell reaction .	310
B.2.8	Thermal conductivity of Microtherm insulation: data plot and fit	311
B.2.9	Cold face temperatures of Microtherm insulation	312
B.2.10	Heat capacities of RSOFC system gases: data plot and fit	313
B.2.11	Heat capacity of copper metal data plot and fit	314

List of Tables

1.1.1	Electrical energy storage methods	30
1.2.1	Comparison of fuel cell types	32
1.3.1	A comparison of SOFC fabrication techniques	40
1.3.2	SOFC companies and details of their products and manufacturing	40
1.3.3	Comparison of dip-coating slurry formulations and sintering parameters	42
1.3.4	Comparison of Ag/Cu/Ti brazing methods	43
1.3.5	Proposed materials and manufacturing methods of RSOFC	45
1.5.1	Degradation mechanisms of LSM-YSZ and Ni-YSZ SOFC electrodes	50
1.5.2	Solid-state Energy Conversion Alliance targets	51
2.1.1	Water and polyethylene glycol based extrusion recipes	68
2.1.2	Water and cellulose based recipes for the mechanised screw extruder	70
2.1.3	Thermoplastic extrusion recipes for the mechanised screw extruder	71
2.1.4	YSZ tape casting recipe 1 and dip coating recipes Y-7.4A and Y-3.4B	73
2.1.5	NiO/YSZ dip-coating slurry recipes	75
2.1.6	Varying Ag:Cu ratio in a braze: different compositions tested	82
2.1.7	Braze-LSM compositions tested	82
2.1.8	Braze interlayer sample descriptions	83
2.1.9	Sample descriptions for brazing samples with titanium coating	84
2.2.1	Polishing method for SEM sample preparation	85
3.1.1	Increase in area specific polarisation resistance for tape cast samples over 140 h	107
3.2.1	In plane electrical conductivity of symmetrical pellet cells with different current collectors	112
3.2.2	Literature values for five processes identified in impedance spectra	117
3.2.3	Comparison of literature values for process C, and results from this work	117
4.1.1	Selected water or polyethylene glycol based recipes for extrusion	124
4.1.2	Cellulose-water ratios for absorption experiment	128
4.1.3	Extrusion recipes with varying cellulose-water ratios and characteristics of tubes made from them	128
4.2.1	Water and cellulose based extrusion recipes for the mechanised screw extruder	132

4.2.2	Thermoplastic extrusion recipes for the mechanised screw extruder	133
4.2.3	Mass loss of paraffin wax from extruded tubes after solvent extraction with decane	134
4.2.4	Porosities of LSM tubes made with cellulose and graphite pore formers .	140
5.2.1	Various braze compositions and masses after brazing	150
5.3.1	Properties of brazing materials, fuel cell materials, steel substrates, and alumina	155
5.3.2	Braze:LSM compositions tested	156
5.3.3	Recipes for braze:LSM composites with and without braze interlayers, on 316 stainless steel	157
5.3.4	Characteristics of Ti coated stainless steel	160
5.3.5	Stainless steel, with and without Ti coating, with mass changes after brazing	162
6.2.1	8YSZ tape casting recipe, diluted to make dip-coating slurries Y-7.4A-Y- 7.3D	171
6.2.2	Thickness measurements of 8YSZ electrolytes	176
6.2.3	Thickness of 8YSZ electrolytes made with different dip-coating slurries .	178
6.2.4	8YSZ tape-casting recipe 2, and dip-coating slurries Y-3.4F-Y - 7.3G2 .	185
6.2.5	3YSZ dip-coating slurry recipes, H-K	192
6.2.6	8YSZ dip-coating slurry recipes Y-7.3L and Y-7.4L2	194
6.2.7	Composition of 8YSZ slurries and screen printing inks	196
6.2.8	List of recipe M-gra11 LSM tubes, coated with various screen printing inks	199
6.3.1	NiO/YSZ dip-coating slurry formulations	203
6.3.2	NiO/8YSZ layer thicknesses measured from SEM images	204
6.4.1	Thermal expansion coefficients of RSOFC materials	210
6.4.2	Sealing and leak test results for recipe M-gra7 RSOFC	211
6.4.3	Sealing and leak test results for RSOFC-M-gra8-3, M-gra8-4	211
6.4.4	Sealing and leak test results for RSOFC-M-gra8-5, M-gra8-6	212
6.4.5	Sealing and leak test results for RSOFC-M-gra10-4, M-gra10-6	212
6.5.1	Current collection on various RSOFC	213
7.1.1	Testing of RSOFC with outcomes from each test	220
8.2.1	Dimensions of modelled RSOFC	239
8.3.1	Heat capacities of RSOFC gases	264
8.4.1	RSOFC cycle electrical storage efficiencies, at various current densities and values of the pre-exponential coefficient	277
8.5.1	Comparison of three electrical power and control schemes for the RSOFC system, and their effects on RSOFC stack current	281

Nomenclature

Roman Symbols

304, 316, 330, 430, 441, 446 grades of stainless steel

A area (m^2)

A_V pressure vessel surface area (m^2)

C_p heat capacity ($\text{J kg}^{-1} \text{K}^{-1}$)

i cell current (A)

C charge (C)

d^{10} maximum size of particles in the first (percentage in superscript) of the particle size distribution.

$D_{H_2,m}$ ordinary diffusion coefficient, hydrogen

$D_{H_2O,m}$ ordinary diffusion coefficient, steam

D_{H_2,H_2O} mutual diffusion coefficient, hydrogen and steam mixture

D mass diffusion coefficient ($\text{m}^2 \text{s}^{-1}$)

E_a activation energy (eV)

E Electrical efficiency (%)

F Faraday constant (C mol^{-1})

f_{max} frequency maximum (Hz)

$H_{fus,bronze}$ Enthalpy of fusion, bronze

$i_{density}$ current density (A m^{-2})

i_0 exchange current density (A m^{-2})

J flux ($\text{mol}^2 \text{s}^{-1}$)

l insulation thickness (m)

l wall thickness of pressure vessel (m)

l	length or current path length (m), unless stated as (cm)
L_V	pressure vessel side length: length=breath=height (m)
M	mass (kg)
M	molecular mass (g mol^{-1})
M	moles (mol)
M_{H_2, H_2O}	reduced mass of hydrogen and steam (g^{-1})
n	number of electrons or number of cells
P	partial pressure (Pa) unless stated as (bar)
q_e	electrochemical heat absorbed/produced (W)
Q_i	heat loss through insulation (W)
q	heat (J)
q_m	heat in a mole of hydrogen that is oxidised in fuel cell mode (J)
q_{ohm}	power dissipation from ohmic heating (W)
R	(with subscript) = resistance (Ω)
R	(no subscript) = molar gas constant ($\text{J mol}^{-1} \text{K}^{-1}$)
r	cell radius (m)
T	temperature (K) unless stated to be ($^{\circ}\text{C}$)
t	time (s)
V	volume (m^3)
V_{drop}	voltage drop (V)
V_{Nernst}	Nernst voltage (V)
$V_{standard}$	standard cell voltage (V)
W_m	electrical energy in a mole of hydrogen (J)
W	power (W)
X	mole fraction
Z_C	impedance of a capacitor (F)
Z_{img}	imaginary impedance (Ω)
Z_{real}	real impedance (Ω)

Z_R impedance of a resistor (Ω)

Acronyms

3-YSZ-C commercial 3YSZ screen printing ink

3YSZ or 8YSZ zirconium dioxide doped with 3 mol

AC or ac alternating current

APS atmospheric plasma spraying

ASRp area specific polarisation resistance

CFD computational fluid dynamics

CGO cerium oxide doped with gadolinium oxide

CHP combined heat and power

CTAB cetyl tri-ammonium bromide

CTE coefficient of thermal expansion

DBP dibutyl phthalate

DC dip coating or direct current

DSC differential scanning calorimetry

EDX energy-dispersive X-ray spectroscopy

EtOH ethanol

FIB-SEM focussed ion beam milling-scanning electron microscopy

H-cell handheld extruder-cellulose pore former

I/V Current/voltage

IPA isopropylalcohol

L/D length:diameter ratio

LSM lanthanum strontium manganese oxide

M-cell mechanical screw extruder-cellulose pore former (thermoplastic extrusion mix)

M-cell-W mechanical screw extruder-cellulose pore former (water-based extrusion mix)

M-gra mechanical screw extruder-graphite pore former (thermoplastic extrusion mix)

MEK methyl ethyl ketone

MIP mercury intrusion porosimetry

NMR	nuclear magnetic resonance
OCV	open circuit voltage
P1,2D	propan-1,2-diol
PAA	polyacrylic acid
PEM-FC	polymer electrolyte membrane fuel cells
PP	polypropylene or polyphosphate
PVB	polyvinyl butyryl
PW	paraffin wax
r.m.s.	root mean square
r.p.m.	revolutions per minute
RC	resistor and capacitor in parallel
RPEM-FC	reversible polymer electrolyte membrane fuel cells
RSOFC	reversible solid oxide fuel cells
SA	stearic acid
SECA	Solid-State Energy Conversion Alliance
SEM	scanning electron microscopy
SOFC	solid oxide fuel cells
SP	screen printing
TEA	triethanolamine
TEC	thermal expansion coefficient
TGA	thermal gravimetric analysis
Ticusil	titanium-copper-silver alloy
TPB	triple phase boundary
Tri-X	Triton-X
WS	wet spraying
Y-(number)-(letter)-(number)	YSZ slurry-(solids loading vol. %)-(slurry batch identifier)(iteration number), e.g. Y-7.3-A2
YSZ	zirconium dioxide doped with yttrium oxide

Greek Symbols

β	electron transfer coefficient
γ	pre-exponential coefficient (A m^{-2})
η	overpotential (V)
ϵ	porosity
λ	thermal conductivity (W m^{-1})
μm	microns
ν	diffusion volume ($\text{cm}^3 \text{ mol}^{-1}$)
Φ	State of charge of the system or heat store (%)
π	pi
ρ	resistivity ($\Omega \text{ m}$)
ρ	density (kg m^{-3})
τ	tortuosity or time constant

Superscripts

b	bulk
l	surface of the fuel electrode
r	reactive sites inside electrode

Subscripts

act	activation
$bronze, molten$	molten bronze
$bronze, solid$	solid bronze
$cell$	cell
$cellcon.$	cell connection
$cycle$	A RSOFC system energy storage and release cycle
$diff$	diffusion
$electrical$	electrical
e	electrochemical or electrode

<i>elec</i>	electrolyser mode
<i>fuel.e.</i>	fuel electrode
<i>f.c.</i>	fuel cell mode
<i>h.s.</i>	heat store
<i>intercon.</i>	interconnect
<i>ohmic</i>	ohmic resistance
<i>oxy.e.</i>	oxygen electrode
<i>stack</i>	stack of cells
<i>s</i> or <i>sys</i>	system
<i>tot</i>	total

Chapter 1

Introduction and context

1.1 Energy conversion and storage

1.1.1 Energy: The cause of, and solution to, many of the world's problems

The human race uses ever-increasing amounts of energy, for agriculture, transport, computing, travel, industry, and within our homes. Since the Industrial Revolution, world energy use has climbed steadily, as the world's population has grown, and technology has advanced. These advances would not have been possible without a cheap and plentiful supply of energy - firstly in the form of kinetic energy extracted directly from steam engines, and latterly electrical energy produced by various means. However, most of this energy production worldwide comes from combustion of fossil fuels such as coal, oil, or gas, with only a small percentage of nuclear energy or renewable energy generation such as solar power, wind, wave or tidal power. The energy in fossil fuels comes from hydrocarbons, which produce carbon dioxide when they are burned.

There is now a broad scientific consensus that the increase in carbon dioxide levels seen in the last 300 years since the start of the Industrial Revolution is a result of emissions by mankind, and that this is increasing the strength of the greenhouse effect, causing the earth to warm up. This is sometimes termed anthropogenic global warming. An independent economic analysis of this phenomenon produced for the UK Treasury in 2006 concluded that it was cheaper to address the issue than suffer the unabated effects, such as droughts, famines, loss of biodiversity, spread of disease etc. [1].

Therefore, leaving aside arguments regarding the quantity of energy usage, and assuming that mankind will want to continue to increase the amount of energy consumed, this leads to a question about sustainability. A sustainable energy source is one that is continually replenished, such as wind, wave, tidal, hydro power, and solar power, all of which harvest energy from either the sun, or the orbit of the moon. Therefore, there is a considerable drive across the world to switch from using fossil fuels to generate energy, to renewable energy instead. The UK has set a target of a 34% reduction in greenhouse gas emissions by 2020, from a 1990 baseline, and an 80% reduction target by 2050 [2]. Scotland has committed to a target of 100% of electricity to be generated from renewable

sources by 2020, and is steadily increasing the amount of renewable electricity generation as a percentage of total electricity generation. Fig. 1.1.1 shows the amounts of renewable electricity generated in Scotland over the period 2006-2009, according to the fuel type.

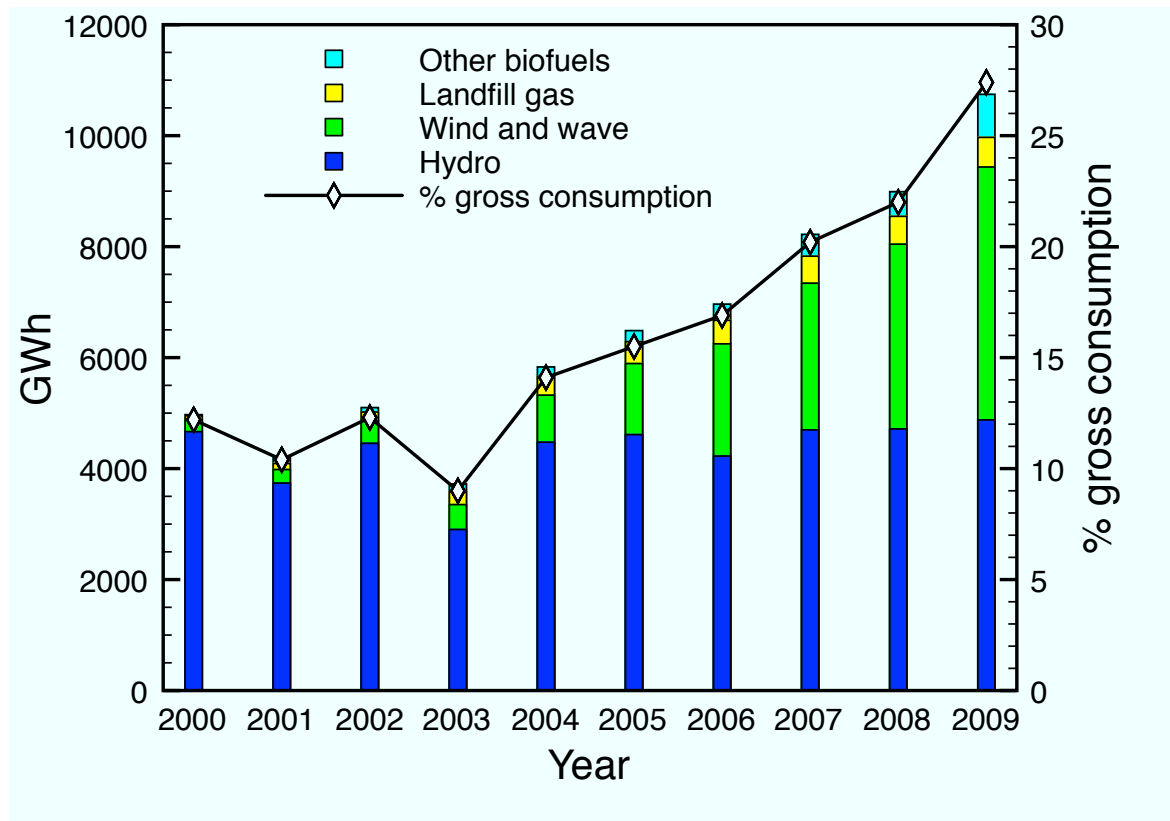


Figure 1.1.1: Renewable electricity generation in Scotland by fuel type, 2006-2009. The percentage of gross electrical consumption that is generated from renewable sources is also shown. [3]

The largest increase in generation is from wind and wave sources. It also shows that the share of renewable electricity as a percentage of the total consumption almost exactly matches renewable electricity generation growth. However, the target of 100% renewable electricity in Scotland by 2020 is very ambitious, and if it is to be met, will necessitate large increases in electricity produced from wave, tidal and wind sources.

1.1.2 Energy storage: UK context

In order for the 2020 target of 100% renewable electricity in Scotland to be met, some form of energy storage must be implemented. Fig. 1.1.2 compares the characteristics of various types of renewable electricity generation methods. It shows that the largest increase in renewable energy generation capacity over this period was in the wind and wave category. However, most of this is wind energy, and it is expected to dominate in the years leading up to 2020. Indeed, there are currently plans for two offshore wind farms in the Firth of Forth, and the Moray Firth, which would have a capacity of 4.8 GW between them. This is double the capacity of Scotland's largest coal-fired power station, at Longannet. However, wind power is both highly intermittent, varying in output considerably from

second to second [4], and also highly unpredictable. This means that a suitable energy storage method must be found, if these energy sources are to generate a large part of the electricity in Scotland. Without energy storage, which matches supply and demand, there would be both interruptions in supply, and oversupply situations, where energy would be wasted.

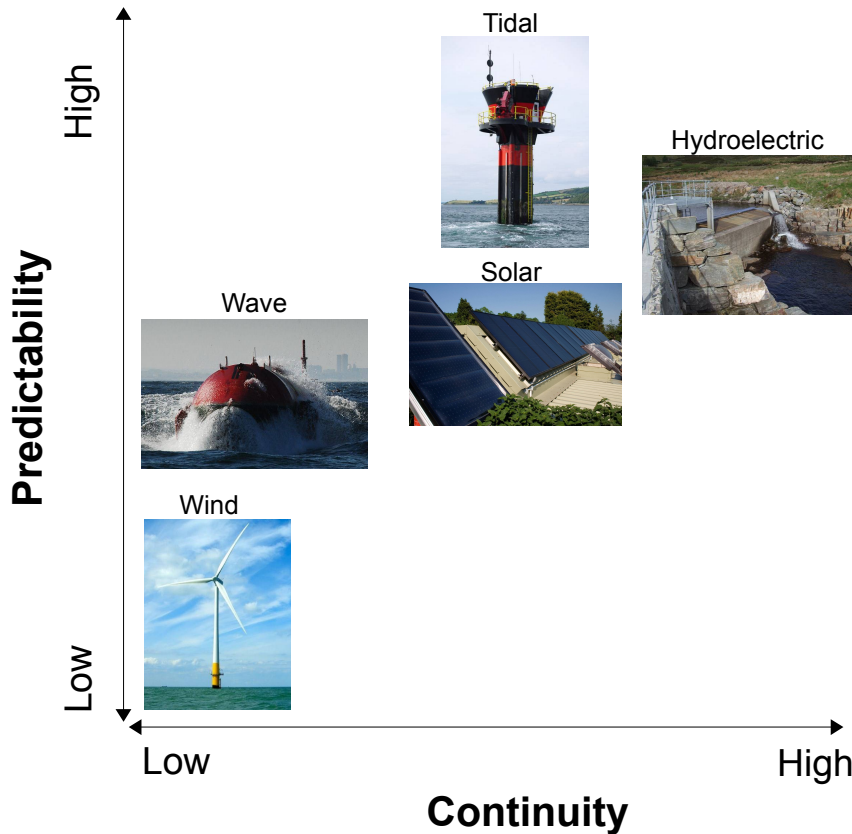


Figure 1.1.2: A comparison of various renewable electricity generation methods, as a function of continuity/availability of power generation, and predictability of power generation. Images shown are: tidal turbine, Strangford Lough, NI [5], hydroelectric dam, Cuileig, near Braemore, Scottish Highlands [6], solar panels, on the Earthship, Brighton [7], wave: Pelamis wave energy converter, Agucadoura Wave Farm, near Porto, Portugal [8], and wind turbine, Kentish Flats offshore wind farm, Thames estuary [9].

1.1.3 Energy storage methods

The UK and Scotland have been storing and releasing electrical energy for many years, in order to balance supply and demand. Demand varies with the time of day and time of year, as fig. 1.1.3 shows. There is a daily demand peak, and variations from day to week to year, so the supply must vary too. This is accomplished in several ways: firstly by exporting and importing electricity from France. Secondly, pumped hydro storage is utilised when the supply exceeds demand. However, there is a limited amount of pumped hydro storage available, because it requires large scale reservoirs of water, which can only be built in specific sites. Thirdly, when demand exceeds supply, the spinning reserve is brought online, which consists of generators that are operating at part load. The load is

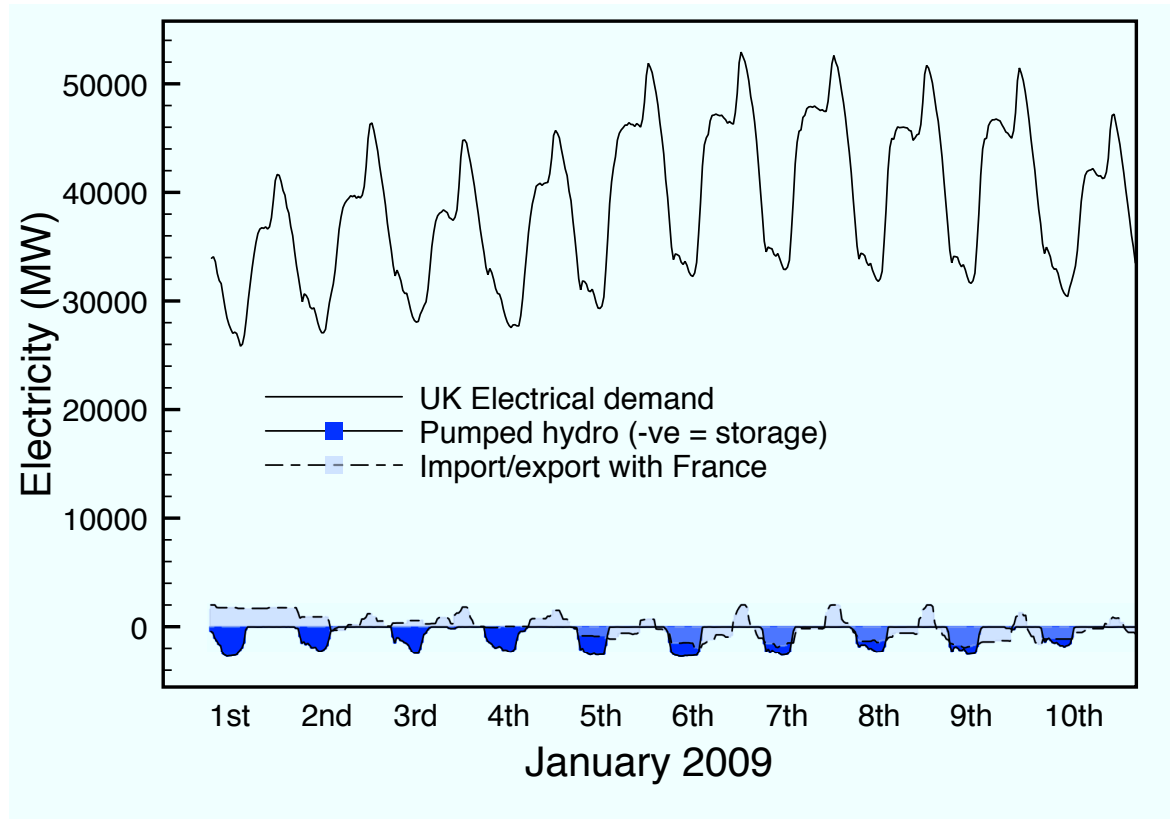


Figure 1.1.3: Electrical demand in the UK for the first 10 days of 2009. [10]

increased to use the spinning reserve capacity. However, it is inefficient to run generators at part load. The majority of the grid demand is met by baseload power stations such as coal, nuclear and gas power stations, which cannot be turned on and off quickly, but are highly predictable. If the majority of the grid were to be run on renewable energy, much more storage will be needed, because it is both more intermittent, and more unpredictable.

There are many different types of energy storage systems currently available or under development, some of which are compared in table 1.1.1.

Technology	Key advantage	Key disadvantage	Round-trip efficiency (%)	Energy type
Compressed air	large scale	needs right geology	50-70 [11]	kinetic
Pb-acid batteries	well-understood	high maintenance	70-80 [12]	chem.
Li-ion batteries	energy density	cost, degradation	80-90	chem.
Pumped hydro	large scale	needs right geology	70-80 [13]	kinetic
Redox flow cells	reliability	toxic chemicals (V)	65-75 [12]	chem.
Reversible SOFC	efficient part load	cost, degradation	>30	chem./heat

Table 1.1.1: Electrical energy storage methods under development. In the energy types column, chem. = chemical energy.

The electrical cycle efficiency of reversible SOFC is not found in the literature, but a

minimum efficiency of 30% - 40% is assumed, as this is the efficiency if energy is stored as hydrogen only, with no heat storage. However, this could be much greater if the heat produced during fuel cell mode could be stored in the system, to be re-absorbed in electrolysis mode. There are also other technologies such as flywheels, supercapacitors etc. which have been examined as energy storage systems, and reviewed [13]. One review compared greenhouse gas emissions over the lifetime of energy generation from nuclear or renewable energy, with three different energy storage technologies. These were pumped hydro energy storage, compressed air energy storage, and redox flow cells for energy storage. A fossil fuelled plant with no energy storage was compared with these. It was seen that greenhouse gas emissions could be substantially reduced with energy storage, compared to a fossil fuelled plant with no energy storage, and the best performing solution used compressed air storage [11]. This work examines a reversible solid fuel cell system (SOFC) as a potential energy storage medium. SOFC have several advantages: as electricity generators they are efficient at part load, and they are fuel flexible, using carbon monoxide (CO) as a fuel, unlike the low-temperature polymer electrolyte membrane (PEM) fuel cells, which are poisoned by CO. They also produce high temperature heat as a by-product of electricity production, so they can be used in a combined heat and power (CHP) mode if this is desired. If this heat is stored from the fuel cell cycle to electrolysis cycle, it may also be used to reduce the electricity input needed for electrolysis. In a reversible SOFC system, the energy storage capacity is partially decoupled from the power rating of the system (size of stack) because energy is partly stored as hydrogen. This gives an advantage over lithium ion batteries, where the energy storage capacity is directly proportional to the number of batteries and power rating of the system. This means that for reversible SOFC systems, cost is not directly proportional to the energy storage capacity, as is true for lithium ion batteries. Redox flow cells rely on large quantities of toxic chemicals such as vanadium compounds, although they can store energy highly efficiently.

1.2 Fuel cells, electrolyzers and reversible fuel cells

1.2.1 Fuel cell types and principles of operation

There are several different types of fuel cells, as in table 1.2.1. They are generally classified according to the electrolyte material used, and the operation temperature. Of these types of fuel cells, polymer electrolyte membrane (PEM-FC) and SOFC are the most studied for energy storage by reversible operation, producing electricity in fuel cell mode, and storing energy in hydrogen by electrolysis. PEM-FC must use only pure hydrogen, because their platinum catalyst is easily poisoned by low levels of carbon monoxide (CO). Hydrogen reacts according to the exothermic reaction equation 1.2.1, to produce liquid water, heat and electricity.



When it is used for energy storage, it is run in electrolysis mode, and splits water according to the endothermic equation 1.2.2.

Fuel cell type	Power range	Operation temp. (°C)	Applications
polymer electrolyte membrane	1-100 kW	80	transport/portable power
alkaline	kW	65-220	remote power e.g. space
phosphoric acid	< 1 MW	205	stationary power
molten carbonate	< 10 MW	650	CHP, stationary power
hybrid direct-carbon	W	700-900	CHP, stationary power
solid oxide	kW-100 MW	750-1000	CHP, distributed power

Table 1.2.1: Comparison of types of fuel cells, by operation temperature and electrolyte type. CHP = combined heat and power.



An analysis of a PEM-FC running reversibly, sometimes called a regenerative PEM-FC, showed that the round trip efficiency, from hydrogen to electricity back to hydrogen was in the range 26% - 42%, depending on the catalyst type and loading used [14]. There are two reasons for this poor energy storage efficiency; firstly that there is a voltage step when the fuel cell is switched from fuel cell mode to electrolysis cell mode - i.e. there is a significant activation energy barrier arising from the oxygen reduction reaction. These losses reduce the cell efficiency considerably. Secondly, the cell temperature is around 80 °C, so heat produced in the reaction is not very useful, because it cannot be used to make steam and do mechanical work.

Solid oxide fuel cells (SOFC) operate at temperatures between 750 °C and 1000 °C, and can use a variety of fuels. However, the reversible SOFC in this study are operated on hydrogen, as it allows Ni-YSZ electrodes to be used. Fig. 1.2.1 shows an operating SOFC and solid oxide electrolysis cell (SOEC) including the half cell reactions. It is important to note that in fig. 1.2.1, the oxygen electrode is the cathode in fuel cell mode, but the anode in electrolyser mode. Therefore, in order to refer to a specific electrode, the terms anode and cathode are not used, but rather the terms oxygen electrode or fuel electrode.

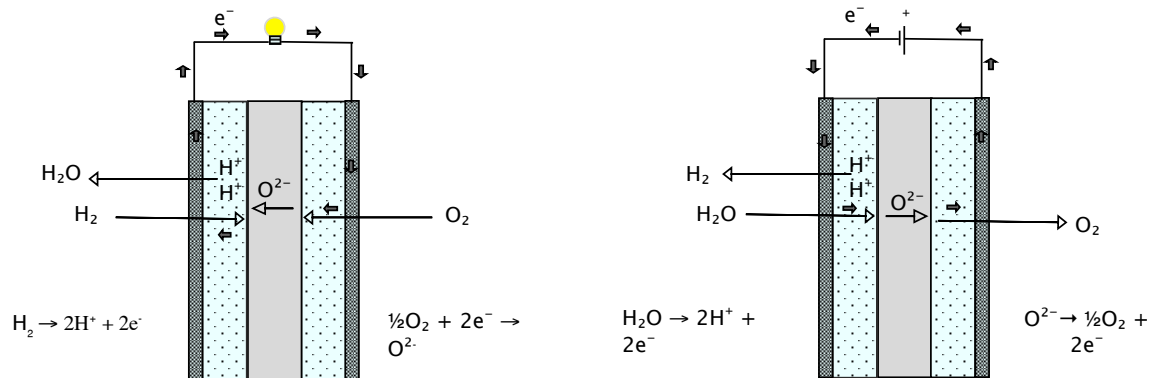


Figure 1.2.1: Solid oxide fuel cell (left) and solid oxide electrolysis cell (right)

Equation 1.2.3 is the reaction in fuel cell mode, and equation 1.2.4 is the reaction in electrolysis mode.



These are the same as the reactions in the PEM-FC, except that in this case, the reactants and products are all in the gas phase. Reversible SOFC are more suited to energy storage than PEM-FC, because with reversible SOFC there is no voltage step when switching from fuel cell mode to electrolysis mode [15], and the heat produced is high-grade. It can be used to produce steam to drive a turbine and generate electricity, stored in the system to improve electrolysis efficiency, or extracted for CHP.

1.2.2 Energy storage by a reversible solid oxide fuel cell system

The reversible SOFC is cycled to store energy, as fig. 1.2.2 shows. The system concept is that heat produced by the exothermic fuel cell reaction equation 1.2.3 should be stored in the system, so that it may be used by the endothermic electrolysis reaction, equation 1.2.4. This is an improvement to the concept of the energy being stored in chemical form as hydrogen only - a cycle efficiency of just 30% is achieved if the heat is discarded.

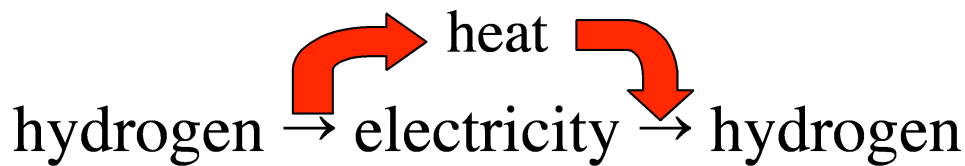


Figure 1.2.2: The reversible SOFC cycle. Heat from the fuel cell reaction is stored in the system and re-absorbed by the electrolysis reaction. [16]

However, if the heat is stored, much higher efficiencies could be achieved. The upper limit to this efficiency depends on two factors:

1. Heat generated by ohmic and polarisation losses in the cell
2. Heat lost from the system

The first factor may be addressed by fabricating a high-performance cell with low resistive losses, and the second by system insulation. The cycle duration will also affect the heat loss from the system - with shorter cycle times, less heat will be lost and the system will be more efficient. Fig. 1.2.3 shows the thermodynamics of the electrolysis cell reaction. In this figure, $T\Delta S^\circ$ is the heat absorbed by the reaction, ΔG° is the standard free energy of reaction - the amount of electrical energy required, and ΔH° is the standard enthalpy of reaction, which is the total energy change of the reaction. These are related according to equation 1.2.5.

$$\Delta H^\circ = \Delta G^\circ + T\Delta S^\circ \quad (1.2.5)$$

The standard voltage of the reaction is also shown in fig. 1.2.3, and is related to the standard free energy of reaction by equation 1.2.6.

$$\Delta G^\circ = -nFE^\circ \quad (1.2.6)$$

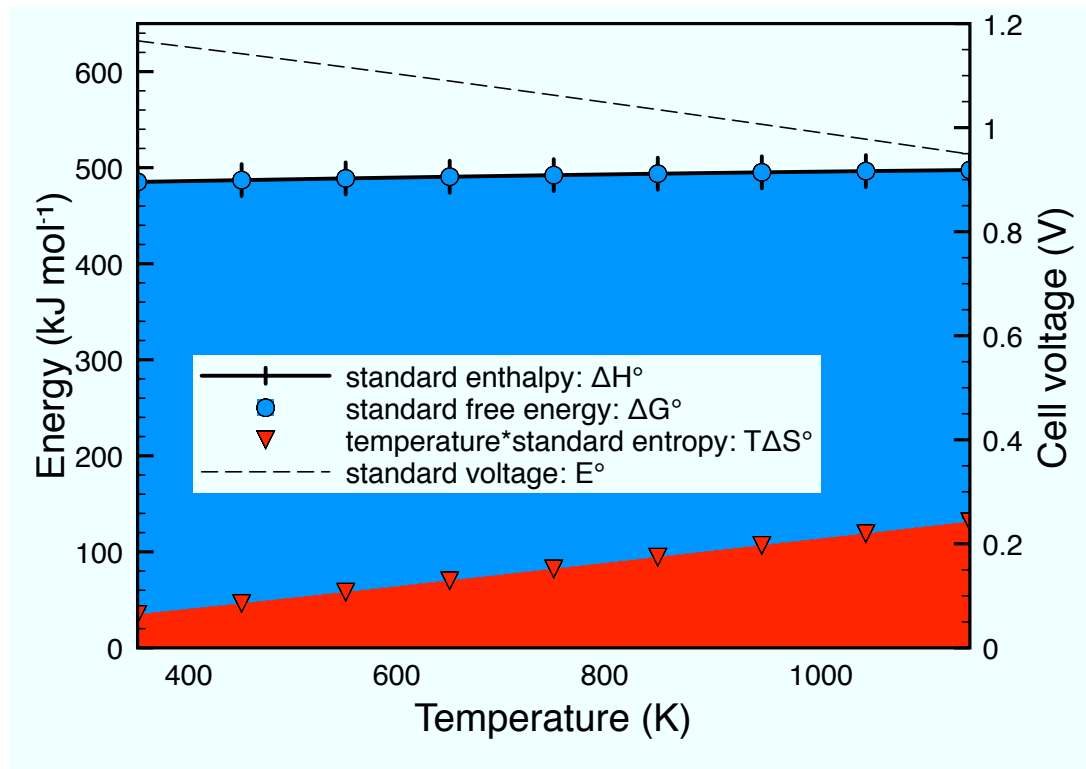


Figure 1.2.3: Thermodynamics of the electrolysis cell reaction: a stacked graph of energy demand for steam electrolysis as a function of temperature, at 1 bar pressure. The red area corresponds to heat input, and the blue area to electrical input. The voltage needed for the reaction as a function of temperature is also shown.

The electrolysis reaction has exactly the opposite entropy, enthalpy and free energy changes as the fuel cell reaction. Therefore, as the temperature of the fuel cell reaction increases, more heat is produced, and less electricity. However, the electrolysis reaction requires less electricity to produce hydrogen, and more heat, at higher temperatures. This means that the electrical to chemical conversion efficiency can exceed 100% in electrolysis mode, if heat is absorbed from the surroundings during electrolysis.

1.3 Reversible SOFC geometry and fabrication

1.3.1 Cell geometry

There are two main SOFC geometries, which may also be used for reversible SOFC; these are planar and tubular, and are shown in fig. 1.3.1. The planar geometry is harder to seal, but provides a high volumetric power density. In the design shown in fig. 1.3.1a, several cells are in series, which increases the voltage obtained from a single substrate.

The tubular design shown in fig. 1.3.1b was used by Siemens-Westinghouse, and has an interconnect running along the cell. This reduces the current path in the support material, improving cell performance. There is also an adapted version of the tubular design, which was pioneered by Siemens-Westinghouse.

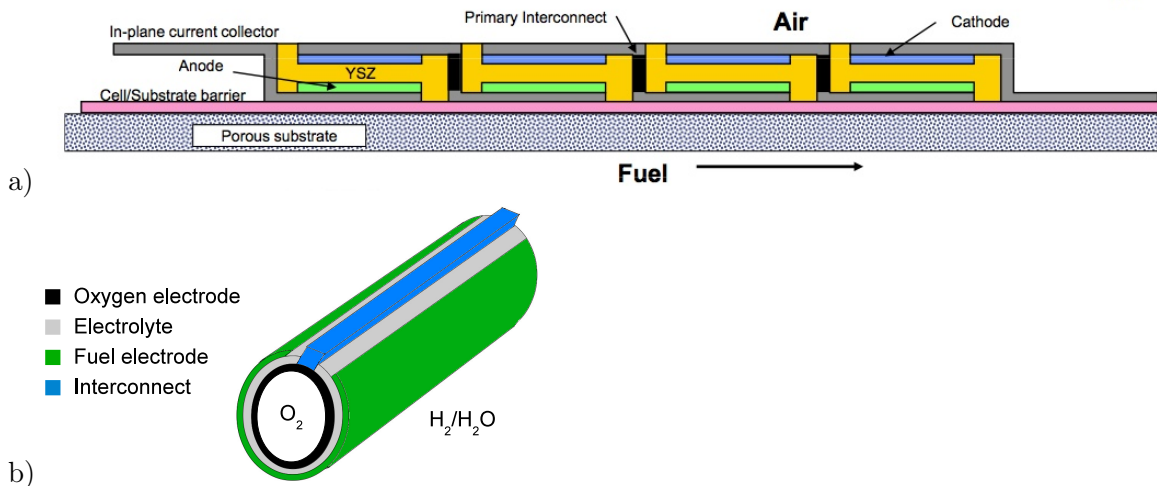


Figure 1.3.1: SOFC geometries: a) planar geometry of a Rolls-Royce Fuel Cell Systems cell. ©2009 Rolls-Royce Fuel Cell Systems (US) inc. and is used by permission. All rights reserved. [17], and b) Tubular SOFC geometry, designed by Siemens Westinghouse [18].

Although the tubular geometry is easier to seal, it generally has longer current paths than the planar cell, which cause ohmic losses in the cell. Reversible SOFC reported in literature are generally not built specifically to run in reverse mode, but are built as fuel cells or electrolyzers, and then run in reverse. Therefore, their geometry is not optimised for reversible SOFC operation.

For pressurised systems, such as the one that was built by Siemens-Westinghouse, tubular cells were used [19]. Sealing is more important as the pressure increases, because any leaks cause hydrogen and oxygen to mix and combust, producing heat. This can lead to a positive feedback cycle, as the heat produced enlarges the hole, causing a bigger leak, and this process is faster if the pressure is higher. Therefore, the geometry chosen for this work is tubular.

1.3.2 Cell materials

The SOFC operates at elevated temperature, so its component materials must be heat resistant, and stable in either oxidising or reducing atmospheres, limiting the choice of materials to ceramics and metals. The active layers in SOFC are quite thin, in the order of tens of μm . This minimises gas diffusion polarisation losses in the cell [20]. These layers are mechanically weak, and therefore are usually supported by a thick layer, which can be one of the active layers, usually the fuel electrode, electrolyte, or oxygen electrode. It may also be an inactive porous ceramic support, as is the case for the Rolls-Royce Fuel Cell Systems planar cell [21], or a metallic interconnect support [22]. Electrolyte supported cells have a large voltage drop across the electrolyte which drastically limits cell performance, so this support

is very seldom used. The fuel and oxygen electrodes are made of a composite of an ionic conductor, and an electronic conductor. The reactions in fig. 1.2.1 can only happen if there is a ‘triple phase boundary,’ (TPB) that is, a junction between a ionic conductor, electronic conductor, and a pore. This is because each reaction involves ions, electrons and gases.

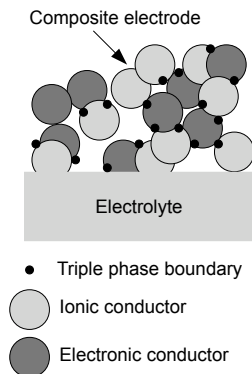


Figure 1.3.2: Triple phase boundaries (TPB) in a composite electrode [16]

Fig. 1.3.2 shows a schematic of a composite electrode, with the triple phase boundaries. The total length of joints between the ionic and electronic conductors and pores in an electrode is called the TPB length. This increases as the particle size decreases, and is proportional to the electrode performance, because it is the place where the fuel cell or electrolysis reactions occur. This was demonstrated by laser patterning an electrolyte substrate, and then filling in the pores with an electronic conductor. Electrical measurements showed that as the TPB length increased, the polarisation resistance of the electrode decreased [23].

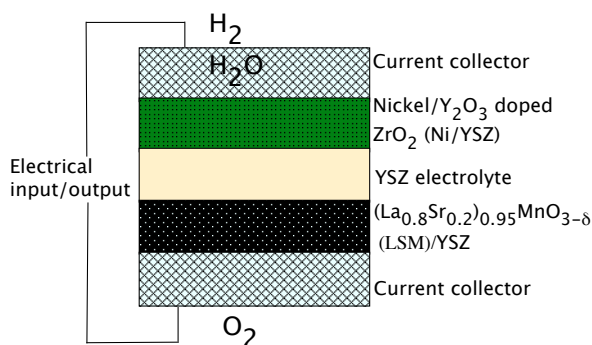


Figure 1.3.3: A schematic of a typical solid oxide fuel cell/electrolysis cell, showing positions of different components. The diagram is not to scale.

Fig. 1.3.3 shows a simple schematic of a typical SOFC/SOEC. The oxygen electrode is typically a composite, made of two materials. Firstly, an electronically conducting perovskite ceramic, A-site deficient, strontium-doped lanthanum manganate (LSM) such as $(\text{La}_{0.8}\text{Sr}_{0.2})_{1-x}\text{MnO}_{3-\delta}$, where A is the La,Sr site and the deficiency is x . The strontium doping increases the electronic conductivity, and the A-site deficiency helps to prevent the formation of the insulating phases, lanthanum and strontium zirconate [24]. This material has been extensively studied and is widely used in

SOFC oxygen electrodes [25]. Secondly, the ceramic ionic conductor is yttrium stabilised zirconia (YSZ). Zirconium dioxide is doped with yttrium oxide in order to stabilise the cubic structure at low temperatures, e.g. 8 mol% Y_2O_3 doped ZrO_2 , which is a fully stabilised YSZ [26]. Without the stabilisation, there are phase transformations from monoclinic to tetragonal to cubic, which cause volume changes in the ceramic. This would cause changes in ionic conductivity, and mechanical damage to thermally cycled cells. YSZ has been very deeply studied, and is known to be stable, fairly unreactive with other perovskites, and quite mechanically tough.

On the fuel electrode side, nickel metal is used as the electronic conductor, typically applied as NiO in a composite with YSZ, and then reduced in situ to form the cermet Ni-YSZ. It is highly electrically conductive, and has excellent catalytic activity for hydrogen oxidation. It is also a good catalyst for carbon formation from hydrocarbons, so SOFC that utilise methane can suffer from coking during operation. Therefore, it was decided to use pure hydrogen as a fuel in the reversible SOFC in order to avoid this problem, because fuel is recycled rather than continuously flowing into the cell. Therefore there is no need for an external source of fuel, which is usually methane rather than hydrogen as it is more readily available. Electrodes based on an all-ceramic design are also under development [27], and one design that has the same material as both fuel and oxygen electrode [28]. Although this has a lower performance than an LSM-YSZ|YSZ|Ni-YSZ cell, developments in this area may make it viable in future, as it has some advantages, such as being more redox-cycle tolerant, sulphur resistant and coking resistant.

1.3.3 Cell microstructure

Various microstructural factors, such as porosity, electrode thickness, particle size, and percolation have a large impact on the cell performance. These arise from the starting materials and fabrication methods. Therefore, an optimised microstructure is crucial to achieve a high performance cell.

The porosity of the electrodes is usually measured as the volume percentage of pores in the electrode, but the pore size distribution is also important. If the porosity is too low, and there is a high flow of gas through the electrode, e.g. at high currents, this can cause a diffusion polarisation resistance to be observed. This may also appear if there is a stagnant layer of gas over the electrode [29]. However, if the porosity is too high, electronic and ionic conductivity will limit cell performance. These effect is particularly important in tubular supports, which are many times thicker than the other active layers.

The effect of particle size distribution on porosity and performance is illustrated by a study on a Ni/CGO (cerium doped gadolinium oxide, an ion conductor) supported tubular cell. Two different sizes of NiO particles were used to make the anode support - $0.5\ \mu\text{m}$ and $2.5\ \mu\text{m}$. Different microstructures were seen by SEM examination, and after reduction, the electronic conductivity was similar in both supports. However, the cell made with $2.5\ \mu\text{m}$ NiO had a maximum power density twice as high as the cell made with $0.5\ \mu\text{m}$ particles, and impedance measurements showed that the difference was due to diffusion in the support. Although the coarser microstructure had a shorter TPB length, the larger pores and high porosity allowed greater diffusion of gases in the support, which improved the performance [30].

Other microstructural parameters of importance are the tortuosity and percolation of the electrodes. Tortuosity is the ratio of the path length of interconnected particles of the same type, e.g. LSM, though a electrode, to the thickness of the electrode. Percolation expresses the fraction of particles of one type that are connected to each other. A percolation threshold for a material in a composite electrode is often seen. This is usually expressed in vol.% of a particular phase, above which value there is a sudden increase in

peroclation. This is about 30 vol% for NiO/YSZ composites [31]. These concepts are often used to predict the ohmic and polarisation resistances of composite electrodes in computer models by modelling inter-particle contact and calculating electronic and ionic pathways [32].

Sealing of the reversible SOFC is also necessary to prevent crossover leakage and direct combustion of fuel gases. Tubular SOFC are usually designed such that one end is closed, and the other is left open as a gas inlet. They are sealed to the gas inlet tube, which may also function as the current collector or interconnect between cells, connecting several cells in series. If this is the case, the seal must be electrically conductive. Glass-ceramics are used for non-conductive seals, and metal brazes for conductive seals.

Glass-ceramics are materials which are designed to soften but not fully melt at a temperature above the SOFC operation temperature, thus filling the joint. When they are cooled to the SOFC operating temperature, they pass through a glass transition temperature, and crystallise, becoming rigid and making a seal. Various types of glass-ceramics have been tested, but the most effective have been silicate based glasses doped with alkaline-earth metals [33]. Another study reported the successful sealing of FeCrAlY steel (22 % Cr, 5% Al, 0.2 % Y, balance Fe), to a fuel cell with sodium aluminosilicate glasses. A MgO filler was also tested, which modified the thermal expansion coefficient of the glass-ceramic, matching it more closely with that of the steel [34].

Braze materials may also be used, if an electrically conductive seal is required. The silver-copper oxide system is the most common braze material used [35]. This consists of a mixture of copper and silver powders, sometimes mixed with an organic binder, that is applied to the fuel cell and gas delivery tube/interconnect. It may be sintered in a vacuum furnace or a reducing atmosphere, or also in air, in which case the copper oxidises. The CuO coats the surfaces of the interconnect and the ceramic fuel cell, allowing the silver to wet them and make a seal between the two components [36, 37]. Such seals have been tested in a fuel cell environment, i.e. with hydrogen on one side and oxygen on the other. Evidence of hydrogen and oxygen diffusion into the seal is seen, but this does not affect its mechanical integrity [38]. The seals have also been subjected to thermal cycling without failure [39], when the fuel cell has been brazed to FeCrAlY steel, which has a similar thermal expansion coefficient to YSZ. The Ag-CuO braze material is quite ductile, but has a higher thermal expansion coefficient than the steel. Furthermore, if braze is placed in a joint which is under mechanical load, it may be squeezed out during brazing when it melts. These problems have been addressed with low CTE filler material, such as alumina, which reduces the CTE of the braze, and increases its viscosity [40].

A tubular support material should have high electronic conductivity, and sufficient porosity to allow diffusion of gas through it. Tubular supports are usually made from either LSM [18, 41] or Ni/YSZ [42, 43]. The advantage of using LSM is that the fuel electrode can be on the outside of the cell, so the hydrogen and steam may circulate in a reversible SOFC system between the cells by convection. If the electrode was on the inside of the cell, steam would build up as the cell was run in fuel cell mode, hydrogen would be depleted, and the performance of the cell would become limited by diffusion

losses. However, the disadvantage of using LSM as the support material is that the YSZ electrolyte must be coated on top of it, and sintered to a high temperature, which may cause lanthanum and strontium zirconate formation. If a NiO/YSZ support is used, the electrolyte may be sintered to a high temperature, and the LSM/YSZ electrode may be coated on at a lower temperature.

The gas delivery tube/interconnect connected to the SOFC is usually made of either a ceramic material, or a stainless steel with a similar thermal expansion coefficient to that of the SOFC materials. Stainless steels such as FeCrAlY or Crofer-22-APU, a special steel developed specifically for fuel cells, are often used. However, coatings have to be applied to these steels to prevent rapid oxidation under fuel cell operating conditions, or poisoning of the fuel cell electrodes with chromium [44].

1.3.4 Fabrication methods

A multitude of different techniques are used in the manufacturing of SOFC, e.g. tape casting, extrusion, dip coating, electrochemical vapour deposition, electrodeposition, screen printing, to name a few. SOFC are highly sensitive to the processing parameters used, such as the particle sizes and compositions of ceramic powders, organic binder systems, sintering ramp rates and component shrinkage rates, thermal expansion matching of different components, anode reduction profiles, etc. Therefore, two cells which are nominally identical, i.e. made at the same time in the same way, may give different performances, if the control of the manufacturing method is not accurate enough. The most common fabrication methods used in industry are shown in table 1.3.1, and materials systems and geometries that were being commercialised in 2010 are shown in table 1.3.2 [16].

The most commonly used method in industry is tape-casting, which is an inexpensive and versatile process which suspends ceramic powder in a matrix of organic binders, making a flexible tape. This can be rolled into shape, or laminated with other tapes to make a support layer, cell electrodes, or both. If the organic components and ceramic powders are optimised so that their burnout temperature and sintering shrinkage respectively, are matched, then cells can be co-sintered.

Extrusion is also used to produce tubes, and it has the advantage that a tube can be produced without any joints, which are necessary in a tubular tape cast cell. This makes the cell more intrinsically robust. It is normally used to produce the support, which can be either LSM [45], or Ni-YSZ [46]. There are two main binder systems used for extrusion of tubes, either aqueous or thermoplastic.

The aqueous system commonly uses the ceramic powder such as LSM, with a cellulose binder and water, and may include other binders, or pore formers such as polymethyl methacrylate [47]. Components are mixed using a high shear mixer, and then left to age for several hours. The ageing period allows the cellulose to fully hydrate: for hydroxyethylcellulose, hydration takes place over a period of several hours. [48]. Nuclear magnetic resonance (NMR) measurements on water absorption on hydroxyethylcellulose have shown that several water molecules bind tightly to each hydroxyl group, in an inner solvation shell. Outside this, there is a second solvation shell, and then free water [49]. Without this

ageing period, the water is not sufficiently bound to the cellulose, and may be squeezed out of it by the high pressures found in an extruder die.

Process	Layer thickness	Components made	Advantages
Screen printing	$>5\ \mu\text{m}$	electrodes, electrolyte	cheap, co-sintering
Extrusion/co-extrusion	$100\ \mu\text{m}$ -mm	electrodes, supports	complex shapes
Tape casting	$>10\ \mu\text{m}$	whole cell	cheap, co-sintering
Dip coating[50]	$>1\ \mu\text{m}$	whole cell	cheap
APS[51]	$>20\ \mu\text{m}$	electrolyte, electrodes	dense electrolyte
Wet powder spraying[52]	$>10\ \mu\text{m}$	electrolyte, electrodes	cheap
Catalyst impregnation	n/a	electrodes	nanosized surfaces

Table 1.3.1: A comparison of cell fabrication techniques. Electrode/electrolyte layers with a thickness $>100\ \mu\text{m}$ are not usually produced, due to gas diffusion losses (electrodes) or high ohmic resistance (electrolytes). Catalyst impregnation may also be called infiltration. Reproduced from [16]. APS = atmospheric plasma spraying.

Company	Geometry	System size	Support	Fabrication methods
Acumentrics[53],[54]	tubular	0.5-5 kW	Ni-YSZ	extrusion, APS, DC
Ceramic Fuel Cells[55]	planar	2kW	Ni-YSZ	tape casting
Ceres Power[56]	planar	0.5-5 kW	steel	WS, SP
Delphi[57], [58]	planar	2-10 kW	Ni-YSZ	tape casting, SP
Hexis[59]	planar	1-3.5 kW	steel	tape casting, SP
Rolls-Royce FCS[17]	planar	1-2 MW	MgO/Al ₂ O ₃	extrusion, SP
Siemens[60]	planar	3-300 kW	LSM	extrusion, APS
Topsoe Fuel Cell[61]	planar	125-250 kW	Ni-YSZ	tape casting, WS/SP
Versa Power Systems[62]	planar	2-30 kW	Ni-YSZ	tape casting, SP
Violet[63]	planar	1-50 kW	YSZ	tape casting, SP

Table 1.3.2: Commercialisation of solid oxide fuel cells. A planar geometry allows for an increased volumetric power density. Most companies use the same cheap fabrication techniques, but a variety of processing parameters, thus producing cells with different microstructures, and performances. Reproduced from [16]. APS = atmospheric plasma spraying, SP = screen printing, WS = wet spraying, DC = dip coating.

Thermoplastic extrusion typically uses a polypropylene binder, with hydrophobic dispersants, and the extrudate is melted inside the extruder barrel, extruded when molten, and cooled. It has been used to make thin-walled YSZ tubes, using a polypropylene and paraffin wax binder. Stearic acid was coated onto the YSZ particles in a high-shear mixer before the other components were added, and this allowed a significant increase in the volume percentage of YSZ in the extrusion mixture [64]. Another thermoplastic binder system was also used to successfully make thin-walled YSZ tubes. It had similar components to the

first system described, except ethylene-vinyl acetate and a commercial co-polymer were substituted for polypropylene [65]. This method has not been applied to the extrusion of support tubes for SOFC, but a gelatinised cellulose-polyethylene composite has been extruded [66].

There are two main types of extruders used to produce tubes. Screw extruders use a rotating screw that draws material along a barrel, and forces it through a die at high pressure, in a continuous feed process. The screw is usually tapered, with the core diameter increasing towards the die. This reduces the volume in the barrel, causing a buildup of pressure which subjects the extrusion mix to a high shear force. Therefore, screw extruders are also used for high-shear mixing. Ram extruders use a piston to force the extrusion billet along a barrel, and then through a die, in a batch process [67].

The die geometry is critical in preventing fracture of the extruded material, particularly for aqueous-based systems. Surface or ‘sharkskin,’ fracture arises because inside the die, the inner core of the extruded part travels faster than the outer part, which is slowed down by friction at the wall. When it exits the die, the outer layer speeds up to match the speed of the inner layer, and the tensile forces cause fracture. It has been shown that increasing the extruder barrel:die diameter ratio reduces the depth and severity of surface fractures [68]. Such surface fractures may also be partially mediated with a die insert, which changes the length of the die [69]. An extrusion model has shown that the die entry angle, which is the angle that the tapered entrance of the die makes relative to the sides of the barrel, affects surface fractures. Increasing the die entry angle also increases surface fractures [70]. The homogeneity of extrusion pastes may also be studied with high-frequency pressure transducer data collected during extrusion [71]. Homogeneity is crucial if an extrusion product which does not vary from batch to batch is to be obtained.

Dip-coating is an inexpensive method to apply a YSZ electrolyte to a tubular cell, where other methods, such as screen printing cannot be used, due to the tubular geometry. The YSZ powder is typically dispersed in a slurry, with a variety of organic binders, dispersants and solvents. Table 1.3.3 shows eight methods of making a electrolyte ceramic slurry for dip-coating. Most methods use YSZ, some with nanoparticles, or in the low μm range, with a poly vinyl butyryl binder. Phosphate or amine-based dispersants are generally used, and a variety of solvents are used, mostly with alcohol or ketone functional groups. Some success in producing dense electrolytes was observed by mixing YSZ slurries with YSZ sols, or by coating both alternately. This allowed the dense layer thickness obtainable by a single sintered layer to be increased to at least 20 μm [72, 73].

One study was able to vary the dense YSZ layer thickness from 8 μm to 80 μm by varying the YSZ powder content and the methyl ethyl ketone:ethanol (MEK/EtOH) to polymeric YSZ sol content of the suspensions used [74]. One study used dip-coated layers of YSZ with intermediate sintering steps, each layer healing the cracks in the previous one. The dip-coating slurry was allowed to settle before dipping, so that any large agglomerates fell out of suspension. This helps to prevent flaws in the YSZ electrolyte [41]. The sintering temperatures and durations used in table 1.3.3 shows that at 1300 °C, at least 3 h are needed for densification of YSZ layer, whereas at 1400 °C, 2 h is sufficient. This depends

very much on the particle size of the YSZ, the green density of the dip-coated layer, and also on the type of YSZ used.

Substrate	Ceramic	Binder/ Dispersant	Solvent	Thickness (μm)	Sintering T. ($^{\circ}\text{C}$), time
LSM [45]	ScSZ, CGO	PVB/diamine	EtOH based	-	1300, 6 h
NiO/YSZ [75]	nano YSZ	-/PAA	water	20-30	1400, 2 h
NiO/YSZ [76]	ScSZ, 3YSZ	PVB/fish oil	IPA, toluene	-	1300, 3 h
NiO/YSZ [47]	CGO	PVB/amine	MEK	-	1400, 1 h
LSM* [41]	nano 3YSZ	PVB/-	EtOH	30	1400
NiO* [77]	YSZ	PVB/TEA	MEK:EtOH	16	1500, 5 h
NiO/YSZ [42]	8YSZ	PVA/fish oil	IPA, toluene	<15	1400, 3 h
NiO/YSZ* [72]	8YSZ	-/PP	MEK:EtOH	10-20	1400, 2 h

Table 1.3.3: Comparison of different electrolyte dip-coating slurries. Binder acronyms are: PVB = polyvinyl butyryl, PVA = poly vinyl alcohol, dispersants: PAA = polyacrylic acid, TEA = triethanolamine, PP = polyphosphate. The ceramics are: CGO = gadolinium doped cerium oxide, ScSZ = scandium doped zirconium oxide., and the solvents are EtOH = ethanol, IPA = isopropyl alcohol, and MEK = methyl ethyl ketone. All samples co-sintered except those marked *.

It was also found that the particle size of the LSM used to make the substrate affected the performance of the cell. Two different particle sizes of LSM were used to make composite oxygen electrodes. The LSM with the larger particles needed to be sintered to a higher temperature than the LSM with the smaller particles in order to achieve the same polarisation resistance [78]. Therefore, because the LSM will be sintered to at least 1300 $^{\circ}\text{C}$ when the YSZ layer is deposited on it, in order to maintain the best cell performance, large particles of LSM should be used.

One of the ways to make a seal on a fuel cell that is also electrically conductive is to use a silver-copper reactive air braze. This is applied in powder form, or mixed with an organic binder, and when heated up, the copper oxidises, coating the surface of the fuel cell, and the gas delivery manifold. The silver fills the gap in the joint by capillary action.

Table 1.3.4 compares various Ag-CuO brazes. Brazes with different levels of CuO have been studied, and the contact angle of the braze when molten was measured for different compositions. As the percentage of CuO increased, the contact angle decreased. CuO precipitates at the ceramic or metal surfaces, and the remainder of the gap in the joint is filled with silver [36]. A strength test of various YSZ:FeCrAlY joints shows that 4 mol.% or 8 mol.% braze gives the strongest joint [39]. Thermal cycling of a YSZ:Crofer-22-APU steel brazed joint in air or 5% H_2 shows that the braze could withstand up to 50 cycles from 70 $^{\circ}\text{C}$ to 750 $^{\circ}\text{C}$ at a rate of 75 $^{\circ}\text{C min}^{-1}$ [37]. For joints with larger gaps, the weight of the pieces to be brazed may cause it to be squeezed out of the joint. This can be avoided if a ceramic filler material is mixed with the braze [40].

Braze composition (mol.%)	Substrate type	Sintering temp. (°C)	Sintering atmosphere
7-17 CuO-Ag [79]	PbMgNb ceramic	1050, 1100	air
1 CuO-Ag [80]	Al ₂ O ₃	946	air
0-69 Cu-Ag [36]	LSCF	1050, 1100	air
1-69 Cu-Ag [39]	YSZ/FeCrAlY, Crofter-22 APU	1050	air
4-69 CuO [37]	Crofer-22-APU	1000	air
4-69 CuO, 0.5 TiH ₂ [81]	LSCF	1050	air
Ag/CuO, ceramics [40]	ceramics, metals	1000	air
2-8 CuO-Ag [38]	Al ₂ O ₃	980, 1100	air
0-69 CuO-Ag [82]	430, 441, 446 steels	800-1300	air
Ticusil, Al ₂ TiO ₅ , TiH ₂ [83]	YSZ, 304, 430 steels	880	vacuum
40 Cu-Ag [84]	316 steel, Cu, Al ₂ O ₃ filler	820	vacuum
66-74 Cu, 1.5-3 Ti-Ag [85]	316 steel, Al ₂ O ₃	850-950	vacuum
66 Cu-2 Ti-Ag [86]	316 steel, Al ₂ O ₃	850	vacuum

Table 1.3.4: A comparison of various brazing methods, with reactive air brazes composed of Ag-CuO, and also brazes containing Ti, sintered under vacuum.

Hydrogen and oxygen are both soluble in silver, so the dual atmosphere stability of a brazed joint was tested using 2 mol.% and 8 mol.% CuO-Ag brazes, joining two pieces of alumina. They withstood a dual atmosphere test at 800 °C for 100/1000 h, with humidified hydrogen on one side of the joint, and air on the other side [38].

Another type of brazed joint uses titanium hydride to react with any oxides on the surfaces of the pieces to be joined, which improves the wetting of the braze to the interfaces. During a dual atmosphere test, Ticusil (a Ti-Cu-Ag alloy) brazed joints, showed extensive void formation in the part of the Ticusil that was not in the joint, which was attributed to steam formation. However, the Ticusil compressed in the joint did not suffer from this [83]. When a small amount of TiH₂ is added to a Ag-CuO braze, it improves wetting of the braze - a SrTiO₃ layer is seen at the braze:LSCF interface. However, it was shown that TiO₂ layers as little as 14-60 nm thick can cause significant resistivity [81]. A 316 stainless steel:alumina joint brazed with a Ti-Cu-Ag braze showed a reaction layer close to the steel containing Ti, Cu, and Ni, Cr and Fe. Therefore, elements from the steel interacted with the brazing material. A Cu/Ag/Ti matrix was seen in the middle of the joint. The joints were free from porosity and cracks [85].

Screen printing may be used to produce electrodes of uniform thickness for SOFC, and is used extensively in industry, as can be seen from table 1.3.2. It may be used to print all the cell layers, and if the shrinkage during sintering of each layer is matched, then cells may be co-sintered [17]. It typically uses a ceramic powder, which is ball-milled with a dispersant in a solvent such as acetone. A binder is added, and the solvent is evaporated, to produce a screen printing ink with a high viscosity and high volumetric solids loading.

Some inks may be thixotropic, or shear thinning, so that when they are being printed and subjected to a high shear force, they run through the screen easily, and slump on the ceramic substrate, removing any traces of the screen mesh. They will then become stiffer, so they do not run on the ceramic substrate. Screen printing may also be used to produce symmetrical cells on YSZ pellets [87], or composite electrodes, with a graded microstructure, i.e. a variation in the ratio of electronic and ionic conductor across the electrode. This improves the electrochemical performance of the electrode [88]. Screen printing inks may also be hand painted onto tubular cells, as they have well dispersed ceramic particles, and a high solids loading. Therefore, they form a layer of high green density on the cell surface with no agglomerates. This may be useful for creating electrolyte layers on tubular cells.

1.3.5 Proposed reversible SOFC design

From this survey of literature, a design for a reversible SOFC may be proposed. Fig. 1.3.4 shows a schematic of the cell, and table 1.3.5 shows the different manufacturing methods proposed for each of the components.

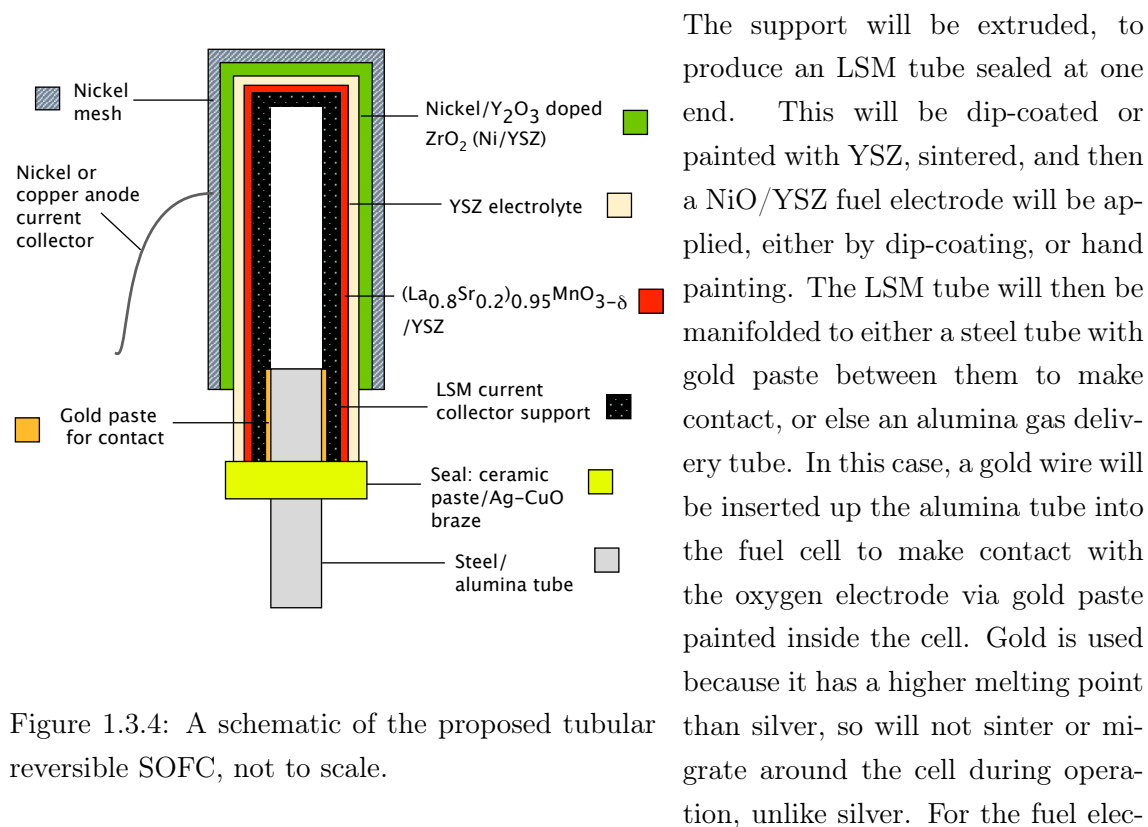


Figure 1.3.4: A schematic of the proposed tubular reversible SOFC, not to scale.

For the fuel electrode current collection, a Ni mesh will be wrapped around the cell, and painted with silver paste if necessary in order to make contact with the fuel electrode.

Component	Material	Manufacturing method
Support	$(\text{La}_{0.8}\text{Sr}_{0.2})_{0.95}\text{MnO}_{3-\delta}$	extrusion
Oxygen electrode	$(\text{La}_{0.8}\text{Sr}_{0.2})_{0.95}\text{MnO}_{3-\delta}/8\text{YSZ}$	painting/YSZ dip-coat
Electrolyte	8YSZ	dip-coat/painting ink
Fuel electrode	NiO-8YSZ	painting ink
Fuel electrode current collector	Ni mesh/Ag paste	mesh wound/painting
Seal/interconnect	Cu-Ag braze or ceramic paste	brazing or painting

Table 1.3.5: Proposed materials and manufacturing methods for the tubular reversible SOFC. The inks used will be screen printing inks. 8YSZ is ZrO_2 doped with 8 mol% Y_2O_3 , or $\text{Zr}_{0.852}\text{Y}_{0.148}\text{O}_{2-\delta}$.

1.4 Reversible SOFC microstructural characterisation

The SOFC has a microstructure on the order of 100 nm - 100 μm , due to the particle sizes of the ceramic powders used to make it, and is therefore suited to examination with a scanning electron microscope (SEM), which can reveal the details of the microstructure. Fig. 1.4.1 shows a diagram of an SEM. It operates in high vacuum, using a beam of electrons incident on the sample, which allows for a higher resolution than an optical microscope, because the wavelength of the electrons is shorter than the wavelength of photons in visible light. The voltage of the electron beam may be adjusted in the kV range. Electrons and radiation are back-scattered from the sample, and detected. An image is produced from the signal. Non-conductive samples to be examined are often coated with gold in an evaporation or sputtering process. This prevents the surface of the sample charging under the electron beam which distorts the image. However, samples that have a mixture of a conductive and non-conductive phases, such as a reduced Ni-YSZ fuel electrode, may be imaged without a gold

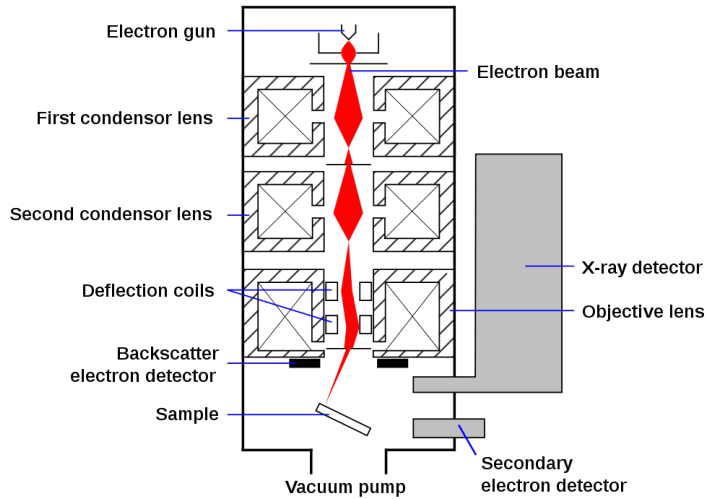


Figure 1.4.1: Schematic of a scanning electron microscope (SEM), not to scale [89].

coating at low accelerating voltages. This method was applied to a cross section of Ni-YSZ electrode, using a field emission-SEM and a secondary electron detector. Particles which are less conductive were observed to charge more and appear brighter. Therefore, four phases could be distinguished, as they back-scattered different numbers of electrons at the low accelerating voltage used: YSZ, non-percolating Ni, percolating Ni, and pores [90].

Software can be used to analyse SEM pictures. One study analysed the 2D microstructure from a series of SEM images, then created a 3D model of the microstructure from the information. This was used to inform a computer model of SOFC operation - to relate microstructural features to performance of the cell [91, 92]. SEM images can also be analysed by software to determine levels of porosity, and pore size distributions, based on the contrast between pores and ceramic grains in an SEM image.

Energy-dispersive X-ray spectroscopy may be used to understand qualitatively and quantitatively, the distribution of elements through a sample. It is typically carried out at higher accelerating voltages in an SEM. The incident electrons strike the sample, exciting core electrons in surface atoms into higher energy levels. When these relax to lower energy levels, they emit X-rays which have energies that match the difference between the excited and the ground state energy levels. As each element has different gaps between the electron energy levels, the X-rays emitted are characteristic for that element. A detector measures these X-rays, and can resolve the position of the atoms of each element. If standard samples are employed, the system can be calibrated to measure quantitatively the amount of each element present on the surface in a specific area.

Therefore, by using EDX, phases in the sample can be distinguished. This is useful to detect the formation of undesirable phases, such as lanthanum/strontium zirconates in LSM-YSZ electrodes. It was used to determine where the elements in a Ag-CuO braze segregated to, and showed the formation of Cu-Cr compounds at the interface [39]. This is very useful, as even small amounts of a compound at an interface can have a dramatic effect on the ionic or electronic conductivity across the interface.

There are several advanced techniques for directly measuring the microstructure of the fuel cell, which can be either destructive, such as focused-ion beam (FIB)-SEM, or non-destructive, such as X-ray computed tomography. FIB-SEM was applied to a Ni-YSZ fuel electrode, by using an ion beam to ablate a series of 50 nm layers from the electrode, with SEM images being taken after each layer was removed. The images were analysed by a computer, and a very detailed 3D model of the electrode was obtained. From this, parameters such as the percolation of the Ni and YSZ phases, the TPB length, porosity, tortuosity, etc. could be determined [93]. This is one of the best ways to fully characterise the microstructure, because of the high resolution obtainable in 3 dimensions, down to 20 nm - 30 nm [94, 95]. However, it is quite time-consuming, and only examines a small area of the electrode.

A comparable non-destructive method is X-ray computed tomography, which is extensively used in medicine. X-rays are passed through the sample, and an image is recorded, it is rotated slightly, and then the process is repeated. The resolution is 50 nm or better. The method is more accurate at microstructure and pore characterisation than other methods such as mercury-intrusion porosimetry (MIP), because it can see isolated pores that MIP cannot, and provides better estimates of other parameters [96].

The particle size of the ceramic powders used is also very important in determining the sintering behaviour, and the electrochemical performance of the cell. This can be measured by a particle size analyser, which uses a laser to measure the size of particles in suspension

as they are circulated around the instrument. This is routinely used to measure particle size distributions of ceramic powders, and was used to study the effect of the synthesis conditions of LSM, on the particle size distribution of the product powder [97].

1.5 Reversible SOFC performance

The performance of reversible SOFC may be measured in a similar way to that of SOFC or SOEC. As these are electrochemical cells, one of the chief methods used to understand their performance is electrochemical impedance spectroscopy, which is also called ac impedance spectroscopy, or impedance measurements. In order to understand the processes occurring in a single electrode, symmetrical cells are used. Testing of the whole cell is also essential, and long term tests of the cell in fuel cell or electrolysis mode, reveal the electrical performance of the cell over time. Degradation mechanisms in the cell can then be explored, and optimisation of the cell to produce a high, durable performance.

1.5.1 Symmetrical cell testing

Symmetrical cells are often used to examine the LSM-YSZ oxygen electrode. A typical symmetrical cell geometry is shown in fig. 1.5.1. The cells usually have a YSZ electrolyte support of 1 mm - 2 mm thickness, and LSM-YSZ and LSM layers between 5 μm - 30 μm thick.

Ac impedance is a method that applies a small ac signal, of magnitude in the range 10 mV - 50 mV or mA root mean square (r.m.s) to a cell which is at equilibrium. This is sufficient to gather data without perturbing the cell equilibrium very much. If a sinusoidal voltage is applied, the current response is measured, and vice versa. From this, the complex impedance can be calculated. A very wide range of frequencies can be scanned stepwise, though for measurements on symmetrical cells and fuel cells, typically frequencies in the range: 10 mHz - 1 MHz are scanned. Below this range, measurements take a long time, and above it, no useful data can generally be obtained because of inductive effects arising from the cell contact wires, or the frequency response analyser instrument used to record measurements. The impedance of a resistor (Z_R) is equation 1.5.1, and the impedance of a capacitor Z_C is equation 1.5.2, where ω is the angular frequency.

$$Z_R = R \quad (1.5.1)$$

$$Z_C(\omega) = \frac{1}{j\omega C} \quad (1.5.2)$$

Therefore, the impedance an RC circuit: i.e. a resistor in parallel with a capacitor, is equation 1.5.3. This gives a perfect semicircle on a Nyquist plot ($-Z_{img}, \Omega$ vs Z_{real}, Ω .)

$$Z(\omega) = R - \frac{j}{\omega C} \quad (1.5.3)$$

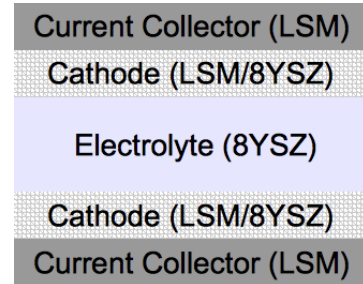


Figure 1.5.1: Symmetrical cell schematic - not to scale.

For an RC circuit, there is a characteristic time constant τ , defined by equation 1.5.4, which shows how fast the process is occurring. Different electrochemical processes will have different time constants.

$$\tau = RC \quad (1.5.4)$$

These RC elements may be combined to make an electrical equivalent circuit, which is a representation of the electrochemical processes occurring in the cell, by electrical circuit elements. This circuit should also include resistor elements to account for the ohmic resistances in the cell electrodes and electrolyte. It is important that the elements in the electrical equivalent circuit are justified by comparison with experimental data, because many different equivalent circuits can be used to fit the same impedance data. In one study, two different impedance circuits were compared, and an analysis of the microstructure of the electrode showed that one was preferred to model the electrode [98].

Measurements can be made on cells such the one in fig. 1.5.1, by connecting a wire to each current collector and doing an impedance sweep, by doing measurements at several frequencies in each logarithmic frequency decade. However, in this case, the resistance of the wires leading to the cell will also be measured. Therefore, in order to examine the resistance of the cell alone, it is better to use four wires - two for applying the ac current signal, and a separate two for monitoring the voltage. The current and voltage wires on each side of the cell should be connected together as close as possible to the cell. The measured resistance will then only be that between the connection point on one side of the cell to the connection point on the other side.

Ac impedance testing on symmetrical cells with LSM-YSZ electrodes has been used to distinguish the limiting electrochemical processes in the cell. One study examined many impedance spectra from literature, and also performed ac impedance measurements on cells, and divided the arcs seen into five different types, named A-E. These were characterised by their capacitance, frequency at peak $-Z_{img}$, activation energy, and dependence of polarisation resistance on P_{O_2} [29]. Diffusion processes are often seen have have larger time constants, and so ac impedance may be used to investigate gas diffusion through porous support tubes [99]. The relationship between oxygen partial pressure and polarisation resistance R_p is usually defined according to the equation 1.5.5, where x is an experimentally determined coefficient.

$$\log R_p = \log P_{O_2}^{-x} \quad (1.5.5)$$

For an LSM-YSZ electrode, a value of 0.5 was found for x , in the P_{O_2} range of 1×10^{-4} atm. to 0.2 atm. Two limiting processes were found for this electrode, a dominant process that occurred at low frequency, which was ascribed to a diffusion polarisation resistance related to oxygen absorption on the electrode surface. The other process was only significant when the electrode was under polarisation, and is not definitely assigned to a physical process, but is often assigned as an activation step of the oxygen reaction [100]. The effect of pressure on the impedance of LSM-YSZ electrodes at higher oxygen pressures has also been determined, for samples with a Sm doped CeO_2 interlayer between the LSM-YSZ and

the YSZ electrolyte. The dominant limiting process had a dependence of the polarisation resistance on oxygen pressure of $x = 0.25$ according to equation 1.5.5, in the range 1 bar to nearly 100 bar. It was ascribed to charge transfer in the oxygen reduction reaction. The other limiting process was invariant with P_{O_2} , and was attributed to transport of oxygen in the electrolyte [101]. Therefore, ac impedance measurements on symmetrical cells may be used to measure the magnitude, and possibly understand the physical nature, of the fundamental processes occurring in the electrode [102].

Impedance measurements may also be used to find the best fabrication parameters for SOFC: measurements on a range of symmetrical cells sintered at different temperatures showed that there was an optimum sintering temperature for LSM-YSZ electrodes. If the sintering temperature is too high, the TPB length and electrochemical performance are reduced. If the sintering temperature is too low, there is insufficient sintering of the LSM and YSZ particles to each other, and the ohmic resistance of the electrode increases, limiting the performance [103]. Ac impedance is able to detect small changes in microstructure, and a review of impedance data gathered on cells with different microstructure, shows completely different impedance spectra [104].

1.5.2 Whole cell testing

Testing of whole SOFC/SOEC is very important, to ascertain their electrical performance. This is accomplished with ac impedance measurements, and I/V curves. These can be measured at a series of fixed currents, or a series of fixed voltages. If the voltage is set, the current is measured, and vice versa. A check for hysteresis is often made to ensure that the cell is in a steady state, e.g. by incrementally increasing the voltage up to the maximum level, then decreasing it, and seeing if the currents are the same in both cases. The application of DC current across the cell has been observed to activate the LSM-YSZ electrode, reducing the manganese ions in the LSM, and improving cell performance [105, 106].

There are a variety of cell degradation mechanisms, which are different for the NiO/YSZ electrode, and the LSM-YSZ electrode. Firstly, the NiO/YSZ electrode, sintered when the cell is fabricated, must be reduced to the active fuel electrode Ni-YSZ, by the flow of hydrogen on the fuel side of the cell. This electrode is susceptible to degradation from a variety of mechanisms, as in table 1.5.1. Coarsening of Ni during testing was observed by two authors [22, 107], which leads to reduced TPB length, and also increased ohmic resistance in the cell. Nickel also oxidises at high steam concentrations, as the P_{O_2} can increase by 2-3 orders of magnitude as the steam concentration increases. During fuel cell operation, hydrogen is consumed, and steam is produced, so the local concentration of steam at the electrode surface may be very high. Ni is partially oxidised, and it was found that at a steam concentration of 40% in the system during electrolysis, irreversible damage occurs to the Ni/YSZ electrode. Redox cycling tests on Ni-YSZ electrodes showed that there was an irreversible linear expansion of the Ni-YSZ electrode, which caused cracking in the cell. This can be mitigated by optimising the Ni-YSZ microstructure. The best temperature to reduce the Ni was found to be 850 °C [108]. Redox cycling can cause

cracking that destroys the cell, if the effect is severe [109].

Table 1.5.1 also shows some degradation mechanisms of the LSM-YSZ electrode. Thermal cycling from 800 °C to room temperature, and then back to 800 °C, of an LSM-YSZ electrode on a YSZ electrolyte, showed a significant increase in resistance from before and after the thermal cycle. This was assigned to a reduction in TPB length during the thermal cycle [110]. Another degradation mechanism in LSM-YSZ electrodes, is delamination from the YSZ electrolyte. This was observed to be a problem for a cell during a 200 h test at 800 °C, and was worse in electrolysis mode than fuel cell mode. It was thought to be a result of oxygen being produced at the LSM-YSZ|YSZ interface, caused by the increased production of lanthanum and strontium zirconate phases, which lead to an oxygen build-up at the interface. The high pressure of the gas then causes delamination. An LSM-YSZ|YSZ|Ni-YSZ cell switched several times between electrolyser mode and fuel cell mode showed some irreversible increase in ohmic resistance, which was attributed to reduction of the YSZ electrolyte at the LSM-YSZ|YSZ interface during cell operation [111]. The key to preventing these degradation mechanisms is optimisation of the microstructure of the electrodes and the cell. However, new materials are also being investigated which may also help to prevent reversible SOFC degradation.

Degradation mechanism, electrode affected	Test conditions/ temperature (°C)	Performance change/effects
Ni coarsening, Ni-YSZ [22]	-0.3 A cm ⁻² , 43% H ₂ O/H ₂ /800	+3.2% R _Ω /1000 h
Oxidation of Ni, Ni-YSZ [112]	OCV, 10-40% H ₂ O/H ₂ /800	larger R _Ω
Redox cycling, Ni-YSZ [108]	9% H ₂ /Ar/700,850,1000	+5% expansion
Thermal cycling, LSM-YSZ [110]	0.1 V, electrolysis/800	larger R _p
Delamination, LSM-YSZ YSZ [113]	0.25 A cm ⁻² /800	larger R _Ω

Table 1.5.1: Degradation mechanisms of the Ni-YSZ and LSM-YSZ electrodes. R_Ω = ohmic resistance, R_p = polarisation resistance.

1.5.3 Reported reversible SOFC performance

In order to illustrate the key goals for commercialisation of fuel cells, table 1.5.2 summarises the goals of the U.S. SECA (Solid-State Energy Conversion Alliance), a U.S. government 10 year partner program with industry to develop various technologies, including fuel cells. The key factors for commercialisation of fuel cells are cost, performance, and durability, as was highlighted by a fuel cell company, Versa Power Systems in 2009 at the SECA annual meeting.[62]. Reversible SOFC have been shown to be capable of a high performance - one study showed a peak of -3.6 A cm⁻² at a cell voltage of 1.48 V in electrolysis mode for a cell tested at 950 °C [15]. Factors affecting the cell performance include the porosity of the support - a performance improvement on one cell was seen when the porosity was graded in the support [114]. However, the performance in this case is less than that measured by other authors [115], which suggests that the cell microstructure is not optimised.

Parameter	Phase I	Phase II	Phase III
Power rating (kW)	3-10	3-10	3-10
Cost per kW	\$800	\$600	\$400
Efficiency (stationary)	35-55%	40-60%	40-60%
Availability over 1500 h	80%	85%	90%
Power drop per 500 h, constant V	$\leq 2\%$	$\leq 1\%$	$\leq 0.1\%$

Table 1.5.2: Solid State Energy Conversion Alliance (SECA) selected targets (US D.O.E. program) [116]. Some of the solid oxide fuel cell manufacturers taking part in the SECA program are; Delphi, Rolls-Royce Fuel Cell Systems, Siemens, United Technologies and Versa Power Systems [16].

A key performance metric for reversible SOFC is their ability to reversibly store energy at high efficiency. This was discussed in section 1.2. Several different systems have been investigated to this end. One early attempt used planar SOFC, and hydrogen gas as an energy storage medium. A 0.075 m^2 cell was demonstrated, which had a resistance of $0.48 \Omega \text{ cm}^{-2}$ [117]. Another system based on SOFC made by Risoe National Laboratory, Denmark, showed a high performance in fuel cell and electrolysis mode. The improvement of electrical efficiency in electrolysis mode by utilising waste heat from nuclear power stations, or geothermal sources was discussed [15]. Another intermediate temperature reversible SOFC system, which was lanthanum gallate electrolyte supported, showed an ohmic resistance of $1 \Omega \text{ cm}^2$ at 800°C , in both fuel cell and electrolyser modes. In fuel electrode supported cells, low porosity in the support limited the cell performance [118].

A larger scale system used LSM-YSZ electrodes on YSZ, and found delamination at current densities of 0.5 A cm^{-2} after a few days operation. This problem was not found for LSCoF perovskites. It was also seen that the oxygen electrode polarisation was dominated by the activation overpotential. A cost model of a system running alternately in fuel cell mode and electrolysis mode, to use cheap electricity at night for electrolysis and produce electricity during the day, showed that this was only economical if there was a differential of at least $0.15\text{-}0.20 \text{ \$ kW hr}^{-1}$ between the daytime and nighttime prices. The storage of heat from the fuel cell cycle to the electrolysis cell cycle was not considered [113].

Another proposed reversible SOFC system which aims to improve electrical-chemical-electrical round trip energy storage efficiency, examined doing so by replacing some of the hydrogen with methane. Thermodynamic calculations showed that little heat is generated or consumed when the cell is cycled between $\text{CO}_2\text{-H}_2\text{O}$ rich and $\text{CH}_4\text{-H}_2$ rich gases. Therefore, only a little energy is lost as heat in the electricity-methane-electricity conversion. In order to avoid coking, the system should be operated at increased pressure ($\sim 10 \text{ bar}$) and a reduced temperature of 600°C [119]. In order to do this, different materials should be used, as the resistivity of YSZ and LSM-YSZ are too high at lower temperatures.

A reversible SOFC cell made of LSM-YSZ|YSZ|Ni-YSZ running on hydrogen and carbon monoxide has also been demonstrated, and the reaction mechanisms in the cell were

examined. Performance was limited by the electrolyte resistance, and charge transfer in the oxygen electrode [120]. A reversible microtubular SOFC has been demonstrated achieves power densities of 0.8 W cm^{-2} in fuel cell and 1.3 W cm^{-2} in electrolyser mode. Very high current densities were achieved, of 6 A cm^{-2} in electrolysis mode, which were attributed to electroreduction of the YSZ [121].

Proton conducting reversible fuel cells have also been investigated, and much better performance was obtained in electrolysis mode, comparable to some YSZ electrolyte systems, than in fuel cell mode [122]. However, the PEM-FC systems suffer from large activation voltages, which reduces their efficiency. Finally, previous research at the University of St Andrews demonstrated the concept of a tubular reversible SOFC, but power output was limited to the low mW range due to oxidation of the steel current collector during sealing [123].

While there has been some work on pressurised SOFC, notably by Siemens-Westinghouse [18], and Rolls-Royce Fuel Cell Systems are proposing a pressurised SOFC-hybrid gas turbine system, there has been little or no research on pressurised reversible SOFC.

1.6 Modelling of reversible SOFC systems

There are a variety of ways to model SOFC systems, from purely thermodynamic models, to fully 3D models with a defined cell geometry, and computational fluid dynamics modelling of the active cell and system. One model of an SOEC system proposes to increase the hydrogen production electrical efficiency by recuperating the heat from the SOEC exhaust, and using it to preheat gases flowing into the SOEC. It was shown for small stacks that increasing the cell voltage above the thermoneutral voltage could increase the hydrogen production efficiency, with heat recuperation. For larger stacks, the system was most efficient at the thermoneutral voltage [124]. Another prior study by the same author, based on a similar cell, except that the system uses a liquid silver electrode instead of LSM-YSZ, proposes to use oxidation of coal to produce hydrogen in electrolysis mode, with hydrogen oxidation to water in fuel cell mode. However, this is not a truly reversible system, since there is net carbon dioxide production [125]. A model of a proton-conducting electrolyte tubular reversible SOFC showed that a hydrogen-electrode supported design is favoured over an oxygen electrode supported design, due to the diffusion polarisation resistances [126]. However, for a YSZ based reversible SOFC, the study showed that the oxygen electrode was the preferred support material for electrolysis mode, and the hydrogen electrode for fuel cell mode [127].

The transient effects seen when switching between fuel cell mode and electrolyser mode has also been modelled. The study shows that steam concentration takes longer to change when the mode is switched, than the oxygen or hydrogen concentrations [128]. For a tubular SOFC geometry, finite volume models have been produced, which divide the fuel cell into sections, and calculate mass and heat flows into and out of each section per unit time, and thus show how heat and mass flows over time. This approach allows the variation of parameters such as temperature and gas composition along the cell, which means that effects such as depletion of fuel as it flows past the cell can be measured. One such model

considers the pressurised operation of a tubular fuel cell, and shows that the diffusion overpotential losses in such a cell are quite small, compared to the activation polarisation losses. One important result from the study was the sensitivity of the model to small changes in the parameters used to model activation energy [129]. Other models on the cell electrodes have shown that their performance is related to the radius of the particles used in the electrode, with a clear optimal size for the particles in the model [130]. There are many different types of SOFC models - dynamic models have been reviewed [131], as well as numerical models [132].

1.7 Thesis and objectives

Building on previous work at the University of St Andrews, where a tape cast reversible SOFC was produced, and tested in fuel cell and electrolysis mode, an oxygen electrode current collector (LSM) supported tubular reversible SOFC will be fabricated, using various methods including extrusion and dip-coating. The support will have an interconnected network of pores, with no cracks or large flaws, and a dense, $<40\text{ }\mu\text{m}$ thick YSZ electrolyte will be coated on top of it. Silver-copper brazes, and braze-LSM composites will also be investigated as a method of applying a seal and current collector to the cells. The cells will be tested to determine their electrochemical performance, by sealing them to a 316 stainless steel or alumina gas delivery tube. If a sufficiently good OCV is achieved, they will be tested with ac impedance measurements, and I/V curves will be recorded in fuel cell mode and electrolysis mode.

Pressurisation of an SOFC system improves performance, and reduces the polarisation resistance of LSM-YSZ electrodes. It also boosts the amount of energy that can be stored as hydrogen, by increasing the density of the gas in the system. The mechanism of performance improvement in the LSM-YSZ electrode will be investigated with pressurised measurements on symmetrical cells. The rate determining steps of the oxygen reduction reaction will be determined for this system, by matching the characteristics of the impedance arcs seen, with characteristics of arcs that have been assigned to rate-limiting steps in the literature. These results will be included in the computer model.

Energy storage by a reversible SOFC system, when electrical energy is converted to hydrogen during electrolysis, and then back to electricity when the system operates in fuel cell mode, is about 30% - 40% efficient. It is proposed that if the heat generated in fuel cell mode is stored in the system, and used in electrolysis mode, a much higher efficiency can be achieved - 50% - 75%. In order to investigate this, a computer model of a reversible SOFC system will be created, in collaboration with another PhD student at the University of Strathclyde. The current density will be assumed, then the voltage drops from ohmic resistance, and activation and diffusion and overpotentials will be calculated for a specified RSOFC geometry. From this, power outputs/inputs and electrochemical heat production/consumption, and ohmic heat production will be determined. The model will be designed such that it does not overheat during the reversible SOFC system cycle. Performance gain due to pressurisation to 70 bar will be quantified. The model will be linked to an electric power and controls system, designed at the University of Strathclyde,

so that the reversible SOFC system can interface with an electrical grid. The electrical storage efficiency over a reversible SOFC system cycle will be determined at different current densities, and the operation conditions and current density for optimum efficiency will be determined.

References

- [1] N. Stern, *Stern Review on the economics of climate change*, Report 1st edition, H.M. Treasury, 2006.
- [2] Elizabeth II, *Climate Change Act 2008, chapter 27*, Act of Parliament, The Stationery Office, 2008.
- [3] National Statistics, *Energy Trends*, Tech. Rep., Department of Energy and Climate Change, UK Government, 2010.
- [4] J. Apt, *J. Power Sources*, 2007, **169**, 369–374.
- [5] Ross, ‘SeaGen’ tidal energy generator, *Strangford Lough*, last checked 17/05/2011. <http://www.geograph.ie/photo/2005923>.
- [6] P. Hookway, *Cuileig Power Station Intake*, last checked 17/05/2011. <http://www.geograph.org.uk/photo/322471>.
- [7] D. Alves, *Brighton Earthship*, last checked 17/05/2011. <http://www.flickr.com/photos/dominicpics/3289308282/>.
- [8] P123, *Pelamis bursts out of a wave*, 2011, last checked 17/05/2011. http://commons.wikimedia.org/wiki/File:Pelamis_bursts_out_of_a_wave.JPG.
- [9] phault, *Offshore wind turbine, Thames estuary*, last checked 17/05/2011. <http://www.flickr.com/photos/pjh/sets/72157600188886762/>.
- [10] National Grid, *Metered half-hourly electricity demands*, 2009, last checked 17/05/2011. <http://www.nationalgrid.com/uk/Electricity/Data/Demand+Data/>.
- [11] P. Denholm, G. L. Kulcinski, *Energy Convers. Manage.*, 2004, **45**, 2153 – 2172.
- [12] C. Ponce de León, A. Frías-Ferrer, J. González-García, D. A. Szánto, F. C. Walsh, *J. Power Sources*, 2006, **160**, 716–732.
- [13] J. Kondoh, I. Ishii, H. Yamaguchi, A. Murata, K. Otani, K. Sakuta, N. Higuchi, S. Sekine, M. Kamimoto, *Energy Convers. Manage.*, 2000, **41**, 1863 – 1874.
- [14] A. Doddathimmaiah, J. Andrews, *Int. J. Hydrogen Energy*, 2009, **34**, 8157–8170.

- [15] M. Mogensen, S. H. Jensen, A. Hauch, I. Chorkendorff, T. Jacobsen in *Proceedings of the 7th European Solid Oxide Fuel Cell Forum (CD-ROM)*, European Fuel Cell Forum, Lucerne, pp. 301–311.
- [16] S. Gamble, *Mater. Sci. Technol.*, 2011, **27**, 1485–1497.
- [17] R. Goettler in *10th Annual Solid State Energy Conversion (SECA) Workshop*, Rolls-Royce Fuel Cell Systems (US) Inc., US DOE.
- [18] S. C. Singhal, *Solid State Ionics*, 2000, **135**, 305–313.
- [19] S. D. Vora in *5th SECA Annual Workshop and Core Technology Program Peer Review Workshop*, Solid State Energy Conversion Alliance (SECA), National Energy Technology Laboratory, Boston, MA, U.S.A.
- [20] A. V. Virkar, J. Chen, C. W. Tanner, J. W. Kim, *Solid State Ionics*, 2000, **131**, 189–198.
- [21] W. Bujalski, C. M. Dikwal, K. Kendall, *J. Power Sources*, 2007, **171**, 96–100.
- [22] G. Schiller, A. Ansar, M. Lang, O. Patz, *J. Appl. Electrochem.*, 2009, **39**, 293–301.
- [23] J. S. Kim, S. I. Pyun, *Electrochim. Acta*, 2009, **54**, 952–960.
- [24] Y. J. Leng, S. H. Chan, K. A. Khor, S. P. Jiang, *J. Appl. Electrochem.*, 2004, **34**, 409–415.
- [25] S. P. Jiang, *J. Mater. Sci.*, 2008, **43**, 6799–6833.
- [26] P. Duwez, F. H. Brown, Jr., F. Odell, *Journal of The Electrochemical Society*, 1951, **98**, 356–362.
- [27] C. Sun, U. Stimming, *J. Power Sources*, 2007, **171**, 247–260.
- [28] D. M. Bastidas, S. Tao, J. T. S. Irvine, *J. Mater. Chem*, 2006, **16**, 1603–1605.
- [29] M. J. Jørgensen, M. Mogensen, *J. Electrochem. Soc.*, 2001, **148**, A433–A442.
- [30] T. Yamaguchi, S. Shimizu, T. Suzuki, Y. Fujishiro, M. Awano, *Electrochem. Solid-State Lett.*, 2009, **12**, B151–B153.
- [31] R. M. C. Clemmer, S. F. Corbin, *Solid State Ionics*, 2009, **180**, 721–730.
- [32] D. Chen, Z. Lin, H. Zhu, R. J. Lee, *J. Power Sources*, 2009, **191**, 240–252.
- [33] K. S. Weil, *JOM*, 2006, **58**, 37–44.
- [34] K. A. Nielsen, M. Solvang, S. B. L. Nielsen, A. R. Dinesen, D. Beeaff, P. H. Larsen, *J. Eur. Ceram. Soc.*, 2007, **27**, 1817–1822.
- [35] J. W. Fergus, *J. Power Sources*, 2005, **147**, 46–57.
- [36] J. S. Hardy, J. Y. Kim, K. S. Weil, *J. Electrochem. Soc.*, 2004, **151**, J43–J49.

- [37] K. S. Weil, J. Y. Kim, J. S. Hardy, *Electrochem. Solid-State Lett.*, 2005, **8**, A133–A136.
- [38] J. Y. Kim, J. S. Hardy, S. Weil, *Int. J. Hydrogen Energy*, 2007, **32**, 3655–3663.
- [39] K. S. Weil, C. A. Coyle, J. T. Darsell, G. G. Xia, J. S. Hardy, *J. Power Sources*, 2005, **152**, 97–104.
- [40] J. Y. Kim, K. S. Weil, J. P. Choi, *Metal-ceramic composite air braze with ceramic particulate*, Patent number WO /2008/115696, 2008.
- [41] A. R. Sahu, A. Ghosh, A. K. Suri, *Ceram. Int.*, 2009, **35**, 2493–2497.
- [42] S. D. Kim, S. H. Hyun, J. Moon, J. H. Kim, R. H. Song, *J. Power Sources*, 2005, **139**, 67–72.
- [43] R. Muccillo, E. N. S. Muccillo, F. C. Fonseca, Y. V. França, T. C. Porfirio, D. Z. de Florio, M. A. C. Berton, C. M. Garcia, *J. Power Sources*, 2006, **156**, 455–460.
- [44] S. P. Simner, M. D. Anderson, G. G. Xia, Z. Yang, L. R. Pederson, J. W. Stevenson, *J. Electrochem. Soc.*, 2005, **152**, A740–A745.
- [45] T. Yamaguchi, S. Shimizu, T. Suzuki, Y. Fujishiro, M. Awano, *Mater. Lett.*, 2008, **62**, 1518–1520.
- [46] Y. Du, N. M. Sammes, *J. Power Sources*, 2004, **136**, 66–71.
- [47] Y. Funahashi, T. Shimamori, T. Suzuki, Y. Fujishiro, M. Awano, *J. Power Sources*, 2007, **163**, 731–736.
- [48] D. S. Roy, B. D. Rohera, *Eur. J. Pharm. Sci.*, 2002, **16**, 193–199.
- [49] D. Capitani, G. Mensitieri, F. Porro, N. Proietti, A. Segre, *Polymer*, 2003, **44**, 6589–6598.
- [50] R. Z. Liu, S. R. Wang, B. Huang, C. H. Zhao, J. L. Li, Z. R. Wang, Z. Y. Wen, T. L. Wen, *J. Solid State Electrochem.*, 2009, **13**, 1905–1911.
- [51] C. X. Li, C. J. Li, G. Y. Yang, *J. Therm. Spray Technol.*, 2009, **18**, 83–89.
- [52] W. Zhou, H. Shi, R. Ran, R. Cai, Z. Shao, W. Jin, *J. Power Sources*, 2008, **184**, 229–237.
- [53] N. Besette in *Solid State Energy Conversion (SECA) Workshop*, Acumentrics Corp., US DOE, of *SECA Annual Workshop Pacific Grove, CA*.
- [54] T. Liktal in *10th Annual Solid State Energy Conversion (SECA) Workshop*, Acumentrics Corp., US DOE.

- [55] J. Fergus, R. Hui, X. Li, D. P. Wilkinson, J. Zhang (Eds.), *Solid Oxide Fuel cells: Materials Properties and Performance 1st ed.*, CRC Press, Inc., Taylor and Francis Group, 6000 Broken Sound Parkway NW, Suite 300, Boca Raton, FL 33487-2742, 2008.
- [56] P. Bance, N. P. Brandon, B. Girvan, P. Holbeche, S. O'Dea, B. C. H. Steele, *J. Power Sources*, 2004, **131**, 86–90.
- [57] R. Kerr in *2009 SECA Annual Review Meeting*, Delphi, US DOE.
- [58] J. Mulot, M. Niethammer, S. Mukerjee, K. Haltiner, S. Shaffer in *Fundamentals and Developments of Fuel Cells Conference 2008*, Electrochemical Society.
- [59] F. Tietz, H. P. Buchkremer, D. Stover, *Solid State Ionics*, 2002, **152-153**, 373–381.
- [60] S. D. Vora in *10th Annual Solid State Energy Conversion (SECA) Workshop*, Siemens, US DOE.
- [61] S. Linderoth, *J. Electroceram.*, 2009, **22**, 61–66.
- [62] B. Borglum in *10th Annual Solid State Energy Conversion (SECA) Workshop*, Versa Power Systems, US DOE.
- [63] A. Devoe, L. Devoe, *A Fuel Cell technology breakthrough, the SOFC stick*, Tech. Rep., Violet Fuel Cell Sticks, 7173 Construction Court, San Diego, CA 92121, 2008.
- [64] T. Jardiel, B. Levenfeld, R. Jiménez, A. Várez, *Ceram. Int.*, 2009, **35**, 2329–2335.
- [65] M. Trunec, *J. Eur. Ceram. Soc.*, 2004, **24**, 645–651.
- [66] N. St-Pierre, B. D. Favis, B. A. R. J. A. Ramsay, H. Verhoogt, *Polymer*, 1997, **38**, 647–655.
- [67] A. Bresciani, H. Reh, W. Bender, *Extrusion in Ceramics (Engineering Materials and Processes) 1st ed.*, F. Handle (Ed.), Springer, ECT GmbH, Kisslingweg 10, 75417 Mulacker, Germany, 2007, chapter 2.
- [68] A. T. J. Domanti, J. Bridgwater, *Trans. IChemE.*, 2000, **78**, 68–78.
- [69] O. L. Kulikov, K. Hornung, *J. Non-Newtonian Fluid Mech.*, 2001, **98**, 107–115.
- [70] A. T. J. Domanti, D. J. Horrobin, J. Bridgwater, *Int. J. Mech. Sci.*, 2002, **44**, 1381–1410.
- [71] B. D. Russell, J. Lasenby, S. Blackburn, D. I. Wilson, *Powder Technol.*, 2003, **132**, 233–248.
- [72] P. Lenormand, D. Caravaca, C. Laberty-Robert, F. Ansart, *J. Eur. Ceram. Soc.*, 2005, **25**, 2463–2646.

- [73] F. Mauvy, P. Lenormand, C. Lahanne, F. Ansart, J. M. Bassat, J. C. Grenier, *J. Power Sources*, 2007, **171**, 783–788.
- [74] M. Gaudon, C. Laberty-Robert, F. Ansart, P. Stevens, *J. Eur. Ceram. Soc.*, 2006, **26**, 3153–3160.
- [75] Y. Zhang, J. Gao, D. Peng, M. Guangyao, X. Liu, *Ceram. Int.*, 2004, **30**, 1049–1053.
- [76] T. L. Nguyen, T. Honda, T. Kato, Y. Iimura, K. Kato, A. Negishi, K. Nozaki, M. Shiono, A. Kobayashi, K. Hosoda, Z. Cai, M. Dokiya, *J. Electrochem. Soc.*, 2004, **151**, A1230–A1235.
- [77] Z. Wang, K. Sun, S. Shen, N. Zhang, J. Qiao, P. Xu, *J. Membrane Sci.*, 2008, **320**, 500–504.
- [78] H. S. Song, W. H. Kim, S. H. Hyun, J. Moon, *J. Electroceram.*, 2006, **17**, 759–764, 2nd International Conference on Electroceramics (ICE-2005), Seoul, South Korea, Jun 12-16, 2005.
- [79] K. M. Erskine, A. M. Meier, S. M. Pilgrim, *J. Mater. Sci.*, 2002, **37**, 1705–1709.
- [80] C. C. Schüler, A. Stuck, N. Beck, H. Keser, U. Täck, *J. Mater. Sci. - Mater. Electron.*, 2000, **11**, 389–396.
- [81] J. S. Hardy, J. Y. Kim, E. C. Thomsen, K. S. Weil, *J. Electrochem. Soc.*, 2007, **154**, P32–P39.
- [82] D. K. Chatterjee, T. D. Ketcham, D. J. St Julien, *Conductive coatings, sealing materials and devices utilizing such materials and method of making.*, Patent number WO2008109100-A1, 2008.
- [83] M. C. Tucker, C. P. Jacobson, L. C. De Jonghe, S. J. Visco, *J. Power Sources*, 2006, **160**, 1049–1057.
- [84] H. Nishi, K. Kikuchi, *J. Nucl. Mater.*, 1998, **258-263**, 281–288, 8th International Conference on Fusion Reactor Materials (ICFRM-8), Sendai, Japan Oct 26-31, 1997.
- [85] O. C. Paiva, M. A. Barbosa, *Mater. Sci. Eng. A-Struct.*, 2008, **480**, 306 – 315.
- [86] A. A. Shirzadi, Y. Zhu, H. K. D. H. Bhadeshia, *Mat. Sci. Eng. A-Struct.*, 2008, **496**, 501–506.
- [87] X. J. Chen, K. A. Khor, S. H. Chan, *Solid State Ionics*, 2004, **167**, 379–387.
- [88] N. T. Hart, N. P. Brandon, M. J. Day, J. E. Shemilt, *J. Mater. Sci.*, 2001, **36**, 1077–1085.
- [89] Steff, *Diagram of a scanning electron microscope with English captions*, 2011, last checked 18th May 2011. http://commons.wikimedia.org/wiki/File:Schema_MEB_%28en%29.svg.

- [90] K. Thydén, Y. L. Liu, J. B. Bilde-Sørensen, *Solid State Ionics*, 2008, **178**, 1984–1989.
- [91] A. Lanzini, P. Leone, P. Asinari, *J. Power Sources*, 2009, **194**, 408–422.
- [92] N. Shikazono, Y. Sakamoto, Y. Yamaguchi, N. Kasagi, *J. Power Sources*, 2009, **193**, 530–540.
- [93] J. R. Wilson, W. Kobsiriphat, R. Mendoza, H. Y. Chen, J. M. Hiller, D. J. Miller, K. Thornton, P. W. Voorhees, S. B. Adler, S. A. Barnett, *Nat. Mater.*, 2006, **5**, 541–544.
- [94] D. Gostovic, J. R. Smith, D. P. Kunderling, K. S. Jones, E. D. Wachsman, *Electrochem. Solid-State Lett.*, 2007, **10**, B214–B217.
- [95] P. R. Shearing, J. Golbert, R. J. Chater, N. P. Brandon, *Chem. Eng. Sci.*, 2009, **64**, 3928–3933.
- [96] J. R. Izzo, A. S. Joshi, K. N. Grew, W. K. S. Chiu, A. Tkachuk, S. H. Wang, W. Yun, *J. Electrochem. Soc.*, 2008, **155**, B504–B508.
- [97] J. X. Wang, Y. K. Tao, J. Shao, W. G. Wang, *J. Power Sources*, 2009, **186**, 344–348.
- [98] J. R. Smith, A. Chen, D. Gostovic, D. Hickey, D. Kunderling, K. L. Duncan, R. T. DeHoff, K. S. Jones, E. D. Wachsman, *Solid State Ionics*, 2009, **180**, 90–98.
- [99] S. Primdahl, M. Mogensen, *J. Electrochem. Soc.*, 1999, **146**, 2827–2833.
- [100] E. Siebert, A. Hammouche, M. Kleitz, *Electrochim. Acta*, 1995, **40**, 1741–1753.
- [101] E. C. Thomsen, G. W. Coffey, L. R. Pederson, O. A. Marina, *J. Power Sources*, 2009, **191**, 217–224.
- [102] S. R. Gamble, J. T. S. Irvine, *Solid State Ionics*, 2011, **192**, 394–397.
- [103] M. J. Jørgensen, S. Primdahl, C. Bagger, M. Mogensen, *Solid State Ionics*, 2001, **139**, 1–11.
- [104] Q. A. Huang, R. Hui, B. Wang, J. Zhang, *Electrochim. Acta*, 2007, **52**, 8144–8164.
- [105] X. J. Chen, S. H. Chan, K. A. Khor, *Solid State Ionics*, 2003, **164**, 17–25.
- [106] M. Liang, B. Yo, M. Wen, J. Chen, J. Xu, Y. Zhai, *J. Power Sources*, 2009, **190**, 341–345.
- [107] P. Tanasini, M. Cannarozzo, P. Costamagna, A. Faes, J. V. Herle, A. Hessler-Wyser, C. Comninellis, *Fuel Cells*, 2009, **5**, 740–752.
- [108] T. Klemensø, C. Chung, P. H. Larsen, M. Mogensen, *J. Electrochem. Soc.*, 2005, **152**, A2186–A2192.
- [109] J. Malzbender, E. Wessel, R. W. Steinbrech, *Solid State Ionics*, 2005, **176**, 2201–2203.

- [110] J. Kong, Y. Zhang, C. Deng, J. Xu, *J. Power Sources*, 2009, **186**, 485–489.
- [111] M. A. Laguna-Bercero, R. Campana, A. Larrea, J. A. Kilner, V. M. Orera, *Fuel Cells*, 2011, **11**, 116–123, Workshop on Solid Oxide Fuel Cells (SOFCs), Albacete, Spain, November 18–20, 2009.
- [112] T. Matsui, H. Fujii, A. Ozaki, T. Takeuchi, R. Kikuchi, K. Eguchi, *J. Electrochem. Soc.*, 2007, **154**, B1237–B1241.
- [113] J. Guan, N. Minh, B. Ramamurthi, J. Rudd, J. K. Hong, P. Riley, D. Weng, *High Performance Flexible Reversible Solid Oxide Fuel Cell*, Tech. Rep., GE Global Research Center, 19310 Pacific Gateway Drive, Torrance, CA 90502, 2006.
- [114] C. M. An, J. H. Song, I. Kang, N. Sammes, *J. Power Sources*, 2010, **195**, 821–824.
- [115] A. Hauch, S. D. Ebbesen, S. H. Jensen, M. Mogensen, *J. Mater. Chem*, 2008, **18**, 2331–2340.
- [116] EG&G Technical Services, Inc., *Fuel Cell Handbook*, Tech. Rep. 7th edition, U.S. Department of Energy, Office of Fossil Energy, National Energy Technology Laboratory, P.O. Box 880, Morgantown, West Virginia, 26507-0880, 2004.
- [117] D. Kusunoki, Y. Kikuoka, V. Yanagi, K. Kugimiya, M. Yoshino, M. Tokura, K. Watanabe, H. Miyamoto, S. Ueda, M. Sumi, S. Tokunaga, *Int. J. Hydrogen Energy*, 1995, **20**, 831–834.
- [118] S. Elangovan, J. J. Hartvigsen, L. J. Frost, *Int. J. Appl. Ceram. Technol.*, 2007, **4**, 109–118.
- [119] D. M. Bierschenk, J. R. Wilson, S. A. Barnett, *Energy Environ. Sci.*, 2011, **4**, 944–951.
- [120] C. J. Moyer, N. P. Sullivan, H. Zhu, R. J. Kee, *J. Electrochem. Soc.*, 2011, **158**, B117–B131.
- [121] M. A. Laguna-Bercero, R. Campana, A. Larrea, J. A. Kilner, V. M. Orera, *J. Electrochem. Soc.*, 2010, **157**, B852–B855.
- [122] F. He, D. Song, R. Peng, G. Meng, S. Yang, *J. Power Sources*, 2010, **195**, 3359–3364.
- [123] P. A. Connor, P. Attidekou, F. G. E. Jones, J. Nairn, J. Rennie, J. T. S. Irvine, *A Reversible Solid Oxide Fuel Cell Energy Storage System*, Tech. Rep., The University of St Andrews, School of Chemistry, University of St Andrews, North Haugh, St Andrews, Fife, KY16 9ST, 2005.
- [124] S. Gopalan, M. Mosleth, J. J. Hartvigsen, R. D. McConnell, *J. Power Sources*, 2008, **185**, 1328–1333.
- [125] S. Gopalan, G. Ye, U. B. Pal, *J. Power Sources*, 2006, **162**, 74–80.

- [126] M. Ni, M. H. K. Leung, D. Y. C. Leung, *J. Power Sources*, 2008, **177**, 369–375.
- [127] M. Ni, M. H. K. Leung, D. Y. C. Leung, *J. Power Sources*, 2006, **163**, 460–466.
- [128] X. Jin, X. Xue, *J. Power Sources*, 2010, **195**, 6652 – 6658.
- [129] S. Campanari, P. Iora, *J. Power Sources*, 2004, **132**, 113–126.
- [130] M. Cannarozzo, A. D. Borghi, P. Costamagna, *J. Appl. Electrochem.*, 2008, **38**, 1011–1018.
- [131] D. Bhattacharyya, R. Rengaswamy, *Ind. Eng. Chem. Res.*, 2009, **48**, 6068–6086.
- [132] S. Kakaç, A. Pramuanjaroenkiij, X. Y. Zhou, *Int. J. Hydrogen Energy*, 2007, **32**, 761–786.

Chapter 2

Experimental and methodology

Introduction

This chapter is concerned with the equipment and experimental techniques used to obtain results, and is divided into three sections. Firstly, fabrication methods used to make symmetrical cells and whole reversible cells are discussed, secondly characterisation methods used to examine the microstructure and determine the optimum fabrication parameters are discussed, and lastly testing procedures and test rig setups are discussed for symmetrical cell testing and whole reversible cell testing.

2.1 Fabrication methods

Process temperature control rings

Process temperature control rings, type 1130 °C - 1400 °C, PTCR-STH (Ferro Electronic Materials BV), were used during the sintering of most of the samples discussed in this work. They are ceramic rings, hereafter referred to as ‘sintering rings,’ which shrink when sintered, to a diameter dependent on both the maximum temperature reached, and the dwell time at that temperature, i.e. the total heat received. The diameter is converted to a temperature via a chart from the company, and the temperatures may be compared from one firing to another. Therefore, the rings monitor the total heat received by the sample, and measure the amount of sintering that a particular sample has received. The amount of sintering that one sample has received may be compared to another one, sintered in the same furnace, or a different furnace, to see if it is sintered less, the same amount, or more. Several furnaces were used in this work, so if the sintering profile is the same, the ring temperature will indicate the level of consistency between furnaces, and the consistency between sintering runs in the same furnace.

2.1.1 YSZ electrolyte pellet manufacture

Pellets of YSZ function as thick electrolyte supports for symmetrical cells. 8 mol.% Y_2O_3 doped ZrO_2 with a surface area of $6.9 \text{ m}^2 \text{ g}^{-1}$ (Daiichi) was used to produce pellets. The mass of powder used was 0.9 g, pressed uniaxially with a force of 0.5 tonnes in a 13 mm

diameter circular stainless steel die. The pellets were sintered with the profile: $2\text{ }^{\circ}\text{C min}^{-1}$ to $1450\text{ }^{\circ}\text{C}$, with a 4 h dwell, and $5\text{ }^{\circ}\text{C min}^{-1}$ to room temperature.

2.1.2 Tape casting

Tape casting is a popular method in industry to produce fuel cells, because it is inexpensive, scalable, and several different cell layers can be produced as tapes, laminated together and co-sintered, reducing fabrication costs[1]. The tapes consist of ceramic powder, and organic binders, pore formers, lubricants, dispersants etc. which burn out during sintering.

Preparation of tapes

An LSM-YSZ tape casting slurry was made from 5% A-site deficient LSM ($\text{La}_{0.8}\text{Sr}_{0.2}\text{MnO}_{3-\delta}$ (Praxair), surface area $8.96\text{ m}^2\text{ g}^{-1}$, and YSZ, 13 mol.% (Unitec Ceramics), $d_{20} = 0.43\text{ }\mu\text{m}$, $d_{50} = 0.65\text{ }\mu\text{m}$, $d_{80} = 1\text{ }\mu\text{m}$, and specific surface area $6.55\text{ m}^2\text{ g}^{-1}$. The masses of ceramic powder used were 5.00 g LSM and 5.00 g of YSZ were used, and the organic components were 2.024 g graphite (99.8%, 325 mesh, Alfa Aesar), 2.376 g glassy carbon ($10\text{ }\mu\text{m} - 20\text{ }\mu\text{m}$, Alfa Aesar), and 11.000 g acetone ($>99\%$, Fisher Scientific). This was milled in a horizontal roller mill (University of St Andrews mechanical workshop) for 18 h at 160 revolutions per minute (r.p.m.) After this, the following chemicals were added: 1.6 g polyethylene glycol (Aldrich), 1.4 g dibutyl phthalate (Fisons Lab. Reagents) and 2.210 g polyvinyl butyryl (97.5%, Kuraray). The contents were milled for 20 min on a planetary ball mill with 10 mm zirconia balls (Whitfield & Sons Ltd.), and then for 4 h on the horizontal roller mill, again with 10 mm zirconia balls at 100 rpm. A YSZ only tape of 8 mol.% YSZ (Daiichi), surface area $6.9\text{ m}^2\text{ g}^{-1}$, was also made using the same procedure.

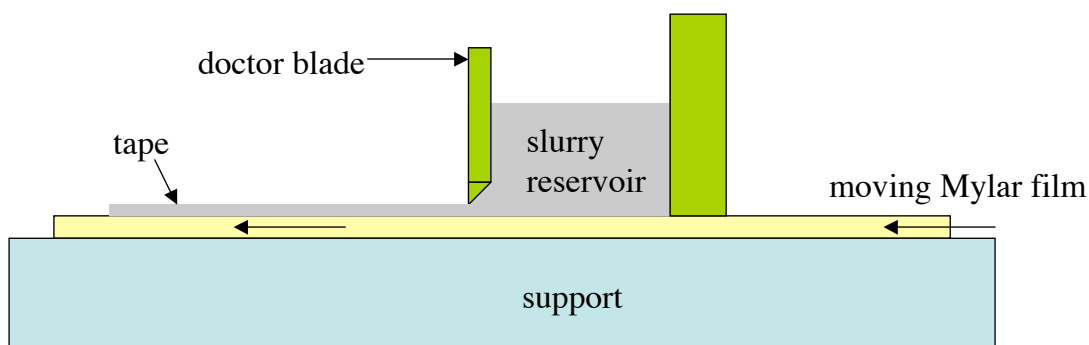


Figure 2.1.1: A schematic of the tape-casting process (not to scale). The Mylar film moves slowly, and a coating of tape casting slurry is produced on it, with the thickness controlled by the doctor blade.

A schematic of the tape-casting process is shown in fig. 2.1.1. The tape casting slurry is placed in the reservoir, and the underlying Mylar film is slowly drawn along the support. A layer of slurry is coated onto it, and a doctor blade is used to control the thickness, as its height can be adjusted. After the tapes are produced, they are left to dry for several hours at ambient temperatures, to let the methyl ethyl ketone and ethanol solvents evaporate.

The resulting tape is about 20 μm thick, and flexible enough to be handled easily without cracking.

Preparation of tape cast cells

Four layers of YSZ were laminated together by manually pressing them together, and a cork borer was used to cut out discs of tape, which had a diameter of 14 mm. Discs of LSM-YSZ tape, of 11 mm diameter were also cut out. These discs were laminated together to produce a symmetrical cell, as in fig. 2.1.2, and sintered with the following profile: From 50 $^{\circ}\text{C}$ - 150 $^{\circ}\text{C}$, 0.3 $^{\circ}\text{C min}^{-1}$, with a 1 h dwell at 150 $^{\circ}\text{C}$, then 0.5 $^{\circ}\text{C min}^{-1}$ to 360 $^{\circ}\text{C}$, 1 $^{\circ}\text{C min}^{-1}$ to 650 $^{\circ}\text{C}$, 0.5 $^{\circ}\text{C}$ to 1000 $^{\circ}\text{C}$, with a 5 h dwell, and then 5 $^{\circ}\text{C min}^{-1}$ to 50 $^{\circ}\text{C}$. The total time is 2350 min, 37.2 h. The second stage

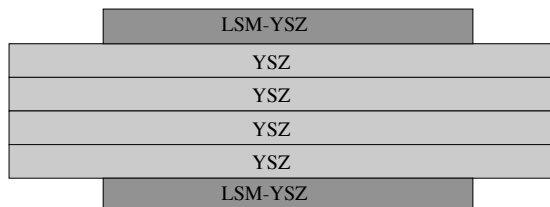


Figure 2.1.2: Tape cast symmetrical cell produced by lamination of tapes

involves heating from 50 $^{\circ}\text{C}$ to 1000 $^{\circ}\text{C}$ at a rate of 5 $^{\circ}\text{C min}^{-1}$, then 2 $^{\circ}\text{C min}^{-1}$ to 1350 $^{\circ}\text{C}$ with a 5 h dwell, and back to room temperature at 5 $^{\circ}\text{C min}^{-1}$. The total time was 925 min, or 15.4 h. Current collection was by a layer of gold paste, (T10112, Metalor Technologies UK Ltd.), which was hand painted onto the electrodes and sintered at 950 $^{\circ}\text{C}$ for 1 h, at a rate of 3 $^{\circ}\text{C min}^{-1}$ heating and cooling.

2.1.3 Screen printing

Screen printing is another technique commonly used in industry, because it is scalable and well understood, and multiple layers can be screen printed, before the cell is co-sintered, which reduces the number of sintering steps. It is important to de-agglomerate the ceramic particles in a screen printing ink, by ball milling or ultrasonic vibration, because this will improve the microstructure of the layer created, preventing very large particles or voids from forming during sintering. It also ensures a homogeneous mixing of different ceramic particle types for composite electrodes.

Production of screen printing inks

Ball milling is used to disperse 5% A-site deficient LSM ($(\text{La}_{0.8}\text{Sr}_{0.2})_{0.95}\text{MnO}_{3-\delta}$) (10 g, Praxair), with hypermer KD1 dispersant (0.2 g) which is a phosphate ester (Uniqema), using 10 mm diameter zirconia milling balls (30) and acetone (>99%, Fisher Scientific) to cover the powders in the milling bottle. It is milled for 18 h at 160 r.p.m in a horizontal roller mill (University of St Andrews mechanical workshop). The zirconia balls are filtered out, and binder is added. The binder is a mixture of butvar (B18, Sigma) and terpineol (Fluka Analytical) in a 1:19 ratio by mass. The amount added is 4.333 g, which is 30 % by mass of powder-binder mixture. The jar holding the ink is then covered with a pierced plastic film and magnetically stirred for several days at room temperature until it has reached a constant mass. At this point all of the acetone has evaporated.

A NiO-YSZ screen printing ink is also made in the same way as the LSM ink, except that instead of 10 g of LSM being used, NiO (6.278 g, Novamet, 99.9%), 4 μm - 6 μm particle size and YSZ (5.067 g), are used instead.

An LSM-YSZ ink was also produced in the same way as the LSM ink, but with different ceramic powders: 5% A-site deficient $(\text{La}_{0.8}\text{Sr}_{0.2})_{0.95}\text{MnO}_{3-\delta}$ (Pi-Kem, 10.000 g) and 8YSZ (Pi-Kem, average size 0.21 μm , surface area 6.7 $\text{m}^{-2} \text{g}^{-1}$) (9.240 g) were used, with hypermer KD1 dispersant (0.38 g).

A YSZ ink was also produced in the same manner, except that 8YSZ (Pi-Kem, average size 0.21 μm , surface area 6.7 $\text{m}^{-2} \text{g}^{-1}$) (10.6000 g) was used instead, with KD1 (0.2160 g), and after milling, butvar/terpineol mixture (4.5465 g). Another YSZ ink was made in the same way, with 3YSZ (10.000 g, TZ-3Y-E, Tosoh, $\sim 16 \text{ m}^2 \text{g}^{-1}$), was used instead, with KD1 dispersant (0.205 g), and then terpineol/butvar mixture (4.2745 g, mixture 18.7:1 by mass) added after milling of the powder in acetone.

Production of screen printed pellet symmetrical cells

Pressed and sintered pellets of YSZ, made as described in subsection 2.1.1, were screen printed with the LSM-YSZ screen printing ink. The screen printer used was an automatic screen printer (248, DEK), with a force of 6 kg, and a print gap of 1.5 mm. After each side of the pellets were printed, they were dried at 85 °C for 20 min. They were sintered with the profile: 3 °C min^{-1} to 1300 °C, a 1 h dwell, then 3 °C min^{-1} to room temperature. A current collection layer of LSM screen printing ink was applied, using a manual screen printer (University of St Andrews mechanical workshop), with a 1 mm - 2 mm print gap. After each side of the pellet was printed, there was a 30 min drying step at 80 °C.

2.1.4 Extrusion

Extrusion was used to produce porous ceramic tubes of $(\text{La}_{0.8}\text{Sr}_{0.2})_{0.95}\text{MnO}_{3-\delta}$, or $(\text{La}_{0.8}\text{Sr}_{0.2})_{0.97}\text{MnO}_{3-\delta}$ LSM (Praxair), which act as a support and current collector for the reversible SOFC. A simple handheld ram extruder was used initially, and then later a mechanised single screw extruder. The extrusion process was developed to produce tubes with a homogeneous and defect free microstructure, suitable for dip coating to make reversible SOFC.

Handheld ram extruder

The handheld extruder ‘Makin’s Professional Clay Gun,’ (The Polymer Clay Pit) was designed to produce decorative clay parts. Fig. 2.1.3 shows the extruder, which is a manual ram extruder propelled by a screw, with a range of different dies and mandrels, examples of which are shown in fig. 2.1.4. The original die was 0.3 mm long, with an external diameter of 18.58 mm, which was 2.1 mm smaller than the inside diameter of the screw cap, allowing it to move relative to the mandrel. It has an internal diameter of 6.50 mm, giving it a die ratio (length/diameter) of about 0.05. The mandrel consists of a perforated disc which allows the extrusion mix to flow through it, and a central rod 4.48



Figure 2.1.3: Handheld ram extruder ‘Makin’s professional clay gun’ (The Polymer Clay Pit).

mm wide, which forms the bore of the tube. This was later replaced by the die assembly shown in fig. 2.1.4. It consists of a mandrel, with a perforated disc as before, with a central rod with diameter of 4.35 mm. The die defines the outside of the tube, and has an inner diameter of 6.50 mm and a length of 5.0 mm, giving a die ratio of 0.77, much greater than the original die ratio. Finally, the extruder cap holds the other components in place. The following components were used in the extrusion recipes: 5% A-site deficient

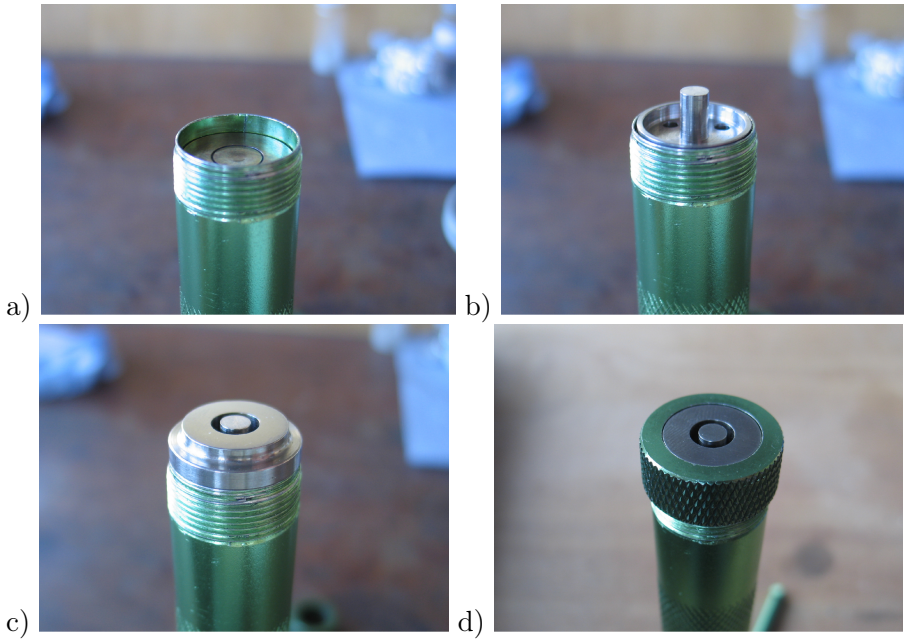


Figure 2.1.4: Handheld extruder die assembly: a) ram, b) mandrel, c) mandrel and die, and d) mandrel, die and cap.

LSM ($\text{La}_{0.8}\text{Sr}_{0.2}\text{MnO}_{3-\delta}$), with particle sizes from the manufacturer of $d^{10} = 0.8 \mu\text{m}$, $d^{50} = 1.2 \mu\text{m}$ and $d^{90} = 4 \mu\text{m}$, density 6.6 g cm^{-3} , surface area $8.96 \text{ m}^2 \text{ g}^{-1}$ (Praxair, Pi-Kem), or 3% A-site deficient LSM ($\text{La}_{0.8}\text{Sr}_{0.2}\text{MnO}_{3-\delta}$), $d^{10} = 0.8 \mu\text{m}$, $d^{50} = 1.3 \mu\text{m}$ and $d^{95} = 2.6 \mu\text{m}$, density 6.6 g cm^{-3} , surface area $3.62 \text{ m}^2 \text{ g}^{-1}$ (Praxair, Pi-Kem). The binder used was cellulose (2-hydroxyethylcellulose), average $M_W = 90,000$ (Aldrich), the lubricants were polyethylene glycol (Aldrich) and propan-1,2-diol, and a solvent, distilled water, was also used. The components were mixed in the proportions in table 2.1.1, and

Recipe no.	LSM (g)	LSM vol.%	cellulose (g)	cellulose vol.%	water (g)	water vol.%	PEG (g)	PEG vol.%
H-cell1	45.00	37.2	1.5	13.6	9.00	49.1	-	-
H-cell2	28.63	39.7	1.00	15.3	-	-	5.53	45.0
H-cell3	20.00	56.1	0.436	13.5	1.490	27.7	0.175	2.9
H-cell4	28.000	37.0	0.736	10.7	5.717	49.8	0.319	2.5
							P1,2D	P1,2D
H-cell5	10.00	36.3	0.687	27.4	1.4143	33.9	0.1057	2.4
H-cell6	30.00	27.4	2.0610	20.4	8.3167	50.1	0.3014	1.8
H-cell7	10.000	35.1	0.687	26.5	1.554	36.0	0.1040	2.3
H-cell8	10.000	28.8	0.687	21.7	2.510	47.6	0.1030	1.9
H-cell9'	15.000	35.3	0.50	12.9	3.341	51.8	-	-
H-cell10'	15.000	36.6	0.50	13.4	3.000	48.3	0.1141	1.8
							PEG	PEG
H-cell11*	15.010	24.3	0.50	8.9	6.000	64.0	0.3	2.8
H-cell12	20.005	33.8	1.778	33.1	2.967	33.1	-	-
H-cell13	20.003	33.8	1.777	33.0	2.971	33.1	-	-

Table 2.1.1: Water or polyethylene glycol based recipes for the manual extruder, full table, PEG = polyethylene glycol, P1,2D = propan-1,2-diol. ' = recipe for LSM squares, * = recipe contains 53 mg CTAB (cetyl tri-ammonium bromide)

ground in a pestle and mortar for 5 min. They were extruded immediately, except for recipes H-cell12 and H-cell13 which were aged overnight in a sealed container to allow the cellulose to fully hydrate. The mixture was extruded by forming it by hand into a cylindrical billet, placing it in the extruder, assembling the die, and slowly rotating the handle attached to the extruder screw. A single long tube was extruded, chopped into sections for sintering, and left to dry overnight. Some of the sections were sealed at one end with a spatula by compressing the open tube end to make a seal while the tube was still wet and malleable. LSM squares were extruded using a different die assembly, with a perforated disc, but no mandrel, and a slot die. Cetyl tri-ammonium bromide (CTAB) (Aldrich) was used as a dispersant in one of the extrusion mixes.

Sintering the tubes

The LSM tubes produced were sintered in a horizontal position on an alumina plate, according to the profile: $0.3\text{ }^{\circ}\text{C min}^{-1}$ to $500\text{ }^{\circ}\text{C}$, then $1\text{ }^{\circ}\text{C min}^{-1}$ to $1000\text{ }^{\circ}\text{C}$, then $3\text{ }^{\circ}\text{C min}^{-1}$ to $1200\text{ }^{\circ}\text{C}$, with a 1 h dwell, and then $3\text{ }^{\circ}\text{C min}^{-1}$ to room temperature. Some of the tubes were sintered in a vertical position, supported by alumina rods on a furnace brick.

Mechanised screw extruder

The mechanised extruder (Rondol) in fig. 2.1.5a uses a single 12 mm diameter screw to mix, de-air and extrude the extrusion mix.



Figure 2.1.5: Mechanised single screw extruder (Rondol) with die assembly a) extruder, b) 12 mm extruder screw, c) screw inside extruder barrel, d) mandrel (left) and die insert (right) e) mandrel and die ring assembled and f) die assembly with heater band, and 4x die ring adjusting screws at 90° intervals around it.

It has two controllable temperature zones; the barrel and the die assembly. A pressure sensor located between the barrel exit and the entrance to the die assembly, records the pressure in bar. It can be seen sticking up from the top left hand side of the extruder in fig. 2.1.5a. The pressure and temperatures can be logged via an RS-485 communications port. The die thermocouple is faulty and so the die temperature cannot be logged, but is measured manually via a thermocouple inserted inside the mandrel which is hollow, so the thermocouple measures the temperature at the centre of the die.

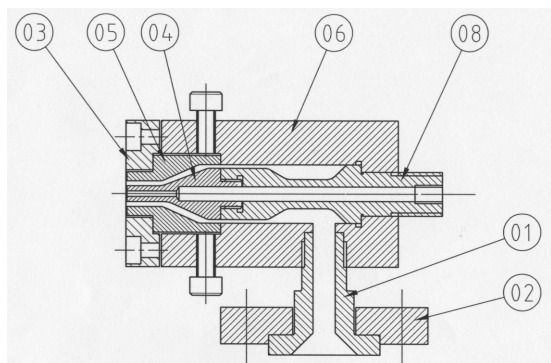


Figure 2.1.6: Mechanised screw extruder: die assembly schematic. 1) Die adapter, 2) Die clamp plate, 3) nozzle clamp ring, 4) mandrel, 5) die insert, 6) die body, and 8) mandrel threads. The heater band is not shown, but surrounds the die body.

The extrusion mix is placed in the aluminium hopper on top of the extruder, and feeds into the extruder as the screw rotates. The speed of rotation is controllable from 0 to 50 r.p.m with a precision of 0.5 r.p.m., and the motor and electronics are water cooled at a flow rate of $2 \text{ dm}^3 \text{ min}^{-1}$ to prevent overheating as they are near the barrel. The extruder screw has a taper in its diameter, becoming thicker towards the die. Therefore, the shear force and the pressure increase along the screw towards the die. This provides a de-airing mechanism, as air is forced backwards along the screw toward the feed intake. In order to assemble the extruder, the screw is attached

inside the barrel, as shown in fig. 2.1.5c, to which the die assembly is bolted. This consists of a mandrel, and a die insert, shown in fig. 2.1.5d,e which together shape the extruded tube. These are then placed inside outer casing of the die, shown in 2.1.5f, and a nozzle clamp ring (not shown) is added to hold the die ring and mandrel in place. Fig. 2.1.6 shows a schematic of the die assembly.

Extrusion procedure: water based recipe

Table 2.1.2 shows the two water and cellulose based recipes that were extruded. The first was recipe M-cell-W1, where 'M' stands for mechanised extruder, 'cell' stands for cellulose and 'W' stands for water-based extrusion mixture. It was mixed in a pestle and mortar, placed in a sealed plastic bag overnight to allow the cellulose to fully absorb the water, and then extruded at 15 r.p.m. The tubes produced were sintered with a ramp rate of $3 \text{ }^\circ\text{C min}^{-1}$ to $1200 \text{ }^\circ\text{C}$, with a 1 h dwell, then $3 \text{ }^\circ\text{C min}^{-1}$ to room temperature. A picture was taken of the sintered tubes. Recipe M-cell-W2 was made in the same way. During extrusion, the speed was varied from 15-55 r.p.m and the temperature from $25 \text{ }^\circ\text{C}$ to $50 \text{ }^\circ\text{C}$.

Recipe no.	LSM mass%	LSM vol.%	cellulose mass%	cellulose vol.%	water mass%	water vol.%
M-cell-W1	80.5	33.6	6.9	31.8	12.5	34.6
M-cell-W2	80.5	33.6	6.9	31.7	12.6	34.7

Table 2.1.2: Water and cellulose based extrusion recipes for the mechanised extruder. The cellulose is 2-hydroxyethylcellulose.

Extrusion procedure: thermoplastic recipe

When extruding LSM tubes, the aim was to try to use the principles of viscous plastic processing, which is a method of processing ceramics, in which organic binders are added to disperse the fine ceramic particles. The mixture is subjected to high shear forces, which break up ceramic powder agglomerates, and the organic binders prevent re-agglomeration. Therefore a stable, finely dispersed and homogeneous, agglomerate free ceramic mixture is produced. This process has been shown to greatly improve the strength of the sintered parts, by reducing the number of microstructural flaws. It can also be optimised to reduce the level of organic components used in the mixture when compared with a conventional process [2]. Table 2.1.3 shows the different extrusion recipes used. The components used are 5% A-site deficient LSM, $(\text{La}_{0.8}\text{Sr}_{0.2})_{0.95}\text{MnO}_{3-\delta}$, 99.9%, with particle sizes from the manufacturer of $d^{10} = 0.6 \mu\text{m}$, $d^{50} = 1.1 \mu\text{m}$ and $d^{95} = 4.3 \mu\text{m}$, density 6.6 g cm^{-3} and surface area $6.79 \text{ m}^2 \text{ g}^{-1}$ (Praxair, Pi-Kem). The binders are polypropylene (ICO Polymer) and paraffin wax (Fisons), the lubricant/surfactant is stearic acid (97%, Acros Organics), and the pore formers are 2-hydroxyethylcellulose (Aldrich, M.W. 90,000) or graphite (325 mesh, 99.8%, Alfa Aesar). Recipes M-gra7 - M-gra11 are all included to show that the tubes extruded from these recipes had a consistent composition.

Recipe no.	LSM mass%	LSM vol.%	PP mass%	PP vol.%	PW mass%	PW vol.%	SA mass%	cell. mass%	cell. vol.%
M-cell1	79.6	32.8	9.0	27.3	7.4	22.8	0.6	3.3	15.0
M-cell2	85.5	42.2	6.1	22.0	5.5	20.2	0.5	2.6	13.9
M-cell3	83.3	38.2	6.9	23.4	6.2	21.5	0.5	3.0	15.0
M-cell4	81.8	35.9	7.0	22.5	6.3	20.7	2.0	3.0	14.3
M-cell5	82.8	37.5	6.9	22.9	6.8	23.0	0.5	3.0	14.7
M-cell6	83.3	38.2	6.9	23.4	6.2	21.5	0.5	3.0	15.0
Recipe no.	LSM mass%	LSM vol.%	PP mass%	PP vol.%	PW mass%	PW vol.%	SA mass%	gra. mass%	gra. vol.%
M-gra7	76.9	38.1	6.4	23.4	5.8	21.6	0.5	10.3	15.0
M-gra8	76.9	38.1	6.5	23.4	5.8	21.5	0.5	10.3	15.0
M-gra9	76.9	38.1	6.5	23.4	5.8	21.5	0.5	10.3	15.0
M-gra10	76.9	38.1	6.5	23.4	5.8	21.5	0.5	10.3	15.0
M-gra11	76.9	38.1	6.4	23.4	5.8	21.6	0.5	10.3	15.0

Table 2.1.3: LSM thermoplastic extrusion recipes. PP = polypropylene, PW = paraffin wax, SA = stearic acid, cell. = cellulose, gra. = graphite. Recipes 1-6 use cellulose pore former, and recipes 7-11 graphite pore former. The abbreviation 'gra' stands for graphite pore former.

The extruder was cleaned before recipe 1 was extruded by passing pure polypropylene through it. The extrusion recipes in table 2.1.3 were prepared by grinding the mixture in a pestle and mortar before extrusion. The extruder was then pre-heated to a barrel

temperature of 170 °C, and a die temperature of 170 °C - 180 °C, and the motor was water cooled with a flow rate of 2 dm³ min⁻¹. For recipes M-cell3 - M-gra11 only, the mixture was passed twice through the extruder without the die assembly present, i.e. the extruder is as shown in fig. 2.1.5c, in order to homogenise it before extrusion. During extrusion, the 4 screws next to the die ring were adjusted to make the die symmetrical and produce straight tubes. A beaker of water was placed below the die, with the water surface about 5 mm below the die face. The tubes were extruded into water because they are molten when they exit the extruder. They would distort under their own weight if not quickly cooled below the melting point of polypropylene, which is 160 °C - 165 °C. As the tube extruded, the bottom end was open. In order to seal the top end, to make a tube suitable to be a reversible cell support, i.e. one end open, one end sealed, scissors were used to cut the tube just below the die face, which dropped into water, and solidified. Extrusion was then stopped, the die face was cleaned by scraping with a metal spatula, and the procedure was repeated. The off-cuts produced were recycled through the extruder. The tubes were then dried at 80 °C for 10 min to remove any water. A piece of software was written using Labview v8.6.1, which recorded the die and barrel temperatures, the pressure just before the die, and the motor current, which is directly proportional to the screw speed.

Solvent extraction of paraffin wax with decane

It was necessary to carry out a ‘de-binding’ process on the extruded tubes, so that they did not crack while sintering. This procedure was carried out for the mixture of recipes M-cell1 and M-cell2, and for recipes M-cell3 - M-gra10 in table 2.1.3. The paraffin wax in the tubes was extracted by immersing them in decane (99%, anhydrous, Aldrich), heated to 60 °C - 80 °C and magnetically stirred, for 0.5 h - 1 h. The mass loss of the tubes was measured by removing one from the solution, and drying it for 10 min at 80 °C. From this, the percentage mass and volume loss were calculated. For recipe M-gra11, diethyl ether (99.5%, Sigma Aldrich) heated to 35 °C was used instead of decane. The tubes were weighed as before to confirm that the paraffin wax had been extracted.

Sintering of the tubes

The tubes were placed on an alumina plate covered with a thin layer of LSM powder, coarsened at 1250 °C and ground in a pestle and mortar. They did not adhere to the plate during sintering. The profile used was 0.3 °C min⁻¹ to 500 °C, then 1 °C min⁻¹ to 1000 °C, and then 3 °C min⁻¹ to the dwell temperature, with a 1 h dwell, then 3 °C min⁻¹ to room temperature. For recipes M-cell1 - M-cell5 in table 2.1.3, the dwell temperature was 1250 °C, for recipe M-cell6, 1330 °C, recipe M-gra7, 1280 °C, and recipes M-gra8 - M-gra11, 1330 °C.

2.1.5 Dip coating

Dip coating is a technique that is normally used to produce thin electrodes or the electrolyte in solid oxide fuel cells. A diluted tape-casting slurry was used as a dip-coating slurry

Recipe	8YSZ (g)	Butvar (g)	Tri-X (g)	PEG (g)	DBP (g)	MEK:EtOH ratio 3:2 (g)	YSZ vol. %
1	30	3.36	0.2	2.49	2.233	8.70:5.80	16.2
Y-7.4A(added)	4.028	0.452	0.027	0.335	0.301	3.52:2.35	7.4
Y-3.4B(added)	2.572	0.288	0.017	0.213	0.191	5.61:3.74	3.4

Table 2.1.4: YSZ tape casting slurry recipe 1, diluted with 3:2 MEK:EtOH to make slurries Y-7.4A(added) and Y-3.4B(added). These are combined with the original Y-7.4A and Y-3.4B slurries to make slurries Y-7.4A2 and Y-3.4B2, which are used for dip-coating. Tri-X = Triton-X, PEG = polyethylene glycol, DBP = dibutyl phthalate, MEK = methyl ethyl ketone, EtOH = ethanol. The solids loading (vol.% YSZ) is also shown.

recipe [3]. It was used to coat many of the earlier LSM tubes. In order to make the slurry, which is called recipe 1, 8YSZ (30.00 g, Tosoh), methyl ethyl ketone (MEK)(>99%, Fisher Scientific) and ethanol (EtOH) (99.9%, BDH) in a 3:2 ratio by mass (14 g), and Triton-X (0.2 g) were placed in a plastic bottle, with 24 zirconia 10 mm diameter milling balls, and milled for 18 h at 160 r.p.m. on a horizontal roller mill (University of St Andrews). Then, butvar (3.2 g), polyethylene glycol (2.49 g), dibutyl phthalate (2.233 g), and some more MEK:EtOH (3:2) (0.5g) were added, and the mixture was shaken for 10 min on an automatic shaker (Vibro Mischer E1, Chemap AG). Finally, it was milled for a further 4 h on the horizontal roller mill.

The slurry was diluted by adding further MEK:EtOH (3:2) to it in different ratios, and then shaken by hand for 5 min, to make dip-coating slurries Y-7.4A, Y-3.4B, Y-3.4C, Y-5.1D, and Y-7.3E, with YSZ solids loadings of 7.4%, 3.4%, 3.4%, 5.1% and 7.3% by mass respectively. After the first few dip-coatings, a further quantity of recipe 1 YSZ tape casting slurry, along with more MEK:EtOH was added to slurries Y-7.4A and Y-3.4B, as in table 2.1.4, because the level of slurry in the glass vials was insufficient for dip-coating the tubes. It was mixed for 15 min in an ultrasonic bath (Ultrawave Ltd.), and then shaken by hand for 5 min. The combined slurries were called Y-7.4A2 and Y-3.4B2, and had the same YSZ solids loading as the Y-7.4A and Y-3.4B slurries.

A further batch of tape casting slurry was made up, called recipe 2, which had a very similar composition to recipe 1, except that the YSZ used was 8YSZ (Pi-Kem, surface area $6.9 \text{ m}^2 \text{ g}^{-1}$, average particle size $0.21 \mu\text{m}$). From it, three YSZ slurries were made by diluting with 3:2 MEK:EtOH as before: slurry Y-3.4F which had 3.4 vol.% YSZ, and slurries Y-7.3G and Y-7.3G2, which had 7.3 vol.% YSZ.

Another type of dip-coating slurry was also made, with 3YSZ (Tosoh TZ-3Y-E ‘easy sinter’ powder, surface area $15.1 \text{ m}^2 \text{ g}^{-1}$, primary crystallite size 26 nm). This powder (35.6355 g) was ball milled with Triton-X (0.2410 g) at 100 rpm overnight, and then butvar (0.3500 g) was added, and 3:2 MEK:EtOH (6.8 g), and it was milled for a further 4 h at 100 rpm, which gave slurry H, with 15.8% vol.% 3YSZ. This slurry was further diluted with 3:2 MEK:EtOH, to give slurries Y-10.0I, Y-7.5J, and Y-4.9K, with 10 vol.%, 7.5 vol.%, and 4.9 vol.% 3YSZ respectively.

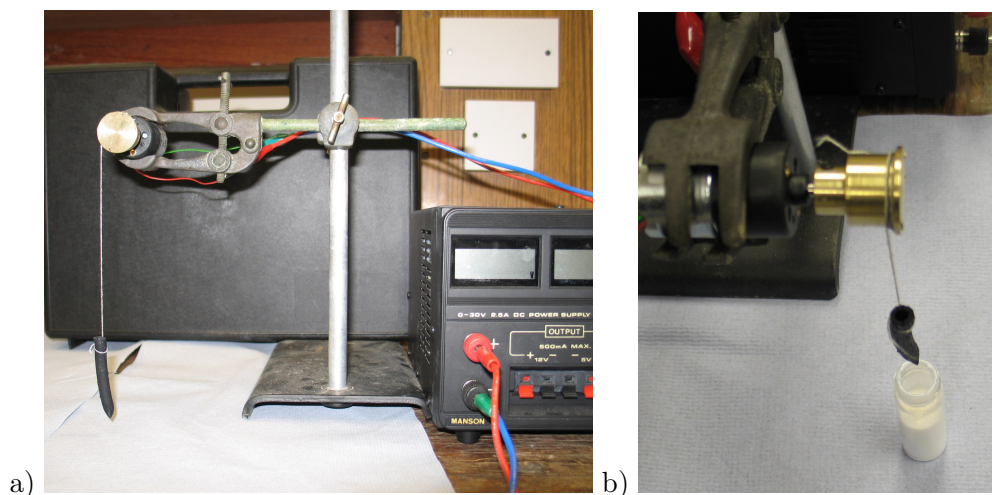


Figure 2.1.7: Electric 12 V DC motor used to dip coat tubes with YSZ electrolyte a) connected to power supply b) ready to dip coat the LSM tube in YSZ slurry.

YSZ electrolyte dip coating by hand

Initial dip coating of LSM tubes by YSZ slurries Y-7.4A and Y-3.4B was carried out by hand. An LSM tube was grasped in tweezers and slowly lowered into the dip-coating slurry, held there for a few seconds, and then slowly raised out again. A porous furnace brick, with thin alumina rods stuck into it vertically, was used to hold the samples as they were dried at 80 °C for 20 min, and during sintering. The tubes were placed on it with the alumina rod inside the tube, holding it upright, with the sealed end at the top. They were sintered at 2 °C min⁻¹ to 500 °C, 3 °C min⁻¹ to 1350 °C with a 1 h dwell, and 3 °C min⁻¹ to room temperature.

YSZ electrolyte dip coating with 12V DC motor.

It is important to control the thickness of the YSZ layer more precisely in order to reproduce the same thickness of YSZ electrolyte each time cells are made. Fig. 2.1.7 shows a 12 V DC motor, which was used to raise and lower LSM tubes into the YSZ dip coating slurry. The speed is proportional to the voltage supplied to the motor. A brass drum with a 2 cm diameter was added to the motor, which winds the thread holding the tube. The voltage was set at 12 V, which gives 18 r.p.m. Therefore, the rate at which the thread is wound is 1.88 cm s⁻¹. In order to switch between raising and lowering the tube, the polarity of the motor was reversed.

The dip-coating procedure is as follows: a thin string was tied around the open end of the LSM tube, and it was lowered into the slurry until only about 5 mm of the tube protruded from the surface of the liquid. It was held there for 5 s, and then the motor polarity was reversed and it was raised up from the slurry. Sometimes, a tube would contact the side of the glass vial as it was being raised, which would scrape the YSZ slurry from the tube, damaging the dip-coated layer. After the tube was fully out of the slurry, the inside lip of the vial was touched to the bottom of the tube for a couple of seconds to allow the excess slurry to drain off. A bent paper clip was inserted into the tube to hold

Recipe no.	NiO/YSZ ink (g)	IPA (g)	Ink:solvent (mass ratio)	Solids (vol.%)	Solids (mass%)	Tubes dipped (LSM recipe no.)
1	6.585	3.228	2.0x	8.1	39.8	4
2	9.516	4.678	2.0x	8.1	39.7	6,7
3	13.588	5.495	2.47x	8.9	42.2	8

Table 2.1.5: NiO/YSZ dip-coating slurry formulation and LSM tubes dipped. IPA = isopropanol.

it, the thread was untied, then the tube was placed on a vertical alumina rod stuck into a furnace brick, and sintered. It was noted that when the YSZ slurry was shaken before dipping, the coating was more homogeneous. Therefore, there is some settling of YSZ in the slurry.

The tubes were dried at 80 °C in a drying oven for at least 10 min, to evaporate the dip-coating solvents. They were then sintered at 1 °C min⁻¹ to 500 °C, 3 °C min⁻¹ to the dwell temperature, which was usually 1350 °C, but occasionally 1400 °C, with a 1 h dwell, and then cooled at 3 °C min⁻¹ to room temperature. Many of the dip-coated tubes were photographed after dip-coating, and also after sintering.

NiO/YSZ fuel electrode dip coating with 12 V DC motor

A NiO/YSZ screen printing ink was used to dip-coat the earlier LSM tubes. It was made as described in section 2.1.3, was diluted with isopropanol (99.8%, BDH), in a 2:1 ratio by mass, to make recipe 1, table 2.1.5. Further NiO/YSZ ink and isopropanol was added to this composition to make recipes 2 and 3 in the same table. LSM tubes from extrusion recipes 4, and 6 - 8 were dipped in the NiO/YSZ slurries as in table 2.1.5. The tubes were all sintered with the following profile: 1 °C or 2 °C min⁻¹ to 80 °C, 0.5 h dwell, 1 °C or 2 °C min⁻¹ to 500 °C, 3 °C min⁻¹ to 1350 °C, 2 h dwell, 3 °C min⁻¹ to room temperature. The amount of heat received by the samples was monitored with the use of 1130 °C - 1400 °C sintering process control rings, type PTCR - STH (Ferro Electronic Materials BV). The rings shrink according to the maximum temperature reached, and the dwell time. They can be used to compare the amount of heat energy that the sample has experienced in one sintering, to another.

2.1.6 Hand painting of reversible cell layers

LSM-YSZ oxygen electrode layer

The LSM-YSZ electrode is on the oxygen side of the cell, and is the cathode in fuel cell mode, and the anode in electrolysis mode. It is made by hand painting the LSM-YSZ screen printing ink onto the outer surface of the LSM tubes. Coats on the earlier LSM tubes were applied to the outer surface, except for a roughly 5 mm long section at the open end, and coats on the later LSM tubes were applied to the whole outer surface of the tube. The manufacture of the screen printing ink is described in section 2.1.3. After painting,

the tubes are placed with the open end down, on vertical alumina sticks, and dried at 80 °C for 0.5 h. They are sintered either at 2 °C min⁻¹ to 500 °C, then a 3 °C min⁻¹ ramp rate to 1300 °C, a 1 h dwell, then 3 °C min⁻¹ to room temperature, or by sintering at 1 °C min⁻¹, or 2 °C min⁻¹ to 500 °C, then 3 °C min⁻¹ to 1200 °C, with a 1 h dwell, then 3 °C min⁻¹ to room temperature. Photos were taken before and after the sintering for some of the tubes painted with LSM-YSZ ink.

YSZ electrolyte layer

Some of the later LSM cells had one of three different YSZ inks painted on them to form the electrolyte layer. The 8YSZ and 3YSZ inks were made as described in subsection 2.1.3, and a 3YSZ commercial ink, referred to as 3YSZ-C, was also used. The LSM cell was held with a bent paperclip inserted inside it, so that the whole outer surface of the cell could be painted, and a small brush was used to apply the ink. This avoids the problem seen with dip-coated cells, that the portion of the cell with the string around it which holds the cell during dipping, cannot be coated with YSZ.

Then, the painted cells were left at room temperature for 10 min, to allow any brush-strokes in the ink to settle out, before drying at 80 °C or 90 °C for 10 min - 15 min, to evaporate the volatile components of the ink vehicle. They were then sintered with the profile 1 °C or 2 °C min⁻¹ to 500 °C, then a 3 °C min⁻¹ ramp rate to 1350 °C, a 1 h dwell, then 3 °C min⁻¹ to room temperature. Occasionally, a dwell temperature of 1330 °C or 1400 °C was used instead of 1350 °C. Most of the cells were photographed before and after sintering.

NiO/YSZ fuel electrode layer

A NiO/YSZ screen printing ink from subsection 2.1.3 was used to paint NiO/YSZ fuel electrodes onto some of the later cells. A band of ink was painted around the outside of the cell, near the sealed end, but not covering it. This was done to avoid touching any rough parts of the YSZ electrolyte. These arise from the rough line on the top of the LSM cell, where the tube is sealed by cutting during the extrusion process. If there are any holes in the YSZ here, the NiO/YSZ would penetrate them and short circuit the cell. The drying and sintering process for the NiO/YSZ ink is the same as for the YSZ ink above.

2.1.7 Sealing reversible SOFC

Sealing onto 316 stainless steel pipe

RSOFC were sealed to 316 stainless steel 3.125 mm outer diameter tubes, by clamping the steel tube and the RSOFC in position, cleaning the surface to be joined with ethanol or acetone, and applying a layer of Ceramabond VFG-552 ceramic adhesive (Aremco) to bridge the gap and make a seal. The sealant is then left to air dry, for 1 h - 2 h, then cured by heating at 2 °C min⁻¹ to 90 °C for 2 h, and then 250 °C or 260 °C for 2 h, then cooled to room temperature at 3 °C min⁻¹. Various other heating/cooling rates and dwell temperatures were also used.

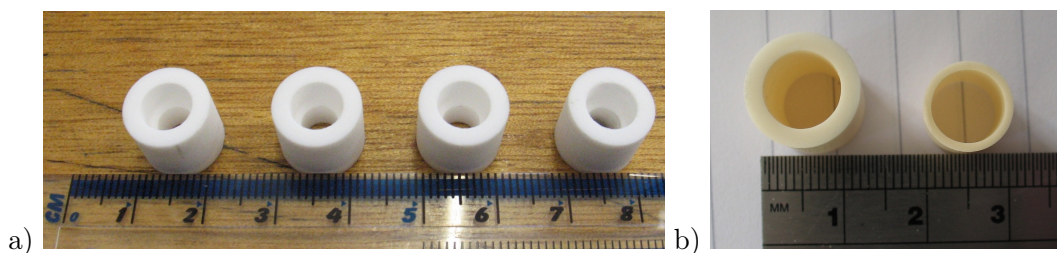


Figure 2.1.8: Ceramic rings used in sealing RSOFC to alumina gas delivery tubes: a) MACOR glass ceramic rings, smaller bore 5 mm (lower half), larger bore 7 mm (upper half), outer diameter 12 mm, and b) alumina rings, 8 mm bore, outer diameter 10 mm or 14 mm.

Sealing onto an alumina tube

Several types of alumina tube were used - the first was a 5 mm outer diameter, with 4x 0.5 mm bores in it, and the second type was a 5 mm outer diameter, with a single 3 mm diameter bore in it. The third type was a 6 mm outer diameter, with a 4 mm bore. The 4-bore alumina was used for the RSOFC-H-cell4-5, and single bore alumina was used for all subsequent reversible SOFC. The ceramic adhesives used for sealing were Ceramabond 552-VFG (Aremco), and Toku P-24 sealant (Tokuriki Research Chemical Co., Ltd). They were applied in the same way as described above for the steel tube support, except that after drying, they were cured with a variety of different ramp rates, and dwell temperatures.

Sealing using MACOR/alumina rings

In order to improve the sealing of the alumina/RSOFC joint, the area to be sealed was reduced, by encasing it in a MACOR ring. MACOR is a glass ceramic material, which was machined into a ring, as shown in fig. 2.1.8a. Short sections of alumina tubes were also cut for the same purpose, in fig. 2.1.8b. All these rings were cleaned with acetone to remove grease before using them. They were attached to the joint using either Ceramabond or Toku sealants.

2.1.8 Leak testing reversible SOFC

Four different experimental setups were used to carry out leak tests using oxygen gas. In the first, the stainless steel supported cell was attached to a manifold with a pressure sensor, but isolated from it by a valve. The manifold pressure was adjusted to about 100 mbar - 125 mbar, and then the valve was opened to expose the cell to the pressure. There was a relatively small volume of oxygen inside the manifold, so the pressure changed measurably even if the leak was small. The pressure transducer was connected to an E725 pressure display (RDP), and the voltage output from this was logged by an MX-100 logging voltmeter and connected PC, and converted to a pressure using software. Thus, the pressure drop over a period of 5 min was recorded. In later leak tests, a lower starting pressure was used, about 60 mbar.

The second experimental setup was used for the cells that had an alumina gas delivery tube. It was the same except that in order for the tube to fit the manifold, a short section

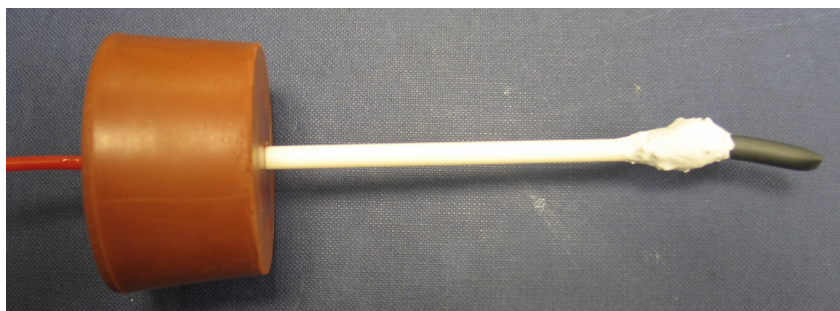


Figure 2.1.9: Leak testing apparatus: A rubber bung has two holes bored in it, which allows rapid leak testing of several cells: The red pipe leads to the manifold and pressure sensor. A reversible SOFC is shown fitted to the bung, ready to be leak tested. The bung is clamped during leak testing to prevent movement, and possible damage to the cell.

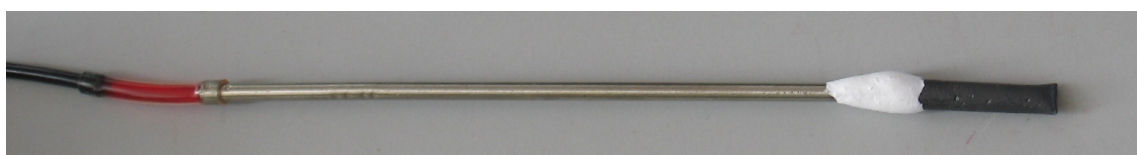


Figure 2.1.10: Red dye leak test setup - pre test. The red dye can be seen in the transparent tube attached to the stainless steel support tube.

of 316 stainless steel 3.125 mm pipe was cut and attached to the end of the alumina tube with silicone sealant. The pipe and tube were cleaned with acetone before applying the sealant, which was typically left to cure over several hours.

The third experimental setup in fig 2.1.9 used a different manifold that did not require the stainless steel pipe - the alumina tube could be put directly into it. It consisted of a rubber bung with a hole slightly smaller than the diameter of the alumina pipe, which the pipe was pushed into in order to make a seal. This was an effective method of quickly doing leak testing. A blocked section of alumina pipe as used to leak test the rubber bung setup, and it had zero leakage over 7 min.

The fourth method of leak testing was by using the cell testing jig, in the pressure vessel. The stainless steel tube from the cell was plugged into it, which seals with a rubber ring, and then the cell was tested by measuring the pressure drop over 5 min.

To determine the location of leaks, three different methods were used. Firstly, the cell and seal were immersed in water, and a pressure of 250 mbar - 300 mbar was applied to the inside of the cell. The bubbles observed showed the leak location. Secondly, soap solution (Teepol) was placed on the outside of the cell, and a pressure of 250 mbar - 300 mbar was applied to the inside of the cell. Bubbles were observed, indicating where the leaks were. The third method is shown in fig. 2.1.10. A solution of 0.75 g of red food colouring in 50 ml water was put in the manifold. When a pressure of 200 mbar - 250 mbar was applied to the inside of the cell, the dye was pushed up into the cell, and red spots on its surface indicated the location of leaks. This method was useful for showing how porous the ceramic seal was. As it is translucent, a faint red colour could be seen underneath the surface of the white ceramic in porous areas, even if there was no leak.

2.1.9 Current collection and short circuit testing for the reversible SOFC

Current collectors were applied to both the oxygen and fuel electrodes. A noble metal must be used for the oxygen electrode as it is a highly oxidising environment, with pure oxygen at several bar pressure inside the cell. However, a wide range of metals may be used on the fuel electrode side, as it is a reducing environment.

Silver and copper current collection

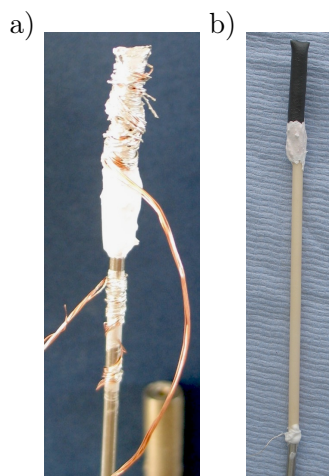


Figure 2.1.11: a) RSOFC-H-cell4-4 with copper current collecting wires, with silver paste as prepared, b) RSOFC-H-cell4-5. The oxygen electrode current collector is a silver wire which is inside the cell, and runs down the bore of the alumina tube, and comes out through the silicone joint between the alumina and the stainless steel (bottom). There is no fuel electrode current collector applied to the cell.

Initially, copper was used in conjunction with silver for the current collection on the fuel electrode side, because copper is cheap and has an excellent electrical conductivity, just slightly less than silver. The inside of the cell was painted with silver paste (Alfa Aesar), before the sealing took place, to electrically connect the oxygen electrode to the stainless steel gas delivery tube and current collector. Copper wires (0.44 mm diameter) were wrapped around the RSOFC, and the steel tube support, and then painted with silver paste, as shown in fig. 2.1.11, to make contact with the cell. A multimeter was used to check for a short circuit across the cell. The resistance of the cell at room temperature should be about 80 M Ω , assuming a typical cell geometry of 5 cm long, a diameter of 0.6 cm, and an electrolyte thickness of 50 μm .

Silver current collection

Other cells had current collectors applied in the same manner as in fig. 2.1.11a, except that the copper wires were replaced with silver wires. The later reversible cells, RSOFC-H-cell4-5 and subsequent cells, had an alumina tube instead of the steel tube. In order to collect current on the oxygen electrode side of the cell, a silver wire was folded into a u-shape at its end, then the u was bent in half to make a 3D shape, which was pushed inside the cell to the top with silver paste. The trailing silver wire was threaded through the bore of the alumina support. It comes out at the silicone joint between the alumina and the stainless steel gas delivery tube, in fig. 2.1.11b. The latter is necessary, because the reversible SOFC testing jig is designed to fit 3.125 mm stainless steel pipe tubes. The silicone is applied after the end of the alumina and the stainless steel tube have been cleaned with ethanol to remove any grease on their surfaces. The fuel electrode current collector is applied in the same manner as before, then the cell is tested for short circuits across the electrolyte.

Nickel and gold current collection

Silver melts just above fuel cell operation temperatures, so a better current collector on the fuel electrode side is nickel. Copper wire and nickel mesh was used, along with nickel paste, for some of the earlier cells. The paste was made by mixing an organic solvent such as butanol with nickel metal powder ($\sim 3 \mu\text{m}$, 99.7%, Sigma Aldrich). Subsequent cells

were made with a nickel wire and mesh, wound around the NiO/YSZ fuel electrode of the RSOFC. On the oxygen electrode side, the silver was replaced by gold wire and paste on the inside of the cell. This gold wire was sometimes connected to a silver wire lower down inside the alumina tube, where the temperature was lower during testing, for reasons of economy.

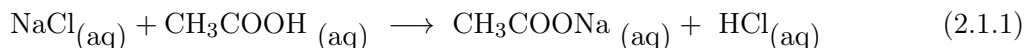
2.1.10 Brazing

Brazing is a method to produce a gas-tight joint, from a metal alloy. It is applied as a paste, powder or foil, and then melted to form the brazed joint. It may be used to seal fuel cells, giving an electrically conductive seal, and can be used to make metal-ceramic or ceramic-ceramic joints. Therefore, it can function as a current collector as well as a seal.

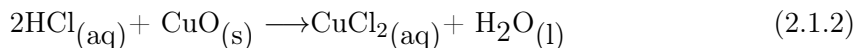
A reactive air braze is brazed in air, and consists of a component which oxidises, which wets the surfaces to be joined, and a noble metal, which provides electrical conductivity and fills the joint. One such braze is a copper-silver mixture, which oxidises when brazing to silver-copper(II) oxide.

Silver-copper brazes

In order to make silver-copper brazes, silver powder ($2\ \mu\text{m}$ - $3.5\ \mu\text{m}$, 99.9%, Aldrich), and copper powder (Fisons) were mixed. However, copper powder oxidises over time in storage, taking on a black appearance, which is a surface Cu(II)O layer. In order to reduce this to metallic copper, NaCl (5 g) was dissolved in distilled water (20 ml) with glacial acetic acid (10 g), which reacts to form dilute hydrochloric acid according to reaction equation 2.1.1. Then oxidised copper powder (7 g) was added, and the solution was left for 3 min, or else boiled for 5 min, when the copper oxide was slow to reduce.



During this time, the reaction in equation 2.1.2 occurred, and the colour of the copper powder changed from black to a shiny coppery colour.



Then the liquid was decanted, and the copper particles were rinsed with distilled water, dried at $80\ ^\circ\text{C}$, and examined by SEM. In order to make brazes, the silver and copper powders were mixed according to the desired ratio in the braze.

An initial trial of the braze material used the following composition: copper powder: 0.258 g, silver powder: 1.0368 g, butvar B-98 (Sigma): 0.1 g, and polyethylene glycol: 0.428 g. This is a Ag-Cu ratio of 29.8 mol.% copper, with the balance silver. The braze was applied inside two LSM tubes (cellulose and water based) that had been extruded by hand and then sintered. Two short lengths of 3.125 mm diameter 316 stainless steel pipe were cut, filed at one end so that they would fit inside the LSM tubes, cleaned with acetone, and then fitted inside the LSM tubes. The brazing paste was also applied to the LSM-steel joint in a ring around its diameter. Some of the braze mixture was also placed

on an LSM tube split lengthwise. The samples were brazed at $5\text{ }^{\circ}\text{C min}^{-1}$ to $1000\text{ }^{\circ}\text{C}$ for 0.5 h, then $5\text{ }^{\circ}\text{C min}^{-1}$ to room temperature.

A similar experiment was also performed with a 40 mol.% CuO, balance Ag braze, except that only 2 tubes were made.

Variation of the silver-copper ratio in the braze

In order to examine the effect of varying the silver-copper ratio of the braze, five different compositions with different ratios were prepared as in table 2.1.6, by mixing the powders with a small amount of polyethylene glycol. The brazes were then applied to an LSM tube - stainless steel joint as before. Some of the tubes were weighed before and after application of the braze to determine the mass of braze used. The samples were then brazed with the heating rate of $5\text{ }^{\circ}\text{C min}^{-1}$ to $1000\text{ }^{\circ}\text{C}$ with a 0.5 h dwell, and then cooled at $5\text{ }^{\circ}\text{C min}^{-1}$ to room temperature. The samples were mounted in resin and cross sectioned across the brazed joint, and SEM pictures were taken, and EDX was carried out on the samples.

Braze no	mol.% Cu	Cu powder (g)	Ag powder (g)	Polyethylene glycol (g)
1	0	0.000	0.3236	0.1
2	4	0.0076	0.3107	0.1
3	8	0.0153	0.2977	0.1
4	16	0.0305	0.2718	0.1
5	32	0.0610	0.2201	0.1

Table 2.1.6: Braze compositions - varying the Ag-Cu ratio in the braze.

Braze:LSM composite pellets

Braze:LSM (vol.%)	Mass Cu (g)	Mass Ag (g)	Mass LSM (g)
20:80	0.0381	0.7443	2.0682
30:70	0.0569	1.1115	1.8017
40:60	0.0763	1.4886	1.5512

Table 2.1.7: Braze-LSM composite experiment. The braze used was 8 mol.% Cu with the balance Ag.

A braze may also contain a filler material, which functions to reduce the coefficient of thermal expansion of the braze, and decreases mismatch of the expansion coefficients of the steel and the fuel cell components. This may also function as a matrix to hold the braze, allowing it to fill a wider gap. Therefore, a composite material of the braze powder and LSM powder was made, by mixing these powders and pressing pellets with a pressure of 3000 kg. The compositions are shown in table 2.1.7.

The LSM was added to lower the thermal expansion coefficient of the braze. It is thought that this will help to prevent delamination at the braze-fuel cell interface. Two pellets were made with each composition in table 2.1.7. One of these was placed on a

square of copper sheet, and the other was placed on a square of 316 stainless steel. The six samples were then sintered with the profile: $5\text{ }^{\circ}\text{C min}^{-1}$ to $1000\text{ }^{\circ}\text{C}$ for 0.5 h, then $5\text{ }^{\circ}\text{C min}^{-1}$ to room temperature. The samples were photographed after sintering, and the mounted in resin, cross sectioned and prepared for SEM. Images were taken, and EDX was performed on the braze:steel interface.

Brazing unsintered LSM to steel with braze interlayer

In order to investigate the braze:LSM composite further, two different compositions were made, with an 8 mol.% Cu, balance Ag braze, as a composite with LSM, with either 30 vol.% braze or 40 vol.% braze. These composites were thoroughly mixed by hand in a 1:1:1 volumetric ratio with 2-hydroxyethyl cellulose (Aldrich, M.W. 90,000) and distilled water, and pressed between Mylar[®] sheets by hand to give flat discs. An LSM tape casting tape was made as described in section 2.1.2, except that the ceramic component was entirely LSM. The discs of the mixture, and the LSM tape, were placed on 316 stainless steel flat discs. The effect of including a braze:LSM composite interlayer between the LSM tape and the steel for some of the samples was investigated. The matrix of samples made is shown in table 2.1.8. The samples were sintered at $5\text{ }^{\circ}\text{C min}^{-1}$ to $1000\text{ }^{\circ}\text{C}$, with a 0.5 h dwell, then $5\text{ }^{\circ}\text{C min}^{-1}$ to room temperature, photographed, mounted in resin and cross sectioned. They were examined by SEM and EDX.

Sample no.	Sample type (layer 1 layer 2 layer 3)	Braze:LSM ratio (vol.%)
1	Braze:LSM+organics braze interlayer 316 stainless steel	30:70
2	Braze:LSM+organics 316 stainless steel	30:70
3	Braze:LSM+organics braze interlayer 316 stainless steel	40:60
4	Braze:LSM+organics 316 stainless steel	40:60
5	LSM tape braze interlayer 316 stainless steel	n/a
6	LSM tape 316 stainless steel	n/a

Table 2.1.8: Unsintered LSM with cellulose binder and water (organics), with and without braze interlayers, on a 316 stainless steel pellet, and LSM tape on 316 stainless steel, with and without a braze interlayer. The braze is 8 mol.% Cu in all cases.

Braze:LSM composite on Ti coated 316 and 430 stainless steel

In this experiment, braze:LSM composite pellets were brazed to steel samples that had been modified by evaporating titanium onto them, in order to see if this aided adhesion, or helped to prevent corrosion of the steel during sintering. For this experiment, a fresh batch of copper powder from the oxidised copper powder (Fisons), was prepared in the same manner as before, as the previous batch had run out.

The steel substrates were prepared in a vacuum using an evaporator (University of St Andrews) designed for evaporation of gold onto SEM samples, which consists of two tungsten filaments in a vacuum chamber. A piece of titanium foil is placed inside the coil of one of

the tungsten filaments, and the steel samples to be coated are placed about 10 cm below the coil.

Sample type (layer 1 layer 2 layer 3 ...)	Brazing temp. (°C)
316 Brazo:LSM	1000
430 Brazo:LSM	1000
Ti 316 Ti Brazo:LSM	1000
Ti 430 Ti Brazo:LSM	1000
Ti Ti 316 Ti Ti Brazo:LSM	950
Ti Ti 430 Ti Ti Brazo:LSM	950
Ti Ti 316 Ti Ti	950
Ti Ti 316 Ti Ti	950

Table 2.1.9: Braze:LSM composite pellets on steel substrates, either 316 or 430 stainless steel, coated with either 0,1 or 2 layers of evaporated titanium, brazed at either 1000 °C or 950 °C for 0.5 h.

pellets with a diameter of 5 mm were pressed uniaxially with a pressure of 75 kg, giving a final thickness of 2 mm. The samples were sintered with a heating rate of 3 °C min⁻¹, a 0.5 h dwell at 1000 °C or 950 °C, and a cooling rate of 3 °C min⁻¹. After sintering, the samples were photographed, mounted in resin, cross sectioned, and examined by SEM and EDX.

The vacuum chamber is then evacuated in a two-stage process that reduces the air pressure to $<1 \times 10^{-5}$ mbar. Electrical current is passed through the tungsten filament, heating it white-hot, and the titanium melts and then evaporates, coating everything around the coil in a thin layer of titanium. The vacuum is then released, and the steel is inverted, in order to coat the other side. Multiple layers of titanium were deposited on some samples by repeating the process. Two types of stainless steel, 316 and 430, were used in this experiment. Those that were coated had either one or two layers of titanium, as shown in table 2.1.9. Six of these steel substrates had a composite braze:LSM braze pellet brazed to them. The braze was 8 mol.% Cu, balance Ag, and was mixed with LSM in a 40:60 ratio by volume. Six braze:LSM composite pel-

2.2 Characterisation methods

2.2.1 Optical microscopy

An optical ML 2000 Microscope (Meiji Techno Co. Ltd.) was used to examine LSM tubes produced, and particularly to identify any cracks in dip-coated YSZ electrolytes. The microscope has an adapter to fit a Canon Powershot G6, 7.1 megapixel digital camera, which was used to take some optical micrographs, at magnifications of 100x, 200x, 500x, and 1000x.

2.2.2 Scanning electron microscopy (SEM)

A scanning electron microscope (SEM, JSM 5600, Jeol) was used to examine samples at the small scale.

Powder examination

The powders examined in the SEM were sprinkled onto sticky conductive carbon paper, and held upside down so the excess fell off. Alternatively, suspensions containing powders were placed on carbon paper and allowed to dry before SEM examination.

Samples mounted in resin

The majority of samples examined by SEM were mounted in resin. The sample was placed in a mould greased with high vacuum grease (Dow Corning). EpoFix resin and hardener (Struers) were mixed in a 6:1 ratio by volume, poured over the sample, and placed in a glass vacuum chamber, or Citovac vacuum chamber (Struers). The air was evacuated for 2-3 min until all bubbles of air inside the sample had expanded out, and then the samples were taken out, and left overnight to cure.

The disc of resin with the sample was then sectioned with a Minitom diamond saw (Struers) and polished on a Metaserv 2000 grinder/polisher (Buehler) according to the procedure in table 2.2.1. They were then gold coated, by an high vacuum gold evaporation method, using equipment made by the University of St Andrews.

Polishing media	Duration	Lubricant
600 grit SiC paper	2 min	water
1200 grit SiC paper	3 min	water
Cloth with 6 μm diamond paste	10 min	Metadi fluid (Buehler)
Cloth with 3 μm diamond paste	5 min	Metadi fluid (Buehler)
Cloth with 1 μm diamond paste	3 min	Metadi fluid (Buehler)

Table 2.2.1: Polishing process for resin mounted SEM samples. In between each step, the resin discs were ultrasonicated in an ultrasonic bath (Ultrawave Ltd.) in water for 2 min to clean them.

Fractured and conductive samples

Some samples such as YSZ coated LSM tubes were fractured, and the fracture surface was examined in the SEM. The less conductive YSZ contrasted with the more conductive LSM under the electron beam. These samples not mounted in epoxy, because the thin solid YSZ layers are easily damaged. The vacuum that is applied to draw air out of all the pores and infiltrate liquid epoxy resin, puts pressure on the YSZ layer, causing it to shatter. Then, as the epoxy cures, it shrinks, which also puts pressure on the YSZ layer. Therefore, the samples are best examined without being mounted in epoxy resin.

2.2.3 Energy dispersive X-Ray spectroscopy (EDX)

A scanning electron microscope (JSM-5600, Jeol) was used to carry out energy dispersive X-ray spectroscopy. Various samples were examined, and elemental composition was determined over a set area (map), along a line, (line scan) or a single point (spectrum).

Furthermore, by combining data from two different elements, maps of particular phases were produced.

2.2.4 Thermal gravimetric analysis

Thermal gravimetric analysis is a technique which accurately measures mass changes in a sample during a heating profile, and can be carried out in either a reducing or oxidising atmosphere, with a variety of gases. It was used in this work to measure the temperatures at which organic components of the extrusion recipes combusted. This is important to understand, as organic components that persist to hotter temperatures will have a greater impact on pore formation in the LSM substrate. Typically, 10 mg - 20 mg of the organic component was placed in a platinum crucible in a thermal gravimetric analyser (TG-1000-M, Rheotherm), and was heated at $5\text{ }^{\circ}\text{C min}^{-1}$ to $900\text{ }^{\circ}\text{C}$ or $950\text{ }^{\circ}\text{C}$. The mass loss as a function of temperature was plotted, which showed the temperatures that the components burned out at, and allows comparison between them.

2.2.5 Particle size distribution analysis

Particle size distribution measurement may be carried out by several methods, but the one used in this work is laser diffraction. The particles to be examined are suspended in a solvent, and flow past a laser. When the laser hits the particles, the light is scattered. Smaller particles create a greater scattering angle, but weaker intensity of light, and larger particles are the opposite. In this way, a particle size distribution measurement can be made. In-situ ultrasonication can also be used to break up agglomerates in the slurry to be examined.

LSM used for extrusion

A Hydro 2000S Mastersizer (Malvern) was used to make particle size distribution measurements on the LSM used for extrusion. 20 mg - 30 mg of LSM was dispersed in a solution of 2 % by mass Triton QS-44 dispersant in isopropanol (99.8%, BDH), using an Ultrawave ultrasonic bath (Ultrawave Ltd.) for 2 min, and then the particle size distribution was recorded three times.

YSZ dip-coating slurries

A selection of YSZ dip-coating slurries were measured in the particle size analyser. The typical procedure was similar to that used for the LSM, but the samples were not ultrasonicated. They were shaken for 1 min by hand, allowed to settle for 24 h, and then the suspended layer was sampled. The slurries were then shaken for a further 1 min, and the mix of the settled and suspended layers was sampled. The suspended layer is that which is coated onto the tubes, and the mix of the two layers shows how well the YSZ is dispersed in the slurry.

YSZ screen printing ink

The particle size distribution of three screen printing inks; a 3YSZ ink, an 8YSZ ink, and a commercial 3YSZ ink, were measured with the particle size analyser. Three measurements were made on each ink, firstly on the ‘as made’ ink, secondly after 1 min ultrasonication in situ, and thirdly after 10 min ultrasonication in situ. A comparison of the measurements allowed the dispersion of the particles in the ink to be determined. The first measurement shows the agglomerates, the second measurement shows the hard agglomerates, and the third measurement shows the primary particle size.

2.3 Testing symmetrical half cells

2.3.1 AC impedance on tape cast cells at ambient pressure

The tape cast samples in this section were tested in jigs with a 2 electrode, 2 wire configuration. The tape cast cells from section 2.1.2 were tested in a jig which held two samples. Electrical contact was made to the cell electrodes by platinum bead contacts, which were spring loaded. The resistance of the probe was measured, and subtracted from the series resistance of the impedance results. The tape cast sample tested in oxygen was tested in a separate sealed jig, with a slow flow of oxygen through it. The current collection was carried out by a fine platinum mesh which was spring loaded and pressed against the sample. All three cells were tested at a range of temperatures between 500 °C - 900 °C, by measuring the impedance, using a sinusoidal a.c. potential of 50 mV root mean square, and measuring at various frequencies between 0.1 Hz to 100kHz or 1 MHz. The results were fitted to an electrical equivalent circuit as shown in fig. 2.3.1, and the total polarisation resistance obtained was corrected for the cell area, which was measured with digital callipers (Guo Gen)

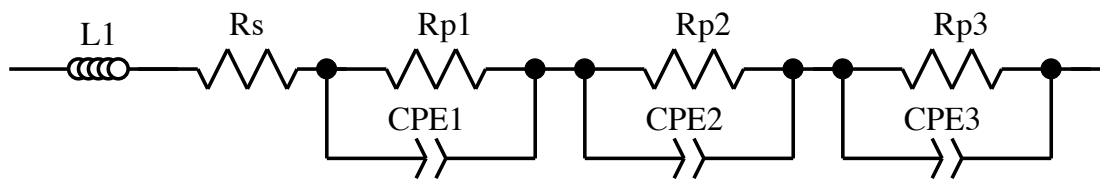


Figure 2.3.1: Electrical equivalent circuit used to model ac impedance results. L1 = inductor, Rs = series/ohmic resistance, Rp = polarisation resistance, CPE = constant phase element. For some results, only two impedance arcs could be resolved instead of three, so a simplified equivalent circuit was used, which did not have Rp3 and CPE3.

Thermal ageing test

After the initial impedance spectra were measured at various temperatures, the cells were held at 900 °C at OCV for about 160 h, in order to see how the impedance results changed over time. Impedance spectra were taken periodically. The samples tested in air had a static atmosphere of air around them, and the samples tested in oxygen had a very slow flow of oxygen over them.

2.3.2 Impedance spectroscopy on pellet symmetrical cells at high pressure

Testing procedure

The pellet symmetrical cells in this section were tested in a jig with a 2 electrode, 4 wire configuration. They were made as described in subsection 2.1.1, and an LSM-YSZ oxygen electrode and LSM current collector were applied as described in section 2.1.3. The cells were placed in the test setup shown in fig. 2.3.2a. The setup is a 2 electrode, 4 wire

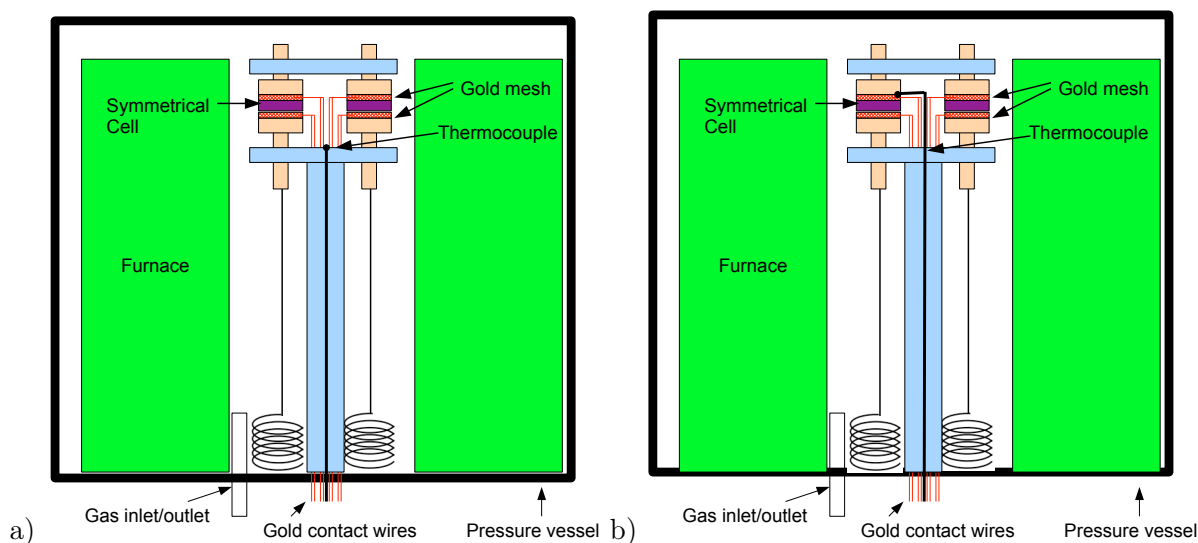


Figure 2.3.2: Symmetrical cell test setup: a) with thermocouple tip on ceramic base plate, and b) with thermocouple tip next to the sample.

setup. Therefore, the ohmic resistance measured corresponds only to the short distance between the point at which the two wires on each side of the symmetrical cell merge, and the electrode surface. This greatly reduces the effect of jig resistance on the measurement. In order to eliminate the remaining resistance from the results, impedance measurements were carried out at a range of temperatures, without a sample in the jig - it was shorted out - and the ohmic resistance of the jig was determined. This was subtracted from any impedance results obtained, so that only the resistance of the symmetrical cell itself was counted.

The experiments are carried out in pressurised pure oxygen, and a pressure transducer is used to measure the gas pressure, which is equal to the P_{O_2} . Gas is added or vented via a valve in the pressure vessel until the correct pressure is reached. When an experiment is carried out, after the pressure vessel is assembled, it is purged by increasing the oxygen pressure to 5 bar above atmospheric pressure and then venting gas to reduce it to just above atmospheric pressure three times, which means that $(1/6)^3 = 1/216$ or 0.46% of the air present at the start is left. There is also a tap on the base of the vessel so any water which condenses on the base of the vessel during testing may be removed. Pressures and temperatures are monitored using an MX-100 data logger (Yokogawa) connected to a computer.

The electrochemical impedance spectroscopy measurements are performed at various temperatures and pressures on the symmetrical cells using an Ivium Compactstat (Ivium) impedance analyser. The impedance was measured at about 70 frequencies between 1 MHz and 0.1 Hz, by passing a sinusoidal a.c. voltage of 10 mV across the sample, and measuring the current response. From this, the real and complex impedance are calculated and recorded through a software interface (Iviumsoft) with a desktop computer. The data are exported in a comma separated values (csv) format and imported into the program Zview v2.8. The data were fitted to the electrical equivalent circuit in fig. 2.3.3. Data with negative values of imaginary impedance was not modelled - this data has a negative imaginary impedance, because of distortion from inductance in the wires of the jig. Therefore, the inductance was also not modelled. Two resistor/CPE parallel units were used, because the spectra had two visible arcs.

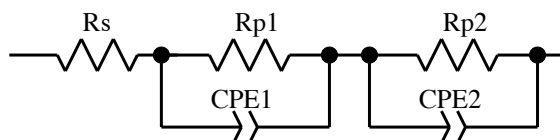


Figure 2.3.3: Electrical equivalent circuit used to model impedance data from high pressure measurements. R_s = series/ohmic resistance, R_p = polarisation resistance, CPE = constant phase element.

Conductivity of the symmetrical cells

The in-plane conductivity of the symmetrical cell electrode was quantified by measuring the resistance across the electrode surface, for various pellet samples. A multimeter was used to measure resistance across the electrode surface. The pointed metal contacts were pushed onto the electrode surface at both edges of the circular electrode, which is approximately 8 mm in diameter, and the resistance was measured. The sample was rotated by 45 degrees and measured again. This was done a total of four times, and the results were averaged. One sample had a gold grid painted onto it - in this case care was taken to avoid touching the grid with one of the contacts, so that the resistance of electrode and grid was measured, not the resistance of the grid alone.

Testing temperature calibration

In order to check that the sample temperature thermocouple in fig 2.3.2a was accurately measuring the temperature of the symmetrical cells, a second thermocouple, not shown in the figure, was placed next to the cell, physically touching it. This showed that the thermocouple position in 2.3.2a underestimated the symmetrical cell temperature by about 60 °C - 80 °C. Therefore, the test setup in figure 2.3.2b was adopted, with the thermocouple tip actually touching the jig next to the sample.

However, as the impedance measurements on the symmetrical cells had already been carried out before this calibration, the temperatures that they had been measured at were incorrect. Therefore, a spare YSZ pellet made in the same furnace at the same time as the pellets used to make the tested symmetrical cells, was painted with gold paste (Alfa Aesar) on both sides, dried at 80 °C for 0.5 h, and impedance measurements were made on it at various temperatures. The resistivity of the pellet was calculated from its area and

thickness, and $\log(\text{resistivity})$ was plotted against $1000/T$, and a linear trend line was fitted to it with Microsoft Excel. Then, the ohmic resistance of the symmetrical cells that were measured was adjusted for the probe resistance, and the remainder of the resistance was assumed to be entirely due to the electrolyte. This neglects the small contribution from the LSM-YSZ electrodes, as they are much more conductive than the YSZ electrolyte, and about fifty times thinner. This resistance was converted to a resistivity and compared to that measured for the YSZ pellet with gold electrodes, where the testing temperature was known. Therefore, the temperature at which the pellets had been tested was calculated and it was found to be about 60-80 °C higher than the nominal temperature, agreeing with the measurements made by the thermocouple.

2.4 Testing of RSOFC

2.4.1 Test setup

The test setup used to perform electrochemical tests on the RSOFC is shown in fig. 2.4.1. This setup allows testing of RSOFC in electrolysis and fuel cell modes, by doing I/V curves and impedance measurements, under pressure up to 5 bar, at temperatures up to 1000 °C. The cells fit into a jig clamped at the bottom of the pressure vessel. It has six holes for cells, each designed to receive a 3.175 mm diameter stainless steel tube into it, which are sealed by a push fit against a rubber O-ring. However, usually only one cell is tested at a time. In this case, the unused holes are blocked with 3.175 mm diameter stainless steel rods. Fig. 2.4.2a shows the jig, with one cell in it. The cell is wired to the electrical feed-throughs in the base of the pressure vessel, as in fig. 2.4.2b. The furnace is then fitted, and connected, so that the cell is inside it next to the furnace thermocouple, as in fig. 2.4.2c.

Various temperatures and pressures are logged by the MX-100 data logger, by converting voltage signals to the appropriate units. The data are recorded by the logging software on the PC. These data include the furnace temperature (which is also assumed to be the RSOFC temperature), the pressure vessel base temperature, the gas temperature inside the vessel, halfway from the base to the top, the oxygen and hydrogen/steam pressures, and the cell OCV. Oxygen gas can be added or vented via the solenoid valves shown in fig. 2.4.1. A furnace controller (not shown) is used to control the furnace temperature.

The test setup was modified in later tests, to allow it to be used for pressurised testing. It is crucial to balance the pressure across the cell when it is being tested under pressures greater than 1 atmosphere, otherwise the pressure differential might cause the cell to crack. In order to do this, the oxygen pressure and the hydrogen/steam pressure are monitored, and fed into the Picolog data logger, which sends a digital signal to the PC. Software custom-written using the Labview software, measures the pressure differential, and if it exceeds a certain value, sends a signal to the add or vent solenoid valves, to add or release oxygen gas. Therefore, the oxygen pressure is balanced against the fuel pressure. The fuel pressure can be manually controlled by opening a valve on the hydrogen cylinder.

The setup was also modified to allow oxygen to flow past the inside of the cell, by

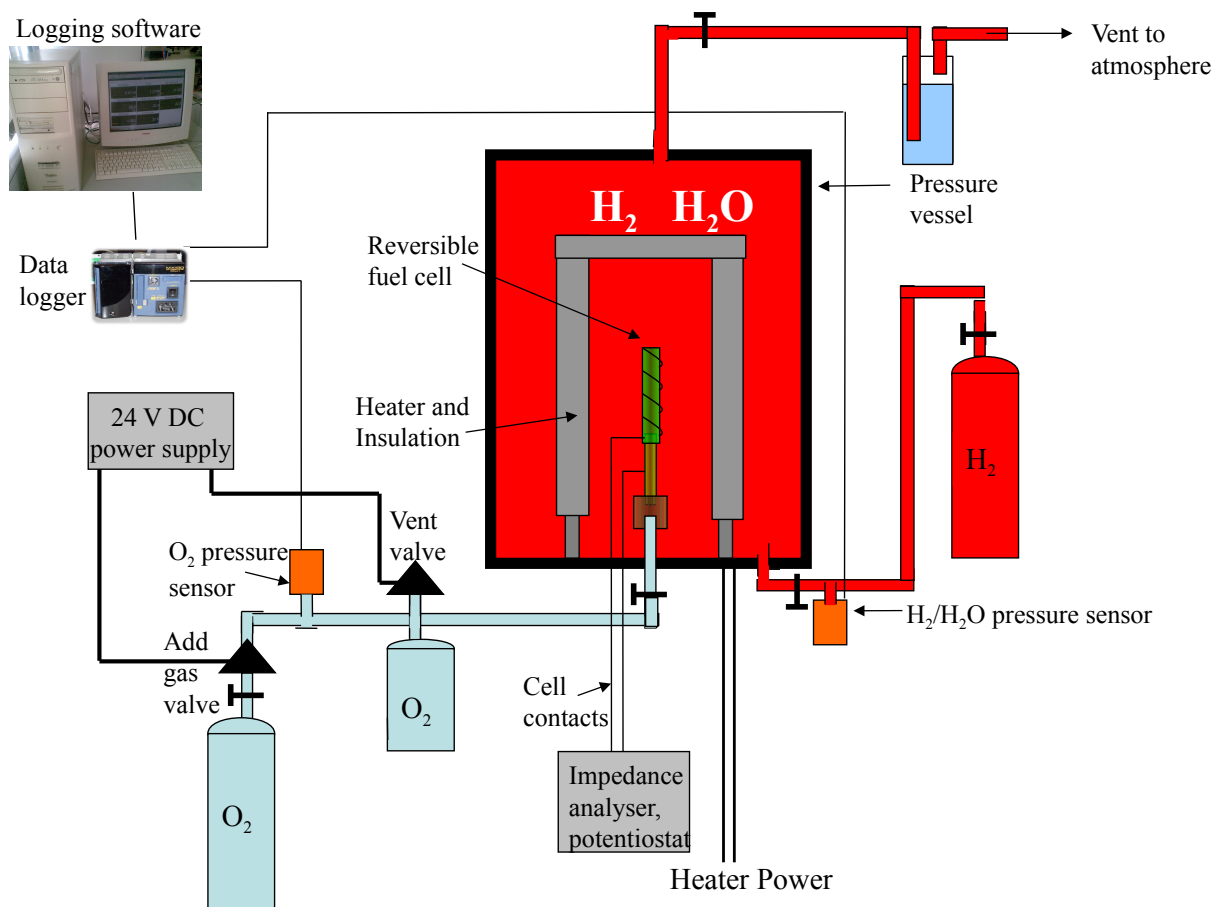


Figure 2.4.1: A schematic of the first test setup for electrochemical testing of RSOFC.

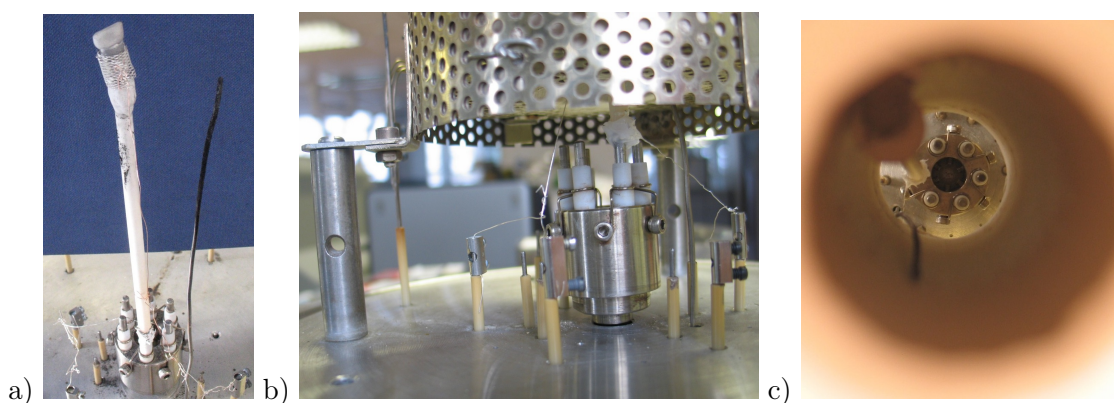


Figure 2.4.2: RSOFC fitted in the pressure vessel, before it is assembled for testing: a) A RSOFC fitted and wired into the pressure vessel jig. The fuel electrode current collection wire runs down the outside of the alumina gas delivery tube. The oxygen electrode current collection wire runs down the inside of the alumina tube, and comes out at the alumina-steel silicone joint. Image b) shows the 4 wire cell connections at the base, with the furnace in place, and c) shows the cell inside the furnace, with the furnace thermocouple.

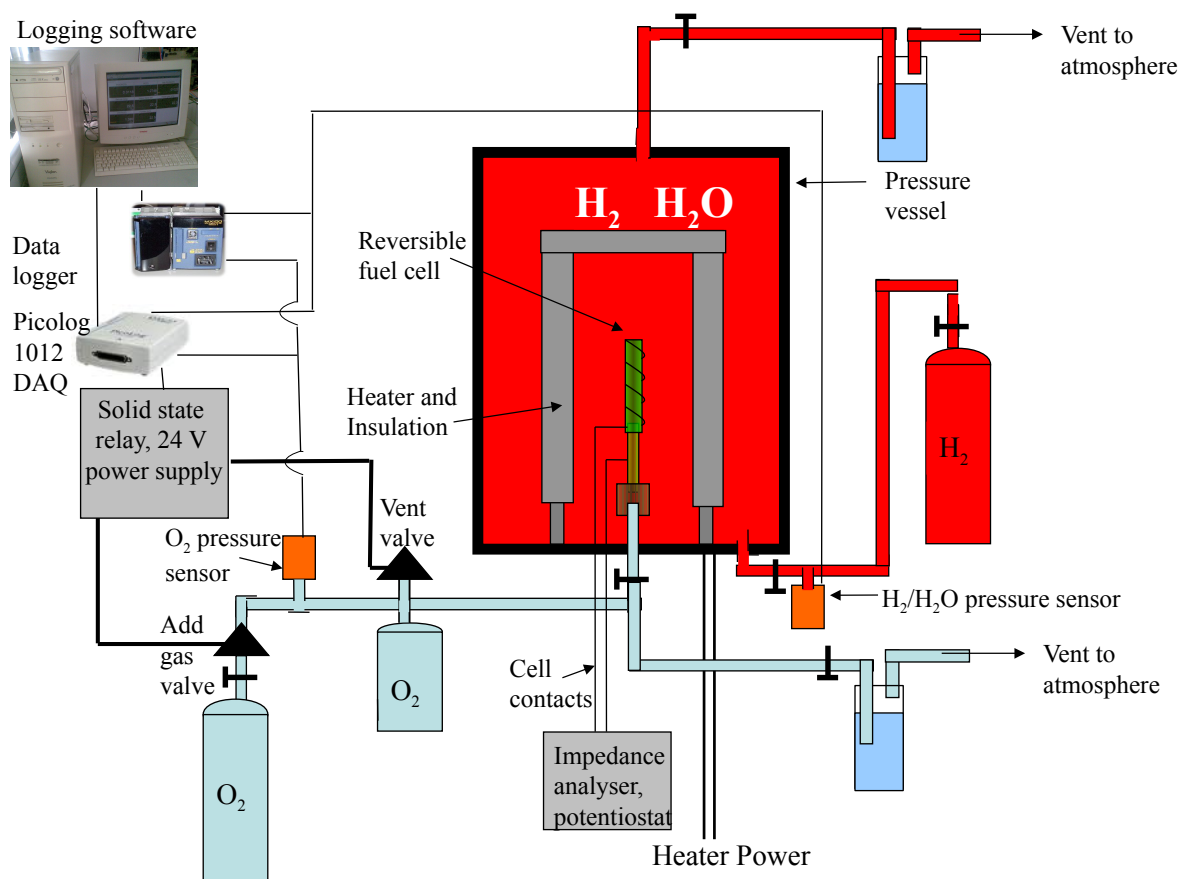


Figure 2.4.3: A schematic of the second test setup for electrochemical testing of RSOFC, which was modified from the setup in fig. 2.4.1, to allow oxygen to flow past the cell continuously.

adding an exhaust and bubbler to the oxygen line to the cell, as fig. 2.4.3 shows.

2.4.2 Testing procedure

In order to carry out a test, after the cells were wired in to the testing jig and the furnace was bolted on, the sides and the lid of the pressure vessel were bolted on to the base, which are sealed with large O-rings. The furnace is used to heat at various rates, ranging from $0.4\text{ }^{\circ}\text{C min}^{-1}$ to $3\text{ }^{\circ}\text{C min}^{-1}$. In the initial tests, flowing 5% H_2/Ar was used when heating the cells, and static oxygen on the oxygen side. For later tests, a switch was made to flowing oxygen, and then after another few tests, the fuel electrode was heated in static air to $700\text{ }^{\circ}\text{C}$ or $800\text{ }^{\circ}\text{C}$, then flowing 5% H_2/Ar . This was so the reduction of the cell happened at high temperature, which affects the morphology of the Ni particles produced in the fuel electrode.

The electrical resistance of the cells was often measured before, during and after testing, by using a multimeter across the feed-throughs at the pressure vessel base when the cell was wired in. In-situ leak tests were also carried out by applying a positive pressure of

oxygen inside the cell, then isolating it and measuring the pressure drop over 5 min with the pressure sensor.

Leak tests of the cells after testing were also carried out by applying a positive pressure inside the cell, and immersing it in water. Large leaks could be identified by streams of bubbles arising from the cell. A red dye was also used inside the cell, and a positive pressure was applied. This forced the dye out of any holes in the seal or the cell electrolyte, and showed the locations and severity of the leaks.

Impedance measurements

Impedance measurements were carried out with a Zahner frequency response analyser (IM6e, Zahner elektrik). A typical scan measured the impedance at a range of frequencies between 0.1 Hz and 100 kHz. Above 66 Hz, it measured 20 cycles per frequency, and 10 frequencies per logarithmic frequency decade, and below 66 Hz, it measured 5 cycles per frequency, and 4 frequencies per decade. This is to balance the conflicting demands of obtaining a good signal:noise ratio at low frequencies, and also a reasonably short collection time. A sinusoidal ac signal of 10 mV root mean square was used, and the current response was measured. From this, the complex impedance was calculated. The instrument was also sometimes used to record the OCV of cells.

2.5 Modelling a reversible SOFC system

In order to accurately model a reversible fuel cell system, some values obtained from experiment or literature sources were plotted. Most of these plots are shown in appendix B. The equations derived from these plots are referred to as semi-empirical equations, because they are based on empirical data collection. These are discussed below.

2.5.1 Data collection and analysis for semi-empirical equations

Equations for $V_{standard}$

This parameter is the standard voltage for the fuel cell/electrolysis reaction in eqs. 2.5.2 and 2.5.4. It is used to determine the Nernst voltage and cell output voltage in a reversible fuel cell. It can be calculated according to equation 2.5.1, where n is the number of electrons in the reaction, and F is Faraday's constant, $96485.34 \text{ J mol}^{-1} \text{ C}^{-1}$, and ΔG° (J mol^{-1}) is the free energy of reaction, which varies with temperature. A series of values of free energy at different temperatures is obtained for the fuel cell and electrolysis reactions 2.5.2 and 2.5.4, by using the program HSC Thermodynamics (Outokumpu Research Oy). This program uses thermodynamic data sets for hydrogen and steam [4], and oxygen [5].

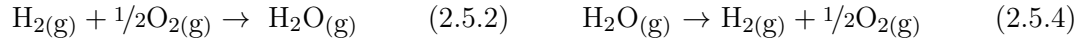
$$\Delta G^\circ = nFV_{standard} \quad (2.5.1)$$

The free energy values are used to calculate $V_{standard}$ values, which are plotted against temperature (K) for both fuel cell mode and electrolysis mode, using Microsoft Excel, and linear trend lines are used to give the equations 2.5.3 and 2.5.5, which relate $V_{standard}$ to

the temperature of the reaction. It was decided that the parameter $V_{standard}$ would be rendered as a positive value in both cases, for ease of calculation in the software model.

Fuel cell mode

Electrolysis mode



$$V_{standard} = (-0.00028090T_s + 1.277058) \quad (2.5.3) \quad V_{standard} = (-0.00028090T_s + 1.277058) \quad (2.5.5)$$

Equations for ohmic resistances of reversible cell components

The ohmic resistance of cell components can be calculated, if their geometry and resistivity is known. The resistivity of the support was calculated by plotting a graph of resistivity against temperature from literature data for the compound $\text{La}_{0.8}\text{Sr}_{0.2}\text{CoO}_3$ [6]. This compound was chosen as it has a high electronic conductivity, and has been used as the electronic conductor in composite oxygen electrodes for SOFC. The software Microsoft Excel was used to fit a trend line to the data, and produce equation 2.5.6.

$$\rho_{support} = 0.01 \exp\left(\frac{-316.1}{T_s} - 2.8719\right) \quad (2.5.6)$$

A similar process was carried out for the resistivity of the electrolyte, giving equation 2.5.7.

$$\rho_{electrolyte} = 0.01 \exp\left(\frac{4062.9}{T_s} - 2.4332\right) \quad (2.5.7)$$

The interconnect and cell connection are both made of nickel metal, so data [7] on nickel conductivity with temperature was used to plot a graph in Microsoft Excel, and a linear trend line was fitted, giving equation 2.5.8. This equation is also valid for the cell connection.

$$\rho_{intercon.} = 6 \times 10^{-10} T_s - 1 \times 10^{-7} \quad (2.5.8)$$

The mechanism of diffusion inside the fuel electrode microstructure

There are at least two commonly used different methods of modelling diffusion between the anode surface, and the reactive sites within the anode. The diffusion of gases through the porous microstructure can be modelled as either molecular (Fickian) diffusion or Knudsen diffusion. Knudsen diffusion uses the assumption that the mean free path of the molecules, i.e. the average distance between intermolecular collisions in the gas, is greater than the pore diameter. This means that the molecules are more likely to hit the pore walls than hit each other. This assumption is valid for very small pores (nm), low gas pressures,

and high temperatures. However, molecular diffusion assumes the opposite, i.e. that the mean free path of the molecules is much less than the pore diameter, so the molecules are much more likely to hit each other than the pore walls. This assumption is valid for larger pores, on the order of μm , and higher pressures, and lower temperatures. The model in [8] assumes Knudsen diffusion. In order to see if this assumption is appropriate for this model, the mean free path of pure hydrogen and pure steam gases can be calculated. This is done by equation 2.5.9, where l is the mean free path (m) k_B is the Boltzmann constant, $1.38065 \times 10^{-23} \text{ J K}^{-1}$, d is the diameter of the molecule, (m), which for a hydrogen molecule is $7.4 \times 10^{-11} \text{ m}$, and for water is $3.2 \times 10^{-10} \text{ m}$. It assumed that the temperature is 1173 K , the pressure is $7 \times 10^6 \text{ Pa}$ (70 bar).

$$l = \frac{k_B T_s}{\sqrt{2} \Pi d^2 P} \quad (2.5.9)$$

Using equation 2.5.9, the mean free path of hydrogen is $0.095 \mu\text{m}$, and the mean free path of steam is $0.0051 \mu\text{m}$. However, as there is a 50:50 mix of hydrogen and steam, the average mean free path of the molecules is likely to be close to $0.01 \mu\text{m}$, which is two orders of magnitude less than the assumed pore size of $1 \mu\text{m}$. Therefore, molecular diffusion will dominate, at high pressures such as 70 bar, so the equations in [8] are inappropriate for this model - they overestimate the diffusion coefficient, and therefore underestimate the diffusion polarisation resistance. Therefore, equations for molecular diffusion used for modelling diffusion in the gases above the fuel electrode were adapted for use inside the fuel electrode.

Diffusion on the oxygen electrode surface

Symmetrical cell ac impedance measurements were carried out and analysed as described in section 2.3.2. The results showed that the dominant process was a surface diffusion process, rather than mass transport of oxygen gas through the electrode microstructure. A surface plot of the values of surface diffusion polarisation, called $R_{diff,surface}$ was plotted as a function of temperature and pressure, using the software program Mathematica (Wolfram), in fig. 2.5.1.

$$R_{diff,surface} = 2.45311 \times 10^{-5} \exp\left(\frac{8853.38}{T}\right) P^{-0.532568} \quad (2.5.10)$$

Equation 2.5.10, which describes a 3D surface which fits the points, is also shown in the figure. A power law dependence was used to model the pressure dependence, as in [9], and an Arrhenius-type exponential term was used to model the temperature dependence. The constants were then determined by trial and error. In a similar way, the maximum frequency of each impedance arc was also plotted as a function of pressure and temperature. The surface obtained was fitted by equations which described the dependence of the maximum frequency on the temperature and pressure. This is eq. 2.5.11.

$$f_{max} = 1.5809 \times 10^{10} \exp\left(\frac{-1.98253 \times 10^4}{T}\right) P^{0.807662} \quad (2.5.11)$$

In doing this, an assumption is made that there is no chemical capacitance from the

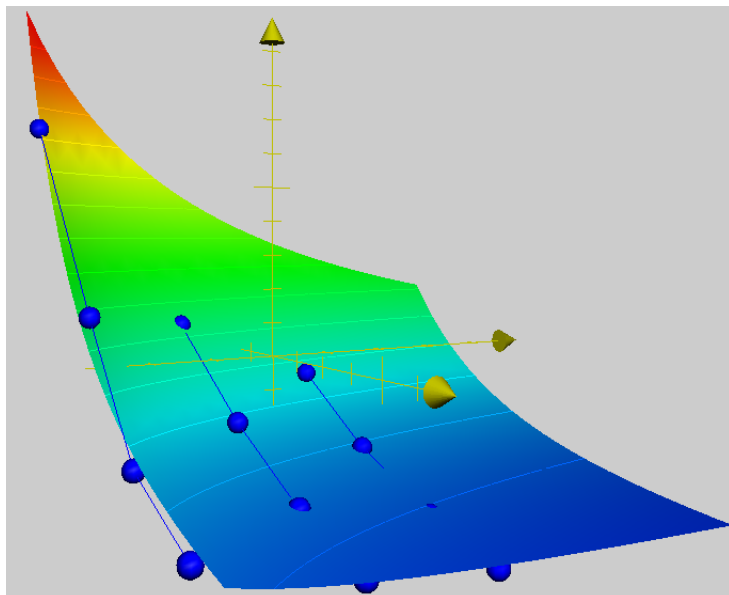


Figure 2.5.1: $R_{diff,surface}$ as a function of temperature and pressure. The vertical axis is $R_{diff,surface}$, in the range $0\ \Omega$ - $1.5\ \Omega$, the axis pointing towards the observer is temperature ($800\ ^\circ\text{C}$ to $1000\ ^\circ\text{C}$, far to near), and the axis pointing away from the observer is pressure, from 1 bar to 5 bar, left to right. Data are from symmetrical cell measurements, and the surface plot was obtained by trial and error. The plot and fit was obtained in collaboration with Dragos Neagu, a PhD student at the University of St Andrews.

YSZ. It has been shown that a gadolinium doped cerium oxide electrolyte (CGO), is partially reduced under reducing conditions, becoming a mixed ionic-electronic conductor. This results a large low frequency arc being seen in the impedance spectra, which has a large capacitance of 1 F at $582\ ^\circ\text{C}$. This is a chemical capacitance - which represents chemical diffusion in the electrolyte [10]. However, as this effect depends on the reduction of the electrolyte, it is unlikely to be seen for YSZ electrolytes. Therefore, the capacitance seen is likely to be related to the LSM-YSZ electrode, not the YSZ electrolyte.

These results were extrapolated to higher pressures in the model, in order to predict $R_{diff,surface}$, and the maximum frequency and capacitance, up to 70 bar. It has been shown for LSM-YSZ electrodes, that the trend in polarisation resistance as a function of pressure, seen at low pressures such as 1 bar - 3 bar, continues to at least about 100 bar [11].

Heat production and consumption from fuel cell and electrolysis reactions

Heat production and consumption in the reversible SOFC system may be quantified if the number of moles of reactant, and the heat produced/consumed per mole, are known. The fuel cell reaction, equation 2.5.2, produces heat, and the electrolysis reaction, equation 2.5.4, consumes heat. HSC thermodynamics software was used to obtain thermodynamic data for the formation enthalpy and entropy of steam, oxygen and hydrogen at 1 bar pressure. However, no data was available at 70 bar, so data from the NIST standard reference database 69 [12] of the entropy and enthalpy of the gases at 1 and 70 bar was also obtained, and the differential in the data between these two pressures was calculated.

This was added to the HSC thermodynamics data to give values of entropy and enthalpies of formation at 70 bar. The NIST data could not be used directly, as it had a difference zero enthalpy and entropy reference point than the HSC data. Therefore, the enthalpy and entropy of hydrogen, oxygen and steam were calculated at 70 bar. Equation 2.5.12 relates the enthalpy (ΔH), which is the total energy available in the reaction, to the amount of free energy (ΔG), and the heat energy, which is the entropy multiplied by the temperature ($T\Delta S$). By plotting the heat energy for one mole of hydrogen against temperature, and using a linear trend line in the software Microsoft Excel, the gradient is found which gives the dependence of heat energy on temperature for the reaction.

$$\Delta G = \Delta H - T\Delta S \quad (2.5.12)$$

The semi-empirical equation 2.5.13 multiplies the heat produced by one mole of hydrogen, by the number of moles of hydrogen consumed per second per cell in the system (M_{H_2}) by the number of cells in the system n , to give the system heat production rate q_e (W). The same equation may be used to calculate the amount of heat absorbed from the system, by the reaction in electrolysis mode.

$$q_e = nM_{H_2}(42.3241T - 4473.97) \quad (2.5.13)$$

Similar equations were also produced for the dependence of enthalpy and Gibbs free energy with temperature at 70 bar pressure. Equation 2.5.14 calculates the enthalpy, W_{fuel} of a specified number of moles of hydrogen M_{H_2} , and equation 2.5.15 calculates the Gibbs free energy W_m available in 1 mole of hydrogen, as a function of temperature.

$$W_{fuel} = M_{H_2}(4.76042T + 243825) \quad (2.5.14)$$

$$W_m = -37.5636T + 248299 \quad (2.5.15)$$

Heat loss from the system

Heat is lost from the system through the pressure vessel walls, which are insulated with a commercial high-performance microporous insulation, with the brand name Microtherm®. Values of thermal conductivity are taken from data on the Microtherm website [13]. The thermal conductivity of the insulation was plotted as a function of temperature, and fitted with a quadratic function using the software Excel 2003 (Microsoft), to give equation 2.5.16, in which λ is the thermal conductivity ($W\ m^{-1}\ K^{-1}$) and T is the system temperature (K). The coefficient values are $a = 2.54132 \times 10^{-8}$, $b = 1.93343 \times 10^{-5}$, and $c = 0.0257471$.

$$\lambda = aT^2 - bT + c \quad (2.5.16)$$

An online calculator on the Microtherm website [14] was used to calculate values of the cold face temperature of the insulation T_c , assuming it was 0.2 m thick, and that the hot face temperature was equal to the system temperature. These values were fitted to a linear

trendline using the software Excel 2003 (Microsoft), giving eq. 2.5.17.

$$T_c = 0.0225455T + 279.627 \quad (2.5.17)$$

It can be seen from eq. 2.5.16 that the thermal conductivity of the insulation has a non-linear dependence on temperature. Therefore, the heat loss was calculated by integrating eq. 2.5.16 with respect to temperature, and evaluating it between the limits T_c and T . This equation is divided by the insulation thickness l (m) and multiplied by the surface area of the insulation A_V (m²) to give eq. 2.5.18. This equation was written by a colleague.

$$Q_i = A_V \left[\left(\frac{a}{3l}T^3 - \frac{b}{2l}T^2 + \frac{c}{l}T \right) - \left(\frac{a}{3l}T_c^3 - \frac{b}{2l}T_c^2 + \frac{c}{l}T_c \right) \right] \quad (2.5.18)$$

Heat capacities of the system gases

The heat capacities (J kg⁻¹ K⁻¹) of hydrogen, oxygen, and steam were calculated as a function of temperature, at a pressure of 70 bar using data from the NIST standard reference database 69 [12]. The data was plotted in Microsoft Excel, and linear trend lines were fitted to it, so the heat capacities C_p of these gases as a function of temperature could be calculated. For hydrogen, equation 2.5.19, for oxygen, equation 2.5.20, and for steam, equation 2.5.21, where T is the system temperature (K).

$$C_{pH_2} = 1.50216T + 13491.0 \quad (2.5.19)$$

$$C_{pO_2} = 0.144437T + 951.593 \quad (2.5.20)$$

$$C_{pH_2O} = 0.182118T + 2207.90 \quad (2.5.21)$$

Heat capacity of the heat store

The heat store is a copper-tin bronze alloy, which is assumed to have a melting point of 1010 °C or 1283 K, from the copper-tin phase diagram [15]. As there was no data available on the heat capacity of this alloy, data for the heat capacity of copper was used instead to model the bronze heat capacity. As the bronze is mostly copper, their heat capacities are very similar, and assumed to be the same in the model. The data for the heat capacity of copper in the range 610 °C to the melting point of copper at 1084 °C, was plotted in Microsoft Excel, and a linear approximation was fitted to the data, which is equation 2.5.22.

$$C_{pbronze,solid} = 0.1594T + 293.09 \quad (2.5.22)$$

2.5.2 Assembling the software model and obtaining results

The equations for the model were written at the University of St Andrews, and were assembled using the software Matlab, with the Simulink module (Mathworks), at the University of Strathclyde, by Andy Ren, an electrical engineering PhD student. This allows the various equations to be represented by blocks which perform the calculations. These were linked to each other, to allow data to flow through the model. It is based on modelling a single cell, then extrapolating to two parallel sets of 400 cells in series. By setting key parameters, such as state of charge, which is the mol.% hydrogen on the fuel side of the system, the system pressure, and starting temperature, various simulations were performed using the model, to investigate the effect of these parameters on the performance of the modelled RSOFC system. A sensitivity analysis was also carried out, to determine the effect of varying the pre-exponential coefficient used in the equations to predict activation energies. The results were obtained as tables, and plotted as graphs.

2.6 Conclusions

This chapter has described the methods used to fabricate, characterise, and test reversible solid oxide fuel cells, with particular focus on materials processing and the manufacturing of the cell. This is deliberate, as the microstructure of the reversible cell depends on the way it is fabricated. In order to find the best manufacturing method, an understanding of such things as rheology, particle size distribution, sintering, etc is used in conjunction with trial and error, to produce a cell. These are characterised by various methods, and the electrochemical performance of the cell is tested. These three facets of fabrication, characterisation and testing are therefore inextricably linked, because the cell can only be improved when they are related to each other and considered as a whole. In industry, they are usually carried out in tandem, with the goal of achieving a high performance, durable cell [1].

References

- [1] S. Gamble, *Mater. Sci. Technol.*, 2011, **27**, 1485–1497.
- [2] F. A. Mesquita, M. R. Morelli, *J. Mater. Proc. Tech.*, 2003, **143-144**, 232–236.
- [3] J. T. S. Irvine, F. G. E. Jones, P. A. Connor, *Improvements in Solid Oxide Fuel Cells and related devices*, Patent no. wo/2003/036746, The University of St Andrews, College Gate, North Street, St Andrews KY16 9AJ, 2003.
- [4] M. W. Chase-Jr, C. A. Davies, J. R. Downey-Jr., D. Frurip, R. A. McDonald, A. N. Syverud, *JANAF thermochemical tables part II, J. of Phys. and Chem. Ref. Data 3rd ed., Vol. 14*, 1985.
- [5] I. Barin, *Thermochemical Data of Pure Substances, Part I*, VCH Verlags Gesellschaft, Weinheim, 1993.
- [6] A. Petric, P. Huang, F. Tietz, *Solid State Ionics*, 2000, **135**, 719–725, 12th International Conference on Solid State Ionics, Halkidiki, Greece, Jun 06-12, 1999.
- [7] Isabellenhuetten, *Super Pure Nickel*, Tech. Rep., Isabellenhutte Heusler GmbH I& Co. KG, www.isabellenhuetten.de, 2009.
- [8] S. Campanari, P. Iora, *J. Power Sources*, 2004, **132**, 113–126.
- [9] E. Siebert, A. Hammouche, M. Kleitz, *Electrochim. Acta*, 1995, **40**, 1741–1753.
- [10] A. Atkinson, S. A. Baron, N. P. Brandon, *J. Electrochem. Soc.*, 2004, **151**, E186–E193.
- [11] E. C. Thomsen, G. W. Coffey, L. R. Pederson, O. A. Marina, *J. Power Sources*, 2009, **191**, 217–224.
- [12] NIST, *NIST Chemistry WebBook*, last accessed 01/08/2011. <http://webbook.nist.gov/chemistry/>.
- [13] Microtherm, *Microtherm Standard Panel*, Datasheet from <http://www.microtherm.uk.com/>, Microtherm, België, Industriepark Noord 1, BE-9100 Sint-Niklaas, 2011.
- [14] Microtherm nv, *Thermal calculator*, last accessed 25/08/2011. <http://www.microtherm.uk.com/high/EXEN/site/calculator.aspx>.
- [15] N. Saunders, A. P. Miodownik, *J. Phase Equil.*, 1990, **11**, 278–287.

Chapter 3

Oxygen electrode testing with symmetrical cells

3.1 Tape-cast symmetrical cells

3.1.1 Introduction

Symmetrical cells are used to study one of the two electrodes in a fuel cell or electrolysis cell in isolation from the other. This chapter is concerned with how the performance of the LSM-YSZ electrode is affected by changes in temperature and oxygen partial pressure. In this case, the limiting processes being studied in the electrode will be one of the steps involved in the oxygen reduction or oxidation reactions on the LSM-YSZ electrode. Electrochemical impedance spectroscopy is often used on symmetrical cells to identify and quantify the limiting processes in the electrode.

One of the ways to make symmetrical cells is by tape-casting, a technique which binds the ceramic powders used to make the cell layers into a flexible organic matrix. They can then be laminated together to produce thicker versions of the same cell layer, or different tapes can be laminated to produce a whole cell. If the burnout and shrinkage behaviour of the tapes are optimised, the whole cell may be co-sintered in a single step. Accordingly, tape-cast symmetrical cells of LSM-YSZ|YSZ|LSM-YSZ were produced, and gold paste was applied to both sides of the cell and cured at high temperature, to act as a current collector. They were then tested at high temperature using impedance spectroscopy.

3.1.2 Impedance spectroscopy results

Impedance spectroscopy was carried out on three nominally identical tape-cast cells. Two cells named A and B were tested in the same jig, in air, and a third cell named C was tested in pure oxygen in a different jig. The impedance spectra of samples A and B were fairly similar. Figure 3.1.1 shows measurements on samples B and C at 900 °C. It can be seen that the polarisation resistance has a similar magnitude for the two samples. It is composed of at least two arcs, which can be seen most distinctly for sample B. The dominant arc is a low frequency arc, with a peak frequency between 10 Hz and 100 Hz, which suggests that a diffusion limitation process dominates the spectra.

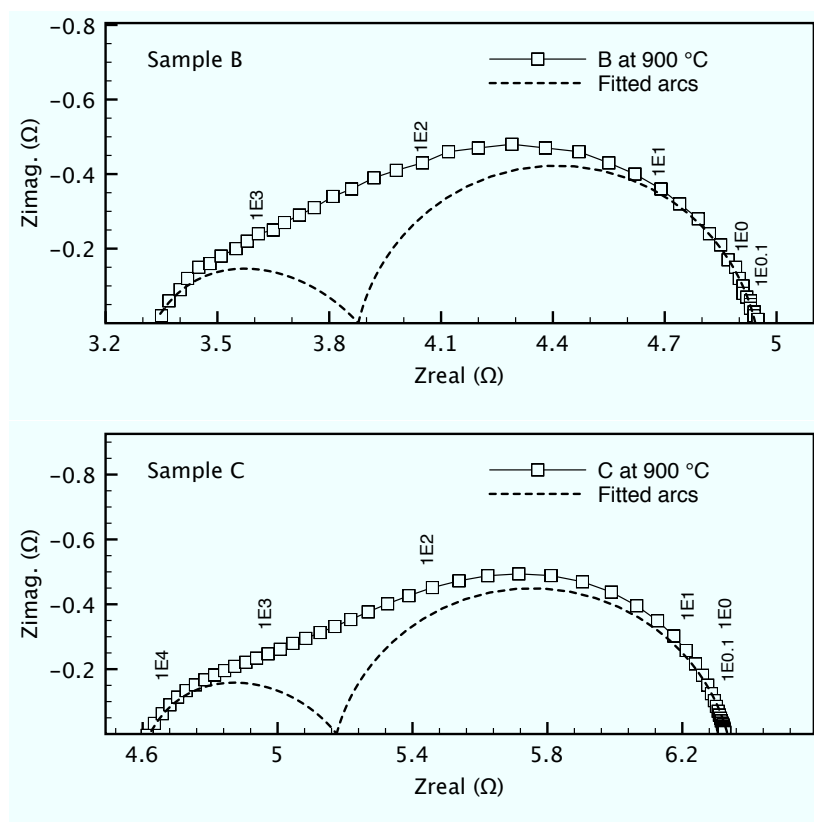


Figure 3.1.1: Impedance spectra of tape cast samples at 900 °C, tested in air (sample B) and in oxygen (sample C), not normalised for cell area. Frequency decades are marked in hertz. The individual arcs, calculated by equivalent circuit modelling of the data are also shown as dashed lines.

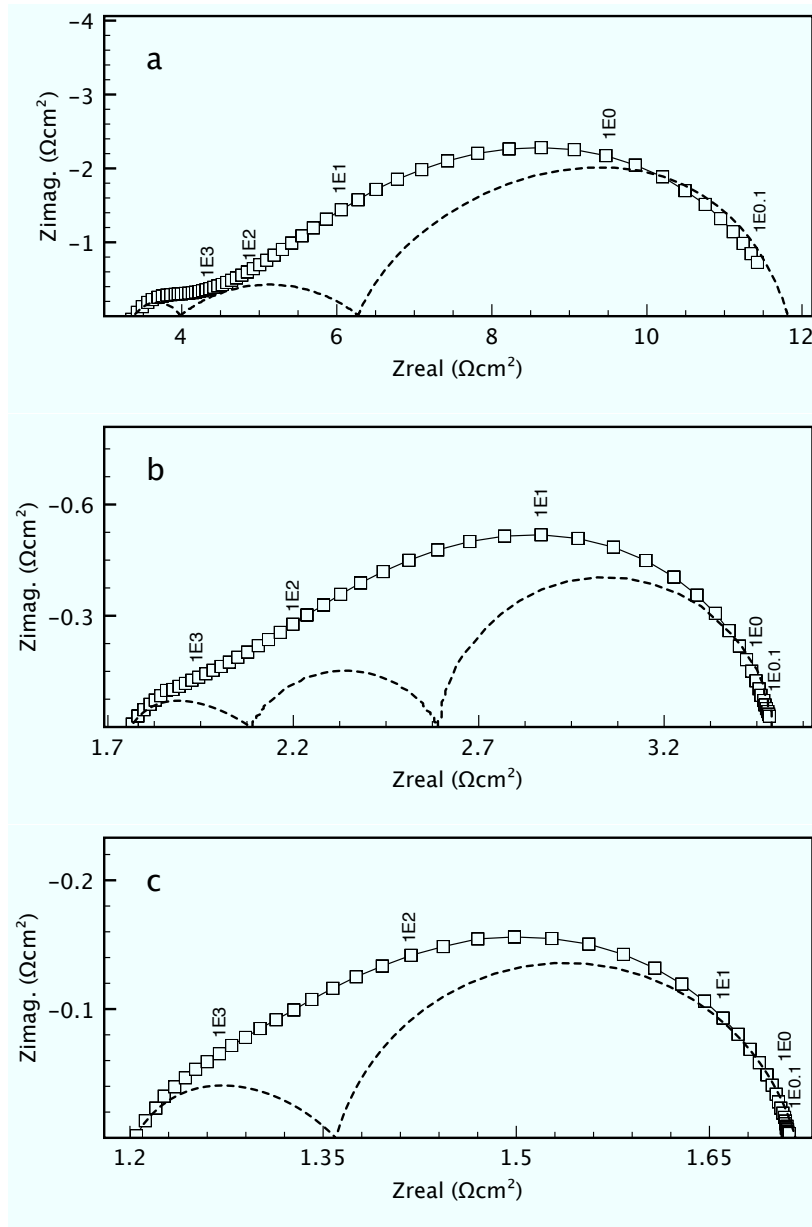


Figure 3.1.2: Impedance spectra at various temperatures for a tape cast symmetrical cell - sample A. Data are normalised to the cell area, and the frequency decades are shown, a) 696 °C, b) 794 °C and c) 900 °C. The individual arcs from the modelling fit are also shown as dashed lines. The spectrum at 900 °C was modelled with two arcs instead of three.

Figure 3.1.2 shows impedance spectra at various temperatures for sample A. The spectrum for 696 °C shows most clearly of all these spectra that there are three processes in the sample. There is a small high frequency process above 1000 Hz, a bigger process about 100 Hz, and the dominant, low frequency process around 10 Hz - 0.1 Hz. The three processes are most distinct at the lowest temperature, because the lowest frequency process shifts to a lower peak frequency as the temperature decreases from 900 °C to 696 °C. As the temperature increases, the magnitude of the lowest frequency arc decreases significantly, and the arcs overlap more. The area specific polarisation resistance of the three samples was calculated by modelling to an electrical equivalent circuit with the program Zview.

The fit to the data in shown in B. It is plotted in an Arrhenius plot in fig. 3.1.3.

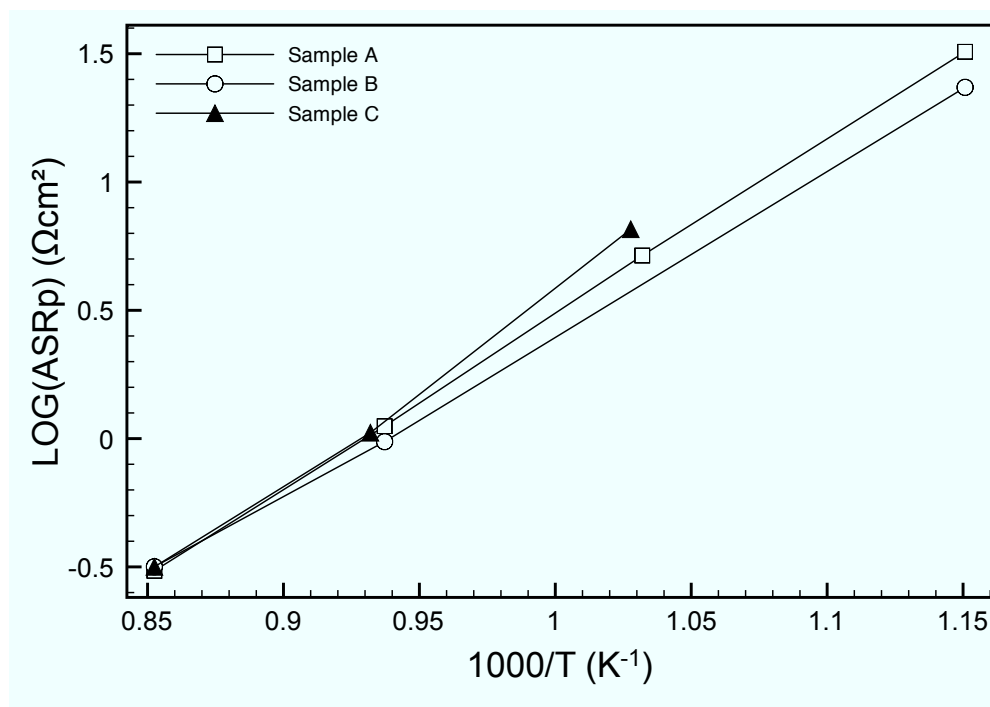


Figure 3.1.3: Area specific polarisation resistance of symmetrical cell electrodes, samples A, B and C.

The impedance spectrum for sample C at the lowest temperature could not be modelled with the equivalent circuit. This is because there was a large low frequency arc, which was incomplete because the frequency scan stopped at 0.1 Hz, so its magnitude could not be determined. The activation energy of sample A is 1.60 eV, sample B is 1.48 eV, and sample C is 1.77 eV. Although the samples are nominally identical, they have slightly different activation energies, which may arise from slight variations in the microstructure. From fig. 3.1.3, the difference is more pronounced at lower temperatures, at which the diffusion arc is more dominant. The diffusion arc may vary in size from sample to sample, because one sample might have a thicker current collection layer than the other, which would increase the size of that diffusion arc, and affect the activation energy of the sample. Microstructural changes in the gold current collection layer during testing would also produce a change in this arc. This was examined more fully by doing a week long test of the cells.

3.1.3 Thermal ageing of symmetrical cells

The cells were then thermally aged at 900 °C for about a week at open circuit voltage (OCV), in order to determine the stability of the cell. Impedance spectra were taken periodically, and fitted to a similar electrical equivalent circuit as before. The initial area specific polarisation resistance values are compared with the ones after about 140 h in table 3.1.1, and the results as a function of time are shown in fig. 3.1.4.

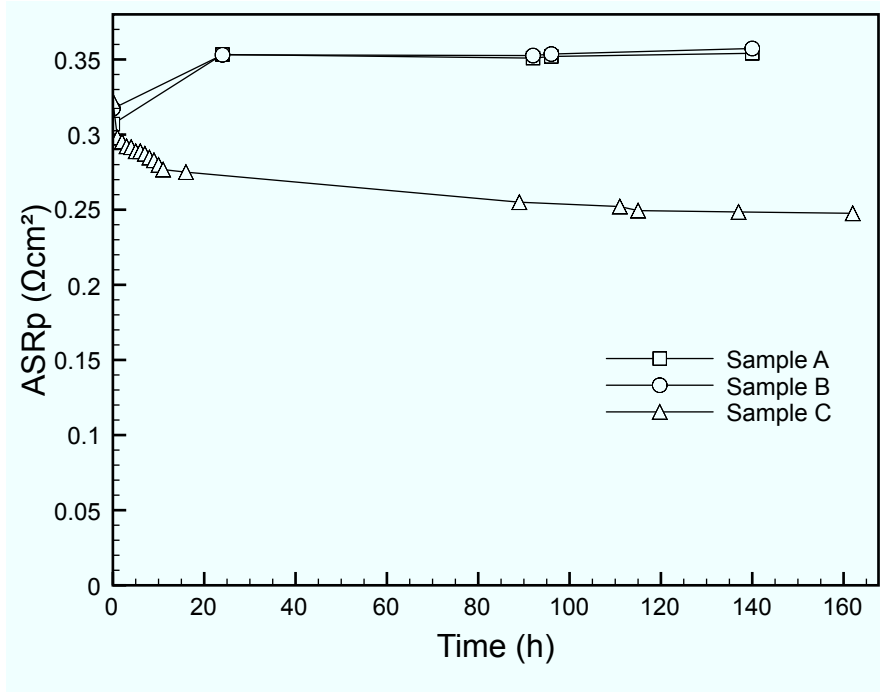


Figure 3.1.4: Area specific polarisation resistance of samples A, B and C tested at 900 °C over time. Samples A and B were tested in the same jig in air, and sample C was tested in oxygen in a different jig.

Time (h)	ASRp sample A air, (Ω)	ASRp sample B air, (Ω)	ASRp sample C oxygen, (Ω)
0	0.305	0.317	0.316
140	0.344	0.354	0.241

Table 3.1.1: Area specific polarisation resistance at 900 °C for tape cast symmetrical half cells, Au|LSM-YSZ|YSZ|LSM-YSZ|Au

It can be seen that there is an increase with time in the polarisation resistance of samples A and B, but a decrease for sample C. Most of the change observed occurs during the first 24 h. Fig. 3.1.5 shows the initial and final impedance arcs for sample B, plotted on the same axes, and also for sample C.

In both cases, the size of high frequency arc has remained the same. The low frequency arc has changed in magnitude, but the position of the frequencies has not changed. This means that the nature of this limiting step has not changed, but it has become more or less intense. This arc is thought to be related to a diffusion polarisation resistance [1]. This suggests that the diffusion polarisation of the sample has reduced during the test for sample C, but increased during the test for samples A and B. In order to interpret the differences, the microstructure of the samples, and how it changes during testing must be considered.

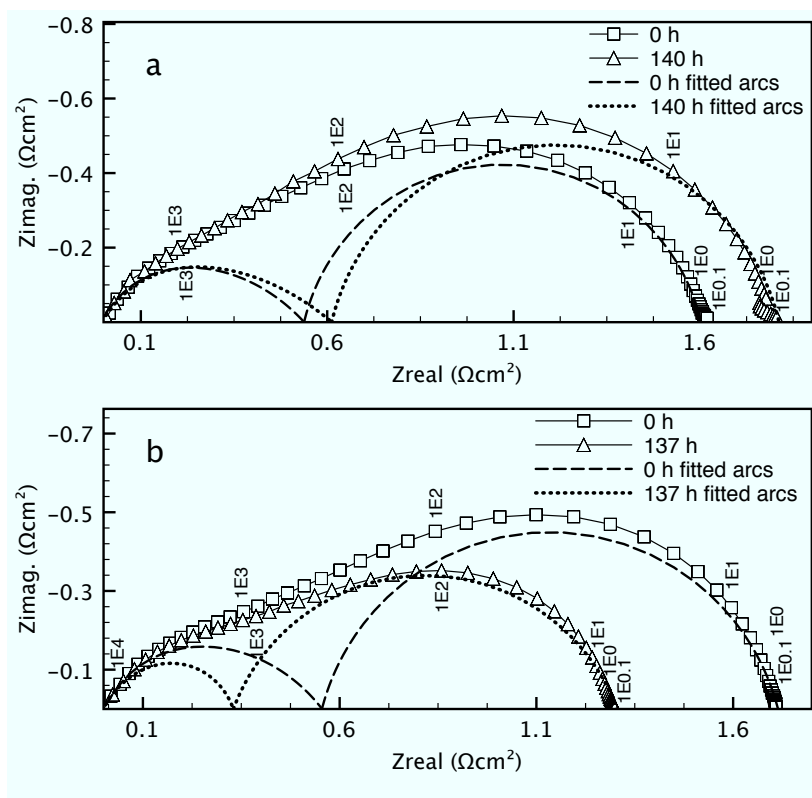


Figure 3.1.5: A comparison of impedance arcs normalised for cell area with the ohmic resistance component removed, before and after thermal ageing at 900 °C for 140 h/137 h, respectively, a) sample B tested in air, and b) sample C tested in oxygen. Frequency decades are marked in hertz. The individual arcs from equivalent circuit modelling are also shown.

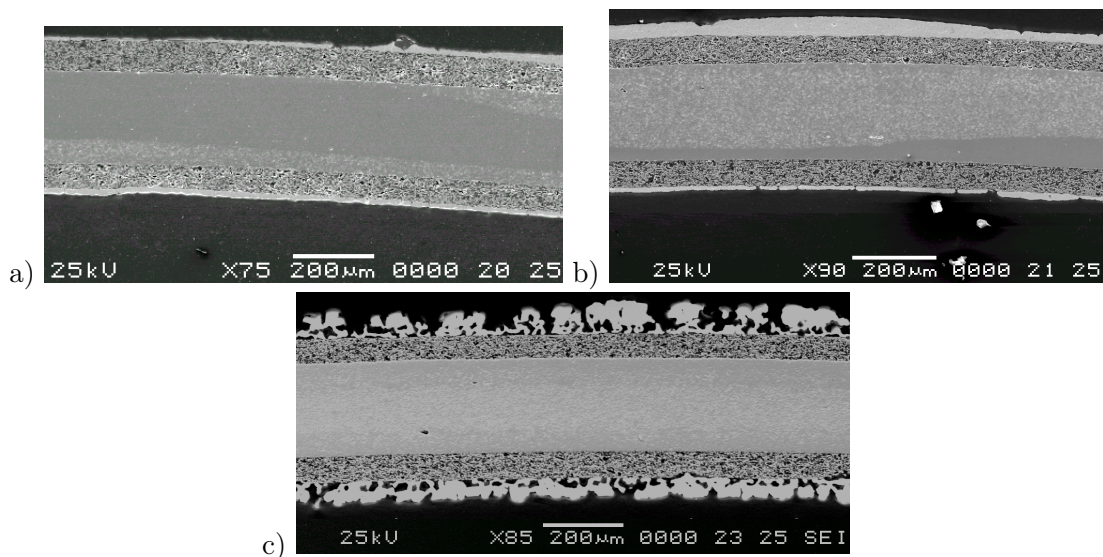


Figure 3.1.6: Tape cast samples a) before testing b) after testing in air at 900 °C for 140 h c) after testing in oxygen at 900 °C for 162 h. The cell tested in air was contacted to the jig with a platinum bead, but the cell tested in oxygen was contacted by a platinum mesh.

The samples are nominally identical as they were made in the same way and at the same time, but sample C is in a jig in oxygen, with a platinum mesh contacting the gold

current collector, whereas samples A and B are in a jig in air, each with a platinum bead contacting the gold current collector. Figure 3.1.6a shows a cross-section of an untested sample made at the same time as samples A, B and C. The gold current collection layer is quite dense, and it is likely that this increases the diffusion polarisation resistance, seen as the low-frequency arc in the impedance spectra. It may be seen in a cross section of sample A in 3.1.6b after 140 h of testing in air at 900 °C, that the current collection layer is almost totally dense. This will limit the diffusion of oxygen to the electrode, and cause the diffusion polarisation arc in the impedance spectrum to increase, if the density has increased during the thermal ageing process. This may be contrasted with the cross section of sample C in fig. 3.1.6c; after 162 h testing in oxygen at 900 °C, where the current collector is quite porous. This corroborates the hypothesis that the low frequency arc is related to diffusion, as the post-test microstructure of sample C is more porous than the pre-test microstructure, which matches the reduction in the low frequency arc in the impedance spectrum.

An analysis of the current collection layer of sample C by EDX in fig. 3.1.7 shows that there is platinum present in the gold layer, which has diffused into it from the platinum mesh on the testing jig. It was noted that sample C had a silvery appearance after testing, which is consistent with the presence of platinum. However, samples A and B had a golden appearance after testing, so they did not contain as much platinum.

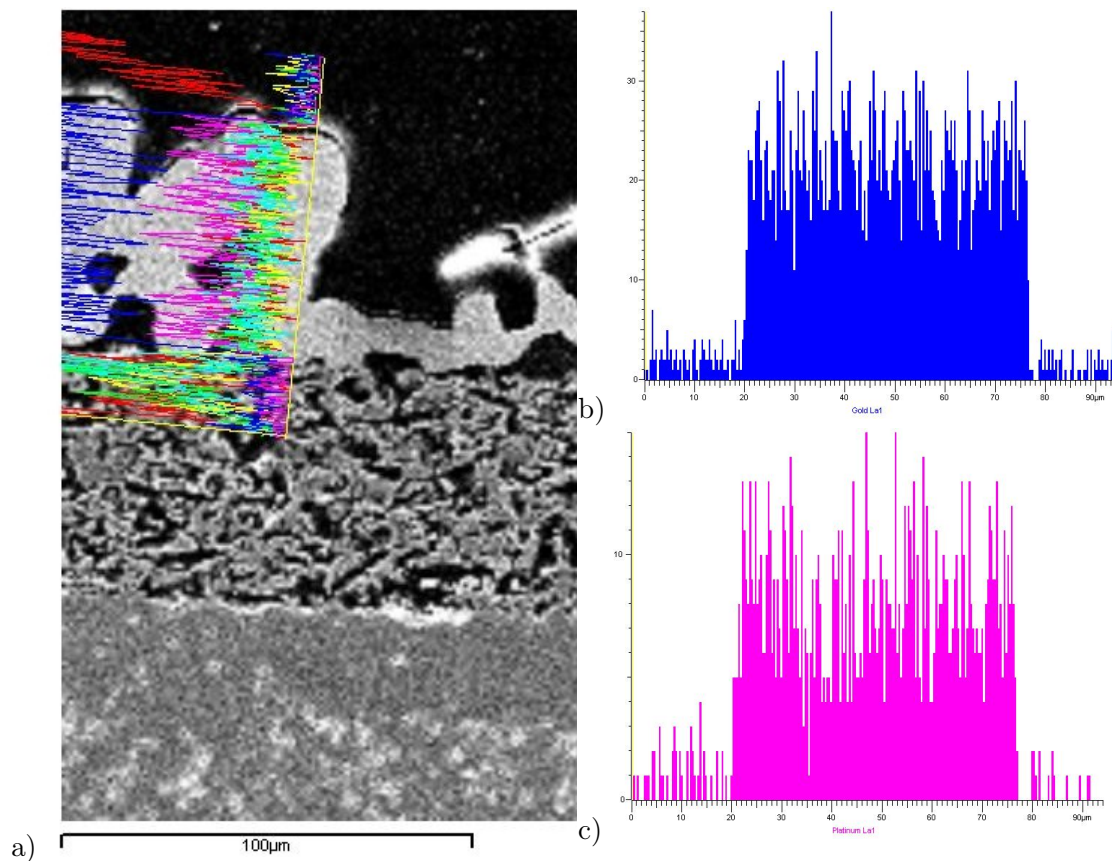


Figure 3.1.7: EDX on tape cast symmetrical cell, after testing in oxygen at open circuit voltage for 162 h, a) line scan sum spectrum with SEM image, b) line scan of gold, c) line scan of platinum.

The alloying of platinum and gold in sample C may have changed the wetting properties of the metal, reducing its wetting of the ceramic, and causing it to become more porous. Some gold may also have diffused out of the current collection layer, creating porosity, and alloyed with the platinum mesh. The unstable current collector makes it very difficult to determine the effect of changing the partial pressure of oxygen from 0.21 bar to 1 bar, therefore no definite conclusions about the effect of the partial pressure of oxygen on electrode performance can be reached by comparing the performance of samples A and B, with sample C.

The results obtained have implications for the type of current collection layer that should be used on symmetrical cells. A gold paste current collection layer painted on to the whole electrode surface has been shown to cause an increased diffusion polarisation resistance because is almost totally dense. Furthermore, when a gold current collector is used in a jig with platinum contacts, alloying will take place. In fig. 3.1.4, most of the change in the polarisation resistance, which is dominated by the diffusion arc, took place in the first 24 h. Therefore, it is reasonable to conclude that the alloying process will quickly affect the performance of symmetrical cells. The platinum-gold phase diagram shows that at near 100% concentration of platinum, a liquid phase forms with gold at a temperature of just 1000 °C, which is only 100 °C more than that used during testing [2]. This suggests that an alloy may form by solid state diffusion quite easily.

3.2 Pellet symmetrical cells

3.2.1 Introduction

This work investigates the relationships between LSM-YSZ cathodes and their area specific polarisation resistance under an elevated oxygen pressure beyond 1 bar, using symmetrical pellet cells. These cells are widely used to understand the performance of fuel cell electrodes, by relating arcs in impedance spectra to physical processes occurring in the electrode. The oxygen reduction reaction has been studied extensively in Sr doped LaMnO_3 / Y_2O_3 doped ZrO_2 (LSM-YSZ) cells. Several parameters may be used to differentiate the arcs, such as capacitance, the time constant (or maximum frequency), dependence of polarisation resistance on P_{O_2} , and activation energy. By systematically studying LSM-YSZ electrodes made or tested under different conditions, different arcs in the spectra can be associated with specific electrochemical processes in the electrode, by comparison with the available literature. It has previously been demonstrated with three electrode cells that LSM/YSZ composite cathodes with a CGO inter-layer between the cathode and the electrolyte, that increasing the oxygen partial pressure up to 1 bar oxygen, decreases the polarisation resistance (R_p) of the electrode exponentially [3]. The dependence of the polarisation resistance on oxygen pressure follows a power law, where $R_p = P_{\text{O}_2}^{-x}$. A value of $x = 0.5$ was found for this dependence, where the process is thought to correspond to dissociative adsorption of oxygen at the triple phase boundary [4]. In another study two arcs in the impedance spectra were distinguished, one was invariant with oxygen partial pressure, and was attributed to transport of oxygen ions, and the other was attributed to

O^- surface diffusion, with a $P_{O_2}^{-x}$ dependence of $x = 0.25$ [5].

Research at Siemens-Westinghouse shows improved performance with increased gas pressure in the SOFC system [6]. Pressurisation also increases the volumetric energy storage density of the system by compressing the fuel. The effect of high pressure oxygen, ($P_{O_2} > 1$ bar) on the ohmic and polarisation resistance of LSM/8YSZ composite cathodes for solid oxide fuel cells (SOFC) has not been widely studied, but is of interest for high pressure SOFC, and therefore reversible SOFC. One study of a 2% A-site deficient LSM/YSZ composite electrode between pressures of 1-100 bar oxygen found that the impedance spectra resolved to two arcs over the pressure range studied. One had a $P_{O_2}^{-x}$ dependence of $x = 0.25$, and was attributed to charge transfer, and the other was smaller and nearly independent of P_{O_2} , and was assigned to transport of oxygen ions in the YSZ [7].

In this work, 8YSZ pellets are prepared with LSM-YSZ electrodes and are tested at different temperatures and oxygen pressures. Impedance is performed to determine the area specific polarisation resistance of the LSM-YSZ electrodes, and the impedance spectra are measured and interpreted by comparison with the electrochemical literature.

3.2.2 Symmetrical cell testing

Current collection on symmetrical cells

In order to avoid the problem of gold-platinum alloying seen with the tape cast cells, a jig was made with gold contacts, so that there would be no thermodynamic driving force for alloying of the jig contacts and the current collector on the symmetrical cells. Then pellets of YSZ were coated with LSM-YSZ electrodes, and a gold grid current collector was painted on them, as in fig. 3.2.1. This did not cover the whole LSM-YSZ electrode surface, which meant that there was no limitation of diffusion of oxygen into the electrode. However, it was found that the gold grid was an inadequate current collector because areas of the LSM-YSZ electrode not covered by gold had a very high in-plane resistance. This was measured for a pellet symmetrical cell in table 3.2.1 as being about 16 k Ω across a distance of 8 mm at room temperature. The gold grid only contacts the parts of the electrode under it, leading to an uneven current and potential distribution in the electrode. This will cause an incorrect value for the area specific resistance of the electrode to be determined, as the active, measured area of the electrode will be limited to the area under the gold grid, which is a minor fraction of the geometrical area.



Figure 3.2.1: Gold current collector grid on LSM-YSZ electrode, pellet symmetrical cell. The electrode is about 8 mm in diameter.

Sample no.	Current collection	Reading no. 1 (k Ω)	2 (k Ω)	3 (k Ω)	4 (k Ω)	Average resistance (k Ω)
1	gold grid	15.9	14.6	16.5	16.9	16.0
2	LSM	0.57	0.31	0.46	0.31	0.41

Table 3.2.1: In-plane electrical conductivity of pellet symmetrical cells with LSM-YSZ electrodes at room temperature, measured across the diameter of the electrode surface, about 8 mm. For sample 1, the contacts touched the electrode surface rather than the gold grid that was painted on it.

A current collection layer must have at least these three properties, in order to function properly:

- It should be in contact with the entire LSM-YSZ surface
- It should be thin and porous so it does not impede the diffusion of oxygen
- It should not chemically interact with the testing jig.

A current collector which satisfies all three requirements is a porous layer of LSM. This is the electronic conductor used in the composite LSM-YSZ oxygen electrode, and so it is chemically compatible with it. It also has a high conductivity, and will not interact with gold or platinum meshes in the testing jigs. It forms a porous layer, even at high temperatures such as 1300 °C, and has been frequently used as a current collector in other studies of LSM-YSZ symmetrical cells [8]. Table 3.2.1 shows that that cells with a layer of LSM have a much lower resistance across the electrode at room temperature, and when the cell is tested at higher temperature, the resistance will be very small, as LSM is a semiconductor. Therefore, the cells with a gold grid were not tested, and the remaining cells had an LSM layer applied to both sides by screen printing and sintering.

Temperature calibration for testing

After impedance measurements were performed on the symmetrical cells at a range of temperatures and pressures, it was seen that the ohmic resistance of the pellets, which is almost all due to the thick YSZ electrolyte, was less than that expected for each measurement temperature. Tests with multiple thermocouples showed that the sample temperature thermocouple had been placed too far from the samples during testing, and so it had underestimated the testing temperature. Therefore, a calibration and correction was made for the testing temperature, based on the ohmic resistance of the sample.

3.2.3 Impedance spectroscopy results

Electrochemical impedance spectroscopy data are obtained for two nominally identical symmetrical cells named A and B, tested in the same jig, at a range of temperatures and oxygen pressures. The microstructure of the electrode is shown in fig. 3.2.2 where a sample that was tested is compared with a sample that was made at the same time, but not tested. A 5 μm - 10 μm thick porous LSM layer can be seen, on top of a 5 μm - 10 μm thick

LSM-YSZ layer which is denser, which is on top of the grey dense YSZ electrolyte. The microstructures of the layers before and after testing are very similar. It can be seen that the LSM layer is quite porous, so it should not present a diffusion barrier to the oxygen coming into the cell. Although a higher performance LSM-YSZ electrode would have been achieved by reducing the sintering temperature of the LSM-YSZ electrode to 1100 °C - 1200 °C [8], the temperature of 1300 °C was chosen. This was because the reversible SOFC is LSM supported, so it will be sintered to at least 1300 °C in order to densify the YSZ electrolyte that will be coated on top of it.

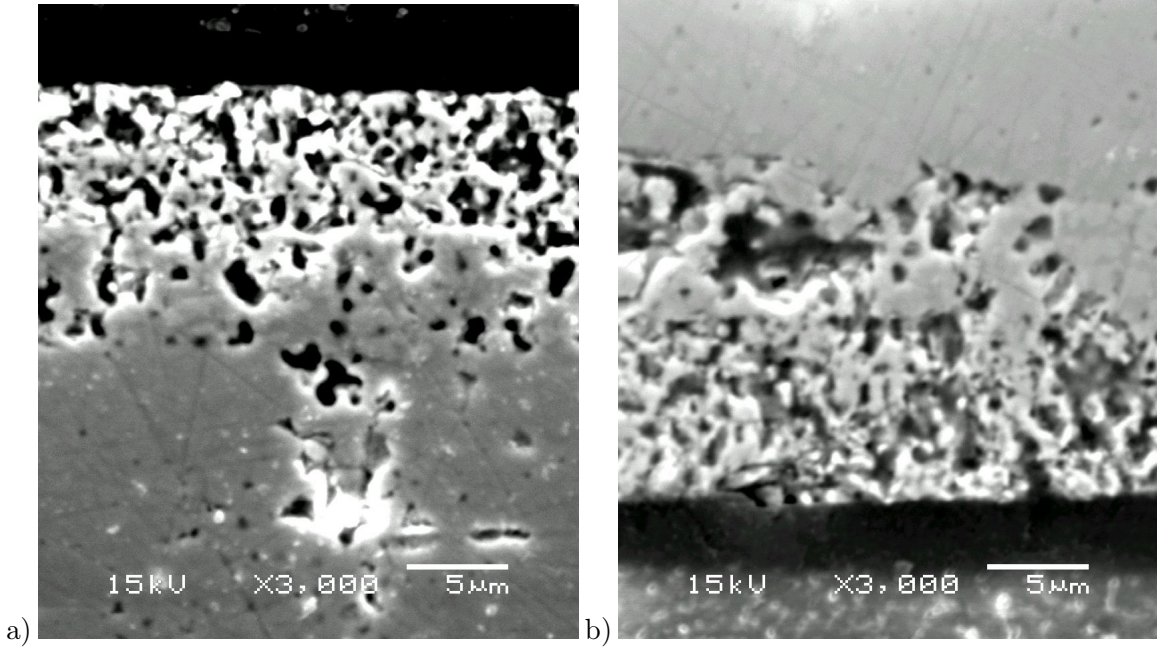


Figure 3.2.2: Microstructure of symmetrical cell: YSZ pellet with LSM-YSZ electrode sintered at 1300 °C and LSM current collector sintered at 1200 °C : a) untested sample, and b) tested sample.

Impedance spectra for sample A at various temperatures are shown in fig. 3.2.4, which shows that there is a dominant low frequency arc, which was named arc C, and a small high frequency arc, which was named arc B. The spectra are fitted to the electrical equivalent circuit shown in fig. 3.2.3.

Only data above the Nyquist plot x-axis was fitted. The ohmic and polarisation resistance for the two arcs in the spectra are determined. The polarisation resistance is corrected for the electrode area to give the area specific polarisation resistance (ASRp), and plotted in fig. 3.2.5. As the oxygen pressure increases from 1 bar - 3 bar, the polarisation resistance of the samples decreases.

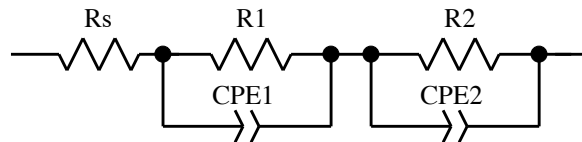


Figure 3.2.3: Equivalent electrical circuit used in modelling impedance data (R_s = ohmic resistance, R_1 = polarisation resistance 1, $CPE1$ = constant phase element 1, etc)

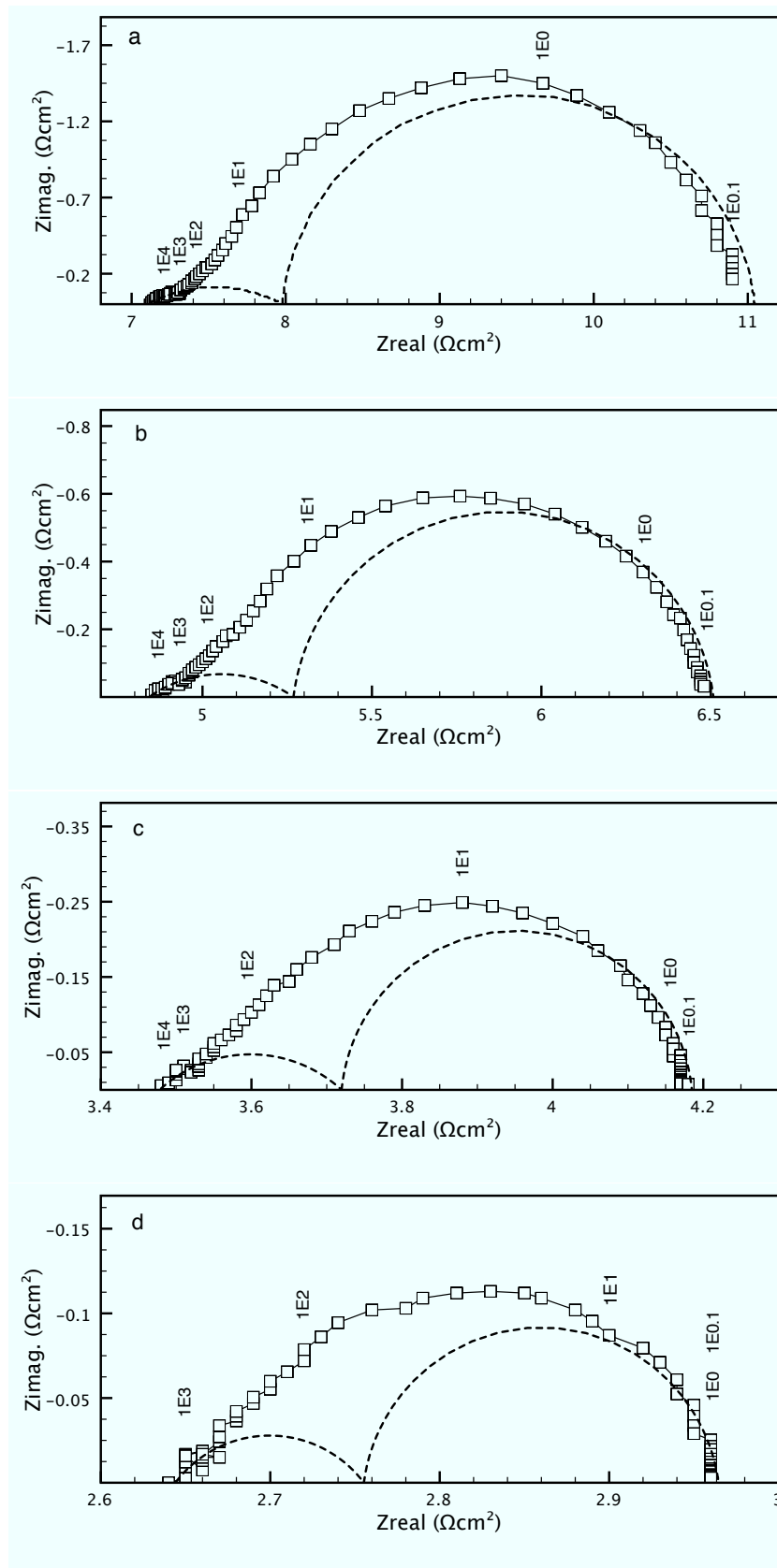


Figure 3.2.4: Impedance spectra obtained from sample A at various temperatures, $P_{\text{O}_2} = 1$ bar, a) 793 °C, b) 843 °C, c) 890 °C, d) 932 °C. Each frequency decade is marked in Hz. The two electrode processes are most distinct at lower temperatures. The modelled arcs from the equivalent circuit modelling are shown as dashed lines.

This is in accordance with other work which tested three-electrode cells which had composite LSM and YSZ electrodes and a samaria-ceria inter-layer between the electrodes and electrolyte. A similar trend of decreasing polarisation resistance with increasing oxygen pressure over the whole measured range of 1 bar to ~ 100 bar was observed [7]. The magnitude of the polarisation resistance of both samples is very similar, which indicates that they have a similar microstructure, and there is no difference between them arising from the testing method. The activation energies of both samples are within the range 2.0 eV - 2.2 eV. This is similar to the value of about 2 eV previously found for 50:50 LSM:YSZ composite electrodes. However, the activation energy was observed to change with temperature, because there were two different processes in the sample with different activation energies [9]. In this work, the activation energy also varies slightly with temperature, which can be seen in fig. 3.2.5.

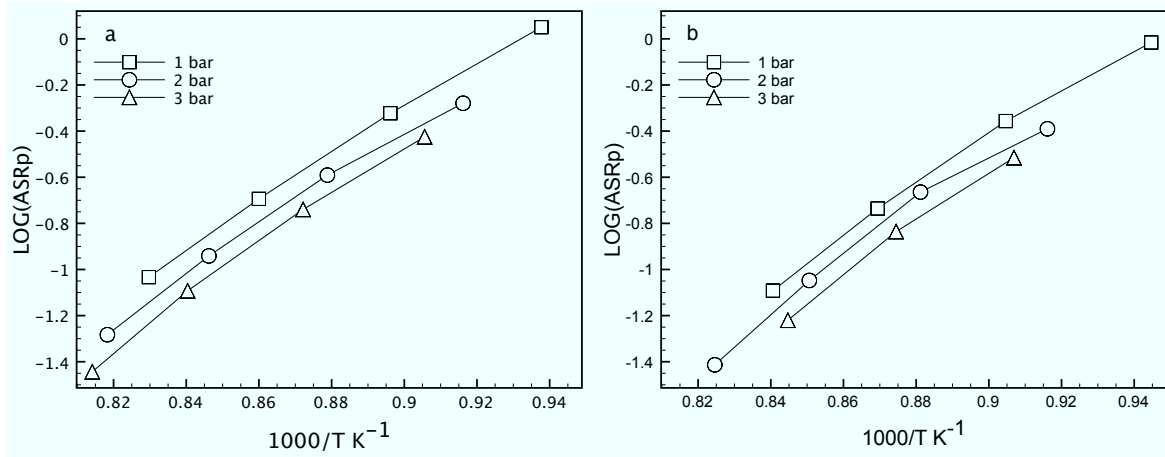


Figure 3.2.5: Area specific polarisation resistance as a function of temperature and absolute oxygen pressure, for two nominally identical symmetrical cells a) for sample A and b) for sample B. The scaling is equivalent to allow direct comparison.

3.2.4 Assignment of arcs in impedance spectra

The arcs in the impedance spectra each represent a physical process occurring in the electrode. These processes may have different characteristics, e.g. different time constants, or their magnitude may have a different dependence on temperature or P_{O_2} . By determining these characteristics for each arc, it can be related to a physical process, by comparing it to previous analyses in the electrochemical literature.

Assignment of arc C

Fig. 3.2.6 shows the area specific polarisation resistance of arc C for sample A. The activation energies obtained for arc C were in the range 2.01 eV - 2.13 eV. It can be seen that this arc has a P_{O_2} dependence, which could not be directly calculated from fig. 3.2.6 because the measurements at each pressure are at different temperatures.

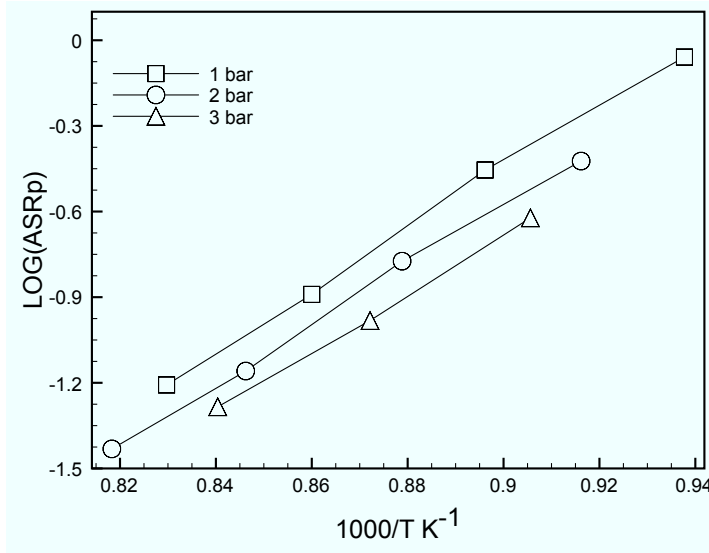


Figure 3.2.6: Area specific polarisation resistance of sample A, arc C as a function of temperature and absolute oxygen pressure.

Therefore, a linear trend line was fitted to the data at each pressure using the program Microsoft Excel, and then the area specific polarisation resistance was calculated at various temperatures between 800 °C - 950 °C, and plotted in fig. 3.2.7.

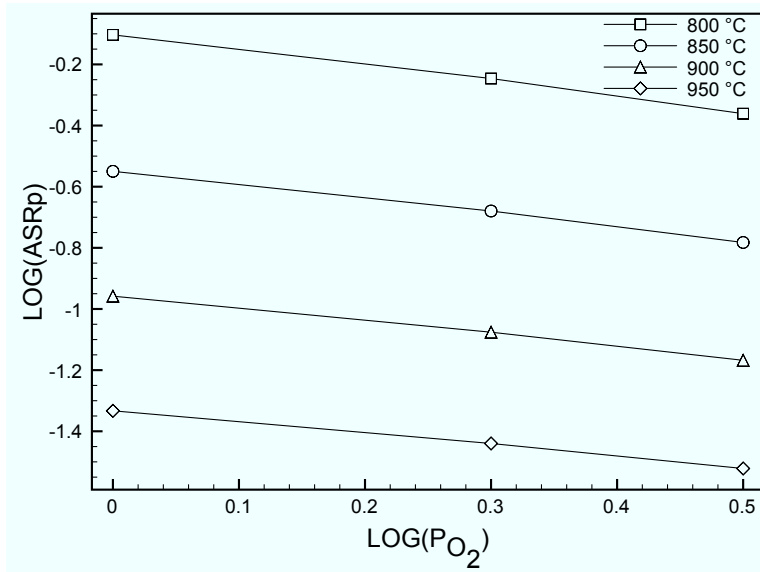


Figure 3.2.7: Area specific polarisation resistance of sample A, arc C of the symmetrical cell as a function of temperature and absolute oxygen pressure. Values obtained by interpolation from fig. 3.2.6.

The slope of these lines are $-x$ in equation 3.2.1, and x has a range of 0.39-0.53 in the temperature range 800 °C - 950 °C.

$$\text{ASRp} \propto P_{\text{O}_2}^{-x} \quad (3.2.1)$$

The capacitance of arc C in sample A, normalised for cell area was calculated from the

frequency in Hz of the point at maximum imaginary impedance in each spectrum, and the modelled value of the ASRp of arc C for that spectrum. The calculated capacitance values are in the range of 0.062 F cm^{-2} - 0.15 F cm^{-2} , and there seems to be no dependence of the capacitance on pressure, and very little, if any, dependence on temperature. The peak frequency for the arcs in the impedance spectra varied from 1.2 Hz - 79.1 Hz. The calculated parameters for arc C may be compared with parameters of arcs in the literature that have been assigned to physical processes, so that it may also be assigned.

One study of impedance arcs, which summarised the findings of various authors, described the characteristics of five distinct processes that could be present as arcs in impedance spectra [10]. The parameters of these arcs are shown in table 3.2.2.

Arc	f_{max} (Hz)	E_a (eV)	x in $P_{O_2}^{-x}$	Process description
A	5×10^3 - 10^4	1	0	Transport/transfer oxygen intermediates/oxygen ions between LSM/YSZ, or YSZ in composite
B	10^2 - 5×10^3	2	-	Competitive elementary process in oxygen reduction mechanism
C	0.1 - 10^4	1.5 - 1.9	0.14 - 0.5	Dissociative adsorption, transfer of species at TPB, and surface diffusion
D	1.4 - 10	0	0.6 - 1	Gas diffusion in stagnant gas layer over electrode
E	~ 0.03 - 0.4	-	-	Assumed to relate to TPB segregates

Table 3.2.2: Literature values for five different processes identified in ac impedance spectra. The information in this table, and all references are found in [10].

Arc C in this work was compared with these five processes, and it closely matches one in particular, called process C in table 3.2.2. The characteristics of arc C from this work, and process C in the literature, are compared in table 3.2.3. It can be seen that arc C in this work, almost entirely falls in the ranges of each characteristic identified in the literature for process C. In literature, process C is present in nearly all impedance spectra of LSM-YSZ solid oxide fuel cell cathodes, and the capacitance increases as the sintering temperature of the electrode increases.

Condition	Literature range	This work
Frequency range (Hz)	0.1 - 1×10^4	1.2 - 79.1
Activation energy (eV)	1.5 - 1.9	2.0 - 2.1
x in $p(O_2)^{-x}$	0.14 - 0.5	0.39 - 0.53
Capacitance (F cm^{-2})	8×10^{-5} - 0.4	0.062 - 0.15

Table 3.2.3: Comparison of literature values for process C [10] and results from this work, sample A, arc C.

A value of 0.4 F cm^{-1} is given for an electrode sintered at 1300°C for 2 h, tested at 850°C in air, and an experimental range of $80 \mu\text{F cm}^{-1}$ - 0.4 F cm^{-1} is given for process

C, for electrodes sintered between 850 °C - 1300 °C. The electrodes sintered in the present experiment at 1300 °C for 1 h, should therefore have a capacitance near the top of this range as they were sintered for 1 h rather than 2 h. The capacitance of a sample tested at 865 °C, at $P_{O_2} = 2$ bar was 0.12 F cm^{-2} . The capacitance decreases with temperature very slightly, but does not vary with pressure, which implies that it does not arise from mass transport of gas in the pores of the electrode by diffusion. As the capacitance is of a similar magnitude to that measured in literature, it is suggested that it may arise from a passivation of the triple phase boundaries due to adsorbed oxygen intermediates such as O^- or possibly segregates such as silica or lanthanum zirconate [8]. Passivation may also rise from species such as MnO_x and SrO on the surface of the LSM. These can be removed with acid etching, leading to a large decrease in polarisation resistance [11]. In another work using fuel cells with LSM-YSZ electrodes, a low frequency arc arising from the LSM-YSZ electrode, had an activation energy of 2.09 eV, which is similar to arc C in this work. The arc was attributed to dissociative adsorption and diffusion of oxygen on the electrode surface [12]. The range in peak frequencies observed for arc C in this work was 1.2 Hz - 79.1 Hz. In an investigation of the impedance of symmetrical cells, a similar maximum frequency was also found for the dominant arc, in the 10 Hz to 35 Hz range, for samples sintered at 1300 °C, and it was found that this frequency was principally affected by the sintering temperature of the electrode [8]. Lower sintering temperatures lead to a higher peak frequency - at sintering temperatures below 1050 °C, the peak frequency was $>100 \text{ Hz}$. Process C is attributed to dissociative adsorption of oxygen on the surface of the cathode, transfer of oxygen intermediates at the triple phase boundary, and surface diffusion of oxygen [10]. There is disagreement in the literature about what arc C may represent. It is suggested the arc may be affected by segregates of silica or SrO and MnO_x at the triple phase boundary.

The value of x in $P_{O_2}^{-x}$ is 0.39 - 0.53 in this work, which is similar to that found by Siebert *et al.* over the P_{O_2} range of 1×10^{-5} - 1 bar [4]. Therefore, the arc is assigned primarily to the surface diffusion of adsorbed dissociated oxygen, at the triple phase boundary.

Assignment of arc B

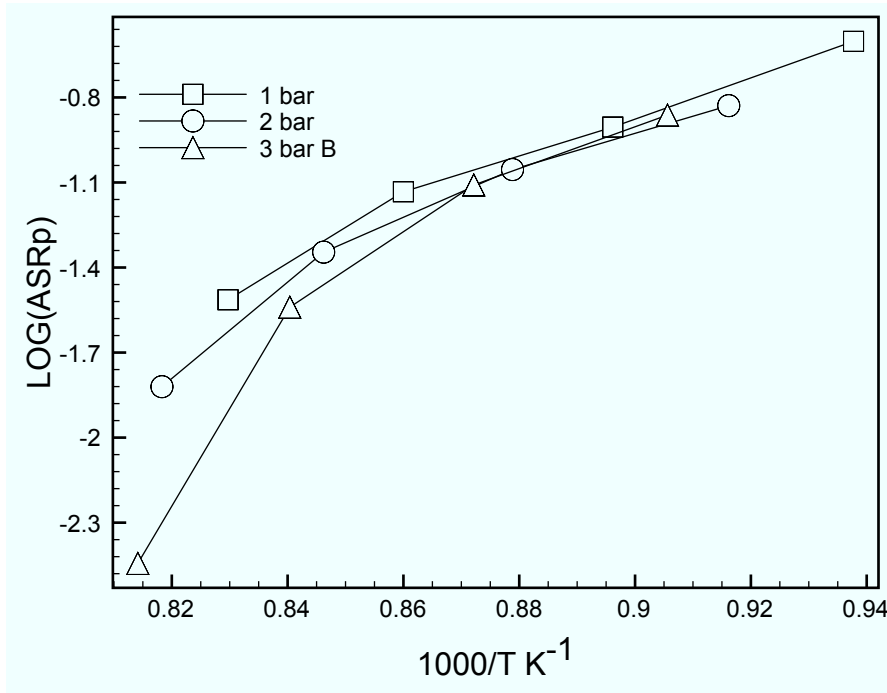


Figure 3.2.8: Area specific polarisation resistance of sample A, arc B as a function of temperature and absolute oxygen pressure. The anomalous value at high temperature for the 3 bar measurements is a result of the difficulty in modelling this arc because it was not clearly distinguished from arc C on the spectrum.

The area specific polarisation resistance of arc B obtained from the spectra by equivalent circuit modelling is shown in fig. 3.2.8. It has a near-zero dependence on P_{O_2} , within the margin of modelling error. This arc was harder to model than arc C using the equivalent circuit in fig. 3.2.3 because it was more affected by inductance from the wires and cables in the testing jig. Furthermore, as arc B is quite small compared to arc C, a small error in modelling C can lead to a larger error in the magnitude of arc B.

The peak frequency of arc B, i.e. the frequency at the maximum imaginary impedance, was calculated from the equivalent circuit modelling of the spectra, using the polarisation resistance and capacitance values. The range of frequencies was 17 Hz - 310 Hz. This arc was also compared to the remaining four processes seen in impedance spectra, A, B, D and E, shown in table 3.2.2. Of these, process E can be definitely ruled out because it typically occurs at frequencies of ~ 30 mHz, much lower than arc B. The resistance of process D is highly dependent on the P_{O_2} , which arc B is not. Process A is reported to have no P_{O_2} dependence, and a maximum frequency of $\sim 1 \times 10^4$ Hz, which is higher than that measured for arc B. Process B is reported to be very similar to process A, except that it has a maximum frequency in the range 1×10^2 - 5×10^3 Hz. Therefore, arc B in this work is most likely to be process B, because the frequency range matches best of all the processes, and the P_{O_2} dependence of arc B and process B are both zero. It is stated that processes A and B are hard to separate, and may be attributable to the flow of oxygen ions/intermediates through the YSZ or triple phase boundaries. There may be a

contribution from reaction products between LSM and YSZ such as lanthanum zirconates. However, as 5% A-site deficient LSM was used to make the cathode, due to the high sintering temperature of 1300 °C, it is unlikely that a significant quantity of lanthanum zirconates could have formed.

3.3 Conclusions

Tape cast symmetrical cells

Symmetrical cells were tested for 1 week under open circuit voltage to assess the stability of the cells and the performance of the LSM-YSZ electrode. It was found that the method of current collection must be correct, to ensure that the whole electrode is being tested. If a gold grid is used, some parts of the electrode may be inactive due to the low in-plane conductivity of LSM-YSZ cathodes. When a gold current collection layer covers the whole cell, it may become dense and hinder gas diffusion into the cell. Furthermore, the gold current collector must not be allowed to touch other noble metals in the testing jig - it will alloy with them and change its microstructure, which affects the measured polarisation resistance of the electrode under test. Due to this effect, no conclusions can be drawn from these experiments about the effect of P_{O_2} on the electrode.

Pellet symmetrical cells

Symmetrical cells were tested between 850 °C- 950 °C at P_{O_2} of 1 bar - 3 bar. The initial results gave a lower than expected ohmic resistance for the cells, which was attributed to an underestimation of the sample temperature during measurement. A correction was made to the measured data to account for this. A good method of current collection for the LSM-YSZ electrode is to use a layer of pure LSM, which has a high in-plane conductivity, and so ensure that the whole LSM-YSZ electrode is adequately contacted.

A inverse correlation between P_{O_2} and area specific polarisation resistance was found in the range studied. The impedance spectra were modelled using an equivalent circuit, and two arcs were seen. The dominant arc, named C, was assigned to surface diffusion of adsorbed dissociated oxygen species near the triple phase boundary, by comparing its capacitance, peak frequency, activation energy and the dependence of the polarisation resistance on P_{O_2} , with literature values. Various factors are thought to affect this arc, such as segregates of silica at the triple phase boundary, or SrO and MnO_x on the LSM active surface. The second, smaller, arc seen was named B, and was assigned to the flow of oxygen ions/intermediates through the YSZ or triple phase boundaries. It is thought to be affected by the formation of insulating phases such as lanthanum zirconate.

Impedance spectroscopy has been used to determine the nature of the rate limiting steps for these LSM-YSZ electrodes, and the effect of increasing P_{O_2} above 1 bar has been investigated. The results show improvement in electrode performance at open circuit voltage as the P_{O_2} is increased.

References

- [1] K. Huang, *J. Electrochem. Soc.*, 2004, **151**, H117–H121.
- [2] G. C. Bond, *Platinum Metals Rev.*, 2007, **51**, 63–68.
- [3] S. Bebelis, N. Kotsionopoulos, A. Mai, F. Tietz, *J. Appl. Electrochem.*, 2007, **37**, 15–20.
- [4] E. Siebert, A. Hammouche, M. Kleitz, *Electrochim. Acta*, 1995, **40**, 1741–1753.
- [5] J. D. Kim, G. D. Kim, J. W. Moon, Y. I. Park, W. H. Lee, K. Kobayashi, M. Nagai, C. E. Kim, *Solid State Ionics*, 2001, **143**, 379–389.
- [6] S. C. Singhal, *Solid State Ionics*, 2000, **135**, 305–313.
- [7] E. C. Thomsen, G. W. Coffey, L. R. Pederson, O. A. Marina, *J. Power Sources*, 2009, **191**, 217–224.
- [8] M. J. Jørgensen, S. Primdahl, C. Bagger, M. Mogensen, *Solid State Ionics*, 2001, **139**, 1–11.
- [9] M. Juhl, S. Primdahl, C. Manon, M. Mogensen, *Journal of Power Sources*, 1996, **61**, 173–181.
- [10] M. J. Jørgensen, M. Mogensen, *J. Electrochem. Soc.*, 2001, **148**, A433–A442.
- [11] S. P. Jiang, J. G. Love, *Solid State Ionics*, 2001, **138**, 183–190.
- [12] S. P. Jiang, J. G. Love, Y. Ramprakash, *J. Power Sources*, 2002, **110**, 201–208.

Chapter 4

Extrusion

Extrusion is a widely used technique to produce tubular or planar fuel cell supports, because it has a low cost, and can produce complicated cross sections in one step [1]. In this chapter, it is used to produce porous tubular supports for a reversible solid oxide fuel cell, that also function as current collectors, on the oxygen side of the cell. The tubes are extruded from a paste which is a mixture of fine particles of 5% A-site deficient $(\text{La}_{0.8}\text{Sr}_{0.2})_{0.95}\text{MnO}_{3-\delta}$ (LSM) ceramic powder, a solvent, and organic additives. The tubes are sintered at $\geq 1200^\circ\text{C}$, allowing the organic components to burn out, which produces short, porous, LSM tubes, which can be used as the support for a reversible solid oxide fuel cell. This chapter is divided into two sections - the first one for a handheld ram extruder, and the second one for a mechanised screw extruder. Different solvents and organic binder systems are examined, and the effect of pre-coarsening the LSM powder before extrusion is investigated in the second section.

4.1 Extrusion with handheld ram extruder

4.1.1 Comparison of two solvents for the extrusion mix

LSM powder was used with 2-hydroxyethylcellulose (cellulose) as a binder. Two solvents, distilled water and polyethylene glycol (Aldrich) were compared, by recipes H-cell1 and H-cell2 respectively in table 4.1.1. 'H' stands for handheld extruder, and 'cell' stands for cellulose pore former, and the number stands for the iteration of the recipe. Polyethylene glycol usually functions as a lubricant in extrusion. The method was previously successfully employed to make micro-tubular cells, with water as the solvent [2].

Upon extrusion of the water based recipe, de-watering took place; water migrated through the extrusion mix toward the die, causing tubes extruded first to be wetter than the later ones. This had the effect of increasing the pressure needed to extrude, as extrusion proceeded, and finally the mixture became so stiff, it could not be extruded. This effect was studied with cellulose and water mixtures, and it was seen that below a certain threshold velocity, more de-watering took place. It was also seen that with a higher solids content, the threshold velocity increased [3]. The tubes that were extruded had a rough surface, and varied in thickness. The L/D die ratio (length of die:diameter of die) was very low, ~ 0.05 ,

Recipe no.	LSM mass%	LSM vol.%	cell. mass%	cell. vol.%	water mass%	water vol.%	PEG vol.%	P1,2D vol.%
H-cell1	81.1	37.2	2.7	13.6	16.2	49.1	-	-
H-cell2	81.4	39.7	2.8	15.3	-	-	45.0	-
H-cell3	90.5	56.1	2.0	13.5	6.7	27.7	2.9	-
H-cell4	80.5	37.0	2.1	10.7	16.4	49.8	2.5	-
H-cell5	81.9	36.3	5.6	27.4	11.6	33.9	-	2.4
H-cell12	80.8	33.8	7.2	33.1	12.0	33.1	-	-

Table 4.1.1: Selected water or polyethylene glycol based recipes for the manual extruder. PEG = polyethylene glycol, P1,2D = propan-1,2-diol, cell. = 2-hydroxyethylcellulose.

which has been linked to surface roughness [4]. The variation in thickness may be due to an inhomogeneous extrusion mixture, which would mean that parts of it would extrude more easily than others, producing curved tubes which vary in thickness. It was also noted that the mandrel fitted the die loosely. Therefore, it may wiggle about during extrusion, or sit at an angle to the direction of extrusion, causing one side of the tube to have a thicker wall than the other side. Extrusion of the polyethylene glycol based recipe proceeded smoothly, though some cracks were observed in the green extruded tubes. However, they were straighter and had a more consistent thickness than the water based ones, because polyethylene glycol acts a lubricant during extrusion, so the mixture extrudes much more easily.

After sintering, the microstructure of the tubes is shown in fig. 4.1.1, where it can be seen that very large cracks are present in tubes made with polyethylene glycol, but not in the water based tubes. This can be explained by considering the porosity of the tubes before sintering. The water based tube has a network of pores formed by water evaporation, whereas the polyethylene glycol based tube has no pores. It has been shown that for tubes with no porosity before sintering, cracks often form in the tubes as organic components burn out during sintering [5].

4.1.2 Extrusion die ratios (length: diameter) and surface fracture

Die swell was observed in the previous extrusions, i.e. the tube diameter increased as it came out of the die. To counteract this, a new die was employed with a much longer bore of 5.00 mm, which greatly increased the L/D die ratio from 0.05 to 0.77. This die was a better fit to the extruder than the previous one, thus producing tubes of more even wall thickness, as it did not move about during extrusion. The extrusion recipe was reformulated to make recipe no. H-cell3, in table 4.1.1. Polyethylene glycol was largely replaced with water, in order to avoid tube cracking during sintering. However, a small amount was retained in the recipe, so it would act as a plasticiser and lubricant. The tube shrinkage during sintering can also be reduced by increasing the volume percentage of ceramics. One study on the extrusion of alumina, successfully extruded a composition with about 57 vol.% ceramic powder [6]. Therefore, the volume percentage of LSM was increased to this value in recipe

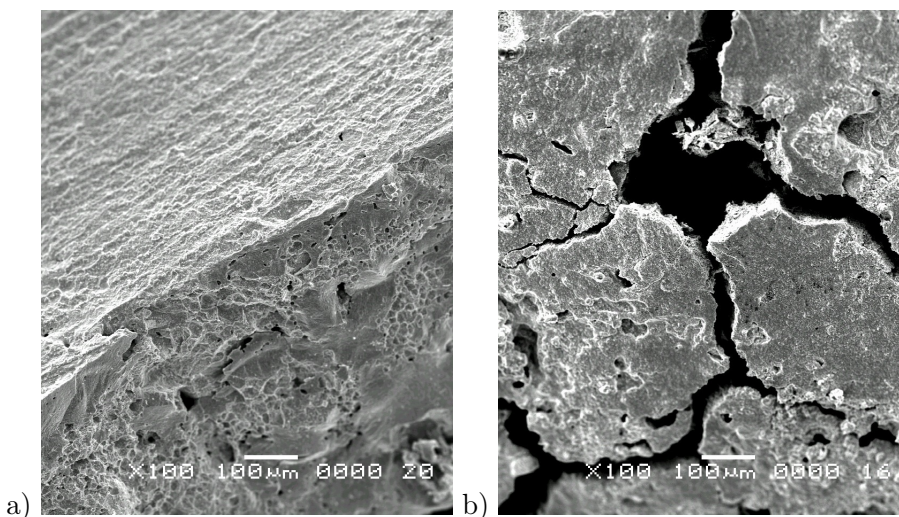


Figure 4.1.1: LSM tubes extruded and sintered at 1200 °C for 1 h at 100x magnification, a) LSM tube, fractured longitudinal cross section viewing inner wall, recipe H-cell1 - water based, b) and LSM tube outer wall surface, recipe H-cell2 - polyethylene glycol based.

H-cell3. However, this mixture was too dry and powdery to be extruded, probably because the components of recipe H-cell3 were mixed by hand in a pestle and mortar, so they were insufficiently homogeneous. In the study which extruded the 57 vol.% alumina mixture, a high shear Z-blade mixture was used to achieve a highly homogeneous extrusion mix [6]. Therefore, the LSM recipe was modified to reduce the volume percentage of LSM, and recipe H-cell4 in table 4.1.1 was made. However, during extrusion, the die became partially blocked, and only $\frac{3}{4}$ of the full diameter of the tube extruded, as the mixture was still inhomogeneous. It has been shown that if the components of extrusion mixtures are blended in a high shear mixer, the flaws in the final products are reduced, and a higher solids loading (volume percentage) of up to 60 % by mass of ceramic particles can be used in the extrusion mixture [7]. This is called viscous plastic processing, because of the behaviour of the mixture. It works by using high shear mixing to break down agglomerates of ceramic particles, and using additives to act as surfactants, lubricants etc., which coat the surface of the ceramic particles to prevent re-agglomeration [8]. Therefore mixing the extrusion mixture components in a pestle and mortar will not provide enough shear force, and will lead to problems with extrusion, and flaws in the product giving it a lower strength, and surface blemishes. These flaws and pinholes will cause holes in the YSZ electrolyte layer when it is dip-coated onto the tube, leading to a leaky cell.

Surface fracture and replacement mandrel

The extrusion recipe was changed by replacing polyethylene glycol with propan-1,2-diol, as it is chemically similar to glycerol, a plasticiser used in extrusion, with the aim of improving the flow of the material through the extruder. The volume percentage of cellulose was increased, so the tube would be more porous after sintering, as it was previously quite dense. This recipe is H-cell5 in table 4.1.1. Fig. 4.1.2 shows three extruded tubes before they are cut into sections. As the tubes were extruded, they had an uneven wall thickness,

and initially came out curved, as one side of the tube extruded faster than the other side. As extrusion proceeded, they straightened under their own weight. This is because the mandrel used was a loose fit, and so was able to move off-centre relative to the die during extrusion, so the die assembly became asymmetrical. The mandrel was replaced with a precision machined, larger bore mandrel for subsequent extrusions, which was a tight fit to the extruder, so it did not move around during extrusion.



Figure 4.1.2: LSM tubes as extruded. The curvature at one end is due to die asymmetry. ‘Dragons teeth’ markings can be seen on the surface of the tube topmost in the picture. A pen (biro) is included for scale.

Some markings, sometimes called ‘sharkskin,’ or ‘dragons teeth,’ can also be seen on the topmost tube. They arise from the flow inside the die. The outer layer of the tube is slowed relative to the inner layer by friction with the die wall. When the outer layer comes out of the die, it must accelerate to the same speed as the inner layer, which stretches it and causes the ‘dragon’s teeth’ markings. Research into the extrusion of starch pastes in a ram extruder has shown that this effect is dependent on the extrusion ratio (length of die:diameter of barrel). As the L/D die ratio decreases below 1, there is increasing surface fracture in a ‘dragons teeth’ pattern [4]. This matches the surface fracture pattern shown in fig. 4.1.2, where the die used had a ratio of 0.77. This problem can be mitigated by increasing die length to bring the ratio above 1. It has also been shown that the use of a die with a divergent exit, i.e. where the die bore tapers to a larger diameter towards the die exit, helps to prevent this surface fracture. Computational fluid dynamics (CFD) modelling of dies with divergent exits of different length, shows as the divergent section becomes longer, from 3 to 8 mm, the stretching of the tube becomes less. Surface fracture is not seen at longer divergent section lengths. It is also shown that coating the interior of the die with a fluoropolymer reduces the friction between the extrusion mix and the inner die wall, which reduces surface fracture [9]. A geometrical solution to surface fracture is to use a steel die insert, which is an extension of the mandrel inside the die, and juts out from the die orifice. It was shown that the use of a die insert allows faster rates of extrusion without causing ‘dragon’s teeth’ surface fracture. It is suggested the insert causes a pressure build-up, stabilising the extruded piece. [10] This may be because the pressure build up slows down the speed of the inner layer, and reduces the differential in speed between its inner and outer layers as it exits the die, therefore reducing stretching, stress

and surface fracture.

4.1.3 Understanding water absorption of cellulose

Some problems with de-watering and inhomogeneity in the extrusion mix were observed during extrusion. This is partly related to the kinetics of the water absorption of cellulose. It has been shown that the hydration of hydroxyethylcellulose is gradual process with a timescale of hours - it will absorb 5.5 times its own mass in water, swelling considerably, over a period of 10 h, forming a viscous gel [11]. Therefore, it is important to allow the cellulose time to hydrate and come to an equilibrium with the water when preparing an extrusion mixture. It was hypothesised that the best extrusion mixture might be produced from cellulose that had sufficient water to form a gel, but no more water, as this would prevent de-watering during extrusion. In order to determine what the minimum cellulose-water ratio was to form a gel, a series of compositions of water and cellulose were examined. Table 4.1.2 shows the different compositions and results obtained after 24 h. Some compositions formed a gel, proving the necessity of ageing the extrusion mix before extrusion in order to allow the water to hydrate the cellulose and come to equilibrium with it. Fig. 4.1.3 compares a cellulose-water mixture that has just been mixed, with one aged for 24 h. Previous compositions that had been extruded immediately after being mixed had shown signs of de-watering, as the water had not yet been absorbed by the cellulose.



Figure 4.1.3: Cellulose-water mixture just mixed (left) and aged for 24 h (right). When they are initially mixed, a suspension of cellulose particles in water is formed, then after 24 h, a translucent gel, as the cellulose has been fully hydrated.

cellulose (g)	water (g)	water:cellulose (mass ratio)	observations (after 24 h)
0.427	0.244	0.57:1	$\frac{3}{4}$ of cellulose still dry
0.407	0.297	0.73:1	$\frac{3}{4}$ of cellulose wet
0.409	0.412	1.01:1	$\frac{3}{4}$ cellulose wet
0.408	0.506	1.24:1	nearly all cellulose wet
0.423	0.652	1.54:1	$\frac{1}{2}$ wet cellulose, $\frac{1}{2}$ gel
0.427	0.786	1.84:1	cloudy gel formed
0.407	0.800	1.97:1	cloudy gel formed
0.409	0.900	2.20:1	cloudy gel formed
0.408	0.986	2.42:1	cloudy gel formed
0.423	1.304	3.08:1	cloudy gel formed

Table 4.1.2: Cellulose-water absorption experiment. All compositions were aged for 24 hr. The last five compositions were made up from the first five, by adding more water. The total water added is shown in the table.

Above a mass ratio of 1.84:1 (water:cellulose), there is enough water to form a gel with the cellulose, and at 1.53:1, there is insufficient water. Assuming that the optimum amount of water in an extrusion recipe is that which just hydrates the binder, the best water:cellulose ratio for an extrusion recipe is between 1.54:1 and 1.84:1. This was tested by preparing extrusion mixes with varying water:cellulose ratios, and ageing them overnight.

LSM (g)	cell. (g)	water (g)	water:cell. (mass ratio)	sintering shrinkage (longitudinal, %)	water (vol.%)	water molecules: cell. unit
5.138	0.511	1.376	2.69:1	22	45.8	8.5-10.6
5.348	0.511	1.148	2.25:1	23	40.9	7.1-8.9
5.558	0.511	0.942	1.84:1	17	35.7	5.8-7.3
5.768	0.511	0.840	1.64:1	17	32.7	5.2-6.5

Table 4.1.3: Variation of the cellulose:water mass ratio in extrusion mixes, with longitudinal tube shrinkage during sintering at 1200 °C for 1 h. Cell. = 2-hydroxyethylcellulose. The possible range of the the number of water molecules per repeating unit of the cellulose is also shown. The range depends on the degree of substitution of the cellulose hydroxyl groups, which is assumed to be between 1 and 3 hydroxyethyl groups per repeating unit, giving the range shown here.

Table 4.1.3 shows the different compositions, and fig. 4.1.4 shows the tubes produced by extruding them. It can be seen that the best tubes are produced with a water:cellulose ratio of 1.64:1, i.e. just enough water to hydrate the cellulose and form a gel, but no more. As the water content increases, there is more free water in the mixture not bound to the cellulose, so the stiffness decreases, and de-watering may occur.

The cellulose used in these experiments is 2-hydroxyethylcellulose, a cellulose derivative



Figure 4.1.4: LSM tubes extruded from the compositions in table 4.1.3. The water: cellulose mass ratio is shown in the picture on each tube. As the water content reduces, the tubes are smoother, and have less holes in the surface.

made by substituting hydroxyethyl groups for some of the hydroxide groups on the cellulose.

Fig. 4.1.5 shows the repeating monomer in 2-hydroxyethylcellulose, which has a varying molecular mass according to the degree of substitution by the hydroxyethyl group. Assuming that between 1 and 3 of the hydroxyl groups are substituted, the range of the molecular mass of the 2-hydroxyethylcellulose repeating monomer may be calculated. If a water: cellulose mass ratio of 1.64:1 is also assumed, then it can be determined that there are between 5.2 and 6.5 water molecules per 2-hydroxyethylcellulose repeating monomer. As there are three substituent groups on

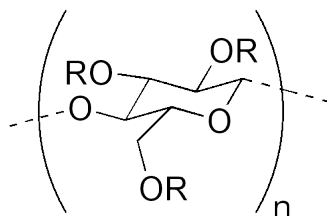


Figure 4.1.5: 2-hydroxyethylcellulose repeating unit. 2-hydroxyethyl cellulose is a derivative of cellulose made by substituting hydroxyl groups with hydroxyethyl groups.

each monomer, either $-OH$ or $-O-CH_2CH_2OH$, this means there are about 2 water molecules per OH group. It is suggested that this water is tightly bound to these groups, and any further water is more loosely bound, which reduces the viscosity of the cellulose-water mixture. A study of a mixture of hydroxyethyl cellulose and carboxymethyl cellulose used DSC (differential scanning calorimetry) and solid state NMR to study the position of water after hydration. DSC measurements looked at the proportion of non-freezable water, i.e. the water that is tightly bound to the functional groups on the cellulose. It found that there were 5.8 water molecules per repeating unit of the cellulose, which form the inner solvation shell. NMR measurements indicate that there are 6-9 water molecules bound tightly to each repeating unit of the polymer, and that if more water was added, it is bound loosely [12]. These values are in good agreement with the results obtained from the cellulose-water absorption experiments. Table 4.1.3 shows the calculated number of water molecules per repeating unit of the cellulose, assuming that each repeating unit is substituted with between 1 and 3 hydroxyethyl groups. It was observed from fig. 4.1.4 that

the tube with a water:cellulose ratio of 2.69 lengthened under its own weight as it came out the extruder, to such an extent that gaps appeared in the tube. This indicates that at a water:cellulose ratio of 2.69, there is excess water in the mixture, that is not bound. The range of water molecules per cellulose repeating unit for this composition is 8.5-10.6. As some of this water is loosely bound, the true number of tightly bound water molecules per repeating unit must be less than this range. Therefore, appropriate cellulose-water ratios in extrusion mixes may be predicted by considering the ratio of hydroxyl groups in the cellulose, to the number of water molecules.

4.1.4 Pinholes in extruded tubes - air bubbles

As the fourth composition in table 4.1.3 gave a relatively smooth tube, recipe H-cell12 in table 4.1.1 was extruded, which consists of about $\frac{1}{3}$ LSM, $\frac{1}{3}$ cellulose and $\frac{1}{3}$ water by volume. Fig. 4.1.6a shows a length of extruded tube. It is malleable just after extrusion, and is cut into sections in fig. 4.1.6b, so that they can be dip-coated after sintering. Fig 4.1.6c contrasts the tubes before and after sintering. It can be seen that there is significant shrinkage during sintering.

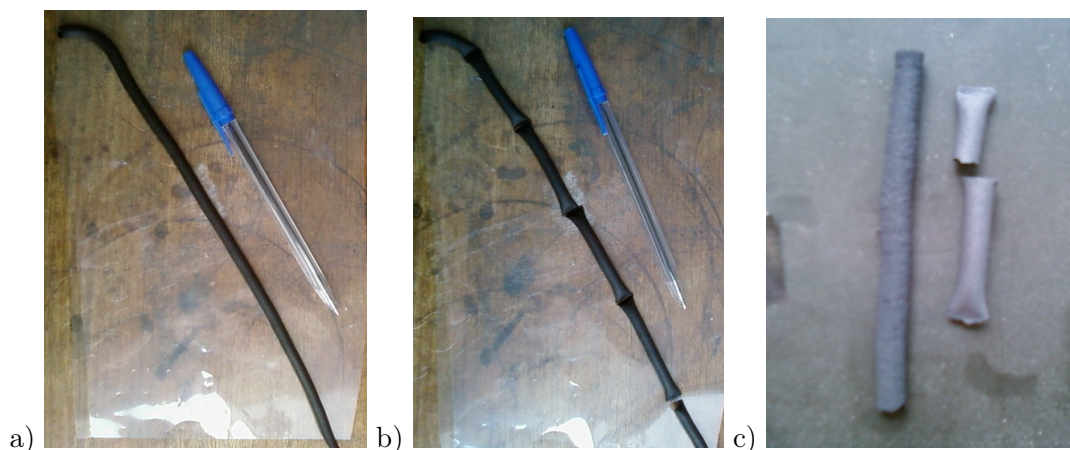


Figure 4.1.6: Tube extruded with recipe H-cell12, table 4.1.1 shown with a pen (biro) for scale, a) as extruded, b) after sectioning with a spatula - each section is subsequently cut in half to produce two tubes sealed at one end and c) tube as extruded (left) and tubes after sintering with one end sealed (right).

The tubes, although fairly smooth, still have pinholes, as shown in fig. 4.1.7. A pinhole such as this would prevent a dense YSZ electrolyte coating being successfully deposited on the tube. Pinholes in the tube surface are likely to be caused by air trapped in the mixture. An extruder with a de-airing feature would prevent this [13]. If the cellulose is insufficiently mixed with the other components and is present in large lumps, it will leave leave holes when it burns out.

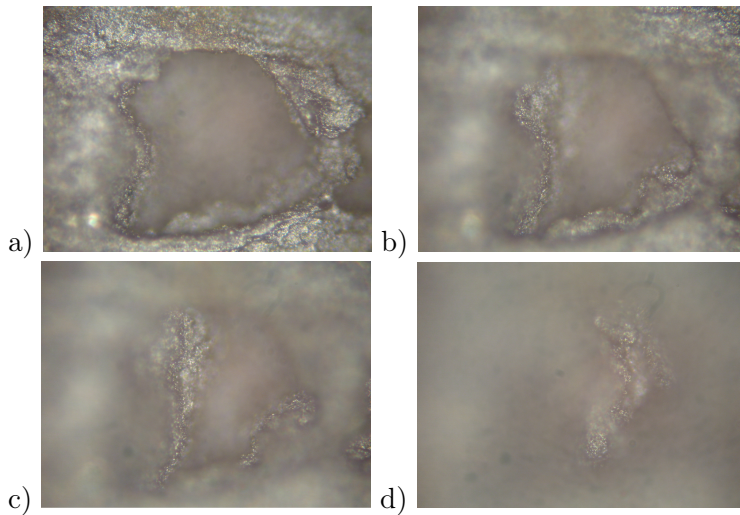


Figure 4.1.7: LSM tube surface after sintering at 1200 °C for 1 h, recipe H-cell12 table 4.1.1, optical micrographs showing central pinhole, taken at different focal lengths to show the depth of the hole. The pinhole is about 0.1 mm wide.

4.2 Extrusion with mechanised screw extruder

The mechanised screw extruder (Rondol) allows high-shear mixing of the extrusion mix, and the high pressures generated force air away from the die. The screw speed and temperature of the mix can be precisely controlled, and the pressure recorded, allowing for reproducible process conditions and tubes of a consistent quality.

4.2.1 Water and cellulose based extrusion

A recipe similar to recipe H-cell12 in table 4.1.1 was made up and extruded in the mechanical extruder. It was called recipe M-cell-W1, where 'M' stands for mechanised extruder, and 'W' stands for water-based extrusion mixture, and the number stands for the recipe iteration, and is shown in table 4.2.1. Fig. 4.2.1 shows the tubes produced after sintering at 1200 °C for 1 h. It was noted that all of them had longitudinal cracks, and also cracks perpendicular to the bore of the tube, so they broke into pieces easily. However, the individual pieces were strong. Extrusion was attempted once more, using recipe M-cell-W2 in table 4.2.1. The tubes produced were initially smooth in appearance, but after half the mix had been extruded, their surface became rough, as the surface of the tubes peeled off and adhered to the die ring as they came out



Figure 4.2.1: LSM tubes after sintering at 1200 °C for 1 h, showing rough surfaces and longitudinal cracks.

of it. Variation of extrusion speed up to 55 r.p.m and heating of the mixture to 50 °C did not improve the quality of the tubes. The ‘dragons teeth’ surface fractures that are also seen on the tubes, arise as the slow-moving outer layers of the tube, next to the outer die wall, speed up as they exit the die, to match the faster-moving inner layers in the bulk of the tube. The L/D die ratio is related to the frequency of fractures: possibly because the tensile stresses and loss of ductility in the mix as it is deformed and enters the die, are reduced by using a longer die. They also decrease in frequency and depth as the volume percentage of water in the mix increases [4]. The longitudinal cracks on the tubes in fig.

Recipe no.	LSM mass%	LSM vol.%	cellulose mass%	cellulose vol.%	water mass%	water vol.%
M-cell-W1	80.5	33.6	6.9	31.8	12.5	34.6
M-cell-W2	80.5	33.6	6.9	31.7	12.6	34.7

Table 4.2.1: Mechanised extruder water and cellulose based extrusion recipes

4.2.1 are in the direction of extrusion, and indicate a ‘cutting lamination,’ or ‘weld line.’ This is a plane of weakness within the tube, and is created when the extrusion mix within the die divides in two to go around either side of the mandrel. A thin layer enriched in water and cellulose forms at the interface between the mandrel wall and the extrusion mix, as this reduces friction. This is the ‘wall slip’ layer. For the extrusion of a biscuit dough, this wall slip layer was identified by magnetic resonance imaging [14]. When the two parts of the extrusion mix are reunited on the other side of the mandrel, they are just laminated together and do not mix. Insufficient mixing occurs because the distance between the recombination point and the die exit is too short, or else because the pressure is too low within the extruder. The laminated joint of two slip layers will have very few LSM particles present in it, so when the tube is sintered, a gap is formed. Therefore, the tubes will appear solid when extruded, but fall apart after sintering into longitudinal halves when the strip enriched in cellulose has burnt out [13]. Some tubes that are split longitudinally may be seen in fig. 4.2.1. The problem of laminations could be reduced by using a recipe with more lubricants in it - as these will reduce friction at the die wall, or by using a die with a fluoropolymer coated interior, which would also reduce friction at the wall. Another method to eliminate laminations is to lengthen the die geometry, to allow the extrusion mix to more time to homogenise and remove the lamination.

4.2.2 Thermoplastic extrusion: cellulose pore former

This type of extrusion was compared to water and cellulose based extrusion. A molten polymer system, with a polypropylene/paraffin wax binder, and a stearic acid dispersant/lubricant was used. Recipe M-cell1 in table 4.2.2 was prepared and then extruded through the mechanised screw extruder. In this designation, ‘M’ stands for mechanised screw extruder, ‘cell’ stands for cellulose pore former, and the number stands for the recipe iteration. The pressure was 1 bar, which was much lower than that observed for the water and cellulose based recipes. The tubes produced had a plastic stripe down their side - a

residue of the polypropylene that was used to purge the extruder before extrusion of recipe M-cell1. Tubes were extruded into cooling water, which helped prevent elongation of the molten tubes under gravity as they came out of the extruder die. After sintering the tubes in a horizontal position at 1250 °C for 1 h, they had slightly adhered to the alumina plate they were lying on, which caused flaws in their surfaces. The tubes also sagged slightly during sintering, and had radial cracks. As the extrusion pressure was low, there was scope to increase the stiffness of the mixture. Therefore, an increased volume percentage of LSM was used in recipe M-cell2, table 4.2.2. To prevent the tubes sticking to the furnace plate, some LSM powder was sprinkled on it. When recipe M-cell2 was extruded, the extrusion

Recipe no.	LSM mass%	LSM vol.%	PP vol.%	PW vol.%	SA vol.%	cell. mass%	cell. vol.%
M-cell1	79.6	32.8	27.3	22.8	2.0	3.3	15.0
M-cell2	85.5	42.2	22.0	20.2	1.8	2.6	13.9
M-cell3	83.3	38.2	23.4	21.5	1.9	3.0	15.0
M-cell4	81.8	35.9	22.5	20.7	6.7	3.0	14.3
M-cell5	82.8	37.5	22.9	23.0	1.9	3.0	14.7
M-cell6	83.3	38.2	23.4	21.5	1.9	3.0	15.0
Recipe no.	LSM mass%	LSM vol.%	PP vol.%	PW vol.%	SA vol.%	gra. mass%	gra. vol.%
M-cell7	76.9	38.1	23.4	21.6	1.9	10.3	15.0
M-cell8	76.9	38.1	23.4	21.5	1.9	10.3	15.0

Table 4.2.2: LSM thermoplastic extrusion recipes. PP = polypropylene, PW = paraffin wax, SA = stearic acid, cell. = 2-hydroxyethylcellulose, gra. = graphite. Recipes M-cell1-M-cell6 use cellulose pore former, and recipes M-gra7-M-gra8 graphite pore former. Recipes M-gra9 to M-gra11 are almost identical to recipes M-gra7 and M-gra8, and so are not shown in this table. In these designations, 'gra' stands for graphite pore former.

pressure went up to 20 bar, the die became mostly blocked, and only $\frac{1}{8}$ of the diameter of the tube extruded. This is attributed to an extrusion mixture that was too stiff, with too great a volume percentage of LSM in it, and possibly also inhomogeneous. Therefore, the die was disconnected, and the extrusion mixes from recipe M-cell1 and M-cell2 were mixed together to reduce the volume percentage of LSM. They were passed through the barrel of the extruder without the die assembly twice, in order to homogenise the mixture. Tubes were extruded at a pressure of 7 bar. Some tubes were sintered with the first part of the sintering profile only, to 400 °C and then back to room temperature. They had large cracks in them, which demonstrates that the binder burnout stage is responsible for the radial cracks seen after sintering. A further experiment in sintering was carried out; a 1 h dwell at 250 °C was added to the program, to try to prevent cracking, but was also unsuccessful. This problem was solved in the literature by creating porosity in the tubes before sintering, by using a solvent, n-heptane, to dissolve and extract the paraffin wax in the extruded tubes. The porosity allows gases produced as the organic components of the

tubes burn during sintering to escape, rather than building up inside it and causing cracks.

Solvent extraction of paraffin wax

In order to create porosity in the tubes before sintering, a solvent extraction using decane was carried out on some tubes extruded from the mixture of recipes M-cell1 and M-cell2. The mass losses are shown in table 4.2.3.

Tube no.	Initial mass (g)	Final mass (g)	Mass loss (g)	Mass loss (%)
1	2.502	2.377	0.125	5.0
2	2.242	2.141	0.101	4.5
3	2.727	2.593	0.134	4.9
4	2.985	2.844	0.141	4.7

Table 4.2.3: Mass loss of paraffin wax from four nominally identical LSM tubes made from a mixture of recipes M-cell1 and M-cell2 in table 4.2.2, after drying at 80 °C for 20 min, after solvent extraction of paraffin wax by immersion in magnetically stirred decane at 63 °C for 1 h, then 80 °C for 0.5 h.

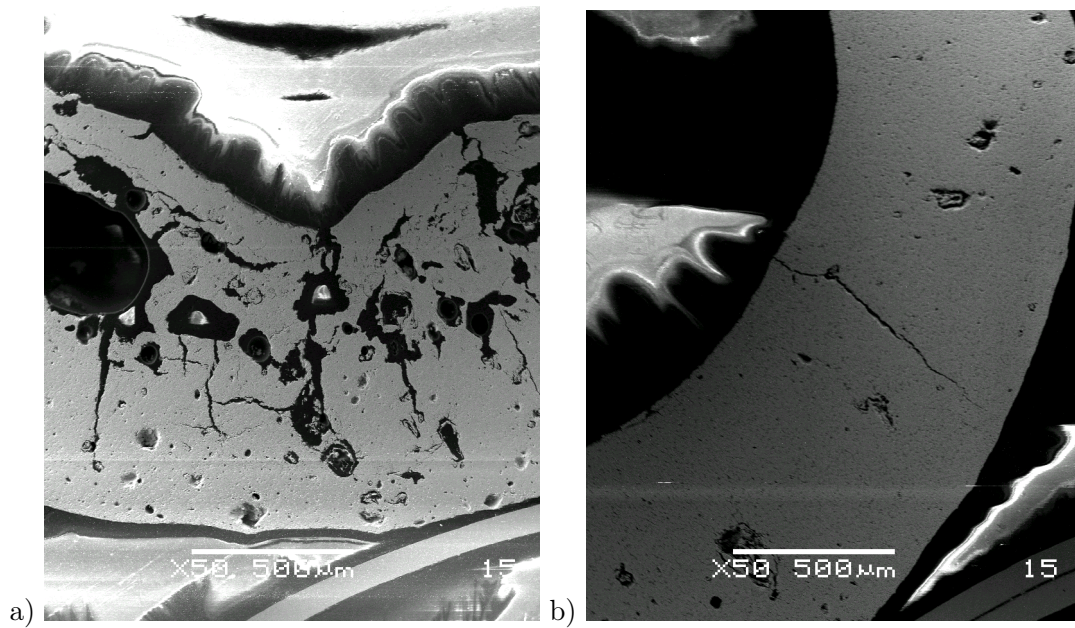


Figure 4.2.2: LSM tubes after sintering at 1250 °C for 1 h, a) recipe M-cell1 no solvent extraction, and b) mix of recipes M-cell1 and M-cell2, solvent extracted before sintering. Large cracks in a) are absent in b), as the removal of the paraffin wax by solvent extraction creates porosity, allowing gases from combustion of the organic components to escape during sintering, without cracking the cells. White areas are from charging effects in the SEM.

The precise amount of paraffin wax in the tubes is not known, but is between 5.5% and 7.4% of the mass, and most likely $\sim 6.5\%$. Therefore, about $\frac{3}{4}$ of the wax has been extracted by this method, making the tubes about 15 vol.% porous. Two LSM tubes are contrasted in fig 4.2.2, one that was sintered without solvent extraction, and one that was sintered after solvent extraction of paraffin wax. Recipe M-cell3 in table 4.2.2 had a volume percentage of LSM that was midway between that of recipes M-cell1 and M-cell2, as a compromise between maximisation of the solids loading, and prevention of blocking of the die during extrusion. Extrusion was attempted, but the die became blocked, so the mixture was homogenised by extruding it twice through the barrel with the die removed. The solvent extraction of paraffin wax with decane 70-80 °C for $\frac{3}{4}$ h resulted in a tube losing 4.4% in mass.

Recipe M-cell4 in table 4.2.2 was homogenised twice with the extruder barrel only, and then extruded in short (5 cm) sections. Each section was sealed at one end. Fig 4.2.3 shows a cross section of the sealed end of one of the tubes. It can be seen that the tube has been successfully sealed with no cracks visible in this cross section. The large cavities in the tube microstructure form when lumps of cellulose in the extrusion mix burn out during sintering. The cellulose may aggregate in large lumps, because it is hydrophilic because of its hydroxyl groups, but the other organic components such as paraffin wax and polypropylene are hydrophobic because they are hydrocarbons. Therefore, the cellulose will tend to separate from the other components of the extrusion mix and form large lumps, even after high shear mixing by extrusion through the barrel. This is why the tube microstructure is very dense, apart from large holes where lumps of cellulose have burnt out during sintering. Recipe M-cell6 in table 4.2.2 was extruded, and tubes were sintered at 1330 °C for 1 h. If the LSM tube is not sintered to at least 1330 °C before the YSZ coating, it will shrink during the YSZ sintering [15], which makes it difficult to obtain a dense, crack free YSZ electrolyte coating.

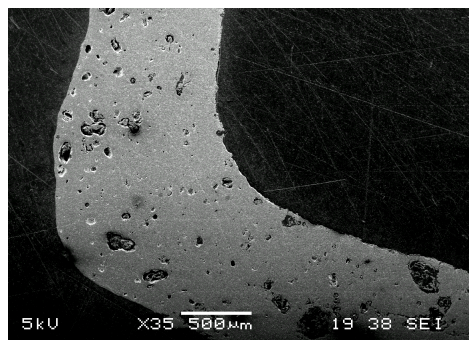


Figure 4.2.3: LSM tube after sintering at 1250 °C, 1 h, extruded from recipe M-cell4, table 4.2.2. Large pores can be seen, which arise from lumps of cellulose in the extrusion mix, which burn out during sintering, leaving cavities.

Thermal gravimetric analysis of extrusion components

The extrusion recipe components were analysed by thermal gravimetric analysis, so that burnout temperatures could be determined. Fig. 4.2.4 shows a plot of mass loss (%) on heating, for polypropylene, paraffin wax, stearic acid, cellulose, and graphite. The polypropylene, paraffin wax, stearic acid and cellulose start to evaporate/burn out below 200 °C, and are mostly gone by 300 °C. Therefore, a slow ramp rate in this part of the sintering program is essential, to allow the gases produced time to escape the tube without cracking it. However, at 400 °C, only about 10% of the polypropylene and paraffin wax

remains, so a faster sintering ramp rate is appropriate above this temperature. The graphite persists to 750 °C, and then gradually burns. Therefore, as graphite is still present even at high temperatures, creating porosity, it will create a much more porous tube than a cellulose pore former, which burns out at low temperatures before the LSM starts to sinter.

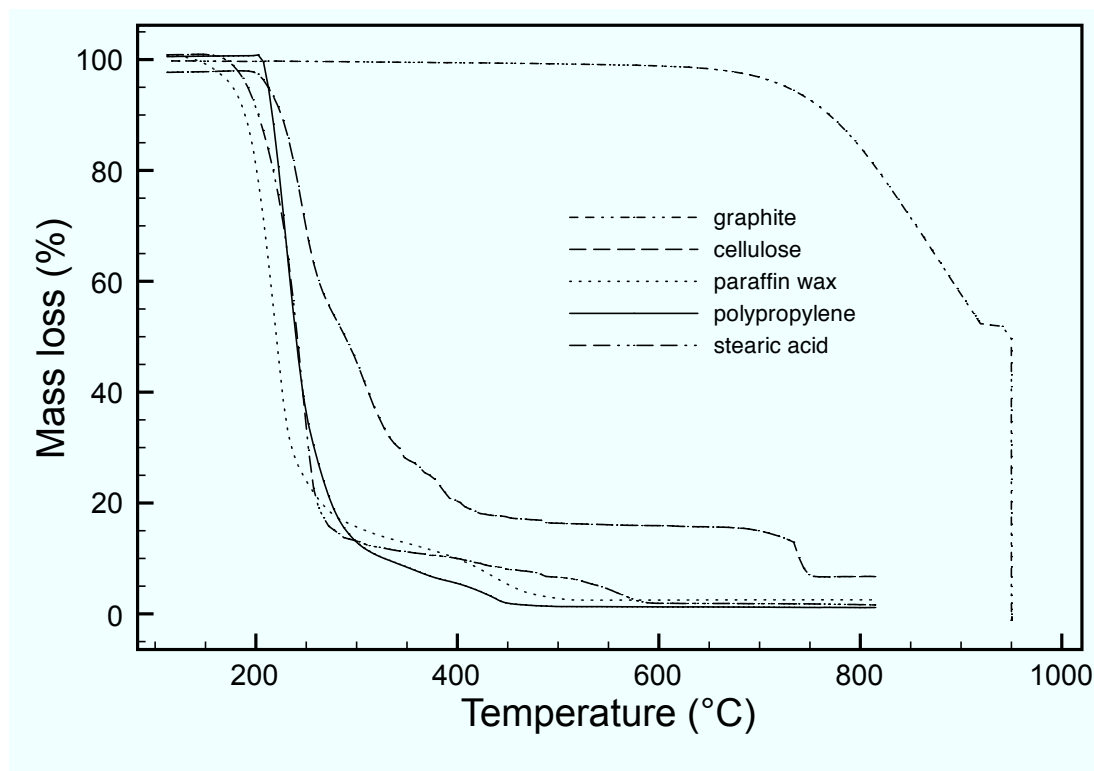


Figure 4.2.4: Thermal gravimetric analysis of extrusion recipe organic components, heating rate 5 °C min⁻¹. The graphite was only burned away after a 1 h isotherm at 950 °C. It persists to much higher temperatures than cellulose, and is therefore a more effective pore former.

4.2.3 Thermoplastic tube extrusion: graphite pore former

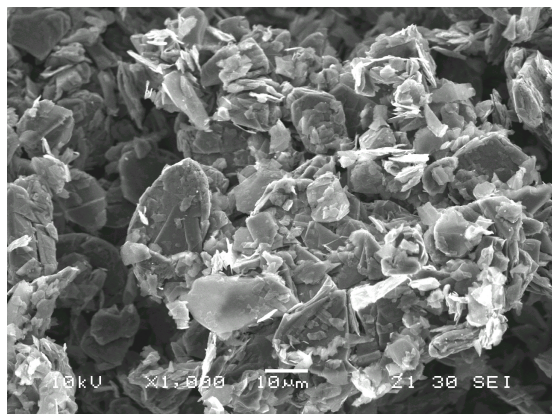


Figure 4.2.5: Graphite pore former (325 mesh, <44µm.)

Recipe M-gra7 in table 4.2.2, where gra stands for graphite, uses graphite as a pore former instead of cellulose, because the cellulose formed large lumps in the mix, rather than being evenly distributed. Graphite is also a lubricant, because of its structure of strongly bonded flat layers of carbon in a hexagonal pattern, and weak bonds between layers, thus allowing them to slip over each other easily. This should also help to prevent the ‘dragon’s teeth surface defects on the extruded tubes, which are exacerbated by friction between the extrusion

mix and the walls of the die. Fig. 4.2.5 shows the graphite used: 325 mesh, or $<44\mu\text{m}$.

LSM coarsening and particle size distribution

The LSM tubes need to be sintered to at least $1330\text{ }^{\circ}\text{C}$ so that they can be successfully coated with a dense YSZ electrolyte. The LSM tubes made previously were very dense, because at the sintering temperature of $1330\text{ }^{\circ}\text{C}$, the small LSM particles used are very sinter-active. They form necks with each other as they sinter in order to reduce their surface energy, which reduces the porosity, and leads to a dense microstructure as the tube shrinks. Although this microstructure has a high electrical conductivity because the particles are well-connected, if it is too dense, gas diffusion through the cell is inhibited. It has been shown that for SOFC cathodes, in order to produce a less dense microstructure, LSM with a bigger initial particle size can be used [16].

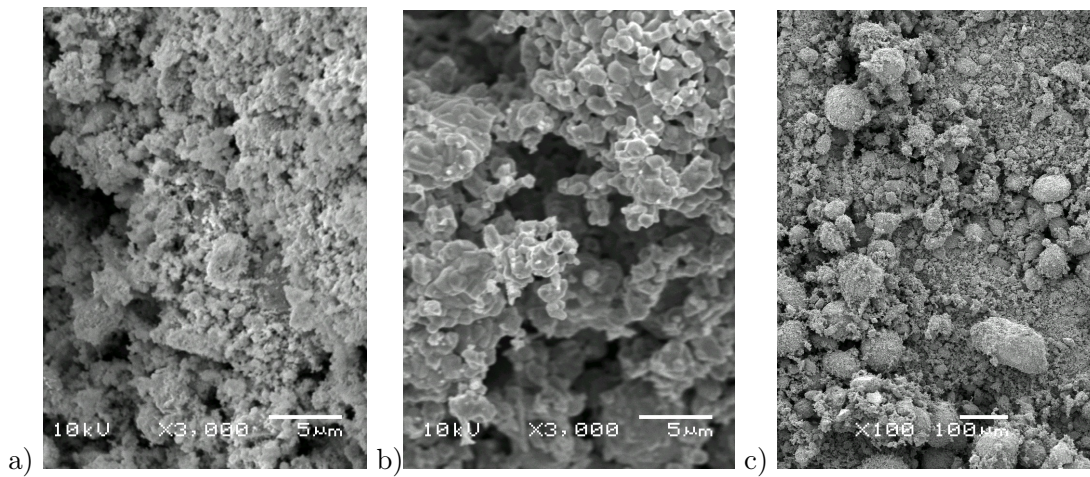


Figure 4.2.6: LSM powder a) pre-calcining, b) after calcining at $1300\text{ }^{\circ}\text{C}$ for 1 h, c) after calcining at $1300\text{ }^{\circ}\text{C}$ for 1 h (low magnification). A wide range of particle sizes can be seen in b), c) from $\sim 1\text{ }\mu\text{m}$ to $>100\text{ }\mu\text{m}$.

The same principle is employed here by sintering LSM at $1300\text{ }^{\circ}\text{C}$ for 1 h to coarsen it, and then grinding in a pestle and mortar. It has been demonstrated that this temperature is sufficient to cause the LSM particles to sinter together [15]. Fig. 4.2.6 shows LSM powder which has been calcined and ground, and also powder which has not been calcined. It can be seen that calcining increases the particle size significantly, which is quantified by particle size distribution measurements in fig. 4.2.7. There is a wide distribution of particle sizes in the coarsened LSM powder from $\sim 1\text{ }\mu\text{m}$ to $>100\text{ }\mu\text{m}$, and it can be seen that there is a slight bimodal distribution of the particle sizes, with the main peak at around $30\text{ }\mu\text{m}$ with a shoulder at $3\text{ }\mu\text{m}$. During sintering, the large particles will scavenge some of the surrounding smaller particles, and undergo coarsening. This will produce a tube which is not very dense, with some quite large particles present in it, linked by a network of smaller particles. The tube is unlikely to densify and shrink much during sintering, because the large particles do not sinter together, as they are separated by the network of smaller particles. Therefore, during cell operation at high temperature for prolonged periods, the microstructure is likely to be mechanically stable, because the large particles are not very

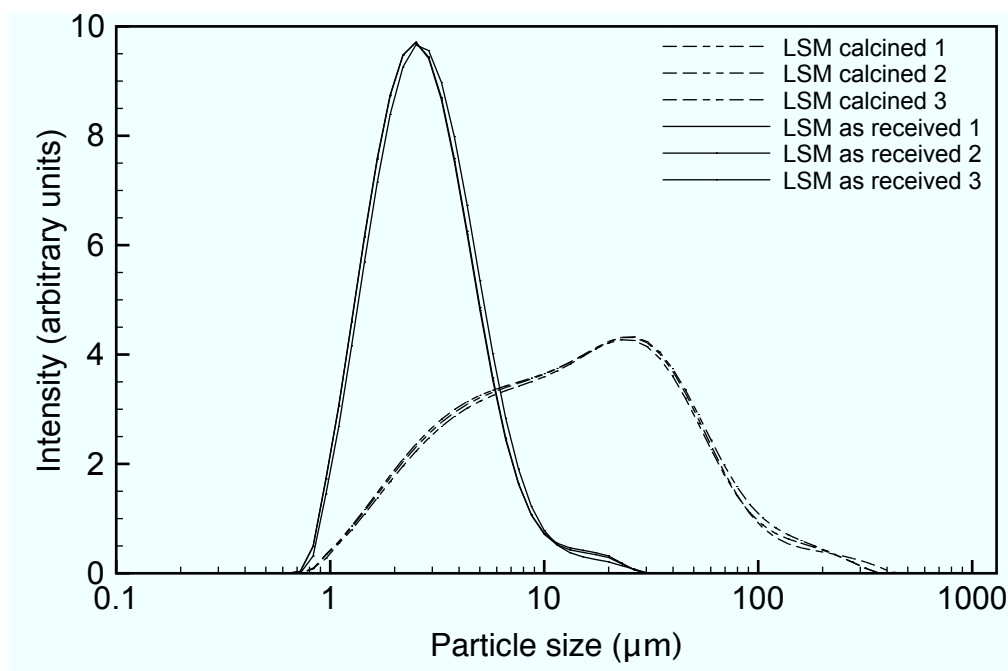


Figure 4.2.7: Particle size distribution measurements on LSM (as received, i.e. not calcined) and LSM calcined at 1300 °C for 1 h. Three measurements are taken for each sample.

sinter active. A study of LSM-YSZ cathodes measured the effect of particle coarsening during cell operation. Three LSM powders were used, with mean particle sizes of 1.54 μm , 5.98 μm and 11.31 μm . The cathode made with the smallest particles showed the greatest initial performance as it had a large surface area and therefore high triple phase boundary length. However, during cell operation at 900 °C for just 100 h, the performance quickly deteriorated as the LSM particles agglomerated. However, the cathode made with the largest LSM particles had a lower initial performance, which was virtually unchanged during cell operation as the larger particles were not sinter active [17]. This demonstrates the strong influence of LSM particle size on the stability of the electrode. A porous support should be a good current collector, provide mechanical support, and allow gas diffusion through it. It is not electrochemically active, so a fine particle size is unnecessary. A larger particle size is preferred, to produce a more mechanically stable support during cell operation.

Recipe M-gra7 was extruded twice through the extruder barrel to homogenise it. The tubes were extruded at the same speed as the recipe containing cellulose, but the pressure was lower at 4 bar - 6 bar, because graphite is an excellent lubricant. They also had fewer surface flaws than those made with cellulose, because the friction between the die wall and the extrusion mix was reduced due to the graphite lubricant. Therefore there is scope to increase the volume percentage of LSM used in the extrusion mix without causing the extruder die to block. After solvent extraction with decane, the tubes produced were sintered at 1280 °C for 1 h. A lower sintering temperature was used, so that when the YSZ electrolyte was dip-coated onto the tubes, the shrinkage of the YSZ during sintering would be matched more closely by shrinkage in the LSM substrate, helping to prevent cracking.

However, after sintering the LSM tubes at 1280 °C, they were quite friable, mechanically weak, and hard to handle, because the particles were poorly connected. Therefore, a higher sintering temperature is needed.

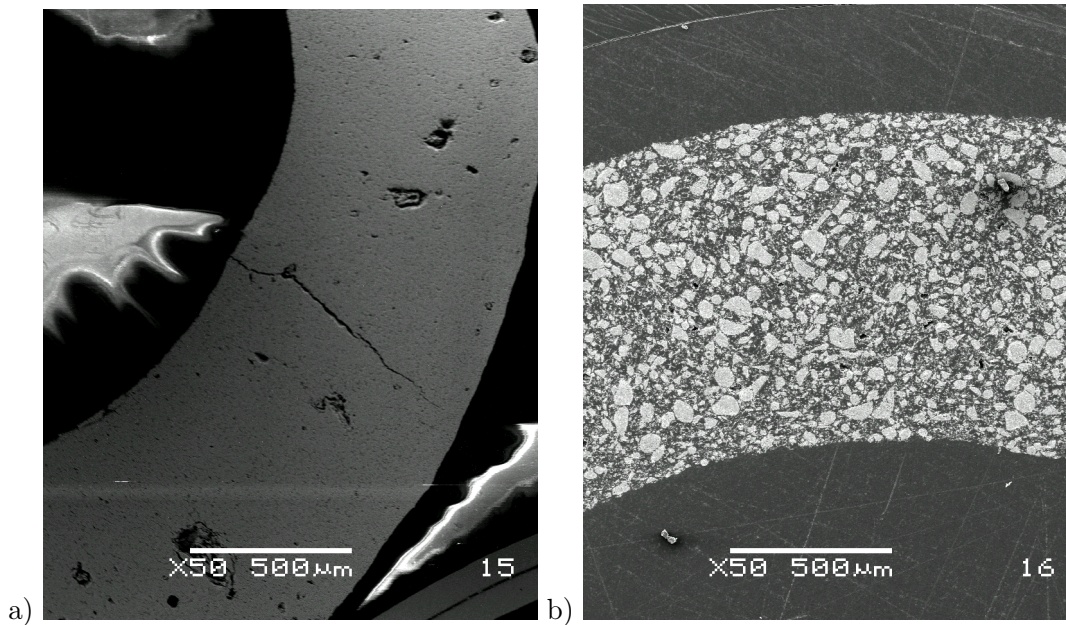


Figure 4.2.8: LSM tubes after sintering a) made with cellulose pore former, sintered to 1250 °C, (white areas adjacent to the tube are due to charging in the SEM), and b) made with graphite pore former, and coarsened LSM, and sintered to 1280 °C. The microstructure of b) is much more porous than that of a), with no large holes or cracks.

Tubes made with cellulose and graphite pore formers are contrasted in fig. 4.2.8. It was noted that the tubes were larger and less dense than the tubes made with a cellulose pore former. The LSM used in the tube with the graphite pore former was pre-coarsened, which gives interconnected porosity throughout the tube, and a homogeneous microstructure. However, large holes are seen in the microstructure of the tube made with cellulose pore-former, fig. 4.2.8a. If these occur on the tube surface, they make the deposition of a dense YSZ electrolyte layer very difficult. The large holes arise from lumps of cellulose, which may form in the mix because the cellulose is hydrophilic, whereas the other components such as paraffin wax and polypropylene are hydrophobic. However, the graphite used, shown in fig 4.2.5, is more hydrophobic than cellulose so mixes well with other hydrophobic components of the extrusion mix.

The coarsened LSM powder in fig. 4.2.6 shows a wide particle size distribution. Fig 4.2.8b shows that in the tube, the large particles are connected by the more sinter active small particles, which makes a strong yet highly porous network, ideal characteristics for a conductive support tube.

4.2.4 Porosity analysis of tubes with ImageJ software

The volume percentage of porosity in the LSM tubes made with the graphite and cellulose pore formers is compared in table 4.2.4.

Picture no.	Tube type	Sintering temperature (°C)	Porosity (vol. %)
1	LSM, graphite pore former	1300	55.0
2	LSM, graphite pore former	1300	58.7
3	LSM, cellulose pore former	1250	23.5
4	LSM, cellulose pore former	1250	21.5

Table 4.2.4: Porosities of LSM tubes made by extrusion, with two different pore formers, graphite and cellulose. The porosities were obtained by analysing levels of gray tone in SEM pictures with the ImageJ software [18] - the darker areas are pores. Fig. 4.2.9 shows SEM pictures 1 and 4, and the identification of pores. The LSM powder used in the graphite tubes was pre-coarsened at 1300 °C before extrusion.

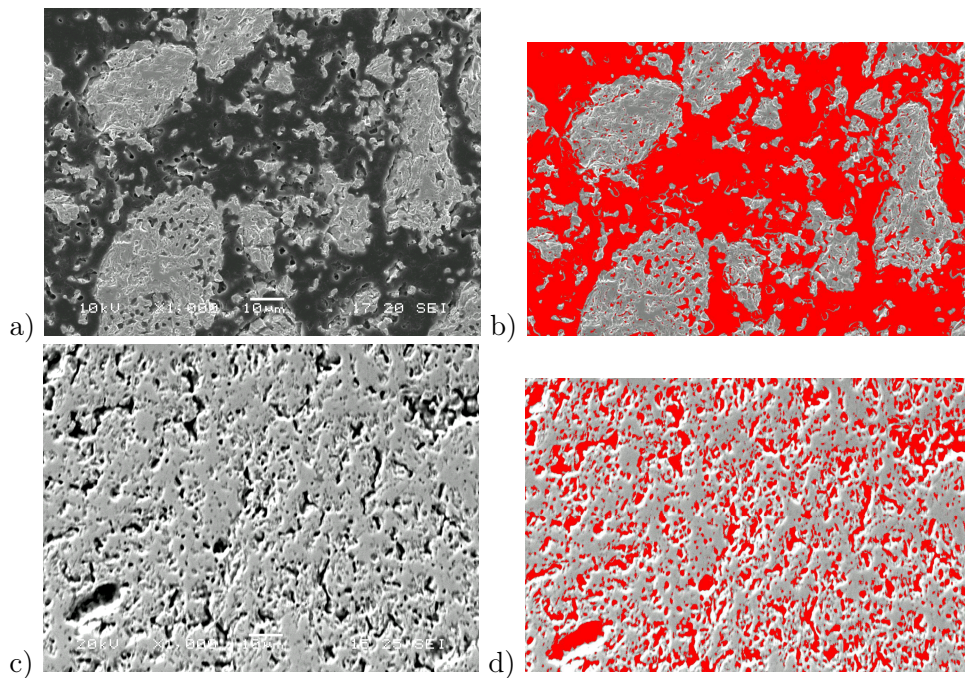


Figure 4.2.9: Cross section of LSM tubes at 1000x magnification a) made with graphite pore former b) made with graphite pore former with pores highlighted in red c) made with cellulose pore former d) made with cellulose pore former with pores highlighted in red. Imaging software ‘ImageJ’ [18] was used to colour the pores red, according to the grey tone - darker areas are pores.

The porosity of the tubes made with graphite pore former, with the coarsened LSM, was almost twice that of the tubes made with cellulose pore former, and LSM that had not been coarsened. Fig. 4.2.9 shows the microstructure of the two tubes. It is not clear from the figure, whether the porosity in the tube made with cellulose is connected. However, the porosity in the tube made with graphite is obviously connected. Therefore, the microstructure of the tube made with cellulose may be too dense to allow gas to flow through it easily. As the YSZ electrolyte is deposited and sintered to >1300 °C, the tube will continue to densify. It also was noted that the tubes made with graphite were less dense, and had a larger diameter than the tubes made with cellulose. This can be attributed to the coarser LSM particles, which are less sinter active, and also the bimodal distribution

of LSM particles, which means that small particles separate the large particles, preventing them from touching each other and sintering together, to make a dense microstructure. This less dense microstructure reduces the mechanical strength of the tubes, although they were still robust and easily handled without breaking.

Recipe M-gra8 was extruded, and the barrel temperature, pressure just before the die, and motor current was recorded, using custom written software developed using Labview v8.6.1®.

The data is shown in fig. 4.2.10. There are many small spikes in the motor current, from 0 A to 0.4 A, as the extruder was turned on and off to extrude each tube individually. They correspond with pressure spikes of about 4-5 bar, which is the pressure needed to extrude. This is compared with a measurement of 1 bar taken during the homogenisation of the extrusion mix, at the same temperature and screw speed, with the die removed. Therefore, by subtraction, the die exerts a back pressure of about 3 bar - 4 bar on the extrusion mix. It can also be seen that the barrel temperature declines during extrusion, and rises when extrusion is halted. As new material feeds into the extruder when the screw turns, it melts and cools the barrel by a few degrees. The die temperature is not recorded in fig. 4.2.10 because of a fault with the extruder, but it was measured to be about 170 °C.

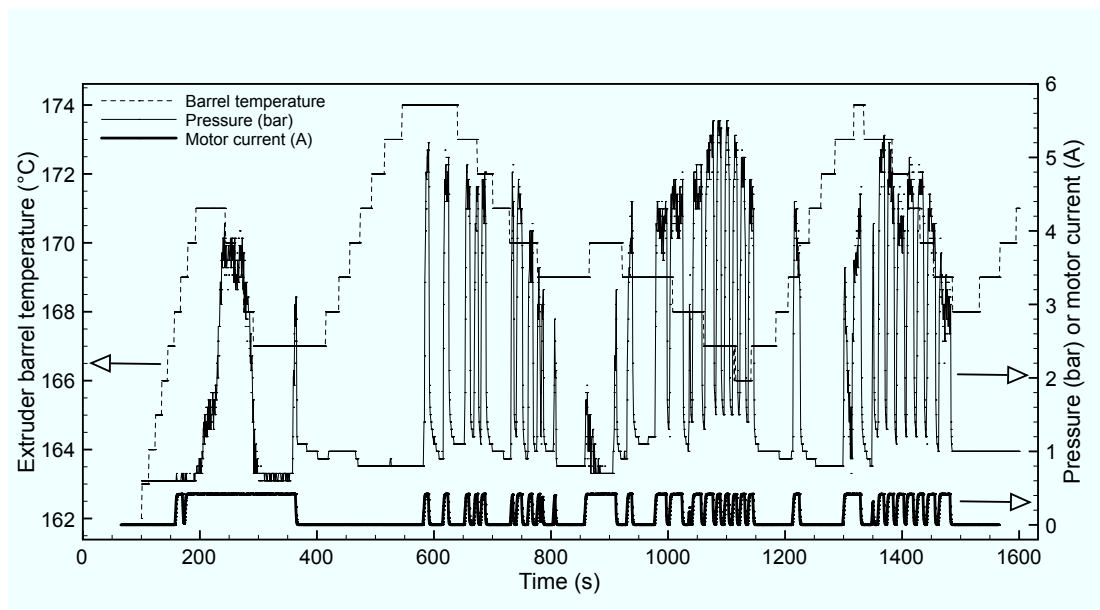


Figure 4.2.10: Extrusion of recipe M-gra8: Barrel temperature, pressure before the die, and motor current are shown for the duration of extrusion. 20-30 LSM tubes are extruded, with the rotation of the extruder screw halted between tubes. Each small peak in the motor current corresponds to the extrusion of one tube.

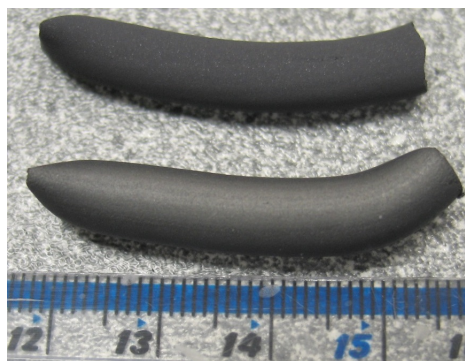


Figure 4.2.11: LSM tubes as extruded (bottom), and after sintering at 1330 °C for 1 h (top).

The sintered tube in fig. 4.2.11, has a matte appearance as all the organic components have burned out, leaving a porous tube. However, the extruded tube has a shiny appearance because of the polypropylene and paraffin wax. Both tubes have a similar size, which shows that there is not much shrinkage during sintering. A higher sintering temperature of 1330 °C was used for this recipe and all subsequent ones, so that the tubes would be mechanically robust. Recipes M-gra9 to M-gra11, which had an almost identical composition to recipes M-gra7 and M-gra8, were also extruded and sintered in

the same manner. For recipe M-gra11, diethyl ether was used instead of decane to perform the solvent extraction, and was able to extract the wax more quickly. The recipe M-gra11 tubes were also cut to a longer length, so that when the tubes are tested, the seal and the active area could be further apart. This means that the seal is cooler, which protects it.

4.2.5 Conclusions

In conclusion, two different extruders were used to extrude LSM tubes. Firstly, a small handheld ram extruder was used to extrude tubes with an LSM, water and cellulose based mixture. The die and mandrel were replaced with better fitting versions, which improved the tube quality, symmetry of the walls, and reproducibility. The new die greatly increased the die ratio (length:diameter) from 0.05 to 0.77, the maximum possible value given the limitations of the extruder. However, this was not sufficient to prevent surface fractures such as ‘dragon’s teeth.’ This is in accordance with the literature, which states that the die ratio must be greater than 1 to prevent this phenomenon. They are caused by tensile stresses in the tube surface as the slow moving surface layer accelerates to match the speed of the faster moving bulk layers of the tube as it comes out of the die.

It was seen that the mixing the components of the extrusion recipe by hand in a pestle and mortar did not produce a homogeneous mixture. It leads to a tube with a rough surface, and causes variations in wall thickness, or large pits in the tube. When a higher volume percentage of LSM was used, the extruder became blocked. These levels of LSM could be successfully used in literature papers, because the mixture was subjected to high shear mixing before extrusion, which produced a mixture that could be extruded. Experiments carried out to determine the optimum cellulose-water ratio by testing the water absorption capabilities of cellulose showed that the optimum water:cellulose mass ratio was about 1.63, as this was just sufficient to hydrate the cellulose to form a gel. This amount of water was calculated to correspond to approximately 2 water molecules per OH group in the cellulose. Extrusion of tubes with varying amounts of water showed that addition of more water caused increased surface roughness, and a loss of mechanical integrity in the extruded tubes. It was also seen that air bubbles were present in the extruded tube, some

of which were on the surface, causing pinholes. This makes dip-coating the electrolyte and subsequent layers very difficult.

Therefore, a mechanised screw extruder was used to extrude LSM tubes instead. A cellulose, water and LSM recipe was tried initially. However, a 'cutting lamination' or 'weld line' was observed, arising from the extrusion mix parting to go around the mandrel inside the die, and then reuniting. This caused a line of weakness in the extruded tubes, which resulted in longitudinal cracks after sintering. It is a function of the recipe, extrusion pressure, and die shape. 'Dragon's teeth' surface fractures were also observed. This is a function of the die ratio (length:diameter), and friction between the inner die wall and the extrusion mix, which can be reduced by coating the die or changing the lubricants in the extrusion recipe.

Therefore a thermoplastic recipe was employed, with LSM powder, polypropylene and paraffin wax binder, stearic acid as a surfactant and lubricant, and cellulose as a pore former. Extrusion was carried out above the melting point of polypropylene, at about 170 °C. The initial tubes produced, sagged during sintering, so the volume percentage of LSM was increased. This caused the pressure during extrusion to increase to 20 bar, and the die became blocked. High shear mixing was carried out by extruding the mix through the barrel only, and then tubes were successfully extruded at a pressure of 7 bar. It is necessary to employ high shear mixing, to provide a homogeneous extrusion mix according to the theory of viscous plastic processing. It was also confirmed that it is necessary to use decane as a solvent to extract the paraffin wax in the tubes and create porosity before sintering. This allows gases produced by the binder burnout to escape and prevents tubes cracking during sintering.

The tubes produced had a very high density, and isolated large pores due to lumps of cellulose - it was an unsatisfactory pore former. The LSM powder was pre-coarsened by sintering at 1300 °C, which greatly broadened the particle size distribution, with many large particles. TGA measurements showed that the cellulose burned out at low temperatures, whereas graphite persisted to at least 750 °C, so it was used as a pore former instead. Imaging software was used to analyse SEM pictures of tubes made with cellulose and graphite pore formers, showing that the volume percentage porosity was about 23% and 57% respectively. Tubes made with graphite had no 'dragon's teeth' surface fractures, and extruded at a pressure of 4-5 bar, because the graphite pore former also acts a lubricant. The coarsened LSM used in the tubes with the graphite pore former is not very sinter active, so the tubes are robust and are unlikely to sinter further during cell operation at high temperature. It was seen that 1280 °C was insufficient to sinter the tubes as they were mechanically weak. However, 1330 °C proved sufficient.

The total pressure in the extruder during thermoplastic extrusion of a LSM and graphite based mixture was 4 bar - 5 bar, of which 1 bar could be attributed to the barrel, and 3 bar - 4 bar to the die, so it exerts a significant back pressure on the mix, which increases the shear force, helping to homogenise and de-air it.

Therefore, LSM tubes with the correct properties to be used as reversible solid oxide fuel cell supports have been made. They are produced by extrusion of a thermoplastic

mixture of coarsened LSM and organic components, with a graphite pore former, using a mechanical screw extruder. The tubes have sufficient porosity to allow easy gas diffusion, enough mechanical strength to support the cell, and a smooth surface so that the other layers may be dip coated, so a reversible solid oxide fuel cell can be made.

References

- [1] S. Gamble, *Mater. Sci. Technol.*, 2011, **27**, 1485–1497.
- [2] T. Yamaguchi, S. Shimizu, T. Suzuki, Y. Fujishiro, M. Awano, *Mater. Lett.*, 2008, **62**, 1518–1520.
- [3] S. Mascia, M. J. Patel, S. L. Rough, P. J. Martin, D. I. Wilson, *European Journal of Pharmaceutical Sciences*, 2006, **29**, 22–34.
- [4] A. T. J. Domanti, Phd thesis, Pembroke College, Cambridge, Department of Chemical Engineering, University of Cambridge, 1998.
- [5] T. Jardiel, M. E. Sotomayor, B. Levenfeld, A. Várez, *Int. J. Appl. Ceram. Technol.*, 2008, **5**, 574–581.
- [6] R. Greenwood, K. Kendall, O. Bellon, *J. Eur. Ceram. Soc.*, 2001, **21**, 507–513.
- [7] N. M. Alford, K. Kendall, J. D. Birchall, *Sintered ceramic articles of high strength due to reduced flaw size - obtd. by shaping drying and sintering fine particulate dispersion in liq. medium subjected to high shear mixing*, Tech. Rep., Derwent Primary Accession Number: 1988-301241 [46], 1987.
- [8] F. A. Mesquita, M. R. Morelli, *J. Mater. Proc. Tech.*, 2003, **143-144**, 232–236.
- [9] H. V. Pol, Y. M. Joshi, P. S. Tapadia, A. K. Lele, R. A. Mashelkar, *Ind. Eng. Chem. Res.*, 2007, **46**, 3048–3056.
- [10] O. L. Kulikov, K. Hornung, *J. Non-Newtonian Fluid Mech.*, 2001, **98**, 107–115.
- [11] D. S. Roy, B. D. Rohera, *Eur. J. Pharm. Sci.*, 2002, **16**, 193–199.
- [12] D. Capitani, G. Mensitieri, F. Porro, N. Proietti, A. Segre, *Polymer*, 2003, **44**, 6589–6598.
- [13] A. Bresciani, H. Reh, W. Bender, *Extrusion in Ceramics (Engineering Materials and Processes) 1st ed.*, F. Handle (Ed.), Springer, ECT GmbH, Kisslingweg 10, 75417 Mulacker, Germany, 2007, chapter 2.
- [14] D. I. Wilson, S. L. Rough, *Chem. Eng. Sci.*, 2006, **61**, 4147–4154.
- [15] A. Ghosh, A. K. Sahu, A. K. Gulnar, A. K. Suri, *Scripta Mater.*, 2005, **52**, 1305–1309.

- [16] H. S. Song, W. H. Kim, S. H. Hyun, J. Moon, *J. Electroceram.*, 2006, **17**, 759–764, 2nd International Conference on Electroceramics (ICE-2005), Seoul, South Korea, Jun 12-16, 2005.
- [17] J. H. Choi, J. H. Jang, J. H. Ryu, S. M. Oh, *J. Power Sources*, 2000, **87**, 92–100.
- [18] W. Rasband, software, ImageJ version 1.44i, National Institutes of Health, USA, 2010.

Chapter 5

Brazing

5.1 Introduction

5.1.1 A brazed joint as a seal and interconnect

In this work, an LSM supported tubular fuel cell is under development. The type of LSM used here is a 5% A-site deficient perovskite ceramic, with the formula $(\text{La}_{0.8}\text{Sr}_{0.2})_{0.95}\text{MnO}_{3-\delta}$. The LSM support tube needs to be connected to a gas delivery tube, such as 316 stainless steel. This is a low cost gas delivery tube, which could also function as a current collector. In order to do so, the steel tube must be both electrically connected to the LSM support, and sealed to the YSZ electrolyte on top of the LSM. Various solutions to sealing the cell have been discussed [1], including silver-copper oxide metallic brazed seals [2]. These have high electrical conductivity, and can be made gas-tight. They are termed “reactive air brazes,” because the copper constituent oxidises during brazing to give copper(II)oxide, allowing the silver to wet the ceramic and the metal surfaces to be joined, and making a gas-tight seal. These brazes are relatively inexpensive compared to other noble metal brazes, and do not melt at fuel cell operation temperatures, but can be melted and applied below temperatures which would damage the fuel cell. These brazes have been successfully applied in air to ceramic-ceramic joints [3],[4] and ceramic-metal joints, with steels such as FeCrAlY and on a special steel designed for fuel cell operation, Crofer-22-APU [5]. They have also been applied to other stainless steels such as the 430 and 316 grades, in a vacuum furnace in a patented process [6]. In this work, brazing LSM to these other stainless steels in air is attempted.

5.2 Silver-copper brazes

5.2.1 Initial trial of copper-silver braze

The copper powder used in the brazing experiments was reduced prior to use with dilute hydrochloric acid, as it had turned black with CuO. Fig. 5.2.1a shows the copper powder after reduction. The particle size is about 2 μm . A silver-copper braze was made with 29.8 mol.% copper, with the balance silver, and applied at the joints between two sintered tubular LSM cells and two 316 stainless steel gas delivery tube/current collectors.

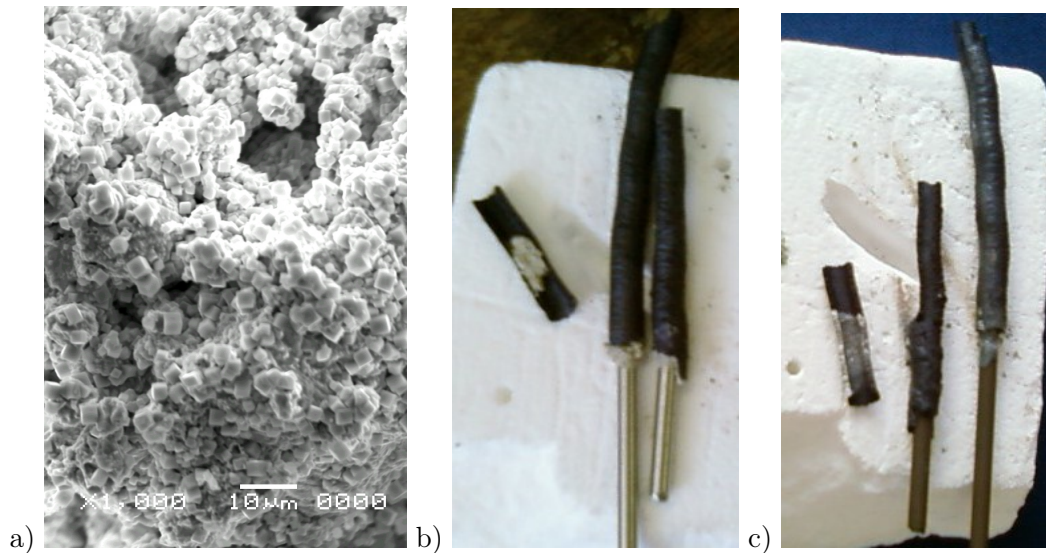


Figure 5.2.1: a) Microstructure of the reduced copper particles, b) samples before brazing, and c) samples after brazing at 1000 °C for 0.5 h.

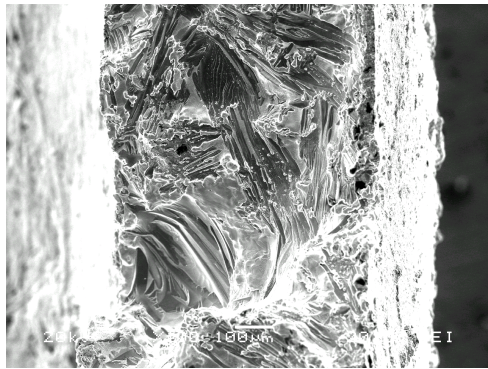


Figure 5.2.2: Braze absorbed into LSM tube microstructure

Fig. 5.2.1b and c shows the samples before and after brazing at 1000 °C for 0.5 h in air. The copper oxidises and coats the ceramic and the steel, allowing the silver to wet both. It can be seen that the braze has melted and soaked into the porosity of the LSM half-tube. It was examined by SEM (Scanning Electron Microscopy), and the surface is shown in figure 5.2.2, where it can be seen that the braze has completely penetrated the LSM microstructure, due to capillary action when liquid. The braze in

fig. 5.2.1c can also be seen near the joint on the LSM tube surfaces which have the steel gas delivery tube. After brazing, the half tube was much stronger than an LSM tube that had not been brazed, when they were both manually broken. It can be seen that the silver forms a continuous structure with almost no pores, so the electrical conductivity of braze bulk in the joint will be high. One of the LSM tube/steel tube joints adhered strongly, and the other one poorly.

5.2.2 Silver-copper braze (40 mol.% Cu)

A similar procedure was carried out for a braze containing 40 mol.% Cu, with the balance silver. Fig. 5.2.3 shows the Ag-CuO phase diagram, where it can be seen that this composition is in the region of two immiscible liquids at 1000 °C, so it should wet the steel and the LSM well.

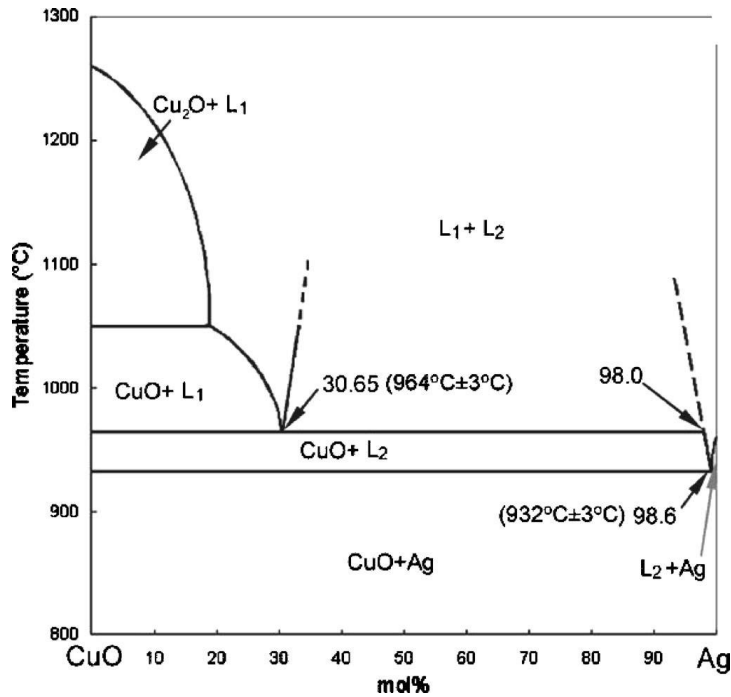


Figure 5.2.3: Silver-copper oxide phase diagram [7].

Fig. 5.2.4 shows the tubes before and after brazing at 1000 °C for 0.5 h, where it can be seen that the braze has melted and penetrated the LSM tubes, and also wet the surface of the steel. However, when the samples were examined, the LSM tubes were not fully sealed to the steel tube. This is because the braze had been drawn into the tube by capillary action, and did not totally fill the gap between the steel and the LSM tube. This gap varied around the tube circumference, but in places, it was too great for the braze to bridge it. The 316 stainless steel tubes have oxidised and turned a brown colour during brazing.

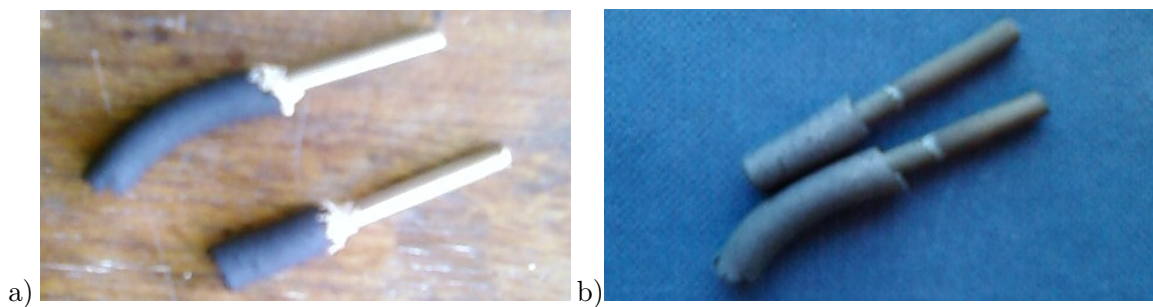


Figure 5.2.4: LSM tubes and stainless steel supports - a) after application of braze paste, b) after brazing at 1000°C for 0.5 h.

5.2.3 Variation of the braze silver-copper ratio

The Ag:Cu molar ratio affects the wetting of the braze onto the steel and ceramic. It has been demonstrated for braze on a lanthanum strontium cobalt ferrite oxide ceramic (LSCF) that the contact angle of the molten braze at temperatures between 1000 °C and 1100 °C decreases with increasing CuO content up to 34 mol.% CuO [8]. Therefore, if

the braze contains these levels of CuO, it wets the ceramic quite well. However, the joint strength is reduced as the CuO content is increased, because the microstructure of the braze at the joint changes, so the strongest joints are those with 4 mol.% - 8 mol.% CuO [9]. Therefore, a range of Ag:Cu ratios will be examined. Table 5.2.1 shows the different compositions. The braze was used to join a 316 stainless steel tube to an LSM tube, and the samples were brazed at 1000 °C for 0.5 h. The masses of the samples before and after brazing are also shown in the table.

Cu (mol.%)	Mass LSM, (g)	Sample mass post brazing (g)	Braze mass post brazing (g)
0	2.232	2.213	0.044
4	2.631	2.613	0.047
8	-	2.502	0.034
16	2.332	2.314	-
32	2.656	2.633	-

Table 5.2.1: Braze compositions with varying Cu content from 0 - 32 mol.%, with the balance Ag. The samples lose mass during brazing as the organic components of the braze burn out, and this mass gain exceeds the mass gain from the copper oxidation. Not all masses were recorded.

Figure 5.2.5 shows the samples after brazing.

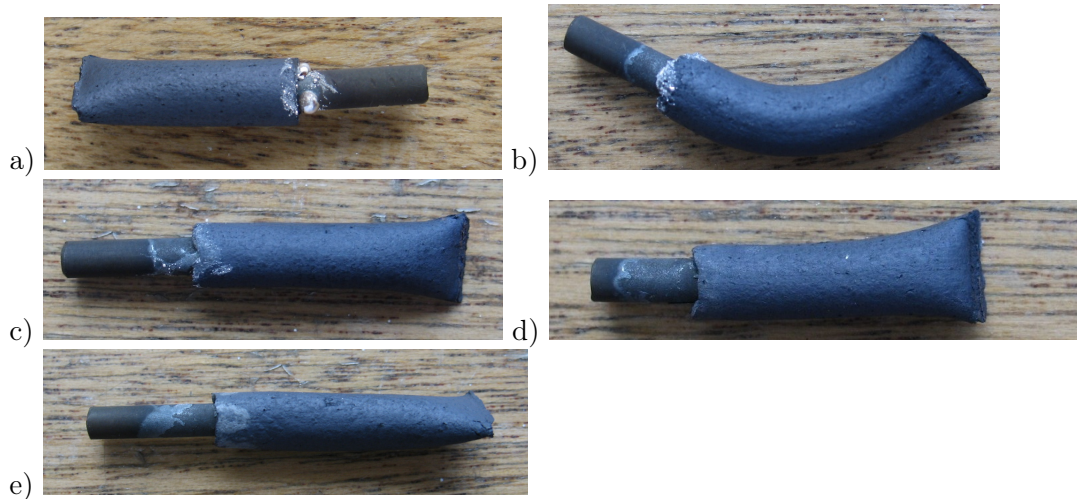


Figure 5.2.5: Photos of samples after brazing a) 0 mol.% CuO, b) 4 mol.% CuO, c) 8 mol.% CuO, d) 16 mol.% CuO, and e) 32 mol.% CuO, with the balance Ag, in the braze. Samples were brazed at 1000 °C for 0.5 h.

The 0 mol.% CuO composition did not wet the steel very well, but the compositions containing CuO did. As the percentage of CuO increases, there is less free silver sitting on the surface of the steel or LSM tube. All the LSM tubes adhered to their steel support tubes.

In order to look at the samples more closely, a cross section of the brazed joint was examined by SEM. Fig. 5.2.6 shows the 4 mol.% CuO sample. The silvery colour in the pores of the LSM is the braze, and it can be seen that it joins the steel tube to the LSM tube, where they are close together - less than about 150 μm apart. However, on the right hand side, where they are further apart, the braze does not bridge the gap. Several distinct layers may be seen between the bulk steel and the bulk LSM tube. These were examined in more detail by EDX (Energy dispersive X-ray spectroscopy), as shown in fig. 5.2.7, where the elemental composition of the bulk steel, the bulk LSM/braze and the layers in between is shown.

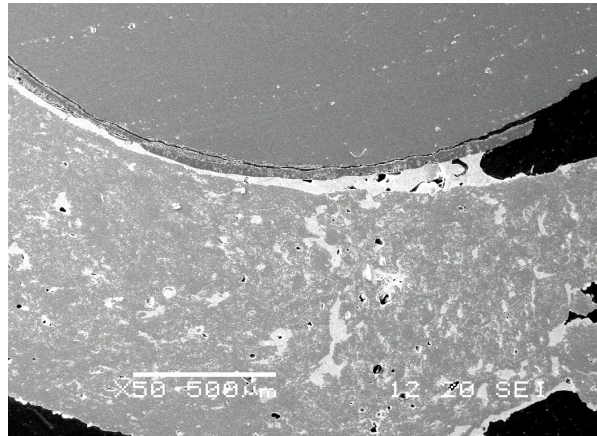


Figure 5.2.6: A cross section of the LSM tube (bottom) brazed to the 316 stainless steel support (top), with 4 mol.% CuO, balance Ag braze.

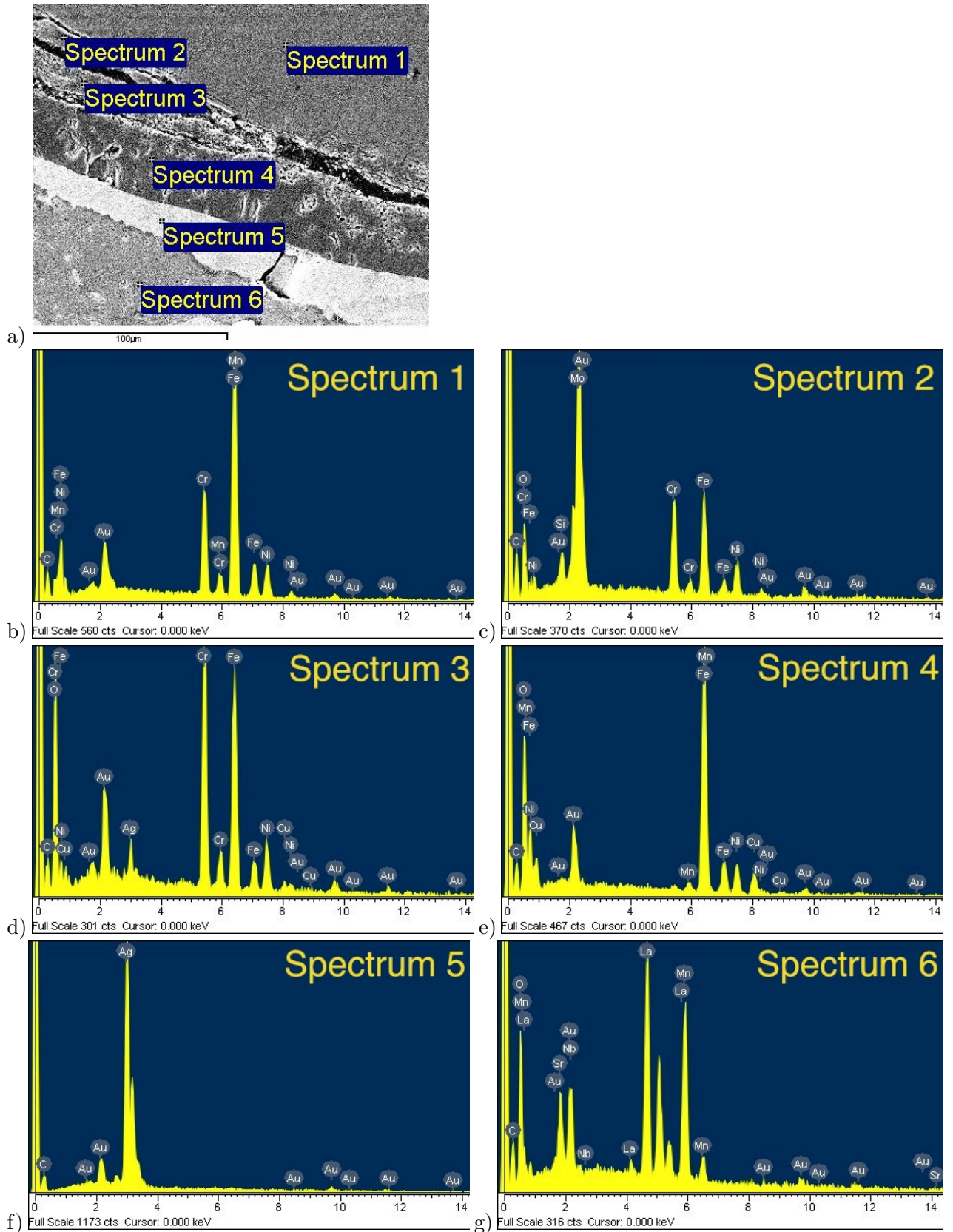


Figure 5.2.7: Analysis of various phases in the braze/steel interface a) locations of spectra b) spectrum 1, c) spectrum 2, d) spectrum 3), e) spectrum 4, f) spectrum 5, and g) spectrum 6.

In these spectra, the gold comes from the coating on the SEM sample, and not from the

sample itself. Spectrum 1 in fig. 5.2.7b is of the bulk steel, and shows the presence of Mn, Fe, Cr, and Ni as expected for 316 stainless steel, which has the composition Fe, 16%-18.5% Cr, 10%-14% Ni, 2-3% Mo, <2% Mn, and <1% Si. Spectrum 2 is of the surface oxide layer, and shows a fairly similar profile. Spectrum 3 shows Fe, Cr, Ni, Ag, and Cu - the first layer with the braze materials in it, and spectrum 4 shows Fe, Ni, Mn, and Cu. Chromium is conspicuously absent from this layer, which is about 20 μm thick. This implies that the braze layer may be able to prevent chromium diffusion into the LSM electrode, which is detrimental to its performance [10]. Spectrum 5 shows pure silver with no other elements present, and spectrum 6 shows La, Mn, Sr but no silver. Therefore, when the braze is molten, it reacts with the oxide layer on the surface of the metal, forming another oxide layer on top, which contains elements from the steel as well and the braze constituents, but does not contain Cr.

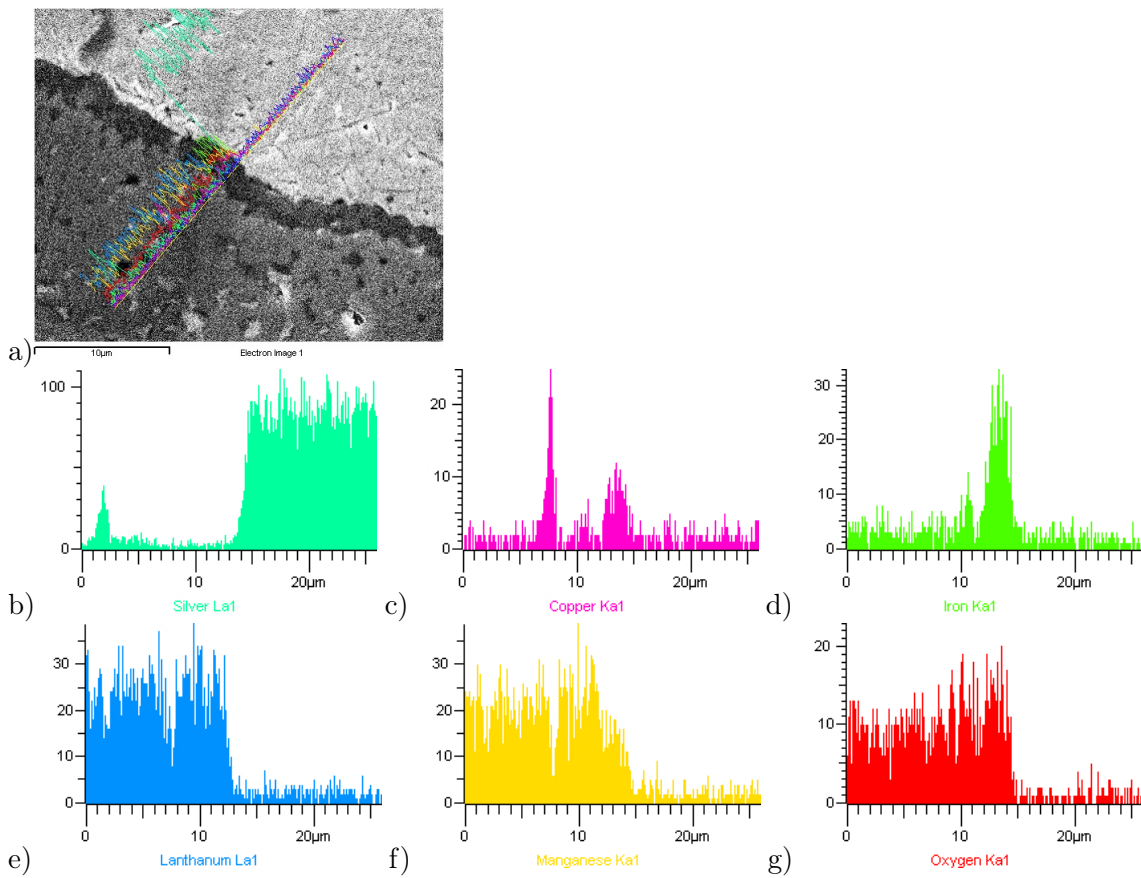


Figure 5.2.8: a) LSM tube brazed to 316 stainless steel tube with 4 mol.% CuO braze, balance Ag. The image shows the thin dark layer between the bulk LSM and the Ag layer, the stacked line scan. Line scans for b) Ag, c) Cu, d) Fe, e) La, f) Mn, and g) O are also shown.

The silver wets the second oxide layer quite well, as can be seen in fig. 5.2.7a. However, there is delamination of the base oxide layer from the steel. From the image in fig. 5.2.7, a thin dark layer can be seen between the silver layer and the bulk LSM. This is examined in more detail in fig. 5.2.8. EDX line scans show that the thin dark layer is composed of Fe, Mn, Cu and O, between 11 μm - 15 μm along the line scan. They also show a peak for copper in the LSM tube at about 8 μm along the line scan, indicating that

CuO is drawn into the LSM microstructure along with the silver. There is a corresponding dip in La and Mn intensity at this point, indicating that these elements have not alloyed with the copper oxide.

Cross-sections of the samples with 8 mol.% - 32 mol % CuO are shown in fig. 5.2.9. As the CuO content increases above 8 mol.% CuO, there is less Ag in the gap between the LSM tube and the steel tube. The 16 mol.% and 32 mol.% CuO brazes do not show any silver between the LSM and steel tubes. This is probably because the CuO wets the LSM very well, and so when there is more CuO, it is drawn into the tube leaving less silver behind to fill the gap. It may also be significant that the phase diagram in fig. 5.2.3 shows that above 30.65 mol.% CuO, the braze forms two liquids rather than a solid phase of copper oxide and a Ag-CuO liquid phase, which also makes it more mobile. Therefore, the 4 mol.% braze or 8 mol.% brazes seem the most suitable brazes for sealing 316 stainless steel tubes to LSM tubes, because they fill the gap between the LSM and steel tubes most effectively. However, if the gap between the steel and the LSM surface is greater than 150 μm , the silver will not bridge it. This means that either steel and LSM tubes should be machined so that they are a close fit to each other, or else a filler material should be used to help bridge the gap. A porous filler material would allow the braze to soak into it by capillary action as it does into the tube, allowing the braze to seal the joint. The 4 mol.% braze is the most effective composition for filling in the cracks and porosity of the LSM, sealing the tube. Another issue that is significant is the oxide layer on the surface of the steel seen in all samples. Although it is thin, it will lower the mechanical integrity and electrical conductivity across the brazed joint.

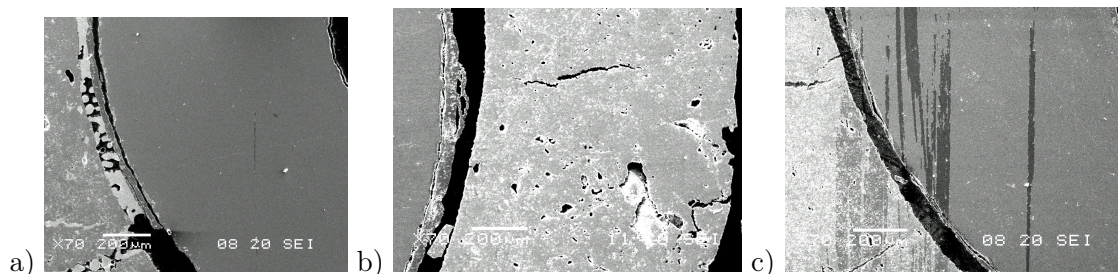


Figure 5.2.9: Cross sections of LSM tubes brazed with Ag-CuO braze to 316 stainless steel supports, with a CuO content of a) 8 mol.%, b) 16 mol.% and c) 32 mol.%. The scratches on the surface of c) are due to damage to the gold coating on the sample.

5.3 Braze-LSM composites

5.3.1 Introduction

In a brazed joint where steel and ceramic are joined, the braze is sandwiched between them, filling the gap. In determining the robustness of the joint, it is important to consider the thermal expansion coefficients of the different materials, and their ductility. For a 316 steel|Ag-CuO|LSM joint, the braze and the steel have similar thermal expansion coefficients. However, the braze and the reversible fuel cell ceramic, in this case LSM, have quite different thermal expansion coefficients, as in table 5.3.1. This mismatch has been

observed to lead to delamination at a braze:YSZ interface, after repeated thermal cycles of the joint [9]. This problem has been addressed with the use of filler materials in the braze, such as alumina, which lower the thermal expansion coefficient of the braze, reducing the mismatch between the braze and the fuel cell ceramic. This also has the effect of creating a thermal expansion coefficient that is midway between that of the braze and the ceramic, thus dividing thermal stresses over two interfaces rather than one. This approach has been patented for Ag-CuO brazes, for brazing in air, using a filler such as titanium dioxide. Various other materials are also listed, including perovskite ceramics. [11]. LSM has been examined as a filler material in a braze made without CuO, i.e. silver and LSM only, to braze an LSM cathode to a Crofer-22 APU steel interconnect. It was seen that if more than 50 vol.% LSM was used in the braze, cracks appeared in the joint. Compositions with less than 50 vol.% LSM withstood 50 thermal cycles between 250 and 800 °C, over a period of 500 h. [12]. It was decided that LSM should be investigated as a filler material, to make a braze:LSM composite.

Material	Thermal expansion coefficient (10^{-6} K^{-1})	Density (g cm^{-3})
Silver	22.4 [13]	10.49 [13]
Copper	20.2 [14]	8.93[14]
Copper(II) oxide		6.31[15]
Ticutil	18.5 [16]	9.4
LSM	11.8 [17]	6.6
YSZ	10.5 [16]	6.0
Stainless steel 316	19.9 [18]	7.99[18]
Stainless steel 430	10.5 [16]	7.75
Alumina	~ 7 [16]	~ 4

Table 5.3.1: Properties of brazing materials, fuel cell materials, steel substrates, and alumina

5.3.2 Comparison of copper and steel substrates

A Cu|braze+alumina|316 stainless steel joint has been successfully produced using a 28 mol % CuO braze, with the balance silver and alumina particles, brazing to 820 °C in vacuum [19]. In this experiment, the adhesion of braze:LSM composites to copper and 316 stainless steel substrates will be compared. For the braze component of the composite, an 8 mol.% Cu braze was chosen. This composition previously showed good adhesion to both LSM and steel, wets the steel well, and also filled the gap between the LSM tube and the steel tube. The braze was mixed in three different volumetric ratios with LSM powder, to make braze:LSM composites, as in table 5.3.2.

These were pressed into pellets with a pressure of 375 MPa on them. Two pellets of each composition were made, and one was placed on a copper square, and one was placed

Braze (vol.%)	LSM (vol.%)	Mass Cu (g)	Mass Ag (g)	Mass LSM (g)
20	80	0.0381	0.7443	2.0682
30	70	0.0569	1.1115	1.8017
40	60	0.0763	1.4886	1.5512

Table 5.3.2: Braze:LSM composites. All the brazes are 8 mol.% copper, balance silver.

on a 316 stainless steel disc. The samples were brazed to 1000 °C for 0.5 h in air. A picture of the samples before and after brazing is shown in fig. 5.3.1.

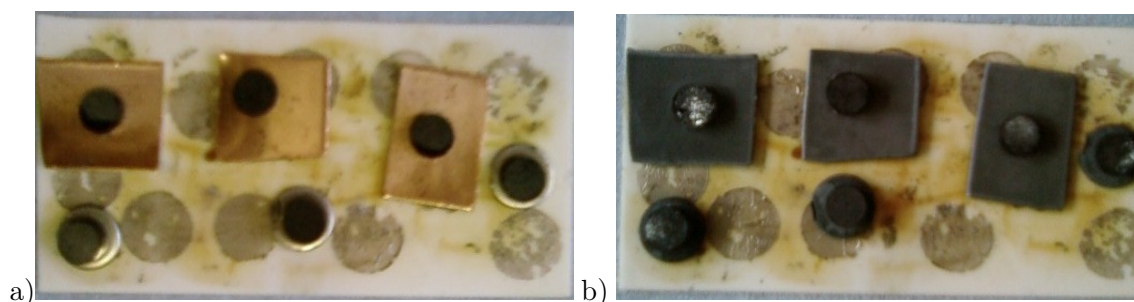


Figure 5.3.1: Braze:LSM composite samples on either copper squares a) before brazing at 1000 °C for 0.5 h, and b) after brazing.

The copper developed a thick spall of CuO and Cu₂O, which shattered after brazing, causing the pellets to drop off when the samples were handled. This was because the air atmosphere was too oxidising for the copper. Although LSM is unstable when exposed to a reducing atmosphere, a low oxygen atmosphere such as a nitrogen atmosphere during brazing may prevent oxidation of the copper. The pellets with 30 vol.% and 40 vol.% braze adhered to the 316 stainless steel substrates, but the pellet with 20 vol.% braze did not. Fig. 5.3.2 shows a cross section of the samples mounted in resin after brazing. There are many large cracks in the pellet running parallel to the pellet|steel interface. Bubbles may also be seen in the resin in these cracks, which shows that they were present before the samples were mounted in resin. They may be due to pressing the pellet with too much force, and inducing stresses in it which cause the cracking as the braze melts. Neither composition adheres to the steel very well, with a gap between the steel and the pellet. The pellets and steel are not perfectly flat, and the braze does not fill the gap, as it prefers to stay within the LSM matrix, because of capillary action when molten. The 20 vol.% braze pellet did not adhere to the steel at all, probably because all of the silver remained within the LSM matrix, and none made contact with the steel.

The braze:LSM composite|steel interface was examined in more detail at the the point where the gap between the two was narrowest in fig. 5.3.2a, by EDX. Fig. 5.3.3 shows the interface at this point, with line scans across the interface of various elements. The bulk steel can be seen from 0 μm - 24 μm , and then there is a layer of Cr, Cu, and a little Ni and Fe to 26 μm , then a layer of Fe and Ni to 34 μm , then a gap until 42 μm . Finally, there is a layer of La, Cu and Ag, and what may be traces of Ni and Cr. Oxygen was not measured,

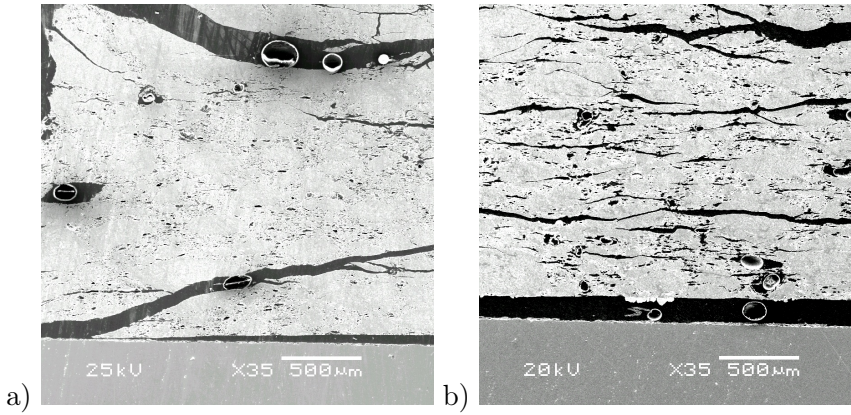


Figure 5.3.2: Cross section of braze:LSM composite pellets on 316 stainless steel pellet after brazing, a) 30 vol.% braze b) 40 vol.% braze

but is likely to be present in all of the layers. Therefore a copper chromium corrosion layer forms on the surface of the steel where it is exposed to the braze. It is interesting that there is a corrosion layer with chromium, and a separate one free of chromium, as seen before in subsection 5.2.3. In another brazing study, at the interface between 4 mol.% CuO braze and Crofer-22-APU, a high chrome stainless steel, the Cu-Cr precipitates observed were suggested to be CuCr_2O_3 and CuCr_2O_4 [5].

5.3.3 Braze interlayers

The braze:LSM composite was further investigated, by applying it to a 316 stainless steel substrate in a different way. Rather than pressing a braze:LSM composite pellet as a mixture of the different powders, they were mixed with cellulose and water, in a 1:1:1 ratio by volume, in order to make a paste, and then applied to the steel substrate. The effect of using a pure braze interlayer between this mixture and the steel was also investigated. Two samples were made with an LSM tape produced by tape casting, instead of the braze:LSM, cellulose and water paste. The six samples that were made are described in table 5.3.3.

Sample type (layer 1 layer 2 layer 3)	Braze:LSM ratio (vol.%)	Mass braze interlayer (g)	Mass mix. /tape (g)
Braze:LSM+organics braze interlayer 316 steel	30:70	0.064	0.121
Braze:LSM+organics 316 steel	30:70	0	0.277
Braze:LSM+organics braze interlayer 316 steel	40:60	0.067	0.148
Braze:LSM+organics 316 steel	40:60	0	0.169
LSM tape braze interlayer 316 steel	30:70	0.270	0.039
LSM tape 316 steel	40:60	0	0.034

Table 5.3.3: Braze:LSM composites, made with an 8 mol.% CuO braze, either 30 vol.% or 40 vol.% braze, with the balance LSM, mixed with cellulose and water (organics) to give the composition: 1/3 braze:LSM, 1/3 cellulose, 1/3 water by volume. Some of these mixtures had a pure braze interlayer between them and the steel, and some did not.

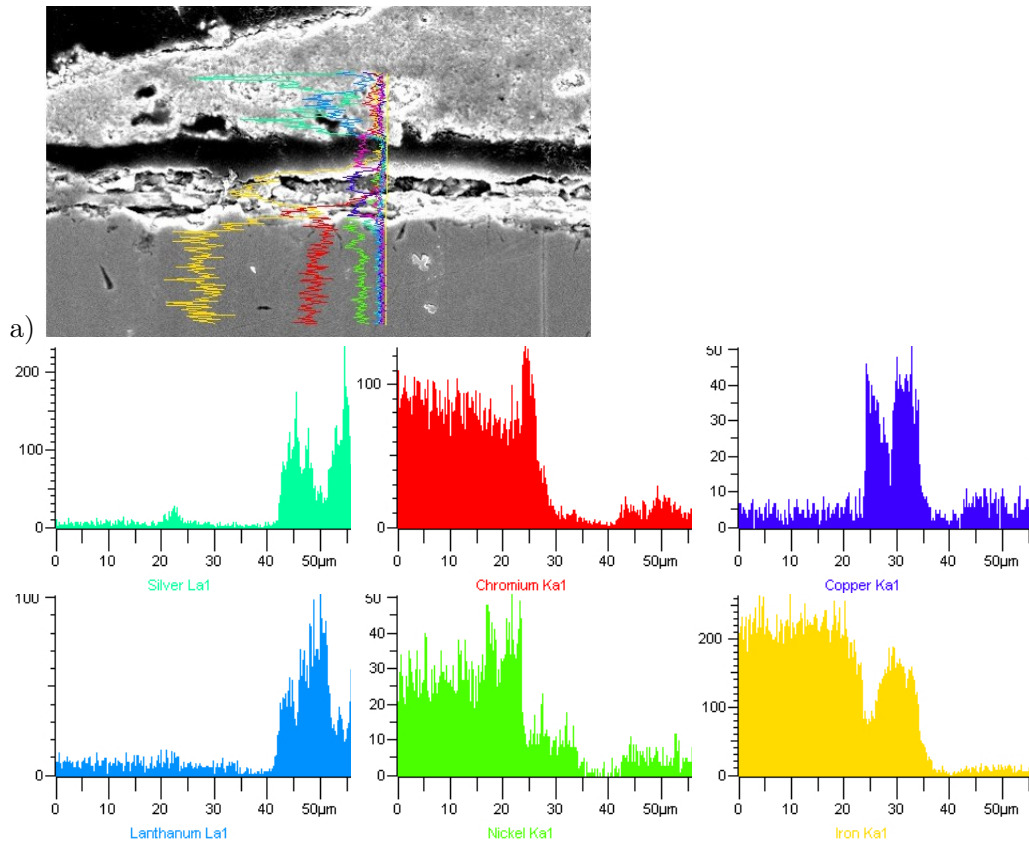


Figure 5.3.3: EDX analysis of the braze:LSM composite and steel interface in sample with a 30 vol.% braze pellet.

A picture of the samples after brazing for 0.5 h at 1000 °C is shown in fig. 5.3.4. It can be seen that the braze interlayer has penetrated the entire composite layer, and the composite layer in these samples unexpectedly adheres less well to the steel pellets than in the samples without a braze interlayer.



Figure 5.3.4: Brazed samples from table 5.3.3. The top row of samples have a braze interlayer, and the bottom row of samples do not. the samples on the left column have 40:60 braze:LSM ratio by volume, and those in the middle column have a 30:70 ratio. The two samples on the right column are the LSM tape samples.

The samples made with LSM tape do not adhere to the 316 stainless steel substrate at all. The four samples with the composite layer were mounted in resin, cross sectioned and examined by SEM. Fig. 5.3.5 shows cross sections of the steel:composite interface for all four samples. The 30 vol.% and 40 vol.% braze samples look quite similar. However, the samples with a braze interlayer do not adhere to the steel substrate, and the composite layer is relatively crack-free. The samples without a braze interlayer do adhere to the substrate, but the composite layer is cracked, because it adheres well to the steel, so when it shrinks during sintering, and as the braze melts, it experiences stresses parallel to the composite:steel interface. It is constrained in its sintering by the steel, which does not shrink during sintering. This effect causes the large vertical cracks in the layers, and leads to the braze not saturating the LSM matrix of particles in the composite layer. However, the presence of the braze interlayer in the other samples means that the composites do not stick to the steel, so their sintering is unconstrained and they do not crack, and the braze saturates almost all of the pores in the LSM matrix. Both sets of samples also exhibit an oxidation layer on the surface of the steel. This will impede the electrical conductivity across the joint.

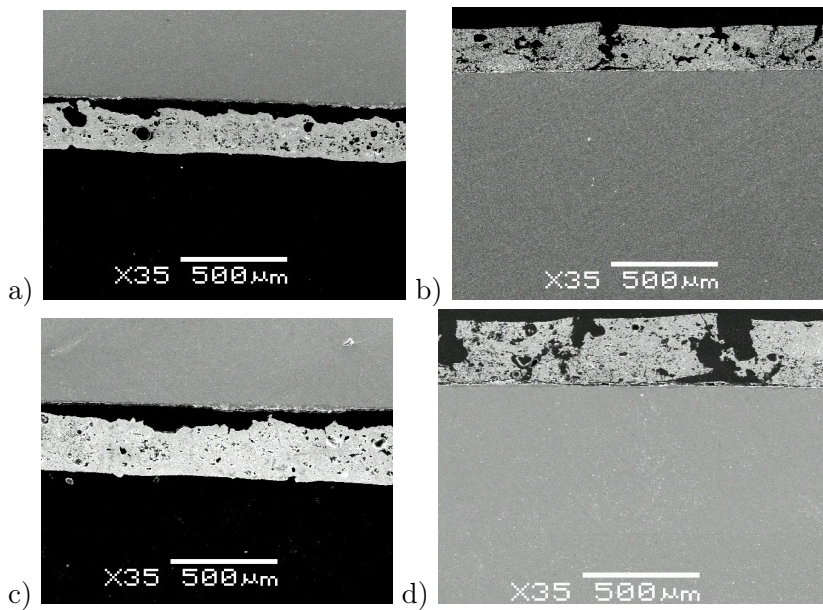


Figure 5.3.5: Cross section of braze:LSM composite, with cellulose and water, sintered to 1000 °C for 0.5 h, on 316 stainless steel substrates a) 30 vol.% braze with pure braze interlayer b) 30 vol.% braze with no interlayer, c) 40 vol.% braze with pure braze interlayer b) 40 vol.% braze with no interlayer.

5.3.4 Titanium coated stainless steel substrates

The protection mechanism for high chrome stainless steel is that chromium forms a passivating layer of metal oxide, rich in Cr_2O_3 , which prevents further oxidation, but is not very electrically conductive [20]. However, when the samples are brazed to 1000 °C in air, a black oxide layer forms, as in fig. 5.3.4, which was shown to contain multiple elements from the steel. This layer may also not be electrically conductive, and the previous tests have shown

Steel type	No. Ti coats	Mass (g)	Mass after coating with Ti (g)
316	0	3.0924	n/a
430	0	0.4932	n/a
316	1	3.8282	3.8280
430	1	0.6318	0.6317

Table 5.3.4: Titanium coated steel samples brazed with composite braze:LSM pellets. The masses after coating with titanium are shown, and both samples appear to have lost mass. This may be due to evaporation of water vapour from the surface as the samples are exposed to high vacuum during the coating process.

that it has a poor adherence to the steel. Therefore, modification of this layer by evaporation of titanium onto the steel surface before brazing was attempted, to see if this improved the corrosion resistance of the steel. A braze:LSM composite pellet was brazed to the steel. Two types of steel were compared, stainless steel 316 and 430. The 316 is an austenitic stainless steel, and the 430 is ferritic. As a consequence, the 430 has a much lower thermal expansion coefficient, as in table 5.3.1, quite similar to that of the fuel cell materials. An 8 mol.% CuO braze was used, with balance silver, in a 40:60 braze:LSM volumetric ratio.

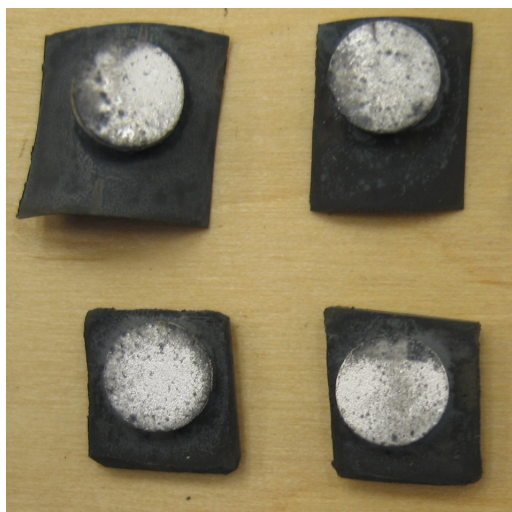


Figure 5.3.6: Stainless steel 430 (top) and 316 (bottom) with pellets of 8 mol.% CuO, balance silver braze, in a 40:60 braze:LSM volumetric ratio, after brazing at 1000 °C for 0.5 h. The samples on the left had a titanium coating prior to brazing, whereas those on the right did not.

Table 5.3.4 shows the four samples that were made. It can be seen that samples had a lower mass after the titanium coating. This is either due to instrumental error on the weighing balance, or the presence of some water on the sample which evaporated in the high vacuum used to coat the titanium onto the sample. From these results, it can be seen that the Ti layer is very thin. It cannot be seen in the SEM, however, it is present on the surface. This is shown by comparing it with a control sample. A sample of 430 stainless steel was coated with titanium, and then heated up to 900 °C for 2 h, and compared to a control sample that had no titanium coating, and had the same heat treatment. The sample with titanium had a distinctive blue colour, whereas the other sample had a brown colour. Fig. 5.3.6 shows the samples after brazing at 1000 °C for 0.5 h. All the braze

pellets adhered to the steel substrates, although the 430 steel warped during sintering, so that only a small part of the pellet was touching it. It can be seen that there is no visible difference in the black corrosion layer between samples that were coated with titanium,

and those that were not. The samples were cross sectioned and examined in SEM. Fig. 5.3.7 shows the interface between the braze:LSM composite pellets and the steel for all four samples. At the microscopic scale, no difference in the interface surface can be observed

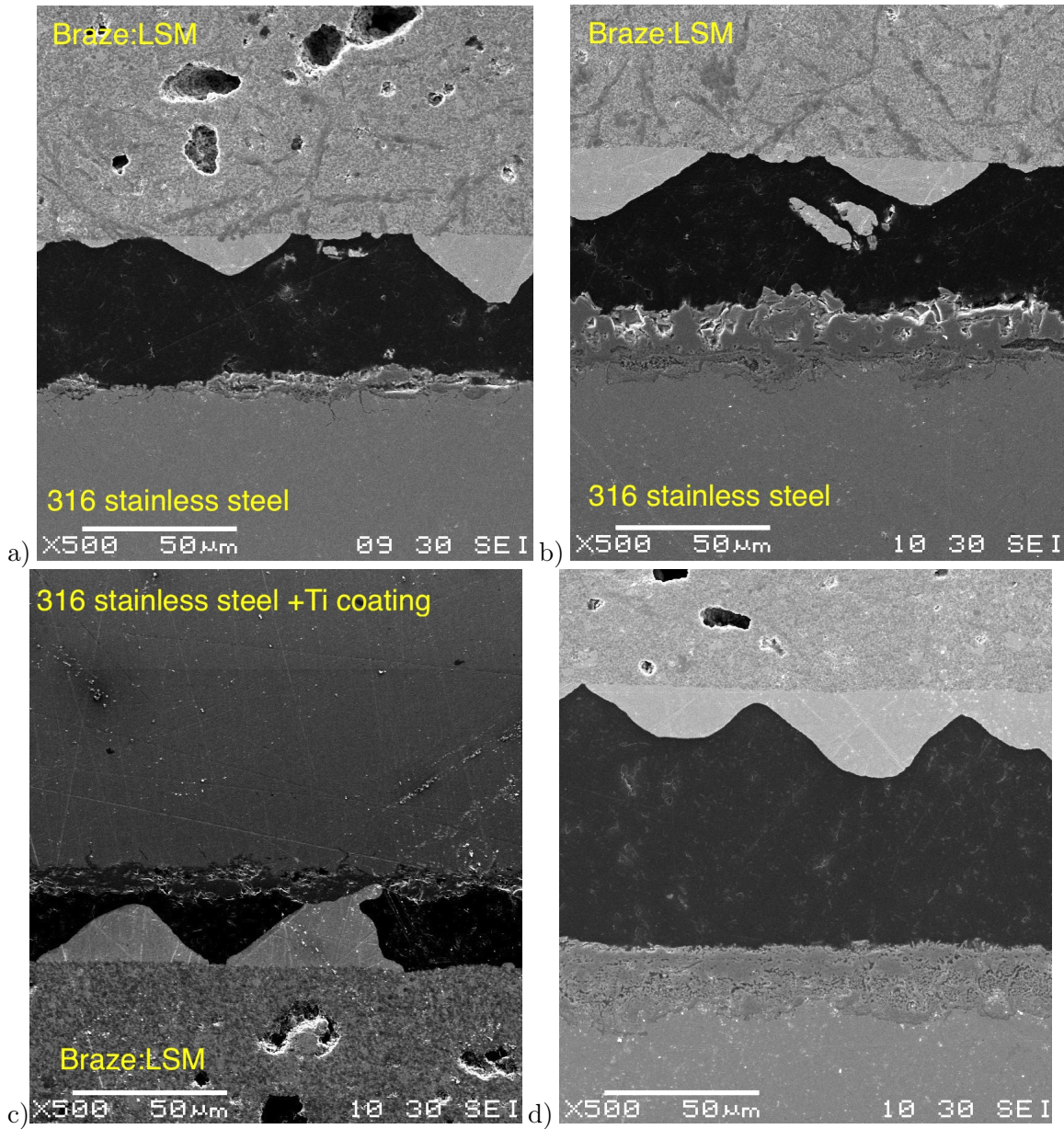


Figure 5.3.7: Stainless steel 316 (left column) and 430 (right column) with no Ti coating (top) and a Ti coating (bottom), with composite pellets made of 8 mol.% CuO, balance silver braze, in a 40:60 braze:LSM volumetric ratio, after brazing at 1000 °C for 0.5 h, a) 316+composite, b) 430+composite, c) 316+Ti+composite, and d) 430+Ti+composite.

between the samples with and without a Ti layer. This is probably due to the very low amount of titanium that was deposited by evaporation, less than 0.1 mg cm^{-2} . In order to modify the surface corrosion layer, more titanium should be deposited. It may be seen from all the images that silver comes out of the matrix of LSM particles, to form lumps of pure silver on the surface, which connect with the steel substrate when the gap is small enough between them. If the braze:LSM composite pellets and the steel were flatter and

thus closer together, there might be a continuous joint between them. However, there is still a significant corrosion layer on the surface of both steels, although it appears much thicker on the 430 stainless steel. The 430 does not contain as much nickel as the 316 stainless steel, and so is less corrosion resistant.

A further four samples were prepared. Table 5.3.5 shows the samples that were prepared. The masses of the samples were weighed at various points before and after brazing, to try and understand the processes occurring in the samples. The expected mass change when the copper in the braze pellet is oxidised was calculated. It is very similar to the value of the mass change for the 316 steel sample, but the mass change recorded for the 430 sample is much less than expected. It is unlikely that the sample has lost mass during the brazing, so the mass has probably been incorrectly recorded.

Sample type	No. Ti coats	Mass steel (g)	Mass pellet (g)	Mass change post brazing (g)	Expected mass gain Cu to CuO (g)
316	0	1.0582	n/a	0.0004	n/a
430	0	0.1126	n/a	0.0010	n/a
316+pellet	2	1.0675	0.2668	0.0162	0.0163
430+pellet	2	0.1208	0.2663	0.0019	0.0163

Table 5.3.5: Samples of 316 and 430 stainless steel, with or without Ti coating and braze:LSM composite pellets brazed to them.

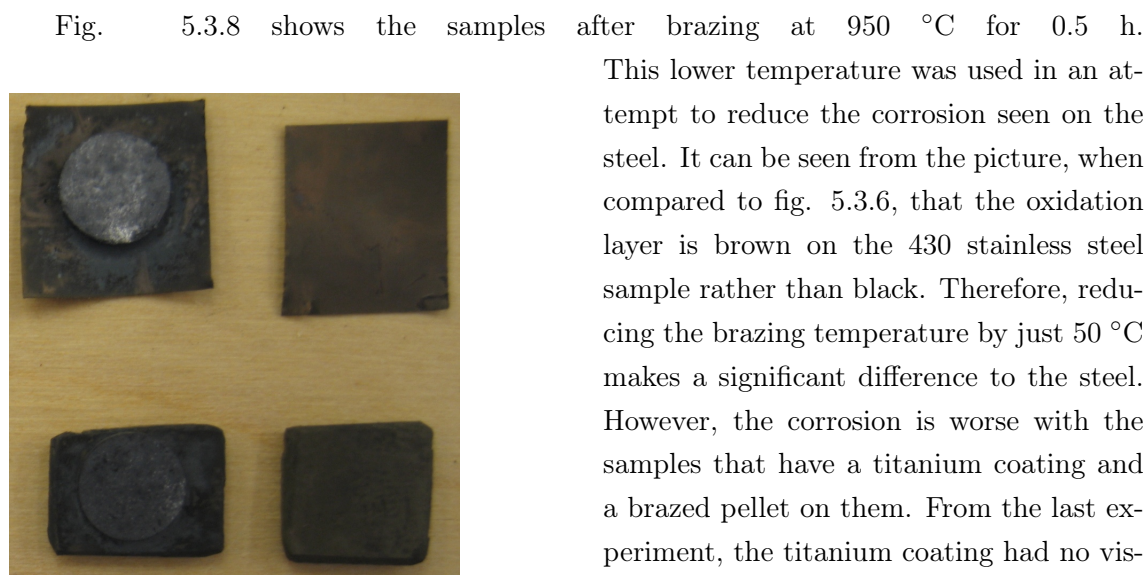


Figure 5.3.8: Stainless steel 430 (top) and 316 (bottom) with pellets of 8 mol.% CuO, balance silver braze, in a 40:60 braze:LSM volumetric ratio, after brazing at 950 °C for 0.5 h. Two samples had a titanium coating (left) prior to brazing, whereas the others did not (right).

silver allows the diffusion of dissolved oxygen into its structure [21].

It can also be seen that there is much less visible silver on the surface of the composite. The samples are brazed to 950 °C rather than 1000 °C, so they are in a different region of the Ag-CuO phase diagram in fig. 5.2.3, the CuO + liquid 2 phase, rather than the CuO + liquid 1 phase. Therefore, it seems that silver is less mobile in liquid phase 2. The phase transition between these two regions occurs at 964 °C, which is the melting point of silver. There are no lumps of silver on the surface of the composite pellet, which means that it does not adhere to the surface of the steel very well. Therefore, 964 °C seems to be a minimum temperature for this braze to fully melt in an air atmosphere. Fig. 5.3.9 shows the cross sections of the samples in the SEM.

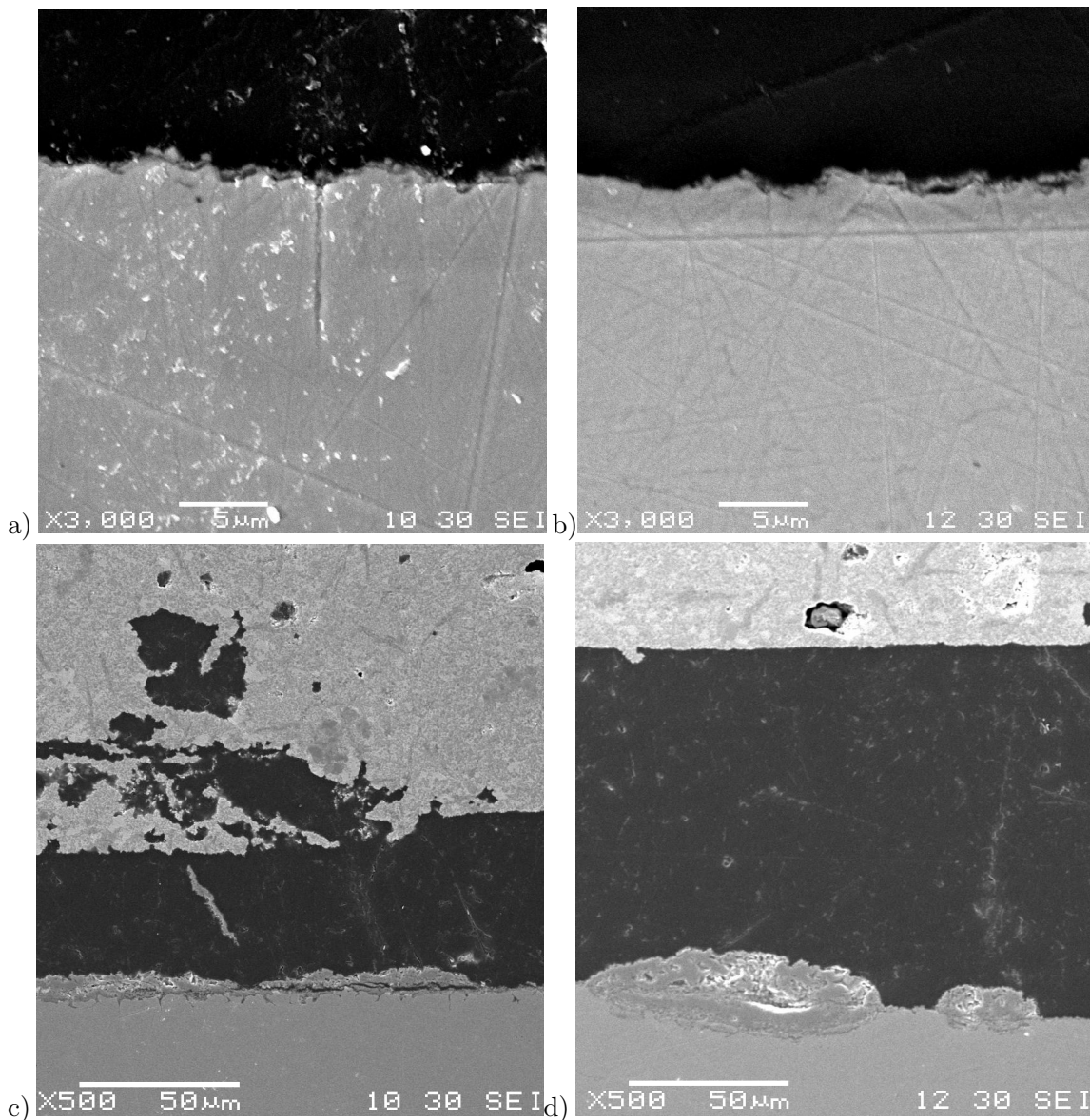


Figure 5.3.9: Stainless steel 316 (left column) and 430 (right column) with a) and b) no coatings, c) and d) 2 layers of evaporated Ti, and then a composite pellet made of 8 mol.% CuO, balance silver braze, in a 40:60 braze:LSM volumetric ratio. All four samples were sintered to 950 °C for 0.5 h.

It can be seen that there is a very thin layer of corrosion on the 316 and the 430 stainless

steels, which is enough to give it a brown appearance. Based on previous results, the layer on the surface of both steels which have braze:LSM composite pellets on them is probably a mixed oxide, with elements from the steel, and also copper inclusions from the braze. There is also a very thin corrosion layer on these samples, much less than on the samples sintered to 1000 °C in fig. 5.3.5. By careful adjustment of the sintering temperature to the minimum necessary to fully melt the braze, and also reducing the dwell time at the maximum temperature from 0.5 h to e.g. 5 min, it may be possible to reduce this corrosion even further.

5.4 Conclusions

Ag-Cu brazing

It was seen from the first experiments carried out, that the Ag-Cu braze mixture was unable to bridge the large gaps between the 316 stainless steel tube support, and the LSM tube, and that the steel tube oxidises during brazing, forming a brown or black oxide layer. When varying the silver-copper ratio of the braze, it was seen that as the fraction of CuO increased, less silver was seen in the steel-LSM joint. Therefore, the best CuO:Ag ratios were those with 4 mol.% or 8 mol.% CuO.

When this interface was examined by EDX to identify the elements in each layer, several different layers could be identified with different compositions and microstructures. The first was a corrosion layer from the steel, containing elements from it only, then another layer also containing copper and silver. Then there was a non-chromium containing layer, and no chromium in subsequent layers, which suggests that chromium diffusion is limited out of the steel by the presence of the braze. There was a pure silver layer, and then a very thin copper:iron:LSM layer, and then the LSM bulk tube. Therefore, copper wets the surface of the LSM. This complex layer chemistry needs to be studied further to fully understand the electrical conductivity and stability of these phases.

Braze:LSM composites

When LSM:braze composite pellets were brazed onto steel and copper substrates, they adhered to the steel substrates, except for the 20 vol.% braze composite, because the braze was absorbed into the matrix of LSM particles by capillary action and did not bond with the steel. The microstructure of the composite was an LSM matrix saturated with braze, but it had cracks perpendicular to the direction of pellet pressing, which are probably due to stresses caused during pressing. The copper substrates were destroyed by oxidation in air during brazing.

When braze interlayers were applied between a cellulose:water:LSM mixture and steel substrates, they melted into the mixture during brazing, and therefore the LSM:braze mixture did not adhere to the substrates. However, when no braze interlayer was used, the mixture did adhere to the steel substrates, but suffered cracking as it shrank during brazing.

Evaporation of titanium onto the steel substrates appears to have no effect in reducing corrosion of the steel, probably because the layer deposited was so thin. It could not be seen by SEM and its mass was too small to be measured by the lab. balance - less than 0.1 mg per sample.

Braze:LSM composite pellet samples brazed at 1000 °C had much more silver visible on their surface afterwards than samples brazed at 950 °C. The samples brazed to the higher temperature have a different composition according to the Ag-CuO phase diagram, when they are at 1000 °C. The oxidation of the steel support is less severe at 950 °C than 1000 °C, but a brown layer of oxide is still seen. The braze may worsen the oxidation of the steel. A steel sample with a braze composite pellet on it had a black oxide layer, whereas that without a braze composite pellet was brown.

Therefore, the steels used, stainless steels 316 and 430, suffer from oxidation when brazing, which leads to an oxidation layer which is not penetrated by the braze. This is likely to give low electrical conductivity across the joint, poor mechanical strength, and porous joints. Brazing with silver and copper would work better with steels that can withstand the temperatures necessary, or a protective atmosphere during brazing that would allow the brazing temperature to be lowered and prevent oxidation of the steel substrates.

References

- [1] J. W. Fergus, *J. Power Sources*, 2005, **147**, 46–57.
- [2] K. S. Weil, *JOM*, 2006, **58**, 37–44.
- [3] K. M. Erskine, A. M. Meier, S. M. Pilgrim, *J. Mater. Sci.*, 2002, **37**, 1705–1709.
- [4] C. C. Schüler, A. Stuck, N. Beck, H. Keser, U. Täck, *J. Mater. Sci. - Mater. Electron.*, 2000, **11**, 389–396.
- [5] K. S. Weil, J. Y. Kim, J. S. Hardy, *Electrochem. Solid-State Lett.*, 2005, **8**, A133–A136.
- [6] D. K. Chatterjee, T. D. Ketcham, D. J. St Julien, *Conductive coatings, sealing materials and devices utilizing such materials and method of making.*, Patent number WO2008109100-A1, 2008.
- [7] J. S. Hardy, J. Y. Kim, E. C. Thomsen, K. S. Weil, *J. Electrochem. Soc.*, 2007, **154**, P32–P39.
- [8] J. S. Hardy, J. Y. Kim, K. S. Weil, *J. Electrochem. Soc.*, 2004, **151**, J43–J49.
- [9] K. S. Weil, C. A. Coyle, J. T. Darsell, G. G. Xia, J. S. Hardy, *J. Power Sources*, 2005, **152**, 97–104.
- [10] N. Sakai, T. Horita, K. Yamaji, Y. Xiong, H. Kishimoto, M. E. Brito, H. Yokokawa, *Solid State Ionics*, 2006, **177**, 1933–1939.
- [11] J. Y. Kim, K. S. Weil, J. P. Choi, *Metal-ceramic composite air braze with ceramic particulate*, Patent number WO /2008/115696, 2008.
- [12] L. T. Wilkinson, J. H. Zhu, *J. Electrochem. Soc.*, 2009, **156**, B905–B912.
- [13] URL Accessed 26/04/2011. <http://www.matweb.com/search/DataSheet.aspx?MatGUID=63cbd043a31f4f739ddb7632c1443d33>.
- [14] URL Accessed 26/04/2011. <http://www.matweb.com/search/DataSheet.aspx?MatGUID=9aebe83845c04c1db5126fada6f76f7e>.
- [15] URL Accessed 26/04/2011. <http://www.matweb.com/search/DataSheet.aspx?MatGUID=c1db7a2dc38342739041049ad336cff9>.

- [16] M. C. Tucker, C. P. Jacobson, L. C. De Jonghe, S. J. Visco, *J. Power Sources*, 2006, **160**, 1049–1057.
- [17] F. Tietz, I. A. Raj, M. Zahid, D. Stöver, *Solid State Ionics*, 2006, **177**, 1753–1756.
- [18] URL Accessed 25/04/2011. <http://www.lenntech.com/stainless-steel-316l.htm>.
- [19] H. Nishi, K. Kikuchi, *J. Nucl. Mater.*, 1998, **258-263**, 281–288, 8th International Conference on Fusion Reactor Materials (ICFRM-8), Sendai, Japan Oct 26-31, 1997.
- [20] J. P. Chilton, *Principles of Metallic Corrosion 2nd ed.*, The Royal Institute of Chemistry, 1969.
- [21] I. Kontoulis, B. C. H. Steele, *Solid State Ionics*, 1991, **47**, 317 – 324.

Chapter 6

Reversible SOFC preparation

This chapter discusses the preparation of reversible solid oxide fuel cells (RSOFC), starting from the extruded LSM tubular supports, and finishing with a RSOFC ready for electrochemical testing. The LSM tubular supports are painted with an LSM-YSZ ink to make the oxygen electrode, then dip coated with YSZ slurries, or painted with YSZ inks. The second method gave a dense electrolyte. The NiO/8YSZ fuel electrode is also applied via dip-coating a slurry or painting an ink. A gas delivery tube is sealed to the cell using ceramic adhesive, and current collectors are applied to both electrodes. Finally, the cell is leak tested with gas, and checked to ensure there are no electrical short circuits across it. The objective is to obtain a leak tight cell, ready for testing, to determine its electrical performance as a RSOFC. A dense 3YSZ electrolyte was obtained with the ink painting method, and a cross section of the cell shows a porous LSM support, and Ni/8YSZ fuel electrode. However, the sealant used to connect the cells to the gas delivery tube was either porous or cracked during curing, so no leak-tight cells could be made.

6.1 Painting LSM-YSZ oxygen electrode

In this chapter, the LSM tubular supports are referred to according to the LSM extrusion recipe used to produce them, e.g. recipe H-cell6 LSM tubes. This designation means: a tube extruded by the handheld extruder (H), with a cellulose pore former (cell), recipe no. 6. Cells extruded with graphite pore former have the designation 'gra,' instead of 'cell.' Details of these recipes are found in chapter 4 on extrusion.

LSM tubes with cellulose pore former

The extrusion recipe H-cell6 LSM tubes had large pinholes on the surface, created as cellulose agglomerates burned out during tube sintering. In order to fill in these pinholes to provide a more homogeneous surface for dip coating a YSZ electrolyte, an LSM-YSZ screen printing ink was applied by hand painting and sintered at 1300 °C. This layer normally functions as a composite electrode on the oxygen side of the reversible SOFC. It was intended that the YSZ electrolyte would sit on top of this layer. The technique of hand painting rather than dip coating was used, as some of the holes in the LSM tube were

quite large. If dip-coating had been attempted, an air bubble would have been trapped in the hole by a thin layer of LSM-YSZ ink, leaving a void with a very fragile coating. This would burst during sintering, leaving a large hole in the coating, making the application of a dense YSZ electrolyte impossible. Although this method filled in some of the pores, the largest ones were not filled by this method, as the layer was less than $50\text{ }\mu\text{m}$ thick, and some of the pores were about $500\text{ }\mu\text{m}$ in diameter.

LSM tubes with graphite pore former.

Extrusion recipe M-gra7 LSM tubes were made with coarsened LSM, and graphite pore former. Although they were more porous than the cellulose based tubes ($>55\%$ porous, vs 22% porous), they did not have the large pinholes in the surface seen with tubes made with cellulose pore former, but rather lots of small, evenly distributed pores. An LSM-YSZ electrode painted on and sintered at $1200\text{ }^{\circ}\text{C}$ had a homogeneous appearance.

Comparison of tubes painted with LSM-YSZ and unpainted tubes



Figure 6.1.1: A painted coat of LSM-YSZ ink before drying, on LSM tubes made from extrusion recipe M-gra8.

In order to determine the function and necessity of the LSM-YSZ layer for the LSM tubes made with graphite pore former, LSM recipe M-gra8 tubes were made with the layer, and without it, and sintered to $1200\text{ }^{\circ}\text{C}$. This is discussed further in subsection 6.2.4. Fig. 6.1.1 shows the wet layer of ink glistening on the tubes after painting. The bare LSM substrate can also be seen at the bottom of each tube - it is porous but has no large pores visible to the naked eye. An LSM-YSZ layer was also used for some of the subsequent LSM tubes, which were made to similar recipes.

6.2 Producing the 8YSZ electrolyte

The reversible SOFC will only perform well when it has a dense and flaw-free 8YSZ electrolyte. According to the Nernst equation, the presence of even a small leak will considerably reduce the voltage obtained from the cell. Therefore, this section discusses the production of a dense 8YSZ electrolyte, free of cracks and pinholes. This dense layer must be produced on the surface of a porous LSM substrate tube. It should not be greater than $50\text{ }\mu\text{m}$ thick, as its contribution to the cell resistance increases linearly with thickness. However, it should be sufficiently thick to withstand at least a 100 mbar pressure differential across it, which may arise during testing.

A previous study on dip coating of 8YSZ successfully produced a dense electrolyte layer after sintering, on a porous NiO/YSZ substrate, using a mixture of 8YSZ particles

and a 8YSZ sol, in an azeotropic methyl ethyl ketone:ethanol (MEK:EtOH) based slurry, similar to a YSZ tape casting mixture [1]. It has also been shown that this can be achieved without the 8YSZ sol, again using a tape casting based slurry [2]. Another YSZ dip-coating slurry is based on an azeotropic MEK:EtOH mixture, with a triethanolamine dispersant, polyvinyl butyryl binder and the plasticisers polyethylene glycol and diethyl-*o*-phthalate [3]. It was shown that of various solvent combinations, the MEK:EtOH mixture allowed the YSZ particles to stay suspended for the longest time. NiO/YSZ support tubes were dipped in it twice and dried at 70 °C, and then they were sintered at 1500 °C for 5 h, to obtain dense, crack free YSZ coatings about 16 μm thick.

In this work, a similar recipe normally used for YSZ tape casting was employed, which had a solids loading of 16.2 vol.% - recipe 1 in table 6.2.1 [4]. However, it was too viscous to use as a dip coating slurry, so two diluted slurries were made, called ‘Y-7.4A’ and ‘Y-3.4B,’ shown in table 6.2.1. In this designation, ‘Y’ stands for YSZ, the number is the solids loading of the slurry, and the final letter stands for the recipe iteration.

Recipe/ slurry	8YSZ (g)	Butvar (g)	Tri-X (g)	PEG (g)	DBP (g)	MEK:EtOH ratio 3:2 (g)	8YSZ vol.%
1	30.00	3.36	0.20	2.49	2.23	8.70:5.80	16.2
Y-7.4A	4.09	0.46	0.027	0.34	0.31	3.60:2.40	7.4
Y-3.4B	1.92	0.22	0.013	0.16	0.14	4.15:2.77	3.4
Y-3.4C	2.44	0.27	0.016	0.20	0.18	5.32:3.54	3.4
Y-5.2D	2.67	0.30	0.018	0.22	0.12	3.59:2.40	5.2
Y-7.3D	3.26	0.37	0.022	0.27	0.24	2.89:1.92	7.3

Table 6.2.1: 8YSZ tape casting recipe 1, diluted with 3:2 MEK:EtOH to make slurries Y-7.4A, Y-3.4B, Y-3.4C, Y-5.2D and Y-7.3D, which are used for dip coating LSM tubes. Tri-X = Triton-X, PEG = polyethylene glycol, DBP = dibutyl phthalate, MEK = methyl ethyl ketone, EtOH = ethanol. The solids loading (vol.% 8YSZ) is also shown for all recipes.

The particle size distribution measurements on the Y-7.4A and Y-3.4B slurries in fig. 6.2.1, show a clear bimodal distribution. The 8YSZ is quite well suspended, as there is only a small difference between the suspended and mixed layers. Some large agglomerates can be seen in the settled 8YSZ layer, of 20 μm - 25 μm .

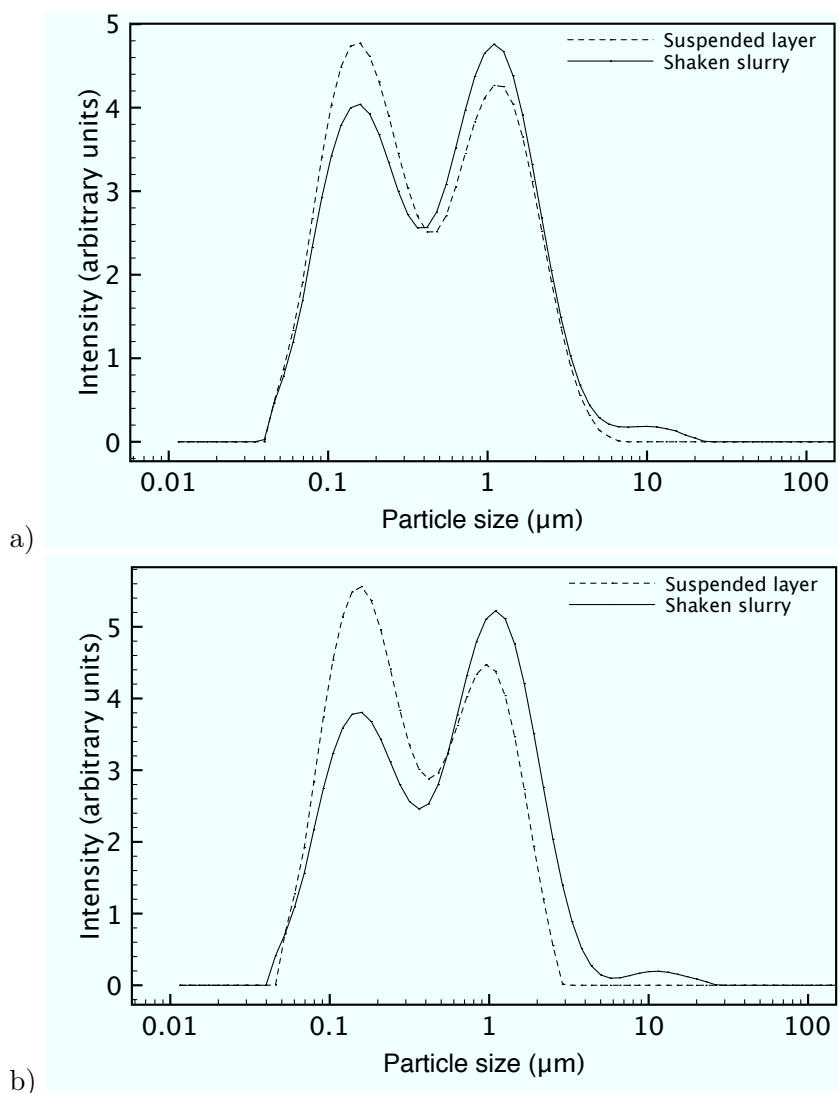


Figure 6.2.1: Particle size distribution measurements on 8YSZ slurry G: The slurry is shaken, left to settle for 24 h, and then a sample is taken from the suspended layer. The slurry is then shaken vigorously by hand for 1 min, to mix the settled and suspended layers together, and another sample is taken: a) 8YSZ slurry Y-7.4A, and b) 8YSZ slurry Y-3.4B.

6.2.1 Dip coating 8YSZ slurries Y-7.4A and Y-3.4B

Three LSM tubes from extrusion recipe H-cell2 were dipped initially, one with 1 coat of Y-7.4A (1xY-7.4A), one with 2 coats of Y-7.4A (2xY-7.4A), and one with one coat of Y-3.4B (1xY-3.4B), and sintered at 1350 °C. This sintering temperature was chosen as a compromise between having the sintering temperature as high as possible, to densify the 8YSZ, but not so high that it caused the reaction of YSZ with LSM to make lanthanum and strontium zirconates [5]. Previous studies have demonstrated dense 8YSZ electrolytes made from ceramic particles, which were sintered between 1300 °C and 1500 °C, e.g. [6]. In order to produce a dense layer at lower temperatures than this, hydrated 8YSZ nanoparticles [7] or a 8YSZ sol with ceramic particles [1] need to be used. The surface of the tubes was examined using an optical microscope, and representative pictures of the 8YSZ electrolyte are shown in fig. 6.2.2. Cracks in the 2xY-7.4A sample are apparent,

which may be due to shrinkage of the layer during sintering, which creates tensile stresses. There are no cracks in the 1xY-7.4A sample, probably because it is thin enough that the shrinkage during sintering does not cause cracks. A large air bubble is also apparent on the 2xY-7.4A sample picture. This is likely to arise as a result of a surface flaw in the substrate tube, such as a pinhole. It can be seen that this causes a break in the electrolyte, and therefore, a leak.

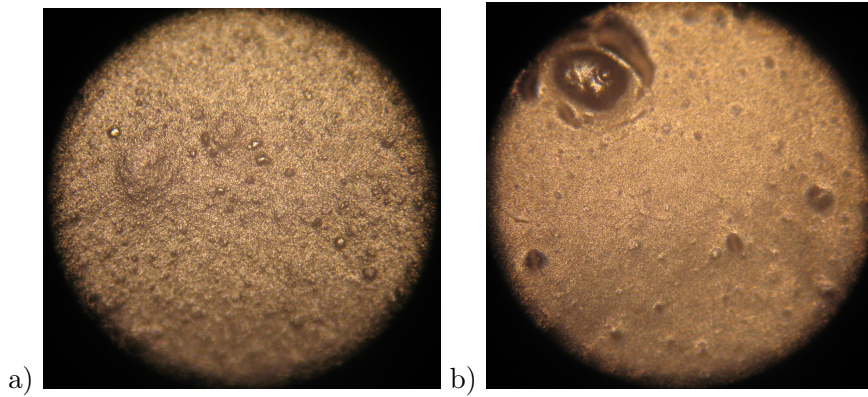


Figure 6.2.2: Sintered 8YSZ electrolyte surface on LSM tube - optical micrographs at 100x magnification, a) 1x dip coat of Y-7.4A and b) 2x dip coat of Y-7.4A. Fine cracks, and a large air bubble may be seen in the surface of b).

Thickness and microstructure of the 8YSZ electrolyte

The microstructure of the electrolytes created by dip coating with the slurries is shown in fig. 6.2.3.

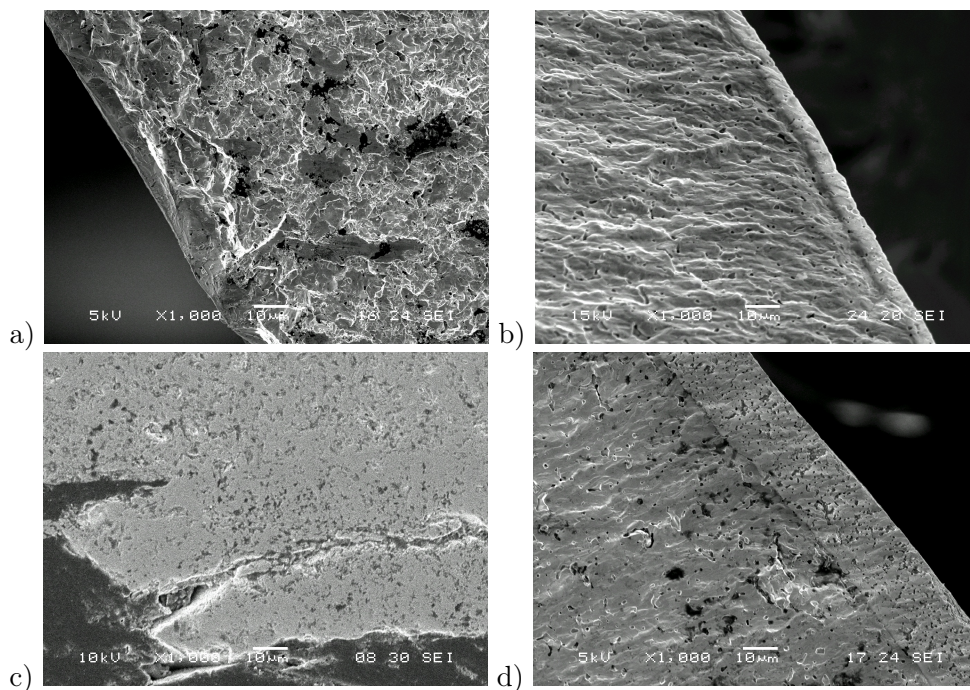


Figure 6.2.3: Fractured cross sections of LSM tubes dip coated with 8YSZ electrolyte slurries Y-7.4A and Y-3.4B, and sintered at 1350 °C, a) 1xY-7.4A, b) 1xY-3.4B, c) 2xY-7.4A showing a pinhole in the coating, not fractured but mounted in epoxy resin and polished, and d) 2xY-7.4A. Magnification is 1000x in all micrographs.

The 1xY-7.4A and 1xY-3.4B layers appear to be fairly dense, but the 2xY-7.4A layer is much thicker, and quite porous. This may be due to the thickness - the tensile stresses created as the layer shrinks during sintering prevent full densification. By comparison of fig 6.2.3a and 6.2.3c, it can be seen that the thickness of a single 8YSZ layer of the ‘Y-7.4A’ concentration varies significantly. In 6.2.3a, the layer is $< 10 \mu\text{m}$ thick, and in 6.2.3d, two layers are $20 \mu\text{m}$ thick in total, but in 6.2.3c a single layer is $> 20 \mu\text{m}$ thick. At least three factors affect 8YSZ layer thickness. Firstly, it will be thickest at the bottom or sealed end of the LSM tube, as the tubes are dipped in the slurry with the sealed end pointing down. This is because the 8YSZ slurry will settle down the tube a little after dipping. This effect can be easily observed on the dipped tubes, e.g. in fig. 6.2.6 because the slurry is a white colour, and the degree of colour shows the thickness of the coating.

Secondly, the speed of withdrawal of the tube from the slurry affects the coating thickness. This is due to a mechanism called liquid entrainment. The slurry adheres to the tube surface if the tube is withdrawn faster than the slurry can drain from the surface. It is affected by factors such as slurry density, surface tension, and withdrawal velocity [8]. The more quickly the tubes are withdrawn, the thicker the 8YSZ slurry coating. It has been shown that the thickness of a dip-coated NiO/8YSZ layer could be varied between $5 \mu\text{m}$ - $33 \mu\text{m}$, when the speed of withdrawal was varied between 25 mm min^{-1} - 125 mm min^{-1} [9]. Therefore, in order to obtain consistently thick layers, and to be able to accurately control the thickness, the withdrawal speed must be precisely controlled. It also follows that an increase in the viscosity of the solution will also lead to thicker 8YSZ layers, as less slurry will run off the tube. The third factor affecting the thickness of 8YSZ dip coated

layers is the solids loading of the slurry. A comparison of fig. 6.2.3a and b shows that the 1xY-7.4A slurry, with a solids loading of 7.4 vol.%, produces a layer almost twice as thick as the 1xY-3.4B slurry, which has a solids loading of 3.4 vol.%.

6.2.2 Dip-coating 8YSZ slurries Y-3.4C, Y-5.2D and Y-7.3D

Three different slurry concentrations, called Y-3.4C, Y-5.2D, and Y-7.3D from table 6.2.1, were dip-coated at constant speed using a 12 V DC motor, onto LSM extrusion recipe H-cell4 tubes, which had a cellulose pore former. Fig. 6.2.4 shows the tubes after sintering. The tubes were named according to the number of dip-coats on each, and the slurry used. They were sintered after each coat at 1330 °C, for 3 h after the second dip-coat. The 1xY-3.4C, 1xY-5.2D, and 1xY-7.3D tubes were named RSOFC-H-cell4-1, H-cell4-2, and H-cell4-3 respectively, and the 2xY-3.4C, 2xY-5.2D and 2xY-7.3D tubes were named RSOFC-H-cell4-4, H-cell4-5, and H-cell4-6. It can be seen from fig. 6.2.4, that the 8YSZ

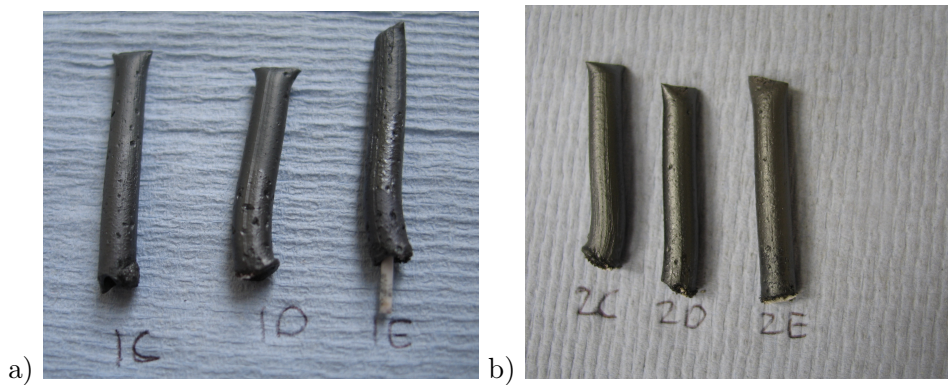


Figure 6.2.4: LSM tubes dipped in three different 8YSZ slurry concentrations Y-3.4C, Y-5.2D and Y-7.3D, and sintered to 1350 °C. Image a) dipped and sintered once, and also coated with a layer of NiO/8YSZ. RSOFC-H-cell4-3 still has the alumina rod inside it that is used to hold it upright during sintering. The shiny area in the middle of the tube is the 8YSZ coating, and matte part at the top is the NiO/8YSZ. Image b) shows tubes dipped and sintered twice with 8YSZ only.

coating gives a shiny appearance, but all six tubes produced had an uneven surface. This arises from the large holes in the tubes, left from the burnout of the cellulose pore former.

A cross section of RSOFC-H-cell4-5 in fig. 6.2.5a shows the dense LSM microstructure, except for the large holes created by the cellulose pore former. These range in size from 20 μm to >100 μm , even up to 500 μm . In places these are on the surface of the tube and interrupt the 8YSZ electrolyte coating, and can be seen in fig. 6.2.4. Therefore, in order to produce a flaw free electrolyte, the homogeneity of the substrate LSM tube needs to be improved. Table 6.2.2 indicates that a single dip coat of slurry concentration Y-5.2D gives an average layer thickness of 8 μm , but this varies considerably due to the roughness of the LSM substrate.

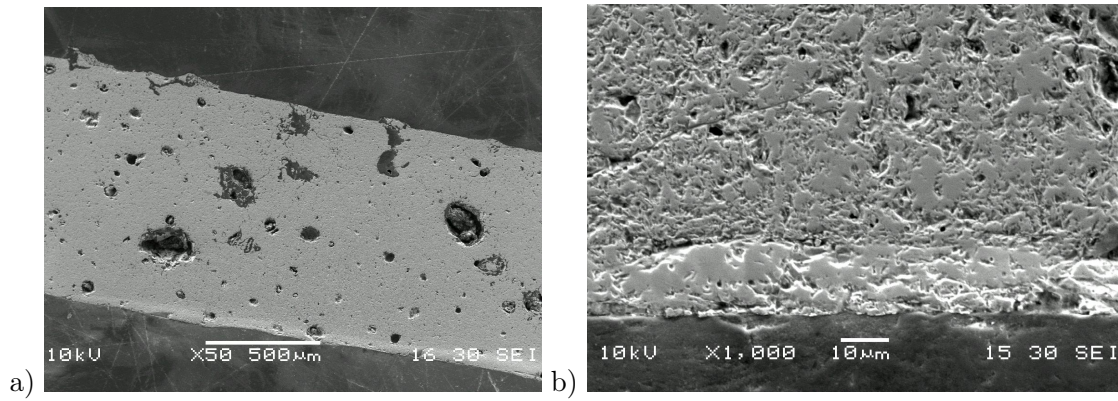


Figure 6.2.5: Cross section of LSM tube, RSOFC-H-cell4-5, 8YSZ coated, a) 50x magnification and b) 1000x magnification

Region	8YSZ thickness measurements (μm)	Average thickness (μm)
1	8.8, 8.9, 9.4, 8.2, 7.8, 5.0	8.0
2	15.9, 13.3, 14.1, 17.5, 16.3, 17.2	15.7

Table 6.2.2: Layer thickness of 8YSZ electrolyte on RSOFC-H-cell4-5. Region 1 is a portion of the tube with only 1 coat of 8YSZ, and region 2 is a portion of the tube with 2 coats. The values were measured using the ImageJ software [10] on SEM images.

6.2.3 Dip-coating 8YSZ slurries Y-7.4A2 and Y-3.4B2

LSM tubes produced from extrusion recipe M-gra7, which used a graphite pore former rather than cellulose, had a much more homogeneous microstructure, with no large pores. It was about 57 vol.% porous, and the longest distance between any two particles was $<30 \mu\text{m}$. These tubes were dip-coated with 8YSZ slurries Y-7.4A2 and Y-3.4B2, which were made by adding more recipe 1 tape casting slurry, and MEK:EtOH 3:2 to the Y-7.4A and Y-3.4B slurries from table 6.2.1, so that the solids loading of each slurry was kept the same. Eleven LSM tubes made with extrusion recipe M-gra7 that been coated with LSM-YSZ already, were dipped in Y-7.4A2 or Y-3.4B2 slurries and sintered to 1350°C , and then dipped and sintered again.

Fig. 6.2.6a shows some cracking on the sealed ends of the tubes after the first dip coat of Y-7.4A2 slurry. This is because this end is at the bottom when dip-coating, coming out of the slurry last, so excess slurry runs down the tube and gathers there. The thick layer of 8YSZ produced is susceptible to cracking, as the organic components in it are trapped as it sinters, then produce carbon dioxide and steam as they burn, which cracks the layer. Tubes dipped in slurry Y-3.4B suffer less from this problem, as the slurry is less viscous, so the drop at the bottom is smaller, or almost non-existent. After dipping, touching the end of the tube to the inside of glass vial allows excess drain off. However, with the thicker slurry Y-7.4A, some excess slurry remains. Fig. 6.2.6b shows the tubes after the second dip coat. The blue coloration in this photo is due to the blue background it was taken against, which has affected the colour balance. This is the case for some of the photos of tubes in later figures as well. In this photo, the Y-7.4A2 slurry coated

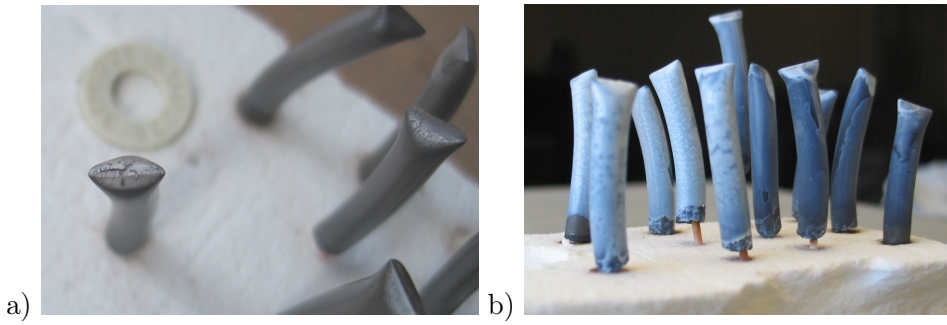


Figure 6.2.6: Extrusion recipe M-gra7 LSM tubes pre-coated with LSM-YSZ, a) after dip coating with 8YSZ slurry Y-7.4A2 once and sintering at 1350 °C, some cracking may be seen on the end of the tube, b) after dipping again with slurries Y-7.4A2 (left) or Y-3.4B2 (right).

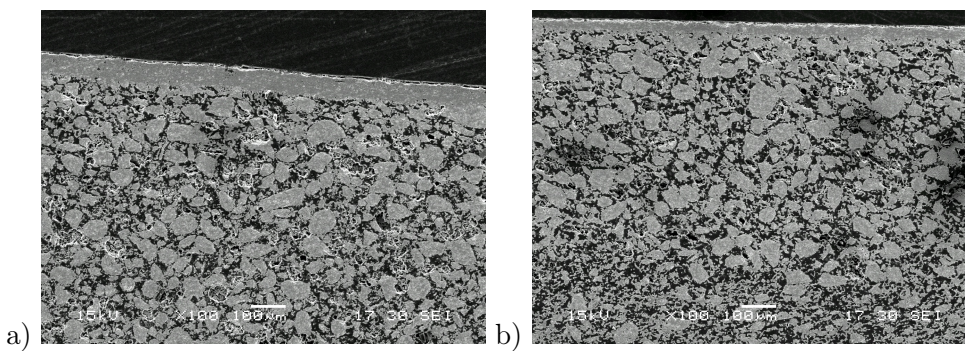


Figure 6.2.7: 8YSZ electrolyte produced by dip coated and sintering at 1350 °C, on extrusion recipe M-gra7 LSM tubes with an LSM-YSZ coating a) 2xY-7.4A2 dip coats, and b) 2xY-3.4B2 dip coats.

tubes have a whiter appearance than the Y-3.4B2 slurry coated tubes, because the solids loading in slurry Y-7.4A2 is higher than in the Y-3.4B2 slurry. After the second sintering, the tubes dipped with Y-7.4A had cracking where the coat was thick, and one tube had micro-cracking over much of the tube surface. The tubes dipped with slurry Y-3.4B had a mostly intact surface, except for a couple of tubes which had cracks where a drop of slurry had remained at the top of the tube.

Microstructural analysis of the 2xY-7.4A2 and 2xY-3.4B2 8YSZ slurry dipped and sintered LSM tubes

Fig. 6.2.7a shows the 8YSZ electrolyte obtained by dip-coating twice with Y-7.4A2 8YSZ slurry, and fig. 6.2.7b shows the electrolyte from 2 coats of slurry Y-3.4B2. The Y-7.4A2 electrolyte is thicker than the Y-3.4B2 electrolyte, because the Y-7.4A2 slurry has a greater solids loading than the Y-3.4B2 slurry. The 8YSZ electrolyte thickness, measured from SEM images is shown in table 6.2.3a. Two trends are apparent - firstly, that the thickness of the 8YSZ layer is dependent on the concentration of the 8YSZ slurry. Two dips of the Y-7.4A2 concentration gives a sintered layer that is 20-25 μm thicker than the Y-3.4B2 concentration, at a similar position on the tube. The layer thickness of the outer layer of 8YSZ in the Y-3.4B2 dipped sample in table 6.2.3b is about 20 μm on average,

a)

Reading no.	8YSZ slurry/position on tube. Thicknesses in μm .							
	A2/top	A2/top	A2/base	B2/top	B2/top	B2/base	B2/base	B2/base
1	51	51	72	36	41	47	45	32
2	64	54	72	32	28	50	49	58
3	59	47	71	27	29	51	49	49
4	52	50	75	29	22	56	48	54
5	59	42	72	29	33	51	47	38
6	59	45	71	27	25	46	51	31
Average	57	48	72	30	30	50	48	44

b)

Reading no.	8YSZ slurry/layer position/position on tube. Thicknesses in μm .			
	A2/inner/base	A2/outer/base	B2/inner/base	B2/outer/base
1	35	31	38	20
2	36	36	35	19
3	32	34	32	19
4	31	35	33	17
5	37	33	47	20
6	32	34	40	18
Average	34	34	38	19

Table 6.2.3: Measured thicknesses of 8YSZ electrolytes, made with two dips of either Y-7.4A2 or Y-3.4B2 8YSZ slurry, sintered at 1350 °C, on extrusion recipe M-gra7 LSM tubes, pre-coated with LSM-YSZ. In these tables, the slurry designations are abbreviated to A2 and B2. Six measurements of thickness per SEM image were taken using the ImageJ software [10]. The position on tube refers to where measurements were taken: near the sealed end (base) or near the open end (top). The layer position refers to whether the layer was next to the tube (inner) or on top of this, on the outside of the tube (outer). Table a) readings are for the whole thickness of the electrolyte layer, and table b) are the individual layer thicknesses. The error in all the measurements is $\pm 4 \mu\text{m}$.

which is thinner than the inner layer of the same sample. The SEM image shows that there are several breaks in the outer layer - this could be due to the tube accidentally scraping the side of the vial holding the slurry, as it came after dip coating, which thinned the layer. Secondly, the thickness of the 8YSZ layer depends on the position on the tube that the measurements are taken. For both Y-7.4A2 and Y-3.4B2 slurries, the 8YSZ layers are thicker near the base of the tube, and thinner near the top of the tube. This is because the 8YSZ slurry runs down the tube after dip coating, to the base, creating a thicker layer. This is quite a significant effect, making a layer that is about 20 μm thicker at the base for both slurry concentrations.

Densities of the 8YSZ layers

Fig. 6.2.8 indicates that the density of the 2xY-7.4A2 8YSZ layer was 88%, and the density of the 2xY-3.4B2 8YSZ layer was 87%, therefore the electrolyte might not be leak-tight.

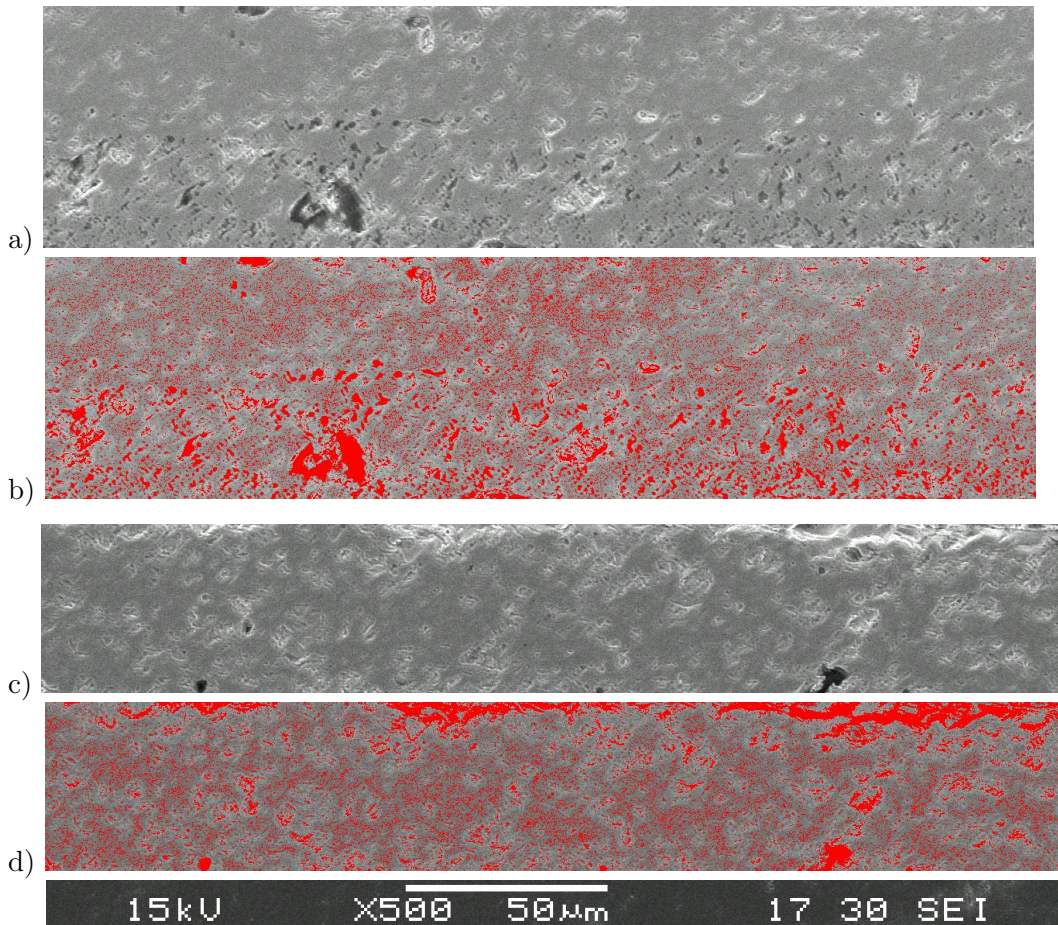


Figure 6.2.8: Volume percentage porosity analysis of sintered 8YSZ layers, with scale, a) 2xY-7.4A2 8YSZ layer b) 2xY-7.4A2 8YSZ layer, pores in red, c) 2xY-3.4B2 8YSZ layer, and d) 2xY-3.4B2 8YSZ layer, pores in red. The image analysis was carried out using the program ImageJ. The volume percentage porosity of the 2xY-7.4A2 layer is 12%, and the porosity of the 2xY-3.4B2 layer is 13%.

Defects in a layer of YSZ can sometimes be healed by the application of another layer of YSZ, and it has been shown that small cracks or pores in one layer of YSZ, can be filled in by the next dip-coating, if the conditions are optimised. One study of YSZ dip-coating on a porous LSM-substrate showed that it may take several coats of YSZ to obtain a dense, crack free layer [11].

EDX analysis of the electrolyte layer

EDX analysis was carried out to determine if there was LSM present in the dense layer of 8YSZ electrolyte. Fig. 6.2.9 shows the line scans for the elements yttrium, zirconium, and lanthanum, and a combined line scan which also includes manganese. At 20 μm on the x-axis there is a clear peak in the lanthanum signal, and corresponding dip in the

zirconium and yttrium signals, which shows that there is a particle of LSM in the middle of the 8YSZ layer. This may be because some or all of the 8YSZ slurry has soaked into the LSM substrate during dip-coating. This makes a dense LSM-8YSZ layer, which would short-circuit the cell, if it penetrated through the entire thickness of the 8YSZ electrolyte.

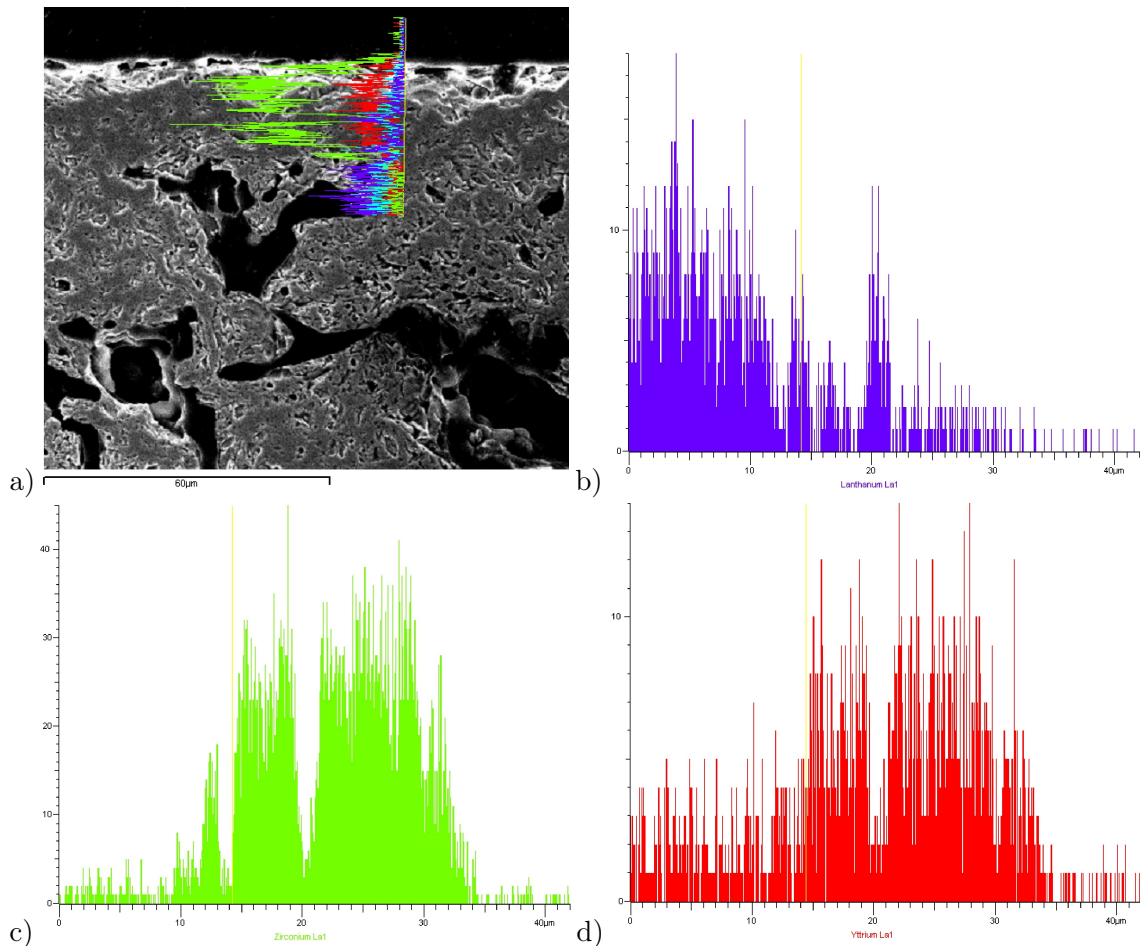


Figure 6.2.9: EDX line scan of selected elements in a 2xY-3.4B2 8YSZ dip coated electrolyte, 1 layer of 8YSZ near open end of an extrusion recipe M-gra7 LSM tube, with an LSM-YSZ coating, a) EDX line scan of zirconium (green), lanthanum (dark blue), yttrium (red), and manganese (light blue), b) lanthanum line scan, c) zirconium line scan, and d) yttrium line scan.

6.2.4 Dip coating 8YSZ slurry Y-3.4B2

In order to ascertain the necessity and function of the LSM-YSZ painted layer on the LSM tubes, some extrusion recipe M-gra8 LSM tubes that had been pre-coated with LSM-YSZ were compared with some that had not. They were all dip-coated with four coats of 8YSZ slurry Y-3.4B2, with intermediate sintering steps at 1350 °C. Fig. 6.2.10 shows the tubes after the first dip-coat and sintering. The tubes which have a layer of LSM-YSZ on them have a white appearance where they have been dip-coated, which shows that 8YSZ is present on the surface, but the tubes without the LSM-YSZ coating have much less white on their surface, indicating that the 8YSZ has been absorbed into the tube. After sintering,

a shiny layer can be seen on the tubes pre-coated with LSM-YSZ, which indicates a dense surface layer, but this is not seen on the tubes without an LSM-YSZ pre-coating.

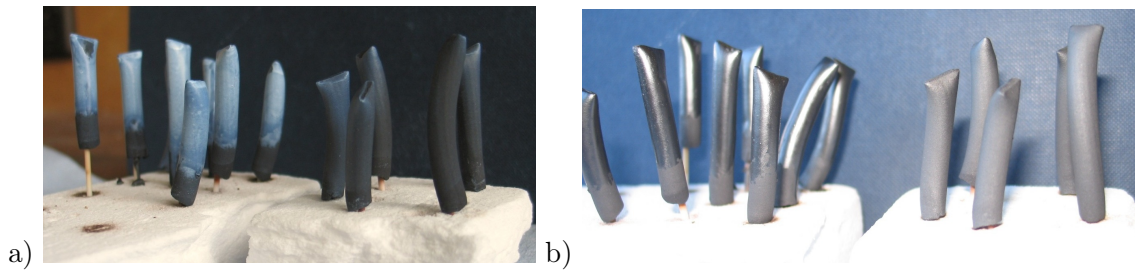


Figure 6.2.10: 8YSZ dip-coated on extrusion recipe M-gra8 LSM tubes, a) after dip-coating, b) after dip-coating and sintering. The tubes on the left in each picture had a painted and sintered layer of LSM-YSZ before dip-coating 8YSZ, and the tubes of the right were bare before dip-coating 8YSZ.

Fig. 6.2.11a shows the same set of tubes after the second dip-coating with 8YSZ slurry Y-3.4B2. There is no discernible difference between the green 8YSZ slurry coating colour on the tubes with the LSM-YSZ pre-coating (left) and those without (right). This indicates that the first coat of 8YSZ is sufficient to partially seal the tubes without the LSM-YSZ coating, preventing further absorption of the 8YSZ slurry into the LSM microstructure.

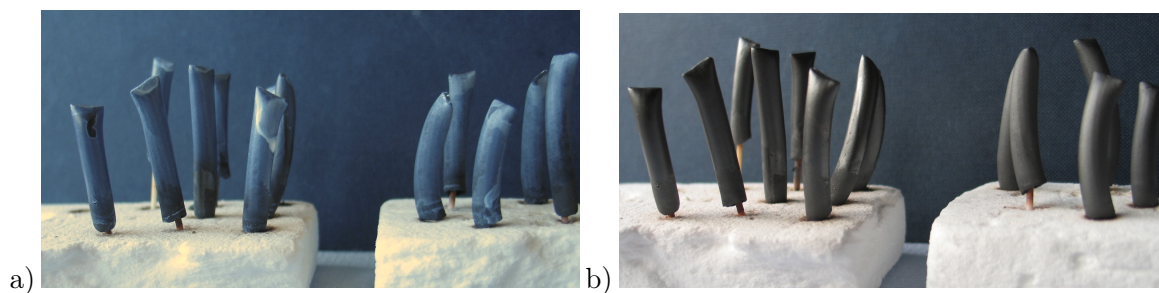


Figure 6.2.11: The second 8YSZ dip-coating on extrusion recipe M-gra8 LSM tubes, that were previously dip-coated as in fig 6.2.10. Image a) shows tubes after dip-coating with 8YSZ slurry Y-3.4B2. Both the tubes which were pre-coated with LSM (left) and those that were not (right) show the same colour of coating, indicating that 8YSZ is sitting on the surface in both cases. Image b) show the tubes after sintering at 1350 °C.

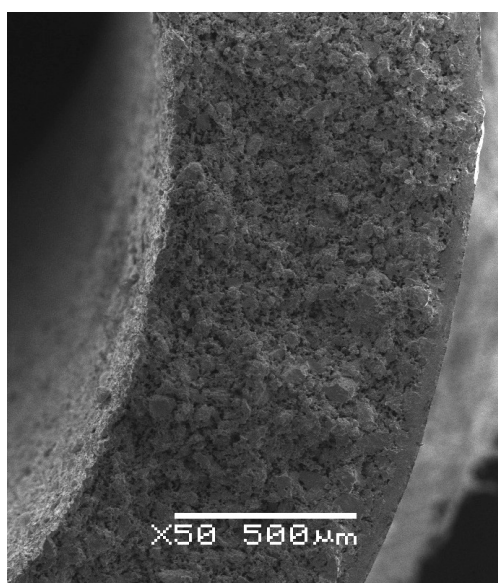


Fig. 6.2.11b shows the tubes after sintering at 1350 °C for 1 h. The tubes with an LSM-YSZ pre-coating are perhaps slightly more shiny than the tubes without. A fractured cross section of one of the tubes with a LSM-YSZ pre-coating, after a third dip-coat and sintering of 8YSZ slurry Y-3.4B2 is shown in fig. 6.2.12. The homogeneous microstructure of the LSM tube substrate, and the fairly dense layer of 8YSZ on the tube outer surface can be clearly seen.

Figure 6.2.12: Fractured cross section of LSM tube, extrusion recipe M-gra8, with a LSM-YSZ layer, then 3x 8YSZ Y-3.4B2 slurry layers, with intermediate sintering at 1350 °C.

Comparison of tubes with or without an LSM-YSZ pre-coated layer, by EDX and SEM.

Fig. 6.2.13 shows the EDX analysis of a cross section of a reversible SOFC made with LSM extrusion recipe M-gra8. It can be seen that some of the 8YSZ slurry penetrates at least 30 μm into the LSM support tube, making a porous area of mixed LSM and 8YSZ. There is also a fairly dense layer of mixed LSM and 8YSZ, which probably arises from the painted and sintered layer of LSM-YSZ, the pores of which were filled in by the 8YSZ when it was dip-coated onto the tube. There is then a mostly dense layer of pure 8YSZ electrolyte, about 20 μm thick, and 8YSZ can also be seen in the outermost NiO/8YSZ layer. The images in fig. 6.2.14 are the cross sections of two LSM tubes, a) with a layer of LSM-YSZ on it, b) with no layer of LSM-YSZ, both coated with 4 layers of dip coated

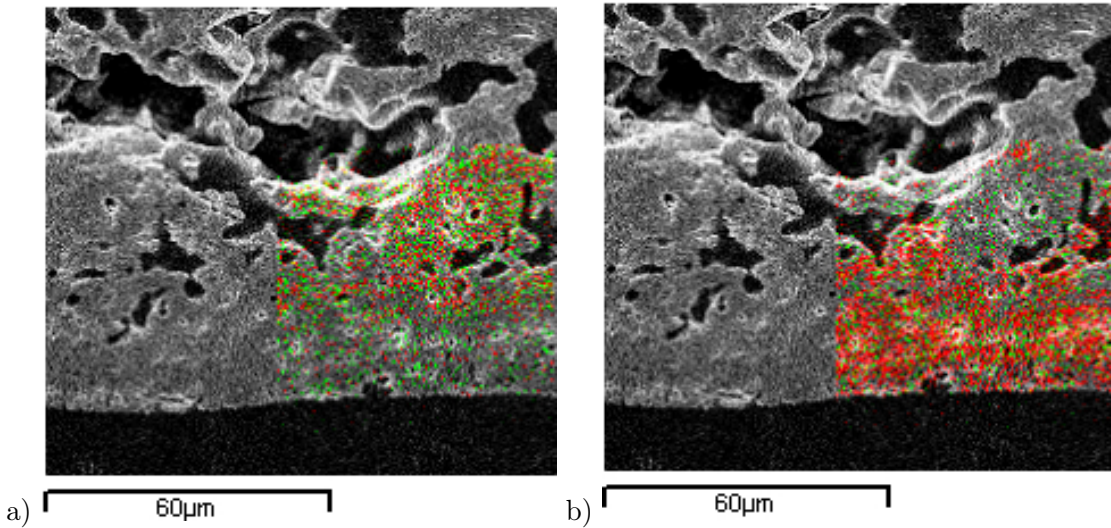


Figure 6.2.13: EDX analysis of a cross section of reversible SOFC. The layers, going from top to bottom, are the porous LSM tube substrate, then 4x Y-3.4B2 8YSZ slurry dip-coats, then 1x NiO/8YSZ slurry dip-coating, and the resin the sample is mounted in at the bottom (black layer). Image a) is an elemental map of manganese (green) and lanthanum (red), which shows the LSM phase. Image b) has zirconium (red) and yttrium (green), which shows the 8YSZ phase.

8YSZ Y-3.4B2 slurry. A fairly dense 8YSZ electrolyte can be seen on the surface of both tubes. It can be seen that the tube in fig. 6.2.14a with the LSM-YSZ layer has less 8YSZ penetrating into it. This is because this layer blocks some of the large pores in the tubes that would otherwise allow the uptake of 8YSZ slurry deeper into the LSM support.

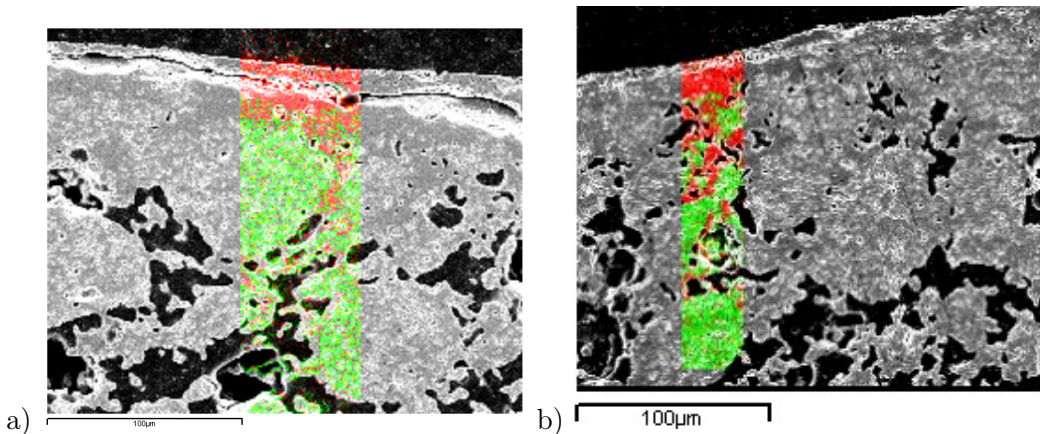


Figure 6.2.14: EDX analysis of recipe M-gra8 LSM tubes with or without an LSM-YSZ layer, with 4 dip-coated layers of Y-3.4B2 8YSZ slurry, a) with an LSM-YSZ layer, and b) with no LSM-YSZ layer. Red = zirconium (8YSZ phase) and green = lanthanum (LSM phase). There is a dense layer of 8YSZ electrolyte, a dense layer of mixed LSM and 8YSZ, and a porous LSM layer with a little 8YSZ in it.

On the tube without a pre-coated LSM-YSZ layer, there is a thin dense layer of 8YSZ, then a dense mix of LSM-YSZ beneath it on fig 6.2.14b, where the 8YSZ has penetrated the LSM-YSZ layer and filled the remaining pores, making it dense. It penetrates at least 100 μm into the LSM support tube, making a porous LSM-YSZ matrix.

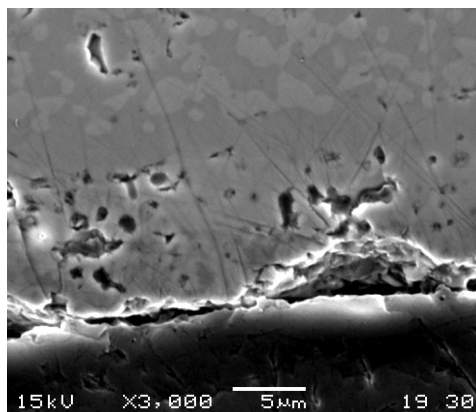


Figure 6.2.15: Cross section of an LSM tube with a LSM-YSZ layer, with four dip-coats of 8YSZ Y-3.4B2 slurry, and a NiO/8YSZ surface layer.

This layer would act as a composite oxygen electrode during a RSOFC test. A picture of the dense LSM-YSZ phase is shown in fig. 6.2.15. EDX analysis shows that the light areas have lanthanum, strontium and manganese (LSM phase), and the dark areas mainly zirconium (8YSZ phase). There is a very thin layer of dense 8YSZ below the LSM-YSZ dense phase (mixed colours), then a porous layer of pure 8YSZ, and at the outer surface, a $\sim 5 \mu\text{m}$ thick layer of NiO/8YSZ. The pure 8YSZ layer in fig. 6.2.15 is quite thin. This is because most of the dip-coated 8YSZ slurry is absorbed into the LSM-YSZ layer and fills in

the pores, as the 8YSZ particles are quite small. If all the 8YSZ slurry is absorbed into the LSM-YSZ layer in some areas in the tube surface, so it completely penetrates the electrolyte, or if there is a surface flaw in the 8YSZ, then the electrolyte will short circuit because the LSM is electrically conductive. The presence of the dense LSM-YSZ layer in the electrolyte will also reduce the ionic conductivity, and may cause delamination during electrolysis. This is because oxygen ions flowing from the oxygen side of the tube will meet an LSM particle in the dense region, and be oxidised to oxygen gas. This will create pressure in the dense composite, and crack it [12].

6.2.5 Dip-coating 8YSZ slurries Y-3.4F and Y-7.3G

A new set of LSM tubes made from extrusion recipe M-gra9, which had a similar composition to recipe M-gra8, were sintered at 1250°C , rather than 1330°C . The lower sintering temperature allows the tubes to sinter and shrink when the 8YSZ coating was applied to them. It was hoped that this would improve its density, by more closely matching shrinkage rates. However, these tubes were quite friable, as the LSM had not sintered as much. A fresh batch of 8YSZ tape-casting slurry, and dip-coating slurries made from it by dilution are in table 6.2.4.

Recipe/ slurry	8YSZ (g)	Butvar (g)	Tri-X (g)	PEG (g)	DBP (g)	MEK:EtOH ratio 3:2 (g)	8YSZ vol.%
2	3.472	2.63	0.16	1.96	1.75	6.90:4.60	16.1
Y-3.4F	3.54	0.40	0.02	0.30	0.26	7.61:5.07	3.4
Y-7.3G	6.00	0.67	0.04	0.50	0.45	8.89:5.33	7.3
Y-7.3G2	5.95	0.67	0.04	0.5	0.44	8.82:5.29	7.3

Table 6.2.4: 8YSZ tape casting recipe 2, diluted with 3:2 MEK:EtOH to make slurries Y-3.4F, Y-7.3G and Y-7.3G2, which are used for dip coating LSM tubes. Tri-X = Triton-X, PEG = polyethylene glycol, DBP = dibutyl phthalate, MEK = methyl ethyl ketone, EtOH = ethanol. The solids loading (vol.% 8YSZ) is also shown for all recipes.

Particle size distribution measurements on slurry Y-7.3G are shown in fig. 6.2.16. They show that the slurry is suspended well, with little settling over 24 h, except some large 8YSZ agglomerates up to 25 μm in size.

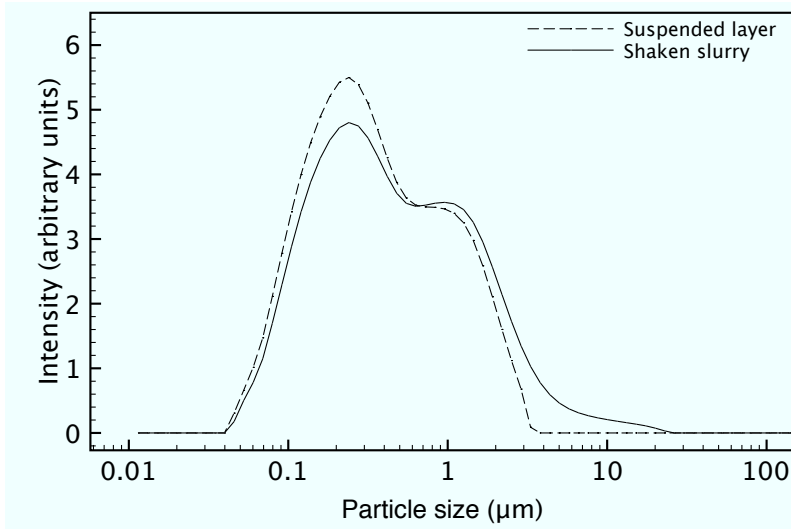


Figure 6.2.16: Particle size distribution measurements on 8YSZ slurry Y-7.3G: The slurry is shaken, left to settle for 24 h, and then a sample is taken from the suspended layer. The slurry is then shaken vigorously by hand for 1 min, to mix it thoroughly, and sampled again.

Fig. 6.2.17 compares the 8YSZ surface microstructure of recipe M-gra9 LSM tubes, dipped with 1 coat of Y-7.4A2 8YSZ slurry from subsection 6.2.3, sintered at 1350 °C, and the same tubes then dipped with 1 coat of slurry Y-3.4F from table 6.2.4, and sintered at 1400 °C. Many cracks can be seen in the 8YSZ coating of the 1xY-7.4A sample, which are mostly filled in by the 1xY-3.4F dip-coating, though many pores remain. Some large agglomerates can be seen on the surface, which have cracks around them that are not entirely filled in by the 1xY-3.4F coating. After a second coating of slurry Y-3.4F, fig. 6.2.18a shows a rough surface with pinholes but no cracks, and b) shows the large 8YSZ grains, up to 10 μm in size. Two of these tubes were named RSOFC-M-gra9-1 and M-gra9-2.

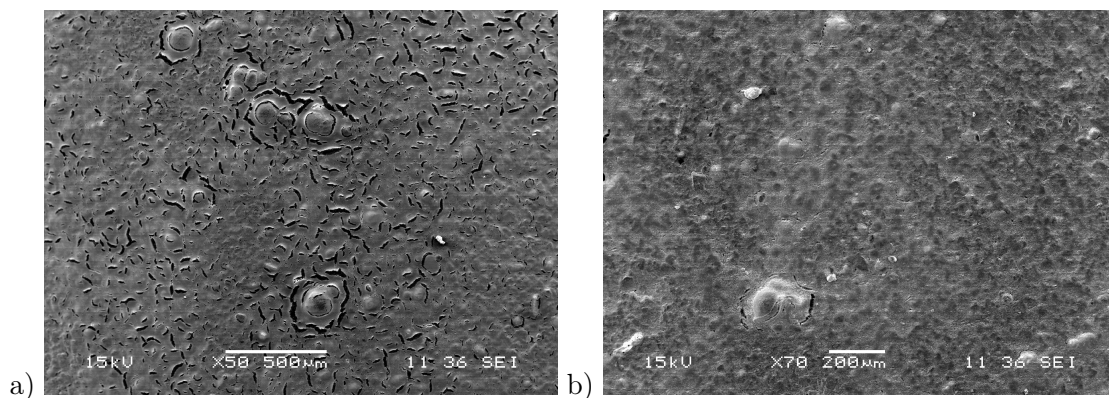


Figure 6.2.17: Comparison of the surface of the 8YSZ electrolyte on a) an LSM tube coated with 1x8YSZ Y-7.4A, sintered at 1250 °C, (50x) and b), a LSM tube coated with 1x8YSZ Y-7.4A, sintered at 1250 °C, then coated with 1x8YSZ Y-3.4F, sintered at 1350 °C (70x).

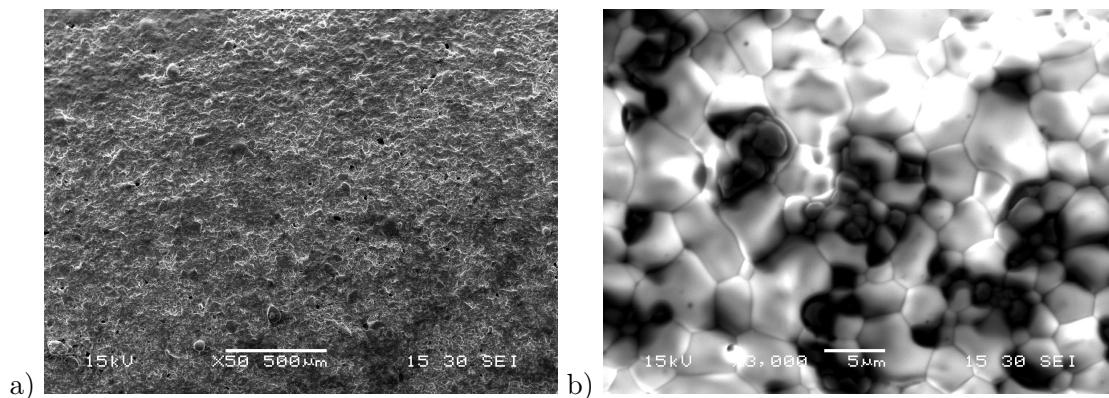


Figure 6.2.18: The 8YSZ surface on recipe M-gra9 LSM tubes, coated with 1xY-7.4A, 2xY-3.4F 8YSZ dip-coated layers, a) 50x, and b) 3000x.

After a third coat of Y-3.4F 8YSZ slurry was applied and sintered, fig. 6.2.19a,b show a fairly dense, bumpy surface, and fig. 6.2.19c shows some pores in the 8YSZ grains. These are not at the grain boundaries, so further sintering is unlikely to remove them. Fig. 6.2.19d,e show a large lump in the 8YSZ surface, probably a 8YSZ agglomerate in the dip-coating slurry. As it sinters, it shrinks, and deep cracks form around it. They are still open after 1xY-7.4A and 3xY-3.4F dip coats of 8YSZ. This is because a flaw or crack in a dip-coating substrate acts as a stress concentration point for any layer that is coated on top of it. Although the green dip-coated layer covers the crack, when the sample is then sintered, stress builds up and the crack is propagated through the new layer as well. This is also the case for the large pinhole seen in fig. 6.2.19f. In one study, cracks and flaws in one 8YSZ layer were healed by dip-coating a fine suspension of 100 nm 8YSZ particles. However, ten coats were necessary to obtain a leak free 8YSZ electrolyte [13].

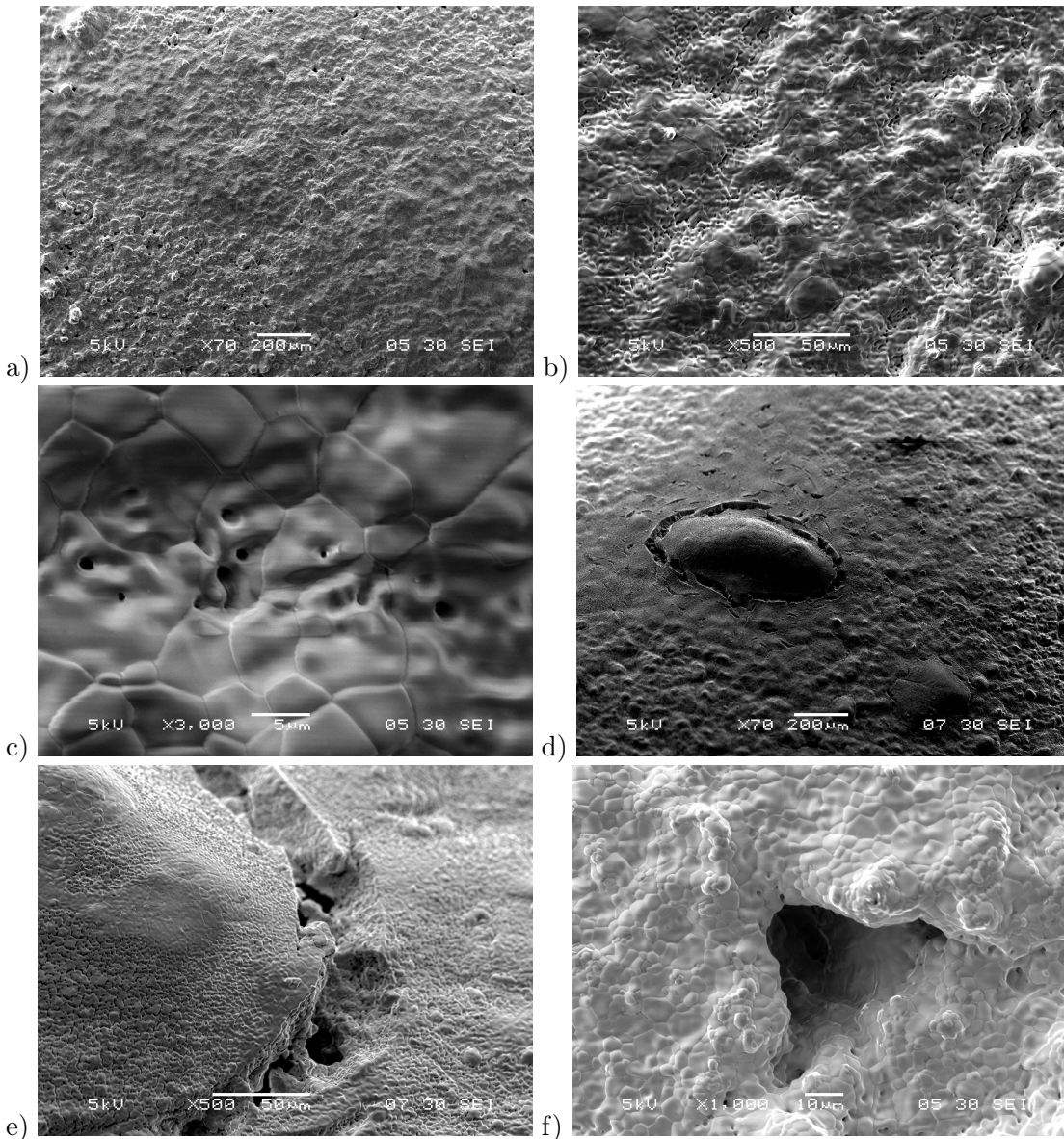


Figure 6.2.19: Pictures of the 8YSZ surface of the 1xY-7.4A, 3xY-3.4F 8YSZ slurry dip coated tube, with intermediate sintering steps, a) surface at 50x, b) surface at 500 x, c) surface at 3000x, d) flaw near sealed end of tube e) flaw near sealed end of tube, crack at side, and f) large hole in electrolyte.

A cross section of the 8YSZ electrolyte is shown in fig. 6.2.20. A lump of 8YSZ in the electrolyte can be seen in fig. 6.2.20a, which probably arises from an agglomerate deposited during dip-coating. The 8YSZ around it is not entirely dense. Fig. 6.2.20b shows that the 8YSZ electrolyte is very thin, and pores penetrate almost the whole way through it. 6.2.20c,d show the 8YSZ electrolyte with a porous layer of NiO/8YSZ below it. Lighter coloured grains of LSM can be seen at the top of the image. The dense pure 8YSZ layer is less than $5\text{ }\mu\text{m}$ thick, even after 1xY-7.4A and 3xY-3.4F dip 8YSZ slurry dip coats. The electrolyte also varies in thickness, so the LSM may permeate it entirely in places, which would short-circuit the cell. In order to increase the thickness of the dip-coated layer, slurry Y-7.3G from table 6.2.4 was dip-coated onto the 1xY-7.4A, 3xY-3.4F tubes, and sintered at $1400\text{ }^{\circ}\text{C}$. The green coating was much whiter than the Y-3.4F slurry coating,

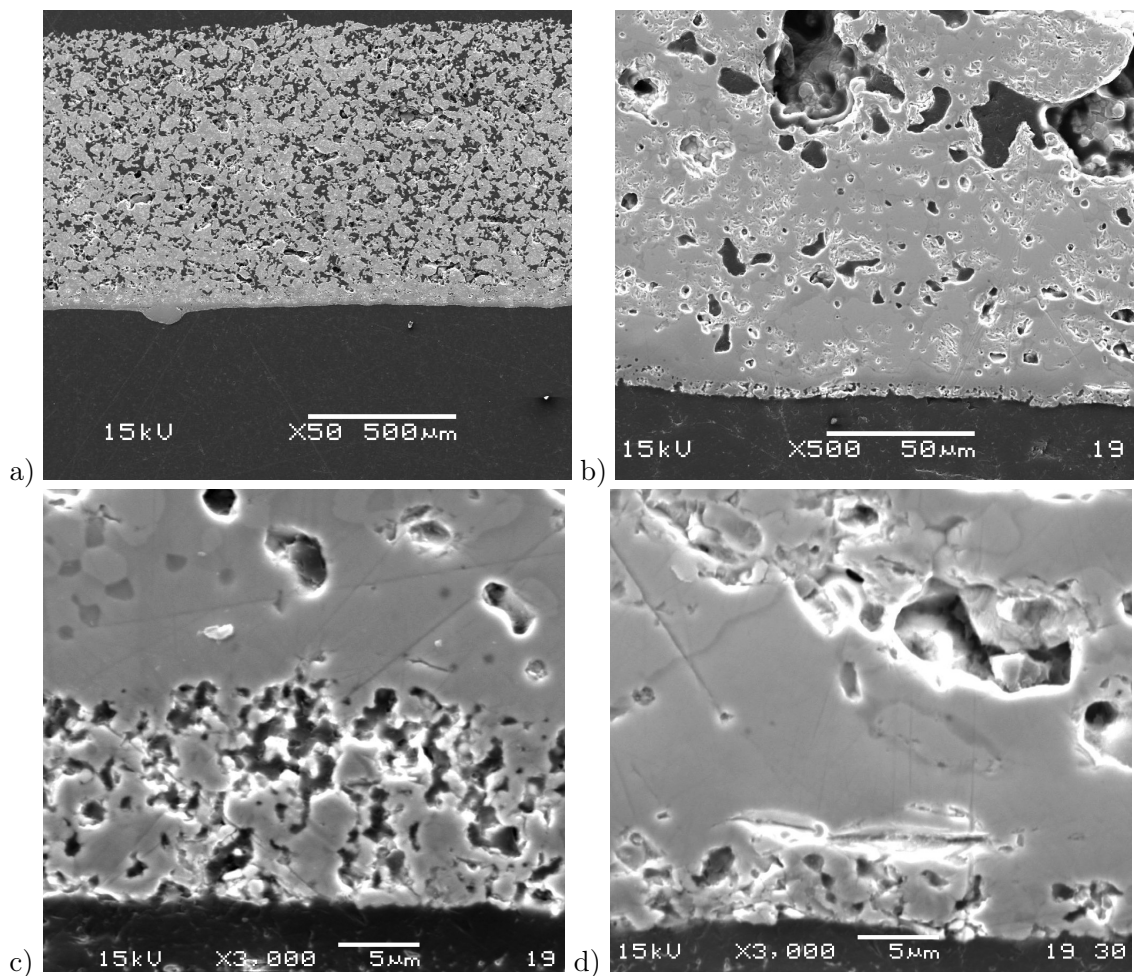


Figure 6.2.20: SEM cross section of 1xY-7.4A, 3xY-3.4F 8YSZ dip-coated tube, which has also had a layer of NiO/8YSZ coated and sintered onto it, a) 50 x, b) 500x, c) 3000x and d) 3000x.

indicating that it was thicker. However, fig. 6.2.21a,b shows that there were $5\ \mu\text{m}$ - $10\ \mu\text{m}$ wide cracks in the surface of the dip-coated layer. Fig. 6.2.21c shows one crack, which has rounded edges which have clearly been sintered, which indicates that the crack occurred during the green state drying or binder burnout step, rather than during sintering. The layer between the cracks is also quite porous.

In order to try to fill in these cracks, the tubes were dipped with 1 layer of slurry Y-3.4F. This was unsuccessful, as fig. 6.2.22 shows. The surface is still cracked, and porous between the cracks.

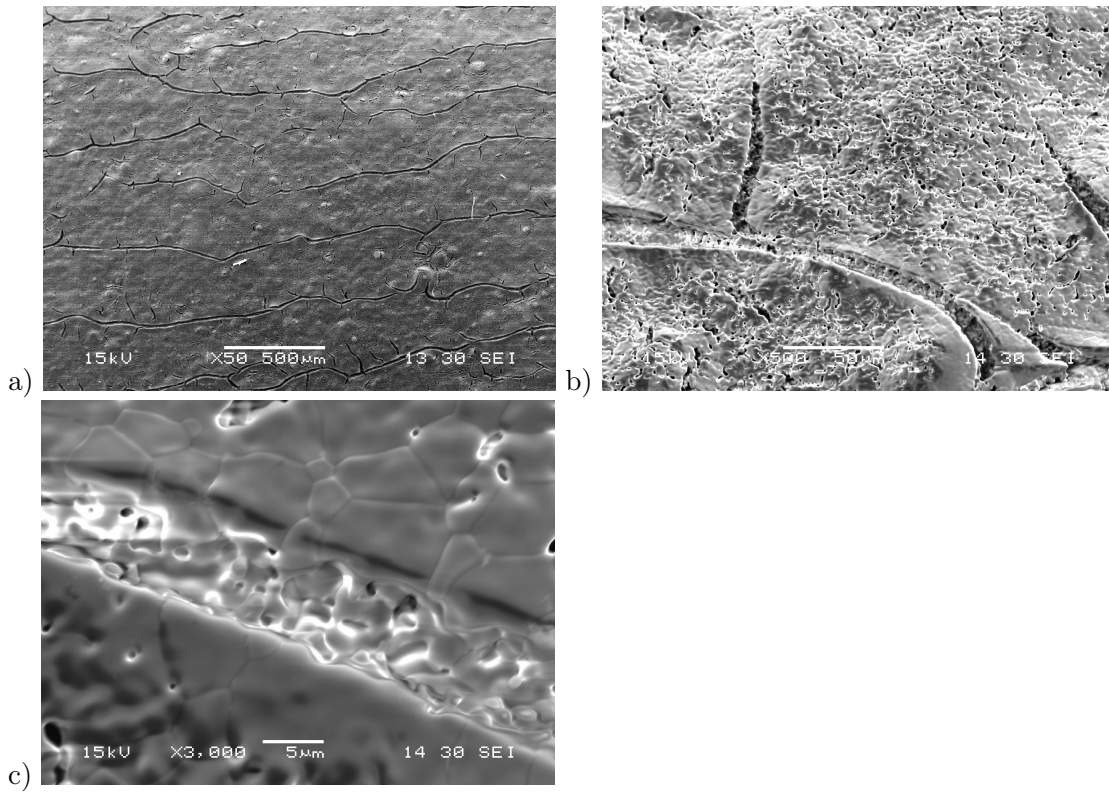


Figure 6.2.21: SEM: surface examination of a tube coated with 1xY-7.3G coating (and other prior coatings), and sintered to 1400 °C.

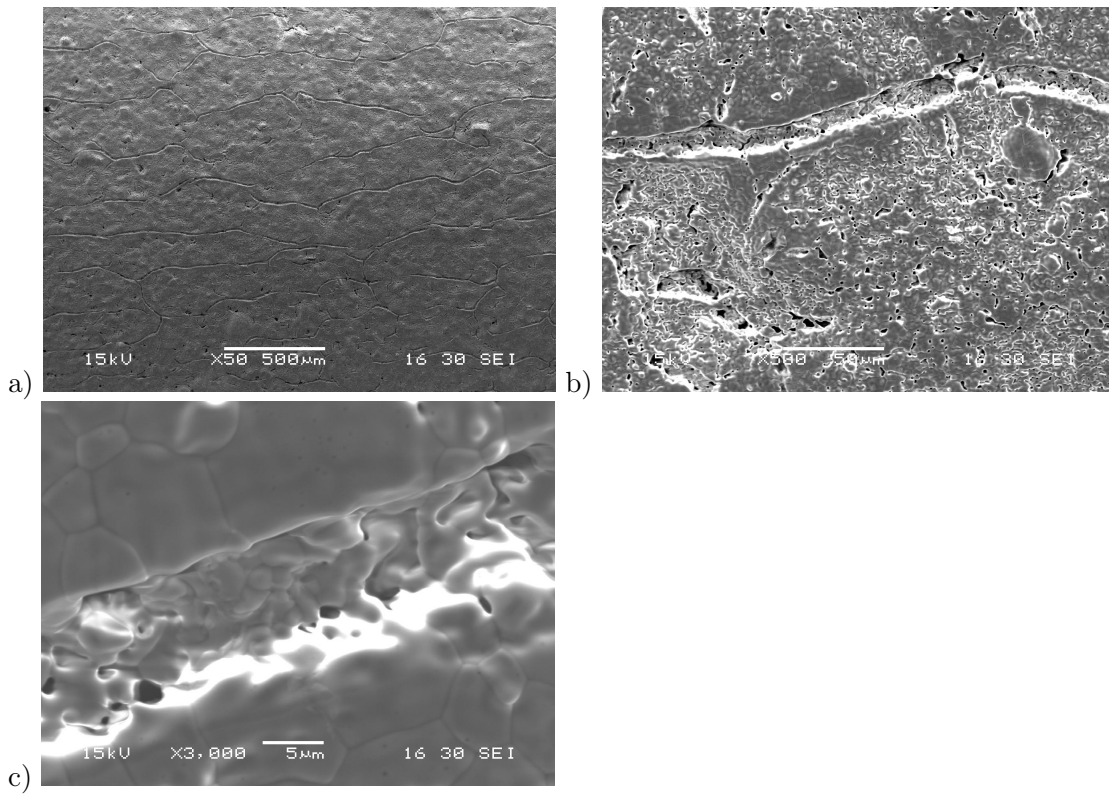


Figure 6.2.22: SEM surface examination of a tube coated with 1xY-7.3G, 1xY-3.4F coatings (and other prior layers), and sintered to 1400 °C.

Fig. 6.2.23a,b show pinholes in the cross section of one of these tubes, fig. 6.2.23c shows the cross section of one of the cracks, and 6.2.23d shows a thin section of the electrolyte. It can be seen that the electrolyte thickness is uneven, and some of the pinholes penetrate its entire thickness.

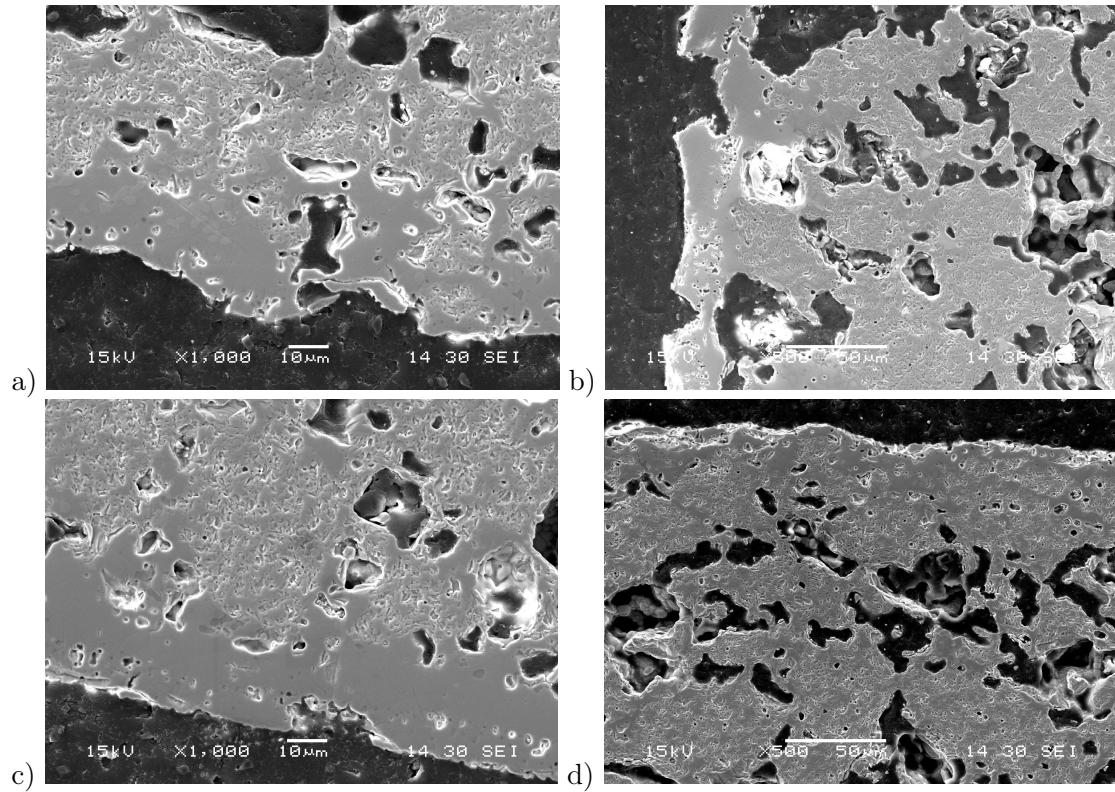


Figure 6.2.23: Cross section of the same sample as fig. 6.2.22.

The remaining tubes were then dip coated with either 1 or two layers of slurry Y-7.3G, and then sintered at 1350 °C. Fig. 6.2.24a,c shows that the 2xY-7.3G coated surface had interconnected cracks, whereas the 1xY-7.3G surface had cracks in one direction only. Fig. 6.2.24b,c shows the cracked and porous 1xY-7.3G surface, and 6.2.24d, e shows the cracked 2xY-7.3G surface, which is dense between the cracks.

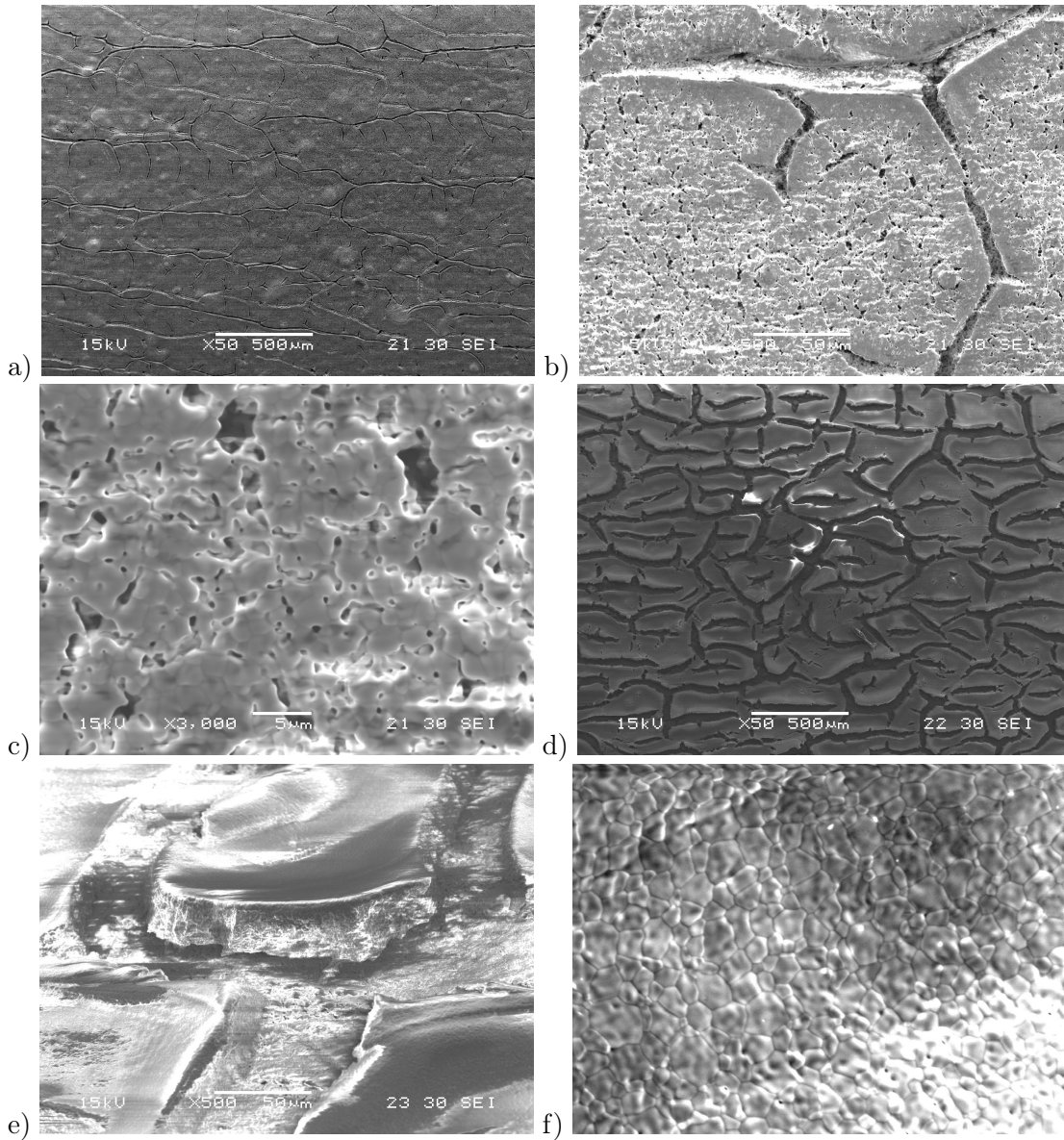


Figure 6.2.24: SEM surface pictures of the tubes dip-coated with 1 and 2 x 8YSZ slurry Y-7.3G: a,b,c) 1 coat of 8YSZ slurry Y-7.3G, and d,e,f) 2 coats of 8YSZ slurry Y-7.3G. The tubes were then sintered to 1350 °C.

There are three stages during which the 8YSZ layer shrinks; firstly as the dip-coating solvent evaporates, secondly as the organic binders burn out during sintering, and thirdly as the 8YSZ particles sinter together. However, shrinkage of the layer is constrained because it is attached to a pre-sintered substrate, that has negligible shrinkage. Therefore, because a thicker dip-coated layer shrinks more than a thin one, it experiences enhanced tensile stresses, which cause more extensive cracking. This is why 2 dimensional cracking is seen

in the 2xY-7.3G layer, but only 1 dimensional cracking in the 1xY-7.3G layer. The 2 dimensional cracking seen on the 2xY-7.3G layer serves to relieve stresses in both the x and y directions in the plane of the layer, so it is then unconstrained by the substrate. Although the cracks are wider in this case, this allows the islands of 8YSZ between the cracks to shrink more, and become quite dense, as in fig 6.2.24f. However, the largely 1 dimensional cracking on the 1xY-7.3G sample only relieves the constraint in one direction, so the islands between the cracks cannot shrink and densify as much, so the surface is still porous as in fig. 6.2.24c. In order to produce a 8YSZ microstructure without cracking, the shrinkage of the green 8YSZ layer could be reduced, by reducing the volume of organic binders in the slurry. This would reduce shrinkage in the binder burnout stage, and help to prevent cracking.

6.2.6 Dip-coating 3YSZ slurries H, Y-10.0I, Y-7.5J, and Y-4.9K.

The YSZ used to make dip-coating slurries was changed to 3YSZ, (Tosoh easy sinter grade), which has a small addition of alumina to act as a sinter aid. A range of slurries with different concentrations of 3YSZ were made up as in table 6.2.5, with a lower percentage of organic binders than previous slurries. The dibutyl phthalate and polyethylene glycol which act as plasticisers, were removed, as was the KD1 dispersant.

Recipe/ slurry name	3YSZ (g)	Butvar (g)	Tri-X (g)	MEK:EtOH ratio 3:2 (g)	3YSZ vol.%
H	36.6355	0.36	0.16	14.85:9.90	15.8
Y-10.0I	3.54	0.07	0.05	4.85:3.23	10.0
Y-7.5J	6.00	0.05	0.03	4.92:3.28	7.5
K	5.95	0.03	0.02	5.13:3.42	4.9

Table 6.2.5: 3YSZ dip coating slurry recipes. Tri-X = Triton-X, MEK = methyl ethyl ketone, EtOH = ethanol. The solids loading (vol.% 3YSZ) is also shown for all recipes.

Fig. 6.2.25a shows tubes coated with 1 layer of slurries Y-10.0I, Y-7.5J, or Y-4.9K before sintering, where it can be seen that the 3YSZ layer is quite thick, and fig. 6.2.25b shows the tubes after sintering at 1350 °C. The higher 3YSZ solids loadings give thicker layers and more extensive cracking. It was also noted that 24 h after dip coating, the slurries had almost completely settled out, which suggests that the 3YSZ in the slurries is agglomerated and the suspension unstable.

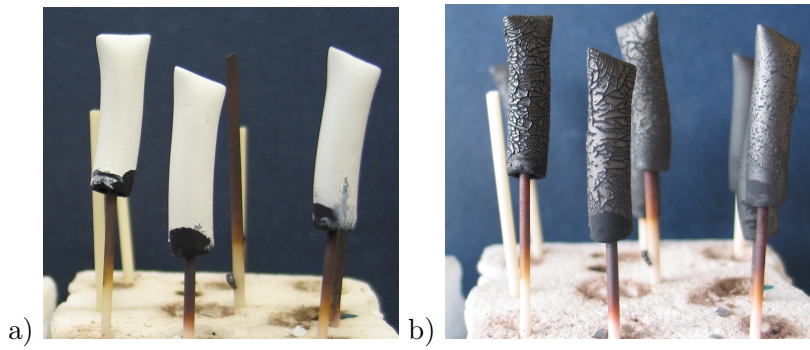


Figure 6.2.25: LSM tubes dipped with 3YSZ slurries Y-10.0I, Y-7.5J, and Y-4.9K, from left to right a) after dip-coating, and b) after sintering at 1350 °C.

Particle size distribution measurements on slurry Y-4.9K in fig. 6.2.26 showed that the suspended layer, which was almost transparent, had particles of about 100 nm in size, whereas when the slurry was shaken, agglomerates of up to 25 μm were seen. Therefore, this recipe is not optimised to disperse the 3YSZ particles very well.

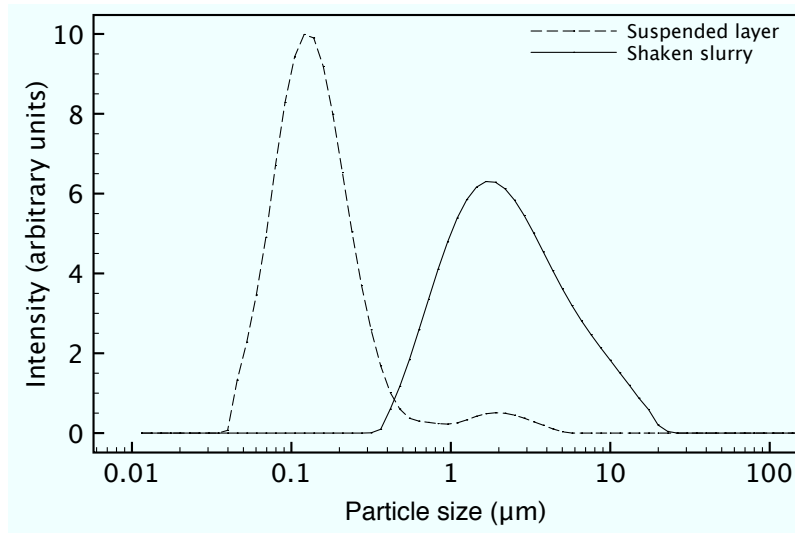


Figure 6.2.26: Particle size distribution measurements on 3YSZ slurry Y-4.9K, of the suspended layer, and after shaking the slurry to mix the suspended and settled layers.

6.2.7 Dip coating 8YSZ slurries Y-7.3G and Y-7.3G2 on recipe M-gra10 LSM tubes



Figure 6.2.27: LSM tubes dip coated with 8YSZ slurries and sintered at 1350 °C. LSM tubes sintered, with a sintered LSM-YSZ coating prior to dip coating: Left foreground 2xY-7.3G, right foreground 1xY-7.3G. Tubes not sintered prior to 8YSZ dip-coating, middle and left background 2xY-7.3G, middle and right background 1xY-7.3G. so is not shiny.

A comparison was made of the effect of putting one or two dip-coated layers of slurry Y-7.3G onto recipe M-gra10 LSM tubes, which are similar to recipe M-gra8 and M-gra9 LSM tubes. Two types of tubes were used: firstly those sintered at 1300 °C and coated with LSM-YSZ, and secondly extruded, unsintered LSM tubes, after the solvent extraction of paraffin wax. Fig. 6.2.27 shows the tubes after sintering at 1350 °C, that the 1xY-7.3G and 2xY-7.3G coatings are both without flaws, but are not shiny, whereas the LSM tubes that were previously unsintered have a mud cracked shiny layer of 8YSZ. This is due to the greater shrinkage of the previously unsintered tubes, and cracking of the 8YSZ layer, which allows densification of the 8YSZ, giving a shiny appearance. The previously sintered LSM tubes do not shrink as much, and the layer does not crack, so the 8YSZ on them cannot sinter dense, and

6.2.8 Dip coating 8YSZ slurry Y-7.3L and Y-7.4L2.

A fresh batch of 8YSZ tape casting slurry was made, similar to recipe 2 in table 6.2.4. A dip-coating slurry obtained from it by dilution, shown in table 6.2.6, called slurry Y-7.3L, was used to dip-coat LSM tubes, which had an LSM-YSZ layer on them. One, two or three coats of slurry Y-7.3L were applied. The four slurry Y-7.3G coated tubes from fig. 6.2.27 also had a single coat of slurry Y-7.3L, and all tubes were sintered at 1350 °C.

Recipe/ slurry name	8YSZ (g)	Butvar (g)	Tri-X (g)	PEG (g)	DBP (g)	MEK:EtOH ratio 3:2 (g)	8YSZ vol.%
Y-7.3L	7.96	0.90	0.06	0.67	0.59	7.04:4.69	7.3
Y-7.4L2	6.28	0.72	0.05	0.54	0.47	5.64:3.76	7.4

Table 6.2.6: 8YSZ dip coating slurry recipes Tri-X = Triton-X, PEG = polyethylene glycol, DBP = dibutyl phthalate, MEK = methyl ethyl ketone, EtOH = ethanol. The solids loading (vol.% 8YSZ) is also shown for all recipes.

Fig. 6.2.28a shows the 1xY-7.3G and 2xY-7.3G tubes after sintering, and 6.2.28b

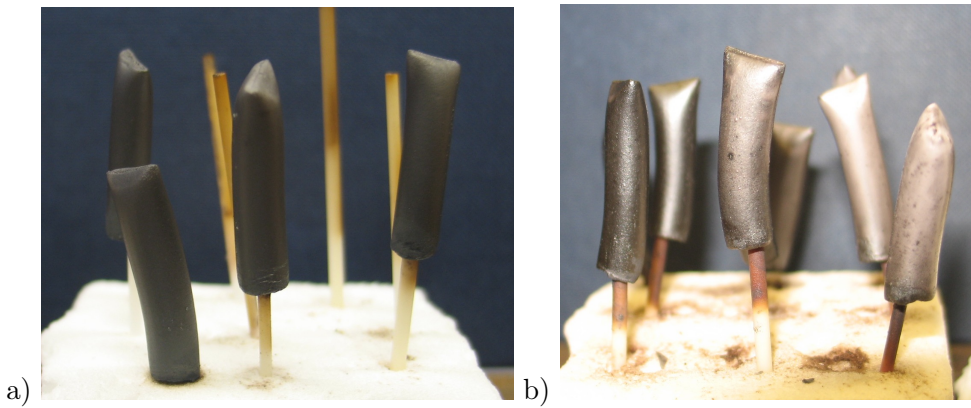


Figure 6.2.28: Recipe M-gra10 LSM tubes with an LSM-YSZ coating, after sintering at 1350 °C 1 h, a) left, 1xY-7.3G, middle and right, 2xY-7.3G 8YSZ slurry dip coated tubes, and b) left, 1xY-7.3L, middle 2xY-7.3L, and right, 3xY-7.3L 8YSZ slurry dip coated tubes.

shows the 1xY-7.3L, 2xY-7.3L and 3xY-7.3L tubes after sintering. It can be seen that with more coats of slurry Y-7.3L, the tubes have a whiter appearance, and become less shiny. Therefore, this 8YSZ layer is unlikely to be fully dense. A cross section of the slurry Y-7.3L coated tubes in fig. 6.2.29 shows that the 8YSZ varies between 10 μm - 30 μm thick, but is porous in all cases.

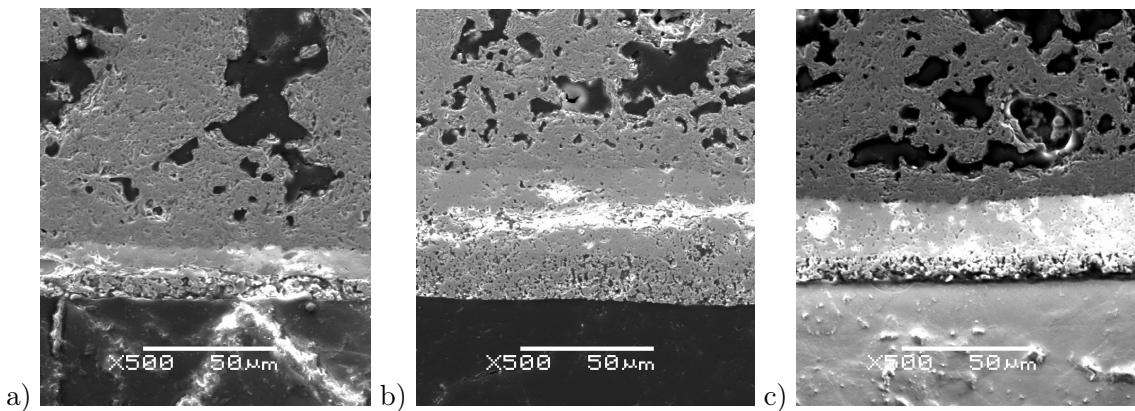


Figure 6.2.29: SEM cross sections of 8YSZ dip-coated tubes, also with a porous layer of NiO/8YSZ on them (bottom): a) 10-13, 1xY-7.3L, b) 10-14, 2xY-7.3L, and c) 10-15, 3xY-7.3L. The 8YSZ electrolyte is the layer just above the porous NiO/8YSZ layer at the bottom of the images.

Some of the tubes were then painted with another coat of slurry Y-7.3L. Longitudinal cracks along the tube in the dried 8YSZ coating were observed, which form as the slurry dries. This shows that some cracking occurs as the solvent evaporates. The tubes were sintered to 1350 °C, dipped and sintered again, and the longitudinal cracks along the tube were noticed again. In order to prevent this cracking, a different organic binder system could be used, which lowers the percentage of solvent and organic components, and increases the 8YSZ solids loading.

6.2.9 Painting with 8YSZ inks

8YSZ screen printing ink

Table 6.2.7 shows the solids loading of 8YSZ dip-coating slurries and screen printing inks.

Composition type	8YSZ (vol.%)	volatile organics (vol.%)	non-volatile organics (vol.%)
8YSZ slurry Y-7.3L as made	7.4	81.3	11.3
8YSZ slurry Y-7.3L after drying	39.4	0.0	60.6
8YSZ ink as made	25.9	68.3	5.8
8YSZ ink after drying	81.5	0.0	18.5

Table 6.2.7: Volume percentages of 8YSZ and organic components in dip-coating slurry Y-7.3L and 8YSZ screen printing ink, before and after drying at 80 °C to remove volatile components (MEK/EtOH or terpineol). Percentages do not sum to 100% due to rounding.

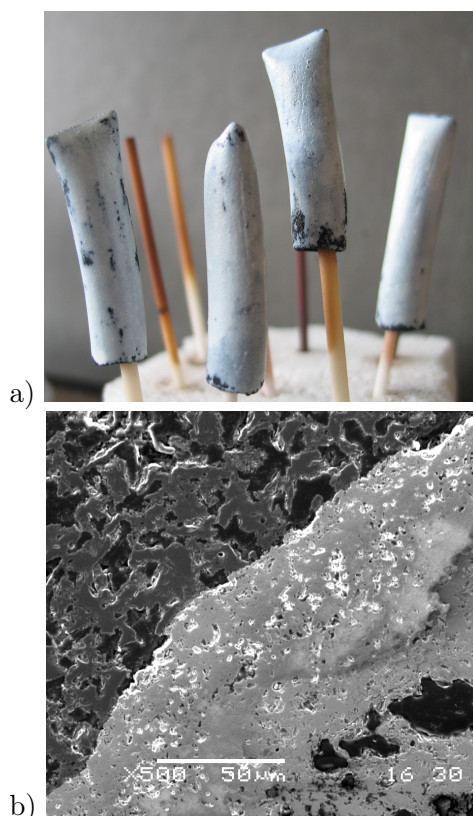


Figure 6.2.30: a) Recipe M-gra10 LSM tubes pre-coated with a sintered LSM-YSZ layer, with a painted layer of 8YSZ screen printing ink. The ink did not wet parts of the tube where bare LSM is exposed because of holes in the LSM-YSZ layer, and b) cross section of RSOFC-M-gra10-4, with Toku ceramic paste (top left), 8YSZ layer (middle), and LSM substrate (bottom right).

The screen printing inks have a much higher solids loading than the slurries. Therefore, the shrinkage of the 8YSZ layer should be much less during both drying and sintering, which will help to prevent crack formation. These inks must be painted on the tubes rather than dip-coated as they are quite viscous. A single coat of 8YSZ screen printing ink was applied to 1xY-7.3L, 2xY-7.3L and 3xY-7.3L tubes, which were named RSOFC-M-gra10-4, M-gra10-5, and M-gra10-6, and also some recipe M-gra10 LSM tubes painted with LSM-YSZ, which were named RSOFC M-gra10-7, M-gra10-8, M-gra10-9, and M-gra10-10. The ink wetted the LSM-YSZ layer well, but not the parts that were not coated with LSM-YSZ, as fig. 6.2.30a shows. The tubes were sintered at 1350 °C. A cross section of RSOFC-M-gra10-4 in fig. 6.2.30b, shows that its 8YSZ electrolyte layer is 20 μm - 30 μm thick, but not dense. The tubes were then coated with another two layers of 8YSZ ink, along with another two tubes called RSOFC M-gra10-11 and M-gra10-12, with sintering steps at 1350 °C after each layer of 8YSZ applied. However, the 8YSZ

ink did not make a dense layer on the tubes, although it was thicker than the slurry Y-3.4B2 dip-coated layer.

Commercial 3YSZ ink

A commercial 3YSZ ink, hereafter referred to as 3YSZ-C, was examined to see if it might be useful in preparing a dense electrolyte layer. Its particle size distribution was compared with that of the 8YSZ screen printing ink, in fig. 6.2.31.

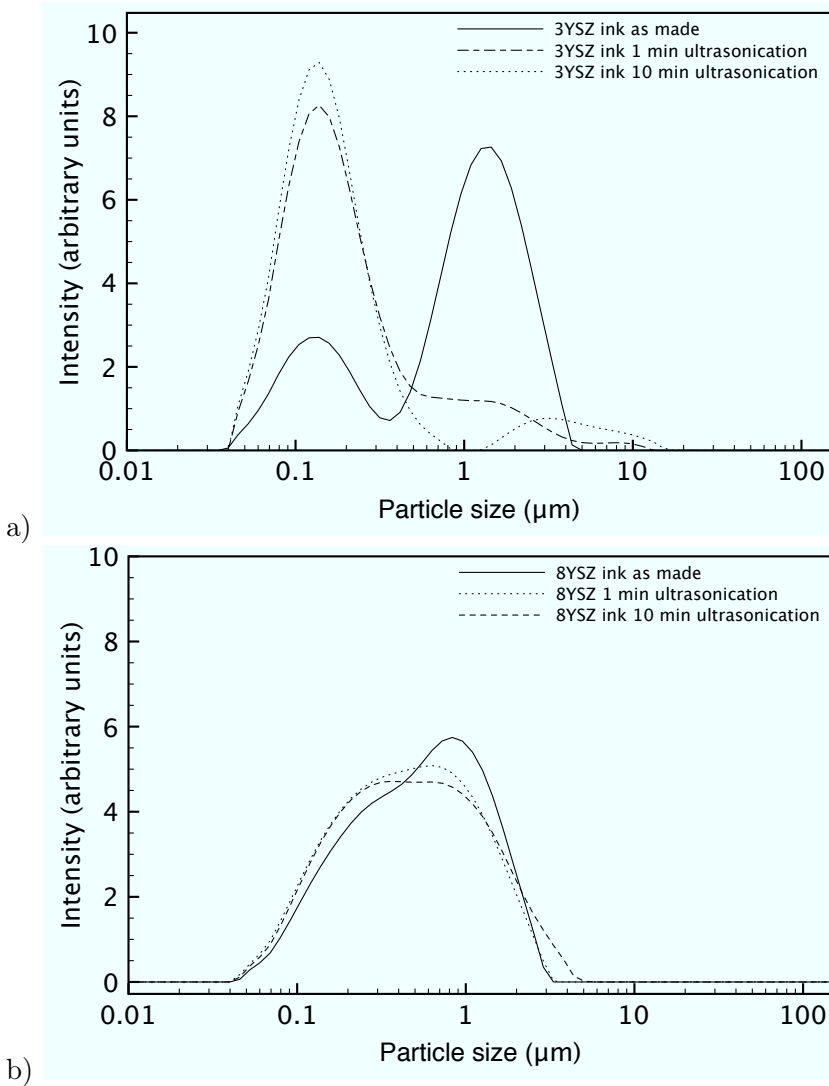


Figure 6.2.31: Particle size distribution measurements on two YSZ screen printing inks used for painting YSZ electrolytes onto LSM supports. Measurements were made on the ink as made, and after 1 min and 10 min ultrasonic vibration in the particle size analyser, a) 3YSZ-C ink, and b) 8YSZ Pi-Kem ink.

The measurements on the 'as made' inks show that there are few agglomerates in the 8YSZ ink, but the 3YSZ-C ink has loose agglomerates just over 1 μm in size. The 1 min ultrasonication breaks almost all of these agglomerates in the 3YSZ-C ink, and the 10 min ultrasonication shows the primary particle size is 0.1 μm , and that of the 8YSZ ink is about 0.2 μm to 1 μm . Therefore, the 3YSZ-C ink will be much more sinter-active,

requiring a lower sintering temperature to achieve full densification. This is advantageous, as lower sintering temperature decrease the likelihood of the YSZ reacting with the LSM substrate, and there is less coarsening of the LSM-YSZ oxygen electrode, which should improve the electrochemical performance of the cell [14]. Recipe M-gra10 LSM tubes with a prior sintered coat of LSM-YSZ painted with either 1, 2 or 3 coats of 3YSZ-C ink, sintered at 1350 °C, and named RSOFC M-gra10-27 - M-gra10-29 respectively are shown in fig. 6.2.32a.

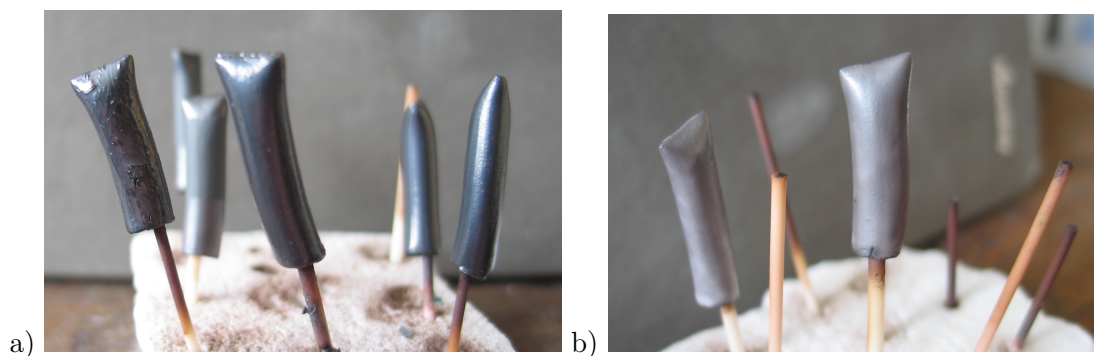


Figure 6.2.32: Comparison of tubes painted with YSZ ink and sintered at 1350 °C for 1 h: a) RSOFC-M-gra10-27, M-gra10-28 and M-gra10-29, 3YSZ-C ink, left 3 coats, middle 2 coats, right 1 coat, and b) RSOFC-M-gra10-7, and M-gra10-9, both 1 coat 8YSZ ink.

Fig. 6.2.32b shows RSOFC M-gra10-7 and M-gra10-9, which had 1 coat of 8YSZ ink and were sintered at the same time as RSOFC-M-gra10-27 - M-gra10-29. RSOFC-M-gra10-29 has splits and cracks visible in the surface coating, but RSOFC-M-gra10-27 and 10-M-gra28 do not. They are much more shiny than the tubes coated with the 8YSZ ink, which indicates that the electrolyte is more dense.

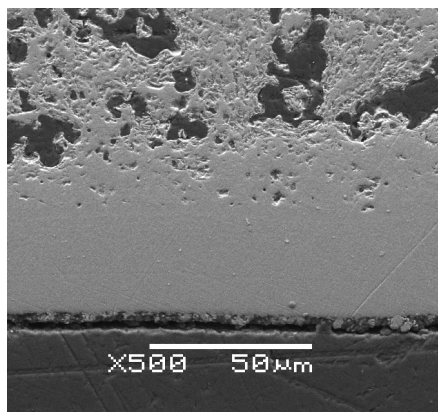


Figure 6.2.33: SEM cross section of RSOFC-M-gra10-27. A dense 3YSZ electrolyte may be seen, with a mixed LSM and 3YSZ layer above it, and then the bulk LSM substrate above that.

A cross section of RSOFC M-gra10-27 is shown in fig. 6.2.33, showing that the electrolyte is quite dense. This tube has no LSM-YSZ coating, so the fairly dense LSM-3Y layer, above the fully dense electrolyte, is produced when the electrolyte layer soaks into the tube when it is painted on.

RSOFC-M-gra10-8 had the following coatings; 2x8YSZ ink, then 1x8YSZ, then 1x8YSZ. RSOFC M-gra10-7 had the same coatings, but an additional 1x3Y coating, and RSOFC M-gra10-9 had the same coatings as 10-8, but an additional four 1x3Y coatings. RSOFC-M-gra10-10 and M-gra10-12, previously coated with 8YSZ ink, and RSOFC-M-gra10-27 had a single coat 3YSZ-C ink. RSOFC-M-gra10-28 and

M-gra10-29 had 2 coats of 3YSZ-C ink and all these tubes were sintered at 1350 °C. One

more coat of 3YSZ-C ink was applied and sintered on RSOFC M-gra10-27 - M-gra10-29. These coatings appeared shiny and dense to the naked eye.

Painting YSZ inks on recipe M-gra11 LSM tubes

More LSM tubes were made from extrusion recipe M-gra11, and were coated as shown in table 6.2.8. The 3YSZ ink was made with Tosoh 3YSZ easy sinter grade.

	Coating no.1	Coating no. 2	Coating no.3	Coating no.4
M-gra10-30	1x3YSZ-C	1x3YSZ-C	-	-
M-gra10-31	1x3YSZ-C	1x3YSZ-C	-	-
M-gra11-1	2xY-7.4L2	2x3YSZ-C	1x3YSZ-C	-
M-gra11-2	2xY-7.4L2	2x3YSZ-C	1x3YSZ-C	1x3YSZ-C
M-gra11-3	2xY-7.4L2	2x3YSZ-C	1x3YSZ	-
M-gra11-4	2xY-7.4L2	2x3YSZ-C	1x3YSZ	-
M-gra11-5	2xY-7.4L2	2x3YSZ-C	1x3YSZ-C	-
M-gra11-6	2xY-7.4L2	2x3YSZ-C	1x3YSZ-C	-
M-gra11-7	2xY-7.4L2	2x8YSZ	1x3YSZ-C	1x3YSZ-C
M-gra11-8	2xY-7.4L2	2x8YSZ	-	-
M-gra11-9	2xY-7.4L2	2x8YSZ	-	-
M-gra11-10	1xLSM-YSZ	2x3YSZ-C	1x3YSZ-C	-
M-gra11-11	1xLSM-YSZ	2x3YSZ-C	1x3YSZ-C	1x3YSZ-C
M-gra11-12	1xLSM-YSZ	2x3YSZ-C	1x3YSZ	
M-gra11-13	1xLSM-YSZ	2x3YSZ-C	1x3YSZ	-
M-gra11-14	1xLSM-YSZ	2x3YSZ-C	1x3YSZ-C	1x3YSZ-C
M-gra11-15	1xLSM-YSZ	2x3YSZ-C	1x3YSZ-C	1x3YSZ-C
M-gra11-16	1xLSM-YSZ	2x3YSZ-C	1x3YSZ-C	-
M-gra11-17	1xLSM-YSZ	2x3YSZ-C	1x3YSZ-C	-
M-gra11-18	1xLSM-YSZ	2x3YSZ-C	1x3YSZ-C	-

Table 6.2.8: Recipe M-gra11 LSM tube coatings to make an electrolyte layer. **3YSZ-C** is a commercial electrolyte ink, **8YSZ** is an ink with a Pi-Kem powder, and **3YSZ** is an ink made with a Tosoh powder. After each coating stage, the tubes are sintered at 1350 °C.

Fig. 6.2.34 shows RSOFC-M-gra11-10 - M-gra11-18, which were pre-coated with LSM-YSZ before the 3YSZ-C ink was applied. Marks running longitudinally along the tubes are brush strokes created during the painting process. The tubes are quite shiny, as are RSOFC M-gra11-1 - M-gra11-6, which were pre-coated with two Y-7.4L2 8YSZ slurry coats before the 3YSZ-C ink was applied. However, this contrasts sharply with RSOFC M-gra11-7 - M-gra11-9, which were painted with 8YSZ ink instead of 3YSZ-C ink. They have a white

appearance, as the 8YSZ electrolyte is not fully dense.



Figure 6.2.34: Recipe M-gra11 RSOFC: Left hand block of tubes, RSOFC-M-gra11-10 - M-gra11-18, after sintering the LSM-YSZ and 2x3Y coatings. Right hand block of tubes: 3 tubes in foreground, RSOFC M-gra11-7 - M-gra11-9, with 2xY-7.4L2 8YSZ slurry coats, then 2x8YSZ coats, and 6 tubes in background, RSOFC-M-gra11-1 - M-gra11-6, also 2xY-7.4L2 slurry coats, then 2x3YSZ-C coats.

Fig. 6.2.35 shows the surface of tubes from fig. 6.2.34.

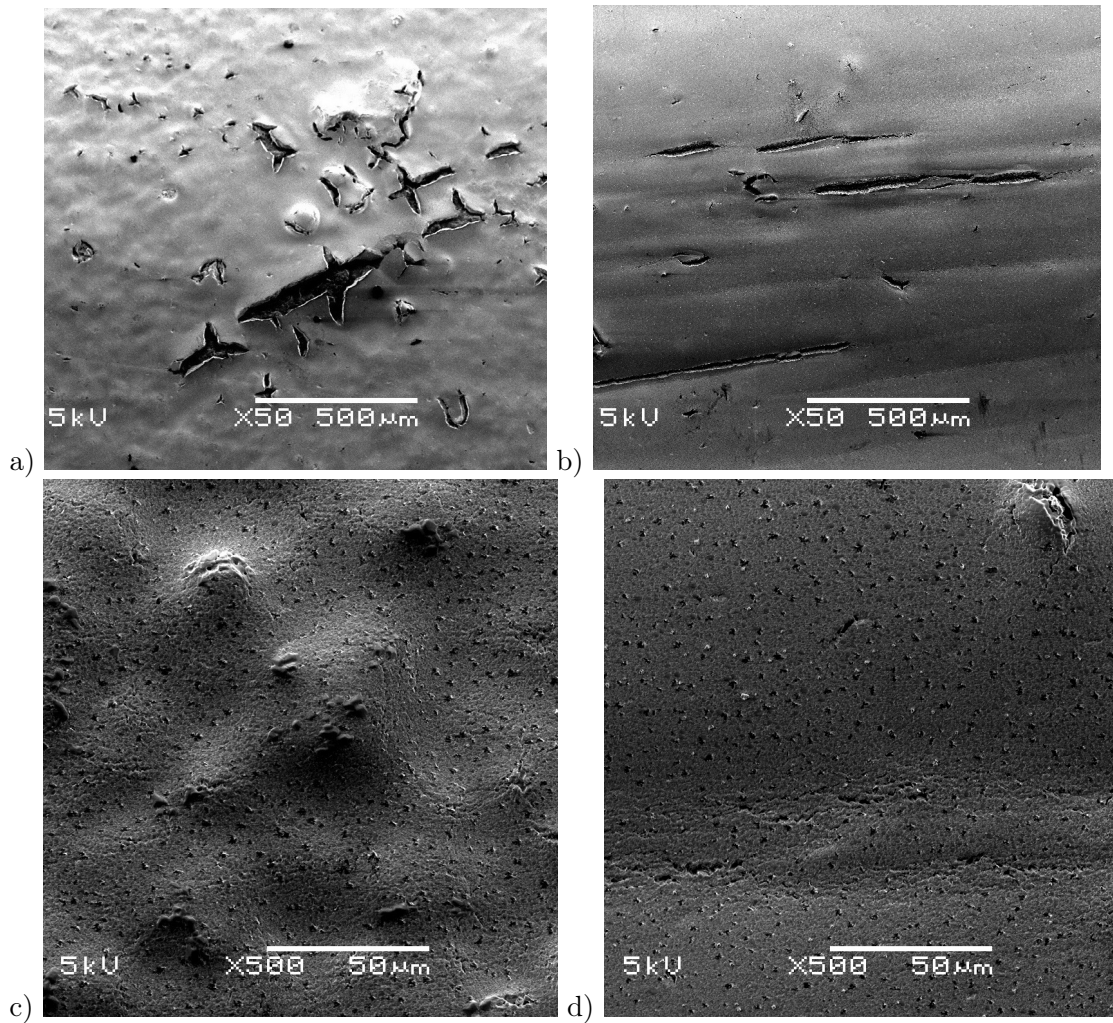


Figure 6.2.35: Comparison of the 3YSZ-C ink electrolyte surface: a, c) recipe M-gra11 LSM tube, with 1 sintered layer of 8YSZ ink, and 2 layers of 3YSZ-C ink, and b, d) 1 sintered layer of LSM-YSZ, and then 2 layers of 3YSZ-C ink.

These were coated with 3YSZ-C ink, but with either an LSM-YSZ sublayer, (a,c, RSOFC M-gra11-10 - M-gra11-18) or a Y-7.4L2 8YSZ slurry sublayer (b,d, RSOFC M-gra11-1 - M-gra11-6). The tubes with the Y-7.4L2 8YSZ sublayer have cracks in the electrolyte layer in two directions, and the surface in 6.2.35c is quite bumpy, probably from 8YSZ agglomerates in the Y-7.4L2 8YSZ slurry. However, the tubes with the LSM-YSZ sublayer has cracks in only one direction, which occur in some of the lines left by the brushstrokes, when the 3YSZ-C ink was painted onto them, but are otherwise smooth, as in fig. 6.2.35d. A distinct line can be seen in this image, which is a close up view of one of the lines in fig. 6.2.35b. The coating appears to be thinner here as this corresponds to a brush stroke in the painted layer, and micro-cracking is observed. Therefore, this flaw is due to the method of application of the ink.

Fig. 6.2.36a shows a tube with an outer layer of 3YSZ-C ink, and fig. 6.2.36b a tube with an outer layer of 3YSZ ink. It can be seen that the tube with the 3YSZ ink has surface flaws in the electrolyte layer, which has a whitish colour, suggesting that it is not fully densified.

A cross section of RSOFC M-gra11-11 in fig. 6.2.37a,c,e shows a dense electrolyte. It had very few flaws, much fewer than previous 8YSZ electrolytes produced. One of the few flaws is shown here. There is a crack in the LSM-YSZ layer which underlies the electrolyte, so it is likely that the flaw in the electrolyte arises because of this. RSOFC M-gra11-12 in fig. 6.2.37b,d, has a dense electrolyte, except for the porous outer surface, the 3YSZ ink layer. A pellet of this powder should densify at 1300 °C,

[15] so the porosity seen here may arise from either constrained sintering, as the substrate is already sintered dense, or else the dispersion of powders in the ink is not optimal, and agglomerates are present. Very few flaws were seen in the cross section examined, except for one pinhole, possibly arising from an air bubble in the first 3YSZ-C ink layer, so there should be little crossover leakage of fuel and oxygen when the cells are tested. In both cells, the fully dense electrolyte layer is about 20 μm to 30 μm thick.



Figure 6.2.36: Comparison of electrolyte inks: a) 3YSZ-C ink RSOFC M-gra11-11, and b) RSOFC M-gra11-12 3YSZ ink made with Tosoh powder.

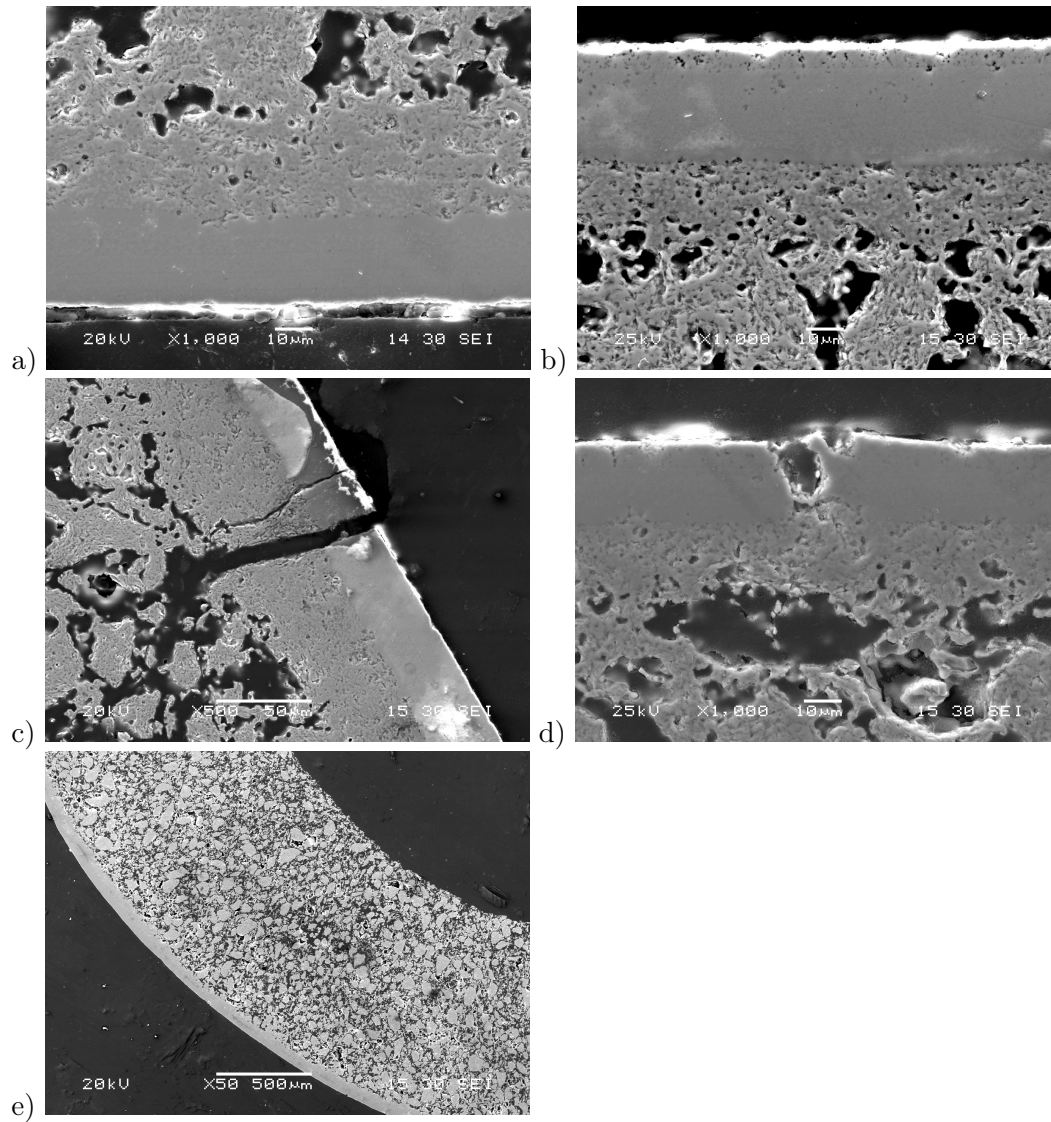


Figure 6.2.37: SEM longitudinal cross section of 3YSZ-C coated RSOFC: a comparison of M-gra11-11, which has 3YSZ-C only, and M-gra11-12, which has an outer layer of 3YSZ, a) M-gra11-11, b) M-gra11-12, c) crack in M-gra11-11, d) pinhole in M-gra11-12, and e) M-gra11-11, a cross section perpendicular to the longitudinal axis of the tube.

Therefore, it may be seen from table 6.2.8 that RSOFC-M-gra11-12 needs just 2x3YSZ-C coats to make it dense; and the porous 1x3YSZ coat need not be applied, so a dense electrolyte may be applied in a single sintering step. This is a significant result which greatly improves on the previous, more porous 8YSZ electrolytes.

6.3 Production of the NiO/8YSZ fuel electrode

In order to produce a NiO/8YSZ fuel electrode, a diluted NiO/8YSZ screen printing ink was dip-coated onto the tubes.

6.3.1 NiO/8YSZ dip coating on Y-3.4C, Y-5.2D, and Y-7.3E 8YSZ slurry coated tubes

A NiO/8YSZ screen printing ink was diluted to make a dip coating slurry called recipe 1, in table 6.3.1.

Recipe no.	NiO/8YSZ ink (g)	Isopropanol (g)	Ink:solvent (mass ratio)	Solids (volume %)
1	6.585	3.228	2.0x	8.1
2	9.516	4.678	2.0x	8.1
3	13.588	5.495	2.5x	8.9

Table 6.3.1: NiO/8YSZ dip-coating slurry formulation. Recipe 1 was made by diluting NiO/8YSZ screen printing ink with isopropanol in the ratio shown. Recipe 2 was made by adding further ink and isopropanol to the slurry, and recipe 3 was also made this way.

RSOFC-H-cell4-1 - H-cell4-6 from subsection 6.2.2, were dipped with the recipe 1 NiO/8YSZ slurry, and sintered to 1330 °C for 2 h. The sintered NiO/8YSZ layer, on RSOFC-H-cell4-5 in fig. 6.3.1 is quite thin, but probably sufficient for electrochemical activity. However, it may have a high lateral electrical resistance. Its thickness was measured using the ImageJ program, and is shown in table 6.3.2. The LSM tubes dipped here have large pinholes in them.

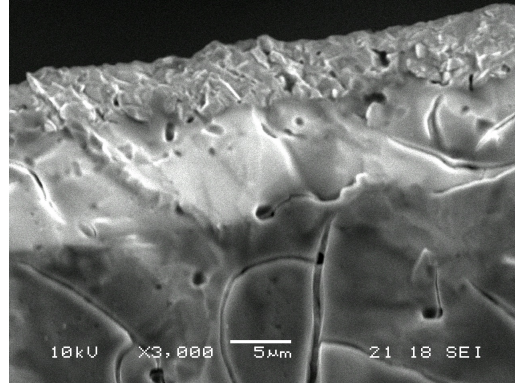


Figure 6.3.1: Fracture surface of NiO/8YSZ layer (top), made by dip-coating recipe 1, table 6.3.1, and sintering at 1350 °C for 1 h. The substrate is a 2xY-5.2D 8YSZ coating (middle white layer) and an LSM tube (bottom dark grey layer).

Reading no.	NiO/8YSZ thicknesses	
	Region 1 (μm)	Region 2 (μm)
1	4.4	4.0
2	5.7	3.8
3	4.6	3.5
4	3.9	3.9
5	4.9	3.6
6	6.0	3.9
Average	4.9	3.8

Table 6.3.2: NiO-8YSZ dip-coated layer thickness after sintering at 1350 °C, measured at two regions of a cross sectioned tube, by analysing SEM images with the program ImageJ. Error in values $\pm 0.5 \mu m$.

Fig. 6.3.2 shows a large pinhole in the LSM tube substrate of RSOFC-H-cell4-5. The quality of the LSM substrate is not only important in producing a pinhole free 8YSZ electrolyte layer, but it is crucial to produce a defect free NiO/8YSZ layer as well.

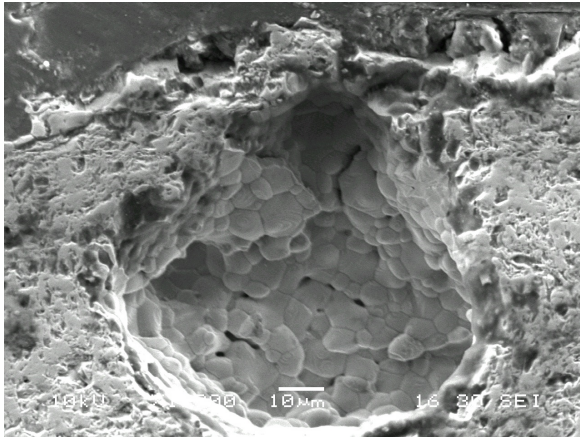


Figure 6.3.2: A large pinhole in the LSM substrate of RSOFC-H-cell4-5. It can be seen that the pinhole disrupts the 8YSZ electrolyte layer.

6.3.2 NiO/8YSZ dip-coating on Y-7.4A and Y-3.4B 8YSZ slurry coated tubes

LSM tubes made from extrusion recipe H-cell6 were also dip-coated with NiO/8YSZ and sintered in the same manner as before, to 1350 °C with a 2 h dwell, sintering ring temperature 1360 °C. Fig. 6.3.3 shows that the surface of the resulting tubes is rough, and has pinholes which cause breaks in the 8YSZ electrode and NiO/8YSZ fuel electrode. Therefore, these tubes could not be used to make reversible SOFC as they are not sealed.



Figure 6.3.3: Recipe H-cell6 LSM, pre-coated with LSM-YSZ, and 8YSZ slurry Y-7.4A or Y-3.4B coats, indicated by the letters in the photograph, with 1 coat of NiO/8YSZ sintered at 1350 °C. The surface of the tubes is rough, as the LSM substrate has pinholes in it, which means that all subsequent layers also have pinholes.

6.3.3 NiO/8YSZ dip-coating on Y-7.4A2 and Y-3.4B2 8YSZ slurry coated tubes

NiO/8YSZ painting on recipe M-gra7 LSM tubes

The tubes made from LSM extrusion recipe M-gra7, with a graphite pore former for improved homogeneity, after previous coatings of LSM-YSZ and Y-7.4A2 and Y-3.4B2 8YSZ slurries, were dip-coated, and sintered twice with recipe 2 NiO/8YSZ slurry from table 6.3.1. As the LSM tubes used had a uniform microstructure, with the maximum distance between particles $<30\text{ }\mu\text{m}$, the NiO/8YSZ coating produced was more uniform, and had no large holes. Four of these tubes, with Y-3.4B2 8YSZ slurry electrolyte, were named RSOFC-M-gra7-2 - M-gra7-5.

NiO/8YSZ painting on recipe M-gra8 LSM tubes

Recipe 3 NiO/8YSZ dip-coating slurry in table 6.3.1, was used to dip LSM recipe M-gra8 tubes, pre-coated with LSM-YSZ and 8YSZ, from subsection 6.2.4, and sintered.

Fig. 6.3.4 shows a picture of the tubes after dip-coating and before sintering, where the green coloured layer of NiO/8YSZ can be clearly seen. Fig. 6.3.5a shows the 8YSZ in one of these tubes, and fig. 6.3.5b shows the nickel. There is fairly dense layer of NiO/8YSZ $\sim 10\text{ }\mu\text{m}$ thick, on the surface of the tube, but its porosity will increase when the NiO is reduced during testing.



Figure 6.3.4: NiO/8YSZ dip coating before sintering on LSM tubes, made with extrusion recipe M-gra8, with LSM-YSZ and 4xY-3.4B2 8YSZ slurry coats on them.

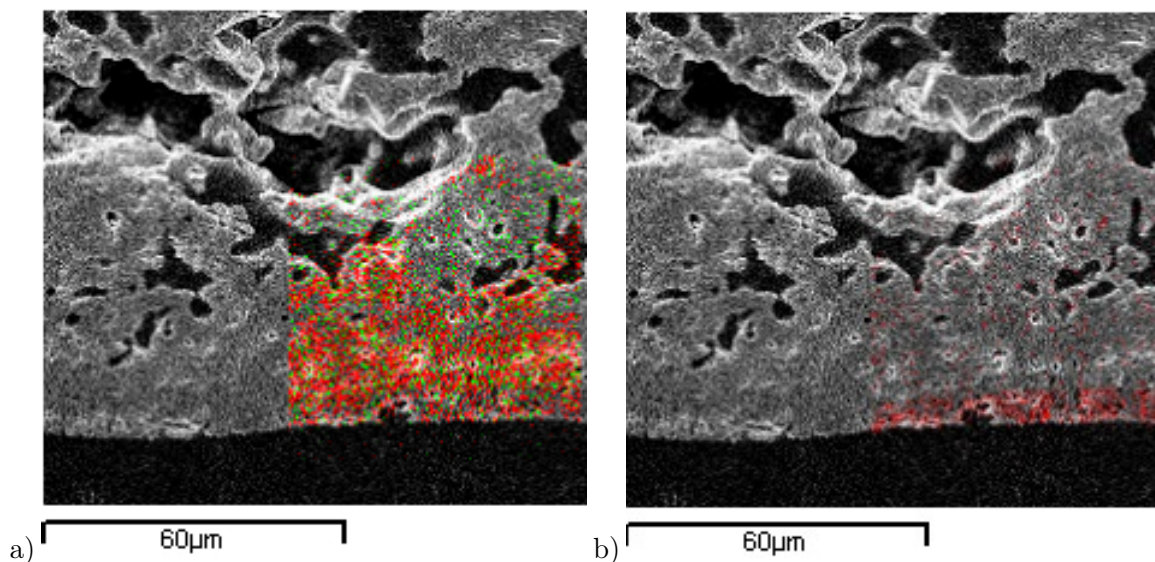


Figure 6.3.5: RSOFC cross section with elemental maps. The layers, going from top to bottom, are the porous LSM tube substrate, then 8YSZ from 4x Y-3.4B2 8YSZ slurry dip-coats, then NiO/8YSZ from a dip-coat, and the resin the sample is mounted in at the bottom (black layer). The images shown are elemental maps of a) zirconium (red) and yttrium (green) which shows the 8YSZ in the electrolyte and NiO/8YSZ fuel electrode, and image b) shows nickel (red).

6.3.4 NiO/8YSZ ink painting on RSOFC

NiO/8YSZ painting on recipe M-gra9 LSM tubes

NiO/8YSZ screen printing ink was painted onto some recipe M-gra9 LSM tubes from subsection 6.2.5, which had 1xY-7.4A 8YSZ slurry, and 2xY-3.4F 8YSZ slurry coating. Fig. 6.3.6a shows the tubes before sintering, and fig. 6.3.6b shows that after sintering at 1350 °C, the NiO/8YSZ ink has run down the tube.

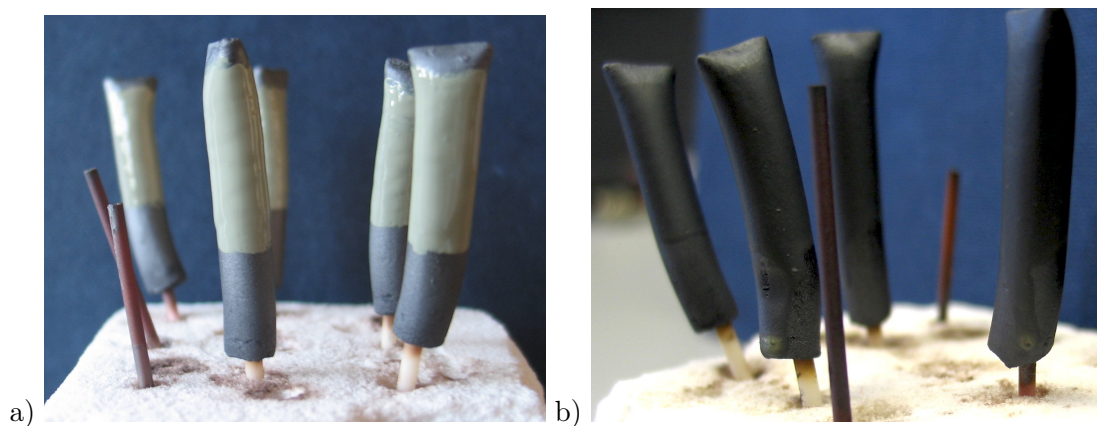


Figure 6.3.6: NiO/8YSZ screen printing ink painted on 1xY-7.4A, 2xY-3.4F 8YSZ coated tubes, a) before sintering, and b) after sintering at 1350 °C. A drip has run down the tube from the NiO/8YSZ coated region, and the green colour of the NiO/8YSZ can be seen at the bottom of the drip.

A band of ink was painted around the tubes, so that the sealed end of the tube would not be covered. This helps to avoid short-circuits in the cell, as the 8YSZ often has flaws at the top of the tube, on the rough LSM surface that is created when the tube is sealed as it is extruded. If there is a break in the 8YSZ, it can be sealed with ceramic sealant, rather than NiO penetrating it and causing a short circuit. It becomes less viscous during sintering as the terpeneol heats up and begins to evaporate, and as there is a thick layer of ink on the tube, it runs down the tube. As the 8YSZ coating is thinner or absent at the tube base, this means that these cells will short-circuit if tested as the fuel and oxygen electrodes will be in direct contact. Two more LSM recipe M-gra9 tubes that had the same 8YSZ coatings were sparingly painted with bands of NiO/8YSZ ink, so the layer was thinner. After sintering, these tubes did not exhibit any drips. These tubes were named RSOFC-M-gra9-1 and M-gra9-2.

NiO/8YSZ painting on recipe M-gra10 LSM tubes

Recipe M-gra10 LSM tubes, coated with LSM-YSZ and then 1xY-7.3G (10-30), 2xY-7.3G (10-31), 1xY-7.3L (10-13), 2xY-7.3L (10-14) or 3xY-7.3L (10-15) 8YSZ slurries from subsections 6.2.7 and 6.2.8 had a band of NiO/8YSZ painted onto them. Fig. 6.3.7a,b shows the tubes before and after sintering, and it can be seen that the NiO/8YSZ ink has not run down the tubes.

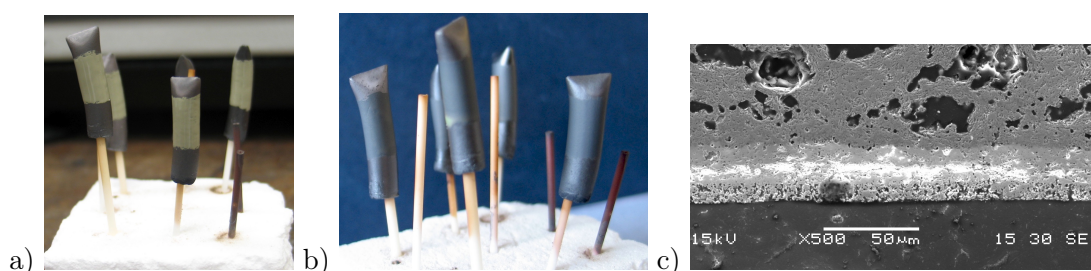


Figure 6.3.7: Recipe M-gra10 LSM tubes with LSM-YSZ coating and either 1xY-7.3G, 2xY-7.3G, 1xY-7.3L, 2xY-7.3L, or 3xY-7.3L 8YSZ slurry coating, painted with NiO/8YSZ screen printing ink a) before sintering, and b) after sintering at 1350 °C, c) cross section showing porous NiO/8YSZ layer at bottom.

Fig. 6.3.7c shows that the NiO/8YSZ layer is about 10 μm thick. NiO/8YSZ ink bands were also painted onto tubes that had the same 8YSZ layers as the previous recipe M-gra10 tubes from subsection 6.2.8 and also another coat of slurry Y-7.3L. The tube that previously had the 1xY-7.3L coating was called 10-1, the 2xY-7.3L tube 10-2, and the 3xY-7.3L tube 10-3. NiO/8YSZ bands were also painted on some tubes that had the same 8YSZ coatings as RSOFC-M-gra10-1, M-gra10-2, and M-gra10-3, and an additional 3 coats of 8YSZ ink, with intermediate sintering steps, as in subsection 6.2.9. The tube that had the 1xY-7.3L coating was named 10-4, the 2xY-7.3L tube was 10-5, and the 3xY-7.3L tube was 10-6. The NiO/8YSZ coating before sintering is shown in fig. 6.3.8. It can be seen that there are some flaws in the 8YSZ, but the NiO/8YSZ coating is smooth and continuous, both before and after sintering.

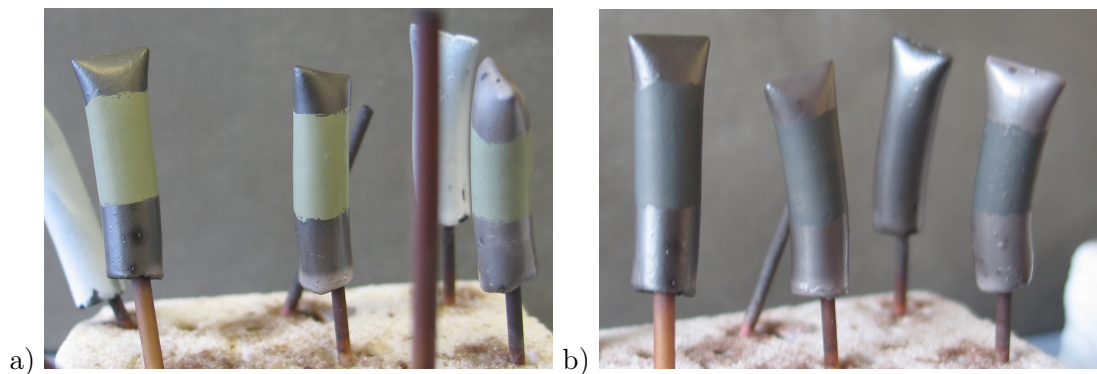


Figure 6.3.8: NiO/8YSZ bands painted on RSOFC-M-gra10-4 (left), M-gra10-5 (middle, and 10-6M-gra (right), a) before sintering, and b) after sintering

RSOFC-M-gra10-7 - M-gra10-9 from subsection 6.2.9 had a NiO/8YSZ band painted on them, and RSOFC-M-gra10-7, and M-gra10-8 looked similar to those observed before. RSOFC M-gra10-10 and M-gra10-12 had the same 8YSZ coatings as M-gra10-9, except one less 8YSZ coating. These tubes were also painted with bands of NiO/8YSZ. It was noted that RSOFC M-gra10-9, M-gra10-10, and M-gra10-12 had longitudinal splits in the electrolyte, and NiO/8YSZ, which may arise from applying and sintering too many electrolyte layers. RSOFC M-gra10-27, M-gra10-28, and M-gra10-29 from subsection 6.2.9 had a band of NiO/8YSZ was painted onto them and sintered, which was smooth and even coating, except for RSOFC-M-gra10-29, because the underlying electrolyte was cracked.

NiO/8YSZ painting on recipe M-gra11 LSM tubes.

NiO/8YSZ bands were painted on various recipe M-gra11 tubes from table 6.2.8, namely M-gra11-1 - M-gra11- 7, M-gra11-10, M-gra11-12 - M-gra11-18. RSOFC-M-gra11-1, M-gra11-2, M-gra11-7, M-gra11-10, and M-gra11-11 were sintered at 1300 °C, and the other cells were sintered at 1350 °C. Fig. 6.3.9 shows some of these cells; the NiO/8YSZ layer looks quite smooth and homogeneous.



Figure 6.3.9: NiO/8YSZ on RSOFC-M-gra11-15 (front left), and M-gra11-18 (front right)

The fuel electrode is painted near the top of the tube, so that the seal at the base is far away from the active area. This allows the seal to be kept cooler than the active area during testing, helping to prevent seal failure. The RSOFC in fig 6.3.9 have a smoother 3YSZ coating than those in fig. 6.3.8, and therefore the NiO/8YSZ fuel electrode is smoother as well, with no flaws or pinholes visible. This NiO/8YSZ layer should have a thickness of about 8 μm , from cross sections of previous tubes. This should be sufficient to provide high electrochemical activity, because most re-

actions happen close to the electrolyte. Nickel also has a very high electronic conductivity, which aids current collection. However, introducing nanoparticles to the layer may boost the performance further. In one study, when nano-sized NiO/8YSZ particles were formed on larger core 8YSZ particles, and then dip coated onto an anode support, to give an ‘anode functional layer’ the performance was increased by a factor of three relative to a cell with no anode functional layer, giving a peak performance of 1.58 W cm^{-2} at 800°C in humidified hydrogen [9]. Therefore, the cell performance is likely to be improved by optimising the NiO/8YSZ microstructure.

6.4 Sealing the reversible SOFC to the support, leak testing

After applying the fuel electrode, a RSOFC is prepared for testing by sealing it to a gas delivery tube. It must be tested to be leak tight before testing in pressurised pure oxygen and hydrogen. Any small leak will cause a flame which burns at about 2000°C , enlarging the hole, and causing the leak to rapidly increase in size in a positive feedback loop.

6.4.1 Sealing to the 316 stainless steel gas delivery pipe and current collector

RSOFC-H-cell4-1 and H-cell4-4 from subsection 6.2.2, were each sealed to a stainless steel gas delivery pipe, which also acts as a current collector, with a alumina-based ceramic adhesive, Ceramabond, and cured at 260°C . When RSOFC-H-cell4-1 was leak tested, the pressure inside it dropped from 170 mbar to 130 mbar in 1 min. RSOFC-H-cell4-4 leaked much more slowly, the pressure dropping from 150 mbar bar to 110 mbar in 4 min.

Identifying leak location with red dye

Fig. 6.4.1 shows where the diluted red food dye has leaked out of the cell. RSOFC-H-cell4-1 has spots of dye on the cell, which come through pinhole leaks in the electrolyte. There are no apparent leaks in RSOFC-H-cell4-4, however, which is probably due to it having twice the electrolyte thickness of RSOFC-H-cell4-1, but there is faint staining of the ceramic sealant, indicating that the seal is partially porous. The ceramic seal on RSOFC-H-cell4-1 is quite stained. Both cells exhibit a leak at the base of the ceramic seal, at the interface between the stainless steel tube and ceramic adhesive. Table 6.4.1 shows the

thermal expansion coefficients of the LSM, 8YSZ, Ceramabond ceramic adhesive, and the 316 stainless steel. The large thermal expansion coefficient mismatch between the ceramic

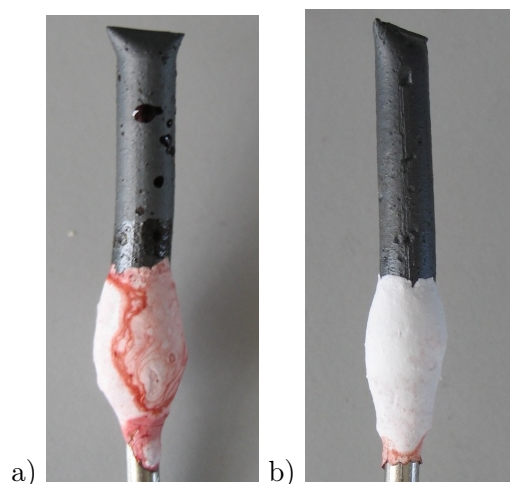


Figure 6.4.1: Red dye leak tests - a) RSOFC-H-cell4-1, and b) RSOFC-H-cell4-4.

sealant and the 316 stainless steel causes the cracking and leakage seen at the base of the ceramic seal. The stainless steel tube expands faster than the ceramic seal as they are heat up, putting it under tensile stress. Ceramics are very strong under compressive stress, but weak under tensile stress, so the seal is likely to fail as seen here.

Material type	Thermal expansion coefficient (p.p.m.K ⁻¹)
LSM [16]	11.8
6YSZ [17]	11
Ceramabond 552 [18]	7.7
316 Stainless steel [19]	16

Table 6.4.1: Thermal expansion coefficients of reversible cell materials, and components used to manifold the cell, presented in the order in which they are connected in the cell. It can be seen that the biggest mismatch between two adjacent materials is the Ceramabond and the 316 stainless steel, almost 10 p.p.m. K⁻¹.

6.4.2 Sealing to an alumina gas delivery tube

As the 316 stainless steel gas delivery tube had a large coefficient of thermal expansion (CTE), an alumina tube was used instead, which has a CTE of about $7 \times 10^{-6} \text{ }^\circ\text{C}^{-1}$ [20]. RSOFC-H-cell4-5 was connected to this tube with Ceramabond. It was leak tested with oxygen and then red dye, and leaked through a large hole in the electrolyte, caused by a pinhole in the LSM tube substrate. However, the ceramic seal did not show any leaks.

RSOFC-M-gra7-2 from subsection 6.3.3 was attached to an alumina support by two layers of Ceramabond, with an intermediate drying step at room temperature. However, while it was curing at 250 °C, the inside of the cell was sealed off from the atmosphere, causing a pressure buildup, which may have created a hole in the electrolyte. There was a slow leak from the cell. Therefore, it is not clear whether this cell had a leaky electrolyte and/or the ceramic seal was leaky. In order to make leak-free cells, RSOFC-gra7-3 - 7-5 from subsection 6.3.3, were manifolded by using Ceramabond to connect them to an alumina tube support., but proved to be leaky. A second layer of Ceramabond was applied, and left to dry but not cured. These cells also leaked, as is shown in leak test 1, table 6.4.2.

Leak identification using soap solution

The location of the leaks was determined by pressurising the cells to 250 mbar - 300 mbar and pouring soapy water over the outside. Very fine bubbles were seen, which indicates a porous ceramic seal. After leak test 1 in table 6.4.2, another layer of Ceramabond diluted with a few drops of water was painted onto the seal, and after air drying, another layer was applied, and it was cured to 260 °C. Leak test 2 in table 6.4.2 was carried out, which shows a reduced leak. Another layer of Ceramabond was applied and cured at 300 °C. Leak test 3 in table 6.4.2 shows that this had a mixed effect on the leaky cells.

Leak test no.	Heat/cool rate ($^{\circ}\text{C min}^{-1}$)	Cure temp. ($^{\circ}\text{C}$)	Start pressure (mbar), change (%)					
			7-3		7-4		7-5	
1	n/a	-	130	-69	100	-100	122	-79
2	2/3	260	123	-35	100	-40	123	-29
3	1/2	300	122	-18	120	-45	122	-32
4	0.5 to 300 $^{\circ}\text{C}$, 3/3	800	-	-	-	-	112	-100
5	0.5 to 300 $^{\circ}\text{C}$, 3/3	800	115	-100	115	-83	115	-83

Table 6.4.2: Sealing and leak test results for recipe M-gra7 reversible SOFC. The curing temperatures refer to the Ceramabond adhesive that was painted onto to the tube and cured before each leak test.

The layer of sealing ceramic was quite thick, so another layer was applied, and it was cured to 800 $^{\circ}\text{C}$, in order to fully sinter all the layers. After this, some large cracks were seen in all the seals. Leak test 4 showed that RSOFC-M-gra7-5 had a large leak from one of the cracks, located by immersing the tube in water and observing the bubbles. Another layer of Ceramabond was applied and cured, but did not seal the cracks, as leak test 5 shows. It is likely that the highly thick layer of Ceramabond will crack during the heating and cooling of the curing cycle. The adhesive is also under tensile stress, because it is on the outside of the tube which expands during heating. Ceramic joints are usually made with compressive seals rather than tensile seals, as ceramics are stronger under compression than tension.

Compressive sealing with MACOR glass ceramic

A MACOR (glass ceramic) ring was used to encapsulate the RSOFC-alumina joint, in order to provide a compressive seal and reduce the area needing to be sealed. Table 6.4.3 shows the leak test results from the cells. After the second leak test, the bubbles in water test showed that cracks were located in the middle of the sealant, and the sealant/MACOR interface.

Leak test no.	Heat/cool rate ($^{\circ}\text{C min}^{-1}$)	Cure temp. ($^{\circ}\text{C}$)/time(h)	Start pressure (mbar), change (%)					
			8-3	Time (s)		8-4	Time (s)	
1	1/2	90/2, 260/2	104.8	-100	10	120	-100	5
2	1/1	90/2, 260/2	60	-100	5	60	-100	5
3	1/1	150/	70	-94	300	70	-100	45
4	n/a	no cure				69.3	-6	300

Table 6.4.3: Sealing and leak test results for RSOFC-M-gra8-3 and M-gra8-4, from sub-section 6.3.4. A MACOR ring was used to seal the cells to the alumina support. A Ceramabond/water mixture was applied before leak test 1, Ceramabond before leak test 2, and Toku sealant before tests 3 and 4. The curing temperatures refer to the ceramic sealant that was painted onto to the tube and cured before each leak test.

They may arise because the MACOR expands, and the sealant shrinks during curing,

causing stresses and cracking at the interface. The Toku ceramic sealant was applied to seal these cracks, but was not fully effective. Table 6.4.4 shows two cells manifolded with the Toku sealant used on its own, with a MACOR ring, and without a MACOR ring. Leakage was 4 times less on the cell with the MACOR ring, than the cell without it. A

Leak test no.	Heat/cool rate (°C min ⁻¹)	Cure temp. °C /time	Start pressure (mbar), change (%)					
			8-5	Time (s)	8-6	Time (s)		
1	2/2	150/2 h	56	-15	300	56	-66	300

Table 6.4.4: Sealing and leak test results for RSOFC-M-gra8-5 and M-gra8-6 from subsection 6.3.4. A MACOR ring was used to seal the cell 5 to the alumina support, but no ring was used for cell 6. The curing temperatures refer to the ceramic adhesive that was painted onto to the tube and cured before each leak test.

cell from LSM recipe M-gra9, named RSOFC-M-gra9-1, from subsection 6.3.4, manifolded with Toku paste, and no MACOR ring, was cured in situ, in the pressure vessel testing jig, by heating at $2^{\circ}\text{C min}^{-1}$ to 175°C , then $3^{\circ}\text{C min}^{-1}$ to the testing temperature.

Two recipe M-gra10 LSM tubes, M-gra10-4 and M-gra10-6, were also manifolded with Toku sealant and leak tested as in table 6.4.5. After the first leak test, more Toku sealant was applied and the

Leak test no.	Heat/cool rate (°C min ⁻¹)	Cure temp. °C /time	Start pressure (mbar), change (%)					
			10-4		Time (s)		10-6	
1	-	no cure	52.5	-12	300	53.9	-24	300
2	2/2	160/15 h	55.3	-4	300	55.3	-14	300

Table 6.4.5: Sealing methods and leak test results for RSOFC-M-gra10-4 and M-gra10-6 from subsection 6.2.9. Toku sealant was applied and dried at room temperature before leak test 1.

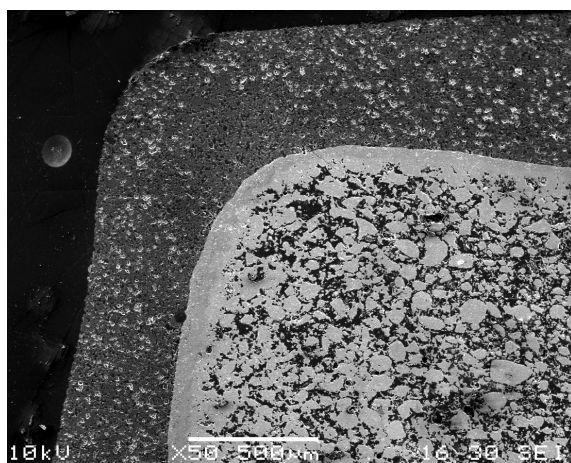


Figure 6.4.2: The sealed end of RSOFC-M-gra10-4 with porous Toku ceramic sealant on the outside.

RSOFC-M-gra10-27 and M-gra10-28 from subsection 6.2.9 were manifolded with Ceramabond sealant, and then Toku sealant as well. They were cured in situ in the pressure vessel testing jig, on the heating ramp of the test. The second leak test shows that the Toku sealant was quite successful at sealing RSOFC-M-gra10-4 and M-gra10-6, fig. 6.4.2 shows that it was quite porous. RSOFC-M-gra10-10 was also manifolded with Toku sealant, and a 10 mm outer diameter, 8 mm inner diameter alumina sealing ring, and cured in situ. However, it was noted that this ring was quite fragile, so a thicker alumina tube with the same bore would be better.

6.5 Current collection and short circuit testing

There are two reversible SOFC current collectors in each cell, which have to function at temperatures of 800 °C - 950 °C. The oxygen electrode current collector is inside the cell, and must be corrosion resistant in the presence of 1 bar - 5 bar pure oxygen. The fuel electrode current collector is on the outside of the cell, so must resist a hydrogen/steam mixture at pressures of 1 bar - 5 bar. Therefore, a noble metal current collector such as silver/gold paste and/or wire current collector was used for the inside of the cell. Silver paste, wires and foil have been used before as current collectors for an SOFC stack operated at lower temperatures, due to the excellent conductivity of silver, and its oxidation resistance [21]. For the cells supported on a steel tube, the steel acts as the connection between the silver paste current collector on the electrode, and the external terminal.

For the current collector on the outside of the cell, a range of metals were tested, including copper, nickel, or silver, in paste, wire or mesh form. After the current collectors were applied, and the cell was sealed, it was tested for electrical short circuits. The resistance of the YSZ at room temperature is about 80 M Ω , assuming a typical RSOFC geometry of an active length of 5 cm, a diameter of 0.6 cm, and an electrolyte thickness of 50 μm , which is an electrolyte area of 9.4 cm². Therefore, the cell resistance should be within an order of magnitude of this value. Table 6.5.1 shows the various RSOFC made, and the current collection used.

Cell ID	Sealing	Current collection (oxygen electrode)	Current collection (fuel electrode)
RSOFC-H-cell4-2	subsection 6.4.1	Ag paste, wire	Ag paste, Cu wire
RSOFC-M-gra8-4	table 6.4.3	Au paste, wire	Ag paste, wire
RSOFC-M-gra8-5	table 6.4.4	Au paste, wire	Ni mesh, paste, Cu wire
RSOFC-M-gra9-1	subsection 6.4.2	Au paste, Au/Ag wire	Ni mesh, paste, Cu wire
RSOFC-M-gra10-4	table 6.4.5	Au paste, Au/Ag wire	Ni mesh, Ag paste, Cu wire
RSOFC-M-gra10-6	table 6.4.5	Au paste, Au/Ag wire	Ni mesh, Cu wire
RSOFC-M-gra10-27	subsection 6.4.2	Au paste, Au/Ag wire	Ni mesh, Cu wire
RSOFC-M-gra10-27	subsection 6.4.2	Au paste, Au/Ag wire	Ni mesh, Cu wire
RSOFC-M-gra10-28	subsection 6.4.2	Au paste, Au/Ag wire	Ni mesh, Cu wire
RSOFC-M-gra10-10	subsection 6.4.2	Au paste, Au wire	Ni mesh, Ni wire

Table 6.5.1: Current collection on various RSOFC.

For RSOFC-H-cell4-4, a combination of copper wire and silver paste was used as in fig. 6.5.1a. It had an electrical short at room temperature, with a resistance of 3.4 Ω between the positive and negative cell terminals. This arises from holes in the electrolyte, penetrated by the silver paste

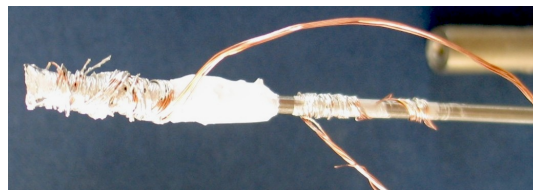


Figure 6.5.1: RSOFC-H-cell4-4 copper current collecting wires, with silver paste.

which makes a short circuit, possibly through some LSM.

Current collection with silver and nickel

A pure silver current collector was used for RSOFC-M-gra8-4 in table 6.5.1. No electrical short circuit was measured across this cell, or any of the subsequent ones in the table, before testing. RSOFC-M-gra8-4 had a leak, which suggests that there were holes in the 8YSZ electrolyte. If this is so, the silver paste is likely to fill them, especially during testing, because silver has a high vapour pressure, and will start to evaporate and flow below its melting point, at temperatures such as 900 °C. Nickel metal does not suffer from this problem as it has a much higher melting point, so is better suited as a current collector than silver in this case.



Figure 6.5.2: RSOFC with nickel mesh current collector, nickel paste, and a copper wire current collector.

Fig. 6.5.2 shows cell 5 from table 6.5.1, which had a nickel mesh wound around it, and was painted with a nickel metal slurry. However, it was seen that the nickel powder falls off the cell easily, so it is not suitable for making contact between the mesh and the fuel electrode. On the oxygen side, a gold wire was used inside the cell. RSOFC-M-gra10-4 in fig. 6.5.3a had a nickel mesh wrapped around it, and silver paste was

painted onto the mesh, so that it made contact with the cell. RSOFC-M-gra10-6 from table 6.5.1, also made with a Ni mesh, is shown in fig. 6.5.3b. No metal paste was used on this cell. RSOFC-M-gra10-27 and M-gra10-28 were manifolded in the same manner as RSOFC-M-gra10-6. RSOFC-M-gra10-10 was manifolded with a Ni mesh, and a Ni wire from the cell, in order that it could be heated up in air. A copper wire would oxidise at the testing temperatures, whereas nickel is more resilient. A Ni foil has been successfully demonstrated as a current collector for a flat planar cell [22].

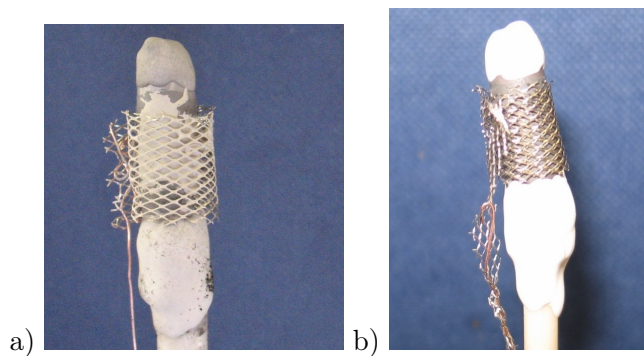


Figure 6.5.3: a) RSOFC-M-gra10-4 with a Ni mesh current collector and silver paste on the fuel electrode, and b) RSOFC-M-gra10-6 with a Ni mesh current collector on the fuel electrode, and a copper wire.

6.6 Conclusions

LSM-YSZ painting

The LSM-YSZ layer functions as a composite electrode, which improves the electrochemical activity of the cell for the oxygen reduction reaction. It also provides a suitable substrate, i.e. one with small homogeneous pores, for YSZ slurry dip-coating or ink painting, that does not allow the YSZ slurry/ink to soak into the LSM support. The LSM-YSZ layer in tubes such as RSOFC-M-gra11-11, M-gra-11-12 is quite porous and distinct, because it was pre-coated and sintered before the YSZ slurry/ink was applied. This LSM-YSZ electrode should give a good electrochemical performance as it has many triple phase boundaries and a porous microstructure. However, for tubes such as RSOFC-M-gra10-27, M-gra10-28, which did not have a pre-coated and sintered LSM-YSZ layer, the SEM cross section shows a dense electrolyte, and between it and the LSM substrate, a fairly dense LSM-YSZ layer. This is produced when the 3-YSZ-C ink soaked into the LSM support. This layer might be too dense to allow easy diffusion of oxygen through it to the active sites in the electrode, so might give a poor electrochemical performance.

YSZ electrolyte production.

8YSZ dip-coating slurries Y-7.4A-Y-7.3E were made with a 8YSZ (Tosoh) powder. However, as the first LSM tubes were made with a cellulose pore former and had large flaws, these electrolytes also had flaws. When the same dip-coating slurries were used on LSM tubes made with a graphite pore former, sufficiently thick electrolyte layers were achieved, but these had only 87% density. Therefore, 8YSZ slurry Y-3.4B2 was used, which had a lower solids loading, to try to achieve a higher density layer. However, this was unsuccessful, and the pre-coated LSM-YSZ layer was seen to penetrate most of the way through the 8YSZ electrolyte, because the dip-coating slurry soaked into it.

Therefore, dip coating slurries Y-3.4F and Y-7.3G with 8YSZ (Pi-Kem) were used to dip the tubes several times, with an increased sintering temperature of 1400 °C. However, surface cracking on the electrolyte was observed, seemingly occurring in the drying/binder burnout phase, which could not be rectified by varying the solids loading in the slurry, or by applying multiple dip-coats. The slurry recipe was varied to reduce the levels of organic components, making slurries H, Y-10.0I, Y-7.5J, and Y-4.9K with 3YSZ (Tosoh) powder, but these were poorly dispersed.

An 8YSZ (Pi-Kem) screen printing ink was painted onto the cells, which had a much higher solids loading than the slurry. The layers produced were thick enough, but not dense enough. A 3YSZ-C electrolyte ink was then tried, and produced highly dense electrolytes with very few flaws. This was attributed to the particle size distribution of this ink, which showed that the ceramic powder was well-dispersed, with a smaller primary particle size than the 8YSZ ink. Therefore, a dense electrolyte can be produced with very few flaws, with or without an LSM-YSZ pre-coating, after just 2 painted coats of ink, and a single sintering step.

NiO/8YSZ dip coating

The initial slurries used to dip-coat the NiO/8YSZ fuel electrode, had a solids loading that was too low, so the layers produced were only $\sim 4 \mu\text{m}$ thick. A slurry with a higher solids loading gave a layer about $7 \mu\text{m}$ - $10 \mu\text{m}$ thick. Subsequent NiO/8YSZ layers were applied in a band shape around the tube, by painting on an undiluted NiO/8YSZ screen printing ink, giving a thickness of about $8 \mu\text{m}$. A modelling study on SOFC electrodes has shown that almost all the electrochemical reactions in the electrode take place in a very narrow region near the electrolyte, so this should be sufficiently thick [23]. The quality of the layer was directly affected by the smoothness of the underlying YSZ electrolyte.

Sealing and leak testing

Initially, a 316 stainless steel tube was used as a gas delivery tube and current collector for the oxygen electrode side of the cell, sealed to it by Ceramabond or Toku ceramic sealant. However, the coefficient of thermal expansion mismatch between the steel and the sealant caused cracking at the interface when it was cured. Therefore, an alumina gas support tube was used instead, with a gold wire current collector on the oxygen side of the cell, but Ceramabond and Toku seals were leaky. The leaks were mostly at sealant/alumina interfaces for the Ceramabond sealant, and through the body of the sealant for the Toku sealant, which was quite porous. MACOR glass ceramic or alumina rings were used to encapsulate the cell-support joint, thus reducing the cross sectional area to be sealed, and making the seal a compressive joint, rather than a tensile joint. This reduced the rate of gas leakage from the cells, but did not eliminate it. When the cells were cured at high temperatures such as 800°C , the leaks became quite severe.

Current collection and short circuit testing

On the oxygen electrode side of the cell, gold paste and wire was used almost exclusively. On the fuel electrode side of the cell, silver, copper, and nickel were used. Silver and copper reacted together to form an alloy. Pure silver wire and paste caused a short circuit in one cell, because the liquid paste penetrated holes in the electrolyte. A nickel mesh and silver paste was then used. When heated to testing temperatures, silver has a high vapour pressure, so diffuses through any holes in the electrolyte, causing a short circuit. Therefore, nickel mesh and powder was used instead, and then for the last cells made, just nickel mesh. This assumes that the lateral conductivity of the fuel electrode is sufficiently good that only a few points of contact between the mesh and the electrode are necessary for adequate current collection.

A RSOFC has been produced, that has a porous and stable LSM support, which does not change structure when subjected to repeated sintering steps at 1350°C . It has a fairly dense LSM-YSZ electrode layer, an almost fully dense 3YSZ electrolyte with very few flaws, and a NiO/8YSZ fuel electrode which is sufficiently thick to have good electrical conductivity. The sealing methods used did not successfully totally seal the cell, but leakage rates were reduced by modifying the sealing method.

References

- [1] P. Lenormand, D. Caravaca, C. Laberty-Robert, F. Ansart, *J. Eur. Ceram. Soc.*, 2005, **25**, 2463–2646.
- [2] T. L. Nguyen, T. Honda, T. Kato, Y. Iimura, K. Kato, A. Negishi, K. Nozaki, M. Shiono, A. Kobayashi, K. Hosoda, Z. Cai, M. Dokiya, *J. Electrochem. Soc.*, 2004, **151**, A1230–A1235.
- [3] Z. Wang, K. Sun, S. Shen, N. Zhang, J. Qiao, P. Xu, *J. Membrane Sci.*, 2008, **320**, 500–504.
- [4] J. T. S. Irvine, F. G. E. Jones, P. A. Connor, *Improvements in Solid Oxide Fuel Cells and related devices*, Patent no. wo/2003/036746, The University of St Andrews, College Gate, North Street, St Andrews KY16 9AJ, 2003.
- [5] H. Yokokawa, *Annu. Rev. Mater. Res.*, 2003, **33**, 581–610.
- [6] M. Gaudon, C. Laberty-Robert, F. Ansart, P. Stevens, *J. Eur. Ceram. Soc.*, 2006, **26**, 3153–3160.
- [7] Q. Zhu, B. Fan, *Solid State Ionics*, 2005, **176**, 889–894.
- [8] M. G. Pontin, F. F. Lange, *J. Am. Ceram. Soc.*, 2005, **88**, 2945–2948.
- [9] D. Yoon, J.-J. Lee, H.-G. Park, S.-H. Hyun, *J. Electrochem. Soc.*, 2010, **157**, B455–B462.
- [10] W. Rasband, software, ImageJ version 1.44i, National Institutes of Health, USA, 2010.
- [11] A. R. Sahu, A. Ghosh, A. K. Suri, *Ceram. Int.*, 2009, **35**, 2493–2497.
- [12] J. Guan, N. Minh, B. Ramamurthi, J. Rudd, J. K. Hong, P. Riley, D. Weng, *High Performance Flexible Reversible Solid Oxide Fuel Cell*, Tech. Rep., GE Global Research Center, 19310 Pacific Gateway Drive, Torrance, CA 90502, 2006.
- [13] C. Xia, S. Zha, W. Yang, R. Peng, D. Peng, G. Meng, *Solid State Ionics*, 2000, **133**, 287–294.
- [14] M. J. Jørgensen, S. Primdahl, C. Bagger, M. Mogensen, *Solid State Ionics*, 2001, **139**, 1–11.

- [15] Last checked 9th June 2011. http://www.tosoh.com/Products/e+basic_grades.htm.
- [16] F. Tietz, I. A. Raj, M. Zahid, D. Stöver, *Solid State Ionics*, 2006, **177**, 1753–1756.
- [17] K. S. Mazdiasni, C. T. Lynch, J. S. Smith II, *J. Am. Ceram. Soc.*, 1967, **50**, 532–537.
- [18] Aremco Products, Inc., *High temperature ceramic adhesives & pastes*, Technical bulletin A2, Aremco, P.O. Box 517, 707-B Executive Blvd., Valley Cottage, NY 10989, 2009.
- [19] S. Molin, M. Gazda, B. Kusz, P. Jasinski, *J. Eur. Ceram. Soc.*, 2009, **29**, 757–762.
- [20] M. C. Tucker, C. P. Jacobson, L. C. De Jonghe, S. J. Visco, *J. Power Sources*, 2006, **160**, 1049–1057.
- [21] Y. Funahashi, T. Shimamori, T. Suzuki, Y. Fujishiro, M. Awano, *Fuel Cells*, 2009, 711–716.
- [22] A. Hauch, S. H. Jensen, S. Ramousse, M. Mogensen, *J. Electrochem. Soc.*, 2006, **153**, A1741–A1747.
- [23] L. C. R. Schneider, C. L. Martin, Y. Bultel, , D. Bouvard, E. Siebert, *Electrochim. Acta*, 2006, **52**, 314–324.

Chapter 7

Electrochemical testing of reversible SOFC

7.1 Introduction

The RSOFC that were made were also tested in order to determine their electrochemical performance. This is normally done by recording impedance spectra and I/V curves. However, I/V curves can only be measured if the cell and the seals which connect them to the gas delivery tubes are relatively leak free, otherwise a good open circuit voltage (OCV) cannot be obtained. Leaks allow mixing of the hydrogen and oxygen gases, which significantly reduces the cell voltage, creates additional heat, and if they are sufficiently large, prevents the NiO/YSZ electrode from reducing to Ni metal. In this case, the cell resistance may be very high, and thus the cell performance will be very low.

7.1.1 Summary of all tests

Table 7.1.1 summarises all of the tubular RSOFC tests that were carried out and their outcomes. All cells were tested for electrical short circuits before and after testing, but only RSOFC-H-cell4-4 had a short circuit before testing. The expected resistance of the YSZ electrolyte, calculated from reference values [1], at room temperature should be $\sim 50\text{ M}\Omega$, assuming a tube diameter of 0.65 cm, a cell active area length of 3 cm, and a YSZ thickness of 20 μm .

RSOFC test no.	RSOFC no.	Comments	Cell resistance after testing
099	4-H-cell4	resistance across cell 3.4 Ω before test	1 Ω - 10 Ω
100	M-gra8-4	One of the contact wires was severed during test	25 Ω
101	M-gra8-5	OCV was 0.004 V at 850 $^{\circ}\text{C}$	70 Ω
102	M-gra9-1	OCV was 0.01 V at 800 $^{\circ}\text{C}$	26 Ω
103	M-gra10-4	OCV was 0.83 V at 400 $^{\circ}\text{C}$, then dropped rapidly	85 k Ω
104	M-gra10-6	OCV <0.05 V at 700 $^{\circ}\text{C}$	163 k Ω
105	M-gra10-27	NiO unreduced after test	>2 M Ω
106	M-gra10-27	Cell resistance was 56 Ω at 580 $^{\circ}\text{C}$	*
107	M-gra10-28	OCV was 0.4 V at 580 $^{\circ}\text{C}$, then dropped rapidly	>2 M Ω
108	M-gra10-10	OCV was 0.7 V at 700 $^{\circ}\text{C}$, then dropped rapidly	>2 M Ω

Table 7.1.1: Testing of RSOFC, with outcomes of each test (*not measured). The cell resistance is measured from the oxygen electrode current collection wire to the fuel electrode current collection wire. Resistances >2 M Ω could not be measured with the instrument used.

7.2 Testing RSOFC with dip-coated YSZ electrolytes

Testing RSOFC-H-cell4-4, T099

RSOFC-H-cell4-4 had a copper wire current collector wound around the cell, with silver paste painted over it to contact the fuel electrode. It had an electrical short circuit across it at room temperature before testing, probably because the silver paste current collector had penetrated holes in the YSZ electrolyte. The presence of the holes in the YSZ can be explained by considering that the LSM support tube for this cell was extruded with a cellulose pore former, so there were large holes in the tube, and therefore in the YSZ electrolyte.



Figure 7.2.1: RSOFC-H-cell4-4 after testing. A copper-silver alloy is present on the cell, which arose as the copper current collection wire on the fuel side formed a eutectic mixture with the silver paste painted on it.

Nevertheless, the cell was heated at 0.8 $^{\circ}\text{C min}^{-1}$ to 802 $^{\circ}\text{C}$, with flowing 5% H_2/Ar on the outside. At this point the electrical resistance across the cell was determined to be $\sim 3 \Omega$, and the open circuit voltage (OCV) was 0.035 V. The cell was heated to 900 $^{\circ}\text{C}$, and after some time, electrical contact across the cell was lost. This is because the silver paste and copper wire on the cell surface formed a eutectic melt, according to the Ag-Cu phase diagram [2]. Therefore, these two metals should not be used

in conjunction with each other in a reducing atmosphere at these temperatures, because it can be seen in fig. 7.2.1 that the contact wires for the fuel electrode have completely

melted, which explains the loss of electrical contact at 900 °C. After testing, the resistance across the cell was measured to be in the range 1 Ω - 10 Ω . It was also noted that the 316 stainless steel support/current collector had oxidised near the cell, due to the high temperature reached during testing. Therefore, all subsequent cells were made with an alumina gas delivery tube, and noble metal paste was painted inside the cell, and a noble metal wire was inserted inside the cell and alumina tube, to act as the oxygen electrode current collector.

Testing RSOFC-M-gra8-4, T100

RSOFC-M-gra8-4 and all subsequent cells had an LSM substrate that was made with a graphite pore former, so there were no large holes in the substrate. This greatly improved the homogeneity of the YSZ electrolyte. No electrical short-circuit was found across the cell in fig. 7.2.2 before testing, so the silver paste had not penetrated the electrolyte. The cell was heated to 150 °C at 3 °C min⁻¹, then to 850 °C. An impedance spectrum was measured, which showed an open circuit. After cooling, a break was found in the silver wire current collector on the outside of the cell, where it had been trapped between the cell MACOR ring and the inner wall of the cylindrical testing furnace. An electrical short circuit of 25 Ω was found across the cell, so either the silver must have penetrated the electrolyte during testing, or else the NiO/YSZ penetrated the electrolyte during cell fabrication. Therefore, this test failed because the electrolyte is not totally dense.



Figure 7.2.2: RSOFC-M-gra8-4 before testing. A silver wire current collector and silver paste were used on the fuel electrode on the cell outer surface. A MACOR glass-ceramic ring was used at joint between the cell and the alumina tube, to improve sealing.

Testing RSOFC-M-gra8-5 and M-gra9-1, T101, T102

RSOFC-M-gra8-5 was heated to 850 °C at 3 °C min⁻¹, and then the OCV was measured to be 0.004 V, and the cell resistance was \sim 5 Ω , and after cooling to room temperature, 70 Ω . Evidently, the NiO/YSZ had penetrated through the YSZ electrolyte as the cell was being made, and when the nickel oxide was reduced to nickel during testing, a short circuit was observed. No silver paste was used on this cell. Fig. 7.2.3 shows the cell after testing, where it can be seen that some of the nickel current collecting powder had fallen off the nickel mesh, and coated the MACOR ring, making it a grey colour. A similar test was conducted on RSOFC-M-gra9-1, and a short-circuit was also observed on this cell after testing. Flaws or pinholes in the YSZ electrolyte which allow the NiO/YSZ fuel electrode to penetrate it and contact the LSM substrate, are the likely cause of the short circuits seen in these tests. Therefore, more work was done on the YSZ electrolyte, to improve its homogeneity, thickness, and density.

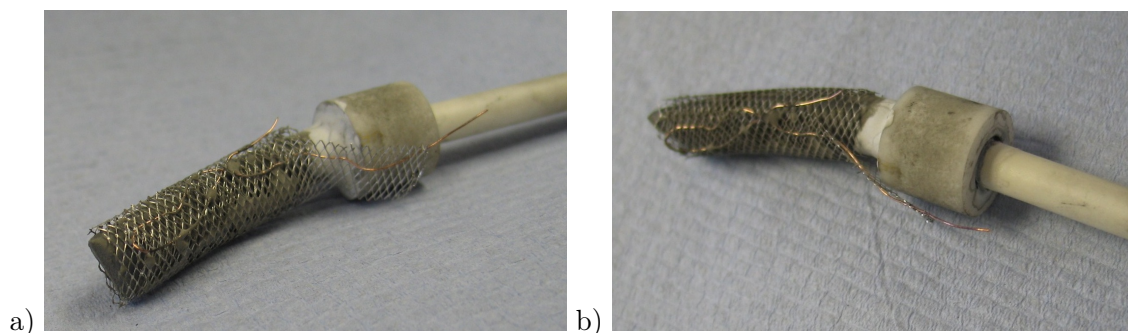


Figure 7.2.3: RSOFC-M-gra8-5 after testing. A Ni mesh, with a Ni paste current collector and a copper current collection wire were used on the fuel electrode side.

7.3 Testing RSOFC with painted YSZ electrolytes

Testing RSOFC-M-gra10-4, T103

When RSOFC-M-gra10-4 was leak tested with oxygen, a 4% pressure drop over 5 min from a starting pressure of 0.053 bar was measured, which was the lowest pre-test leakage of any cell yet tested. Fig. 7.3.1 shows the OCV and oxygen pressure as the cell was heated up at $2\text{ }^{\circ}\text{C min}^{-1}$ to $700\text{ }^{\circ}\text{C}$ in flowing 5% H_2/Ar . Initially, the OCV increased rapidly, to just under 0.8 V at $350\text{ }^{\circ}\text{C}$ as the nickel oxide reduced to nickel, then it stagnated, before starting to increase again to a maximum of 0.83 V. These reduction temperatures are consistent with other studies of the reduction of nickel oxide, which found that it reduced to nickel at temperatures of $150\text{ }^{\circ}\text{C}$ - $300\text{ }^{\circ}\text{C}$ in pure hydrogen [3].

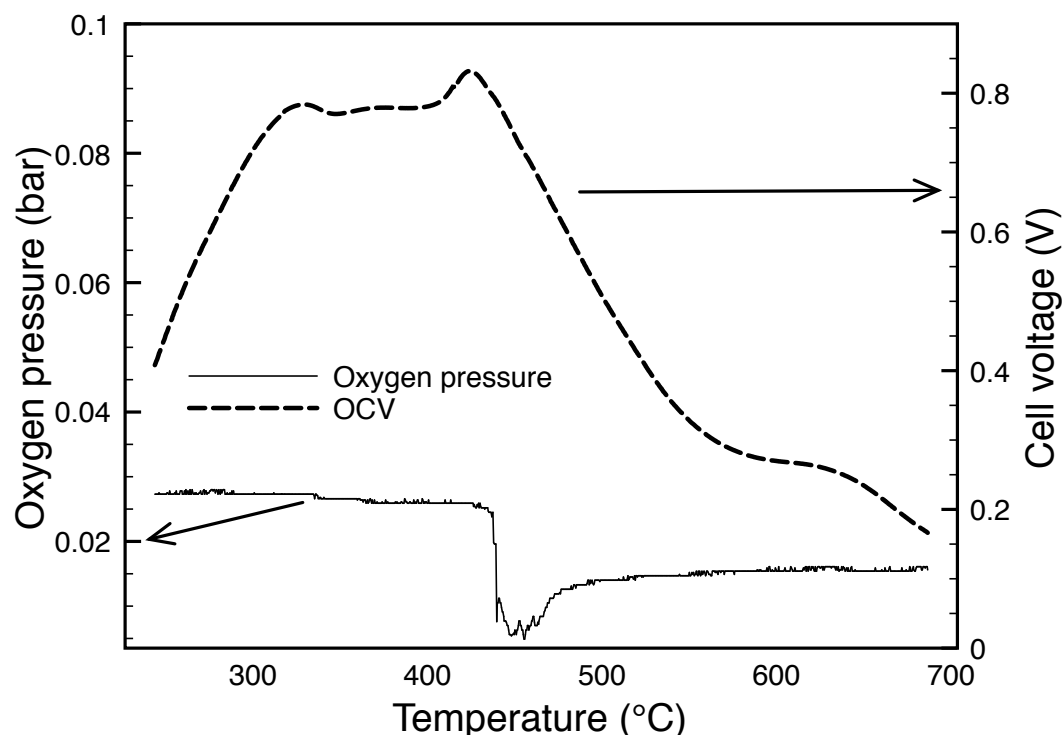


Figure 7.3.1: Temperature and oxygen pressure for RSOFC-M-gra10-4, during heating ramp of test 103, at $2\text{ }^{\circ}\text{C min}^{-1}$. Pressures are relative to atmospheric pressure.

At 440 °C, the OCV started dropping rapidly, in conjunction with a sharp fall in the oxygen pressure inside the cell to near zero. This is probably because a crack in the cell or sealant opened up at this temperature, allowing the fixed volume of oxygen inside the cell and oxygen storage cylinder to escape. When this occurred, a slow flow of oxygen was started into the cell, so the oxygen pressure rose again in fig. 7.3.1. However, this did not prevent the decline in OCV. The resistance across the cell at 700 °C was 300 Ω , and at room temperature, was 85 k Ω . This suggests that there may be a small pinhole in the electrolyte, where some partially reduced NiO/YSZ is contacting the LSM substrate, or else a region of electrolyte which is very thin, so the LSM-YSZ layer fully penetrates it and touches the Ni-YSZ fuel electrode.

Fig. 7.3.2a shows the cell after testing, which shows that the silver paste had coated the cell surface through the nickel mesh.

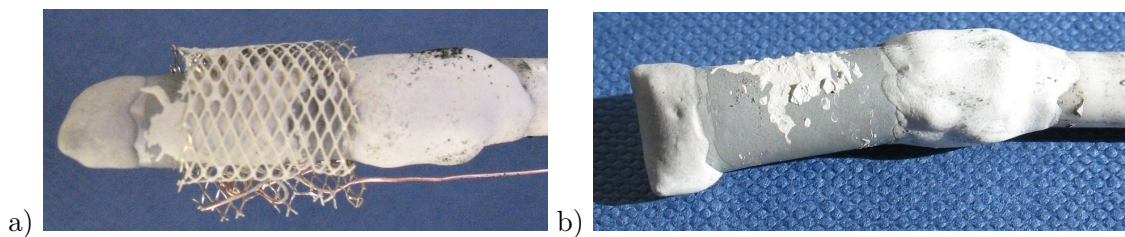


Figure 7.3.2: RSOFC-M-gra10-4, after RSOFC test 103, a) cell after testing and b) with Ni mesh removed.

Fig. 7.3.2b shows the fuel electrode surface after the nickel mesh has been removed. The light gray colour is silver, and the dark grey colour is likely to be reduced nickel, as a resistance of 2 Ω over a 1 cm distance was measured on the dark grey surface. Therefore, the silver paste on the surface of the cell, which functions to contact the mesh to the fuel electrode, may not be necessary. If it diffuses through holes in the YSZ electrolyte and short circuits the cell, it may even harm performance. Fig. 7.3.3 shows a cross section of RSOFC-M-gra10-4 after testing. The cracks in the YSZ electrolyte in images a), c) and d) may have been produced by thermal stresses during testing. It can also be seen that although the electrolyte is 20 μm to 30 μm thick, it is not entirely dense. In image a), two distinct layers can be seen below the electrolyte.

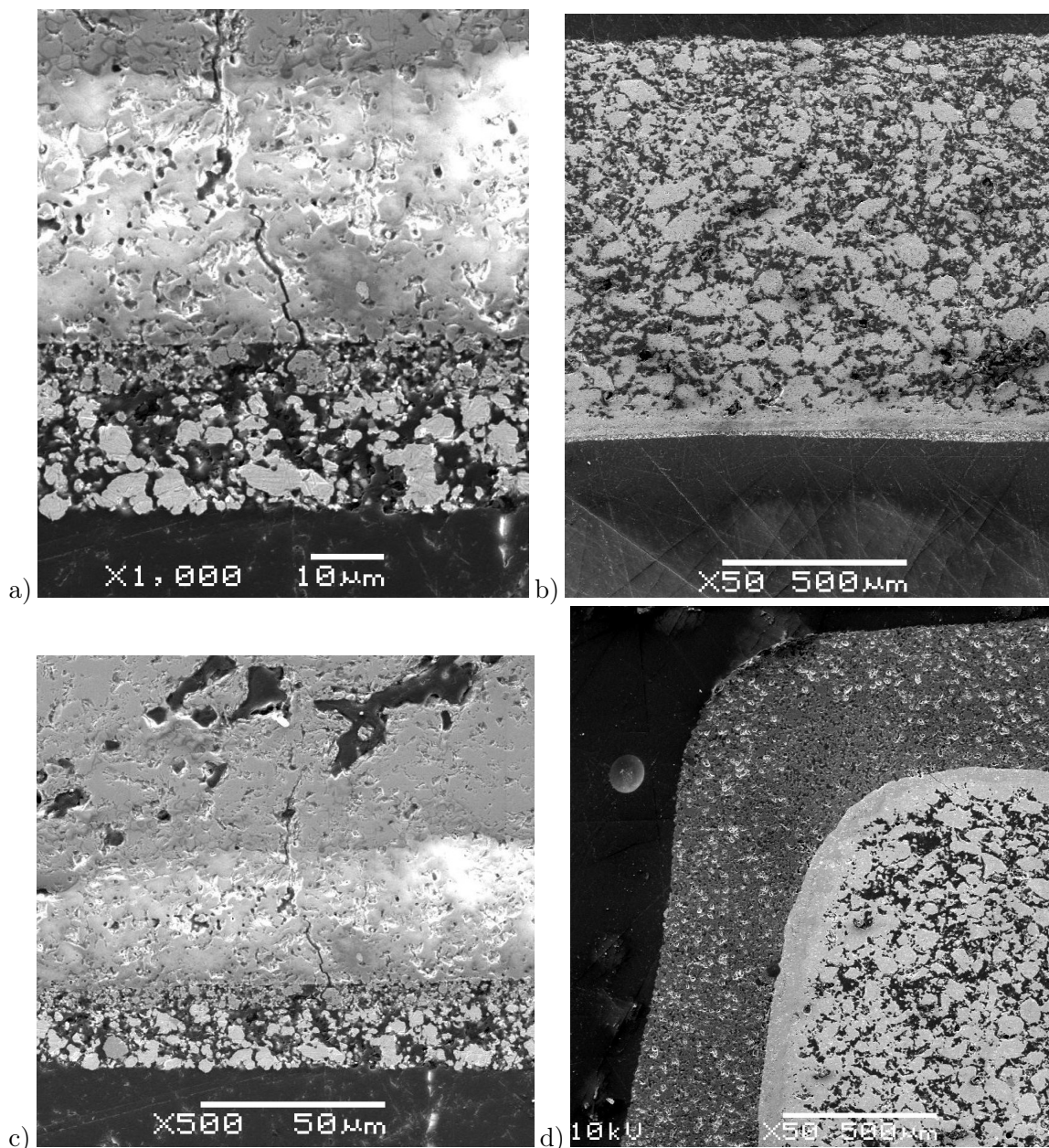


Figure 7.3.3: SEM after RSOFC test 103 analysis of RSOFC-M-gra10-4, a) a crack in the YSZ electrolyte, b) the thickness of the cell, c) another crack in the YSZ electrolyte, and d) the end of the tube. A small crack can be seen on the top horizontal part of the electrolyte. The thick porous layer on the outside of the tube is the Toku ceramic cement.

Fig. 7.3.4 shows an EDX measurement on this area, which shows that there is a $10\text{ }\mu\text{m}$ thick Ni/YSZ layer, and a $20\text{ }\mu\text{m}$ thick silver paste layer. Both layers are porous, so the fuel electrode microstructure should not hinder gas diffusion. A leak test of the cell in situ after the test, showed a pressure drop of 100% from a starting pressure of 0.0546 bar in 1 min. Therefore, the post-test cell is much more leaky than the pre-test cell. This is either due to the cracks seen in the electrolyte in fig. 7.3.3, a crack in the ceramic sealant which developed during testing, or that the sealant became more porous during testing. It can also be seen that the Toku ceramic sealant, which is the outer layer in image d), is quite porous.

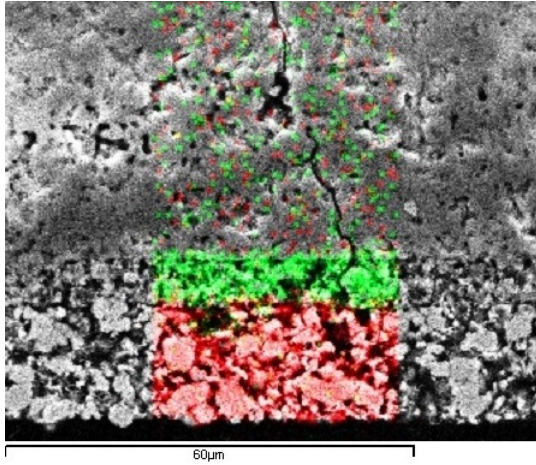


Figure 7.3.4: EDX measurement on the same area as fig. 7.3.3a, with Ag (red) and Ni (green), showing the locations of the silver and nickel layers.

Testing RSOFC-M-gra10-6, T104

RSOFC-M-gra10-6 had a nickel mesh current collector, but no silver paste was applied, to minimise the chance of a short circuit during testing. A leak test in situ before heating the cell, showed that it had a 4% pressure drop over 5 min from a starting pressure of 0.0602 bar. This cell was tested on a modified setup that allowed a continuous flow of oxygen past the oxygen electrode side. At 700 °C, the OCV across the cell was <0.05 V, and the cell resistance was 47 Ω . After cooling down, the cell resistance was 163 k Ω , which is a similar order of magnitude to the last test. An in situ leak test from 0.0623 bar gave a 100% pressure drop over 10 s. A red dye test in fig. 7.3.5 shows leak locations.

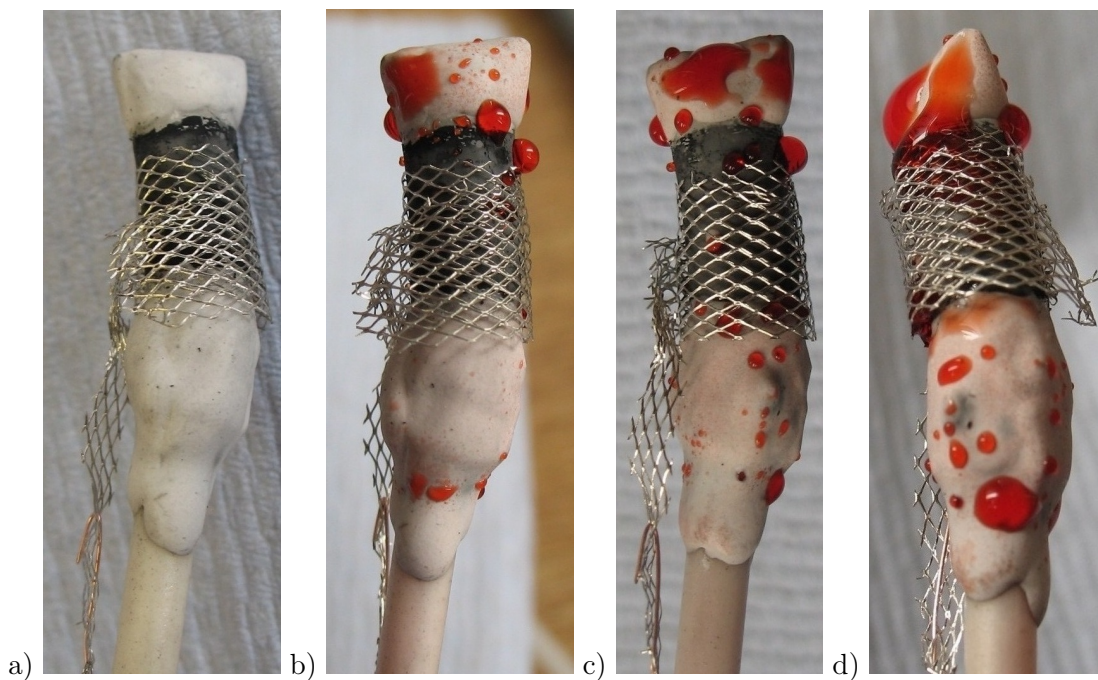


Figure 7.3.5: RSOFC-M-gra10-6 after test 104, leak testing with red dye, a) cell before dye was inserted, b) after 30 s, c) after 1 min., and d) after 2 min.

Image a) shows the cell before the dye was applied. Image b) shows the first sites of dye leakage, which are mainly on the white Toku ceramic sealant, at the top of the cell, although some small leaks can be seen through the active area of the cell, under the mesh. These can be seen more clearly in image c), and image d) shows that the seal at the base of the cell is also leaking. Therefore, the YSZ electrolyte, and the seal, are both leaking. When the resistance across the fuel electrode surface was measured, it was $>2\text{ M}\Omega$, showing that the NiO/YSZ had not reduced to Ni during testing. This explains the large cell resistance seen at room temperature after testing. It is evident that the testing process either caused leaks in the YSZ electrolyte, the seal, or both, as the leakage after testing was much greater than before testing.

Testing of RSOFC-M-gra10-27, T105

A slow ramp rate of $0.4\text{ }^{\circ}\text{C min}^{-1}$ was used to heat up this cell, to cure the Ceramabond ceramic seal in situ, and to avoid cracking the seal by heating it too fast. A slow flow of 5% H_2/Ar was used during the heating ramp. However, a OCV of $<0.05\text{ V}$ was measured for this cell at $700\text{ }^{\circ}\text{C}$, so it was cooled at a rate of $0.5\text{ }^{\circ}\text{C min}^{-1}$ to room temperature. The silicone sealant at the base of the cell was found to have a hole in it, and the resistance of the cell surface was $>2\text{ M}\Omega$, showing that the nickel oxide in the fuel electrode was not reduced. When the silicone sealant was removed, and only the cell and alumina support were leak tested, there was a 100% pressure drop in 25 s, from a starting pressure of 0.0539 bar. It was then leak tested with red dye, as in fig. 7.3.6. It appears that the sealant itself is not porous, but it cracks at the cell|sealant and sealant|alumina interfaces, even when low heating and cooling rates were used.

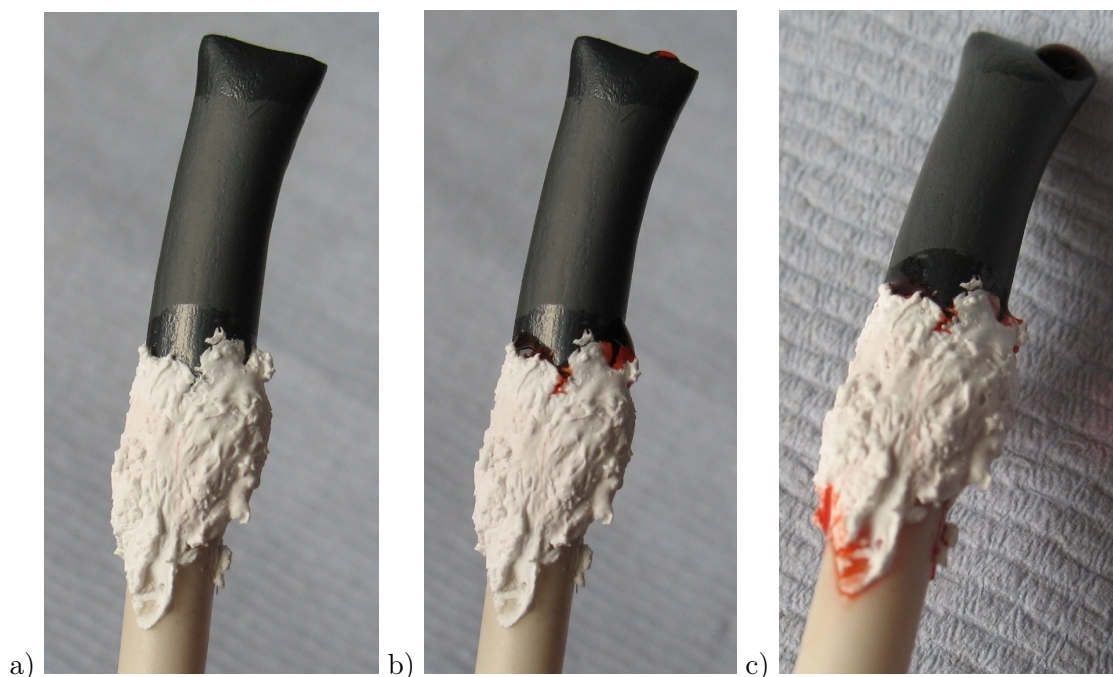


Figure 7.3.6: Red dye leak test on RSOFC-M-gra10-27 from test 105, a) pre-test, b) after 30 seconds, and c) after about 1 min.

Ceramabond 552 is alumina based, and has a thermal expansion coefficient (TEC) of 7.7×10^{-6} p.p.m. K^{-1} [4], YSZ has a TEC of 10.5×10^{-6} p.p.m. K^{-1} , and dense LSM has an TEC of $\sim 12 \times 10^{-6}$ p.p.m. K^{-1} [5], though in the cell, this would be less as the LSM is quite porous [6]. Therefore, there is a thermal expansion mismatch between the RSOFC and the sealant, which causes the cracking seen. The resistance across the cell was >2 M Ω at room temperature, so there was no short-circuit in the cell after testing, so the low OCV is due to gas crossover leakage.

Testing RSOFC-M-gra10-27 again, T106

RSOFC-10-M-gra27 was tested again after application of Toku sealant, which was cured in situ as the cell was heated up at 0.4 $^{\circ}C$ min^{-1} during the test. The OCV at 580 $^{\circ}C$ was 0.07 V, and the cell resistance was 56 Ω . The temperature was increased to 800 $^{\circ}C$, the cell resistance was measured to be about 60 Ω , and the OCV was 0.0012 V, which shows that there was a large leak during testing. The increase in cell resistance with temperature suggests metallic conduction, which suggests that the high resistance arises from the nickel metal. An impedance spectrum was recorded and is shown in fig. 7.3.7.

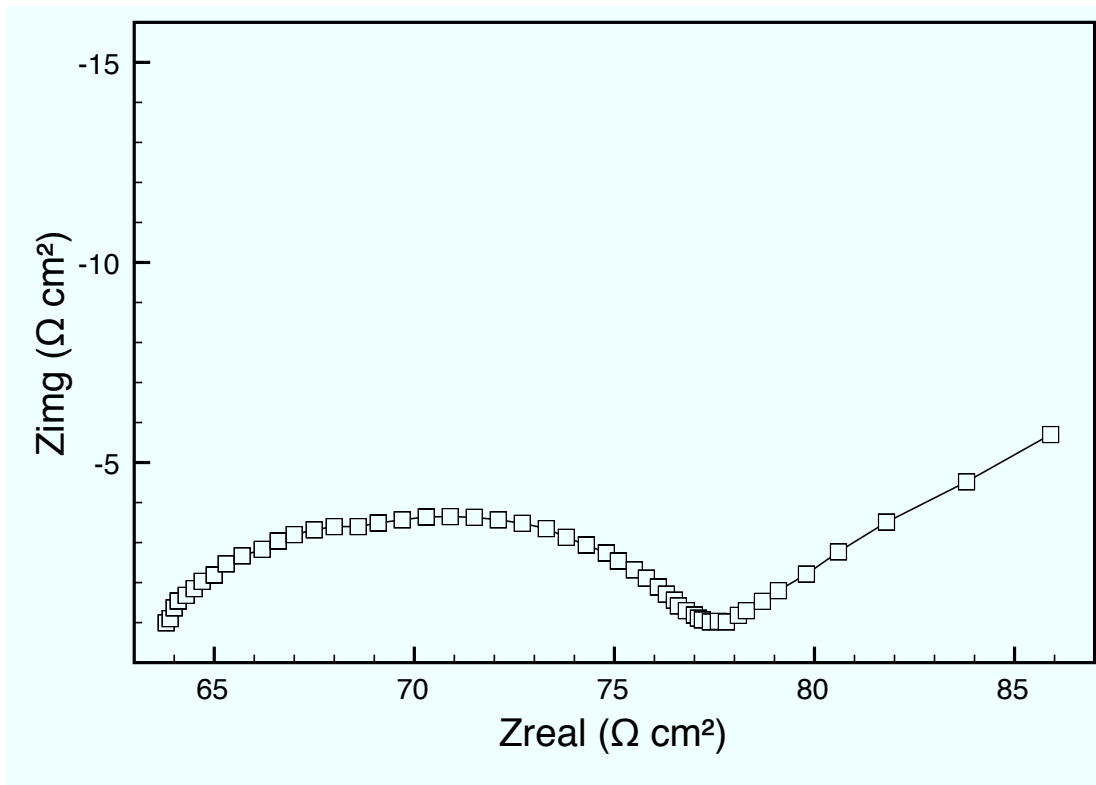


Figure 7.3.7: RSOFC test 106, RSOFC-M-gra10-27: impedance spectrum: OCV 1.2 mV at 800 $^{\circ}C$.

It can be seen that there are at least several features in the impedance spectrum. Firstly, the feature at higher frequency, between 64 Ω and 77 Ω looks like two or three overlapping arcs, the largest of which has a peak frequency of 1607 Hz. At low frequency, there is also a spike which seems to be a diffusion element. It is not clear which arcs are related to the oxygen electrode, and which arcs are related to the fuel electrode, and without

other measurements to compare the arcs with, it is difficult to deconvolute the impedance. In other studies, two or three arcs have been seen in impedance spectra for the Ni-YSZ electrode [7], and also several arcs for the LSM-YSZ electrode [8]. The series resistance is about $63\ \Omega$, which is much higher than would be expected for a high performance cell. The cell is wired into the test rig with four wires, which join near the base of the jig to give two wires. Therefore, the series resistance, going from the oxygen side to the fuel side of the cell, arises from the gold current collection wire, the resistance of the gold paste on the oxygen side, the LSM tube, the YSZ electrolyte, and the NiO/YSZ fuel electrode, nickel mesh, nickel current collection wire, and any contact resistances.

The resistance of the wires, nickel mesh, electrolyte and fuel electrode combined are likely to be only a few ohms, so it is likely that the high resistance comes from a contact resistance between the nickel mesh and the fuel electrode - poor current collection. In this case, most of the electrode would be inactive, which would also increase its polarisation resistance, though several arcs would still be seen, which is consistent with the spectrum recorded, in fig. 7.3.7. If there is any reaction between the LSM and YSZ, resistive phases such as lanthanum or strontium zirconates can be formed [9]. However, the composition of LSM used was 5% A-site deficient, which is known to reduce reactions with YSZ [10]. The cell was cooled at $0.3\ ^\circ\text{C}\ \text{min}^{-1}$ to room temperature, and is shown in fig. 7.3.8.

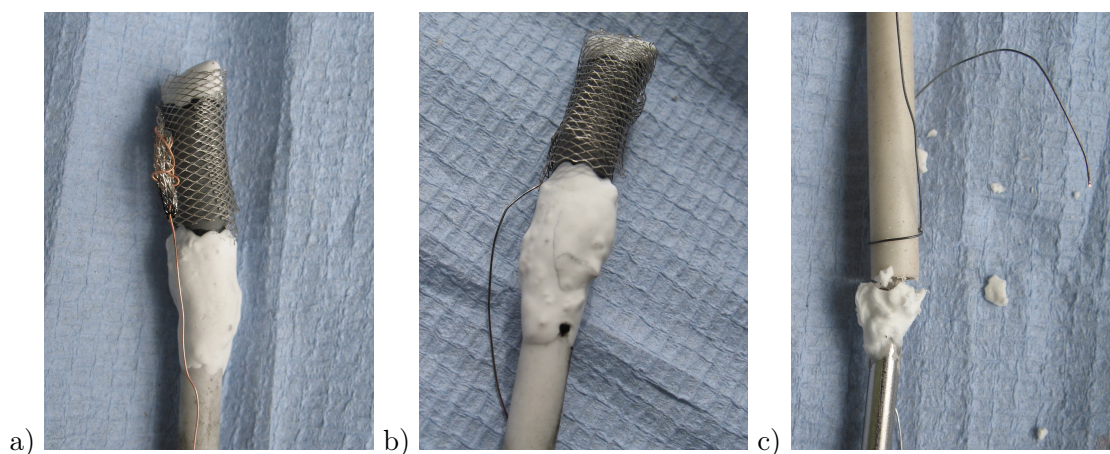


Figure 7.3.8: RSOFC-M-gra10-27 test 106, a) one side, b) the other side. A leak (dark spot) can be seen at the base of the ceramic seal, and c) after testing, the silicone sealant joint was broken and had a crumbly texture.

The fuel electrode appears to have been reduced, as it has a dark grey colour in image a), which is consistent with the measured cell resistance. Image b) shows a large crack in the sealant, and a dark spot, which is probably carbon from the burnout of organic components of the gold paste used to coat the inside of the cell, that has leaked out through a hole in the seal. Image c) shows that the silicone sealant used at the base of the alumina gas delivery tube has become crumbly, and broken, which explains the very low OCV seen at $800\ ^\circ\text{C}$. Failure of the silicone seal happened on this test and not other earlier ones, because the stainless steel tube connected to the cell was longer than usual, so that the silicone joint was higher up in the furnace, closer to the hot zone, and overheated. Image c) also shows that the copper current collection wire has oxidised and turned black

from the oxygen leaking past it out of the cell. A shorter stainless steel tube was used for subsequent tests. When the silicone sealant and stainless steel pipe were removed, and the cell was leak tested without them, there was a 100% pressure drop over 2 s from a starting pressure of 0.0490 bar. This shows that there is a very large leak in the cell/seal/alumina support, probably because of the cracked seal.

Testing RSOFC-M-gra10-28, T107

RSOFC-M-gra10-28 was made with 2 coats of a commercial 3YSZ screen printing ink, which gave a dense YSZ electrolyte. It was heated up at $0.4\text{ }^{\circ}\text{C min}^{-1}$ in a slow flow of 5% H_2/Ar , and a slow flow of oxygen through a pipe connected in a T-junction to the base of the RSOFC alumina support tube. At $580\text{ }^{\circ}\text{C}$, the OCV suddenly dropped from 0.4 V to 0.029 V. When the oxygen flow rate was increased, the OCV increased and fluctuated between 0.04 V and 0.15 V. This indicates a very large leak in the cell. At $800\text{ }^{\circ}\text{C}$, the cell resistance was $44\text{ k}\Omega$, and after cooling the cell to room temperature, it was $> 2\text{ M}\Omega$. Therefore there is no short circuit in the cell. The resistance across the fuel cell electrode surface was $22\text{ }\Omega$ over a distance of 1 cm, so the NiO in the fuel electrode has been partially reduced to nickel.

A red dye test in fig. 7.3.9 showed that there were few if any leaks in the RSOFC, but the Toku sealant used was porous. The cell was then immersed in $\sim 5\text{ cm}$ of water, and 0.25 bar pressure was applied inside the cell relative to atmospheric pressure, and almost zero leakage over 5 min was measured. After drying for 0.5 h at $80\text{ }^{\circ}\text{C}$ and then leak testing the cell by applying 0.25 bar pressure of oxygen inside it, there was a 100% pressure drop in pressure in 20 s. When the cell was again immersed in 5 cm of water, which exerts a pressure of 0.005 bar at that depth, there was no pressure drop when 0.25 bar was put into the cell.

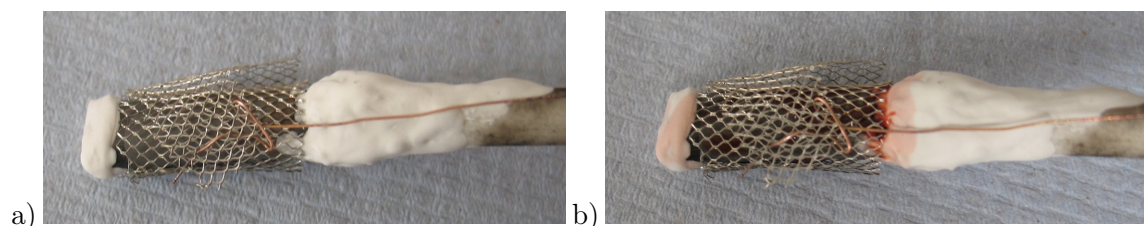


Figure 7.3.9: Red dye test on RSOFC-M-gra10-28, after T107, a) pre red dye b) 2 min after red dye was put inside the cell.

Therefore, the lack of a leak cannot be explained solely by the water pressure at that depth. The gas pressure was then increased to 0.35 bar, at which point the YSZ electrolyte and fuel electrode visibly cracked, and streams of bubbles were seen from the cracks. Therefore, the leak at 0.25 bar pressure was entirely through very small pores in the sealant or electrolyte, which when filled with water, are able to prevent gas going through them, due to capillary forces. The pressure needed to prevent the gas from escaping the pores is a function of their size. As the pressure is quite high in this case, the pores are quite small, on the scale of tens of microns [11].

Fig. 7.3.10 shows a cross section of the cell after these cracks. These cracks were seen periodically along the YSZ electrolyte, probably caused by the high pressure leak test. However, the YSZ electrolyte is otherwise quite dense, and there was no short-circuit observed across the cell after testing. This is why the red dye test, carried out before the immersion test to 0.35 bar, shows no leaks from the active cell area, just the seal.

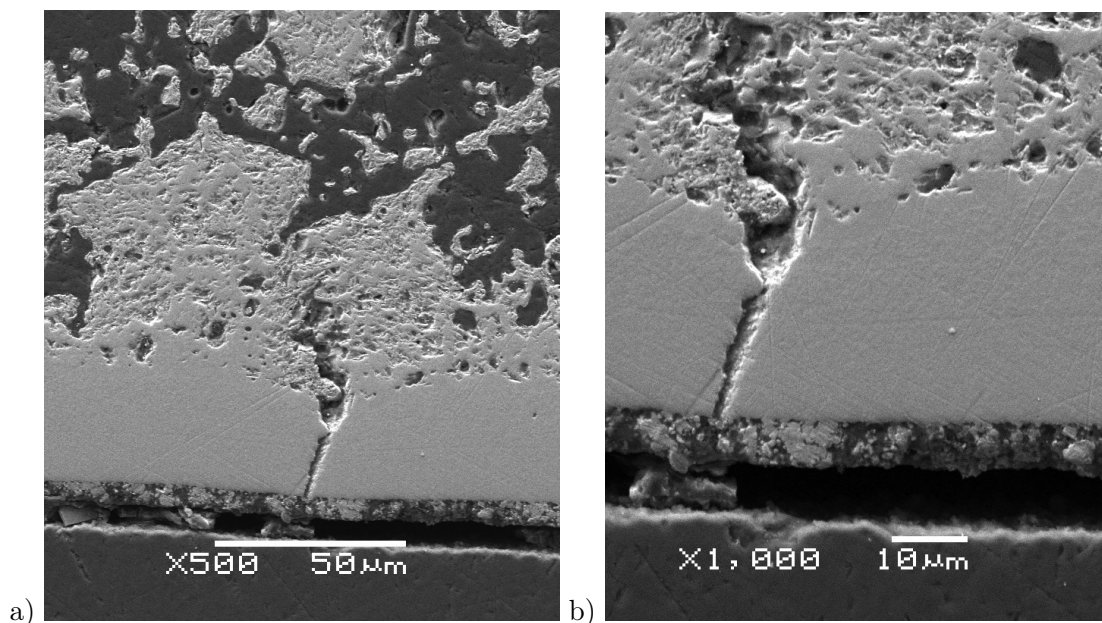


Figure 7.3.10: Longitudinal cross section of RSOFC-M-gra10-28, after T107 and leak tests, a) one of the cracks seen periodically along the electrolyte, and b) the same crack at higher magnification.

Testing RSOFC-M-gra10-10, T108

RSOFC-M-gra10-10 also had a coating of 3YSZ commercial ink, so it had a dense electrolyte. It was sealed with Toku sealant, like RSOFC-M-gra10-28, but it also had an alumina ring over the joint between the alumina gas delivery tube and the fuel cell to aid sealing. Previous tests heated up the cell in 5% H_2/Ar , but a non-reducing atmosphere was used for this test during heating, as the reduction temperature affects the microstructure of the Ni-YSZ fuel electrode. One study compared NiO-YSZ SOFC anodes that had been heated in 5% H_2/N_2 , with ones that had been heated in air to 800 °C, then reduced with 5% H_2/N_2 [12]. The NiO/YSZ electrode reduced during heating, had a more poorly connected microstructure, and 30% lower mechanical strength than the one reduced at 800 °C. This was explained with reference to the reduction and thermal expansion of nickel. In the electrode that was reduced during heating, nickel oxide was reduced to nickel at about 300 °C, and then expanded as it was heated to 800 °C, causing cracking in the YSZ microstructure, because nickel has a higher thermal expansion coefficient than YSZ or nickel oxide. However, as the other electrode was heated up in air, the nickel oxide expansion matched that of the YSZ, so there was no strain on the YSZ microstructure, and then it was reduced to nickel at 800 °C. The grain size of the nickel particles is also affected by the reduction temperature. A study showed that lower reduction temperatures produce

smaller nickel particles, which are more easily oxidised during a redox cycle [13]. Small particles of nickel would coarsen during RSOFC operation, reducing its performance over time.

Therefore, RSOFC-M-gra10-10 was heated at $1\text{ }^{\circ}\text{C min}^{-1}$ to $343\text{ }^{\circ}\text{C}$, then $0.3\text{ }^{\circ}\text{C min}^{-1}$ to $800\text{ }^{\circ}\text{C}$, in static air outside the cell, and flowing oxygen inside it. A nickel current collection wire was used, because a copper current collection wire would have fully oxidised in the air atmosphere during heating. When the cell reached $800\text{ }^{\circ}\text{C}$, the gas outside it was switched to 5% H_2/Ar . The OCV remained near zero for 2.5 h, so the test was cooled down at $0.4\text{ }^{\circ}\text{C min}^{-1}$. When it reached $700\text{ }^{\circ}\text{C}$, the OCV suddenly increased to 0.7 V, and went down to just above 0 V again in a few min. When the cell had cooled down, a leak test showed a 100% pressure drop in 55 s, from a starting pressure of 0.0546 bar. Fig. 7.3.11 shows a red dye test on the cell, which indicates that the Toku ceramic sealant is porous, as the dye leaks through it. There is also a crack in the alumina ring, which is thought to have been caused when it was cut, before the cell was made. The surface electrical resistance across the diameter of the fuel electrode was measured, and found to be $1.5\text{ }\Omega$. Therefore, the NiO in the NiO/YSZ fuel electrode has been reduced during testing. The resistance across the cell after testing was $>2\text{ M}\Omega$, so there was no short-circuit after testing.

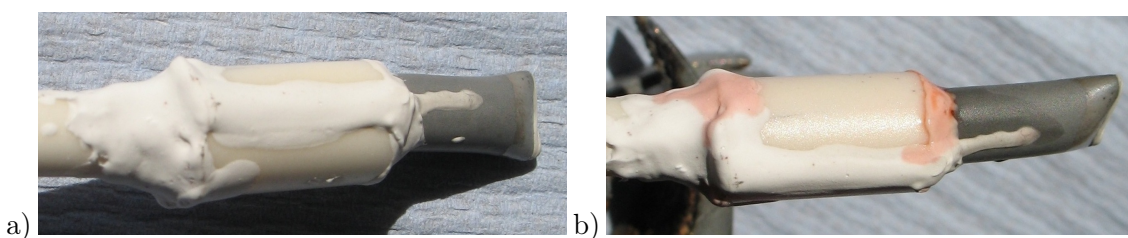


Figure 7.3.11: Red dye test on RSOFC-M-gra10-10, after T108: a) pre red dye, and b) 1 min after red dye was put inside the cell.

7.4 Conclusions

The first four cells tested in T099 - T102 had resistances of $70\text{ }\Omega$ or less at room temperature after testing, indicating that the 8YSZ electrolyte was quite porous, or else thin with flaws in it, so there was a short-circuit through it, where the silver paste had penetrated the electrolyte. The cells in T103 and T104 also had a short circuit after testing, but the resistances were much higher; around $100\text{ k}\Omega$, which indicates a short-circuit through partially reduced nickel in the fuel electrode. Although the cell in T103 had a low surface resistance, this is may be due to the silver paste also used on the cell. The cell in T104 also had a porous Toku ceramic seal, as shown by the red dye test.

The cells in T099-T101 had a dip-coated NiO/YSZ fuel electrode, and subsequent cells had a painted NiO/YSZ electrode. The thickness of both electrodes was similar at $8\text{ }\mu\text{m}$ - $10\text{ }\mu\text{m}$, but the painted electrodes did not cover the top of the cell, which was where flaws in the LSM support and YSZ electrolyte were most likely to be found. All three cells with dip-coated NiO/YSZ had short circuits after reduction, but some of the cells with painted

NiO/YSZ had no short circuit after testing, indicating that the NiO/YSZ electrode had not penetrated the YSZ electrolyte during cell fabrication.

The cell in T105 had no short circuit after test, perhaps because the NiO/YSZ fuel electrode on the cell surface was not reduced at all. Leaks at the interfaces of the Ceramabond seal were observed. When the seal was coated with the Toku sealant, and tested in T106, the seal cracked during testing. Therefore, the Ceramabond sealant tends to form a dense mass, but cracks at interfaces and when the cell undergoes a thermal cycle, whereas the Toku sealant does not crack, but is porous. However, an impedance measurement at 800 °C in T105 showed that the cell itself was electrochemically active, with a polarisation resistance which had several components, in the tens of ohms range.

Tests 107 and 108 both showed some OCV, 0.4 V and 0.7 V respectively, but in both tests, this suddenly declined, indicating that leaks had appeared in the cell. This is either due to cracks in the electrolyte, or more likely, cracks in the seal. These appear because the cell has a greater thermal expansion coefficient than the sealant, putting it under tension, and it cracks. The results from T108 show that heating the cell in air, and then reducing in 5% H₂/Ar at 800 °C, gives a low resistance on the cell surface, similar to cells that were reduced during the heating stage. A cross section of the cell RSOFC-M-gra10-28 show that the electrolyte is dense. The only cracks present are those from testing the cell to destruction with 0.35 bar pressure inside it.

None of the cells tested achieved a good OCV, because of leaks in either the electrolyte, the seal or both. However, the problem of the leaky electrolyte was fixed by changing its fabrication method. A 3YSZ commercial screen printing ink was painted onto the LSM substrate tube, which gave a nearly 100% dense electrolyte, for the RSOFC in T107 and T108.

The leak tests described in this chapter show that for the cells tested, the predominant leak was in the seal, not the electrolyte. The seals were investigated with gas leak tests, immersion leak tests, and red dye leak tests, which showed the nature and location of the leaks. The red dye tests show more leakage from the seals than the electrolytes. Further work is needed to achieve a leak tight seal, perhaps by using a sealant with a thermal expansion coefficient that more closely matches that of the RSOFC, or by using an alternative material, such as a glass ceramic. When these are heated, they melt to form a glassy molten phase, but when cooled below a particular temperature, they go through an amorphous to crystalline phase transition. This transition temperature can be tuned, depending on the composition of the glass, and is usually set above the SOFC operating temperature, so the glass seals are rigid when the cells are in operation [14]. Another type of seal is a self-healing glass seal. If this cracks during cell operation, it has the ability to heal cracks, by flowing to fill them in [15]. In this work, although cells were produced which had a dense electrolyte, a hermetic seal could not be made using the ceramic sealant pastes, so the electrochemical performance of the cells could not be determined.

References

- [1] J. Van herle, R. V. Cavieres, D. Akyuz, K. Barthel, *J. Eur. Ceram. Soc.*, 2001, **21**, 1851–1854.
- [2] A. E. Gheribi, J. Rogez, F. Marinelli, J. C. Mathieu, M. C. Record, *Calphad*, 2007, **31**, 380–389.
- [3] G. Parravano, *J. Am. Chem. Soc.*, 1952, **74**, 1194–1198.
- [4] Aremco Products, Inc., *High temperature ceramic adhesives & pastes*, Technical bulletin A2, Aremco, P.O. Box 517, 707-B Executive Blvd., Valley Cottage, NY 10989, 2009.
- [5] F. Tietz, I. A. Raj, M. Zahid, D. Stöver, *Solid State Ionics*, 2006, **177**, 1753–1756.
- [6] A. R. Sahu, A. Ghosh, A. K. Suri, *Ceram. Int.*, 2009, **35**, 2493–2497.
- [7] M. Mogensen, S. Skaarup, *Solid State Ionics*, 1996, **86-88**, 1151–1160.
- [8] M. J. Jørgensen, M. Mogensen, *J. Electrochem. Soc.*, 2001, **148**, A433–A442.
- [9] S. P. Jiang, J. P. Zhang, K. Föger, *J. Eur. Ceram. Soc.*, 2003, **23**, 1865–1873.
- [10] Y. J. Leng, S. H. Chan, K. A. Khor, S. P. Jiang, *J. Appl. Electrochem.*, 2004, **34**, 409–415.
- [11] A. Jena, K. Gupta, *INJ*, 2005, **14**, 25–30.
- [12] Y. Wang, M. E. Walter, K. Sabolsky, M. M. Seabaugh, *Solid State Ionics*, 2006, **177**, 1517–1527.
- [13] Y. Zhang, B. Liu, B. Tu, Y. Dong, M. Cheng, *Solid State Ionics*, 2009, **180**, 1580–1586.
- [14] J. W. Fergus, *J. Power Sources*, 2005, **147**, 46–57.
- [15] R. N. Singh, *Int. J. Appl. Ceram. Technol.*, 2007, **4**, 134–144.

Chapter 8

Reversible SOFC computer model

8.1 Rationale for the reversible SOFC system and model

The reversible solid oxide fuel cell (RSOFC) system provides temporary energy storage for electrical energy, acting in a load balancing capacity. It uses excess electrical energy from the grid to electrolyse steam to hydrogen and oxygen, and feeds electricity back into the grid when needed, by recombining hydrogen and oxygen in fuel cell mode. It can be used to match intermittent electrical supply from renewable energy sources such as wind, wave and tidal, to varying electrical demand. It is designed to either connect to the electrical grid, or work in an islanded mode in a smaller grid. A dynamic model of a RSOFC system was developed, and implemented in the Matlab software, through a collaboration with the University of Strathclyde, where an electronic power and controls system was also designed for it.

Summary of the model

This chapter is concerned with the development of a RSOFC system model, and evaluation of the system performance. The model describes the electrical and thermal behaviour of a single RSOFC by using electrochemical equations, and then multiplies it by the number of cells to determine the behaviour of the stack. Firstly, the electrical properties of the cell are discussed. The model assumes that the current load on the cell is known. It then calculates the voltage output from the cell, based on the cell current density, system temperature and pressure, and the system state of charge, which is defined as the mole fraction of hydrogen on the fuel side of the cell. The cell voltage is determined by calculating the standard voltage, then the Nernst voltage, and then by subtracting the ohmic and polarisation voltage drops from the Nernst voltage. Once this is known, the cell power output is calculated, and multiplied by the number of cells in the system to give the system power output. Secondly, the heat production by ohmic resistances, and electrochemical heat production in fuel cell mode, or absorption in electrolyser mode, are calculated based on the cell current, and voltage drops. A geometry for the system is proposed, and heat loss through the outer walls is calculated. The heat capacities and thermal mass of the stack are calculated, and a heat store consisting of a high temperature phase

change material is described. Then the dynamic change in temperature during system operation is determined. Finally, by considering electrical energy inputs and outputs to and from the system, an electrical energy storage efficiency is calculated. The equations are implemented using the Matlab software. The model is dynamic and the parameters are interdependent, e.g. the flow of current produces heat, which changes the resistances of the cell components, which affects the current. It is a zero-dimensional model, i.e. the transfer of heat within the system by radiation, convection and conduction is not considered, as the whole system is considered to be at a uniform temperature. Some of the equations used to make this model come from a dynamic, finite volume, fuel cell model [1]. These are some of the ohmic resistance equations, the activation polarisation equations, and most of the diffusion polarisation equations. In this model, the reactants are recycled, so the system is sealed, and is like a rechargeable battery. Fuel utilisation has no meaning, and the system efficiency is described as a percentage electrical cycle efficiency instead.

Description of the model

The equations which describe the model are all written in this chapter. Some of these equations are semi-empirical, with coefficients derived from experimental data. In these cases, the method used to obtain these equations is described in chapter 2. Throughout most of the model, the units length (m), temperature (K), and pressure (Pa) are used, except where units of cm, °C or bar are specified.

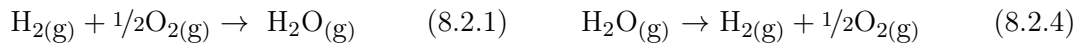
8.2 Cell voltage, geometry, losses, and power.

8.2.1 Nernst voltage and standard voltage

The fuel cell and electrolysis chemical reactions are shown in eqs. 8.2.1 and 8.2.4. From these, the Nernst voltage or open circuit voltage (OCV) may be calculated for both fuel cell mode and electrolyser mode, by eqs. 8.2.2 and 8.2.5.

Fuel cell mode

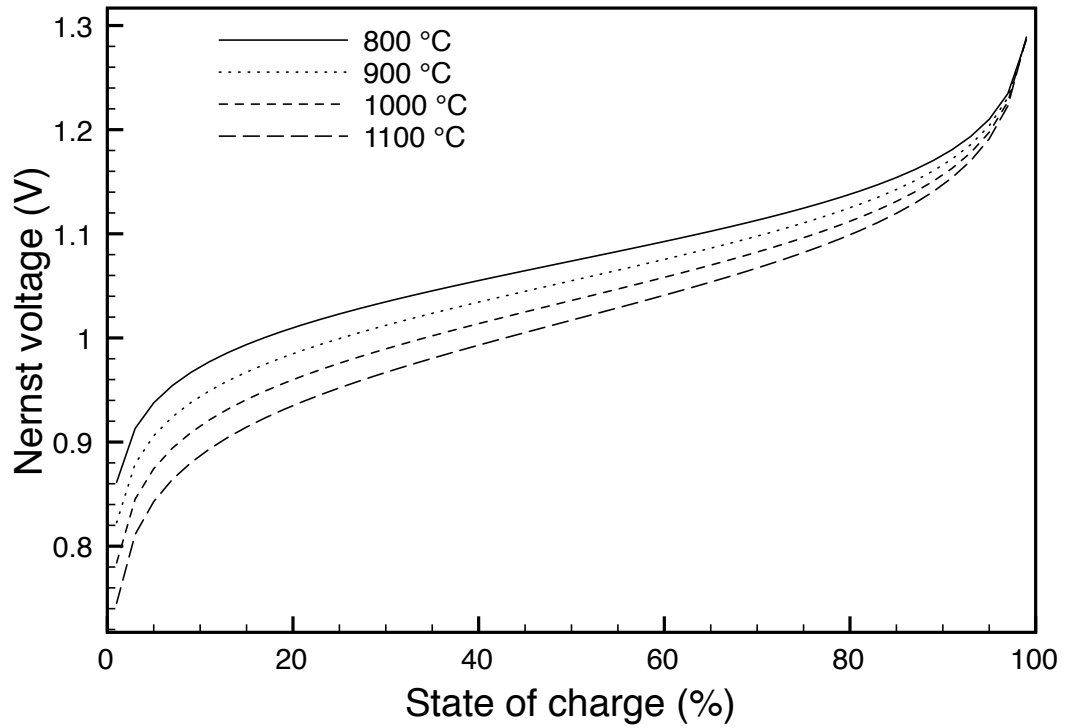
Electrolyser mode



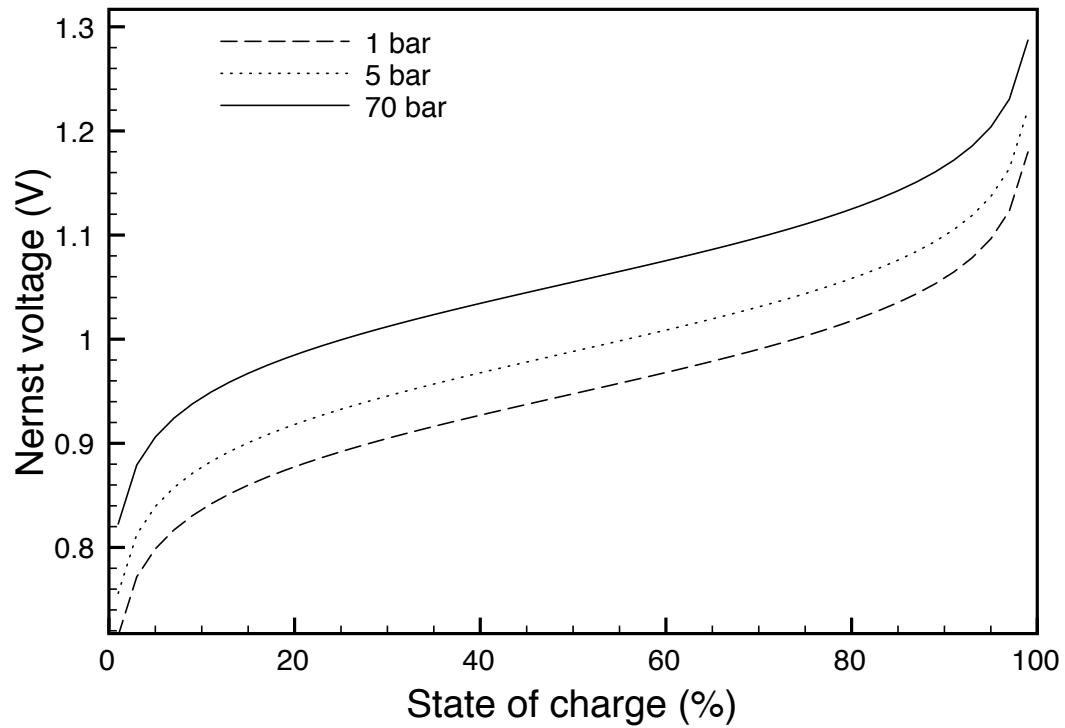
$$V_{\text{Nernst}} = V_{\text{standard}} - \frac{RT}{nF} \ln \left(\frac{P_{\text{H}_2\text{O}}}{P_{\text{H}_2} P_{\text{O}_2}^{1/2}} \right) \quad (8.2.2) \quad V_{\text{Nernst}} = V_{\text{standard}} + \frac{RT}{nF} \ln \left(\frac{P_{\text{H}_2} P_{\text{O}_2}^{1/2}}{P_{\text{H}_2\text{O}}} \right) \quad (8.2.5)$$

$$V_{\text{standard}} = (-0.00028090T_s + 1.277058) \quad (8.2.3) \quad V_{\text{standard}} = (-0.00028090T_s + 1.277058) \quad (8.2.6)$$

It is the voltage of the cell with no losses, and it depends on the concentration of reactants and products (bar) and on the standard voltage $V_{standard}$. This is a temperature dependent voltage calculated by the semi-empirical eqs. 8.2.3 and 8.2.6. Fig. 8.2.1a shows the Nernst voltage for four different temperatures, 800 °C, 900 °C, 1000 °C, and 1100 °C, as a function of the system state of charge. This is defined as the percentage mole fraction of hydrogen, in the hydrogen-steam mixture on the fuel gas side of the system. At higher temperatures, the Nernst voltage is lower, and at higher states of charge, it is higher. The Nernst voltage varies more with state of charge than with temperature over the state of charge range 5% - 95%, and temperature range 800 °C - 1100 °C. Although increasing the cell temperature reduces the Nernst voltage, it also improves the kinetics of the cell reactions, and therefore increases overall cell performance. Fig. 8.2.1b shows that pressurisation of the cell increases the Nernst voltage significantly, and also improves the cell reaction kinetics - a double benefit.



a)



b)

Figure 8.2.1: Nernst potential or OCV of the RSOFC as a function of the state of charge of the system in the range 1% - 99%. The state of charge is the percentage mole fraction of hydrogen on the fuel side of the system. The OCV is plotted, a) at 70 bar pressure and varying temperatures, and b) at 900 °C and varying system pressures. The two graphs are at the same scale.

8.2.2 Cell geometry

The cell geometry is tubular, and its components are described in table 8.2.1, and shown in fig. 8.2.2.

Component	r_{inner} (m)	r_{outer} (m)	Current path (m)	Current path area (m ²)
Support	0.007	0.01	0.075	1.602×10^{-4}
Oxygen electrode	0.01	0.01002	2×10^{-5}	6.283×10^{-3}
Electrolyte	0.01002	0.01004	2×10^{-5}	6.283×10^{-3}
Fuel electrode	0.01004	0.01006	2×10^{-5}	6.283×10^{-3}
Interconnect	0.01006	0.01036	0.05	1.913×10^{-5}
Cell connection	n/a	0.001	0.02	3.142×10^{-6}

Table 8.2.1: Dimensions of components and current paths in the RSOFC.

It has a porous ceramic support tube, with an oxygen electrode, then electrolyte, then fuel electrode, then interconnect on top. The interconnect is assumed to be a nickel mesh extending lengthwise along the tube. Current flows along the support which is 0.1 m long. However, it is assumed that the actual average current path is less than this - 0.075 m, because some of the current leaves the support along its length, entering the oxygen electrode. The current then flows through the oxygen electrode, electrolyte and fuel electrode thickness which are each 2×10^{-5} m, and then on average, halfway along the length of the interconnect, 0.05 m. The current path area for the support tube is the cross sectional area, which is calculated from eq. 8.2.7 using the dimensions in table 8.2.1.

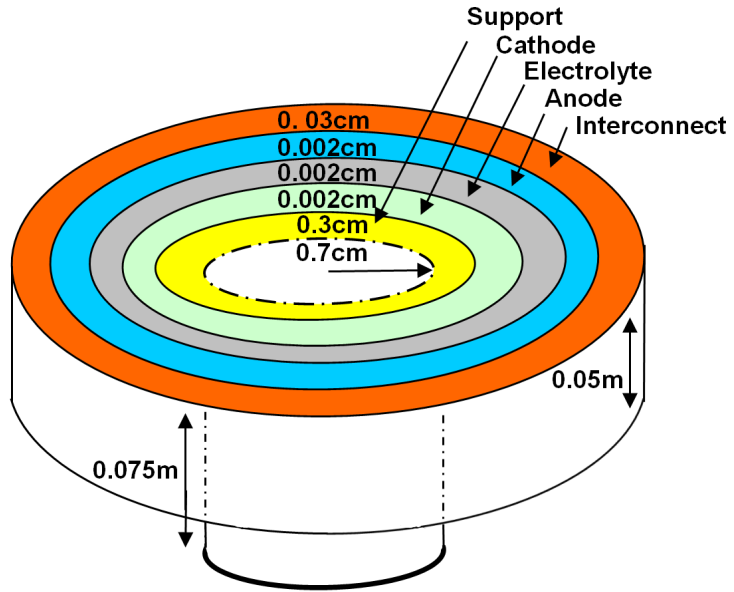


Figure 8.2.2: Schematic of the components of RSOFC. The electrode labelled ‘anode’ in the diagram is the fuel electrode, and the ‘cathode’ is the oxygen electrode. The anode and cathode switch in electrolyser mode.

$$A = \pi (r_{outer}^2 - r_{inner}^2) \quad (8.2.7)$$

The oxygen electrode, electrolyte and fuel electrode current path area is the surface area

of each on the tube, which is calculated from eq. 8.2.8 where r is the inner radius in m, and l is the length of the tube, 0.1 m.

$$A = 2\pi rl \quad (8.2.8)$$

The area of the interconnect is calculated by eq. 8.2.9. It is a mesh, and it is assumed that each strand of the mesh has a square cross section, and has thickness and width of 3×10^{-4} m, and that they are spaced 6×10^{-4} m apart, surrounding the tube. Therefore, it can be assumed that the current path area of the mesh is 1/3 of the area of an solid layer of the same thickness.

$$A = \frac{\pi (r_{outer}^2 - r_{inner}^2)}{3} \quad (8.2.9)$$

The cell connection is a single nickel wire, the same material as the interconnect, and its area is calculated using eq. 8.2.10.

$$A = \pi r^2 \quad (8.2.10)$$

8.2.3 Ohmic resistance of the cell components

In order to calculate the ohmic resistance of the cell components at any temperature, equations for the resistivity of the oxygen electrode, fuel electrode, support, electrolyte, interconnect and cell connection are given as a function of temperature.

The eqs. 8.2.11 and 8.2.12 for the oxygen electrode and fuel electrode are from another model [1].

$$\rho_{oxy.e.} = 8.11 \times 10^{-5} \exp \frac{600}{T_s} \quad (8.2.11)$$

$$\rho_{fuel.e.} = 2.98 \times 10^{-5} \exp \frac{-1392}{T_s} \quad (8.2.12)$$

The resistivity of the support in eq. 8.2.13, the electrolyte in eq. 8.2.14, and interconnect and cell connection, eq. 8.2.15, were derived from literature data.

$$\rho_{support} = 0.01 \exp \left(\frac{-316.1}{T_s} - 2.8719 \right) \quad (8.2.13)$$

$$\rho_{electrolyte} = 0.01 \exp \left(\frac{4062.9}{T_s} - 2.4332 \right) \quad (8.2.14)$$

$$\rho_{intercon.} = 6 \times 10^{-10} T_s - 1 \times 10^{-7} \quad (8.2.15)$$

The resistance of any component can be determined by eq. 8.2.16, where R_i is the ohmic resistance of the component, ρ_i is the temperature dependent resistivity of the component (Ωm), l_i is the current path length (m) and A_i is the area of the section where the current flows.

$$R_i = \frac{\rho_i l_i}{A_i} \quad (8.2.16)$$

The total ohmic resistance for one reversible cell is calculated by eq. 8.2.17.

$$R_{ohmic} = \sum (R_{support} + R_{oxy.e.} + R_{fuel.e.} + R_{electrolyte} + R_{intercon.} + R_{cell.con.}) \quad (8.2.17)$$

Fig. 8.2.3 shows a logarithmic plot of the ohmic resistance of each component of a single RSOFC cell. The cell resistance is dominated by the resistance of the support. This is because it acts as a distributor for the current over the electrode surface, but it is a ceramic material, and has lower conductivity than the nickel interconnect, which distributes current on the fuel electrode side. The next highest resistance comes from the interconnect and cell connection. The electrolyte resistance is also significant at lower temperatures. The fuel and oxygen electrode resistances are very small, because they are very thin, and the current path is across their thickness, so it is very short. In the RSOFC stack, the cells are linked together in two parallel blocks, of 400 cells in series each. This is done to obtain a high voltage with a low current.

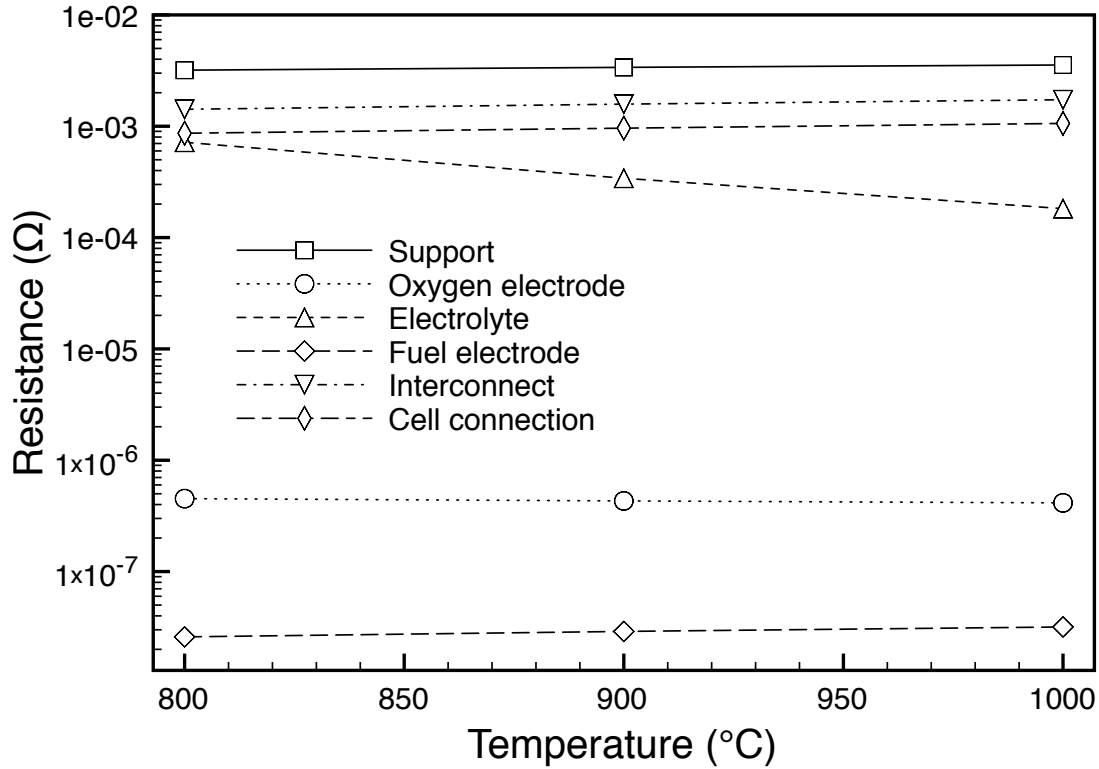


Figure 8.2.3: Ohmic resistance of each component of a single RSOFC, on a logarithmic scale, at 800 °C, 900 °C and 1000 °C.

8.2.4 Activation polarisation resistance

The equations to model the activation polarisation resistance were taken from a dynamic, finite volume fuel cell model [1]. The Butler-Volmer eq. 8.2.18 can accurately model the activation polarisation resistance at high and low polarisation conditions and is assumed

to be the same for fuel cell and electrolyser mode.

$$i_{density} = i_0 \left\{ \exp \left(\beta \frac{nF\eta_{act}}{RT_s} \right) - \exp \left[-(1 - \beta) \frac{nF\eta_{act}}{RT_s} \right] \right\} \quad (8.2.18)$$

In the Butler-Volmer equation, β is the electron transfer coefficient, $i_{density}$ is the fuel cell current density ($A\ m^{-2}$), i_0 is the exchange current density ($A\ m^{-2}$), and η_{act} is the activation polarisation (V). The number of electrons per molecule of fuel reacting is n , which is 2, F is Faraday's constant, $96485.3\ C\ mol^{-1}$, and R is the molar gas constant, $8.31447\ J\ mol^{-1}\ K^{-1}$. The exchange current density can be calculated by eq. 8.2.19 for the fuel electrode, and eq. 8.2.20 for the oxygen electrode.

$$i_{o,fuel.e.} = \gamma_{fuel.e.} \left(\frac{P(H_2)}{P(H_2 + H_2O)} \right) \left(\frac{P(H_2O)}{P(H_2 + H_2O)} \right) \exp \left(-\frac{E_{act,fuel.e.}}{RT_s} \right) \quad (8.2.19)$$

$$i_{o,oxy.e.} = \gamma_{oxy.e.} \left(\frac{P(O_2)}{P(O_2)} \right) \exp \left(-\frac{E_{act,oxy.e.}}{RT_s} \right) \quad (8.2.20)$$

The pre-exponential coefficients $\gamma_{oxy.e.}$ and $\gamma_{fuel.e.}$ both have a value of $7 \times 10^8\ A\ m^{-2}$, for the oxygen electrode and the fuel electrode, respectively. These values were chosen as they were within the range of values reported, determined by experiment on fuel cells [2]. $E_{act,fuel.e.}$ is the activation energy of the fuel electrode, which is $110000\ J\ mol^{-1}$, and $E_{act,oxy.e.}$ is the activation energy of the oxygen electrode, which is $120000\ J\ mol^{-1}$ [1]. P_i stands for the partial pressure of component i (Pa). The Butler-Volmer equation 8.2.18 can be approximated in low polarisation conditions to the linear eq. 8.2.21, and at high polarisation, the second term of 8.2.18 can be neglected, so it is approximated to eq. 8.2.22. This is done in order that the activation loss η_{act} can be calculated [3].

$$\eta_{act} = \frac{RT_s i_{density}}{nF i_0} \quad (8.2.21)$$

$$\eta_{act} = \frac{RT_s}{nF\beta} \ln \left(\frac{i_{density}}{i_0} \right) \quad (8.2.22)$$

The inequality, eq. 8.2.23 is used to determine whether the model is in the high or low polarisation state - if the inequality holds, then it is in the low polarisation state, but if the left hand side of the equation is greater than 1, it is in the high polarisation state. At the switching point between the states, eq. 8.2.23 becomes eq. 8.2.24. Therefore, η_{act} at the switching point can be calculated as a function of temperature. This value is then substituted into eq. 8.2.21 to find the value of $i_{density}$ at the switching point. Below the switching point, eq. 8.2.21 is used to calculate η_{act} . The values of $i_{density}$ and η_{act} at the switching point are substituted into eq. 8.2.22 to find β , it is assumed that β is invariant with current density, and the equation is used to calculate η_{act} above the switching point. This process can be visualised as plotting η_{act} below the switching point, and then the value of β is set such that the high polarisation curve of η_{act} maps onto the low polarisation values smoothly with no step at the switching point. This approach gives

a constant value of $\beta = 0.3465$.

$$\frac{F\eta_{act}}{nRT_s} < 1 \quad (8.2.23)$$

$$\frac{F\eta_{act}}{nRT_s} = 1 \quad (8.2.24)$$

Effect of the pre-exponential coefficient

Fig. 8.2.4 shows the significant effect of varying the pre-exponential coefficients, $\gamma_{oxy.e.}$ and $\gamma_{fuel.e.}$ on the activation losses. Negative currents correspond to electrolyser mode, and positive currents to fuel cell mode. It can be seen the pre-exponential coefficient has a major impact on the activation energy, and by extension the reversible SOFC performance, increasing it dramatically as this factor increases, as has been previously observed [1]. It has been described as depending on cell temperature, and reactant and product concentrations [4]. It also affects the position of the switch between the low and high activation polarisation regimes, seen in fig. 8.2.4 when the linear dependence of activation polarisation on current at low currents, changes to non-linear, Tafel type one at higher currents. At low γ values the switch to a high polarisation regime occurs at a lower current, but with the highest γ value, the switch on the oxygen electrode occurs at a current > 100 A, so is not seen, which is unrealistic. It is expected that at high currents, the potential of the cell is quite different to the standard potential, so the cell should be in the high polarisation region where it displays Tafel type behaviour.

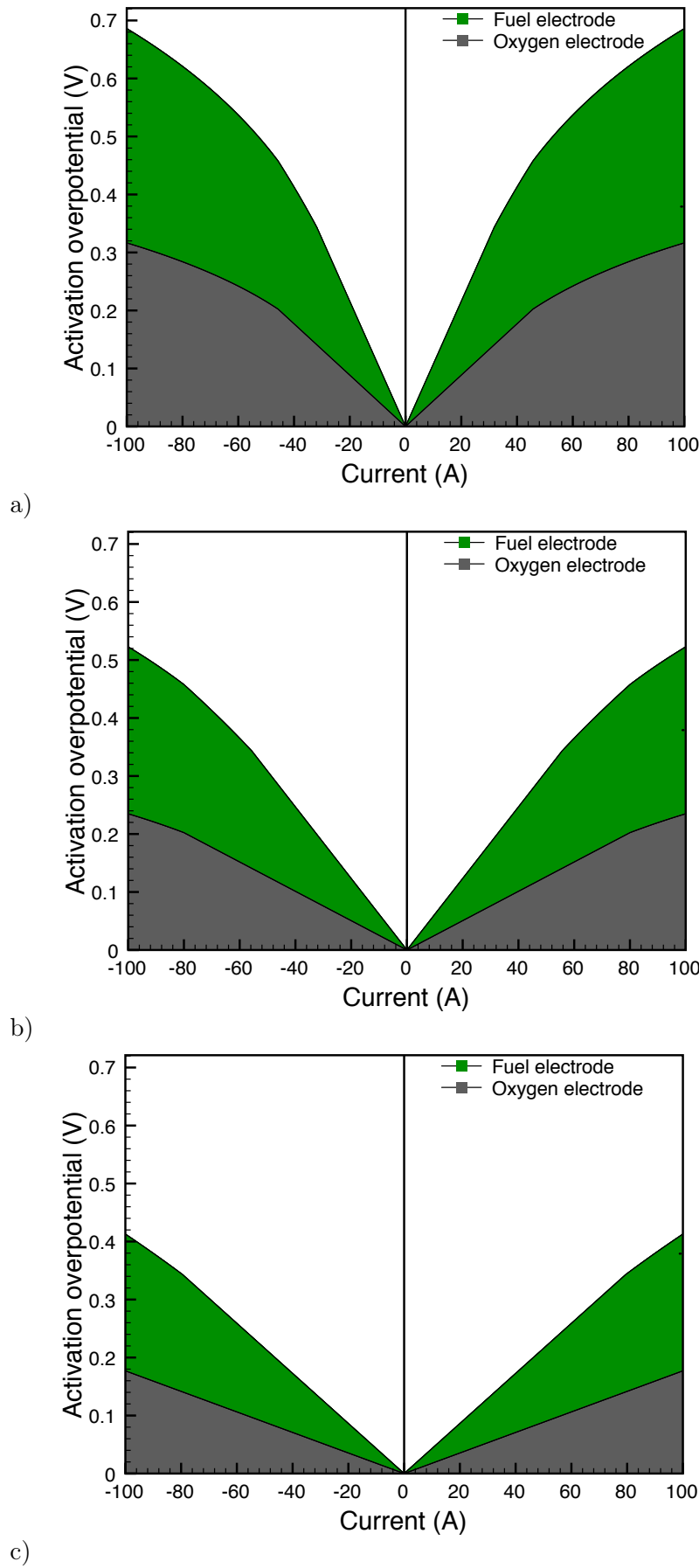


Figure 8.2.4: Activation energy in the RSOFC, at 900 °C, 70 bar pressure, 50% state of charge, for three values of pre-exponential coefficient: a) $4 \times 10^8 \text{ A m}^{-2}$, b) $7 \times 10^8 \text{ A m}^{-2}$, and c) $1 \times 10^9 \text{ A m}^{-2}$. All graphs show cumulative values.

8.2.5 Diffusion polarisation resistance

The diffusion polarisations of the oxygen electrode and the fuel electrode are modelled separately, as overpotentials. The equations presented are valid for the fuel cell mode and electrolyser mode.

Diffusion at the fuel electrode

On the fuel electrode side, there is a mixture of hydrogen and steam, which is modelled with equations from a dynamic, finite volume SOFC model [1] in two stages, as in fig. 8.2.5. The first stage is molecular diffusion along a diffusion gradient from the bulk gas in the system, to the surface of the electrode. The second is molecular diffusion through the pores of the fuel electrode, to the reactive site. To calculate the concentrations of the hydrogen and steam at the reactive surface, the following process is used. Fick's law [5] is the basis for these calculations, but is not used directly in this model. It may be used to calculate the flux of hydrogen to the fuel electrode, where J_{H_2} is the flux of hydrogen to the fuel electrode, in $\text{mol m}^{-2} \text{s}^{-1}$, D is the mass diffusion coefficient ($\text{m}^2 \text{s}^{-1}$), r is the radius of the cell (m), and J_{tot} is the sum of the hydrogen and steam flux, which always equals zero, as one molecule of steam is created for every molecule of hydrogen consumed.

$$J_{H_2} = -\frac{P_{fuel.e.} D}{RT} \frac{dX_{H_2}}{dr} + X_{H_2} J_{tot} \quad (8.2.25)$$

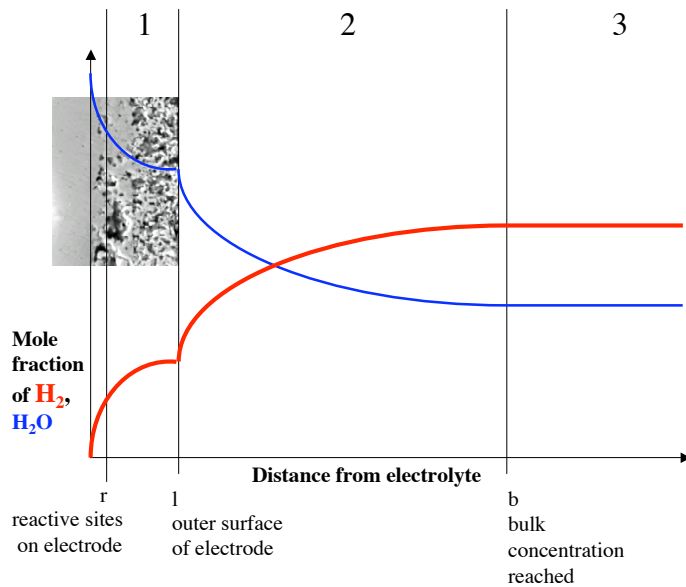


Figure 8.2.5: Concentration of hydrogen and steam within and above the fuel electrode during operation in fuel cell mode, for a state of charge $>50\%$, i.e. the mole fraction of hydrogen in the hydrogen-steam mixture >0.5 . In electrolyser mode, for a state of charge $<50\%$, the two curves would be swapped around. Area 1 shows the diffusion gradient within the fuel electrode pores, area 2 shows a diffusion gradient above the fuel electrode, and area 3 shows the bulk concentrations of hydrogen and steam. This diagram is not to scale.

Diffusion between the gas concentration in the bulk and at the electrode surface

This part of the diffusion is represented by area 2 on fig. 8.2.5. The diffusion coefficients of hydrogen and steam must be calculated before the concentrations at the bulk ^b and the reactive surface ^r can be determined. The ordinary diffusion coefficient of hydrogen $D_{H_2,m}$ in a steam-hydrogen mixture can be calculated using eq. 8.2.26, where D_{H_2,H_2O} is the mutual diffusion coefficient of hydrogen and steam, and X_{H_2} is the mole fraction of hydrogen in the system.

$$D_{H_2,m} = \frac{1 - X_{H_2}}{D_{H_2,H_2O}} \quad (8.2.26)$$

The ordinary diffusion coefficient of steam $D_{H_2O,m}$ in a steam-hydrogen mixture can also be calculated, using eq. 8.2.27.

$$D_{H_2O,m} = \frac{1 - X_{H_2O}}{D_{H_2O,H_2}} \quad (8.2.27)$$

The mutual diffusion coefficient of hydrogen and steam D_{H_2,H_2O} is calculated from a modified Fuller eq. 8.2.28 [6], where T is the system temperature, $P_{fuel.e.}$ is the gas pressure at the fuel electrode (bar in this equation) and ν_i is the diffusion volume of species i ($\text{cm}^3 \text{mol}^{-1}$). The diffusion volume of hydrogen gas is $7.07 \text{ cm}^3 \text{mol}^{-1}$ and steam $12.7 \text{ cm}^3 \text{mol}^{-1}$ [5]. M_{H_2,H_2O} can be calculated from eq. 8.2.29, where M_{H_2} is 2 g mol^{-1} and M_{H_2O} is 18 g mol^{-1} , and will be the same for hydrogen and steam. This mutual diffusion coefficient applies both to electrolyser and fuel cell mode.

$$D_{H_2H_2O} = \frac{0.00143T^{1.75}}{P_{fuel.e.} M_{H_2,H_2O}^{1/2} [\nu_{H_2}^{1/3} + \nu_{H_2O}^{1/3}]^2} \quad (8.2.28)$$

$$M_{H_2,H_2O} = 2 \left[\frac{1}{M_A} + \frac{1}{M_B} \right]^{-1} \quad (8.2.29)$$

When eq. 8.2.25 is integrated, the following assumptions are made: that the hydrogen flux is equal and opposite to the steam flux, so the overall flux is zero as in eq. 8.2.30, and that the flux of hydrogen is directly proportional to the current, as in eq. 8.2.31.

$$J_{H_2} = J_{H_2} + J_{H_2O} = 0 \quad (8.2.30)$$

$$J_{H_2} = \frac{i}{2F} \quad (8.2.31)$$

When eq. 8.2.25 is integrated, as in eq. 8.2.32, the limits taken are l , which is the outer surface of the fuel electrode, and b which is the point above the fuel electrode at which the concentration of hydrogen reaches the value of the bulk concentration, which is assumed to be $5 \times 10^{-3} \text{ m}$ [7]. This gives eq. 8.2.33, where $L_{b,l}$ is the thickness of the diffusion layer between the concentration of gas in the bulk, and the outer surface of the fuel electrode, which gives the molar concentration of hydrogen at the fuel electrode outer surface, where $P_{fuel.e.}$ is the total gas pressure at the anode side (Pa). When the same process is carried out for steam, it gives eq. 8.2.34.

Fuel cell mode

Electrolyser mode

$$\int_{X_{H_2}^b}^{X_{H_2}^l} dX_{H_2} = \int_0^{L_{bl}} -\frac{iRT_s L_{b,l}}{2FP_{fuel.e.} D_{H_2,m}} dr \quad \int_{X_{H_2O}^b}^{X_{H_2O}^l} dX_{H_2O} = \int_0^{L_{bl}} +\frac{iRT_s L_{b,l}}{2FP_{fuel.e.} D_{H_2O,m}} dr$$

(8.2.32) (8.2.35)

$$X_{H_2}^l = X_{H_2}^b - \frac{iRT_s L_{b,l}}{2FP_{fuel.e.} D_{H_2,m}} \quad (8.2.33) \quad X_{H_2}^l = X_{H_2}^b + \frac{iRT_s L_{b,l}}{2FP_{fuel.e.} D_{H_2,m}} \quad (8.2.36)$$

$$X_{H_2O}^l = X_{H_2O}^b + \frac{iRT_s L_{b,l}}{2FP_{fuel.e.} D_{H_2O,m}} \quad (8.2.34) \quad X_{H_2O}^l = X_{H_2O}^b - \frac{iRT_s L_{b,l}}{2FP_{fuel.e.} D_{H_2O,m}} \quad (8.2.37)$$

For electrolyser mode, the equivalent integral is eq. 8.2.35, which is evaluated to eq. 8.2.36 for hydrogen. Note that the sign of the second term has changed, because $X_{H_2}^l$ is now the sum of the bulk concentration of hydrogen, and the hydrogen produced at the fuel electrode during electrolyser operation. It therefore follows that for electrolyser mode, the equations will be the same, but have opposite signs, as hydrogen is being produced, and steam consumed. Therefore the equation for steam diffusion will be eq. 8.2.37.

Diffusion between the electrode surface and the reactive sites in the electrode

Diffusion of gas through the electrode microstructure may be modelled, if the diffusion mechanism is known. Two possible mechanisms are Knudsen diffusion, assumed in [1], or molecular (Fickian) diffusion. Knudsen diffusion relies on the assumption that the gas molecule mean free path length is greater than the electrode pore diameter, and so molecules of hydrogen or steam are more likely to hit the pore walls than each other, whereas molecular diffusion assumes the opposite. The most appropriate mechanism for this model is molecular diffusion - the same type that occurs above the fuel electrode surface. Therefore, the diffusion coefficient of the gases through the fuel electrode pores may be determined by scaling the mutual diffusion coefficients $D_{H_2,m}$ and $D_{H_2O,m}$ by the porosity ϵ (40%) [8] and tortuosity τ (3.0) [1] of the electrode, according to eq. 8.2.38 for fuel cell mode and eq. 8.2.41 for electrolyser mode.

If eq. 8.2.25, and a similar equation in which steam flux replaces hydrogen flux, are integrated along the fuel electrode length (thickness) $L_{fuel.e.}$, which is 2×10^{-5} m, and the hydrogen and steam molar fractions at the fuel electrode reactive surface may be calculated, for the fuel cell mode, according to eqs. 8.2.39 and 8.2.40 respectively. For electrolysis, again the equations take the same form except the sign of the second term is positive, as $X_{H_2O}^r < X_{H_2O}^l$, that is, the mole fraction of steam at the fuel electrode surface l is greater than the mole fraction of steam at the fuel electrode reaction site r . The hydrogen concentration at the reactive surface is given by eq. 8.2.42 and the steam concentration at the electrode surface is given by eq. 8.2.43.

Fuel cell mode

Electrolyser mode

$$D_{H_2,p} = D_{H_2,m} \left(\frac{\epsilon}{\tau} \right) \quad (8.2.38) \quad D_{H_2O,p} = D_{H_2O,m} \left(\frac{\epsilon}{\tau} \right) \quad (8.2.41)$$

$$X^r_{H_2} = X^l_{H_2} - \frac{iRT_s L_{fuel.e.}}{2FP_{an}D_{H_2,p}} \quad (8.2.39) \quad X^r_{H_2} = X^l_{H_2} + \frac{iRT_s L_{fuel.e.}}{2FP_{an}D_{H_2,p}} \quad (8.2.42)$$

$$X^r_{H_2O} = X^l_{H_2O} + \frac{iRT_s L_{fuel.e.}}{2FP_{an}D_{H_2O,p}} \quad (8.2.40) \quad X^r_{H_2O} = X^l_{H_2O} - \frac{iRT_s L_{fuel.e.}}{2FP_{an}D_{H_2O,p}} \quad (8.2.43)$$

The total diffusion polarisation at the fuel electrode can then be calculated by eq. 8.2.44.

$$\eta_{diff,fuel.e.} = \frac{RT}{2F} \ln \left(\frac{X^b_{H_2} X^l_{H_2O}}{X^b_{H_2O} X^l_{H_2}} \right) \quad (8.2.44)$$

Fig. 8.2.6 shows that the diffusion loss on the fuel electrode side of the cell is almost negligible, <0.25 nV at all practical cell current densities.

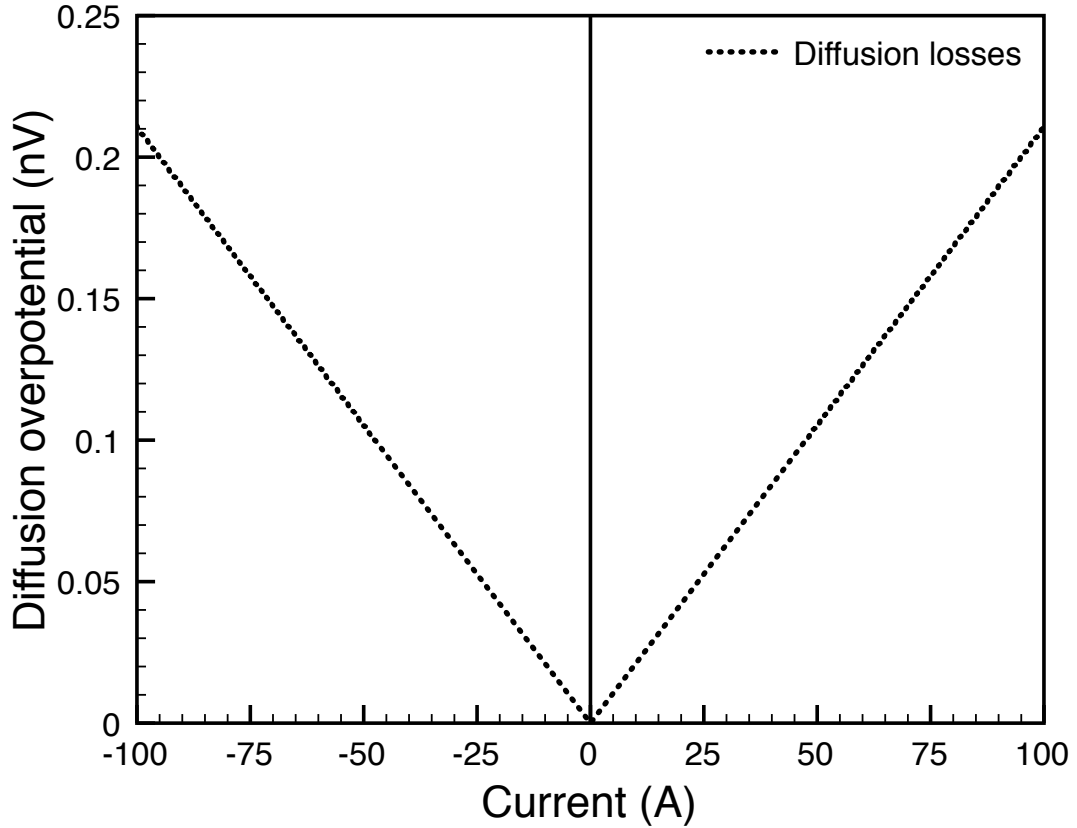


Figure 8.2.6: Diffusion losses at the fuel electrode as a function of RSOFC current, at 900 °C, 70 bar pressure, and 50% state of charge. Negative currents represent electrolyser mode, and positive currents fuel cell mode.

Diffusion at the oxygen electrode

On the oxygen side, as pure oxygen is used, there is no diffusion gradient, so there is no mass transport diffusion polarisation. However, there is a diffusion polarisation, arising from the surface diffusion of oxygen and oxygen species on the electrode. Semi-empirical equations for oxygen surface diffusion were obtained by analysing data from studies of symmetrical half cells of the LSM-YSZ oxygen electrode [9]. The area specific diffusion resistance of the oxygen electrode surface $R_{diff,surface}$ ($\Omega \text{ cm}^2$) can be modelled by eq. 8.2.45, where T is the system temperature in this equation, ($^{\circ}\text{C}$), P is the system pressure (in this equation, bar), and the exponential term uses base e . The equation is valid in the approximate range 1 bar - 70 bar pressure, and 750°C - 1050°C , and is plotted in fig. 8.2.7. In the operating range of the cell, the temperature dependence is more significant than the pressure dependence.

$$R_{diff,surface} = 2.45311 \times 10^{-5} \exp\left(\frac{8.85338 \times 10^3}{T}\right) P^{-0.532568} \quad (8.2.45)$$

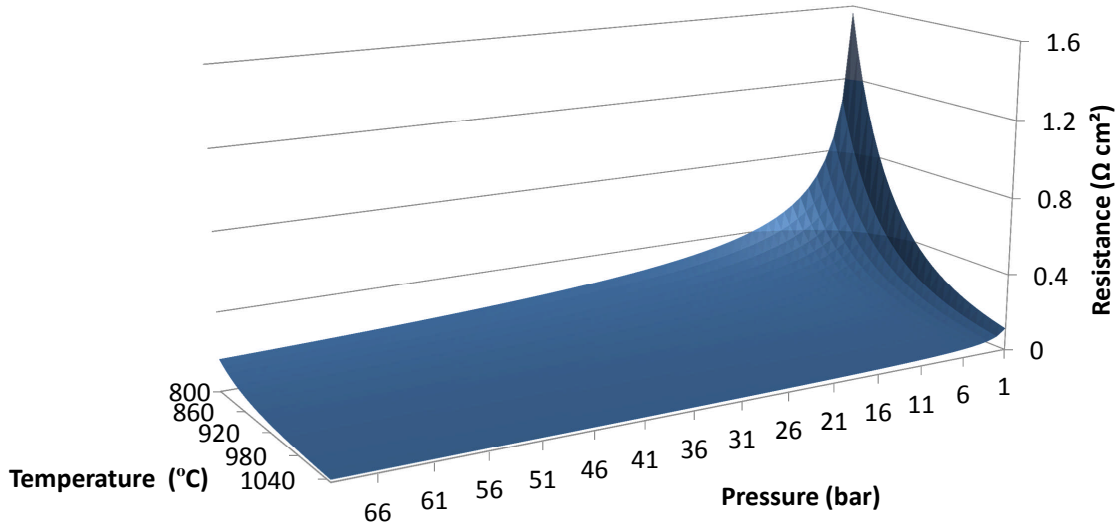


Figure 8.2.7: $R_{diff,surface}$ as a function of temperature and pressure.

In order to calculate the diffusion resistance for a whole cell $R_{diff,surface,cell}$ (Ω), the value of $R_{diff,surface}$ ($\Omega \text{ cm}^2$) calculated in eq. 8.2.45 must be converted to ($\Omega \text{ m}^2$), and normalised by the cell area A (m^2) from eq. 8.3.1. This is accomplished with eq. 8.2.46.

$$R_{diff,surface,cell} = \frac{1 \times 10^{-4} R_{diff,surface}}{A} \quad (8.2.46)$$

The summit frequency f_{max} (Hz) of the diffusion resistance arc $R_{diff,surface}$ ($\Omega \text{ cm}^2$) can be modelled by eq. 8.2.45, where T is the system temperature (in this equation, $^{\circ}\text{C}$), P is the system pressure (in this equation, bar), and exp uses base e . An empirical equation for f_{max} is calculated as a function of system pressure and temperature. The equation is valid from 1 bar - 70 bar pressure, and 750°C - 1000°C .

$$f_{max} = 1.5809 \times 10^{10} \exp\left(\frac{-1.98253 \times 10^4}{T}\right) P^{0.807662} \quad (8.2.47)$$

When the diffusion resistance $R_{diff,surface}$ and the summit frequency f_{max} are calculated, the area specific capacitance $C_{area,specific}$ (F cm⁻²) of the process as a function of temperature and pressure can be calculated using eq. 8.2.48.

$$C_{area,specific} = \frac{1}{R_{diff,surface} 2\pi f_{max}} \quad (8.2.48)$$

In order to calculate the capacitance for a whole cell C_{cell} (F), the value of $C_{area,specific}$ (F cm⁻²) calculated in eq. 8.2.48 must be converted to a value in (F m⁻²), and normalised by the cell area A (m²) from eq. 8.2.55. This is accomplished with eq. 8.2.49.

$$C_{cell} = 1 \times 10^4 C_{area,specific} A \quad (8.2.49)$$

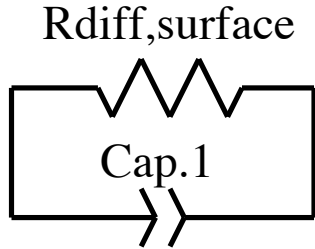


Figure 8.2.8: Randle's cell for modelling the surface diffusion polarisation resistance $R_{diff,surface}$, in parallel with a capacitor Cap. 1.

Now the surface diffusion polarisation and the capacitance can be calculated for a cell at any temperature and pressure in the range 1 bar - 70 bar pressure, and 750 °C - 1000 °C, the voltage behaviour can be calculated using a Randle's cell - a resistor and capacitor in parallel, as shown in fig. 8.2.8.

Diffusion overpotential for the whole reversible cell

The diffusion polarisation overpotential of the whole cell is given by eq 8.2.50. The first term is the fuel electrode diffusion overpotential. The second term is the oxygen electrode surface diffusion overpotential, calculated by multiplying the area-specific surface diffusion polarisation $R_{diff,surface}$ by the current density. As $R_{diff,surface}$ has units of Ω cm², and the current density has units of A m⁻², a conversion factor of 1×10^{-4} is also used to ensure the area units are the same.

$$\eta_{diff} = \frac{RT}{2F} \ln\left(\frac{X^b H_2 X^l H_2 O}{X^b H_2 X^l H_2 O}\right) + 1 \times 10^{-4} R_{diff,surface} i_{density} \quad (8.2.50)$$

Under constant DC current, the capacitor in the circuit in fig. 8.2.8 will charge up in a short period of time and remain fully charged. Then, the circuit behaves as a pure ohmic resistor. Fig. 8.2.9 shows the voltage drop associated with $R_{diff,surface,cell}$, as a function of cell temperature and current density. It may be seen that temperature is a more significant factor than current density in affecting this loss, over the likely operation ranges of system temperature and current density.

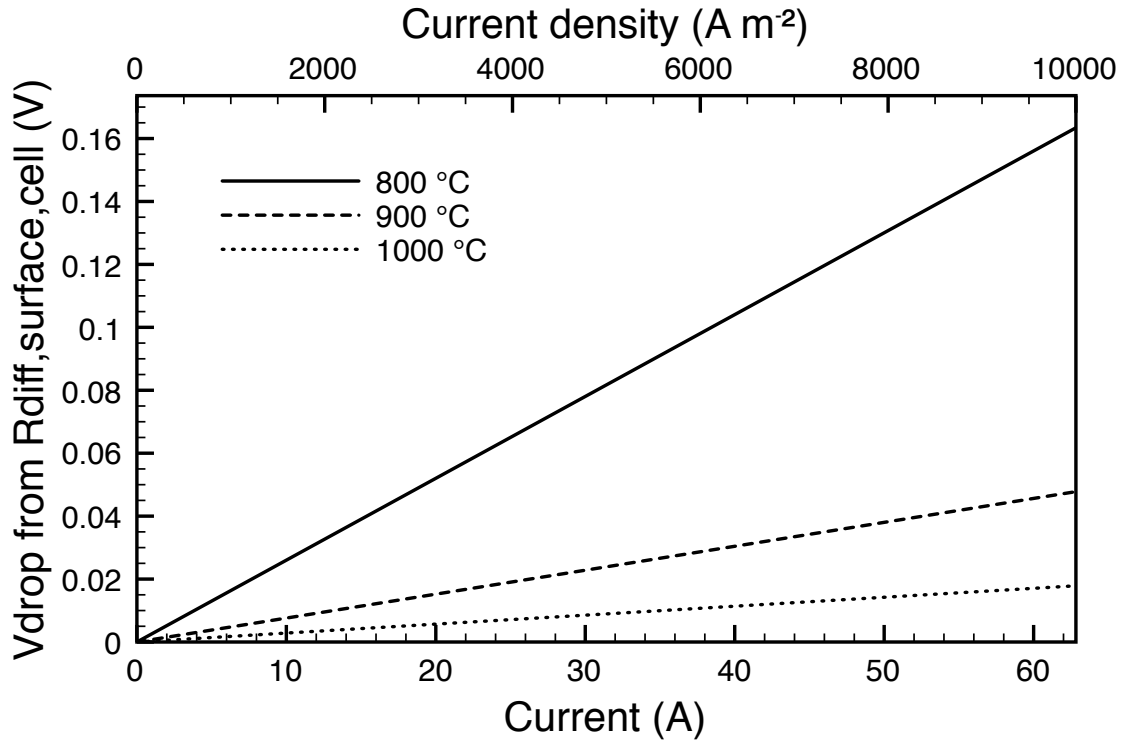


Figure 8.2.9: Voltage drop from $R_{diff,surface}$ at 70 bar pressure, 50% state of charge as a function of cell current and current density at 800 °C, 900 °C and 1000 °C.

8.2.6 Cell voltage and total losses

The losses in the reversible cell are ohmic losses and polarisation losses. The ohmic losses for each cell component were calculated in section 8.2.3 as resistances in ohms. This is converted to a voltage drop for the component i , called $V_{drop,i}$ using Ohm's law, eq. 8.2.51, by multiplying the calculated resistance by the total cell current. The total ohmic voltage loss is then calculated for the reversible cell as in eq. 8.2.52, by taking the sum of the voltage drop across each component.

$$V_{drop,i} = R_i I_{cell} \quad (8.2.51)$$

$$V_{drop,ohmic} = V_{drop,support} + V_{drop,oxy.e.} + V_{drop,fuel.e.} + V_{drop,electrolyte} + V_{drop,intercon.} + V_{drop,cellcon.} \quad (8.2.52)$$

Once the total ohmic losses in the cell $V_{drop,ohmic}$ are known, the cell voltage V_{cell} is calculated for the fuel cell mode according to eq. 8.2.53, by subtracting the ohmic losses and activation and diffusion polarisation losses from the standard voltage. The electrolyser cell voltage can be calculated from eq. 8.2.54, and is the standard voltage plus all the losses. A key assumption is that the current density is uniform through each component in the fuel cell, so the resistance and voltage drop will be the same in each part of the cell. In order to avoid having to make this assumption, and model the system more accurately, a computational fluid dynamics (CFD) model would be required. One such model of an

LSM-(lanthanum strontium manganate) supported tubular fuel cell showed that there was a voltage drop through the LSM [10]. In order to mitigate the effect of LSM support resistance in this model, LSC (lanthanum strontium cobaltate) was used instead of LSM as it has a higher electronic conductivity.

Fuel cell mode

Electrolyser mode

$$V_{cell} = V_{standard} - V_{drop,ohmic} - \eta_{act} - \eta_{diff} \quad V_{cell} = V_{standard} + V_{drop,ohmic} + \eta_{act} + \eta_{diff} \quad (8.2.53) \quad (8.2.54)$$

Fig. 8.2.10 shows the total losses/overpotentials in the fuel cell and electrolyser, as a function of current density, according to eq. 8.2.53 and 8.2.54. The ohmic losses and the activation losses dominate the total cell losses. The diffusion losses are much smaller, because the system is pressurised, which reduces them significantly.

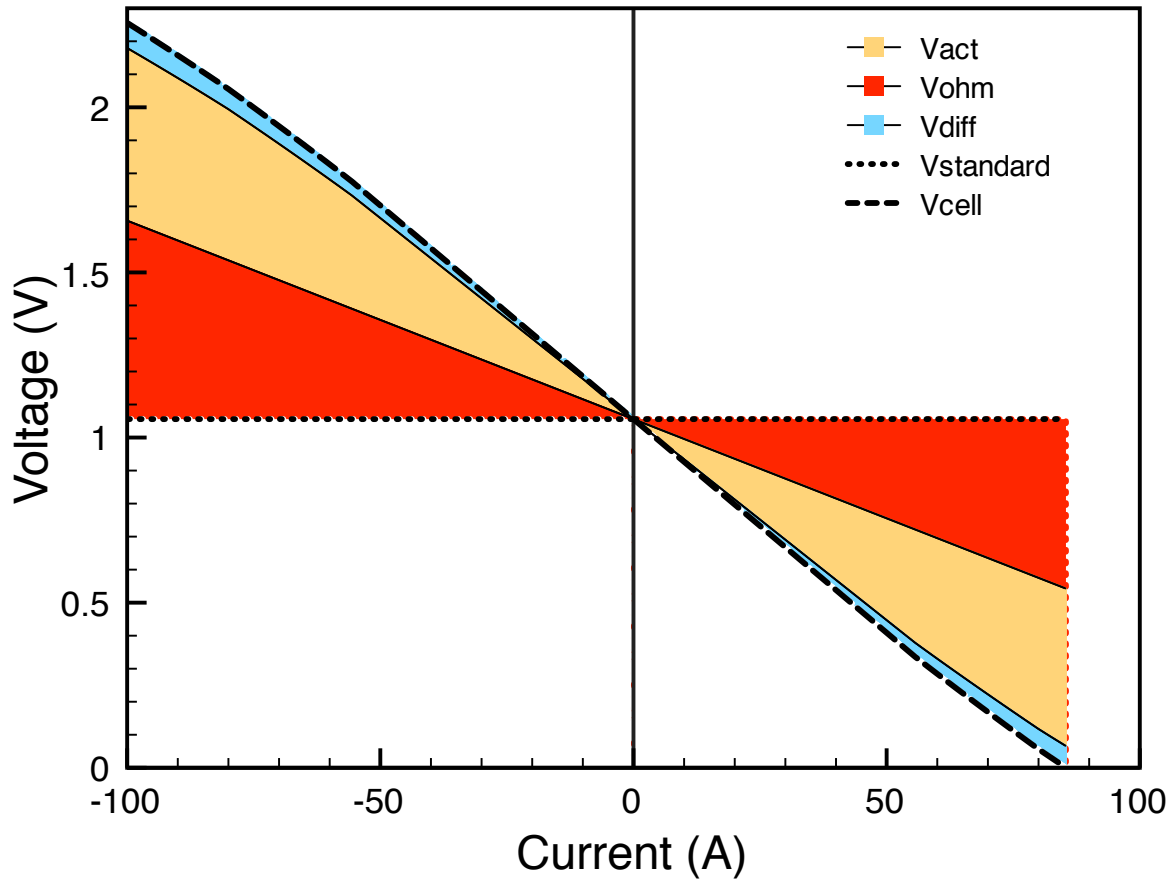


Figure 8.2.10: Cumulative losses/overpotentials in a single RSOFC as a function of current density, as per eq. 8.2.53 and 8.2.54, at 900 °C, 70 bar pressure, and 50% state of charge, as a function of current density. Current is negative in electrolyser mode, and positive in fuel cell mode.

8.2.7 Impedance modelling of the RSOFC

The impedance of a single RSOFC was simulated by the electrical equivalent circuit in fig. 8.2.11. The resistance due to activation losses and anode diffusion losses are treated as purely resistive losses with no capacitive component, in this model.

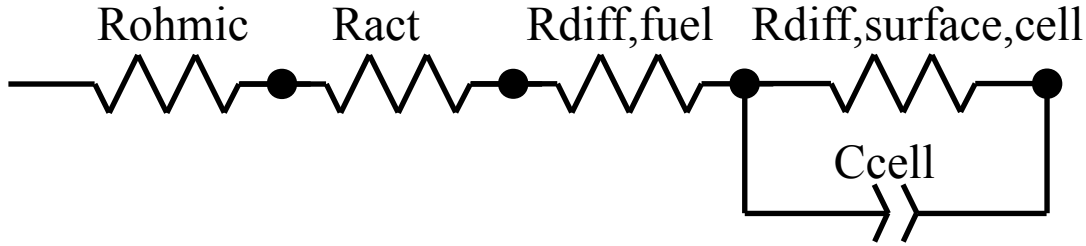


Figure 8.2.11: Electrical equivalent circuit for modelling a single RSOFC. R_{ohmic} is the sum of the ohmic resistances of the cell components, R_{act} is the ohmic resistance from activation losses in the cell, and $R_{diff,fuel}$ is the fuel electrode diffusion resistance. $R_{diff,surface,cell}$ is the oxygen electrode surface diffusion resistance, and C_{cell} is the associated capacitance.

Fig. 8.2.12 shows the calculated impedance spectra of the RSOFC at 70 bar, at 900 °C and 1000 °C.

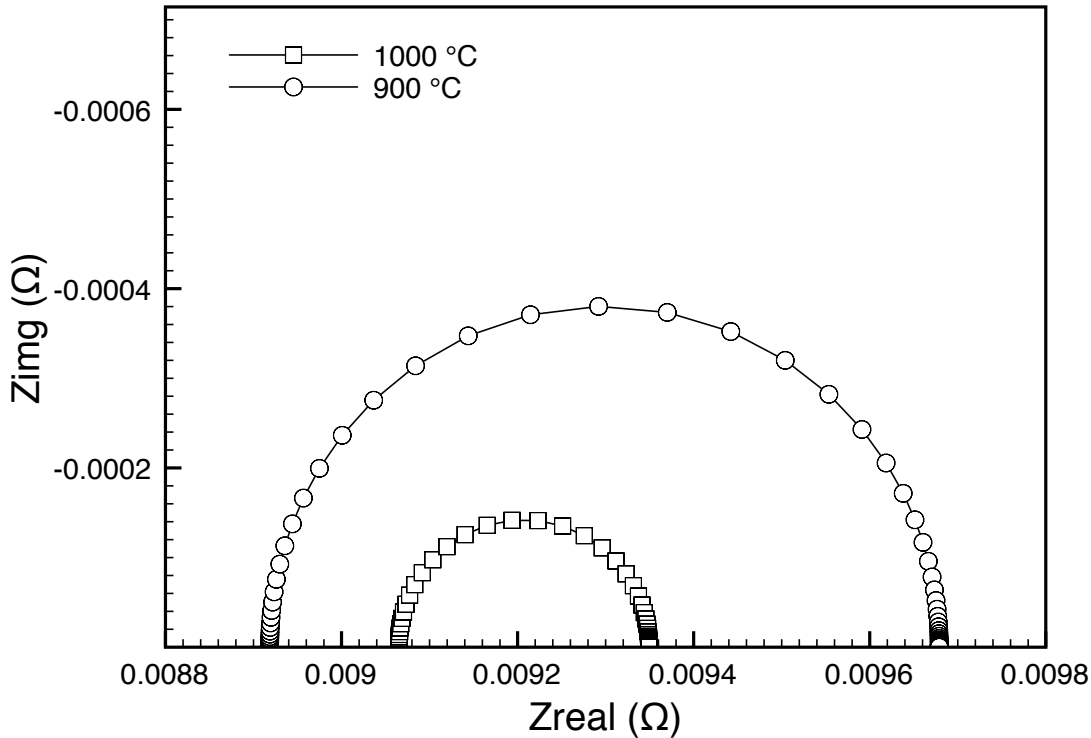


Figure 8.2.12: Impedance of the RSOFC at 900 °C and 1000 °C, at 70 bar. The left hand intercept for each arc is the total series resistance, including the ohmic resistance of the cell, plus the activation polarisation resistance, and the fuel electrode diffusion resistance. The area under the arc is $R_{diff,surface,cell}$ - the oxygen electrode surface diffusion resistance. The points are taken at 7 frequencies per logarithmic frequency decade between 0.1 Hz and 1 MHz.

The magnitude of $R_{diff,surface,cell}$ decreases with temperature considerably. However, the total ohmic resistance, which is the left hand intercept of the impedance arc with the x-axis, increases with temperature. This is because most of this resistance comes from the cell support, which is a metallic conductor.

8.2.8 Power outputs and inputs of the reversible SOFC system

Using the dimensions in table 8.2.1, the active area of the tube can be calculated, and therefore the power output if the fuel cell voltage and current density is known. The active area A of the tube is calculated by eq. 8.2.55.

$$A = 2\pi rl \quad (8.2.55)$$

where r is assumed to be 0.01 m, and l , the length of the active cell area is assumed to be 0.1 m. Therefore the fuel cell active area is 0.006283 m². The power per cell is given by eq. 8.2.56, where the voltage V_{cell} is from eq. 8.2.53. The stack power output W_{stack} (W) when running in fuel cell mode is therefore simply eq. 8.2.57, where n is the number of cells in the system, which is 800. The stack power input W_{stack} when running in electrolyser mode can also be calculated in a similar way, except that V_{cell} is the cell voltage for electrolyser mode.

$$W_{cell} = AV_{cell}I_{density} \quad (8.2.56)$$

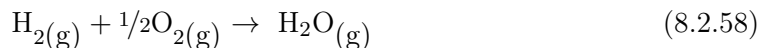
$$W_{stack} = nW_{cell} \quad (8.2.57)$$

8.2.9 Operating range of the reversible system

The safe operating temperature range of the system is defined by the upper limit, which is 1050 °C - above this temperature the microstructure of the cells will be affected, and their performance degradation over time will become significant. The lower limit is defined by the performance - at lower temperatures, especially below 750 °C, the ohmic resistance of the cell will increase significantly. There is also a limit in terms of the voltage and current that can be taken from the fuel cell without damaging it. At high currents and high overpotentials, it has been shown that $Mn^{3+/4+}$ in the LSM reduces to Mn^{2+} , and MnO is exsolved on the LSM surface. If this reacts with any chromium present in the system, it can lead to breakdown of the LSM structure at the triple phase boundaries [11]. It has also been shown that the rate of chromium deposition increases as the current density increases, and that the potential for the electrochemical deposition of chromium is about 0.9 V. Therefore, if the cell is operated below this voltage, chromium will be deposited electrochemically, which leads to an increase in the overpotential of the cell [12]. Sources of chromium in the system might be from the inner walls of a steel pressure vessel, or any steel balance of plant components. In this model, no account has been made for degradation - rather, the short term performance has been examined. However, in order to commercialise RSOFC, the various degradation mechanisms seen in SOFC will have to be addressed. A target of <0.1% drop in power per 500 h, at a constant voltage, was set for commercialised fuel cells [13].

State of charge

The state of charge Φ is the mole percentage of hydrogen in the hydrogen-steam mixture on the outside of the cell - the fuel side. In the fuel cell reaction, eq. 8.2.58, for every molecule of hydrogen consumed, a molecule of steam is produced. Therefore, the total moles of gas on the fuel side is independent of the state of charge.



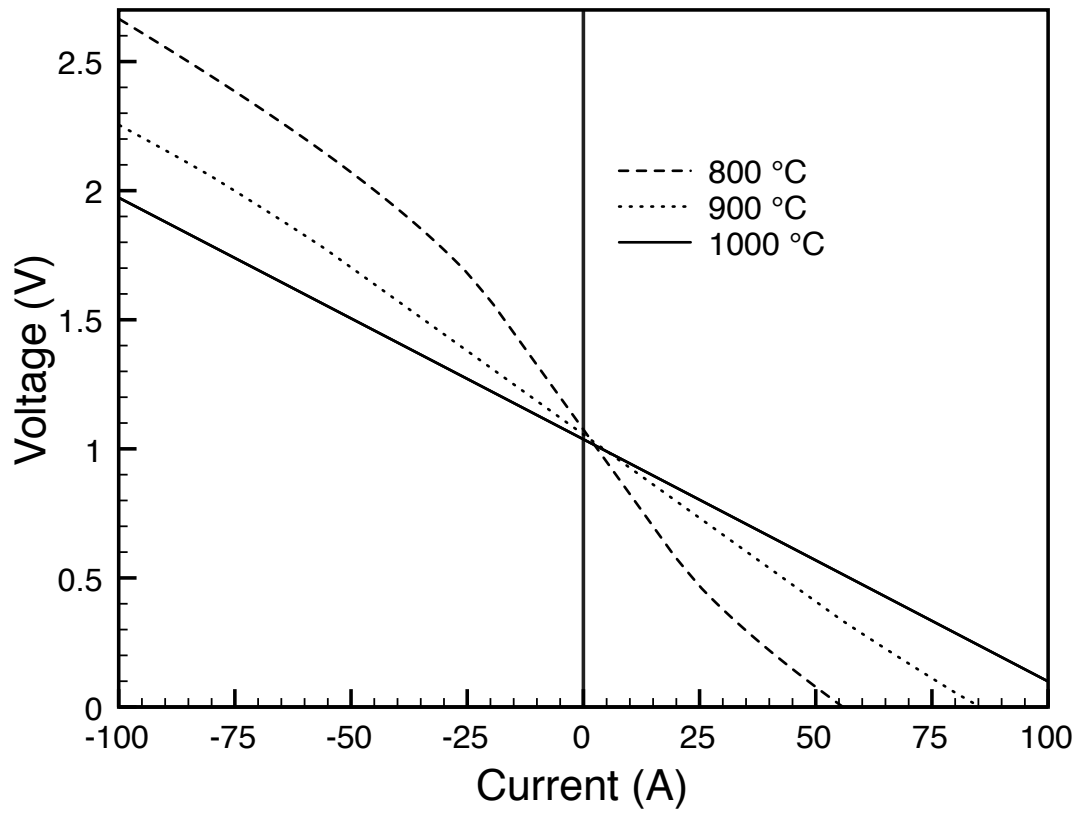
It is assumed in this model for the sake of simplicity, that the pressure of oxygen is always the same as the pressure of the hydrogen-steam mixture, in order that there will be no pressure differential across the cell. In a real RSOFC system, there would have to be a mechanism to balance the oxygen pressure against the pressure of the fuel gases, by adding or removing oxygen to the system.

There are maximum and minimum limits to the state of charge, because at very low hydrogen concentrations, the nickel in the fuel electrode will become oxidised and will expand, damaging it. This has been observed to cause cracking and mechanical failure in the cell during electrolysis [14]. At very high concentrations of hydrogen, near 100% state of charge, there will be very little steam in the system, which will reduce the performance in the electrolyser mode. It will cause a greater diffusion polarisation, and lower exchange current density, so a greater activation polarisation. Therefore, safe operating limits of the state of charge are assumed; the lower limit is 5%, and the upper limit is 95%.

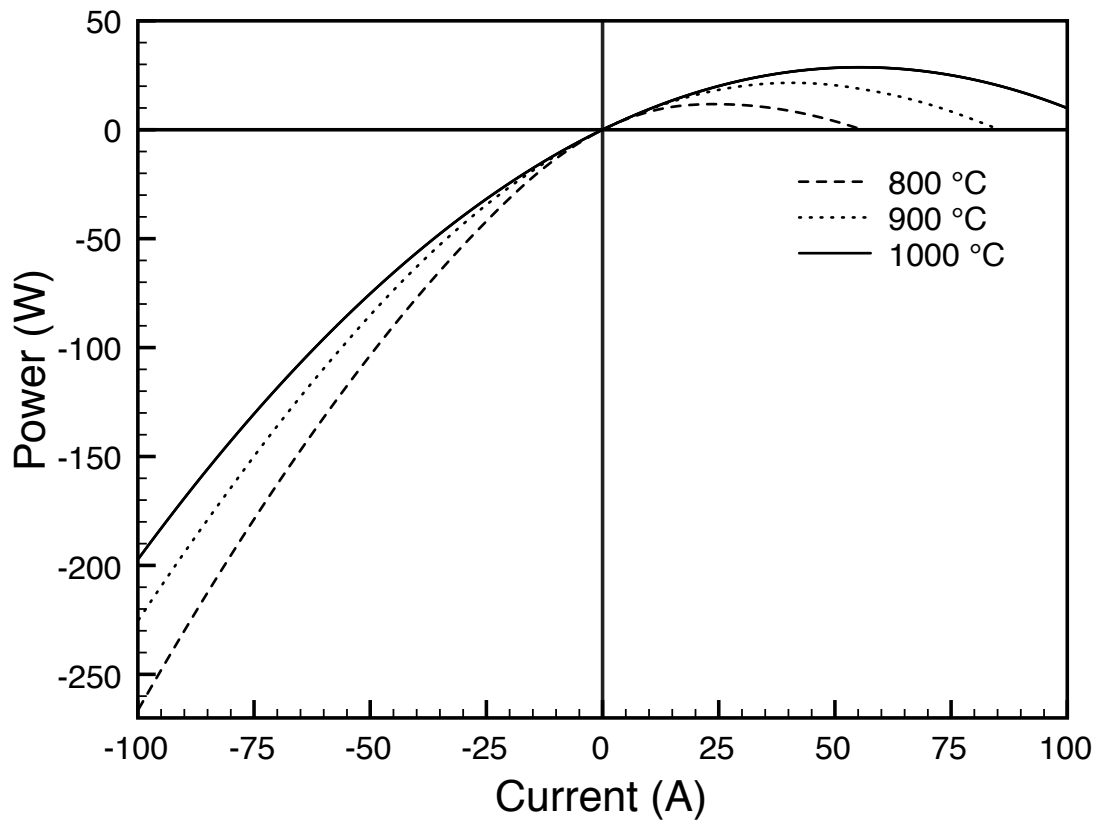
Fig. 8.2.13 shows the calculated performance of a RSOFC with varying temperature. This has a large impact on performance, greatly increasing the maximum power that can be produced from the cell, to 28 W at 1000 °C from 21 W at 900 °C. It has an even larger absolute impact in electrolyser mode, reducing the power needed at -100 A from 224 W at 900 °C to under 196 W at 1000 °C. This is significant, because the the same amount of hydrogen is produced in both cases, because the current is the same, yet the 28 W difference is heat production.

Fig. 8.2.14 shows the calculated performance of the cell at four different pressures, 1 bar, 3 bar, 5 bar and 70 bar. Although performance improves considerably with pressure, the rate of improvement decreases with increasing pressure, e.g. there is a greater performance gain pressurising the system fivefold from 1 to 5 bar than by a factor of fourteen from 5 bar to 70 bar. However, there the absolute gain in performance by pressurising from 5 bar to 70 bar is still significant.

Fig. 8.2.15 shows the calculated RSOFC performance as a function of state of charge, at 1010 °C. As the state of charge increases, the Nernst voltage of the cell increases, and so the cell performance improves. The worst performance in fuel cell mode is at the lowest state of charge, and the worst performance in electrolyser mode is at the highest state of charge. These effects are largely due to the changes in the Nernst voltage shown in fig. 8.2.1, from the different concentrations of hydrogen and steam in the system.

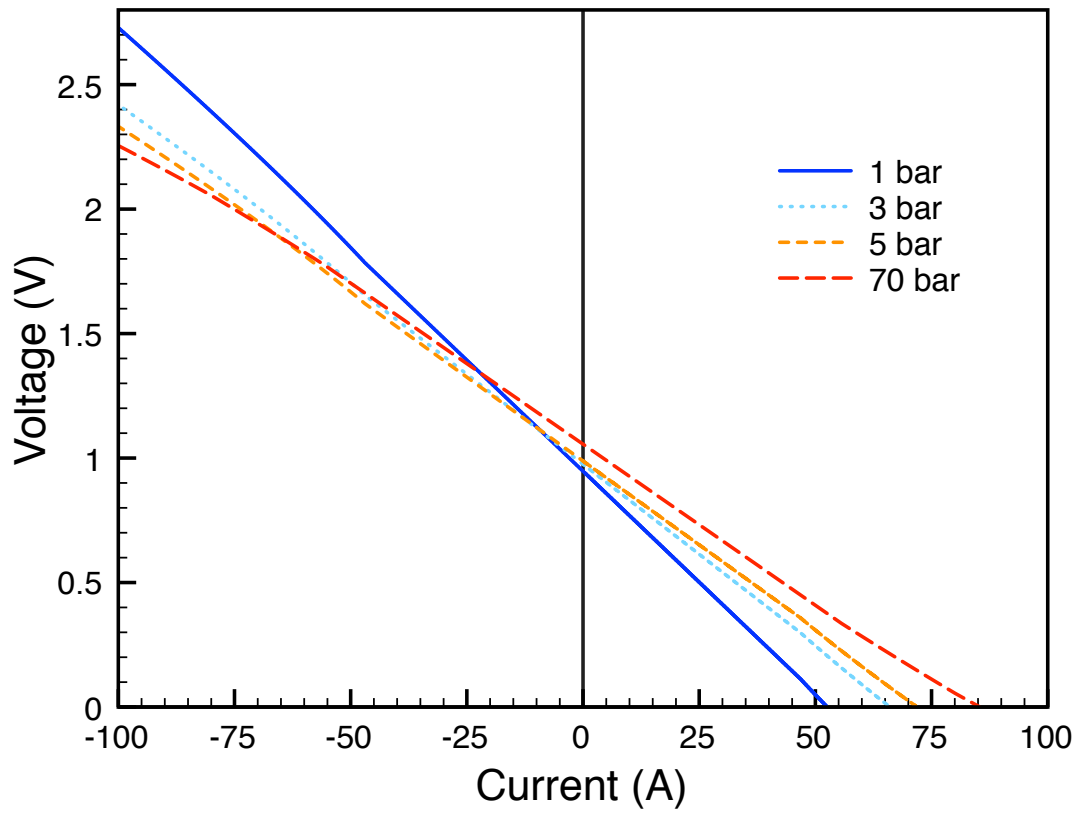


a)

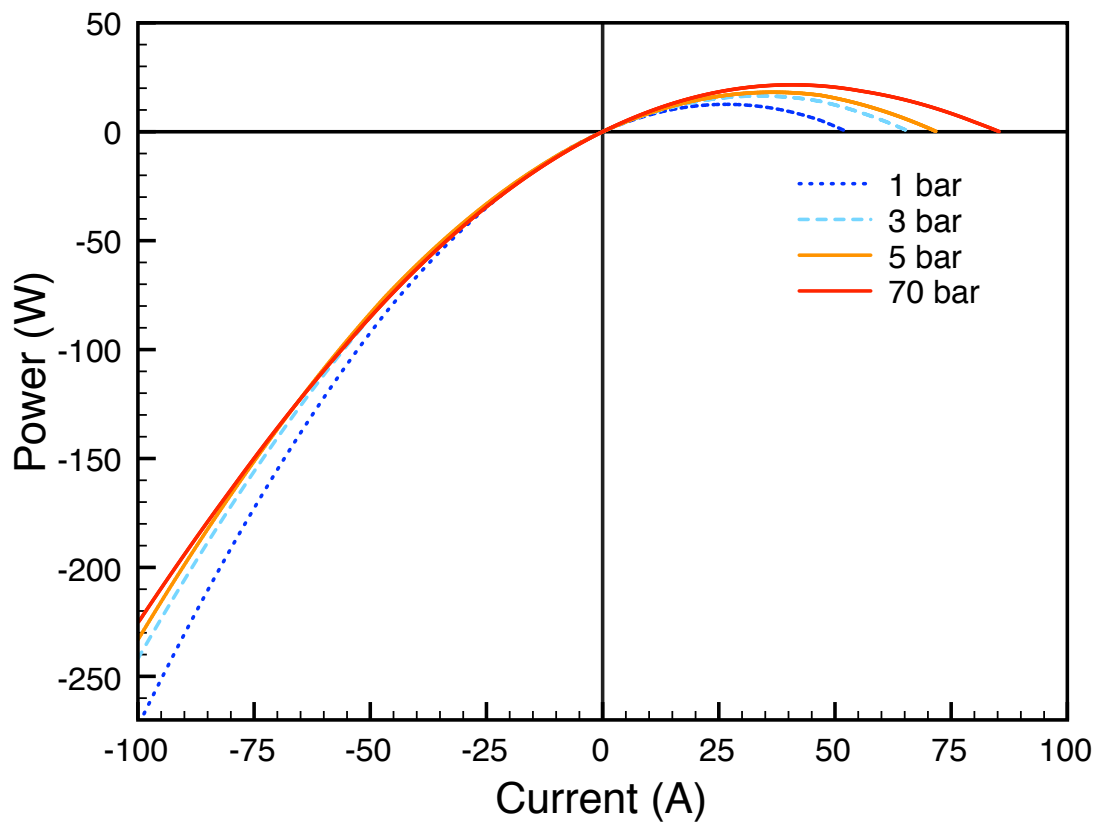


b)

Figure 8.2.13: RSOFC performance at 800 °C, 900 °C and 1000 °C: a) I/V curves, and b) W/I curves, for a single reversible SOFC, at 50% SOC, 70 bar pressure.

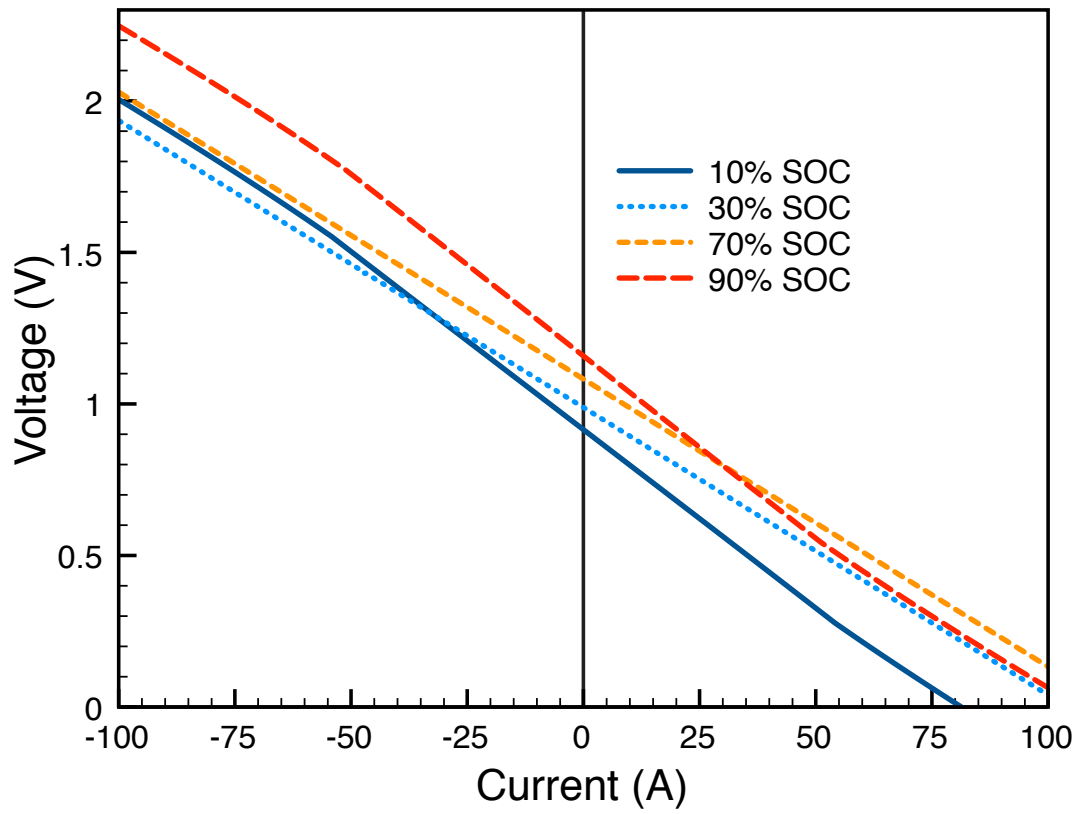


a)

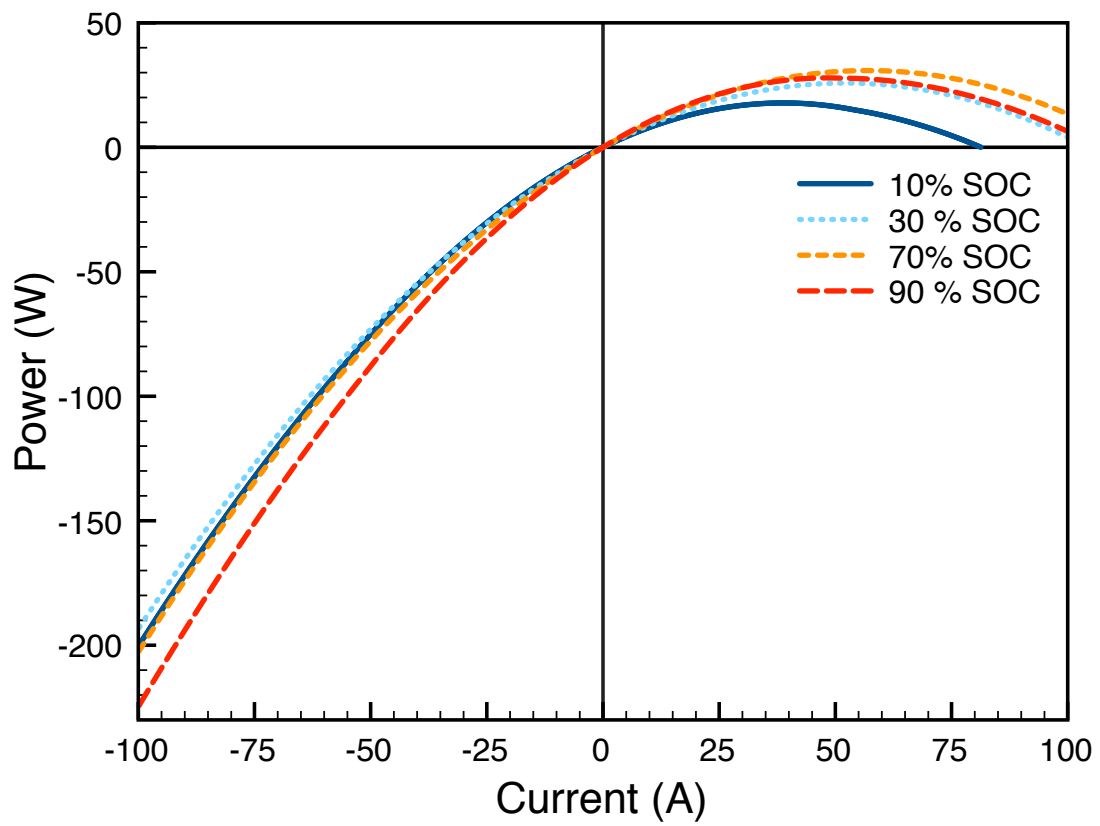


b)

Figure 8.2.14: RSOFC performance at 1 bar, 3 bar, 5 bar, and 70 bar, at 50% state of charge and 900 °C: a) I/V curves, and b) W/I curves, for a single reversible SOFC.



a)



b)

Figure 8.2.15: RSOFC performance at various states of charge, 10%, 30%, 70% and 90%, at 70 bar pressure and 1010 °C: a) I/V curves, and b) W/I curves, for a single reversible SOFC.

8.3 Heat modelling in the reversible cell system

A simplified type of modelling of heat production and consumption in the system, was carried out to test the model and determine the potential for energy storage by the system. The following assumptions were made in order to simplify the model.

1. The system is at a uniform temperature: i.e. any heat produced is instantaneously distributed through the system, and any heat consumed cools the whole system.
2. The external walls of the system are evenly insulated, and the system geometry and thermal conductivity of the material is known, so the rate of heat loss from the system to the surroundings can be calculated.
3. There is no leakage of gas in the system across the reversible cell electrolytes, so all heat generated comes from the electrochemical oxidation of hydrogen rather than combustion.

Of these assumptions, the first is the biggest assumption. In a real system, the cells when operating in fuel cell mode will be hotter than their surroundings, losing heat by conduction, convection and radiation. The model may underestimate the temperature of the cells as a result, and also the performance, which improves with increasing temperature. However, because the model is pressurised to 70 bar, the density of the gases is greatly increased, which will improve their thermal conductivity, and smooth the distribution of heat around the system.

The model may also underestimate the effect of step changes to the current load on the system when in fuel cell mode. It has been demonstrated for a dynamic model of a planar SOFC, that load changes cause a overshoot or undershoot of the cell voltage, which takes time to come back to the new steady-state value at that current density. It was observed that the relaxation times are on the order of 300 s, and were independent of the magnitude of the load change [15]. This may be attributed to fuel depletion/enrichment at the electrode interface, but also the time taken to establish a new equilibrium temperature. If the current is stepped up, the real cell would heat up faster than the model cell, because it would not dissipate heat instantaneously to its surroundings.

Furthermore, different parts of the cell would be at different temperatures - the parts with most resistance would be hottest. This leads to variations in cell performance over its surface. It has been shown for a tubular fuel cell stack, that a simple model of convective and radiative heat transfer is sufficient to predict the performance of the whole cell, but if the local variations are taken into account, a more complex model is necessary [16]. However, in this model, it is assumed that there is instantaneous heat transfer, and so these mechanisms are not modelled at all. The external walls of the system would also not be at an even temperature, so heat loss would vary from one part of the wall to another. This assumption greatly simplifies the model, but is the most significant of all assumptions made, and if the model were to be developed further, should be removed using a CFD model of the system.

Another assumption is that there is no leakage of gas across the electrolyte. This is a fairly accurate assumption, because if leakage is more than negligible, it will cause poor cell performance, especially at a system pressure of 70 bar. Therefore, RSOFC would not be used in a real system if they were leaky.

8.3.1 Electrochemical heat production/consumption

Heat is produced by the electrochemical oxidation of hydrogen, and absorbed by the electrolysis of steam. The heat produced or consumed may be determined from the magnitude of the current flowing through the cell. The cell current i (A) may be calculated from eq. 8.3.1, where A is the active cell area (m^2) as calculated by eq. 8.2.55, and i_{density} is the cell current density (A m^{-2}).

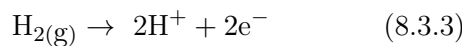
$$i = i_{\text{density}} A \quad (8.3.1)$$

The cell current can be related to the charge flowing per unit time with eq. 8.3.2, where t is the time in seconds, C is the charge in coulombs, and i is the cell current.

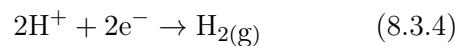
$$C = it \quad (8.3.2)$$

The charge can be converted into moles of hydrogen consumed using the fuel cell reaction half eq. 8.3.3. This shows that for every hydrogen molecule consumed, two electrons flow. Therefore, for every mole of hydrogen consumed, two moles of electrons flow. For electrolyser mode, the opposite is true, for every hydrogen molecule produced, two electrons are required.

Fuel cell mode



Electrolyser mode



The charge can be converted into moles of hydrogen produced/consumed per second using eq. 8.3.5, where F is Faraday's constant, the number of coulombs of charge in one mole of electrons.

$$M_{\text{H}_2} = \frac{C}{2F} \quad (8.3.5)$$

To convert the moles of hydrogen produced/consumed to heat absorbed/generated per unit time for the whole system, a semi-empirical equation may be used. The amount of heat from the reaction q_e (W) depends on the fuel cell temperature T (K) according to eq. 8.3.6, where n is the number of cells in the system. This heat is the entropy change for the fuel cell or electrolysis reaction.

$$q_e = nM_{\text{H}_2}(42.3241T - 4473.97) \quad (8.3.6)$$

In electrolyser mode, hydrogen is produced, so the same amount of heat as in eq. 8.3.6 is consumed.

8.3.2 Ohmic heat production

Ohmic or resistive losses in the cell produce heat, whether in fuel cell mode or electrolyser mode. The term q_{ohm} (W) is the power dissipated as heat by the ohmic resistance in the cell components, and can be calculated using eq. 8.3.7, where n is the number of cells in the stack, i is the cell current (A) from eq. 8.3.1, and R_{ohmic} is the ohmic resistance (Ω) of a cell, from eq. 8.2.17.

$$q_{ohm} = ni^2 R_{ohmic} \quad (8.3.7)$$

Fig. 8.3.1 shows the net heat production/consumption by a single RSOFC as a function of current density.

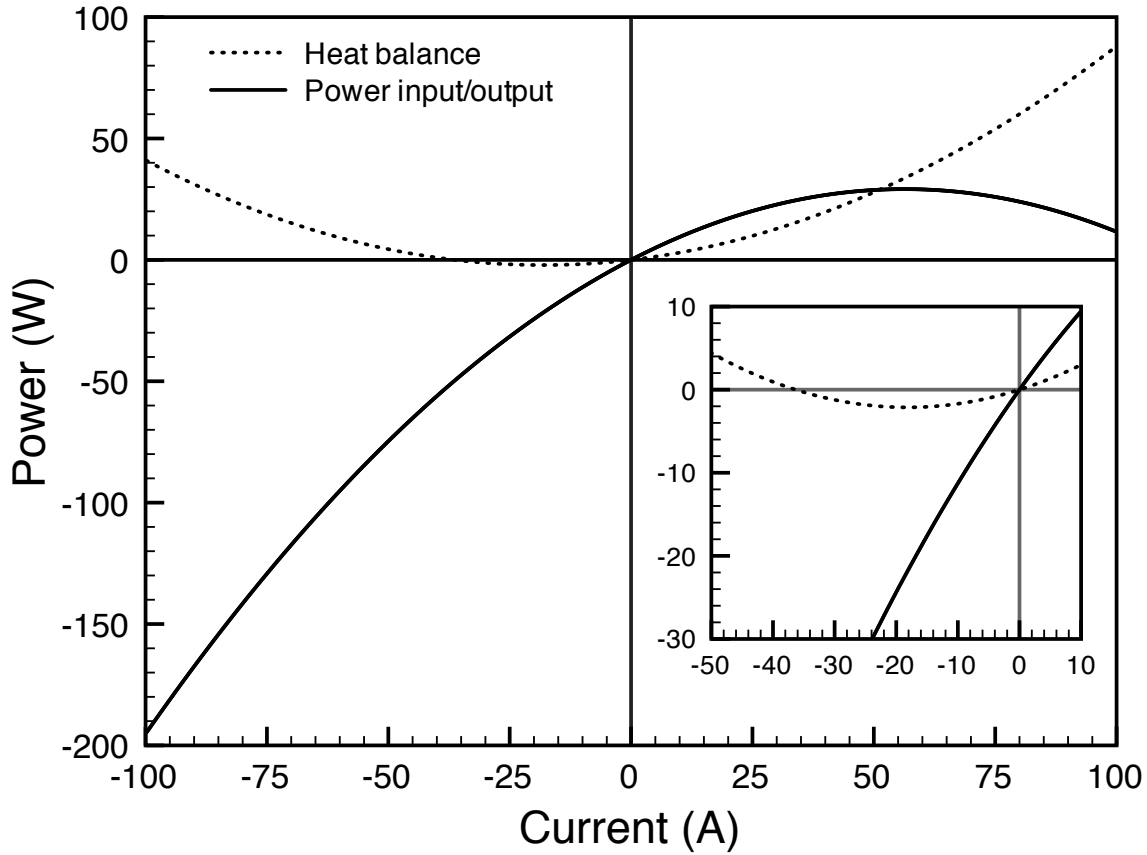


Figure 8.3.1: Net electrical power (W) and heat consumption/production (W) by the RSOFC as a function of current density, at 1010 °C, 70 bar pressure, and 50% SOC. This does not include heat losses from the system. Negative power values indicate electrolyser mode, i.e. power flowing into the system, and positive power values fuel cell mode, i.e. power flowing out of the system. An inset of a magnified portion of the main graph, shows more clearly the range of currents for which heat is absorbed in electrolyser mode.

In fuel cell mode, ohmic and electrochemical heat is produced, so the heat rises rapidly with current. However, in electrolyser mode, the ohmic heat production is offset by electrochemical heat absorption. Therefore, at low currents where the ohmic losses are low, there is a net heat consumption. This can be seen where the heat balance curve dips below the x-axis. Heat is also lost through the system outer walls, though this is not accounted

for on the graph. At 1010 °C, this loss is 2.6 W per cell.

8.3.3 Heat losses to surroundings

The system consists of a reversible cell stack in a pressurised vessel. To calculate heat losses from the system through the walls of the vessel, it is assumed that the vessel is a cube. The total system volume is 4 m³, therefore the internal dimensions of the vessel L_V (m) may be calculated from eq. 8.3.8, and the surface area A_V (m²) from eq. 8.3.9, which is 15.1191 m².

$$L_V = \sqrt[3]{4} \quad (8.3.8)$$

$$A_V = 6L_V^2 \quad (8.3.9)$$

A commercial high-performance micro porous insulation, with the brand name Microtherm® is used to insulate the vessel [17]. It is assumed to have a thickness l of 0.2 m around all the vessel walls. The thermal conductivity of the insulation changes with system temperature according to the semi-empirical eq. 8.3.10, where λ is the thermal conductivity (W m⁻¹ K⁻¹), and the coefficient values are $a = 2.54132 \times 10^{-8}$, $b = 1.93343 \times 10^{-5}$, and $c = 0.0257471$.

$$\lambda = aT^2 - bT + c \quad (8.3.10)$$

The temperature of the cold face of the insulation T_c , on the outside of the system, is calculated from the empirical eq. 8.3.11, as a function of the temperature of the hot face of the insulation. The hot face temperature is assumed to be the same as the system temperature, therefore in this equation it is represented as T .

$$T_c = 0.0225455T + 279.627 \quad (8.3.11)$$

The heat loss through the system walls Q_i (W) is calculated by integrating eq. 8.3.11, multiplying by the area from eq. 8.3.9, and dividing by the thickness of the insulation, to give eq. 8.3.12.

$$Q_i = A_V \left[\left(\frac{a}{3l} T^3 - \frac{b}{2l} T^2 + \frac{c}{l} T \right) - \left(\frac{a}{3l} T_c^3 - \frac{b}{2l} T_c^2 + \frac{c}{l} T_c \right) \right] \quad (8.3.12)$$

Fig. 8.3.2 shows the heat loss through the walls of the system as a function of system temperature. The heat loss from the system increases by 26% when the system temperature increases from 900 °C to 1050 °C. This heat loss is small compared to the maximum electrical power output of the RSOFC system in fuel cell mode, e.g. at 1000 °C, the heat loss is 2.1 kW, and the maximum electrical power output is 22.9 kW. It also shows that the area specific heat loss from the system is quite small - less than 150 W m⁻² when the system temperature is 1050 °C.

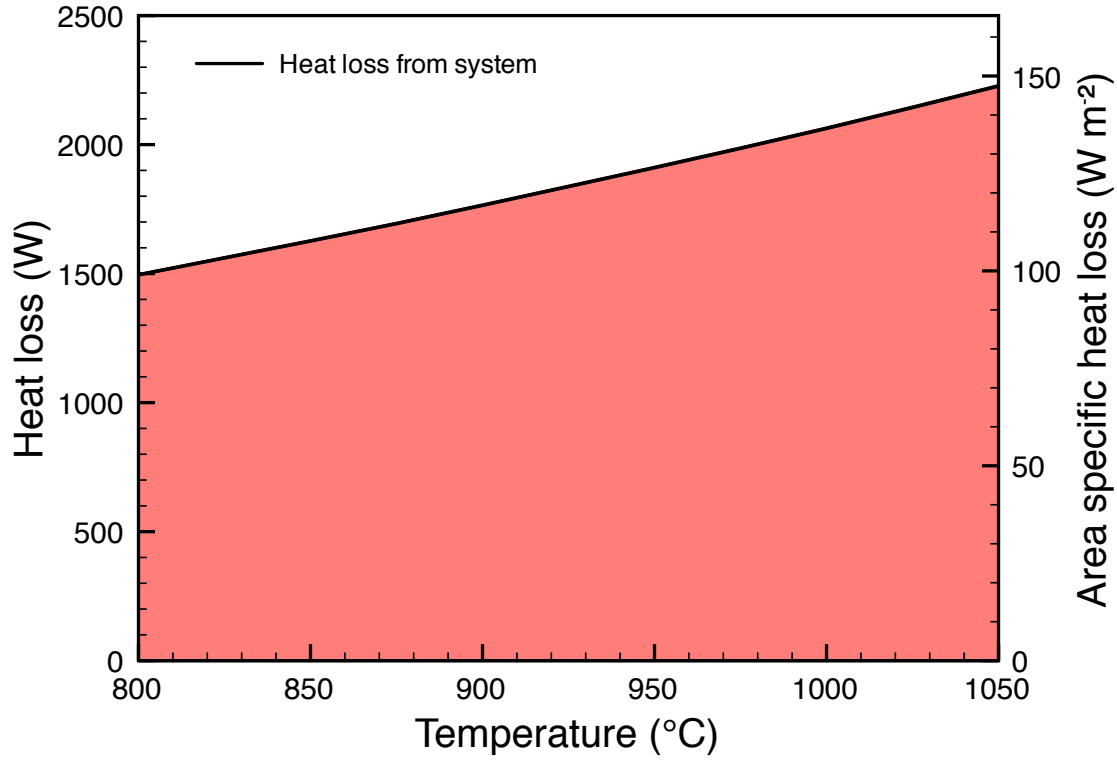


Figure 8.3.2: Total and area specific heat loss through the outer walls of the RSOFC system to the surroundings as a function of system temperature.

8.3.4 Cell and stack geometry and heat capacities.

In order to calculate the thermal mass of the system and its temperature change over time, the masses, volumes and heat capacities of the system components must be known. The total stack mass is calculated from eq. 8.3.13 where n is the number of cells in the stack, M_{stack} is the mass of the stack (kg), and ρ_{cell} is the density of a cell, which is 6000 kg m^{-3} . There is also a solid ceramic base plate connecting the cells, of the same density, and volume $1 \times 10^{-5} \text{ m}^3$ per cell, which are represented by ρ_{base} and V_{base} respectively in eq. 8.3.13.

$$M_{stack} = n (\rho_{cell} V_{cell} + \rho_{base} V_{base}) \quad (8.3.13)$$

The volume of the cell V_{cell} can be calculated from the cell dimensions given in section 8.2.2. A cell diameter of 0.02 m is assumed, and a cell length of 0.1 m. V_{cell} can be calculated by using eq. 8.3.14, where r_{inner} is the inner radius of the tubular cell, 0.007 m, and r_{outer} is the outer radius of the tubular cell, 0.01 m, and l is the cell length, 0.1 m.

$$V_{cell} = \pi (r_{outer}^2 - r_{inner}^2) l \quad (8.3.14)$$

The system volume V_{sys} is assumed to be the sum of the total reversible cell volume and the total base plate volume, according to eq. 8.3.15, where V_{cell} can be obtained from eq.

8.3.14, V_{base} is $1 \times 10^{-5} \text{ m}^3$, and n is the number of cells in the system.

$$V_{sys} = n(V_{cell} + V_{base}) \quad (8.3.15)$$

The specific heat capacity of the cells and bases Cp_{cells} and Cp_{bases} is the same, $400 \text{ J kg}^{-1} \text{ K}^{-1}$, so the total heat capacity of the stack Cp_{stack} (kJ K^{-1}) can be calculated from eq. 8.3.16, where M_{stack} is the mass of the stack from eq. 8.3.13. The value of Cp_{stack} is 593 kJ K^{-1} .

$$Cp_{stack} = M_{stack} Cp_{cells} \quad (8.3.16)$$

8.3.5 Heat capacity of the system gases

The heat capacity of the gases in the system make a significant contribution to the heat capacity of the system. Table 8.3.1 shows the molar heat capacities of the gases used in the reversible cell system. Hydrogen stands out as having a very high gravimetric heat capacity. However, the heat capacity per mole is similar to the other gases.

Gas	Heat capacity C_p ($\text{J kg}^{-1} \text{ K}^{-1}$)	Heat capacity $C_{p,m}$ ($\text{J mol}^{-1} \text{ K}^{-1}$)
Hydrogen	14380	29.05
Steam	1990	35.85
Oxygen	1249	39.97

Table 8.3.1: Heat capacities of the gases in the reversible cell system, at 400 K and 1 bar pressure [5].

The heat capacity ($\text{J kg}^{-1} \text{ K}^{-1}$) of the gases in the system at 70 bar, as a function of temperature is calculated by the following equations. The gravimetric heat capacity of the gases increases slightly with pressure, but their volumetric heat capacity significantly increases as they become more dense with increasing pressure. For hydrogen, eq. 8.3.17, for oxygen, eq. 8.3.18, and for steam, eq. 8.3.19, where T is the system temperature (K). The data for these equations was taken from the NIST standard reference database 69 [18].

$$Cp_{H_2} = 1.50216T + 13491.0 \quad (8.3.17)$$

$$Cp_{O_2} = 0.144437T + 951.593 \quad (8.3.18)$$

$$Cp_{H_2O} = 0.182118T + 2207.90 \quad (8.3.19)$$

The volume of hydrogen and steam in the system V_{H_2, H_2O} (m^3) is calculated in eq. 8.3.20, where the total system volume is 4 m^3 , V_{sys} is the system volume from eq. 8.3.15, i.e. the volume of the cells and base plates, and $V_{h.s.}$ is the volume of the heat store, from eq. 8.3.29. The number of moles of hydrogen and steam in the system n can then be calculated by eq. 8.3.21, at 1173 K, if the system pressure (Pa) is known, and then it is assumed that this is fixed. The moles of hydrogen may be calculated from this using eq.

8.3.22 by multiplying by the state of charge. The number of moles of steam is calculated by eq. 8.3.23.

$$V_{H_2,H_2O} = 4 - V_{sys} - V_{h.s.} \quad (8.3.20)$$

$$n = \frac{(PV_{H_2,H_2O})}{(RT)} \quad (8.3.21)$$

$$n_{H_2} = n\Phi \quad (8.3.22)$$

$$n_{H_2O} = (1 - \Phi)n \quad (8.3.23)$$

The total mass (kg) of hydrogen is calculated by eq. 8.3.24, and the total mass of steam (kg) by eq. 8.3.25.

$$M_{H_2} = 0.00202n_{H_2} \quad (8.3.24)$$

$$M_{H_2O} = 0.01801n_{H_2O} \quad (8.3.25)$$

The number of moles of oxygen in the system can be calculated from eq. 8.3.21, if the system pressure (Pa) and temperature (K) are known, except that V_{H_2,H_2O} is replaced by the volume of oxygen in the system V_{O_2} . This is calculated from the internal volume of each cell, multiplied by the number of cells, according to eq. 8.3.26. Then, the mass of oxygen (kg) in the system is calculated from eq. 8.3.27.

$$V_{O_2} = 0.1\pi r_{cell}^2 n \quad (8.3.26)$$

$$M_{O_2} = 0.03200n_{O_2} \quad (8.3.27)$$

The total heat capacity ($J K^{-1}$) of the gases in the system may be calculated from eq. 8.3.28, where the heat capacity of each gas is multiplied by the mass of the gas (kg), and these heat capacities are added together. For instance, at 1000 °C, the total heat capacity of the system gases is 1324 kJ K^{-1} .

$$\Sigma (C_{p,gases}M_{gases}) = Cp_{H_2}M_{H_2} + Cp_{H_2O}M_{H_2O} + Cp_{O_2}M_{O_2} \quad (8.3.28)$$

System temperature during a fuel cell cycle

The maximum reversible energy storage capability of the system depends on two factors; the amount of heat that can be stored, and the amount of chemical energy in the form of hydrogen that can be stored. A test was run on the model in fuel cell mode with the starting parameters, 95% state of charge, system temperature 900 °C, and pressure 70 bar. The system temperature and electrical power output were recorded as a function of time, at a constant current of 40.8 A per cell, or a current density of 6494 A m^{-2} , and are shown

in fig. 8.3.3. This current was chosen because it is the current at which maximum power from the cell can be drawn at 900 °C.

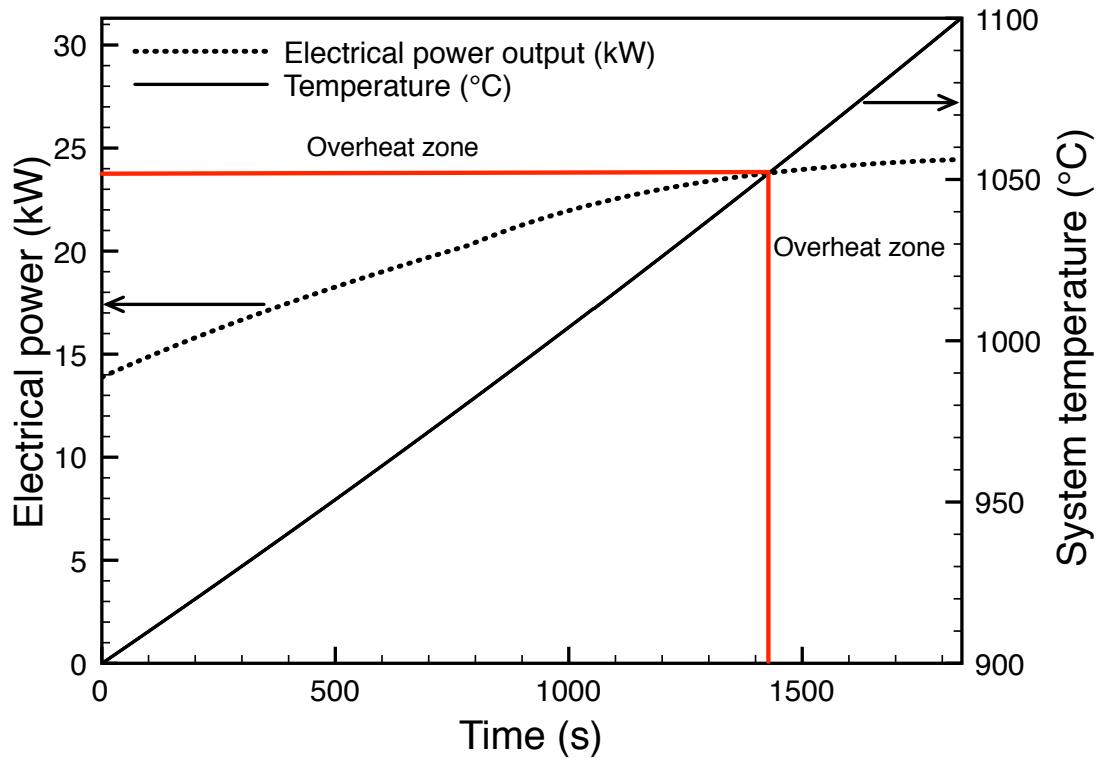


Figure 8.3.3: Electrical power output and system temperature over time, at a current of 40.8 A per cell, starting conditions 95% state of charge, 900 °C, showing the time until the system overheats.

The maximum system temperature is 1050 °C to avoid damaging the RSOFC, and it is marked on the graph with a red line. It can be seen that when the system is run in fuel cell mode, the temperature rapidly increases, and after 23½ min, it has reached 86.5% state of charge and 1050 °C. Therefore, the system has quickly overheated, and is no longer able to produce electrical energy, but must be switched to electrolyser mode, to cool it. The rapid rise in temperature is due to the low heat capacity of the system relative to the heat it produces. Fig. 8.3.4 shows the contribution of different system components to the heat capacity when the system temperature rises from 900 °C to 1050 °C. The gases provide 73.4% of the heat capacity, with the stack supplying 26.6%. Although the gases have a low heat capacity at atmospheric pressure, their volumetric heat capacity at 70 bar is considerably greater.

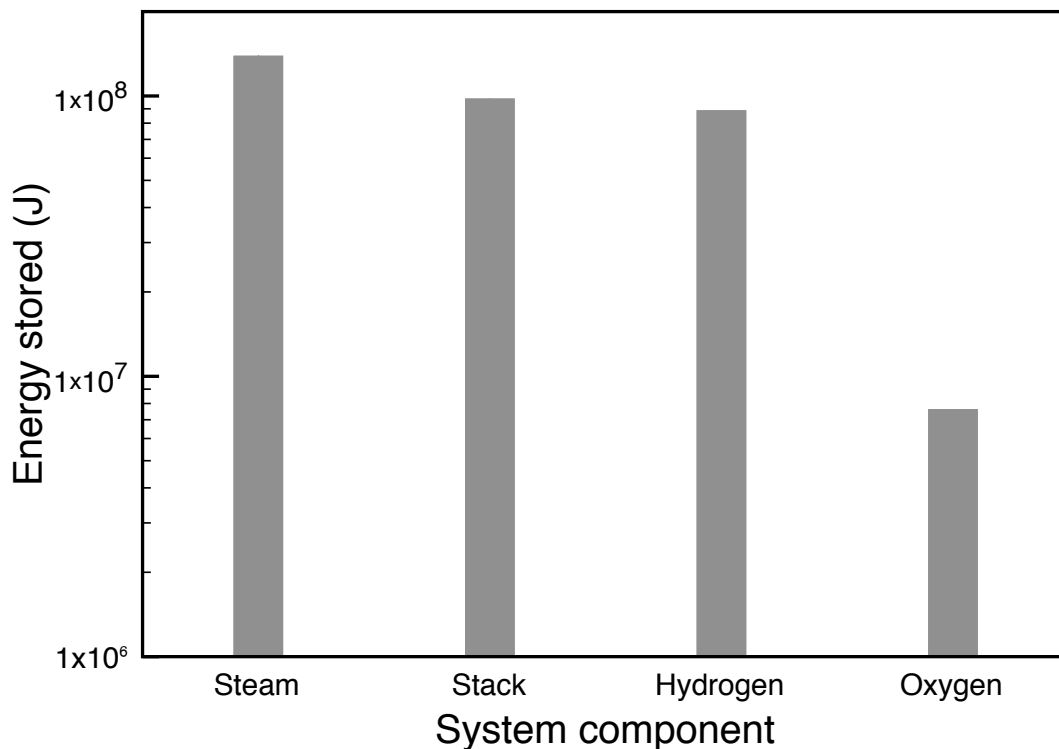


Figure 8.3.4: Logarithmic plot of heat stored by each system component, when the system temperature increases from 900 °C to 1050 °C. The stack includes the cells and bases.

If the heat capacity of the system is increased, it will be able to reversibly store much more energy, and run for longer in fuel cell mode, before it overheats. Two ways to achieve this would be to increase the pressure or volume of the system gases, or add more solid mass to the system. However, increasing the system volume while keeping the stack size and power output constant, would result in greater heat losses through the walls, and increasing the pressure of the gases would add to the expense of the stack. Therefore, the best way to increase the heat capacity of the system is to add more solid mass to it, which has a much higher volumetric heat capacity than the system gases.

8.3.6 The phase change heat store

The reversible SOFC system requires a greater thermal mass, in order to store heat and increase the run-time of the system from 23½ min. The additional of a solid piece of ceramic would be able to fulfil this function. However, a much greater volumetric density of heat storage is obtained by the use of a suitable phase change material, in which a phase transformation between solid to liquid occurs at a particular temperature. In fuel cell mode when the system is heating up, when it reaches the melting point of the material, it melts and stores energy equivalent to the latent heat of melting. When the system is switched into electrolyser mode, it cools to the melting point of the material, which freezes and releases the heat again. Therefore the phase change material acts as a heat store for the system, extending its run time and energy storage potential.

A suitable phase change material for this purpose is a type of bronze, a copper-tin

alloy, 11 weight %/ 6.21 mol. % tin, which melts over a range of temperatures near 1010 °C [19, 20]. For the purposes of this model, is assumed to melt at exactly 1010 °C, or 1283.15 K. The bronze acts as a thermal mass, storing heat as its temperature increases. When it melts, it stores heat equivalent to the enthalpy of fusion (latent heat of melting). Above the melting point, it acts as a thermal mass once again. The heat stored as it heats up and melts during the fuel cell cycle is released in the electrolysis cycle when the system cools. Due to its large thermal mass, it also helps to prevent the system from overheating. The heat store is described in three stages: below, at and above the melting point. The mass of the heat store $M_{h.s.}$ is 500 kg, and its density $\rho_{h.s.}$, which is 7890 kg m⁻³. The volume of the heat store $V_{h.s.}$ is separate from the system volume, and can be calculated from eq. 8.3.29, giving a value of 0.0634 m³.

$$V_{h.s.} = \frac{M_{h.s.}}{\rho_{h.s.}} \quad (8.3.29)$$

The first stage is for temperatures below the melting temperature, i.e. <1010 °C. The semi-empirical eq. 8.3.30, calculates the heat capacity of the bronze below the melting point, $Cp_{bronze,solid}$ (J kg⁻¹ K⁻¹), as a function of system temperature (K). This equation is valid only at $T < 1010^\circ\text{C}$.

$$Cp_{bronze,solid} = 0.1594T + 293.09 \quad (8.3.30)$$

Secondly, if the system temperature is equal to 1010 °C, then eq. 8.3.31 may be used to calculate the total energy (J) stored by the heat store when it completely melts, where $H_{fus,bronze}$ is the enthalpy of fusion for the bronze, which is 3.4x10⁵ J kg⁻¹.

$$E_{h.s.} = H_{fus,bronze} M_{h.s.} \quad (8.3.31)$$

Thirdly, at temperatures >1010 °C, the heat capacity of the molten bronze, $Cp_{bronze,molten}$ is assumed to be constant with temperature in the range 1010 °C - 1050 °C, because the bronze is a liquid, and it has a value of 490 J kg⁻¹ K⁻¹ [19]. Fig. 8.3.5 shows the amount of energy stored by each system component, as the system temperature increases from 900 °C to 1050 °C. The heat stored by the phase change of the heat store represents 31.3% of the total heat stored, and if the heat capacity of the heat store is added to that, 38.1% of the system heat capacity. Therefore, by adding a 500 kg heat store, the heat storage capacity of the system has been significantly increased. The remaining heat is mostly stored by the system gases.

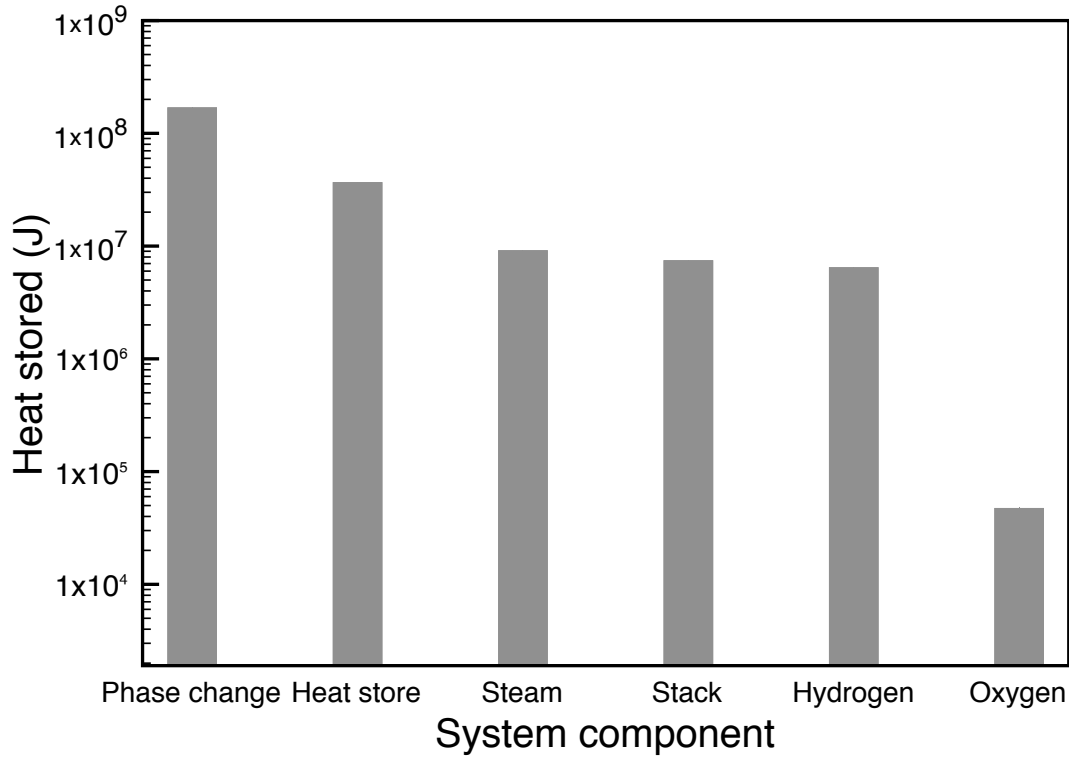


Figure 8.3.5: Logarithmic plot of heat stored by each system component, when the system temperature increases from 900 °C to 1050 °C. The stack includes the cells and bases. The heat stored by the heat store as the temperature increases, and the heat stored when it changes phase are shown separately.

8.3.7 Fuel cell and electrolysis cell heat balances

In order to estimate the heat balance of the system in fuel cell mode, eq. 8.3.32 is used. It is modified from eq. (8) in [21] where M_{stack} is the mass of the reversible cell stack (kg) which can be calculated by eq. 8.3.13, $M_{h.s.}$ is the mass of the heat store (kg), Cp_{stack} is the heat capacity of the stack, which can be assumed to be 400 J kg⁻¹ K⁻¹ [22], and $Cp_{bronze,solid}$ is the heat capacity of the solid bronze, calculated using eq. 8.3.30. The parameter dT is the change in system temperature (K) t is time (s), q_e is the heat generated by the electrochemical reaction per second, q_{ohm} is the heat produced by the ohmic losses per second, and Q_i is the heat loss through the insulation per second. For electrolyser mode, eq. 8.3.33 may be used, because heat is absorbed rather than produced by the reaction.

$$dT = \frac{dt (q_e + q_{ohm} - Q_i)}{(M_{stack} Cp_{stack} + M_{h.s.} Cp_{solid.bronze} + \Sigma (C_{p,gases} M_{gases}))} \quad (8.3.32)$$

$$dT = \frac{dt (-q_e + q_{ohm} - Q_i)}{(M_{stack} Cp_{stack} + M_{h.s.} Cp_{solid.bronze} + \Sigma (C_{p,gases} M_{gases}))} \quad (8.3.33)$$

At a temperature of 1010 °C, as the system generates heat, it is absorbed by the melting of the bronze metal, so the system temperature does not rise. The state of charge of the heat store, represented by the symbol Φ , is defined as the percentage of bronze that has melted,

of the total bronze in the heat store. This is calculated by eq. 8.3.34. The top line of the equation is the total heat that has gone into the heat store: i.e. the integral net heat flow between the time $t = 0$ s, when $T=1010$ °C, and the present moment, e.g. if the system temperature rose to 1010 °C 10 seconds ago, $t=\text{present}=10$ s. When all the metal has melted, the state of charge Φ is exactly 100%, and the temperature of the system begins to rise again. In electrolyser mode, the metal is cooling, so it is progressively solidifying as heat is absorbed by the electrolysis reaction. In this case, $t=0$ is the time at which the heat store state of charge is 100%. The bottom line of the equation is the total energy stored by the heat store as latent heat of fusion $E_{h.s.}$, from eq. 8.3.31.

$$\Phi = \frac{\int_{t=0}^{t=\text{present}} (q_e + q_{ohm} - Q_i) dt}{E_{h.s.}} \quad (8.3.34)$$

In fuel cell mode, at temperatures >1010 °C, the heat capacity of the heat store is constant, because it is a liquid, and eq. 8.3.35 is used to calculate the change in system temperature.

$$dT = \frac{dt (q_e + q_{ohm} - Q_i)}{(M_{stack} C_{pstack} + M_{h.s.} C_{p\text{molten.bronze}} + \Sigma (C_{p,gases} M_{gases}))} \quad (8.3.35)$$

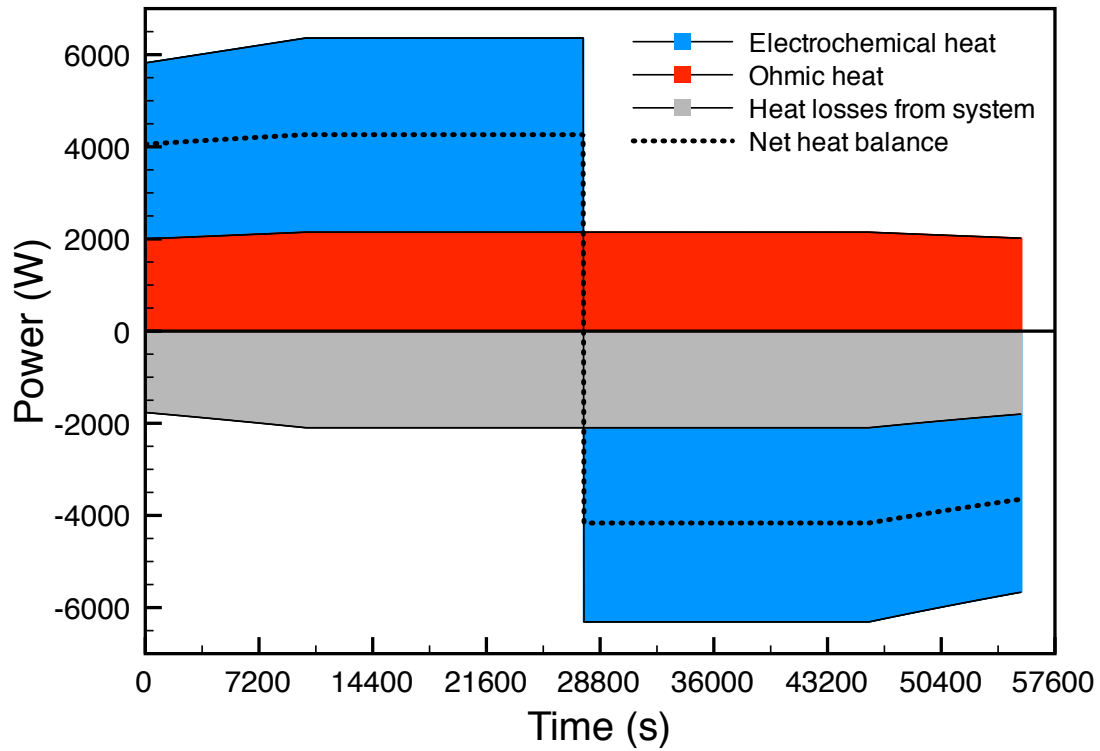
In electrolyser mode, eq. 8.3.36 is used, except that heat is produced rather than being consumed, so q_e is negative.

$$dT = \frac{dt (-q_e + q_{ohm} - Q_i)}{(M_{stack} C_{pstack} + M_{h.s.} C_{p\text{molten.bronze}} + \Sigma (C_{p,gases} M_{gases}))} \quad (8.3.36)$$

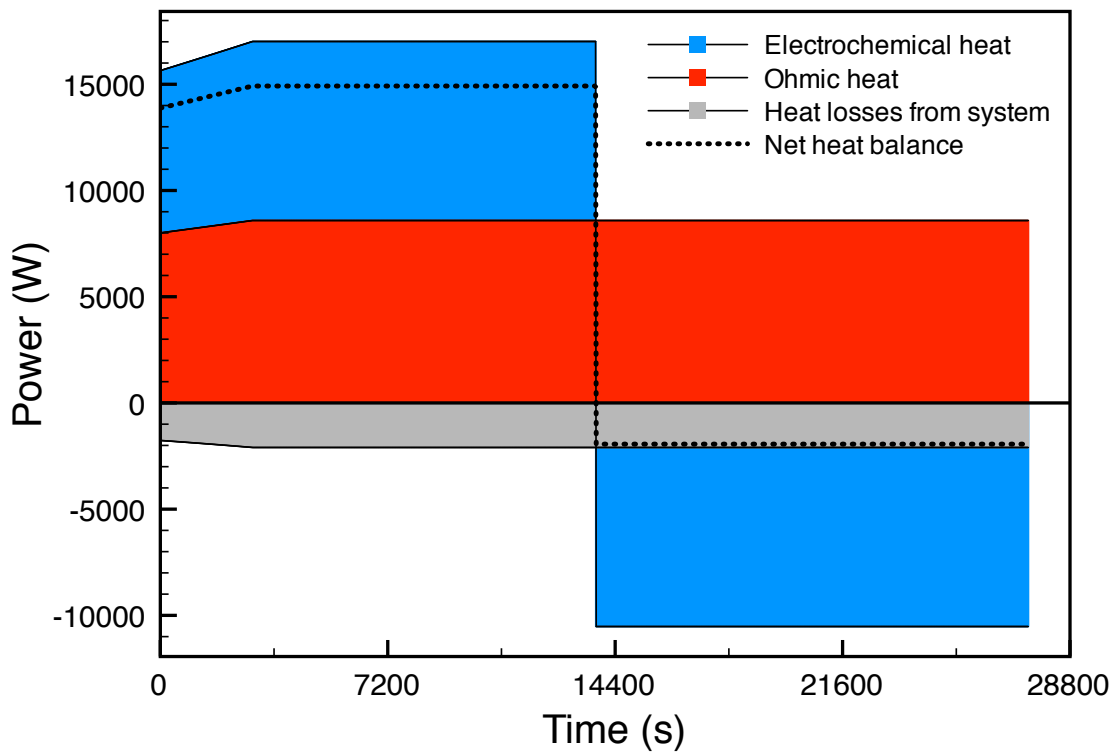
From these equations, the change in the system temperature can be calculated.

Heat production/consumption during a RSOFC cycle.

Fig. 8.3.6a shows a RSOFC cycle run at 40.8 A/-40.8 A per cell, and fig. 8.3.6b shows a RSOFC cycle run at 20.4 A/-20.4 A per cell. The current of 40.8 A per cell was chosen as it is the current that produces the maximum fuel cell power at 900 °C. In both cycles, the starting conditions are 900 °C, 70 bar pressure, and 95% state of charge. The system is run in fuel cell mode until 5% state of charge is reached, then in electrolyser mode until 95% state of charge is attained. The graphs show the heat produced or consumed by the electrochemical reactions as described in subsection 8.3.1, the heat produced by the ohmic losses in the cell from eq. 8.3.7, and the heat lost from the system as in subsection 8.3.3. The net heat balance is also shown. It can be seen that electrical power and heat production is much greater at 40.8 A per cell than 20.4 A per cell, though the heat lost from the system remains constant. In the 40.8 A per cell cycle, the heat produced by ohmic losses q_{ohm} , and the heat absorbed by electrolysis q_e almost exactly cancel each other out during electrolysis. Therefore, the RSOFC is close to thermoneutral operation in electrolyser mode - without counting the heat losses Q_i .



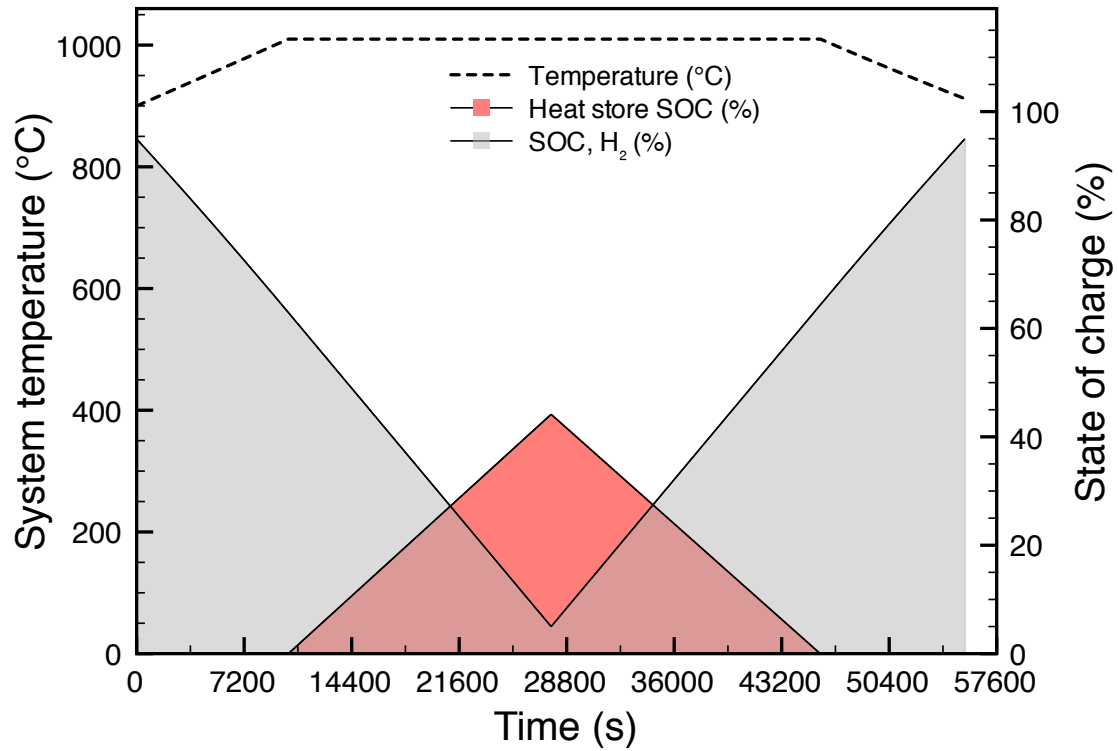
a)



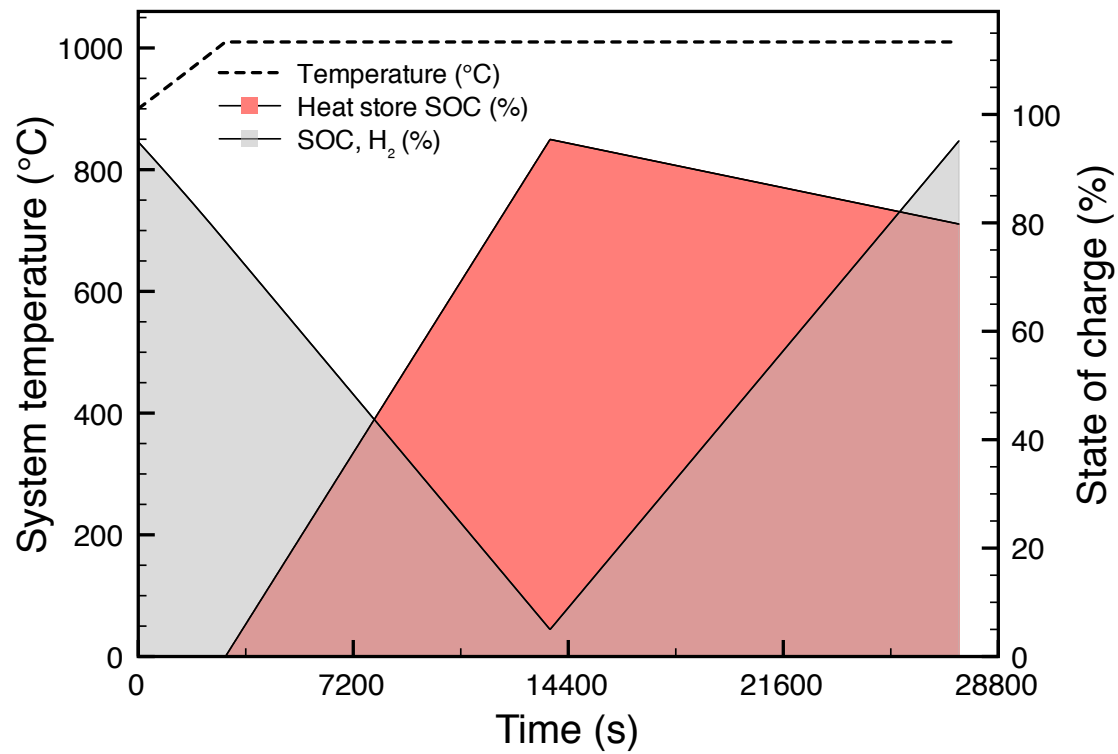
b)

Figure 8.3.6: Stacked heat flows and heat balance in the reversible SOFC system, run in fuel cell mode from 95% state of charge to 5% state of charge, then switched to electrolyser mode until the system returns to 95% state of charge. The cycle in graph a) was simulated at 20.4 A per cell, or 3247 A m⁻² in fuel cell mode, and -20.4 A, or -3247 A m⁻² in electrolyser mode, and the cycle in graph b) at 40.8 A per cell, or 6494 A m⁻² for fuel cell mode, and -40.8 A per cell, or -6494 A m⁻² in electrolyser mode.

Fig. 8.3.7 shows the same RSOFC cycles as fig. 8.3.6. The state of charge (hydrogen), system temperature, and the state of charge of the heat store are shown over the cycle duration. In both cycles, the system temperature rapidly increases to 1010 °C, then holds steady, as the heat store changes phase. When 5% state of charge is reached, the model is switched to electrolyser mode and run until the state of charge of hydrogen rises back to the initial value of 95%. It can be seen that for the cycle at a magnitude of 20.4 A per cell, the system returns to almost exactly the same temperature as the starting temperature. Therefore, multiple cycles could be run at this current, without overheating the system. However, for the cycle at a magnitude of 40.8 A per cell, 80% of the heat store is still molten at the end of the cycle. This is because not all of the heat produced by ohmic losses in the cell in both fuel cell and electrolyser mode, is absorbed by the endothermic electrolysis reaction, so an excess builds up in the system. This reduces the electrical cycle efficiency of the system. This excess would be reduced if the cell had lower ohmic, activation, or diffusion losses. However, this excess heat could be removed from the system, and used in a combined heat and power (CHP) application, which would enable continued cycling.



a)



b)

Figure 8.3.7: Variation in the state of charge, both of the heat store, and the hydrogen, and system temperature over the same RSOFC cycles as fig. 8.3.6. Graph a) shows the RSOFC cycle at 20.4 A per cell, or 3247 A m⁻² in fuel cell mode, then -20.4 A per cell, or -3247 A m⁻² in electrolyser mode, and graph b) shows the RSOFC cycle at 40.8 A per cell, or 6490 A m⁻² in fuel cell mode, then -40.8 A per cell, or -6490 A m⁻² in electrolyser mode. The RSOFC cycle starting conditions in both cases are 70 bar pressure, 900 °C and 95% state of charge.

8.4 Electrical efficiency and energy storage

The electrical conversion efficiency of the RSFOFC system is a measure of how much electricity is produced from the energy in the fuel, in fuel cell mode, or how much electricity is needed to produce the fuel, in electrolyser mode. The RSOFC cycle electrical efficiency is determined as the ratio of electricity in against electricity out during a RSOFC cycle, at a constant current, and where there is no net change in hydrogen state of charge after the cycle. The limits to the system energy storage capacity are discussed.

8.4.1 Electrical efficiency with cell current

Fuel cell mode

In order to calculate the electrical conversion efficiency in fuel cell mode, the energy content or enthalpy of the fuel, W_{fuel} (W) must be determined by using eq. 8.4.1. In this equation, n is the number of cells in the system, M_{H_2} is the moles of hydrogen consumed per second per cell, from eq. 8.3.5, and T is the system temperature. The enthalpy of the fuel W_{fuel} is calculated based on the hydrogen lower heating value (LHV), i.e. when the steam is not condensed, because this is the case within the RSOFC system.

$$W_{fuel} = nM_{H_2}(4.76042T + 243825) \quad (8.4.1)$$

Then the percentage electrical conversion efficiency $E_{electrical,f.c.}$ may be calculated from eq. 8.4.2, where the energy input W_{fuel} is calculated by eq. 8.4.1, and W_{stack} is the electrical power output from the stack when running in fuel cell mode, from eq. 8.2.57.

$$E_{electrical,f.c.} = 100 \left[\frac{W_{stack}}{W_{fuel}} \right] \quad (8.4.2)$$

Electrolyser mode

In electrolyser mode, eq. 8.4.1 may be used to calculate the energy in the fuel produced. The percentage electrical conversion efficiency of the system over one second in electrolyser mode $E_{electrical,elec}$ is defined in eq. 8.4.3 as the energy in the fuel created by electrolysis, W_{fuel} , divided by the energy input, which is the electrical energy used for electrolysis. At low currents, this ratio exceeds 100% because the electricity used is less than the energy in the fuel created, because some of the energy demand comes from heat in the system, absorbed during electrolysis, as the electrolysis reaction is endothermic. However, it does not exceed 100% at moderate or large cell currents, because of the ohmic losses in the cell increase faster with increasing current than the heat absorbed. In equation 8.4.3, W_{stack} is the electrical energy input to the system in electrolyser mode, from subsection 8.2.8.

$$E_{electrical,elec} = 100 \left[\frac{W_{fuel}}{W_{stack}} \right] \quad (8.4.3)$$

The point of maximum electrical efficiency will not correspond to the point of maximum power output in fuel cell mode mode, or maximum power input in electrolyser mode, so a

compromise between these two maxima must be made. The electrical conversion efficiency is defined by eqs. 8.4.2 and 8.4.3. Fig. 8.4.1 shows the electrical conversion efficiency of the cell as a function of cell current. The electrical conversion efficiency is greatest near zero currents for both modes. This is because the ohmic losses in the cell are low in this case. Therefore, in order to maximise electrical storage efficiency, it is best to run the system at lower currents. However, the RSOFC cell current for maximum electrical efficiency over a cycle can only be determined by running a cycle simulation, because the system temperature and state of charge also affects the electrical efficiency.

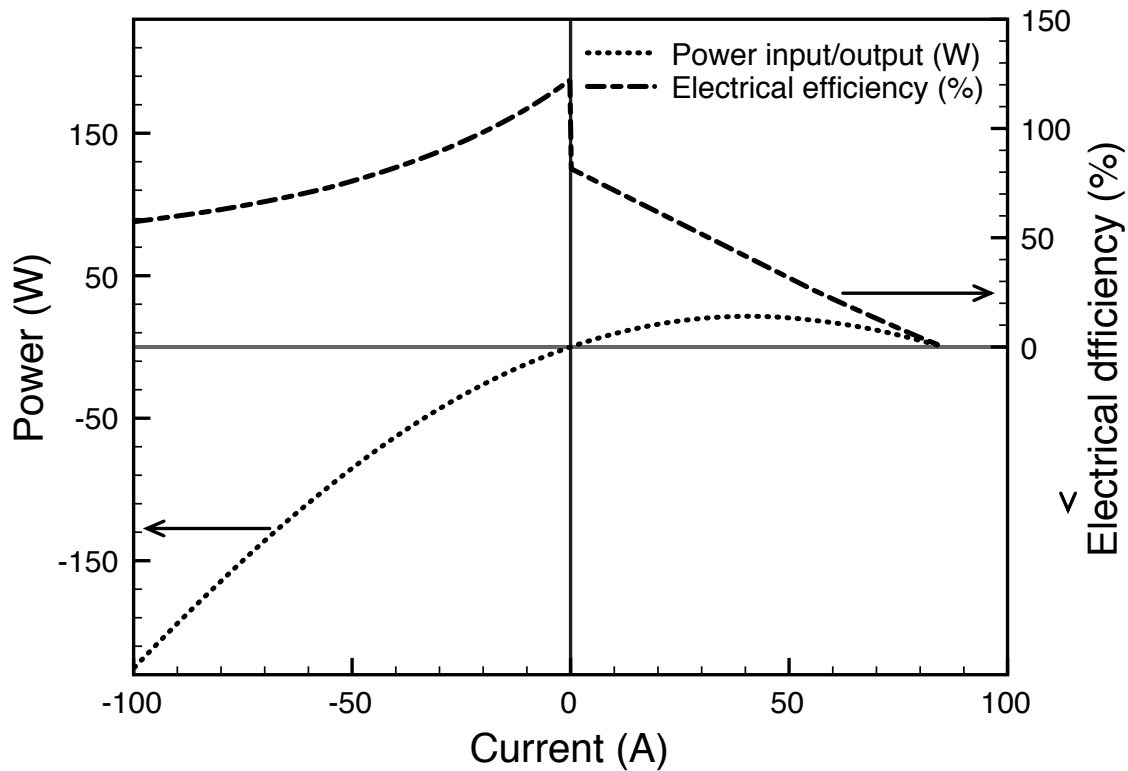
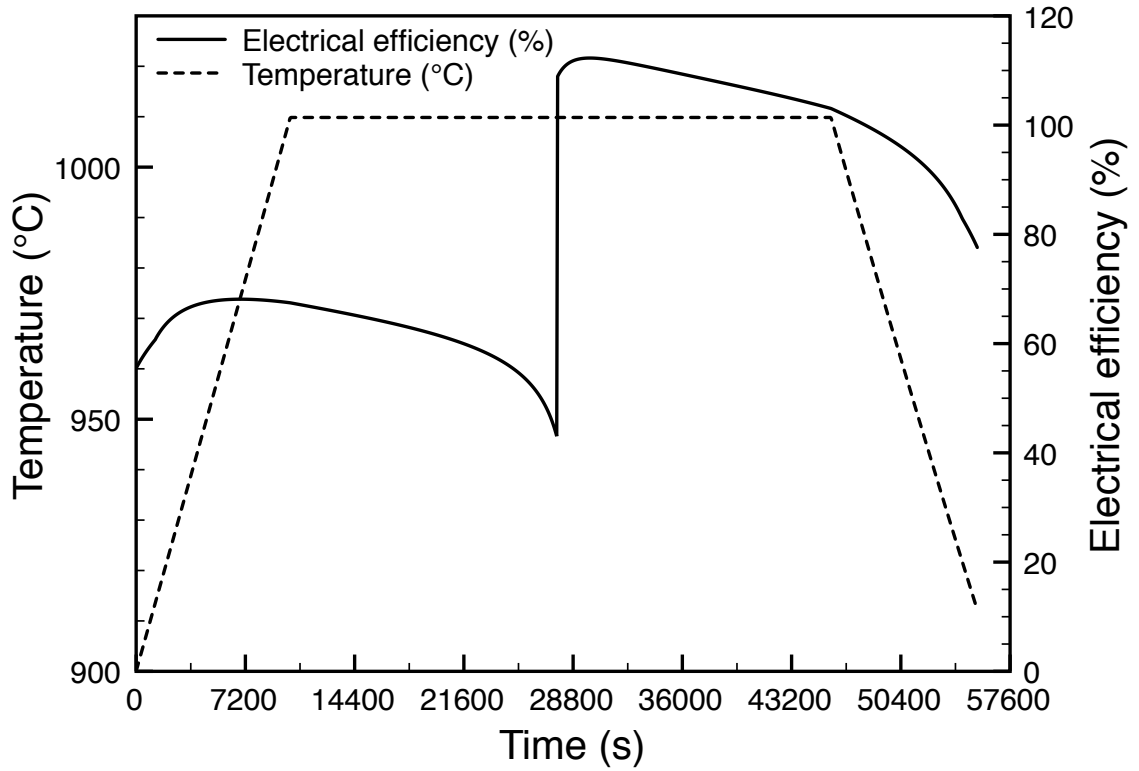


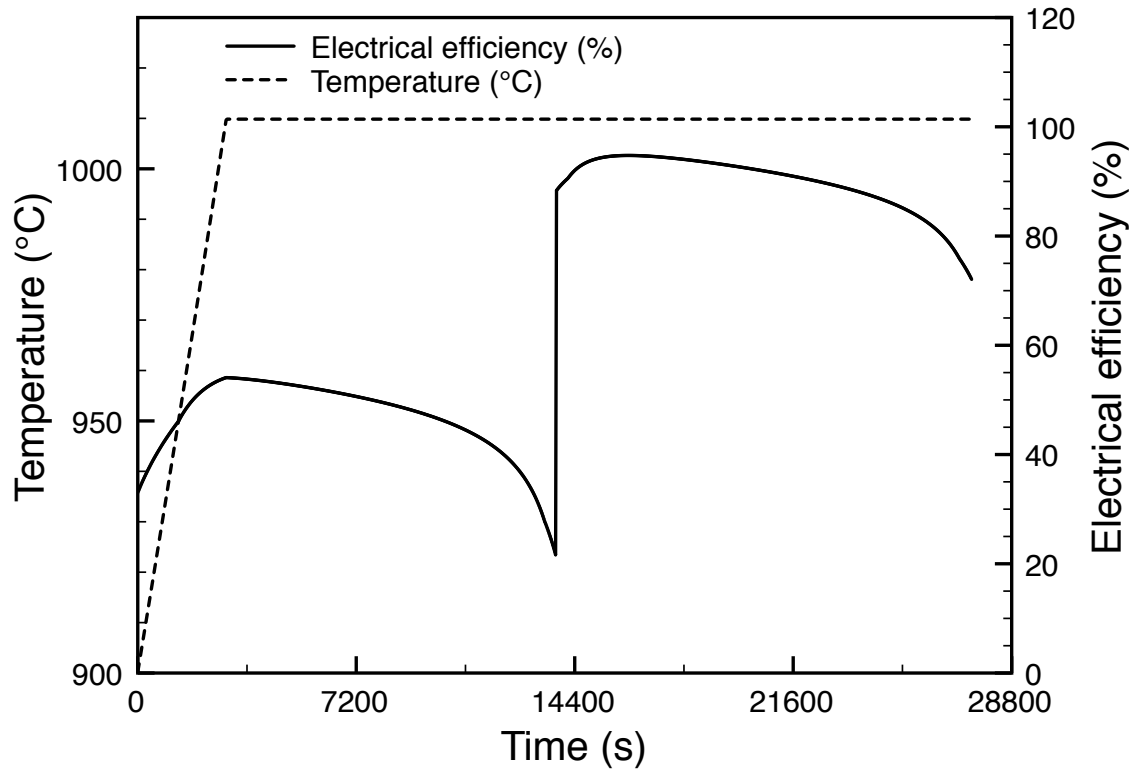
Figure 8.4.1: Power input / output and electrical conversion efficiency with cell current. Positive currents and powers represent fuel cell mode, and negative currents and powers electrolyser mode.

8.4.2 Electrical efficiency during a RSOFC cycle

The electrical conversion efficiency was recorded during the RSOFC cycles shown in figs. 8.3.6 and 8.3.7. The model was run in fuel cell mode, to deplete the state of charge, and then switched to electrolyser mode to return the state of charge to the initial value - this is a single discharge-charge cycle. The electrical conversion efficiency during the cycles is plotted in fig. 8.4.2. It is considerably greater in electrolyser mode than fuel cell mode, because some of the heat from the system is absorbed during electrolysis.



a)



b)

Figure 8.4.2: Electrical conversion efficiency and system temperature during the RSOFC cycle shown in fig. 8.3.6. Graph a) shows the RSOFC cycle at 20.4 A per cell, or 3247 A m^{-2} in fuel cell mode, then -20.4 A per cell, or -3247 A m^{-2} in electrolyser mode, and graph b) shows the RSOFC cycle at 40.8 A per cell, or 6490 A m^{-2} in fuel cell mode, then -40.8 A per cell, or -6490 A m^{-2} in electrolyser mode. The RSOFC cycle starting conditions in both cases are 70 bar pressure, 900 °C and 95% state of charge.

Fig. 8.3.6a shows the RSOFC cycle at a magnitude of 20.4 A per cell. In electrolyser mode, the electrical efficiency reaches a maximum of 112% at about 28800 s or 8 h into the cycle. This is possible, because some of the energy in the hydrogen produced by electrolysis comes from heat in the system. At this point, 1 W of electrical energy, and 0.12 W of heat energy are required to produce an amount of hydrogen gas with an enthalpy of 1.12 W. This demonstrates that it is possible to recover heat energy stored in the system from the fuel cell cycle, and convert it to chemical energy in hydrogen by electrolysis. However, when the system is run at a current magnitude of 40.8 A per cell, as in fig. 8.3.6b, the heat generated by ohmic losses in the system exceeds heat absorbed by electrolysis, so there is no net absorption of heat by the cell during electrolysis, i.e. all the energy in the fuel comes from the electrical energy, and some of the electrical power is wasted on ohmic losses. Therefore, the system cannot recover any of the heat generated in the fuel cell cycle and convert it to chemical energy in hydrogen, as the electrical conversion efficiency never exceeds 100%.

The electrical efficiency for the whole RSOFC cycle $E_{electrical,cycle}$ is calculated from eq. 8.4.4, by dividing the total electrical power production in fuel cell mode $W_{stack,f.c.}$ (W) by the total electrical power consumption in electrolyser mode $W_{stack,elec}$ (W). The quantities $W_{stack,f.c.}$ and $W_{stack,elec}$ are obtained by taking a sum of the power output/input in each second of the cycle, over the time in each mode.

$$E_{electrical,cycle} = 100 \frac{W_{stack,fc}}{W_{stack,elec}} \quad (8.4.4)$$

The electrical cycle efficiency depends on the current density that the system is operated at, and many other parameters, such as the value of the pre-exponential coefficient in the activation energy calculation.

Table 8.4.1 compares five different cycles, with different parameters for each.

Cell current (A)	Current density (A m ⁻²)	Pre-exponential coefficient (A m ⁻²)	Electrical cycle efficiency (%)
10.2	1623	7x10 ⁸	36.3
20.4	3247	7x10 ⁸	64.4
30.6	4870	7x10 ⁸	53.0
40.8	6494	7x10 ⁸	42.0
20.4	3247	1x10 ⁹	67.9

Table 8.4.1: Electrical efficiency during a RSOFC cycle at 70 bar, in the range 95% to 5% to 95% state of charge, at two different values of cell current, and two different pre-exponential coefficients.

It is apparent that the system is more efficient at storing and releasing electricity at lower cell currents, as in fig. 8.4.1. The best electrical cycle efficiency of 64.4% was obtained at a current of 20.4 A per cell. At currents lower than this, the cycle efficiency drops markedly. This can be explained by considering fig. 8.3.1. This shows that the net

heat balance in the cell during electrolysis increases at cell currents with a lower magnitude than about -20 A, so less heat is recycled into energy in the fuel created, so the electrical efficiency decreases. Furthermore, the RSOFC cycle has a longer duration at lower currents, as the rate of fuel usage/production is lower. This means that more heat is lost through the system walls, so the system cools below its optimal temperature operation range of 900 °C - 1050 °C during electrolysis, reducing the efficiency. This is why the cycle at a magnitude of 10.2 A has a much lower efficiency than cycles at higher currents.

In order to improve the cycle efficiency further, the cell resistance should be lowered by optimising the fabrication and geometry of the cell, and the insulation of the system should be improved. This would reduce ohmic losses in the cell, and improve the electrical conversion efficiency, and also prevent loss of energy from the system through the walls. If the cell had negligible resistance, and there was negligible heat loss from the system, almost 100% cycle efficiency would be achieved for energy storage.

The choice of the value of the pre-exponential coefficient also slightly influenced the energy storage efficiency. Different values of pre-exponential coefficient are used in SOFC models [1, 2]. When a coefficient of $1 \times 10^9 \text{ A m}^{-2}$ was used in this model, the electrical cycle efficiency increased to 67.9% at 20.4 A per cell, showing that the cycle electrical efficiency is not very sensitive to this parameter. The efficiencies measured are similar to or slightly lower than the electrical cycle efficiency of redox flow cells, which ranges from 65% - 75% [23].

However, the RSOFC system is more efficient than a reversible polymer electrolyte membrane fuel cell (RPEM-FC), because it can recover heat from the fuel cell cycle during electrolysis to give electrical conversion efficiencies greater than 100%. In a RPEM-FC system, the electrical conversion efficiency cannot exceed 100% because the heat produced in fuel cell mode is wasted. An experimental study found that the electrical cycle efficiency of this system at maximum fuel cell power varied from 26% - 42% depending on the Pt and Ir catalyst loading. Higher loadings generally gave a greater electrical cycle efficiency [24]. It can be seen that the RSOFC cycle in fig. 8.3.6b where the electrical conversion efficiency does not exceed 100%, has a similar electrical cycle efficiency of 42%. However, the surplus heat energy from the RSOFC cycle, is available at a high temperature, which is not the case for redox flow cells or RPEM-FC. Therefore, if this heat could be utilised as well, the overall efficiency of the RSOFC system at higher currents could be further increased. One way to do this would be to couple with RSOFC system with a heat engine, which could extract the heat and produce electricity. This would boost the system electrical efficiency [25]. The heat could also be used directly, in a combined heat and power application, for residential or industrial heating. A report produced for the Scottish government about a recommended renewable heat strategy states that of Scotland's total energy use, 29% is for transport, 19% for electrical equipment/other, and 57% for heat and hot water, of which only 4% was provided from renewable generation in 2006 [26]. Therefore, there is considerable scope to expand renewable heat production, as the RSOFC system lends itself to decentralised power and heat production.

8.4.3 Limits of the energy storage capacity of the system

Energy is stored in the system in two forms: chemical energy in hydrogen, and heat energy, in the thermal mass of the stack, heat store, and system gases. In the RSOFC cycle shown in fig. 8.3.7, the energy storage capacity of the system is limited by the amount of hydrogen in the system. In order to overcome this limitation, the system pressure could be increased, which would improve the system volumetric energy storage density, or the system volume could be increased. However, in the former case, a higher pressure would need a stronger and more expensive vessel. In the latter case, more heat would be lost through the system walls as they would have a larger area, potentially reducing the electrical efficiency of the system.

The energy storage capacity could also be potentially limited by the cycle length. If the system was operating at a lower power level, the cycle time might be longer. In this case, the total heat lost through the walls would be greater, so in electrolyser mode, the system might cool below the optimum temperature range of operation. Therefore, it would have to be switched into fuel cell mode to heat it up again, otherwise the efficiency would be greatly reduced. This is indeed the case for the cycle at 10.2 A - the cycle efficiency is quite low because the system cooled below 750 °C during electrolysis.

8.5 Implementation of the model in software

8.5.1 Model design, power and controls

Model design

In order to produce the RSOFC system software model, and output the results shown, the equations discussed in this chapter were implemented in Matlab/Simulink software at the University of Strathclyde, Glasgow, by a collaborating electrical engineering PhD student. The main model block is shown in fig. 8.5.1.

Power and controls

Most fuel cell system models, are designed to have a continuous flow of gases into and out of the system. These systems seldom or never cycle between fuel cell and electrolyser modes. Typically, fuel or oxidant gas flow rates are used to control cell voltage and temperature, respectively. Fuel utilisation is calculated, and can be used to determine an electrical conversion efficiency [27]. These systems are typically used for either power generation, or in the case of electrolysis, production of hydrogen for energy storage or use in a chemical process.

However, in the RSOFC system, there is only one control input to the model, which is the current drawn from or applied to the RSOFC system, on the left hand side of fig. 8.5.1. This is because the system is self contained and has no inlet or exhaust for gases: rather they are recycled as it charges and discharges. Therefore, the fuel mix or flow rate is not controlled, and so cannot be used to control power production.

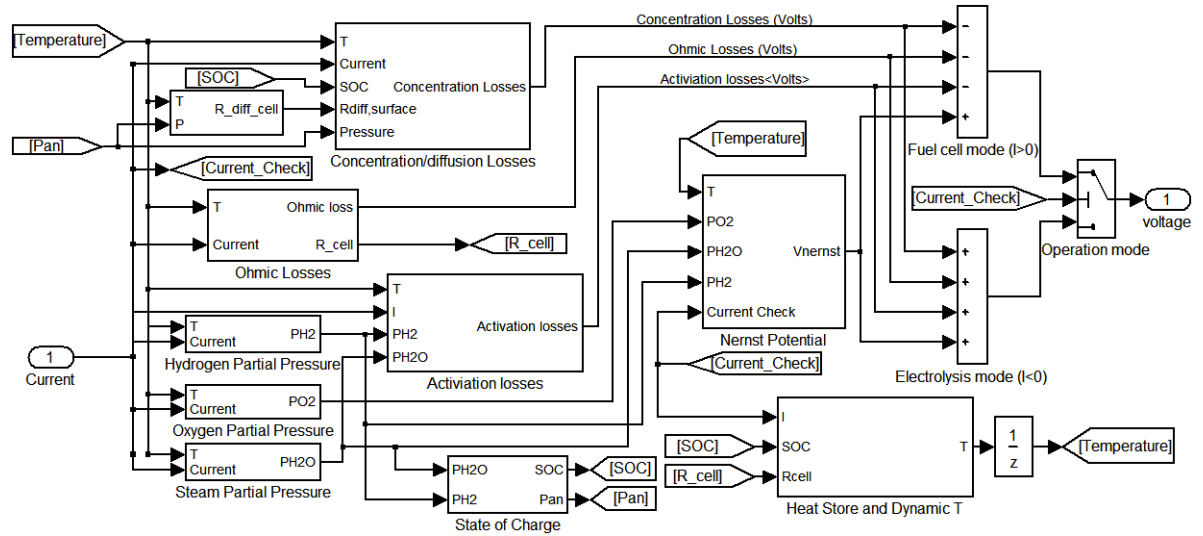


Figure 8.5.1: Main model block for the RSOFC system, in MATLAB/Simulink software, showing data flow through the model. The input current 1 on the left comes from the power electronics block (not shown), which controls the fuel cell system. Each of the rectangular blocks has inputs which feed data into it, and various sub-blocks which perform calculations on the inputs, to produce the outputs. The pentagon shapes show data that is shared across the model.

The amount of current drawn from the system, along with other information such as the state of charge, pressure and system temperature, can be used to predict the system power output. When the RSOFC system is operating, the system temperature is most likely to be 1010 °C, because that is the temperature of the phase change of the heat store. The voltage output from the system is controlled by an electrical power and controls system. This was developed at the University of Strathclyde, in conjunction with the RSOFC system model.

An earlier version of the RSOFC model was connected to an islanded electrical grid, via a three-phase inverter [28]. The RSOFC model was then further developed, and an electric power and controls system was designed that could interact with a small or large electrical grid [29]. It considered the effects on the model and power and controls of variable grid frequency, and variable magnitude, unbalance, and harmonic content of the voltage, all things likely to be encountered in a real-world scenario. Three power and control schemes were considered, which are compared in table 8.5.1.

Each of the schemes tries to achieve different things, but all have consequences for the RSOFC system, because they cause current or voltage ripples of varying magnitude in the stack. The first scheme tries to keep power and reactive power flows constant, which minimises current and voltage ripple on the DC bus and RSOFC system. However, the presence of unbalance or harmonics on the grid causes the inverter currents to experience harmonics. The second scheme yields a steady current, even in the case of harmonics and unbalance in the grid voltages, but has a higher stack current ripple. The third scheme gives a steady power output, and mitigates voltage unbalance or harmonics, but leads to a very large current and voltage ripple in the stack.

Power and control scheme	Goal of scheme	RSOFC stack V variation	RSOFC stack I variation
Grid-connected DC bus ripple minimisation	keep power constant, minimise I, V ripple.	$\pm 0.2\%$	$\pm 0.5\%$
Grid-connected sinusoidal balanced currents	balanced sinusoidal I, mitigate grid V harmonics, unbalance	$\pm 1\%$	$\pm 8\%$
Voltage drive	balanced sinusoidal V, mitigate grid V harmonics, unbalance	$\pm 10\%$	$\pm 69\%$

Table 8.5.1: Power and control schemes for the RSOFC system model, and their effects on the RSOFC stack current. The ripple frequency is 30 Hz for the top and middle power and control schemes, and 20 Hz for the bottom one.

However, since this paper was published, the model has been updated, and the capacitance in fig. 8.2.8 from $R_{diff,surface}$ was extended from just being in the cell impedance simulation, to be part of the main model. This adds a capacitance to the stack, which has the effect of smoothing the current and voltage ripples noted in table 8.5.1, which have similar time constants to the capacitance in $R_{diff,surface}$. However, the magnitude of this smoothing was found to be quite small. Therefore, capacitors have been added to the DC bus of the electrical power and controls system. This has reduced the ripple experienced by the stack, but the work is as yet incomplete.

Studies have shown that the fuel flow rate affects the RSOFC system, and can cause it to have intrinsic capacitance, responding slowly to changes in load current [30]. This capacitance arises from a variety of factors, such as fuel depletion near the electrode due to diffusion limitations, and surface diffusion on fuel cell electrodes [31]. The capacitance could be exploited if a highly variable power source, such as a wind turbine was connected to the RSOFC system. It has been shown that the power output from wind turbines has a significant variation on a second-to-second basis [32]. It would help the RSOFC system to absorb transient variations in power during charging of the system.

The RSOFC system is also suited to sources of energy such as tidal power. The spectrum of output power from tidal turbines varies over a period of hours, from one maximum power output to another [33]. This suits the time scales of energy storage and release demonstrated in this model. Tidal power generation with a RSOFC system could be used to provide baseload power generation, with the RSOFC balancing the peaks and troughs in energy generated from the tidal turbines.

8.6 Further work

The model described here is not a perfect representation of a RSOFC system. In order to improve it, some of the assumptions made to simplify the modelling could be removed, and the model could be validated against empirical data, once it becomes available.

The biggest assumption currently in the model is that of instantaneous heat transfer through the system, which was discussed in section 8.3. This implies that there is one uniform temperature over the whole system. This assumption could be removed from the

model by using a finite volume model. This models the system in three dimensions, dividing it up into small sections. Equations are used to model heat, mass, electric current etc, as they enter and exit each section, conserving each. In this way, heat transfer via radiation, conduction and convection is modelled. This approach allows for a non-uniform current and voltage distribution across the cell [10]. It could also provide a more accurate model of heat flows around the system, which would improve the design of the stack. Rather than being many single cells bolted together, the design could be optimised for maximum performance. Another assumption in the model was that there was no leakage across the cells. This assumption could be removed by measuring experimental leakage rates.

It was also assumed that the activation losses in the model were purely ohmic losses. However, these will have a capacitive element as well. The oxygen surface diffusion polarisation resistance in this model, was based on empirical data obtained from symmetrical cell measurements on the oxygen electrode. However, a reversible cell could be tested, to give data for both electrodes, which would validate the activation and diffusion polarisations, and the capacitive elements of the system. The response of the RSOFC to current and voltage ripples could also be determined by I/V measurements and impedance measurements.

The electrochemical performance of the cells as a function of state of charge, pressure, and temperature should also be validated against experimental data. The cell performance could also be improved, by addressing the two largest losses in the cell: the ohmic resistance, which is dominated by the resistance of the support, and the activation energy.

If the cell design were optimised, the resistance of the support could be reduced. Siemens-Westinghouse initially developed a tubular design, but then moved to a hybrid design of a flattened tube with ribs to aid current collection through the support [34].

The activation energy depends on the exchange current density, which is related to how effective the electrode is at catalysing the reactions in the cell. A lower activation energy and better performance might be obtained by using new materials, or a better microstructure for the cell that increases the number of active catalyst sites.

8.7 Conclusions

The RSOFC system model described here is a zero-dimensional model, i.e. it does not model gas flows using computational fluid dynamics, and consider flows of mass and heat through the system. Instead, cell performance was calculated based on input parameters such as temperature, state of charge, which is the mole fraction of hydrogen, and cell geometry. It was used to investigate the effects of changing parameters on the system, and to model cycles of storing and releasing electrical energy. One of the key assumptions in the model is that the whole system is at a uniform temperature - no account is made for heat transfer by radiation, conduction, and convection, except a heat loss from the system. This means that the model may underestimate the effect of steps in the current load on the cell performance, e.g. if the current load was increased, the cells would heat up more in a real system than in the model, because in a real system they would dissipate heat more slowly. It also means that 'hotspots' might develop in a real system, e.g. at

the interconnects, which would not be observed by this model. This assumption could be removed by making a computational fluid dynamics model of the system. However, this was beyond the scope of the current work. Another assumption was that the cells have zero crossover leakage, across the electrolyte. This is a fairly accurate assumption as leaky cells would not be used in a real RSOFC system, as they would have an inimical effect on performance. A third assumption was that the only capacitative element in the model was from surface diffusion from the oxygen electrode, which was based on experimental data. However, there will also be a capacitative element to the activation energy, which should be investigated experimentally by performing ac impedance tests on RSOFC. This data could be incorporated into the model, in a similar way as to the oxygen electrode.

The electrical performance of the cell has been shown to be positively correlated with system temperature and pressure. The Nernst voltage significantly increased with pressure, giving a better cell performance. Pressurisation also changed the thermodynamics of the system; at a higher pressure, the gases have lower entropy, so more of their enthalpy is available to be converted to electrical energy. Pressurisation has a third benefit; it reduced diffusion overpotentials or losses, so that they became insignificant compared to activation and ohmic losses in the cell.

The ohmic losses from cell components were the most significant losses in the cell, and are dominated by the resistance of the cell support. The cell design could be optimised further to significantly reduce these losses, by changing the shape of the support, e.g. to a flattened tube with interconnecting ribs. However, this would add to the complexity of the design. The activation losses were the other major category of losses. These varied significantly with the pre-exponential coefficient used in the equations, which can only be determined by experiment. There is disagreement in the chemical literature about its magnitude, presumably because it depends on microstructural or chemical features of the cell, which vary from one study to another. The exchange current density is also important, and is a function of the material used as an electrode.

Two kinds of electrical efficiency were described in the model, firstly, an electrical conversion efficiency, i.e. energy in fuel to electrical power produced for fuel cell mode, and vice versa for electrolyser mode. This was much greater for electrolyser mode, because it is endothermic, so heat stored in the system can be absorbed and converted into chemical energy in the hydrogen produced. The second type of efficiency is electrical cycle efficiency, which is a measure of how much electricity can be reversibly produced and then stored again, when the system is run in fuel cell mode and then electrolyser mode. In this case, the same amount of hydrogen was present at the start and the end of the cycle. The cycle efficiency was 42% when the system operated at the current density for maximum power. If the system is operated at $1/2$ of this current density, the efficiency rises to 64.4%. An important conclusion about the system, is that it functions most efficiently for energy storage, when operated at less than maximum power inputs/outputs. This is the opposite of an internal combustion engine, or gas turbine. The cycle efficiency was slightly higher at 67.9% when the pre-exponential coefficient was increased to a value in the middle of the range quoted in literature. A conservative assumption for the pre-exponential coefficient

was used in the model, but validation of the model against experimental data might justify a higher value, improving the cycle efficiency. It could also improve if the surplus heat, which is at high temperature, could be used, e.g. in a combined heat and power application, or if the system was hybridised with a heat engine. There is a large potential for expansion of renewable heat generation in Scotland.

The RSOFC system needs to be integrated into an electrical grid in order to be used. Work was carried out by an electrical engineering collaborator at the University of Strathclyde, to design an electrical power and controls system to act as a grid interface. The capacitance of the cell was included in the main model to see if it would help to smooth harmonics of voltage and current from the inverter. However, it was seen that it was too small to have much of an effect, although if the activation polarisation capacitance was determined by experiment and added to the model, this might provide a more significant level of capacitance for the inverter. Furthermore, in a real system, the uneven heat distribution, and fuel depletion near the electrodes when a transient change in the current density occurs, might also provide some capacitance to smooth transient spikes in voltage and current from the inverter.

The RSOFC system described in this model is able to release and store energy at a reasonable efficiency, i.e. slightly less than that of redox flow cells, but further development of the cell, particularly geometrical optimisation, would reduce losses and greatly improve electrical storage efficiency. However, the efficiency of energy storage is much greater than that of reversible PEM-FC, because heat can be utilised as an energy storage medium, as well as hydrogen.

References

- [1] S. Campanari, P. Iora, *J. Power Sources*, 2004, **132**, 113–126.
- [2] P. Costamagna, K. Honegger, *J. Electrochem. Soc.*, 1998, **145**, 3995–4007.
- [3] S. H. Chan, K. A. Khor, Z. T. Xia, *J. Power Sources*, 2001, **93**, 130–140.
- [4] D. A. Noren, M. A. Hoffman, *J. Power Sources*, 2005, **152**, 175–181.
- [5] R. H. Perry, D. W. Green, *Perry's Chemical Engineer's Handbook 7th ed.*, of *Chemical Engineering Series*, McGraw-Hill, 1997.
- [6] B. E. Pauling, J. M. Prausnitz, J. P. O'Connell, *Properties of Gases and Liquids 5th ed.*, of *The Properties of Gases and Liquids*, McGraw Hill, 2001.
- [7] P.-W. Li, M. K. Chyu, *J. Power Sources*, 2003, **124**, 487–498.
- [8] M. Ni, M. K. H. Leung, D. Y. C. Leung, *Int. J. Hydrogen Energy*, 2007, **32**, 2305–2313.
- [9] S. R. Gamble, J. T. S. Irvine, *Solid State Ionics*, 2011, **192**, 394–397.
- [10] J. M. Klein, Y. Bultel, M. Pons, P. Ozil, *J. Appl. Electrochem.*, 2008, **38**, 497–505.
- [11] S. Wang, T. A. Cruse, M. Krumpelt, B. J. Ingram, P. A. Salvador, *J. Electrochem. Soc.*, 2011, **158**, B152–B158.
- [12] M. Krumpelt, T. A. Cruse, B. J. Ingram, J. L. Routbort, S. Wang, P. A. Salvador, G. Chen, *Journal of the Electrochemical Society*, 2010, **157**, B228–B233.
- [13] S. Gamble, *Mater. Sci. Technol.*, 2011, **27**, 1485–1497.
- [14] J. R. Mawdsley, J. D. Carter, A. J. Kropf, B. Yildiz, V. A. Maroni, *Int. J. Hydrogen Energy*, 2009, **34**, 4198–4207.
- [15] P. Kazempoor, F. Ommi, V. Dorer, *J. Power Sources*, 2011, **In press**, **corrected proof**.
- [16] D. Sánchez, A. Muñoz, T. Sánchez, *J. Power Sources*, 2007, **169**, 25–34.
- [17] Microtherm, *Microtherm Standard Panel*, Datasheet from <http://www.microtherm.uk.com/>, Microtherm, België, Industriepark Noord 1, BE-9100 Sint-Niklaas, 2011.

- [18] NIST, *NIST Chemistry WebBook*, last accessed 01/08/2011. <http://webbook.nist.gov/chemistry/>.
- [19] J. Mahmoudi, H. Fredriksson, *J. Mater. Sci.*, 2000, **35**, 4977–4987.
- [20] N. Saunders, A. P. Miodownik, *J. Phase Equil.*, 1990, **11**, 278–287.
- [21] K. Sedghisigarchi, A. Feliachi, *IEEE T. Energy Conv.*, 2004, **19**, 423–428.
- [22] E. Achenbach, *J. Power Sources*, 1995, **57**, 105–109.
- [23] C. Ponce de León, A. Frías-Ferrer, J. González-García, D. A. Szánto, F. C. Walsh, *J. Power Sources*, 2006, **160**, 716–732.
- [24] A. Doddathimmaiah, J. Andrews, *Int. J. Hydrogen Energy*, 2009, **34**, 8157–8170.
- [25] S. T. Ro, J. L. Sohn, *J. Power Sources*, 2007, **167**, 295–301.
- [26] Renewable Heat Group, the Scottish Government, *Scotland's renewable heat strategy: recommendations to Scottish Ministers: Renewable Heat Group (RHG) Report 2008*, Tech. Rep., Forum for Renewable Energy Development in Scotland, The Scottish Government, St Andrew's House, Edinburgh, EH1 3DG, 2008.
- [27] M. Bavarian, M. Soroush, I. G. Kevrekidis, J. B. Benziger, *Ind. Eng. Chem. Res.*, 2010, **49**, 7922–7950.
- [28] J. Ren, S. Gamble, A. J. Roscoe, G. Burt in *Universities Power Engineering Conference (UPEC), 2009, Proceedings of the 44th International*, Glasgow, pp. 1–5.
- [29] J. Ren, A. J. Roscoe, S. Gamble, G. M. Burt in *Power Electronics, Machines and Drives (PEMD)*, Brighton, 2010.
- [30] F. Mueller, F. Jabbari, J. Brouwer, *Journal of Power Sources*, 2009, **187**, 452–460.
- [31] J. D. Kim, G. D. Kim, J. W. Moon, Y. I. Park, W. H. Lee, K. Kobayashi, M. Nagai, C. E. Kim, *Solid State Ionics*, 2001, **143**, 379–389.
- [32] J. Apt, *J. Power Sources*, 2007, **169**, 369–374.
- [33] J. A. Clarke, G. Connor, A. D. Grant, C. M. Johnstone, *Renew. Energ.*, 2006, **31**, 173–180.
- [34] S. C. Singhal, *Solid State Ionics*, 2000, **135**, 305–313.

Chapter 9

Discussion and conclusions

A reversible solid oxide fuel cell (RSOFC) system is a proposed electrical energy storage system, which could be used to buffer intermittent electrical generation, such as wind or tidal power, providing a constant output of power, or else balancing electrical supply and demand. In this work, the RSOFC were successfully fabricated, the performance of one of their electrodes was tested, and a computer model of a RSOFC system was developed to aid understanding of its performance and electricity storage potential.

The RSOFC are supported by a porous ceramic tube of the oxygen electrode current collector, $(\text{La}_{0.8}\text{Sr}_{0.2})_{0.95}\text{MnO}_{3-\delta}$ (LSM). A pre-coarsened LSM powder was used to extrude the LSM support. It had a 55% porous, stable microstructure of interconnected pores, and the tube did not shrink appreciably after repeated sintering steps at 1350 °C. It is sufficiently porous to prevent mass transport limitations being a significant loss, and RSOFC degradation should be reduced if the support does not sinter and shrink during operation.

The YSZ electrolyte was first applied via a dip-coating process, which produced sintered electrolytes with ~90% density and 20 μm - 40 μm thickness, but this was insufficiently dense to prevent gas leakage through the electrolyte. An LSM-YSZ screen printing ink painted onto the LSM tube, improved the homogeneity of the substrate for YSZ coating and provided a composite electrode to catalyse the oxygen reduction reactions. Two layers of a commercial 3YSZ screen printing ink were then hand painted on top, and a 20 μm - 30 μm thick, almost 100% dense electrolyte was achieved after sintering at 1350 °C. At this density, leakage across the electrolyte should be sufficiently low, that a good open circuit voltage (OCV) could be obtained if the cell were tested. A NiO-YSZ band of screen printing ink was then applied to the outside of the tubes, and a 5 μm - 10 μm thick fuel electrode layer was obtained, which had a resistance of $<2\ \Omega$ across the diameter of the cell outer surface, after reduction at 800 °C in 5% hydrogen/argon. Therefore, a cell with a dense electrolyte, and conductive fuel electrode was produced.

A Ag/Cu reactive air braze used to seal the RSOFC to 316 or 430 stainless steel support tubes did not produce a crack free joint between the cell and the steel, because oxidation layers formed on the steels, at the high temperatures required to melt the braze. The braze did not penetrate the oxidation layers, which cracked and parted from the both types of steel, leaving a void in the joint. The braze did not bridge gaps in the joints greater than

about 150 μm . Although this brazing was unsuccessful, it might work better if it was carried out in an atmosphere with very limited oxygen, such as a nitrogen atmosphere, to prevent steel oxidation.

Therefore, the alumina-based ceramic adhesives Ceramabond VFG-552 and Toku ceramic adhesive were used instead to try to seal the RSOFC to a stainless steel support tube. The joints to be sealed had gaps of 1 mm - 2 mm. However, Ceramabond sealant is recommended to be used to fill gaps of 50 μm - 200 μm - any more than this, and the joints may fail by cohesive shear failure. Upon curing at 260 $^{\circ}\text{C}$, cracks were seen at the Ceramabond/steel interface, which were attributed to a thermal expansion coefficient mismatch of $\sim 8 \text{ p.p.m.K}^{-1}$ between the steel and the Ceramabond. An alumina support tube was used instead, which matches the thermal expansion of the Ceramabond adhesive almost exactly, but has a mismatch of $\sim 3 \text{ p.p.m.K}^{-1}$ with the RSOFC. After the joints were cured at 260 $^{\circ}\text{C}$, a pressure drop experiment showed a pressure drop of 100% from 50 mbar in just 10 s, i.e. from 50 mbar pressure above atmospheric pressure to 0 mbar above atmospheric pressure. A different ceramic adhesive called Toku was used to seal the cells, and a MACOR (glass ceramic) ring was machined to fit over the joint. This allowed for a compressive seal between the cell and support, and reduced the thickness of sealant required. By using a MACOR ring, and Toku sealant, pressure drops as low as 4% over 5 min were achieved. The RSOFC with low leakage were tested, by heating them to 800 $^{\circ}\text{C}$ with flowing 5% H_2/Ar on the outside, and the OCV was recorded as a function of temperature. The best cell reached a maximum OCV of 0.8 V at 440 $^{\circ}\text{C}$ before rapidly dropping to just above 0 V, probably because the sealant cracked. A pressure drop test on the cells after cooling showed a 100% pressure drop from 55 mbar in 1 min. Therefore, the sealant is much more leaky after it has been sintered to 800 $^{\circ}\text{C}$, than after it is cured to 260 $^{\circ}\text{C}$. SEM analysis of a post-test cross section of the cell showed that the Toku ceramic was porous. A red dye leak test on another similar cell after high temperature testing, showed that the leak was mainly present in the Toku sealant. Therefore, the problem may be that the gap in the joint is too large for this sealant to bridge it. This gap could be reduced to 100 μm if the fuel cell and the alumina support were machined so they fit together closely. This aids sealing, and might give a leak-free joint.

An impedance measurement on another cell, which had a very low OCV of 1.2 mV, showed that it was electrochemically active - a polarisation resistance of about 15 Ω was measured for this cell. Therefore, the leakage from the sealant is the most significant problem, rather than the cell itself. The leakage may also cause partial oxidation of the nickel in the fuel electrode, so the polarisation resistance would probably be less if there was no leak.

The effect of pressurisation on the LSM-YSZ oxygen electrode of the RSOFC was examined with symmetrical cells. The polarisation resistance of the dominant arc in the impedance spectra decreased as a function of $P_{\text{O}_2}^{-x}$ in the range 1 bar - 3 bar where x was determined to be 0.39 - 0.53. By a comparison of various measured parameters with literature values, the process was assigned to surface diffusion of atomic oxygen species on the electrode. A smaller arc was assigned to the flow of oxygen ions/intermediates

through the triple phase boundaries in the LSM-YSZ electrode. The data was used to generate equations to predict the oxygen electrode diffusion polarisation over a range of temperatures and oxygen pressures for the RSOFC computer model. The same process could be used on a RSOFC to add the polarisation resistances and associated capacitances to the RSOFC model.

Equations describing the behaviour of a RSOFC were developed, and they were built into a computer model using Matlab with Simulink software, by a collaborator in the University of Strathclyde. The model is controlled solely by the cell current load in fuel cell mode, or input current in electrolysis mode, and calculates the cell voltage and losses over time, based on starting parameters such as temperature, pressure, and state of charge, which is the mole fraction of hydrogen in the system. This differs from most fuel cell models, which typically use inlet gas temperatures, flow rates and compositions to control the system. The RSOFC system described in this work is intrinsically simpler, as it has no inlet or outlet for gases, but is self-contained, like a sealed battery. It relies on internal convection to distribute fuel within the system over the electrodes, rather than pumping gases through the system.

The biggest voltage drop in the cell came from the ohmic losses, of which the largest ohmic resistance of any component was the cell support, $3.4 \text{ m}\Omega$ at 900°C , which was 50% of the total ohmic losses in the cell. These depend on the material used, which is a lanthanum strontium cobaltate ceramic, which has a higher electrical conductivity than other fuel cell ceramic materials such as LSM, but is less conductive than the nickel metal on the fuel electrode side of the cell. The ohmic losses are also a function of the length of the current paths in the cell design. If these were shortened by redesigning the cell geometry, the ohmic losses would be reduced.

The second biggest voltage drop in the cell comes from the activation losses, which depends on the exchange current density. This in turn is a function of the state of charge of the system. At low or high states of charge, where the concentration of hydrogen and steam is more imbalanced in the system, the exchange current density is lower, increasing activation losses. It was also found that the pre-exponential coefficient, an empirical value used in the equations to calculate the exchange current density, is strongly positively correlated with the cell performance. When it is increased from $7 \times 10^{-8} \text{ A m}^{-2}$ to $1 \times 10^{-9} \text{ A m}^{-2}$, the cell power increases by 19 % from 17.5 W to 20.9 W, when the system is at 900°C , 95% state of charge, with a cell current of 40.8 A.

One of the most significant findings of the modelling study was that pressurisation provides a major cell performance improvement. When the system is pressurised from 1 bar to 70 bar, the Nernst voltage increases significantly, from 0.946 V to 1.053 V at 49% state of charge, 900°C , and the diffusion losses decrease to become insignificant beside the ohmic losses. Furthermore, the entropy of the gases in the system is reduced, so every mole of hydrogen that is consumed produces less heat, and more energy is available to be converted into electricity, which boosts the electrical conversion efficiency.

A phase change heat store, in the form of a Cu/Sn alloy that melts around 1010°C , was added to absorb excess heat generated in fuel cell mode, and prevent the system from

quickly overheating. When the heat store had a mass of 500 kg, it increased the time the system could operate at maximum power output without overheating from $\sim 1/2$ h to at least $3 \frac{3}{4}$ h. Heat is stored both in its thermal mass, and as the latent heat of fusion of the alloy. This stores heat at a much higher volumetric density than with a solid material that does not change phase. The composition of the phase change material could be tuned to change the range of temperatures at which the phase change occurs.

At 900 °C and 50% state of charge, at a cell current of 40.8 A, the electrical conversion efficiency between electricity and fuel is 41% in fuel cell mode, and 82 % in electrolysis mode. The electrical storage or cycle efficiency over a RSOFC cycle is determined by discharging the system by running it in fuel cell mode, and then recharging it the original state of charge by running it in electrolysis mode. The total amount of electricity generated in fuel cell mode is divided by the electricity needed to recharge the system by electrolysis. An electrical storage efficiency of 42% for a cycle at 40.8 A per cell was obtained when the system was cycled from 95% state of charge, down to 5%, and back to 95%. There is excess heat in the system at the end of the cycle. This could be used directly in a combined heat and power (CHP) application if heat and power are needed. However, if heat is not needed, the electrical storage efficiency over a discharge-charge cycle can be maximised when the cell is run at lower currents, reaching 64.4% for a current of 20.4 A per cell. In this case, the starting and finishing temperatures of the system are almost identical, because the rate of heat production matches the rate of heat loss from the system. However, when the RSOFC model was run at an even lower current of 10.2 A, the electrical cycle efficiency was reduced to <40%, because the system cooled below its optimal operation temperature during electrolysis. This is because the total heat loss through the walls of the system was greater, because the cycle time was twice as long in this case. If the system insulation were improved, this effect would be mitigated.

The electrical cycle efficiency in the RSOFC system model of 64.4%, compares very favourably with reversible polymer electrolyte membrane fuel cells, which have a theoretical maximum electrical cycle efficiency close to 42%, because they do not use any of the heat generated by the fuel cell reaction, for electrolysis. They also have a large voltage step when switching between fuel cell and electrolysis modes, which is not the case for a RSOFC system, and they also require high noble metal catalyst loadings of e.g. 4 mg cm^{-3} of Pt, or Ir to achieve these levels of performance, metals which have a limited worldwide supply. However, the RSOFC system does not require noble metal catalysts. Furthermore, the RSOFC efficiency of 64.4% is not the theoretical maximum efficiency, and could be greatly improved by reducing the cell resistance, and reducing heat loss from the system. If the cell resistance was negligible, and the insulation was nearly perfect, cycle efficiency would approach 100%.

There is a range of values in the literature for the pre-exponential coefficient in the activation energy equations. This affects system performance and efficiency slightly, e.g. at 20.4 A per cell, electrical cycle efficiency is 64.4% when it is set to $7 \times 10^8 \text{ A m}^{-2}$, and 67.9% when it is set to $1 \times 10^9 \text{ A m}^{-2}$. Experimental validation of the model should confirm an appropriate value for the pre-exponential coefficient.

Power and control electronics developed at the University of Strathclyde were tested with the model under three different electrical power and control schemes, with different inverter designs. They caused different sizes of current and voltage ripples to be imposed onto the RSOFC stack at 20 Hz or 30 Hz. The smallest current ripple of 0.5% was seen in the first scenario. The second scenario had a current ripple of 8%, and the third scenario 69%. The capacitance observed in the cell from the oxygen electrode surface diffusion polarisation was found to be insignificant in smoothing these current and voltage ripples. In order to smooth these ripples, capacitors are being added to the DC bus of the electrical power and controls system. In this model, instantaneous heat transfer is assumed. In a real system, this would not be the case, and so sudden changes in current would be counterbalanced by the cell temperature rising and falling, which would limit the current changes by changing the cell resistance. Therefore, it is expected that in a real RSOFC system, the ripples would have a lower magnitude than that predicted by the model. A computational fluid dynamics model would give a more accurate reflection of the RSOFC system behaviour, by modelling heat transfer via radiation, convection and conduction, and mass flows through the system. Pressurised tests of RSOFC would also help to validate the model against real cell performance, in particular determining the activation losses, and any associated capacitance, and the effect of current and voltage ripples on cell performance.

A RSOFC system could be used to absorb electricity generated from an intermittent and unpredictable source, such as a wind turbine, or an intermittent and predictable source, such as tidal turbine, and convert it to a constant power output. Further development of the RSOFC system model, and power and controls could include simulating an intermittent power source and the fuel cell, using electrical hardware, and measuring their interactions. The design of the hardware fuel cell simulator would be informed by doing individual RSOFC tests with an intermittent power source, in order to measure the time constants of the RSOFC. Time constants in the millisecond range would be expected from the activation and diffusion processes in the cell. In the LSM-YSZ electrode measurements, time constants between 1 Hz - 80 Hz were measured for the surface diffusion polarisation, which corresponds to time constants between 12.5 ms, and 1 s. Time constants in the range of tens of seconds are expected for temperature equilibration, but could not be measured in this work, because the RSOFC tested had leaky seals. Therefore, I/V curves, and the transient behaviour of the RSOFC, could not be measured. A stack of RSOFC could be built, after the sealing problem is solved, to experimentally validate the model predictions of RSOFC performance. This would also allow the investigation of the engineering challenges involved in linking the RSOFC together, e.g. the elimination of hotspots on the interconnecting wires caused by high current flow. It would also show what balance of plant was necessary to run a RSOFC system - e.g. an oxygen balancing mechanism.

To conclude, RSOFC with porous and stable microstructure have been made with a nearly 100% dense YSZ electrolyte, and the effect of pressurisation has been determined for the LSM-YSZ oxygen electrode. The RSOFC system model shows the performance benefits of pressurisation, and the electrical energy storage efficiency of 64.4%. This could be improved by optimising the cell design to reduce ohmic losses, increasing the system

insulation, or by utilising waste heat from the system. Therefore, more research would allow further improvement of the RSOFC system performance, but it already has potential to buffer intermittent sources of electricity, by storing electrical energy efficiently.

Chapter 10

Future work

10.1 Oxygen electrode symmetrical cells

In order to further investigate the pressure dependence of the area specific polarisation resistance for LSM-YSZ symmetrical cells, higher pressures of oxygen could also be investigated. This would confirm the trend seen in this work, beyond 3 bar absolute pressure for oxygen, and would provide useful data for the RSOFC model. Pressures up to nearly 100 bar were previously investigated for a slightly different symmetrical cell system [7].

In order to examine the effect of electrode activation by current, on the LSM in the LSM-YSZ electrode, 3-electrode cells under current load could be used to quantify the relationship between current density, oxygen partial pressure, and area specific polarisation resistance at a variety of different temperatures and activation times. The degradation due to delamination of the LSM-YSZ electrode during electrolysis, as oxygen is formed at the tripe phase boundary interface, could also be studied by ac impedance.

10.2 Extrusion

The extruded tubes made during this work were quite short - between 5 cm - 10 cm in length. This meant that the sealing of the cell had to be carried out at a high temperature, which was problematic. In order to successfully test cells, longer tubes could be extruded, that could be sealed further away from the hot zone of the furnace. This would allow different sealing materials to be used, such as high temperature silicone sealant.

The wall thickness of the extruded tubes was seen to vary around the bore of the tube. This problem was related to the poor capacity for adjustment of the extrusion die, in the mechanical screw extruder. It proved very difficult to finely adjust this to get an even wall thickness of tube, around the whole tube circumference. This problem also caused the tubes to curl: as there was less resistance to the flow of the extrusion melt on the side of the die that had a wider gap for the tube wall, the tube extruded faster on this side than the other, causing curling. Therefore, a new die assembly should be made, which would be capable of precision adjustment, to produce tubes with a more consistent wall thickness.

The LSM powder was coarsened, and a graphite pore former was used, to produce tubes with a ~ 55 vol.% wall thickness. However, this is not an optimised porosity. From

the modelling work, the ohmic losses in the support were much greater than the diffusion losses of oxygen through it, so there is scope for reducing the support porosity, to improve performance. Tubes with different levels of porosity should be made, by varying the LSM pre-coarsening temperature, and the vol.% of graphite pore former, to determine the effect of porosity on RSOFC performance.

It was noted that after extrusion, and cutting of the tubes to seal one end, that the scissors used to cut them left a rough mark on the tube surface. This had been observed to cause the electrolyte to have flaws and holes, allowing gas leakage during testing. Therefore, this surface roughness should be removed before sintering the LSM tubes, to improve the homogeneity of the LSM substrate surface. This could be accomplished by either partially melting the surface to make it smooth, or else abrading away the rough surface. This may improve the quality of the electrolyte layer on this part of the tube, and reduce gas crossover leakage during testing.

10.3 Brazing

The brazing carried out in this work was done in an air atmosphere, which caused extensive oxidation of the steel supports used. In order to avoid this, and produce a solid brazed joint with no voids, brazing in less oxidising atmospheres could be carried out. These could include: nitrogen atmospheres, vacuum brazing, and tungsten-inert gas welding. A collaboration with an industrial partner, perhaps from the electronics industry, may help to determine a suitable brazing method.

In this work, high pressure oxygen and hydrogen are used. These present greater challenges for brazed joints than ambient pressure. This is because oxygen and hydrogen both dissolve in silver, and can react together inside the brazed joint to form steam, which creates bubbles. If the pressure of the gases is higher, this process is likely to be accelerated. Therefore, dual atmosphere testing of the brazed joints under elevated pressure would be necessary to demonstrate their suitability for this application.

There are specially designed fuel cell steel alloys, such as Fecralloy, and Crofer-22-APU. These alloys have lower thermal expansion coefficients, so they are better matched than other steels, with the thermal expansion coefficients of the fuel cell materials. Therefore, if these alloys are available in tubular form, they could be tested with brazed joints to determine their suitability to be fuel cell interconnects, in an elevated pressure RSOFC.

10.4 Reversible SOFC preparation

The RSOFC currently made with the dense electrolyte use a commercial 3YSZ-C screen printing ink, which is manually painted onto them. However, this process is not very reproducible, as layers of different or insufficient thickness could be produced. Therefore, an automated system of applying the 3YSZ electrolyte could be investigated, such as dip-coating, or spraying. This would require the formulation of a suitable slurry, which would involve extensive trials, using a matrix of different parameters, such as solids loading,

binder system, dipping speed/spraying rate, drying times, sintering profiles, number of applied layers, etc.

The NiO-YSZ fuel electrode was also applied by dip-coating and painting. However, it has not been determined if the thickness achieved, 7 μm - 10 μm , provides adequate lateral conductivity for the RSOFC. Therefore, Van der Pauw 4-point measurements could be made on planar Ni-YSZ electrodes made on YSZ pellets, to measure the lateral electrical conductivity. This is especially important during electrolysis, when the presence of steam can raise the partial pressure of oxygen at the fuel electrode, which may oxidise the nickel, reducing its conductivity. Therefore, the conductivity of the nickel as a function of the mol.% of steam at the fuel electrode could be quantified.

The modelling work showed that biggest single category of losses in the model was the ohmic losses from the cell. Therefore, the cell could be redesigned, to reduce this. This could be accomplished by shortening the length of the current paths in the most resistive materials in the cell. Siemens-Westinghouse invented two different cell designs, which address this issue [34]. These could be adapted for the RSOFC.

The mechanical strength of the cells is also very important, because there may be a pressure differential across the YSZ electrolyte. This arises during RSOFC operation, as oxygen is either consumed in fuel cell mode, or produced in electrolysis mode, changing the pressure on the oxygen side of the cell. Therefore, pressure burst tests should be carried out on the tubes, to determine the maximum pressure differential they can hold across the electrolyte, and also to check the consistency of cell strength. Tests could also be carried out to determine the tensile strength of the cells, e.g. 3-point bending flexural testing.

Cell sealing is another key issue; poor sealing of the cells to the gas delivery tubes prevented a successful test of the RSOFC. Therefore, the longer extruded tubes previously mentioned should be coated with electrolyte, and the fuel electrode. A high temperature silicone sealant should be used to seal the cells. Furthermore, other types of high temperature sealants, such as filled silicone sealants, which give less gas permeability, should also be tested.

10.5 Electrochemical testing of reversible SOFC

When a RSOFC has been produced, and successfully sealed to the support, I/V curves and impedance spectra should be recorded under a variety of conditions, e.g. different temperatures and pressures. This will provide important data which could be used to validate the RSOFC model. A systematic study of the effect on the impedance spectra of adjusting the gas compositions during testing, could be used to determine the rate-limiting steps in the reactions, and thus design a better cell. For instance, a test at 1 bar pure oxygen could be compared to a test in pressurised air, with a partial pressure of oxygen of 1 bar, to examine diffusion effects in the cell support. The effect of steam concentration on the cell performance should also be studied. Diffusion effects, and leakage effects, could also be examined, by comparing the effect of using stagnant or flowing gases in the cell.

Energy storage and release cycles, where the cell is cycled between fuel cell and electrolysis modes, would also be very helpful in determining the degradation that arises from

cycling. Degradation modes could include delamination, nickel coarsening, and void formation in the LSM-YSZ electrode. Tests that measure the amount of heat generated and absorbed by the cell, would also be useful to prove the concept of energy storage. This would have to be done by carefully measuring the heat, mass, and electrical energy balances, into and out of the cell, or a small stack of several cells.

10.6 Reversible SOFC computer model

The RSOFC model could be refined and improved, by removing some of the simplifying assumptions used in it. The biggest assumption, is that the system is isothermal, i.e. all areas of the cell, and all cells have an identical temperature and performance. No allowance is made for heat transfer, except heat loss through the walls of the system. Therefore, a computational fluid dynamics (CFD) model would greatly improve the accuracy of modelling. This is typically achieved, by calculating heat and mass flows into and out of the individual cells in a 3D mesh. This would also allow the examination of the intrinsic time constants of the system, due to the time taken for heat and the gases to diffuse through the system. It is expected that these time constants would act as a buffer to absorb some of the rapid changes in electrical supply and demand that might occur in a real-world electricity storage scenario.

One of the largest losses identified in the current RSOFC model is the ohmic or resistive losses from the electrical resistance of cell components. A CFD model would be very useful to determine which parts of the cell were causing the biggest losses, and could guide the design of a better cell - e.g. the parts of the cell that cause the greatest ohmic losses would heat up, and be clearly visible.

The modelling of the electrode microstructure, together with feedback from the cell testing, should show the cell fabrication process could be modified, so that its performance would be increased. Impedance measurements of the cell would also be used to determine the capacitances, and time constants associated with the activation energies of the fuel and oxygen electrodes, so that they could be added to the model. The pre-exponential coefficient in the activation energy equations was shown to be a critical factor in determining the RSOFC performance. Tests on RSOFC could determine this parameter, and this data could be added to the model, to validate the values chosen.

A further way in which the model could be improved is by testing of the phase change material, which will not have a sharp melting point, as assumed in this model, but rather a melting range. The behaviour of this material when cycled many times should be examined, to see how reversible it is, and the melting range determined. This data could be added to the model. The mechanism of heat transfer into and out of the phase change heat store should also be modelled.

In the model cycle simulations shown in this work, a constant current was used. A study of how the electrical storage efficiency is affected by varying the current density in the cell during the cycle would probably show that the electrical storage efficiency could be increased if the cell current was allowed to vary during the cycle. It would also be beneficial to use some real-world data of renewable energy production, and real demand

data, to simulate the charge and discharge of the RSOFC system model. This would allow the suitability of the RSOFC system as an energy storage device, for the different types of electrical generation to be determined and compared. This might show that it was much more suited to one type than another.

Lastly, a practical system to balance the oxygen pressure against the fuel gas pressure would need to be designed, to prevent large pressure differentials building up across the cells during operation. This could either be a mechanical system, or else a chemical oxygen storage and release system.

Appendix A

List of publications

- [1] S. R. Gamble, *Mater. Sci. Technol.*, 2011, **27**, 10, 1485-1497 [article link](#)
- [2] J. Ren, S. Gamble, A. J. Roscoe, G. Burt in *Universities Power Engineering Conference (UPEC), 2009, Proceedings of the 44th International*, Glasgow, 1–5 [pdf download link](#)
- [3] J. Ren, A. J. Roscoe, S. Gamble, G. M. Burt in *Power Electronics, Machines and Drives (PEMD)*, Brighton, 2010 [article link](#)
- [4] S. R. Gamble, J. T. S. Irvine, *Solid State Ionics*, 2011, **192**, 394–397 [article link](#)

Appendix B

Equation fits and semi-empirical equations

B.1 Data from chapter 3

B.1.1 Temperature calibration for pellet symmetrical cell measurements

Fig. B.1.1 shows YSZ resistivity data from impedance data obtained from a YSZ pellet, with platinum electrodes. Impedance spectra were recorded at four different temperatures in air.

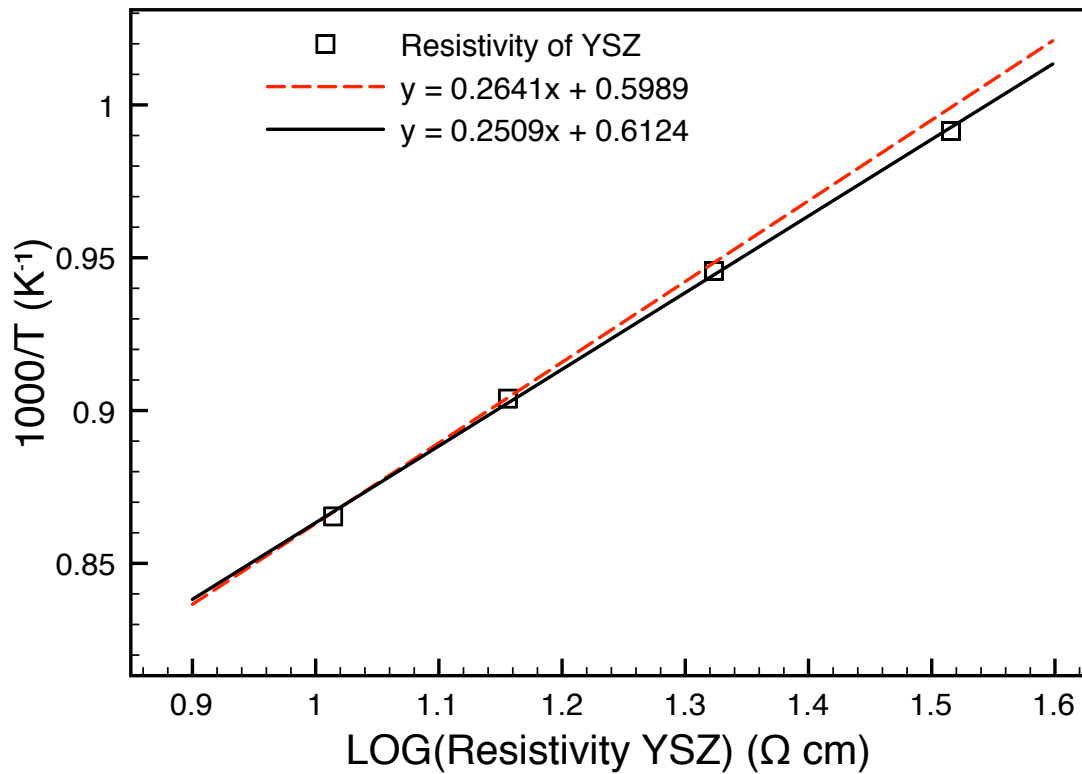


Figure B.1.1: A plot of LOG(YSZ resistivity) against 1000/T, from a fitting of impedance data from a YSZ pellet, and two fits. The black trend line fits the data points shown. The red dashed trend line fits data points that were accidentally lost.

They were then analysed, and the resistivity values obtained from the low-frequency a-axis intercept of the impedance spectra were plotted, and a trend line was fitted to them using Microsoft Excel. An equation of the trend line was recorded, and used to correct the testing temperature of the symmetrical cell tests as is described in subsection 2.3.2. However, the analysis of impedance data was in a file that was accidentally deleted. Therefore, only the trend line equation was preserved, which is the red dashed trend line in fig. B.1.1. However, the impedance data was analysed again, and the resistivity data points obtained are plotted in fig. B.1.1 as the black squares. A new trend line shown in black on the figure, was fitted to these data points, and a second line equation was determined. It is very similar to the first: it predicts temperature values that are less than 0.5 °C from the original trend line across the temperature range shown in the graph.

B.1.2 Example of equivalent circuit modelling fit

Fig. B.1.2 shows an example of the type of fit achieved with the program Zview v.2.8, by modelling the impedance data obtained on tape-cast symmetrical cells, according to an equivalent circuit model. It can be seen that the model fits the measured impedance curves very well.

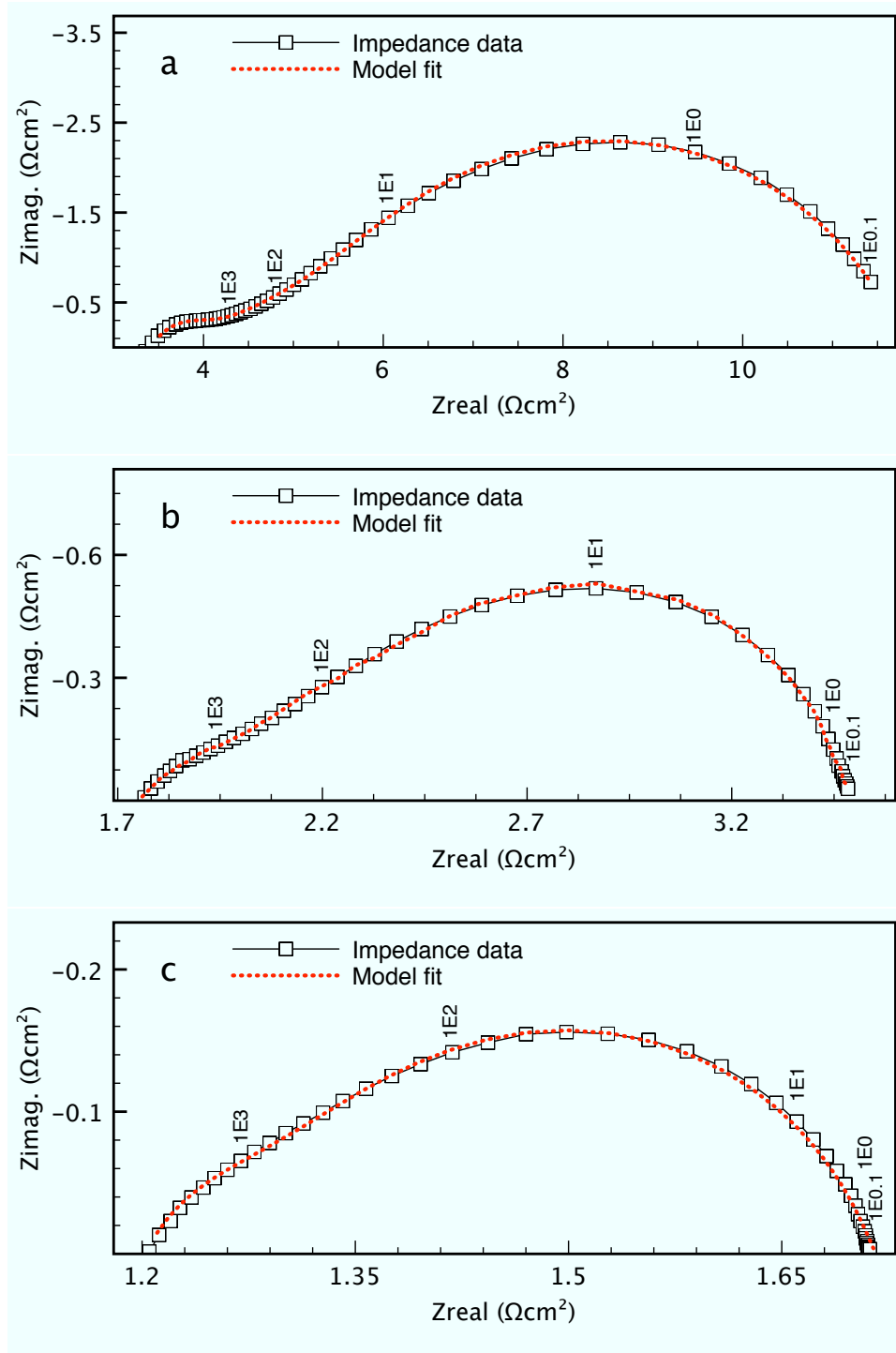


Figure B.1.2: Equivalent circuit model fits of impedance data gathered on symmetrical tape cast cells from fig. 3.1.2.

B.2 Data from chapter 8

B.2.1 Semi-empirical equations: resistivity and surface diffusion losses in the RSOFC

Data for $V_{standard}$

The semi-empirical equations for $V_{standard}$ in fuel cell mode and electrolysis equations, were derived by plotting values of $V_{standard}$, calculated from thermodynamic data, and fitting a linear trend line to them using Microsoft Excel. This is shown in fig. B.2.1 for the fuel cell mode. The same procedure is used for electrolysis mode. The equation of the line of best fit is used to predict $V_{standard}$ at various temperatures, giving eqs. 2.5.3 and 2.5.5.

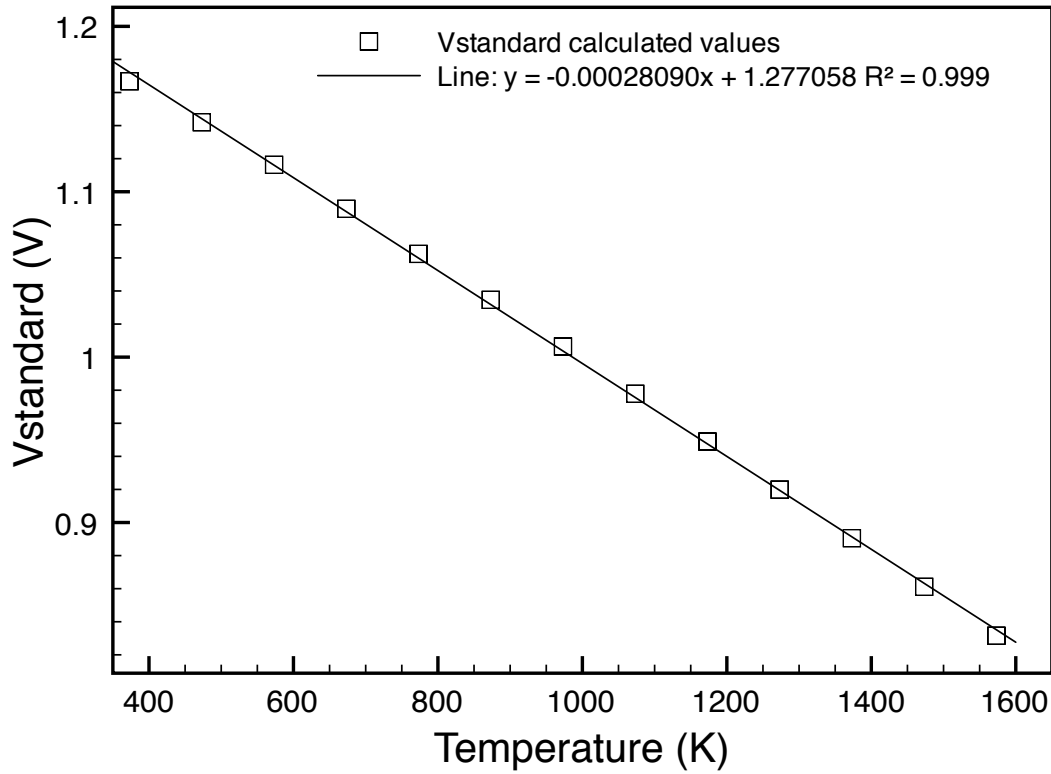


Figure B.2.1: $V_{standard}$ for fuel cell mode, plotted with a linear best fit line, and the equation obtained from it.

Data for LSC support material resistivity

Fig. B.2.2 shows a plot of the resistivity of LSC at three temperatures, which was calculated from conductivity values [1]. A linear best fit line created with Microsoft Excel is also shown. LSC is a perovskite ceramic used as the RSOFC support in the computer model. From this, eq. 2.5.6 was calculated.

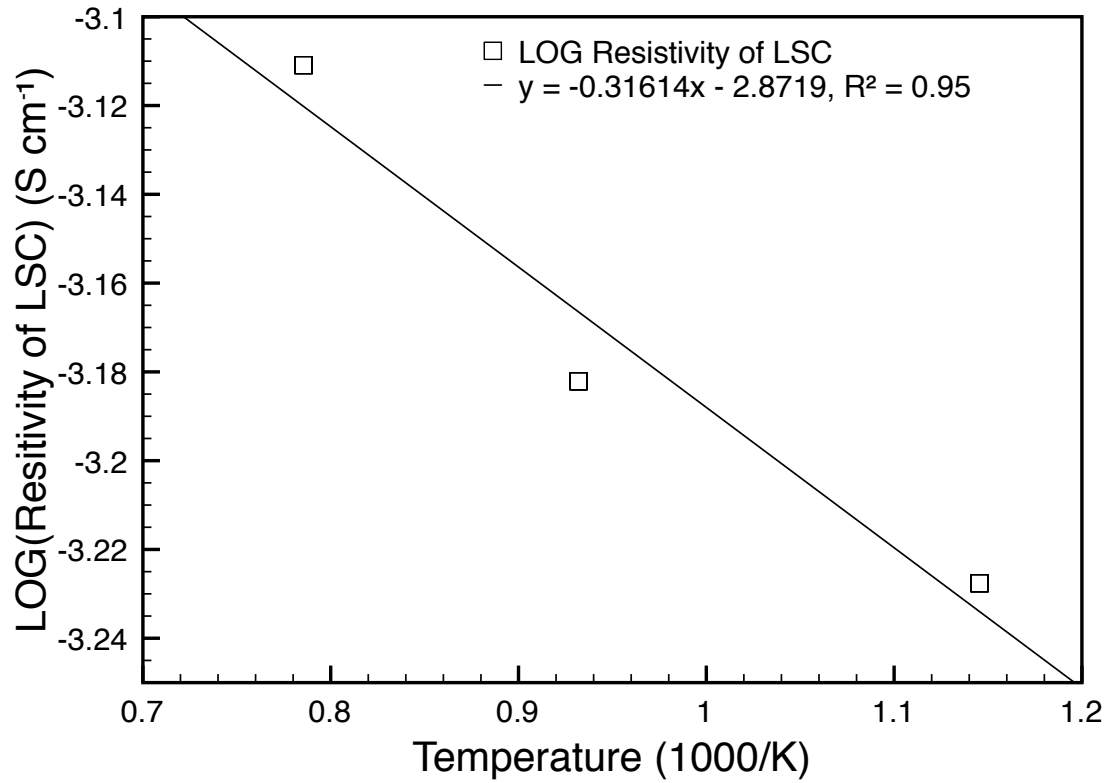


Figure B.2.2: LOG(resistivity) of LSC ($\text{La}_{0.8}\text{Sr}_{0.2}\text{CoO}_{3-\delta}$), used as a support for the RSOFC in the computer model

Data for resistivity of the YSZ electrolyte

Fig. B.2.3 shows a plot of the resistivity of 8YSZ at four temperatures, calculated from conductivity values [2]. A linear fit to the data was performed in Microsoft Excel, and is shown to correlate very closely with the data. From this equation, eq. 2.5.7 was calculated, to predict the YSZ electrolyte resistivity at different temperatures in the RSOFC model.

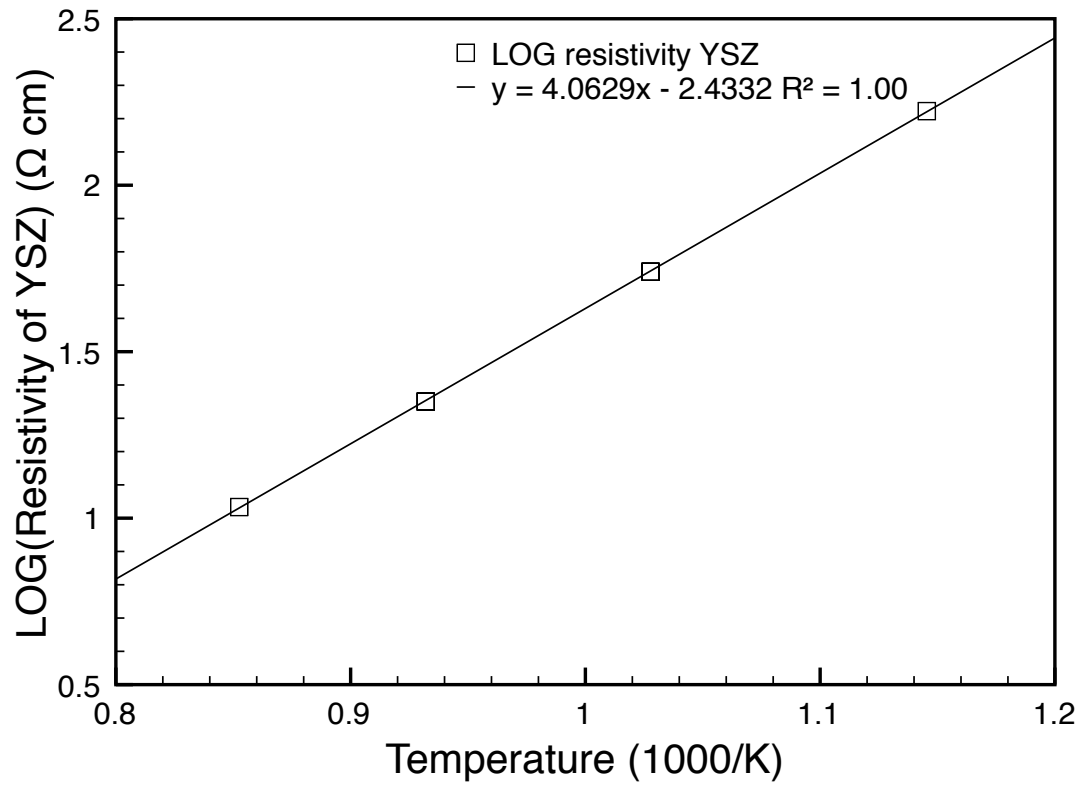


Figure B.2.3: LOG(resistivity) of 8YSZ used as a electrolyte for the RSOFC in the computer model

Data for the resistivity of the nickel interconnect and cell connection

Fig. B.2.4 shows a plot of the resistivity of nickel at six temperatures, calculated from conductivity values [3]. A linear fit to the data was performed in Microsoft Excel, and is shown to correlate very closely with the data. From this equation, eq. 2.5.8 was calculated, to predict the nickel interconnect resistivity at different temperatures in the RSOFC model.

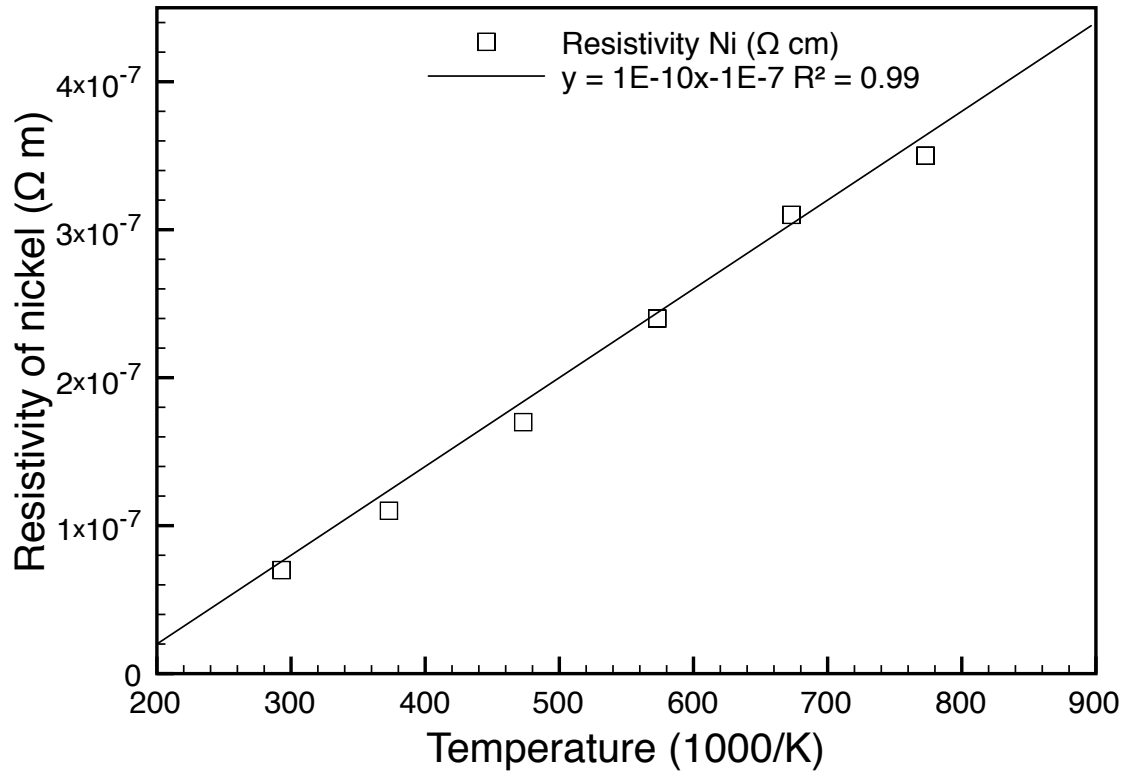


Figure B.2.4: Resistivity of nickel used as an interconnect and cell connection for the RSOFC in the computer model.

Data for the surface diffusion polarisation $R_{diff,surface}$

Symmetrical cell ac impedance measurements were carried out and analysed as described in section 2.3.2. The results showed that the dominant process was a surface diffusion process, rather than mass transport of oxygen gas through the electrode microstructure. The values of surface diffusion polarisation, called $R_{diff,surface}$ was plotted as a function of temperature and pressure, using the software program Mathematica (Wolfram), as the red dots in fig. B.2.5.

$$R_{diff,surface} = 2.45311 \times 10^{-5} \exp\left(\frac{8853.38}{T}\right) P^{-0.532568} \quad (B.2.1)$$

Equation B.2.1, which describes a 3D surface which fits the points, is also shown in the figure.

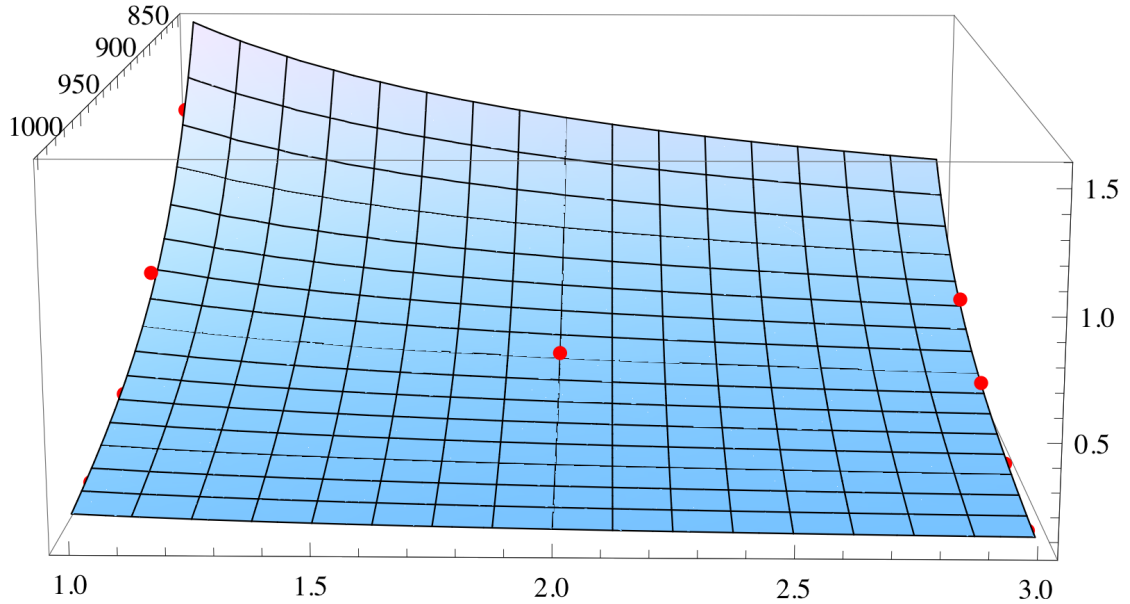


Figure B.2.5: Data of $R_{diff,surface}$ (red points) with 3D surface plot fit using Mathematica. Some points cannot be seen as they are below the surface plot fit.

A graph of the frequency of the point at the maximum negative imaginary impedance f_{max} was also plotted with Mathematica in fig. B.2.6, and a 3D surface fit was made to the data, giving equation B.2.2

$$f_{max} = 1.5809 \times 10^{10} \exp\left(\frac{-1.98253 \times 10^4}{T}\right) P^{0.807662} \quad (B.2.2)$$

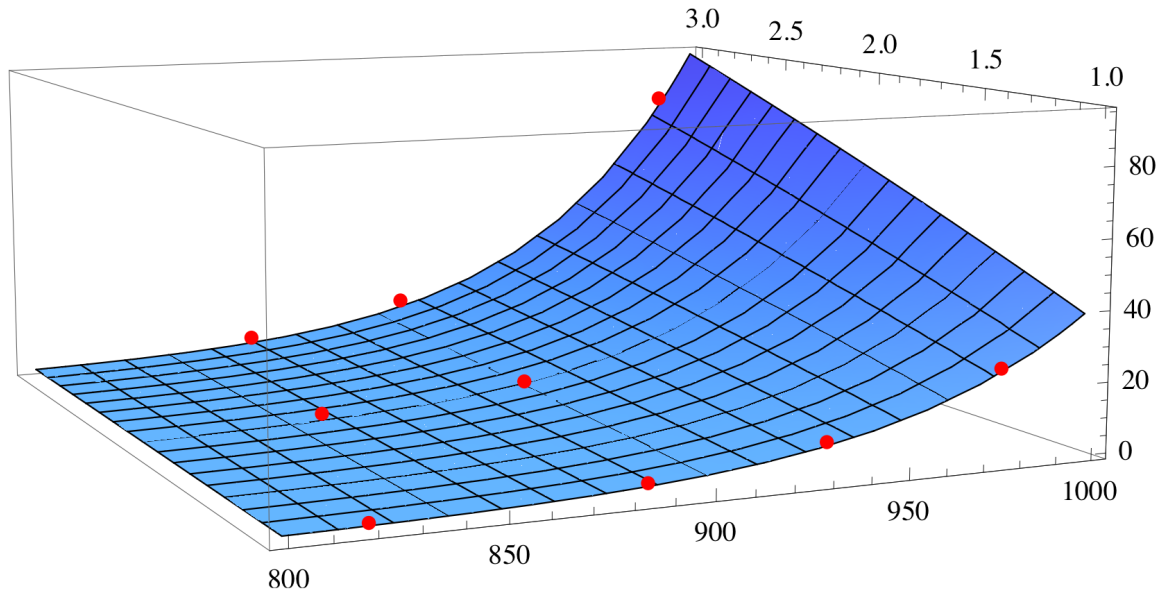


Figure B.2.6: Data of f_{max} for impedance arcs (red points) with 3D surface plot fit using Mathematica. Some points cannot be seen as they are below the surface plot fit.

B.2.2 Semi-empirical equations: thermodynamics, heat production/consumption, and heat capacity

Modelling heat production/consumption: hydrogen oxidation reaction

Fig. B.2.7 shows the data calculated from values found in the NIST database [4] and the HSC thermodynamics software, for the enthalpy, entropy, and free energy of reaction, for the reaction in eq. B.2.3, at a pressure of 70 bar.



These data are plotted as a function of temperature, and then Microsoft Excel is used to create a best-fit line, which correlates closely with the data. Equations 2.5.13, 2.5.14, and 2.5.15 were produced, which model the magnitude of the enthalpy, entropy, and free energy change for the fuel cell and electrolysis reactions.

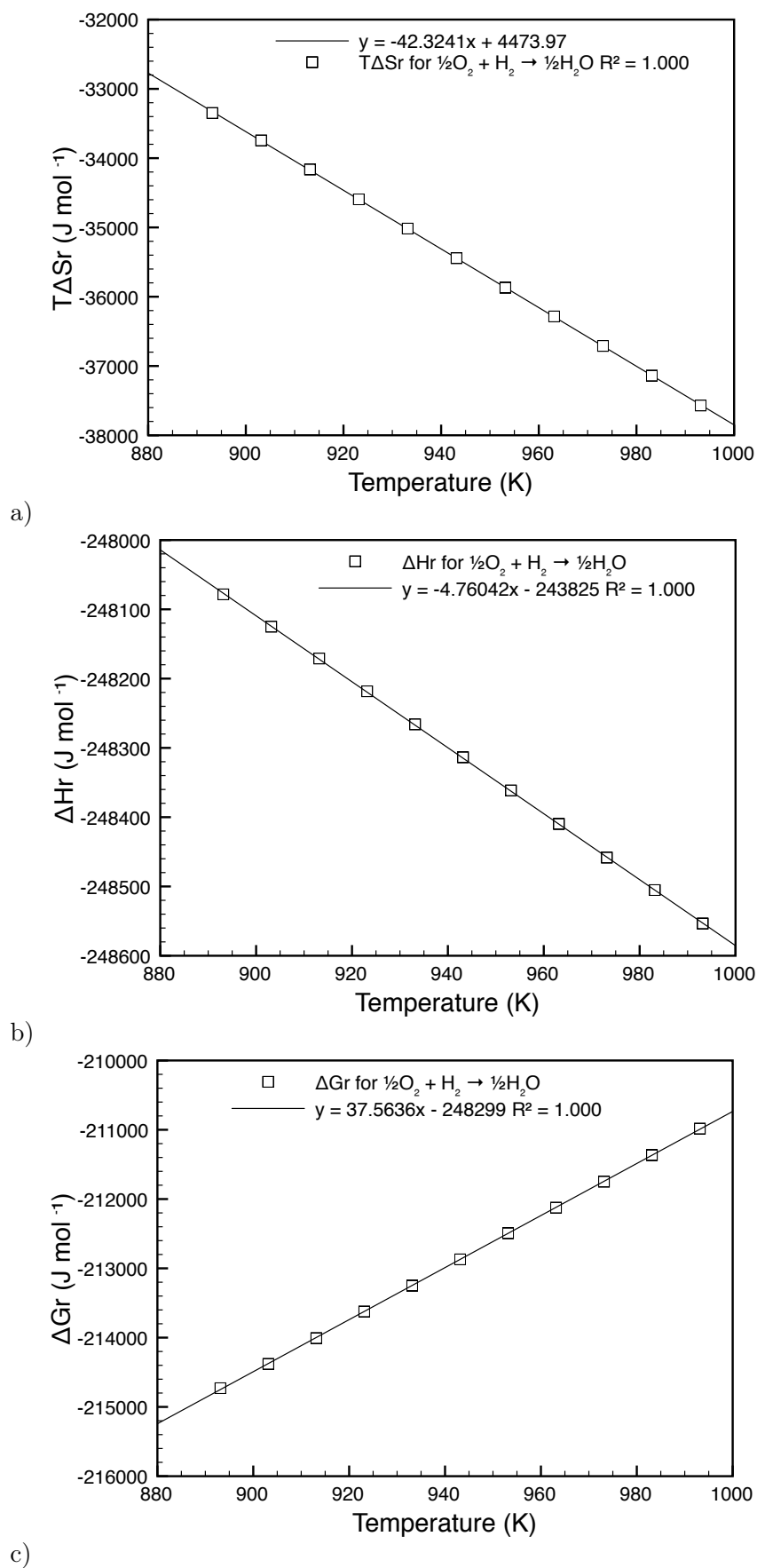


Figure B.2.7: Thermodynamics of the fuel cell reaction. Data for the reaction entropy ($T\Delta S_r$), enthalpy (ΔH_r) and Gibbs free energy ΔG_r are shown, together with linear fits using Microsoft Excel.

Heat loss from vessel walls

The heat loss from the vessel walls, in the modelled RSOFC system was calculated, based on values of thermal conductivity taken from a datasheet provided by the manufacturer of the wall insulation [5]. The thermal conductivity of the insulation is plotted in fig. B.2.8. The data was fitted to a quadratic function, also shown in the figure, using Microsoft Excel 2003, giving eq. 2.5.16.

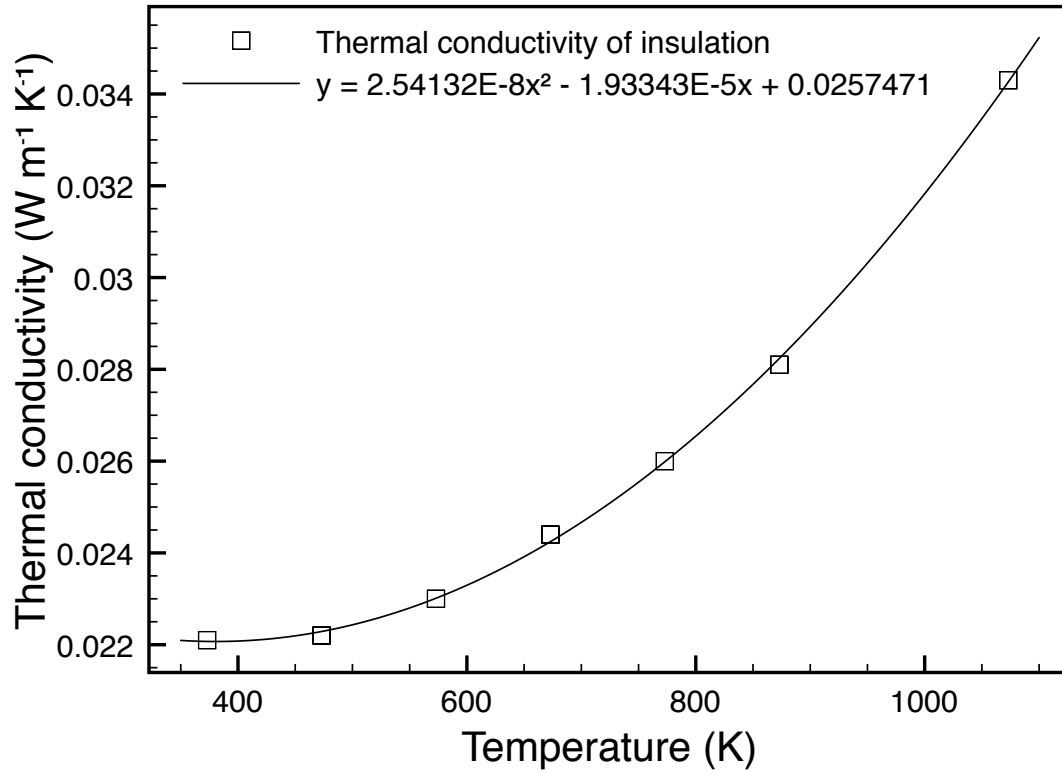


Figure B.2.8: Thermal conductivity of Microtherm microporous insulation as a function of temperature, and line of best fit.

An online calculator on the Microtherm website was used to calculate cold face temperatures for the insulation [6], and these were plotted in fig. B.2.9, and a linear fit line was fitted to them, giving eq. 2.5.17.

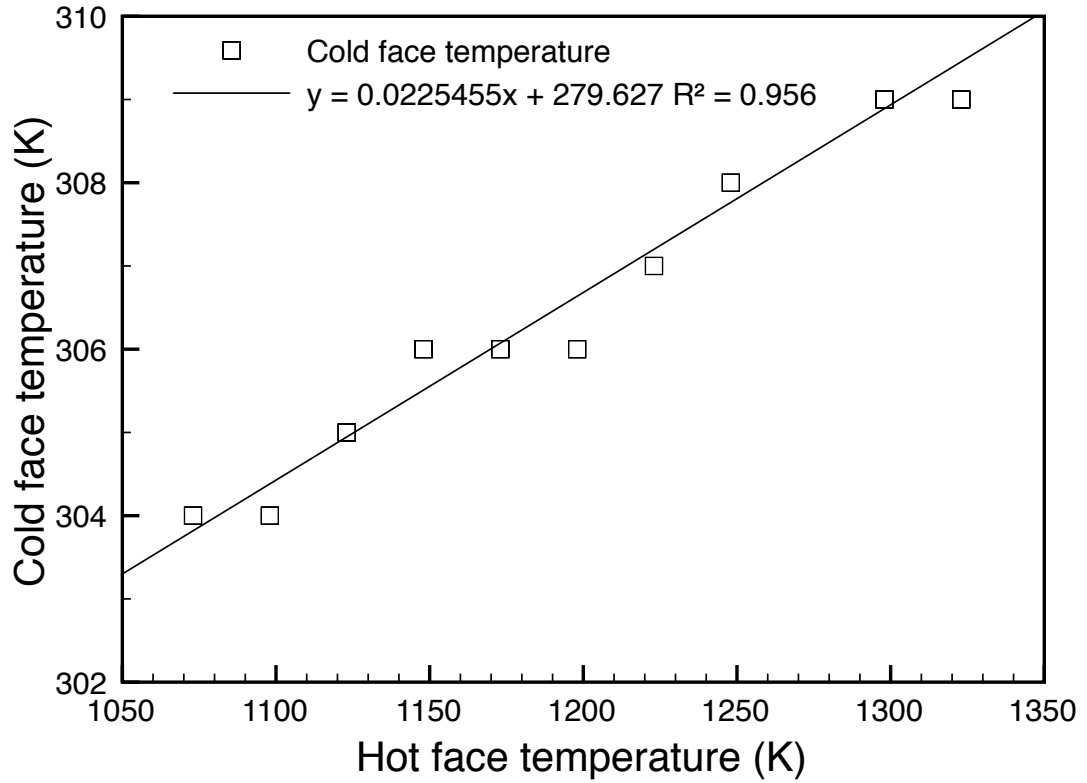
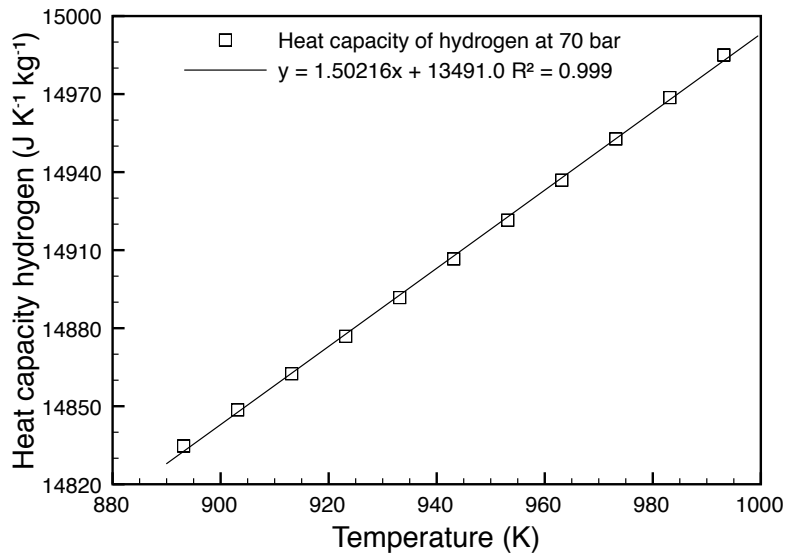


Figure B.2.9: Cold face temperatures of Microtherm insulation, with line of best fit.

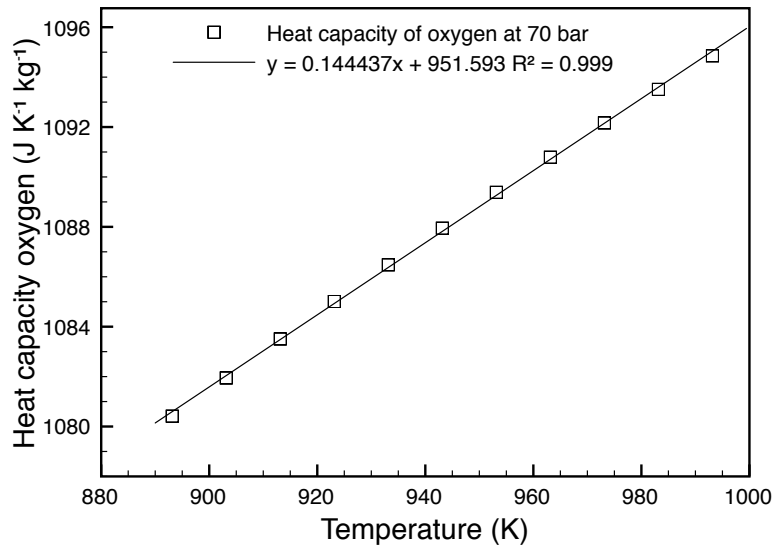
These equations were used to produce eq. 2.5.18, which predicts heat loss from the RSOFC modelled system through the insulated walls.

Heat capacities of system components

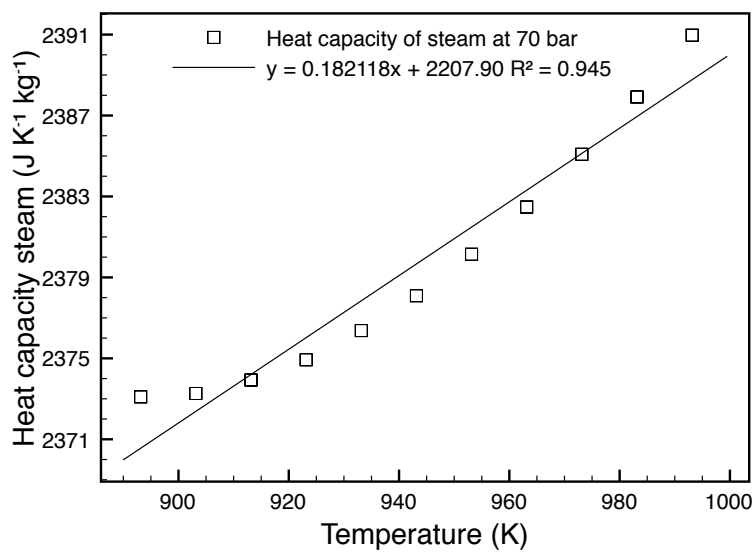
Fig. B.2.10 shows plots of the heat capacities of steam, hydrogen, and oxygen, calculated from data obtained from the NIST database 69 [4]. Linear fits were made to the plots using the software OpenOffice 3.30, and these are shown with the data. Equations 2.5.19, 2.5.20 and 2.5.21 were then obtained from the fits.



a)



b)



c)

Figure B.2.10: Heat capacities of system gases at 70 bar, as a function of temperature.

The heat capacity of the bronze phase change heat store was calculated, by assuming that it is equivalent to the heat capacity of copper, as the bronze is >90% copper. Data on the heat capacity of copper between 610 °C and 1084 °C was plotted in fig. B.2.11, and a linear approximation was fitted to it, to model the heat capacity, producing eq. 2.5.22.

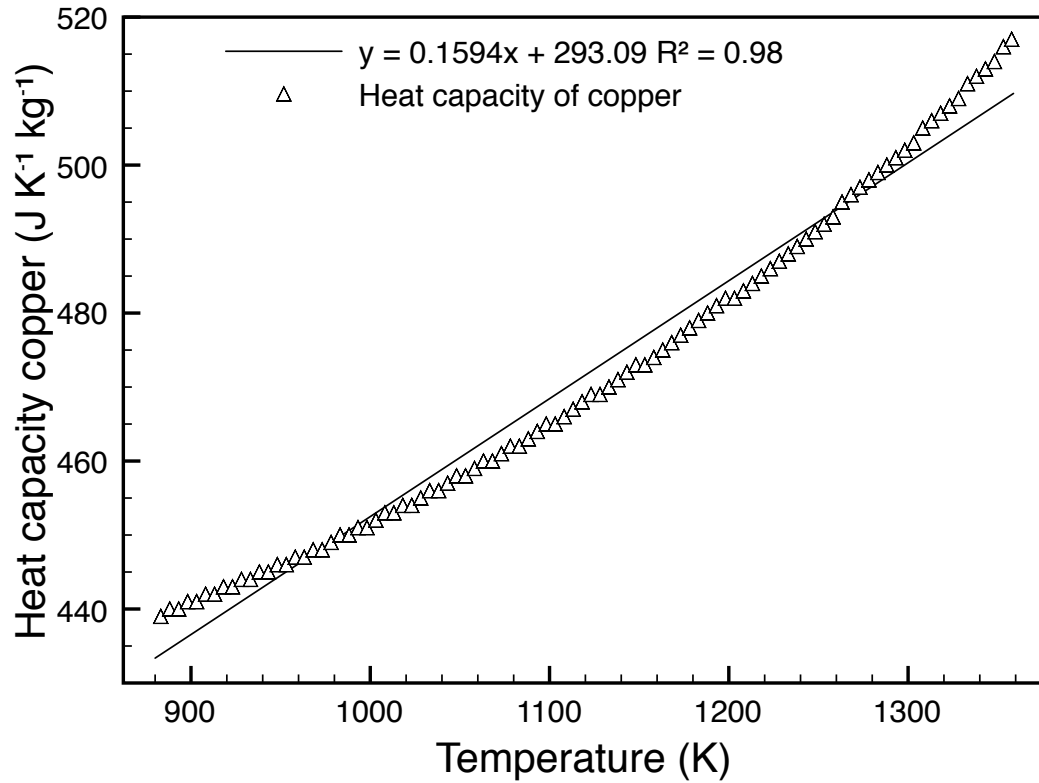


Figure B.2.11: Heat capacity of copper metal, as a function of temperature.

Bibliography

- [1] A. Petric, P. Huang, F. Tietz, *Solid State Ionics*, 2000, **135**, 719–725, 12th International Conference on Solid State Ionics, Halkidiki, Greece, Jun 06-12, 1999.
- [2] J. Van herle, R. V. Cavieres, D. Akyuz, K. Barthel, *J. Eur. Ceram. Soc.*, 2001, **21**, 1851–1854.
- [3] Isabellenhuetten, *Super Pure Nickel*, Tech. Rep., Isabellenhutte Heusler GmbH I& Co. KG, www.isabellenhuetten.de, 2009.
- [4] NIST, *NIST Chemistry WebBook*, last accessed 01/08/2011. <http://webbook.nist.gov/chemistry/>.
- [5] Microtherm, *Microtherm Standard Panel*, Datasheet from <http://www.microtherm.uk.com/>, Microtherm, België, Industriepark Noord 1, BE-9100 Sint-Niklaas, 2011.
- [6] Microtherm nv, *Thermal calculator*, last accessed 25/08/2011. <http://www.microtherm.uk.com/high/EXEN/site/calculator.aspx>.